



Grant Agreement No.: 226479

SafeLand

Living with landslide risk in Europe: Assessment, effects of global change, and risk management strategies

7th Framework Programme
Cooperation Theme 6 Environment (including climate change)
Sub-Activity 6.1.3 Natural Hazards

Deliverable D4.6

REPORT ON EVALUATION OF MASS MOVEMENT INDICATORS

Work Package 4.3 – Evaluation and development of reliable procedures and technologies for early warning

Deliverable/Work Package Leader: GSA/GSA

Revision: 1

April 17, 2012

Rev.	Deliverable Responsible	Controlled by	Date
0	GSA	GeoZS, ICG	29 th March 2012
1	GSA		
2	GSA		

SUMMARY

The document “Report on Evaluation of Mass Movement Indicators” focuses on physical parameters which could be monitored in relation to landslide triggering processes, and which could potentially be used as early warning parameters of slope instabilities.

The first part of the report reviews potentially available monitoring parameters, including basic definitions, units, typical values, and formulas. Not only the well-established parameters are included, but also those with a potential for a future application as early warning parameters.

The second part presents and summarizes results from the SafeLand test sites. The analysis of each of the monitored parameters is described with a focus on investigating the correlation between each of the parameters. An additional goal was to define their critical values (alerts/thresholds) in relation to the triggering of mass movements and to evaluate their role as an early warning parameter on the background of their geological settings.

Note about contributors

The following organisations contributed to the work described in this deliverable:

Lead partner responsible for the deliverable:

Geological Survey of Austria (GSA)

Deliverable prepared by:

Ivo Baroň, Robert Supper & David Ottowitz

Partner responsible for quality control:

International Centre for Geohazards & Geological Survey of Slovenia

Deliverable reviewed by:

Jure Atanackov, Gunilla Kaiser, Matthew J Lato, Dušan Rajver, Michael Roth

English corrections by:

Matthew J Lato

Individual contributors:

Åknes /Tafjord Beredskap: *L.H. Blikra & L. Kristensen*

AMRA: *E. Damiano & L. Picarelli*

Ancona EW Centre: *S. Cardellini*

Geological Survey of Austria (GSA): *I. Baroň, A. Ita, B. Jochum, S. Kauer, J.H. Kim, D. Ottowitz, S. Pfeiler, A. Römer, R. Supper, F. Vecchiotti & A. Zöchbauer*

Geological Survey of Slovenia (GeoZS): *Š. Kumelj & M. Čarman*

International Centre for Geohazards (ICG): *H. Heyerdahl, A. Lam & M. Roth*

International Institute for Geo-information Sciences and Earth Observation (ITC): *A. Stumpf*

Centre National de la Recherche Scientifique (CNRS): *C. Bertrand, TA. Bogaard, J. Gance, J-P. Malet, O. Maquaire, V. Marc, A. Stumpf, A. Tonnellier, J. Travelletti & P. Ulrich*

Centro Servizi di Geingegneria S.r.l. (CSG): *E. Garbarino, A. Gozzi & M. Lovisolo*

Università di Salerno (UNISA): *L. Cascini, D. Peduto & G. Sorbino*

Università degli Studi di Milano-Bicocca (UNIMIB): *F. Agliardi, G.B. Crosta & R. Sosio*

Universitat Politècnica de Catalunya (UPC): *J. Gili & J. Moya*

Université de Lausanne (UNIL): *C. Michoud, M.-H. Derron & M. Jaboyedoff*

Università degli Studi di Firenze (UNIFI): *S. Morelli, S. Segoni & V. Tofani*

Centro Euro-Mediterraneo per i Cambiamenti Climatici (CMCC): *P. Mercogliano*

ZT-Moser-Jaritz: *G. Moser*

CONTENTS

1	Introduction	7
2	Review of monitoring parameters	10
2.1	Slope movement/deformation/activity	11
2.1.1	Displacement	11
2.1.2	Strain	20
2.1.3	Mass loss/Increment balance for landslide EW	32
2.1.4	Macro-cracks and surface fissures	35
2.1.5	Micro seismicity/Acoustic emissions	42
2.1.6	Rockfall event frequency	49
2.2	Hydrologic properties	52
2.2.1	Groundwater level/Pore-water pressure	52
2.2.2	Soil suction	59
2.2.3	Soil humidity	64
2.2.4	Water balance: inflow and outflow, surface flow	69
2.2.5	Surface and subsurface water quality	73
2.3	Ground geophysical properties	88
2.3.1	Geoelectrical parameters	88
2.3.2	Seismic velocity	97
2.3.3	Passive electromagnetic emission	99
2.3.4	Proton magnetic resonance (PMR)	101
2.4	External triggers	105
2.4.1	Meteorological conditions	105
2.4.2	Seismicity/Earthquakes	109
2.4.3	Volcanic activity	112
2.4.4	Tides	118
3	General evaluation of monitoring parameters	120
4	Case histories – analysis of real monitoring data	124
4.1	Åknes (Norway)	127
4.1.1	General description of the test site	127
4.1.2	Design of the monitoring network	132
4.1.3	Analysis of monitoring data	138
4.1.4	End-user involvement and alarm chain	146
4.1.5	Summarized evaluation of parameters	147
4.2	Ampflwang – Hausruck (Austria)	150
4.2.1	General description of the test site	150
4.2.2	Design of the monitoring network	152
4.2.3	Analysis of monitoring data	153
4.2.4	End-user involvement and alarm chain	172
4.2.5	Summarized evaluation of parameters	172
4.3	Ancona (Italy)	173
4.3.1	General description of the test site	173
4.3.2	Design of the monitoring network	177
4.3.3	Analysis of monitoring data	180
4.3.4	Summarized evaluation of parameters	189

4.4	Bagnaschino (Italy)	191
4.4.1	General description of the test site	191
4.4.2	Design of the monitoring network	194
4.4.3	Analysis of monitoring data	195
4.4.4	End-user involvement and alarm chain	209
4.4.5	Summarized evaluation of parameters	210
4.5	Bindo-Cortanova Rockslide (Italy)	211
4.5.1	General description of the test site	211
4.5.2	Design of the monitoring network	213
4.5.3	Analysis of monitoring data	214
4.5.4	Summarized evaluation of parameters	224
4.6	Casella (Italy)	226
4.6.1	General description of the test site	226
4.6.2	Design of the monitoring network	229
4.6.3	Analysis of monitoring data	231
4.6.4	Role as EW parameter	233
4.6.5	End-user role	233
4.6.6	Summarized evaluation of parameters	233
4.7	Gschlifgraben (Austria)	234
4.7.1	General description of the test site	234
4.7.2	Design of the monitoring network	238
4.7.3	Analysis of monitoring data	240
4.7.4	Summarized evaluation of parameters	260
4.8	Jettan - Nordnes (Norway)	261
4.8.1	General description of the test site	261
4.8.2	Design of the monitoring network	265
4.8.3	Analysis of monitoring data	265
4.8.4	Summarized evaluation of parameters	268
4.8.5	Implications for hazard	268
4.9	Mannen (Norway)	271
4.9.1	General description of the test site	271
4.9.2	Design of the monitoring network	274
4.9.3	Analysis of monitoring data	275
4.9.4	End-user involvement and alarm chain	280
4.9.5	Summarized evaluation of parameters	282
4.10	Rosano (Italy)	284
4.10.1	General description of the test site	284
4.10.2	Design of the monitoring network	285
4.10.3	Role as parameter and EW	294
4.10.4	End-user role	294
4.10.5	Summarized evaluation of parameters	294
4.11	Ruinon Rockslide (Italy)	295
4.11.1	General description of the test site	295
4.11.2	Design of the monitoring network	299
4.11.3	Analysis of monitoring data	301
4.11.4	End-user involvement and alarm chain	312
4.11.5	Summarized evaluation of parameters	313
4.12	Sonnblick & Mölltaler Glacier (Austria)	315

4.12.1	General description of the test site	315
4.12.2	Design of the monitoring network	318
4.12.3	Analysis of monitoring data	320
4.12.4	Summarized evaluation of parameters	323
4.13	Super-Sauze (France).....	325
4.13.1	General description of the test site	325
4.13.2	Design of the monitoring network	329
4.13.3	Analysis of monitoring data	333
4.13.4	Summarized evaluation of parameters	349
4.14	Vallcebre (Spain)	351
4.14.1	General description of the test site	351
4.14.2	Design of the monitoring network	352
4.14.3	Analysis of monitoring data	353
4.14.4	Summarized evaluation of parameters	354
4.14.5	End-user involvement and alarm chain.....	355
4.15	Villerville (France).....	357
4.15.1	General description of the test site	357
4.15.2	Design of the monitoring network	359
4.15.3	Analysis of monitoring data	362
4.15.4	Summarized evaluation of parameters	370
5	Discussion.....	372
6	Conclusions	382

1 INTRODUCTION

As stated by the *International Strategy for Disaster Reduction Platform for the Promotion of Early Warning (ISDR)*, the effective early warning (EW) system is comprised of four main elements, including *Risk knowledge*, *Monitoring and warning service*, *Dissemination and communication*, and *Response capability*. Failure in any one part can mean failure of the whole system (web of ISDR: <http://www.unisdr.org/2006/ppew/whats-ew/basics-ew.htm>). The essence of the monitoring element is to keep in mind the basic requirements of the successive EW systems, i.e.: “Are the most effective parameters being monitored?; Is there a sound scientific basis for making forecasts?; Can accurate and timely warnings be issued?” (Figure 1-1).

Risk knowledge	Monitoring and warning service	Dissemination and communication	Response capability
Systematically collect data and undertake risk assessments	Develop hazard monitoring and early warning services	Communicate risk information and early warnings	Build national and community response capabilities
Are the hazards and the vulnerabilities well known? What are the patterns and trends in these factors? Are risk maps and data widely available?	Are the right parameters being monitored? Is there a sound scientific basis for making forecasts? Can accurate and timely warnings be generated?	Do warnings reach all of those at risk? Are the risks and the warnings understood? Is the warning information clear and useable	Are response plans up to date and tested? Are local capacities and knowledge made use of? Are people prepared and ready to react to warnings?

Figure 1-1. The chart of the four elements of effective early warning systems (Source: web of ISDR)

The “Report on Evaluation of Mass Movement Indicators” will try to summarize the state of the art of the monitoring parameters and will present some examples from the SafeLand test sites, which represent prominent European landslides. The report is one of the final deliverables of the SafeLand project, Work Package 4.3 “Evaluation and development of reliable procedures and technologies for landslide early warning”. The aim of the report is to summarize the knowledge acquired from observing the controlling factors, triggers and other monitoring parameters of landslides gained by the SafeLand project, and to explore the role of the critical values of the monitored measures as early warning parameters. It is closely related to other SafeLand project reports (see Figure 1–2).

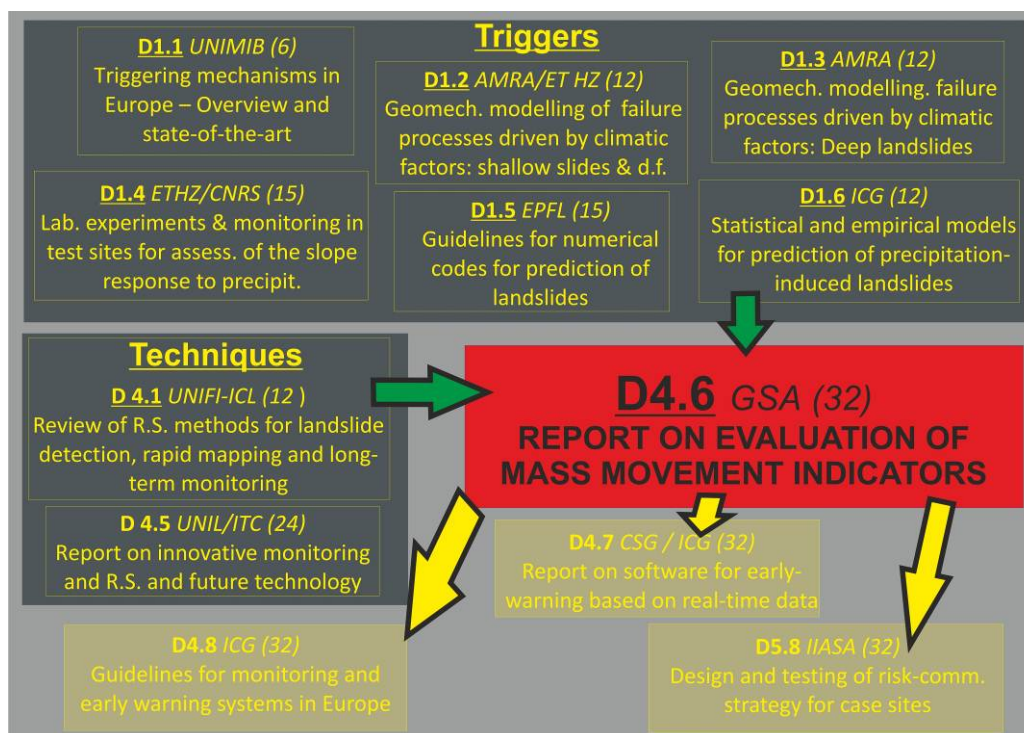


Figure 1-2. Thematic scheme, showing how deliverable D4.6 is related to other SafeLand project reports.

Originally, the report was entitled “Report on geo-indicator evaluation”. The term “geo-indicator” was, however, too broad. The “geoindicators”, as defined by Berger (1996), are measures of any geological processes and phenomena that can change significantly in less than 100 years. They can be used to describe both catastrophic changes (landslides) and those that are slower and more pervasive (soil and sediment erosion). Based on a general agreement by the research group, the title was changed in order to better fit the research aim.

For better clarity of the text, basic terms were defined, i.e.:

- **“Monitoring parameter”** as any phenomenon or factor related to slope (area of interest), which could be quantified and monitored in time;
- **“Mass-movement indicator”** as any monitoring parameter, which characterizes directly or indirectly the dynamic state of mass-movement processes;
- **“Early warning” (EW)** as a social process with a pre-defined set of steps and actions to warn authorities or the public and to prevent/eliminate the impact of any natural disaster;
- and finally, **“Early warning parameter”** (of landslides) as a mass-movement indicator allowing detection of an impending critical activation or acceleration of the landslide(s).

Key issues of any EW are the understanding of the behaviour of those monitoring parameters (which are simultaneously also mass-movement indicators), and especially the evaluation of their role as an early warning parameter by identifying their critical values/thresholds through advanced knowledge of their temporal evolution, correlation and coupling.

The EW parameters are, however, strongly site-specific. They usually depend on (1) the geometry and internal structure of the unstable mass, (2) the deformation pattern (surface and subsurface displacement), (3) the variation in the stress field, and (4) geomechanical and rheological characteristics of the materials.

The first part of the report is a review of monitoring parameters related to slope failure, such as:

- (i) ***Slope movement/deformation/activity parameters*** (displacement, velocity and acceleration, strain, mass loss/increment balance for landslide EW, macro-cracks and surface fissures, micro seismicity/acoustic emissions, rockfall event frequency);
- (ii) ***Hydrologic properties*** (ground water level/pore-water pressure, soil suction, soil humidity, water balance, surface and subsurface water quality);
- (iii) ***Ground geophysical properties*** (geoelectrical parameters, seismic velocity, passive electromagnetic emission, Proton Magnetic Resonance (PMR));
- (iv) ***External triggers*** (meteorological conditions, seismicity/earthquakes, volcanic activity, and tides).

The second part presents data and results from the SafeLand test sites obtained during the project. The analysis of each monitored parameter is described with respect to site-specific conditions and with a focus on investigating the correlation between each of the parameters. The goal was to find possible critical values (alerts/thresholds) and to evaluate their role as EW parameters on the background of their geological settings. The results are briefly summarized in the Discussion and Conclusions chapter.

2 REVIEW OF MONITORING PARAMETERS

This chapter provides a review of monitoring parameters which could be observed in relation to landslides and which also have potential to be applied as a landslide EW parameter. The challenging idea was to include not only the well-established parameters, but also those with a potential future application as indicators or EW parameters.

The chapters on individual parameters include basic definitions and formulas, units, typical values and background signals. Possible applications for landslide monitoring are identified. Each chapter includes illustrating figures and tables, and they are concluded by a list of essential references.

Parameters are grouped in the following chapters:

Slope movement/deformation/activity

- Displacement
- Strain
- Mass loss/Increment balance for landslide EW
- Macro-cracks and surface fissures
- Micro seismicity/Acoustic emissions
- Rockfall event frequency

Hydrologic properties

- Ground water level/Pore-water pressure
- Soil suction
- Soil humidity
- Water balance: inflow and outflow, surface flow
- Surface and subsurface water quality



Ground geophysical properties

- Geoelectrical parameters
- Seismic velocity
- Passive electromagnetic emission
- Proton Magnetic Resonance (PMR)

External triggers

- Meteorological conditions
- Seismicity/Earthquakes
- Volcanic activity
- Tides

2.1 SLOPE MOVEMENT/DEFORMATION/ACTIVITY

The first section describes parameters for **direct monitoring of the actual state of slope failure activity**. These parameters define the dynamic status of a mass movement, **which is suspended, dormant or already activated**. An important issue is the recognition of the reactivation phase, its quantification, the detection of thresholds approaching critical acceleration and, in the ideal case, forecasting the catastrophic phase in order to warn the society in advance. The described parameters comprise displacement, strain, mass loss/increment balance, cracking, micro seismicity/acoustic emissions, and rockfall event frequency.

2.1.1 DISPLACEMENT

Mario Lovisolo

Centro Servizi di Geingegneria S.r.l., Italy

Displacement is the main parameter of active landslides monitoring. The detection of displacements on the surface or in the subsurface is a clear indicator of the activity state of a phenomena. Continuous monitoring allows the possibility of detecting displacements in real-time and therefore of updating in the shortest possible time the conditions of the phenomena under investigation. By analyzing the displacements it is possible to classify the state of activity of active, suspended, quiescent or dormant, reactivated and suspended landslides.

In the case of suspended or quiescent landslides, the scope of monitoring is to detect, through analysis of displacements, the exact moment of reactivation (Figure 2.1.1-1) or to confirm the stability of the phenomena. As the quiescent state before a reactivation may last for years, long-term reliability and stability of instrumentation are essential for an early warning system to detect displacements in real-time.

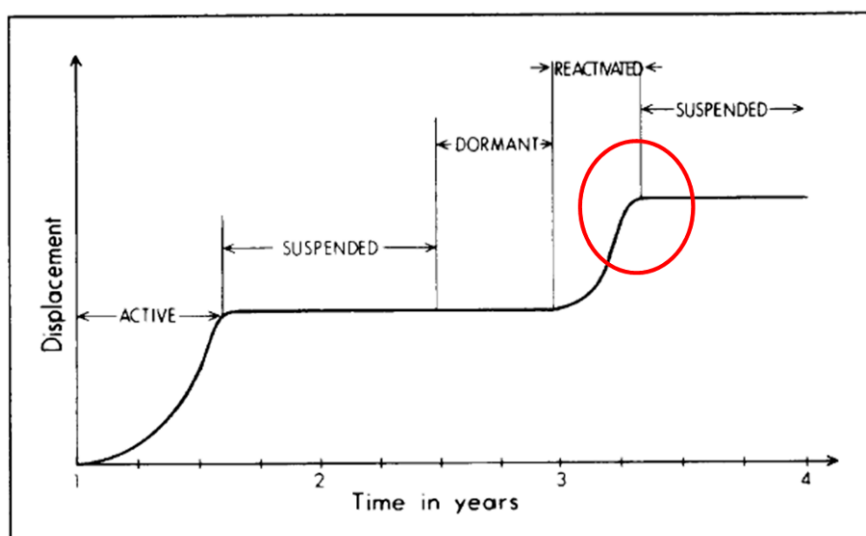


Figure 2.1.1-1. Activity state of landslides (After: Varnes 1996)

Surface and subsurface displacement

For the continuous monitoring of displacements several instruments are available. To detect surface displacements the most common are GPS, laser scanners and interferometers, while for subsurface monitoring the most common are probe and in-place inclinometers, wire and fixed borehole extensometers, and DMS columns.

Through analysis of displacements it is possible to detect the mechanical behaviour of a landslide and consequently to understand its kinematics. Landslides can have different mechanical behaviour according to their morphology and planar profile displacements, for example signal sliding phenomena, or on the contrary, viscous behaviour characterized flow phenomena. In soils with various structures the contemporary development of the two phenomena is possible (Figure 2.1.1-2). By the study of subsurface displacements it is possible to understand which phenomena are developing and their nature and direction. These elements are not detectable with surface monitoring alone because surface displacements can be considered an integral of subsurface displacements, where direction is the vector result of the singular displacements:

$$D_s = \sum_{i=1}^n D_u$$

Where: D_s = Surface Displacement D_u = Underground displacement n = strata

In this way, surface monitoring results alone are not suitable for a complete differential analysis of the active phenomena.

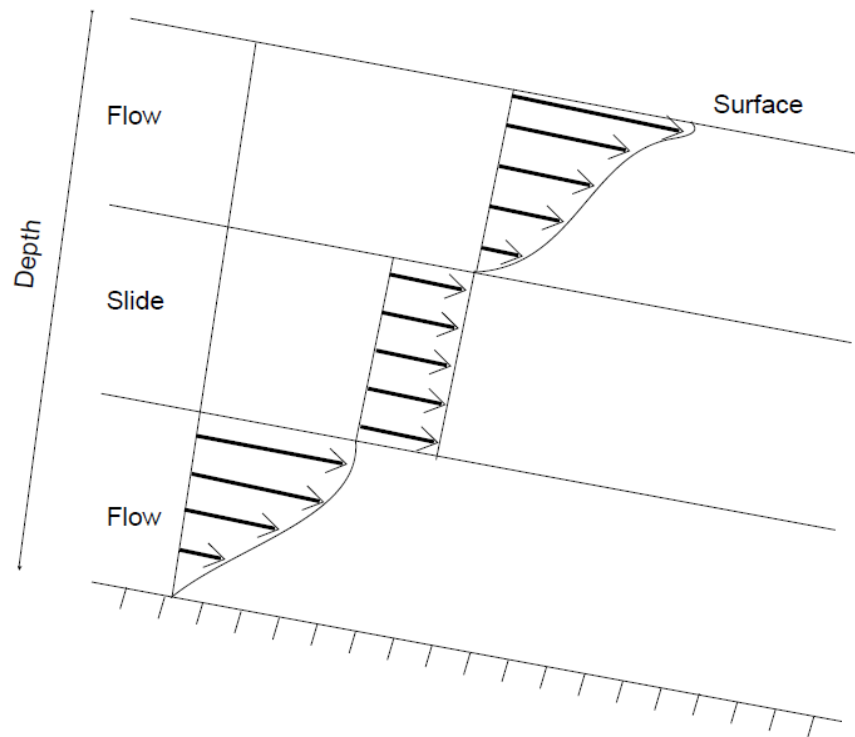


Figure 2.1.1-2. Sketch of different mechanical behaviours of a landslide body

To deeply understand the nature of the detected displacements it is necessary to continuously monitor the entire vertical extent of the landslide. The analysis can be realized through DMS continuous monitoring columns positioned to cover the whole landslide body. The columns are made of instrumented modules, and on each module it is possible to detect the displacements occurring in the soil in real-time, displaying their depth, intensity and direction. This instrument also gives a complete overview of micromovements, raising the monitoring system effectiveness and allowing a deep analysis of the phenomena before the paroxysmal phase.

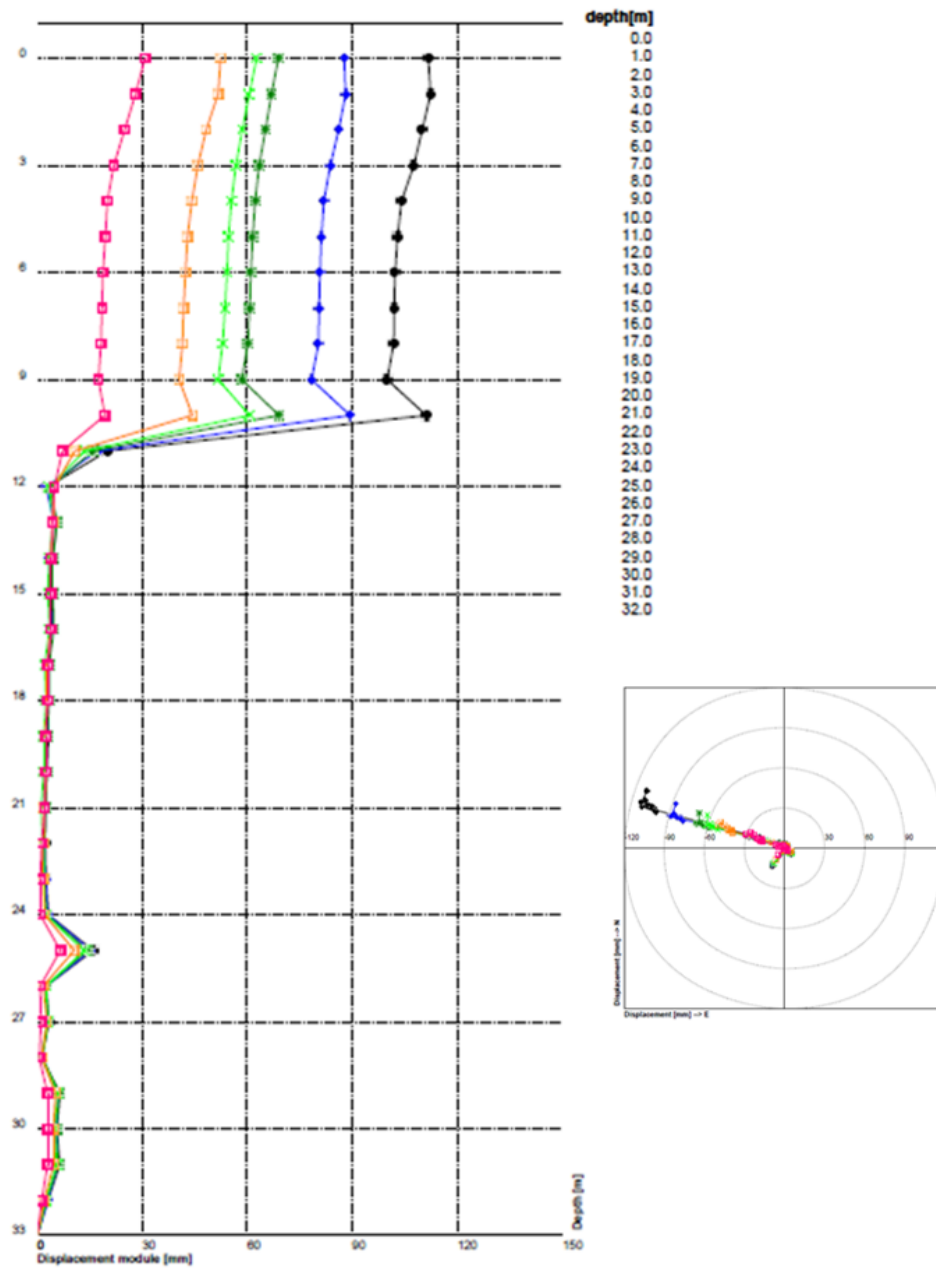


Figure 2.1.1-3. Displacement graph

Cumulative and differential displacement analysis

By means of specific software, displacement data measured in the vertical direction can be visualized both in differential and in cumulative ways. Displacement is calculated along the monitoring column by tilt measurements α (Figure 2.1.1-4).

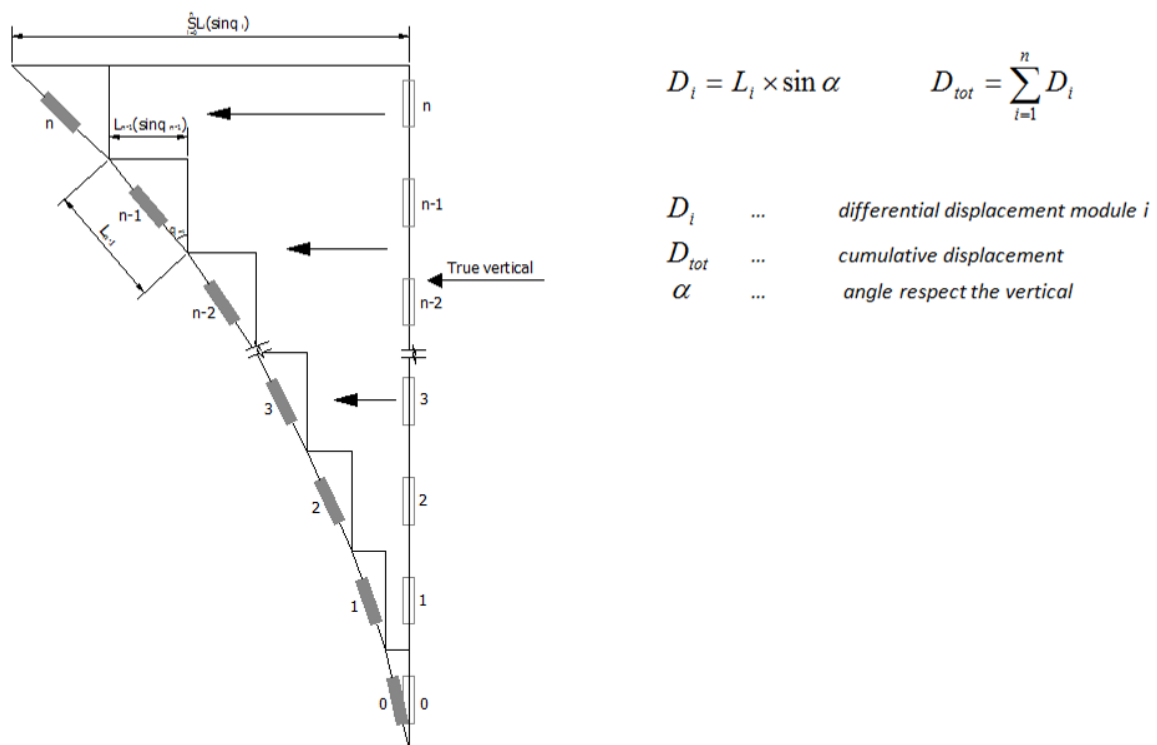


Figure 2.1.1-4. Cumulative and differential displacement

Cumulative displacement allows the amount of displacement occurring in the vertical direction to be visualized more clearly. Differential displacement allows for clear identification of sliding surfaces and the most deformed areas at different depths. Moreover, for early warning applications differential analysis allows new activation zones (which can be identified as outliers) to be visualized more easily.

Velocity and acceleration

Detection of velocity and acceleration of displacements during monitoring is crucial to optimizing warning and intervention times. Phenomena occur with different velocity as a function of their typology, and within the same typology velocity can vary. For instance, rockfalls are characterized by high velocities, as are debris flows. In contrast traditional landslides can be very slow or very fast in function of the morphologic characteristics in which the phenomena is developed.

Moreover acceleration of displacements is an effective indicator of the approach to the critical phase of detachment and consequently it is essential to keep it under close surveillance. Through historical and morphological analysis it is possible to calculate site-specific alarm thresholds and to foresee the approach to the detachment phase, in order to promptly implement mitigation and safety interventions. An example of the use of velocity to choose alarm thresholds is shown in “The Åknes rock slide: monitoring, threshold values and early-warning, Blikra, L.H. 2008” (Figures 2.1.2-5 and 2.1.2-6). Multi-level alarm thresholds are defined on the basis of velocity of displacements. In the case of values exceeding one

threshold, activities and responses shown in the table are to be implemented in function of the threshold exceeded.

Velocity	Alarm level	Activities and alarms	Response
0,1-0,5 mm/d	Level 1 Normal situation	Minor seasonal variations No alarm	EPC staff only Technical maintenance
0,5-2 mm/d	Level 2 Awareness	Important seasonal fluctuations for individual and multiple sensors Values < excess thresholds for Level 2	Increase frequency of data review, compare different sensors Call in geotechnical/geological/monitoring expert
2-5 mm/d	Level 3 Increase awareness	Increased displacement velocity, seen on from several individual sensors Values < excess thresholds for Level 3	Do continuous review, do field survey, geo-expert team at EPC full time Inform police and emergency/preparedness teams in municipalities
5-10 mm/d	Level 4 High hazard	Accelerating displacement velocity observed on multiple sensors Values < excess thresholds for Level 4	Increase preparedness, continuous data analysis Alert municipalities to stand prepared for evacuation
> 10 mm/d	Level 5 Critical situation	Continuous displacement acceleration Values > excess thresholds for Level 4	Evacuation

EPC = Emergency Preparedness Centre in Stranda

Figure 2.1.1-5. Example of alarm level table with activities and responses (L.H. Blikra 2008)

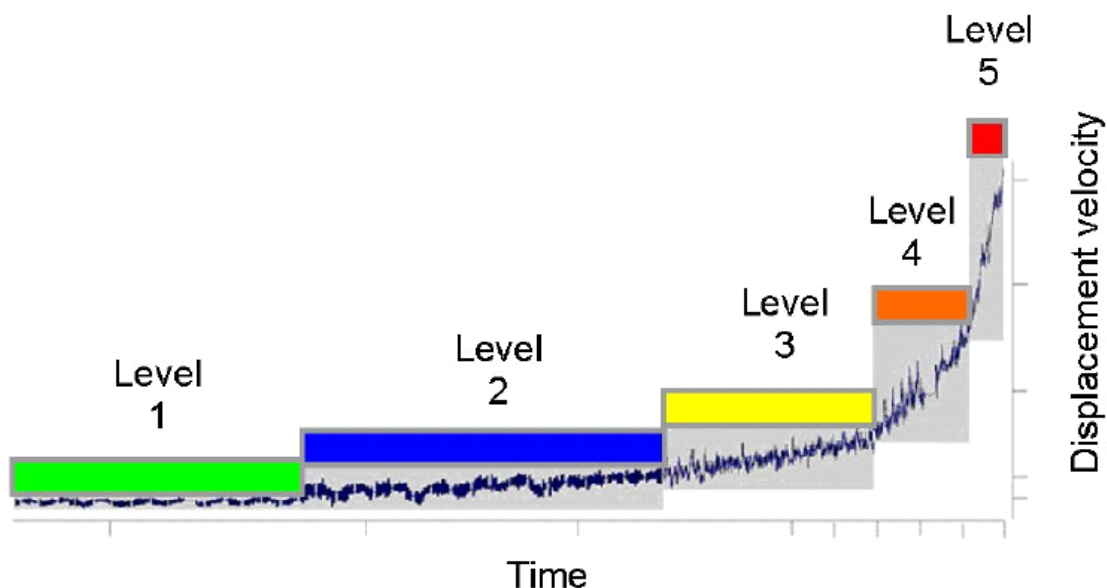


Figure 2.1.1-6. Displacement velocity and alarm level (Blikra 2008)

Displacements are correlated with different phenomena; among them the easiest to correlate is the piezometric level changes. Historical analysis shows how rising of the water table level is often followed by displacements in the sliding area because of changing of pressures and stresses on the body of the landslide. It is also possible to detect a periodicity of displacements in a period of heavy rainfall or snow melting, due to a rise of the water table level. The high

correlation between the two parameters allows for the verification of data detected by the monitoring system and consequently to improve its efficiency.

Settlement

Settlement is the lowering of the topographical surface or of a structure due to deformation of the soil below. If the structure lays over one or more strata of soil that are very compressible, and if those strata are located between strata of uncompressible soil (like sand), settlement depends principally on the characteristics of compressible strata and on intensity and distribution of vertical pressure on that strata. Settlement can be calculated with different models, but it is generally complex to detect it accurately. The available instrumentation (GPS, fixed borehole extensometers, etc.) is often accurate for detection of settlements, establishing reference points at specific depths, and in detecting direction of movement at different depths.

Detection of settlements inside a pipe is not accurate due to the mechanical coupling behaviour existing between the pipe itself and the nude borehole, which affects the measurements lowering the final accuracy of the survey.

Short-term forecasting of slope failures based on displacement

Methods of short-term forecasting of slope failures based on different monitoring parameters were summarized by Busslinger (2009). The following is a brief summary of his report, focusing on displacement velocity.

The approach of Fukuzono (in Busslinger 2009) is based on ***predicting the failure time using the inverse number of surface displacement velocity ($1/v$)***. If the displacement velocity v at a slope surface increases over time, its inverse number ($1/v$) decreases. When ($1/v$) approaches zero, failure occurs (see Figure 2.1.1-7). This method was then successfully developed by other authors.

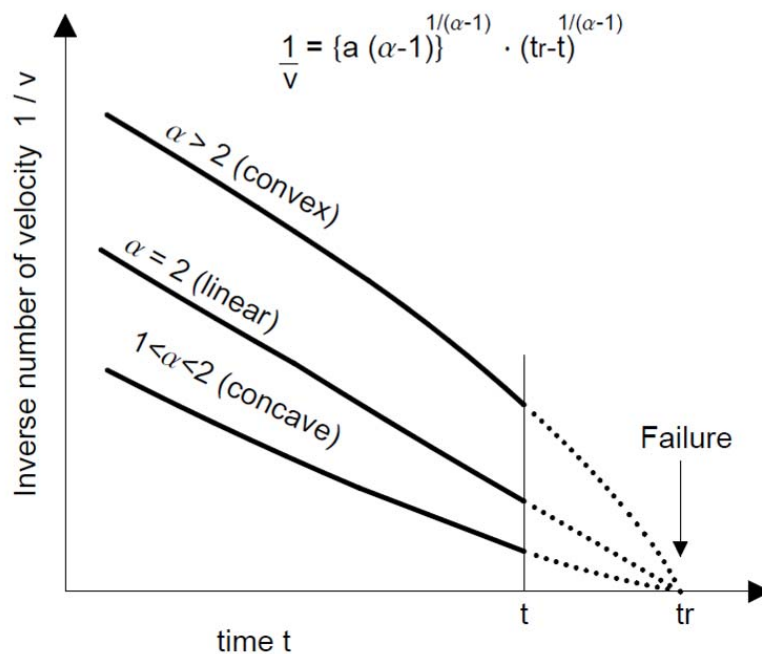


Figure 2.1.1-7. Typical figures for changes of the Inverse number of velocity in surface displacement just before the failure (After Fukuzono in Busslinger)

Rose and Hungr (in Busslinger 2009) summarized the following general **rules for the inverse velocity method**. (i) The method must not be applied in isolation, and displacement monitoring is only one component of a complex process that comprises slope stability management. (ii) The method cannot be used for rockslides dominated by brittle failure, and particular care should be exercised when dealing with relatively small failures in hard rock. (iii) The monitoring data must be processed to remove the effects of instrument error and eliminate records distorted by local movements. (iv) Failure forecasting relies on the identification of consistent trends. The possibility of trend changes, driven by observable or unknown factors, must always be kept in mind. Monitoring must be continued as long as possible prior to failure. The results must be constantly re-evaluated and any established best-fit functions must be revised in view of the latest data. (v) The treatment of cyclic changes depends on the magnitude of their amplitude, relative to the distance from the horizontal axis on the inverse-velocity plot. If the ratio between these two quantities is high, it may be necessary to assume that the low point of any given cycle may produce sudden rupture. (vi) Data fitting using non-linear inverse-velocity trend lines may provide a more accurate assessment of some longer-term trends, but is more complex, which may limit practical use. Crosta and Agliardi (in Busslinger 2009) proposed a method to obtain **alert velocity thresholds** for large rockslides. The method is based on Voight's (1988) accelerating creep theory, where failure is assumed to occur at the time corresponding to a particular rate of displacement. Velocity thresholds can be obtained and incorporated in an emergency concept. This method is only applicable to cases with invariant external conditions.

References:

- Blikra, L.H. (2008): The Åknes rockslide; monitoring, threshold values and early-warning. – In *Landslides and Engineered Slopes*, ed. Z. Chen, J.-M. Zhang, K. Ho, F.-Q. Wu and Z.-K. Li . Proceedings of the 10th International Symposium on Landslides and Engineered Slopes, 30 June - 4 July 2008, Xi'an, China. Taylor and Francis. ISBN: 978-0-415-41196-7. 6 p.
- Buslinger M. (2009): *Landslide time-forecast methods - A literature review towards reliable prediction of time to failure.* – MS. HSR University of Applied Sciences, Institut für Bau und Umwelt, Rapperswil, Switzerland, 31 pp.
- Voight, B. (1988): Materials science law applies to time forecasts of slope failures. – In: Bonnard (Editor): 5th Int. Symp. Landslides Lausanne 1988. Balkema, Rotterdam, 1471-1472.

2.1.2 STRAIN

Jean-Philippe Malet & Julien Travelletti
Centre National de la Recherche Scientifique, France

Displacement monitoring of surface markers on slopes, either in the pre-failure stage or in the case of continuously active landslides subject to period acceleration, indicates often that in the time period (months, days) before large surge displacements, there are always small displacements caused by shear deformation. In general, shear distortions occur within landslides during the early phases of a displacement surge and are caused by the reactivation of failure at residual strength in basal shear zones. These pre-failure strains can be potentially useful precursors of the main movements, and thus embedded in early warning systems. Continuous strain measurements on deformable slopes are also useful observations for a detailed understanding of the failure mechanism in terms of soil and rock mechanics, and for the calibration/validation of coupled hydro-mechanical deformation models. Strain observations are then useful to define the complex interactions between mechanical and fluid properties and states (Van Asch et al., 2007) and reflect spatio-temporal trends in the effective strength and rheological properties of the material. As landslides are not rigid moving bodies, zones of compression and extension are caused by heterogeneity of the moving pattern. This often creates undrained loading in low permeability materials leading to the generation of excess pore water pressure (Figure 2.1.2-1).

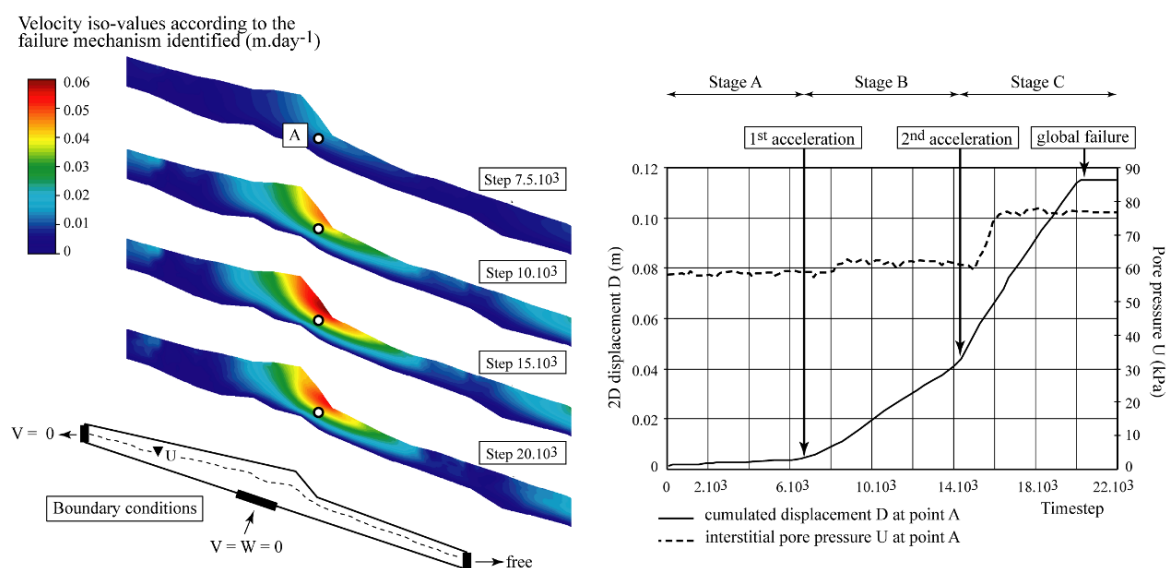


Figure 2.1.2-1. Fully coupled hydro-mechanical simulation of an acceleration of the Super-Sauze mudslide, South French Alps with the GefDyn finite-element code. The soil is described as an elasto-visco-plastic Hujoux material. At the start, the overall safety factor is 1.2. A pore water pressure increase from 56 to 62 kPa over five days leads to a partial acceleration of the soil mass (stage A). Consequent undrained loading and ongoing infiltration lead to a second acceleration (stage B). This local failure is rapid enough to generate excess pore pressures, causing the global failure of the secondary scarp of the mudslide (stage C). This type of analysis permits investigation of the interaction between landslide movements and the development of pore pressures induced by both infiltration and undrained compression of the soil (modified from Malet, 2003).

Strain of objects can be expressed using the stress field that is applied to them. Accordingly, the subject of strain constitutes an important area of interest in geophysics and geodesy in order to obtain information about the stress fields of deforming slope and relief (Brunner, 1979). The concept of strain is closely related to the concept of displacement. To explain it in terms of coordinate change, we can say that, it is the proportion of transformations of coordinates in the direction of axes to those of the initial coordinates. Since it is without a unit and basically expresses a ratio, it is also known as unit strain (Acar et al., 2008). The strain that accumulates within a landslide can be determined using three categories of methods, namely using seismic data, geodetic data or specific geotechnical sensors. The expectation is that the results obtained from the methods should be in accordance with each other. These sections first describe the indirect measurements of strains from geodetic and image processing techniques and, second the direct strain measurements from in-situ sensors. The possible use of seismic data to infer strains is not presented here.

Indirect (remote-sensed) strain measurements from geodetic (GPS) and image processing techniques

The measurements performed by geodetic techniques are repeated at different times in order to determine strains. The time intervals for the measurements used in determination of strain values are designed on the basis of the magnitude of the possible strains or the change in the forces that affects the slope. The basic assumptions for the use of geodetic observations for the determination of strains are linear displacement over the time interval of measurements and uniform strain accumulation (Denli, 1998).

A first indirect estimation of strain values is related to the use of repeated GPS measurements on benchmarks located on landslides. Despite the many advantages that the GPS technique provides, due to the geometrical weakness of the satellite system, inefficiencies of atmospheric modeling used during the evaluation process, and sources of error that cannot be eliminated, the accuracy of the vertical component of the 3-dimensional (3D) positioning information is lower than that of the horizontal component (Featherstone et al., 1998; Krauter, 1999; Çelik et al., 2001). Therefore, two-dimensional (2D) strain tensors must be determined instead of 3D strain tensors and the vertical component must be handled separately.

Homogeneous strain parameters can be obtained from the strain vectors calculated for the points of a geodetic network or from the differences of the repeated observations made on these points. Since the geodetic network is evaluated according to the coordinate system, strain is determined in accordance with this coordinate system. The linear extension of a baseline between the two points of the network is then expressed as:

$$\varepsilon = \frac{S' - S}{\Delta t \cdot S}$$

where: S' expresses the length that has changed at the end of the Δt period while S expresses the unchanged length.

On the other hand, the linear extension of a baseline whose azimuth is t is given as:

$$\varepsilon = e_{xx} \cos^2 t + e_{xy} \sin 2t + e_{yy} \sin^2 t$$

where: e_{xx} , is the change in the unit length in the direction of the x axis; e_{yy} , is the change in the unit length in the y axis and e_{xy} is the shear strain.

Components of the strain tensor are calculated using this basic correlation; the strain analysis involves the division of the geodetic network into triangles and calculation of the components of the strain tensor for the area that each triangle covers. Three equations are established for the three baselines of the triangle, and e_{xx} , e_{xy} and e_{yy} are calculated. The strain tensor components calculated for each triangle are valid for equilibration of the triangle (Deniz and Ozener, 2008).

$$\begin{aligned} D &= e_{xx} + e_{yy} && \text{(dilatancy)} \\ \gamma_1 &= e_{xx} - e_{yy} && \text{(principal shear strain)} \\ \gamma_2 &= 2e_{xy} && \text{(engineering principal shear strain)} \\ \gamma &= \gamma_1 + \gamma_2 && \text{(total shear strain)} \end{aligned}$$

The principal strain parameters are calculated with the equations below:

$$\begin{aligned} E_1 &= \Delta + \gamma && \text{(maximum principal shear strain)} \\ E_2 &= \Delta - \gamma && \text{(minimum principal shear strain)} \\ \beta &= \arctan\left(\frac{e_{xy}}{E_1 - e_{xy}}\right) && \text{(direction of maximum principal shear strain arc)} \end{aligned}$$

GPS observations can be acquired on benchmarks located within a landslide. Application to 18 benchmarks at the Buyukcekmece landslide along the Marmara Sea, Turkey allows an evaluation of the adjusted coordinates and variance-covariance matrix and the horizontal displacements. The control network in the research was then divided into 28 triangles using the Delaunay method to calculate strain parameters (Figure 2.1.2-2). Strain parameter components of e_{xx} , e_{yy} , and e_{xy} can then be calculated for each triangle.

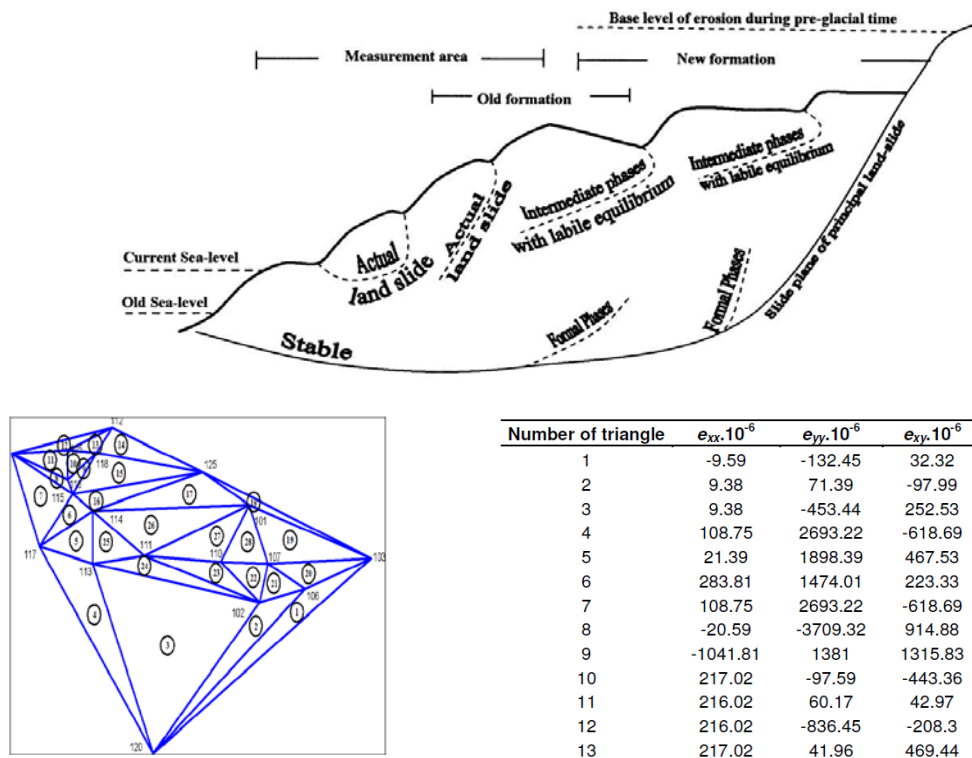


Figure 2.1.2-2. Strain value parameters estimation at the Buyukcekmece landslide (Marmara Sea, Turkey), from the analysis of the deformation of Delaunay triangles through repeated GPS measurements. Top: Location of the measurement area within the landslide body. Bottom left: Delaunay triangles determined from the location of the different benchmarks. Bottom right: Estimation of strain parameter values for the different components of the triangles baselines.

Another technique to infer strain parameter values is to use very dense and multi-temporal point clouds, preferably acquired at the ground using terrestrial laser scanners. An application has been realized by Montserrat and Crosetto (2008) on a rocky slope, and by Travelletti et al. (submitted) within the *SafeLand project* at the Super-Sauze landslide (South French Alps). Their application consisted in calculating the 2D Cauchy's strain tensor E on repeated terrestrial laser observations to characterize small deformation (Pollard and Fletcher, 2010):

$$E = \begin{bmatrix} \frac{du_x}{dx} & \frac{1}{2} \left(\frac{du_x}{dx} + \frac{du_y}{dy} \right) \\ \frac{1}{2} \left(\frac{du_x}{dx} + \frac{dv_y}{dy} \right) & \frac{dv_y}{dy} \end{bmatrix}$$

where: u and v refer to displacement increments along the x-direction and y-direction in the local coordinate system ($u = \Delta X$ and $v = \Delta Y$). A local least squares fitting technique is used to compute the 2D strain tensor at each location of the grid (Pan et al., 2009).

A strain window of $(2m+1) \times (2m+1)$ grid meshes is defined assuming that the displacement distribution follows a linear plane. Therefore, the following equations are solved at each mesh of the grid:

$$\begin{aligned} u(i, j) &= a_1x + b_1y + c_1 \\ v(i, j) &= a_2x + b_2y + c_2 \end{aligned}$$

where: $i, j = -m:m$ are the coordinates in the strain window; $u(i, j)$ and $v(i, j)$ are the displacement components at the location (i, j) ; a_1, b_1, a_2, b_2 are the displacement gradients to be determined, and c_1 and c_2 are constant values.

The overdetermined system of equations is then formulated in a matrix form and is solved in a least squares sense. To find the unknowns a_1, b_1, c_1 , the following equation is used:

$$\begin{bmatrix} 1 & -m & \\ 1 & -m+1 & \\ \vdots & \vdots & \vdots \\ 1 & 0 & 0 \\ \vdots & \vdots & \vdots \\ 1 & m-1 & m \\ 1 & m & m \end{bmatrix} \begin{bmatrix} a_1 \\ b_1 \\ c_1 \end{bmatrix} = \begin{bmatrix} u(-m, -m) \\ u(-m+1, -m) \\ \vdots \\ u(0, 0) \\ \vdots \\ u(m-1, m) \\ u(m, m) \end{bmatrix}$$

The procedure is similar to find the unknowns a_2, b_2, c_2 . The component of the Cauchy strain

tensor are estimated with $a_1 = \frac{du_x}{dx}$, $b_1 = \frac{du_x}{dy}$, $a_2 = \frac{dv_x}{dx}$ and $b_2 = \frac{dv_x}{dy}$.

As the regular grid displays a homogenous distribution of the displacements, the least squares fitting is not influenced by important differences of point densities inside the strain window, thus making the gradient estimations more robust. Because the strain tensor E is real and symmetric, the two eigenvalues e_1 and e_2 corresponding to the change of length per unit of length in the direction having the maximum and minimum extension (positive for extension) without shearing are then computed. The deformation is presented in this study by the surface strain defined as $\epsilon_S = e_1 + e_2$ (positive for extension) and the shear strain defined as $\gamma = |e_1 - e_2|$. A strain window of 3×3 m is selected ($m = 1$ for a grid mesh size of 1 m).

The method has been applied on a series of 10 terrestrial laser point clouds acquired over the period 2007-2010 at the toe of the Super-Sauze landslide. For example, the strain field derived from the acquisition over the periods July - October 2008 and 2009 is used to illustrate the kinematics of the toe. The first step consists in determining the accuracy of the computed strain field. Therefore, a null hypothesis is performed on the stable areas assuming that the strain error in these parts is similar to the strain error in the landslide. The accuracy analysis on the stable parts shows that more than 90 % of the surface strain and shear strain ranges between $\pm 2 \cdot 10^{-3}$ which is therefore considered as the lowest interpretable value. The importance of the compression and shear strain affecting the toe front explains why the correlation computation sometimes tends to fail in that part of the landslide.

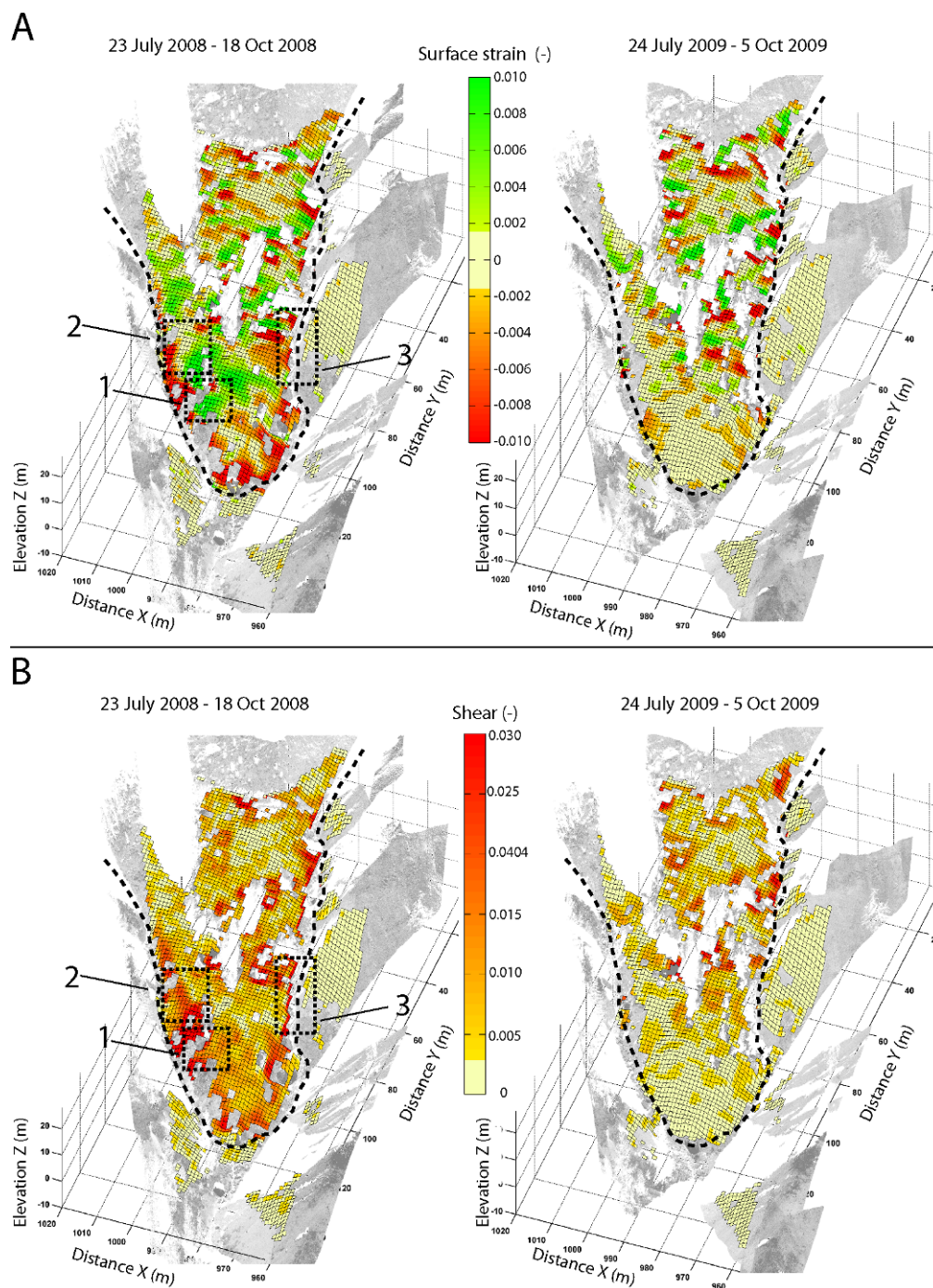


Figure 2.1.2-3. Strain field obtained by TLS measurements related to the acquisition periods of July – October of the years 2008 and 2009. Maps of the surface strain (a positive value means extension) (A) and of the shear strain (B). The strain maps are draped on their corresponding point clouds (intensity values).

The strain analysis allows the discrimination of areas under extension/compression and affected by shearing (Figure 2.1.2-3). Note that because of the finite size of the correlation window and the strain window, a significant smoothing of the strain fields is introduced, associated with a spatial spreading of the structures. The upper part of the toe is characterized by a succession of approximately parallel bands (width of 5 to 10 m) in compression and extension whose main orientation is perpendicular to the sliding direction (Figure 2.1.2–3A). Except at the proximity of the stable part, the upper part is not affected by important shearing

(Figure 2.1.2-3B). The location of the compression and extension zone changes from 2008 to 2009, thus suggesting a possible displacement of these areas with the landslide material. The behaviour of the toe front is very different between the years 2008 and 2009. In 2008, extension is observed, thus inducing compression in the material located in the very front of the toe near the boundary of the landslide (Figure 2.1.2-3A). The consequence of this extension results in the development of tensile fissures identifiable on the field (Figure 2.1.2-4). The toe front is also affected by important shearing concentrated along the landslide boundary. The important shear magnitude in these areas is confirmed by very persistent shear and tensile fissures affecting the landslide material (Figure 2.1.2-4). In 2009, the deformation affecting the toe front is less important than in the previous year because the displacements in that part are very low and uniform.

A more objective validation of the computed strain field will be to compare the ellipse of deformation with the density and the orientation of the fissures automatically determined with object-oriented techniques applied on very high-resolution orthophotographies (Stumpf et al., 2011). Actually both techniques give information on the behaviour of the mudslide and are thus complementary.

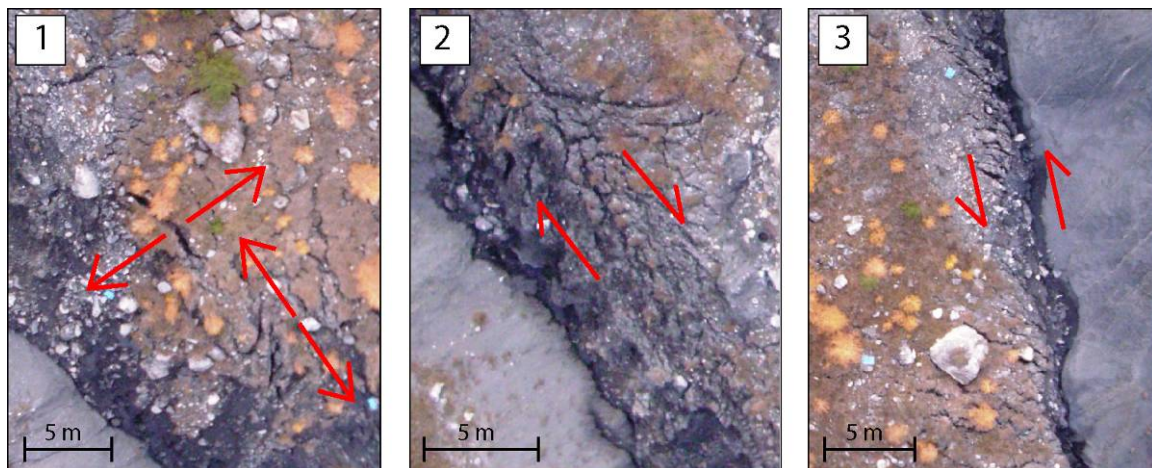


Figure 2.1.2-4. Tensile fracture (1) and shear fracture (2, 3) observed at the front of the toe (block 4 in Figure 2.1.2-9) on an orthophotograph acquired in October 2008 by Niethammer et al. (2010). The location of the pictures is indicated in Figure 2.1.2-3.

Direct *in-situ* strain measurements with FO cables and large strain Rosette

Fiber optic (FO) strain sensors are a promising new technology for advancing the state of the art in *in-situ* landslide monitoring. General performance advantages include high resolution, rapid sampling rate, multiplexing potential, and insensitivity to electrical disturbances (such as lightning). To date, however, there are only a few cases where FO strain sensors have been used for monitoring slope deformations in landslide investigations (Brunner et al., 2007; Woschitz and Brunner, 2008), because the application is restricted to slow-moving landslides characterized by very small strain deformation. Different types of FO sensors are available with varying resolutions and costs. Fiber Bragg grating (FBG) sensors offer a good balance between performance and investment.

Application of FO strain sensors has been tested at the Randa landslide (southern Switzerland), installed at the ground surface and in a deep borehole (Moore et al., 2010). Fiber Bragg gratings are short sections of optical fibre that contain a periodic variation in the index of refraction. When illuminated by broadband light, each FBG reflects a particular

wavelength while transmitting all others undisturbed (Ferraro and de Natale, 2002). In this way, multiple sensors can be placed in a series on the same optical fiber, tuned at nonintersecting wavelength bands. The reflected wavelength is measured by an optical interrogator, and changes proportionally with the FBG strain within a linear regime.

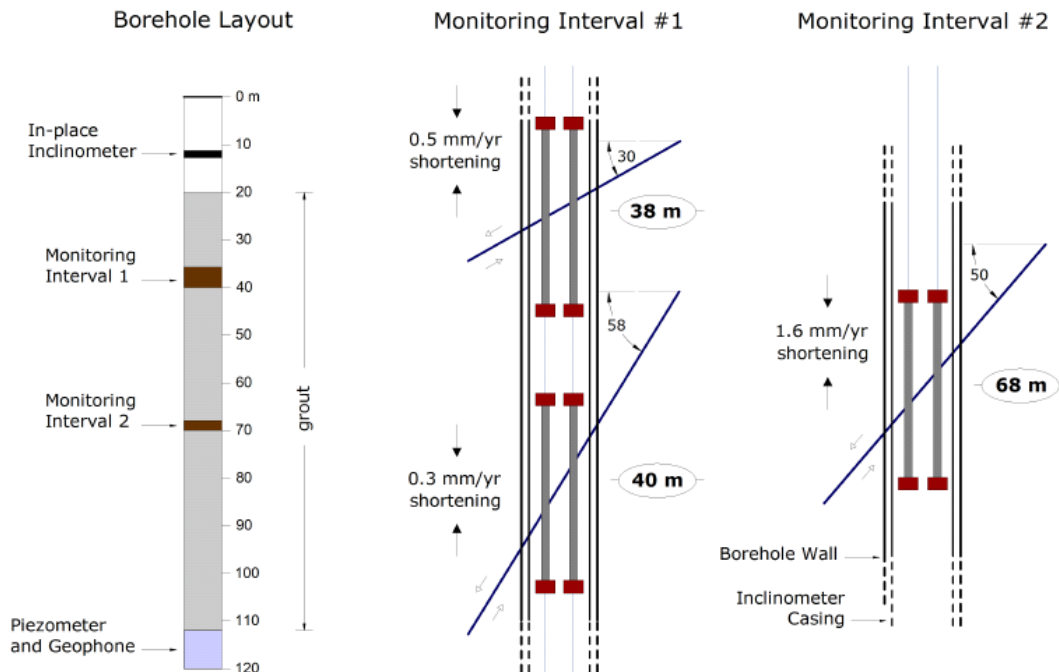


Figure 2.1.2-5. Detail of fiber optic sensor installation in borehole sb120 at the Randa rockslide. Two monitoring intervals were selected to span three active fractures showing normal mode offset (see slip arrows). The expected rates of shortening, calculated from previous extensometer surveys, are shown. Two active parallel sensor chains were installed for redundancy and security, and a third inactive chain (not shown) acts as reserve (in Moore et al., 2010).

FO borehole sensors were emplaced to span known active fractures showing normal mode offset (Figure 2.1.2-5). The targeted fractures were previously characterized in borehole surveys, and slip rates determined from inclinometer and extensometer measurements (Willenberg et al., 2008). The deepest fracture (68 m) dips approximately 50° and has a long-term shear rate of 2.8 mm/year, resulting in an axial shortening rate of 1.6 mm/year. The fracture at 40 m dips roughly 60° and shows an axial shortening rate of 0.3 mm/year, while the fracture at 38 m dips about 30° with an axial shortening rate of 0.5 mm/year. The upper two fractures may be part of a fault zone. The FO sensors measure only the component of deformation in the line of the sensor, or along the borehole axis. Therefore we expect these sensors to shorten (de-stress) over time.

From the long-term displacement and velocity trends (Figure 2.1.2-6), we observe that all borehole sensors are shortening (negative extension values) as expected. Qualitatively, the rates of shortening match with previous extensometer surveys.

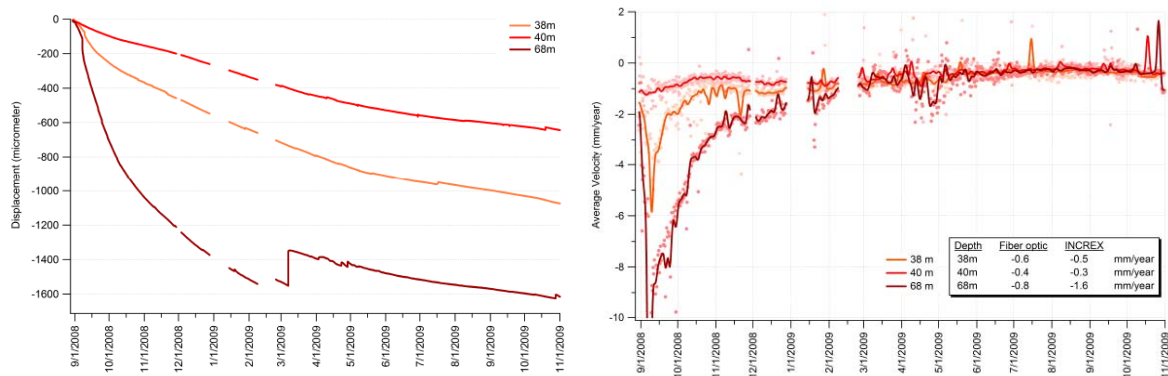


Figure 2.1.2-6. Deformation time series at the Randa rockslide. Right: Deformation time series measurements from the three sensors at different monitoring intervals in borehole sb120 (data from just one sensor chain are shown). All sensors are shortening as expected. Accelerated shortening is seen immediately following sensor installation, which likely results from shrinkage of the grout. A number of transient steps and drops occur throughout the time history. Left: Velocity time series for the different sensors in borehole sb120. Dots indicate calculated half-day average velocities, while the solid lines are the data filtered with a binomial smoothing algorithm. The inset table shows comparison of the long-term average velocities with those determined from previous extensometer surveys. Accelerated shortening is clearly visible in the first 2–3 months of operation. Dates are m/d/y. (in Moore et al., 2010).

The primary performance advantage of FO strain monitoring systems is the improvement in resolution and accuracy. Our system resolution is about two orders of magnitude better than that of the high quality traditional sensors, and rapidly improves with data averaging. We can easily detect sub-micrometer deformations in the long-term record, which allows us, for example, to resolve daily strain patterns or small transients associated with different deformation processes. The possibility of triggered 100 Hz sampling offers the advantage of being able to capture dynamic deformations associated with passing seismic waves, and will enable us to investigate the seismic performance of the unstable rock mass.

FO systems have the general advantage of being insensitive to electrical disturbances such as lightning, which can be a significant source of difficulties for field applications. Furthermore, the optical cabling is robust and suitable for use in harsh landslide environments. Finally, the FBG system offers the possibility of placing many sensors on only a few cables, which makes for easier and more secure installations. The primary disadvantage of FO strain systems is cost. These systems are several times more expensive than their traditional in-situ monitoring counterparts. Another drawback is the relatively large power consumption, which in our case was roughly 50W and required construction of large solar arrays.

Another type of *in-situ* strain sensor is embedded extensometers installed in a Rosette array (separation in orientation of 120°). The measurement technique is based on long gauge (5 m) fibre optical low coherence interferometers, yielding a precision of 2 µm for length changes. The same sensors can also be used for dynamic measurements with a precision of better than 10 nm with sampling rates of 1 kHz. The extensometers are long gauge fibre optical sensors of the SOFO type (Inaudi et al., 1994; Inaudi, 1997) whose advantage is its use of the same embedded sensors for the measurement of the static (absolute) and the dynamic (relative) length changes.

When installing the large strain Rosette in the field and embedding the sensors, the main challenges are the proper connection of the SOFO sensors with the soil and their protection from other disturbances. The set-up of this installation (Figure 2.1.2-7) and results of its investigation are shown in Brunner et al. (2007).

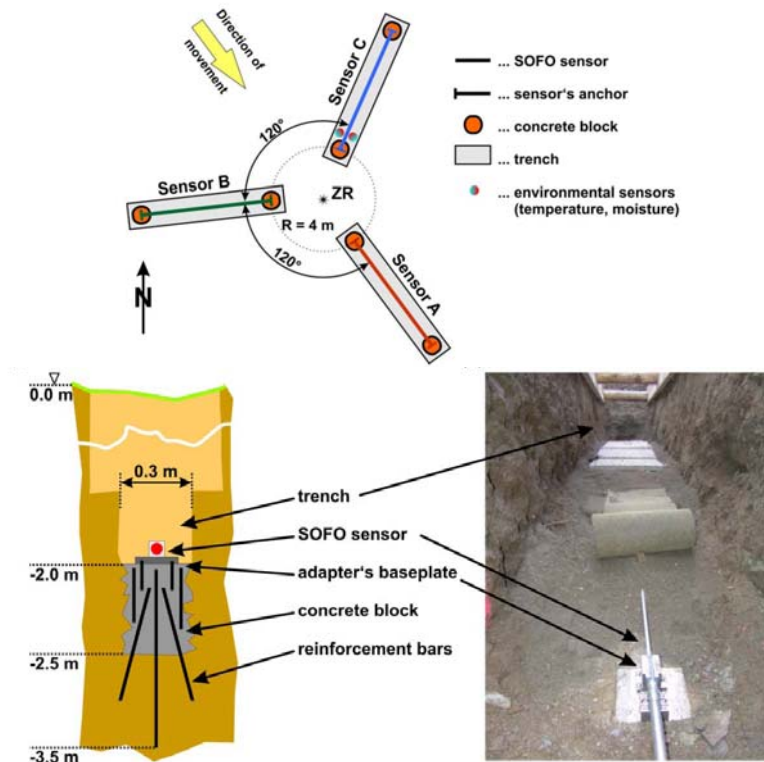


Figure 2.1.2-7. Scheme of the strain Rosette installed at the Gradenbach landslide (Austria) in a trench (Brunner et al., 2007).

Figure 2.1.2-8 shows the collected data of the strain Rosette from 2007 until 2010, which were corrected for temperature changes. The sum of the thermal corrections is less than $12 \mu\text{m}$ for an internal RU temperature difference of about 30°C and a difference of about 7°C for soil temperature.

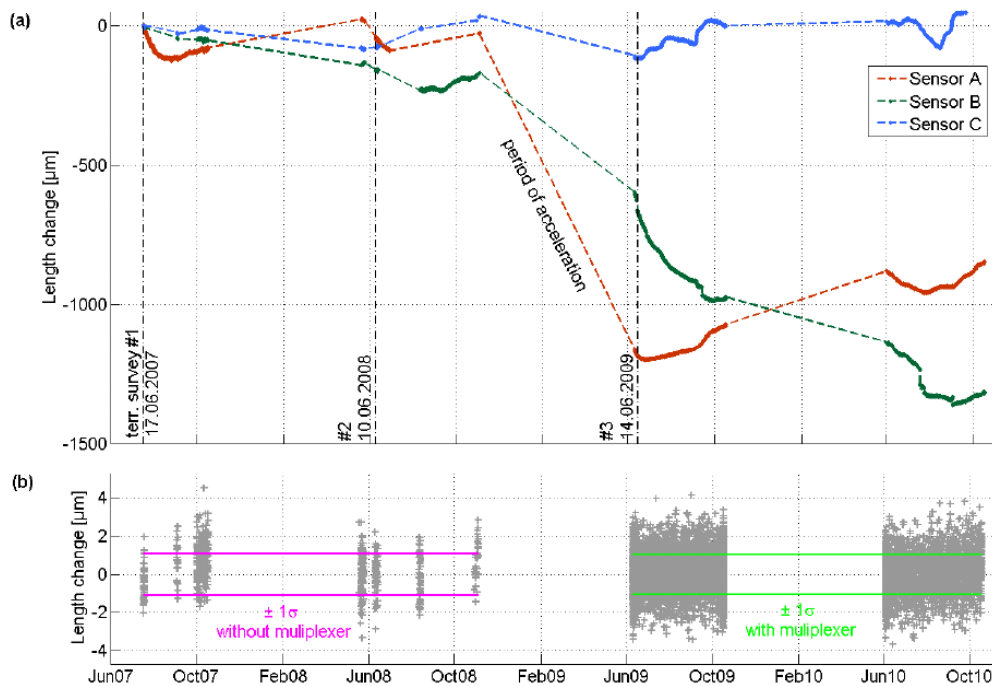


Figure 2.1.2-8. Length change measurements with the three sensors of the strain Rosette and the measurement time of the terrestrial surveys (vertical lines). (b) Length change measurements of the reference sensor.

Error propagation was used to derive the precision of the strain parameters using an ellipse approach for the three sensors. The precision depends inversely on the magnitude of the strain, i.e. the larger the strain the better the precision of the parameters. Using the strain of the third epoch ($\epsilon_1 = -261$ ppm) the calculated precision (1- σ -level) of the principal strain is about 0.6 ppm and the σ of its direction is about 0.1 gon. The computed orientation of the strain ellipse is in agreement with the direction of the slope's motion.

References

- Acar M, Özlüdemir MT, Erol S, Çelik RN, Ayan T (2008). Kinematic Landslide Monitoring with Kalman Filtering, *Natural Hazards and Earth System Science* 8(2): 213-221.
- Brunner FK (1979). On the analysis of geodetic networks for the determination of the incremental strain tensor, *Survey Rev.* 25: 56-67.
- Brunner FK, Coleman R, Hirsch B (1981). A comparison of computation methods for crustal strains from geodetic measurements, *Tectonophysics* 71: 281-298.
- Brunner, F. K., Woschitz, H., Macheiner, K. (2007). Monitoring of deep-seated mass movements, *Proceedings 3rd International Conference on Structural Health Monitoring of Intelligent Infrastructure*.
- Brunner, F.K., Woschitz, H., Macheiner, K. (2007) Monitoring of Deep-Seated Mass Movement. CD-Proc. 3rd Int. Conf. on Structural Health Monitoring of Intelligent Infrastructure (SHMII-3), Nov: 13-16, 2007, Vancouver; 10 p.
- Çelik, R.N., Ayan, T., Denli H.H., Özlüdemir, T, Erol, S, Özöner, B, Apaydın, N, Erinçer, M, Leinen, S, Groten, E. (2001). Monitoring Deformation on Karasu Viaduct Using GPS and Precise Leveling Techniques. *NATO Science Series, Series E: Applied Sciences*, vol. 373, s. 407-415.
- Deniz I, Ozener H (2008). Determination of Velocity Field and Strain Accumulation of Densification Network in Marmara Region, *FIG Working Week 2008, Stockholm, Sweden*.
- Denli HH (1998). Determination of Crustal Movements Analysis in the Marmara Sea Region Using GPS. PhD dissertation, Istanbul Technical University, Istanbul, Turkey.

-
- Featherstone WE, Denith MC, Kirby JF (1998). Strategies for the Accurate Determination of Orthometric Heights from GPS, *Surv. Rev.* 34(267): 278-296.
- Ferraro, P., de Natale, G. (2002). On the possible use of optical fiber Bragg gratings as strain sensors for geodynamical monitoring, *Opt. Laser. Eng.*, 37, 115–130.
- Inaudi, D. (1997). Fiber optic sensor network for the monitoring of civil engineering structures. PhD Thesis, EPFL Lausanne, Switzerland, 262 p.
- Inaudi, D. (2004). Testing performance and reliability of fiber optic sensing system for longterm monitoring. Proc. 2nd European Workshop on Optical Fibre Sensors, Santander, Spain, June, 9-11 2004, 4p.
- Krauter A (1999). Role of the Geometry in GPS Positioning, *Periodica Politechnica Ser. Civ. Eng.* 43(1): 43-53.
- Malet, J.-P. 2003. Les glissements de type écoulement dans les marnes noires des Alpes du Sud. Morphologie, fonctionnement et modélisation hydromécanique. PhD Thesis, Université Louis Pasteur, Strasbourg.
- Monserrat, O., Crosetto, M., 2008. Deformation measurement using terrestrial laser scanning data and least squares 3D surface matching. *ISPRS Journal of Photogrammetry*, 61(1), 142-154.
- Moore, J.R., Gischig, V., Button, E., Loew, S. 2010. Rockslide deformation monitoring with fiber optic strain sensors. *Natural Hazards & Earth System Science*, 10, 191–201.
- Niethammer, U., Rothmund, S., James, M. R., Travelletti, J., Joswig, M. 2010. UAV-based remote Sensing of landslides. *International Archives of Photogrammetry, Remote Sensing and Spatial Information Sciences*, Vol. XXXVIII, Part 5 Commission V Symposium, Newcastle upon Tyne, UK.
- Pan, B., Asundi, A., Xie, H., Gao, J. 2009. Digital image correlation using iterative least squares and pointwise least squares for displacement field and strain field measurements. *Optics and Lasers in Engineering*, 47, 865-874.
- Pollard, D., Fletcher, C. 2010. *Fundamentals of Structural Geology*. Cambridge University Press (Eds.), Cambridge.
- Stumpf, A., Niethammer, U., Rothmund, S., Mathieu, A., Malet, J-P., Kerle, N., Joswig, M. 2011. Advanced image analysis for automated mapping of landslide surface fissures. In Margottini, C. (Ed): *Proceedings of the Second World Landslide Forum*, Roma, 3-7 October 2011, Roma. (in press).
- Travelletti, J., Malet, J.-P., Delacourt, C. Multi-date correlation of Terrestrial Laser Scanning data for the characterization of landslide kinematics. *Earth Surface Processes and Landforms*, 22p. (submitted in September 2011).
- van Asch, Th.W.J., Malet, J.-P., van Beek, L.P.H., Amitrano, D. 2007. Techniques, advances, problems and issues in the modelling of landslide hazard. *Bulletin de la Société Géologique de France*, 178(2): 6-35.
- Willenberg, H., Evans, K. F., Eberhardt, E., Spillmann, T., and Loew, S. (2008). Internal structure and deformation of an unstable crystalline rock mass above Randa (Switzerland): Part II –Three-dimensional deformation patterns, *Eng. Geol.*, 101, 15–32.
- Woschitz, H., Brunner, F. K. (2008). Monitoring a deep-seated mass movement using a large strain rosette, *Proceedings 13th FIG Symposium on Deformation Measurements and Analysis*.

2.1.3 MASS LOSS/INCREMENT BALANCE FOR LANDSLIDE EW

Clément Michoud, Marc-Henri Derron, Michel Jaboyedoff

University of Lausanne, Switzerland

We investigate here the possible use of mass balance in EW systems. This kind of system is regularly used for snow avalanches, in which a local device or a remote sensor (such as Terrestrial Laser Scanning (Sailer et al. 2008)) first records the thickness of the snow mantle particularly in locations where wind is expected to cause its accumulation. Once the volume reaches a predefined critical value, an alarm is automatically sent (Rice et al. 2002). It can even be coupled with a “controlled” gas-explosive system to trigger small avalanches in order to prevent a large accumulation of snow and mitigate the risk caused by huge snow avalanches.

Presently we are not aware of any actual application of this system to landslides. But considering that with shallow landslides, for instance, the soil thickness is the main controlling factor of stability (Melchiorre & Frattini 2011), can we imagine any similar application to earth-, debris- or landslides or flows?

Debris flow source areas:

In active watershed, loose material accumulates over time and can be suddenly released in debris flows (Figure 2.1.3-1). The monitoring of the volume of potentially mobile material in key locations of the watershed could help to prevent large debris flows with long run out. Like with snow avalanches, controlled small volume scouring of source areas could be considered.



Figure 2.1.3-1. Accumulation of potential mobile material during a debris flow event in the Illgraben channel, Switzerland (courtesy of T. Oppikofer).

Landslide foot areas:

Two mass balance processes may affect the stability of a landslide toe. First a progressive erosion of the foot may debuttress the whole sliding mass, such as in quick clays (Jaboyedoff et al. 2009). Secondly, compression ridges may form at the foot of instability, concentrating important stress. The rupture of such a compression zone may provoke a sudden debuttressing of the toe too (Michoud et al. 2010). Regular monitoring of volume changes (positive or negative) at the toe of a landslide can help to prevent a general collapse of the instability.

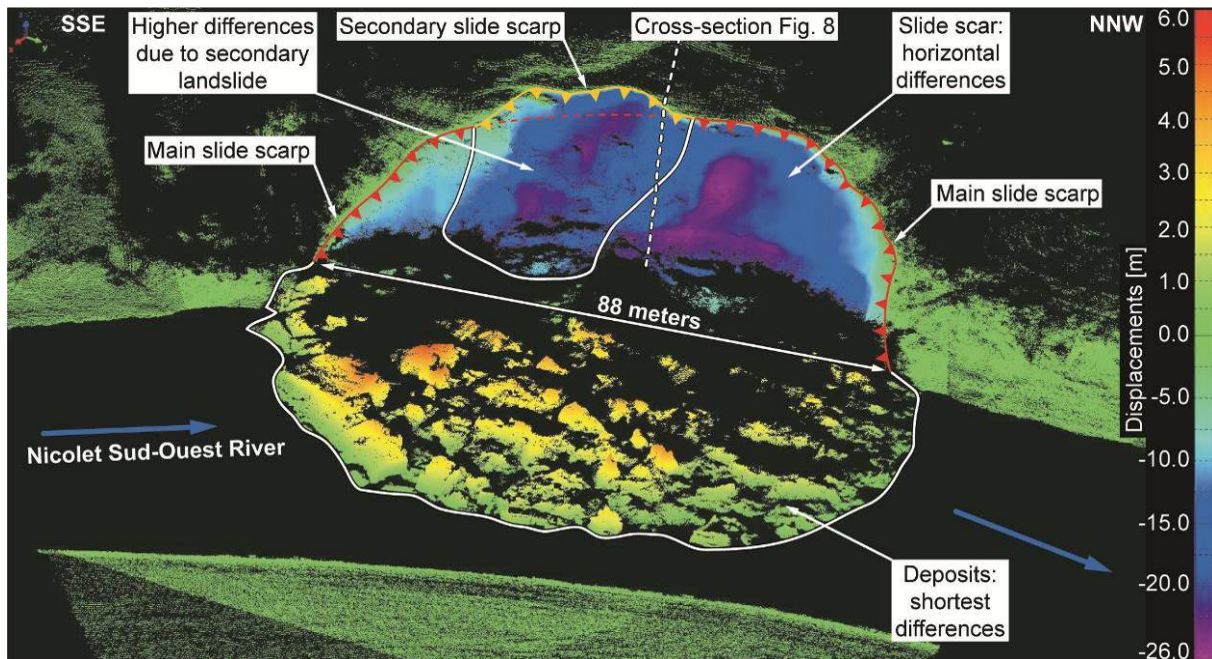


Figure 2.1.3-2. Comparison of the ALS (before) and TLS (after) point clouds of a landslide occurred in clayey soils in 2006 along the Nicolet River, Canada. It underlines the localizations of the first and secondary slide scarps and quantifies the slide volume. It helps to design a new slope profile to stabilize it (from Jaboyedoff et al. 2009).

Presently with laser scanning techniques, it is possible to estimate volume changes and make mass wasting budgets (Figure 2.1.3-2). Then calculating volumes of displaced material allows the fixing of threshold values for alarms based on these mass balances. Indeed, it should be possible to calculate with complex numerical models the maximum material volume at the toe that can be displaced before it collapses. Monitoring systems based on mass balances could then be implemented at the toes of potential instabilities, for which no displacements are observable on the rest of the slope such as for retrogressive landslides in clayey banks along Canadian rivers (Levy et al. in press).

Nevertheless, three major issues must be overcome to implement a monitoring network and establish threshold values. First, as far as we know, there are only few automatic routines allowing continuous monitoring with a TLS device. Moreover, the estimation of mass balances comparing two point clouds are not automatic with traditional acquisitions and need an operator to be exported. Finally, it assumes that threshold values must be estimated with complex models that require a lot of input and a good conceptual model of the landslide to be as reliable as possible for alarms.

These limitations explain why the mass balances concepts are not used in EWS as far as we know today. On the other hand, this new parameter could overcome the difficulties of monitoring only surface displacements in some specific landslide contexts.

References:

- Jaboyedoff M., Demers D., Locat J., Locat A., Locat P., Oppikofer T., Robitaille D., Turmel D. (2009): Use of terrestrial laser scanning for the characterization of retrogressive landslides in sensitive clay and rotational landslides in river banks. – *Canadian Geotechnical Journal*, 46, 1379-1390.
- Levy S., Jaboyedoff M., Locat J., Demers D. (In press.): Erosion and channel change as factors of landslides and valley formation in Champlain Sea Clays: The Chacoura River, Quebec, Canada. – *Geomorphology*, doi: 10.1016/j.geomorph.2011.09.014.
- Melchiorre C., Frattini P. (2011): Modelling probability of rainfall-induced shallow landslides in a changing climate, Otta, Central Norway. – *Climate Change*, 24 pp.
- Michoud C., Nicolet P., Carrea D., Jaboyedoff M. (2010): Glissement au lieu dit Pont Bourquin - Compte-rendu des événements d'août 2010 et premières interprétations. – *Technical Report, IGAR-UNIL*, 31 pp.
- Rice R. Jr., Decker R., Jensen N., Patterson R., Singer S., Sullivan C., Wells L. (2002): Avalanche hazard reduction for transportation corridors using real-time detection and alarms. – *Cold Regions Science and Technology*, 34, 31-42.
- Sailer R., Fellin W., Fromm R., Jörg P., Rammer L., Sampl P., Schaffhauser A. (2008): Snow avalanche mass-balance calculation and simulation-model verification. – *Annals of Glaciology*, 48, 183-192.

2.1.4 MACRO-CRACKS AND SURFACE FISSURES

André Stumpf

International Institute for Geo-information Sciences and Earth Observation, Netherlands /
Centre National de la Recherche Scientifique, France

This sub-section is focused on the significance of surface fissures preceding and accompanying slope failures. They must be distinguished from internal fractures that are not visible at the surface (described in subsection 2.1.5). Several studies that focused particularly on the mapping and mechanical interpretation of surface fractures accompanying landslides can be found in the historical ([Krauskopf et al., 1939](#); [Ter-Stephanian, 1946](#)) or more recent literature ([Fleming et al., 1999](#); [Fleming and Johnson, 1989](#); [Parise, 2003](#)), and surface fractures preceding final failures are frequently mentioned in numerous publications. Ter-Stephanian (1946) suggested a classification scheme based on the mechanical significance of the surface cracks but in present day the terminology still varies among different authors, often adopting concepts from structural geology. The terms ‘crack’ and ‘fissures’ are often used synonymously; “crack” seems more commonly used to refer to the fracturing process (Mode I, II, III, Figure 2.1.4-1a), and “fissures” is more frequently adopted in description of resulting openings in the surface. In certain cases cracks induced by desiccation and by mechanical deformation may have a similar appearance, and particularly in environments with an abundance of swelling clays, special attention should be given to the proper differentiation of those features.

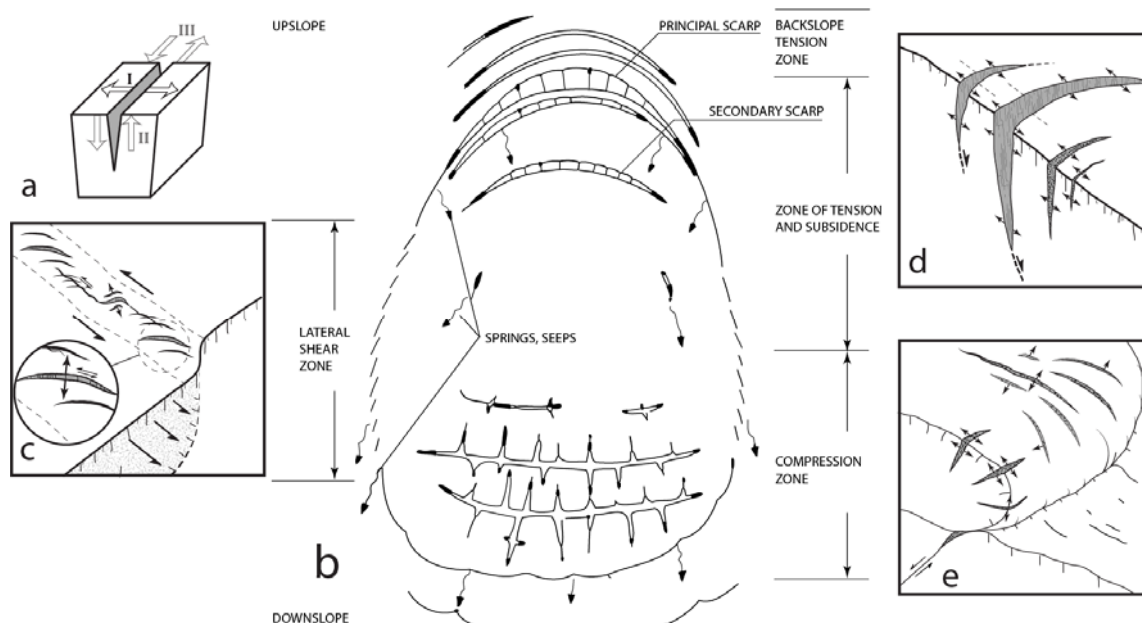


Figure 2.1.4-1. Overview of typical fissure patterns that may occur at the surface of a landslide. (a): The predominant fracture mechanisms for individual cracks is typically Mode I. (b) Different fissure patterns may indicate tension (d), shear (c), or compression occurring preferentially at distinct parts of the the landslide.

From a mechanical point of view, there must be a distinction between rather plastic materials (most soils and unconsolidated sediments) that may experience considerable ductile deformation before the occurrence of brittle fractures and rather brittle materials such as hard rocks. In practice most slope forming materials are deformable to some degree and this division is transient, however, the interpretation of observed fractures must take into account the material characteristics at the time the rupture occurred.

Units:

Individual fissures can be characterized in terms of width, length and depth measured once or frequently to obtain a time series. Their spatial arrangement in terms of orientation, density and the geometry of the fracture surface may provide important indicators to describe past and ongoing mechanical processes.

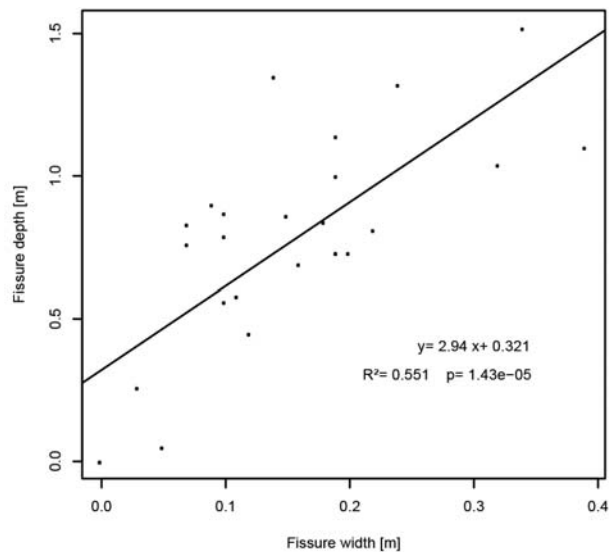


Figure 2.1.4-2. Relationship between fissure width at the Super-Sauze mudslide. Based on data from ([Espinosa, 2009](#))

Typical values:

According to Griffith's crack theory, surface fissures will generally develop from pre-existing material flaws and thus their minimum size is determined by the detection technique rather than by physical constraints. While the typical width of fissures observable in the field ranges from a few millimeters to 100 cm ([Fleming and Johnson, 1989](#); [Krauskopf et al., 1939](#); [Stumpf et al., 2011](#)) there are also examples where such features are several meters wide and hundreds of meters long (e.g. Margielewski and Urban, 2003). Relationships between the width and the depth of the fissures (Figure 2.1.4-2) are suggestive but the parameters of this relationship certainly depend on the material strength and the sub-surface geometry. In more brittle material, a width/depth ratio lower than in plastic materials can generally be expected.

Dependencies on other parameters:

The formation of surface fissures depends on the fracture toughness of the material, the geometry of the slope and the applied forces. Generally there must be a distinction between fissures in hard rock, where brittle fractures have a rather direct link with the applied stresses, and fissures developing in rather plastic materials, where brittle fracturing will only occur after the strain reaches a critical rate. Most soils and soft-sediment can undergo considerable plastic deformation before fracturing and their plasticity typically depends on the saturation of the material. Clay-rich sediments in particular display rather brittle behaviour when dry.

Measurement techniques:

Detailed maps of surface fissures can be obtained through time consuming field surveys by direct observation of the topography (e.g. [Fleming et al., 1999](#); [Meisina, 2006](#)). Relatively large landslide-induced fissures may also be discernible in very high-resolution (VHR) spaceborne images ([Youssef et al., 2009](#)) but typically those structures reach widths that require very high-resolution aerial photography. Only recently, Unmanned Aerial Vehicles (UAVs) are becoming a flexible and cost-efficient tool for the acquisition of imagery with sufficiently high resolution ([Eisenbeiss, 2009](#); [Niethammer et al., 2011](#)). Manual image interpretation can support field campaigns and it has also been demonstrated that pattern recognition techniques provide a more objective and largely automated way to map surface fissures from such images ([Stumpf et al., 2011](#)). For the structural analysis of rock joints and the mapping of larger fissures it has also been demonstrated that terrestrial and airborne LiDAR scans are valuable data sources that enable the localisation of fissures and a better understanding of possible failure mechanisms ([Pedrazzini et al., in press](#); [Sturzenegger et al., 2007](#)). For studies of the landslide hydrology, relating seismic tomography and electrical resistivity measurements to the fissure density in the landslide body has been suggested ([Bièvre et al., 2011](#); [Grandjean et al., 2011](#)). Those techniques require intensive field instrumentation and are at present only applicable for local studies of known hotspots. The development of previously detected fissures can be monitored through repeated field or flight surveys but the installation of fixed crackmeters (crack gauges) is probably the most commonly used technique for monitoring the evolution of cracks (e.g. [Chelli et al., 2006](#); [Froese et al., 2009](#); [Greif et al., 2006](#); [Petro et al., 2004](#); [Read et al., 2007](#)).

Conceptual geotechnical model

Strongly simplified models of the influence of the presence of fissures on the stability of a rock slope are described by Hoek and Bray ([1981](#)) and Hoek ([2007](#)). Due to its simplicity those models are often adopted to estimate slope stability for engineered rock slopes. Figure 2.1.4-3 illustrates the simple case of a tension crack in a planar surface where the probability of a failure will depend on the geometry of the slope and material properties, the position of the tension crack, the depth of the tension crack and the water level inside, and temporarily external forces such as seismic shaking. Hoek and Bray ([1981](#)) emphasized the importance of knowledge about the existence, position and characteristics of such tension cracks to assess the stability of slopes formed in hard rock.

For soils and soft rocks the situation is typically more complex since the plasticity of the material may vary considerably in space and time (Figure 2.1.4-4).

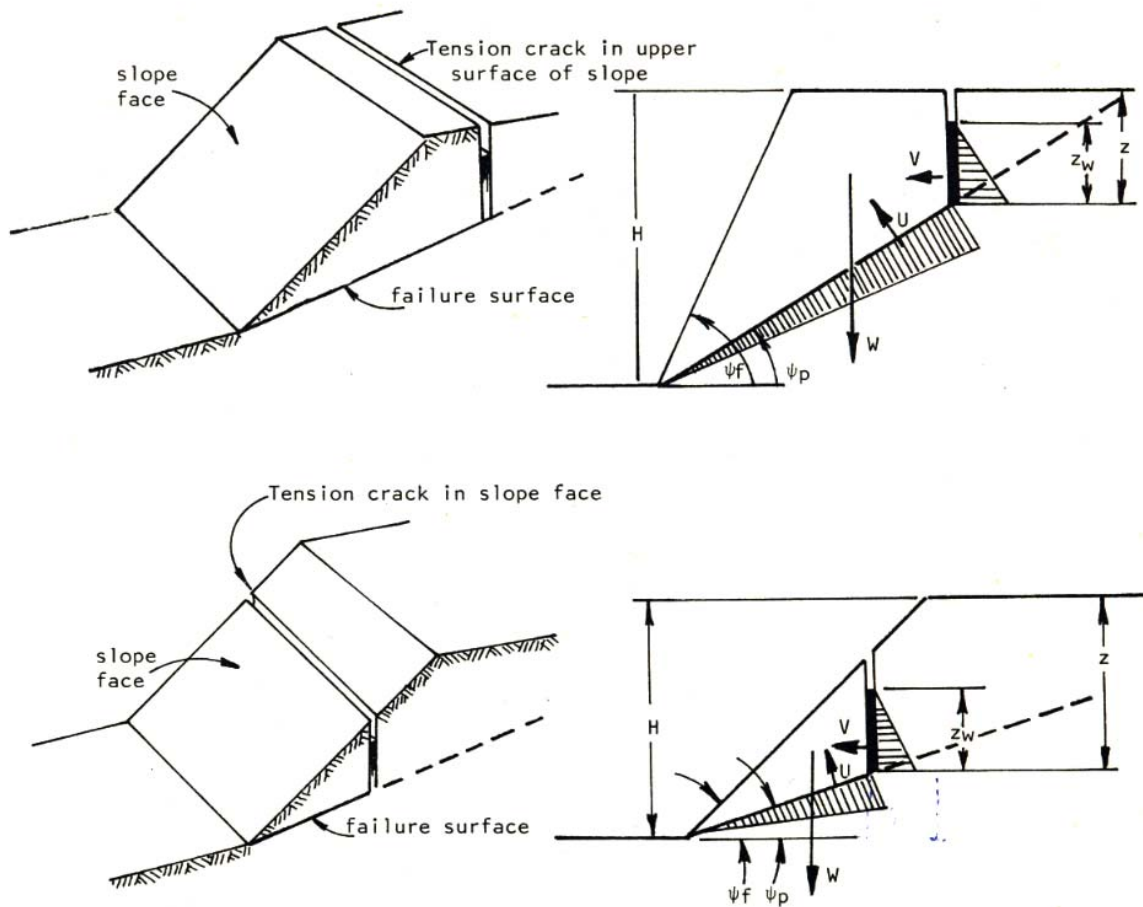


Figure 2.1.4-3. One-dimensional geotechnical model to describe the influence of a tension crack on the stability of a planar slope in hard rock ([modified after Hoek and Bray, 1981](#)).

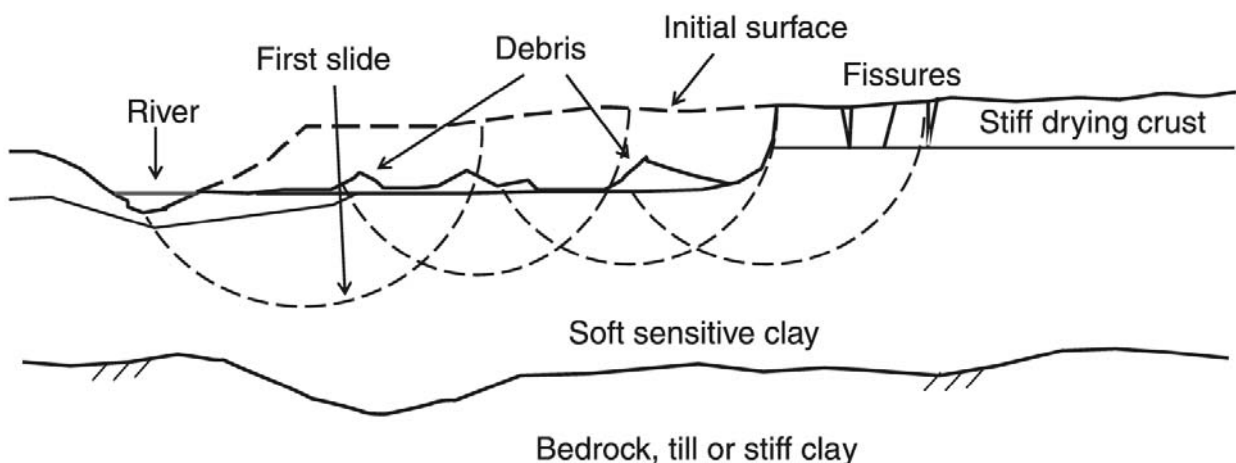


Figure 2.1.4-4. One-dimensional geotechnical model to describe the mechanism of retrogressive failures in sensitive clays ([Quinn et al., 2011](#)) after ([Bjerrum, 1955](#)).

Geotechnical models that involve fracture mechanics to describe landslide types developing soft-rock materials often consider the development of shear zones at the base of the sliding mass as one of the most important processes preceding the failure ([e.g. Quinn et al., 2011](#)). In many cases the surface fissures may occur where the developing shear zones reach the

surface, and thereby provide an indicator for the occurrence of subsequent fast moving events. In return the surface characteristics will also influence hydrological processes, such as infiltration and drainage patterns, which affect the groundwater system and the kinematic response of slopes to hydrological events ([Malet et al., 2003](#); [Malet et al., 2005](#); [van Asch et al., 2009](#)). In particular, open tension cracks modify the infiltration and pore-water response considerably, and their integration into physically-based models may yield more reliable kinematic forecasts and estimates of the hazard level ([Baum and Fleming, 1991](#); [Corominas et al., 2002](#); [Iverson, 2000](#); [Lindenmaier et al., 2005](#); [Malet et al., 2005](#); [van Beek and van Asch, 1999](#)).

Usability as EW parameter:

The presence and characteristics of surface fissures can be relevant inputs for early warning systems from three different directions:

1. The observation of newly occurring surface fissures is a basic qualitative warning sign, which in most cases will raise the alert level and trigger further investigations. The main challenge is therefore the timely detection of such fissures that may often become visible only days or even hours before a catastrophic event. Though very high-resolution remote sensing datasets become more frequently available, reliable techniques for an automatic detection of surface fissures are still largely missing. At present field surveys, image interpretation and observations made by the local population remain the most common information source for the detection of new surface fractures.
2. For the monitoring of known fissures, crackmeters (crack-gauges) are valuable instruments to measure already minimal deformation at the most critical slope sections. The possible integration of such devices in early warning networks has been demonstrated at the Turtle Mountain Monitoring project (http://www.ags.gov.ab.ca/geohazards/turtle_mountain/crackmeter.html, Figure 2.1.4-5)
3. An indirect use of information on the spatial distribution of surface fissures could be a more reliable parameterization of precipitation-based early warning systems, since the presence of fissures will influence the infiltration rate into the landslide body and along potential shear planes.

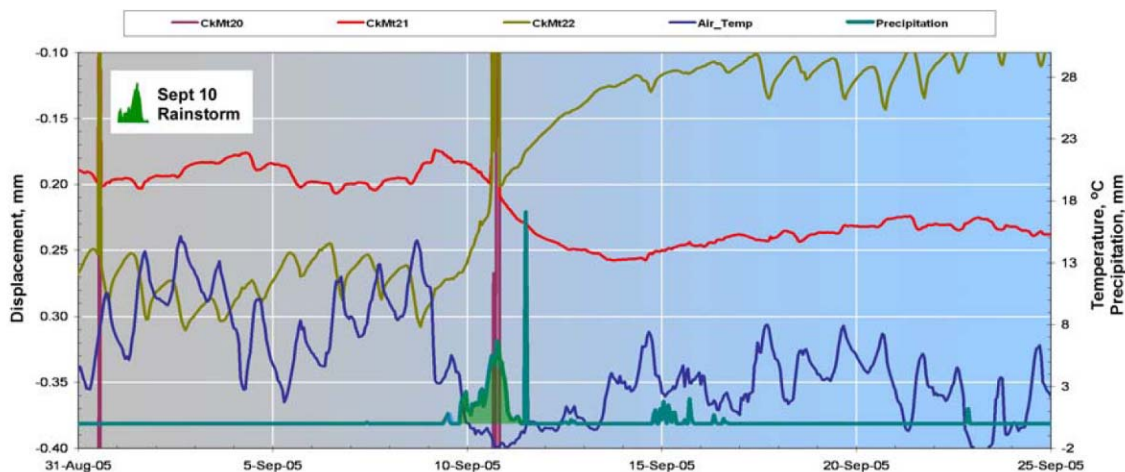


Figure 2.1.4-5. Relationship between displacement rate measured by three crack meters (violet, red, green), temperature (blue), and precipitation as measured over a 25-day period in 2005 at the Turtle Mountain Monitoring Project ([Moreno and Froese, 2007](#)).

References:

- Baum, R.L., Fleming, R.W., 1991. Use of longitudinal strain in identifying driving and resisting elements of landslides. *Geological Society of America Bulletin*, 103, 1121-1132.
- Bièvre, G., Jongmans, D., Winiarski, T., Zumbo, V., 2011. Application of geophysical measurements for assessing the role of fissures in water infiltration within a clay landslide (Trièves area, French Alps). *Hydrological Processes*, n/a-n/a.
- Bjerrum, L., 1955. Stability of natural slopes in quick clay. *Géotechnique*, 5(1), 101-119.
- Chelli, A., Mandrone, G., Truffelli, G., 2006. Field investigations and monitoring as tools for modelling the Rossena castle landslide (Northern Appennines, Italy). *Landslides*, 3(3), 252-259.
- Corominas, J., Moya, J., Hürlimann, M., 2002. Landslide rainfall triggers in the Spanish eastern Pyrenees 4th EGS Plinius Conference on Mediterranean Storms. Universitat de les Illes Balears (Spain), Mallorca, Spain.
- Eisenbeiss, H., 2009. UAV photogrammetry. PhD, ETH Zürich, Zürich, Switzerland, 235 pp.
- Espinosa, A., 2009. Analysis and quantification of preferential flow on the Super-Sauze landslide. MSc, Delft University of Technology, Delft, Netherlands, 80 pp.
- Fleming, R.W., Baum, R.L., Giardino, M., 1999. Map and Description of the Active Part of the Slumgullion Landslide, Hinsdale County, Colorado, Geologic investigations Series Map I-2672. U.S. Geological Survey, p.36.
- Fleming, R.W., Johnson, A.M., 1989. Structures associated with strike-slip faults that bound landslide elements. *Engineering Geology*, 27(1-4), 39-114.
- Froese, C.R., Moreno, F., Jaboyedoff, M., Cruden, D.M., 2009. 25 years of movement monitoring on South Peak, Turtle Mountain: understanding the hazard. *Canadian Geotechnical Journal*, 46(3), 256-269.
- Grandjean, G., Bitri, A., Krzeminska, D.M., 2011. Characterisation of a landslide fissure pattern by integrating seismic azimuth tomography and geotechnical testing. *Hydrological Processes*, n/a-n/a.
- Greif, V., Sassa, K., Fukuoka, H., 2006. Failure mechanism in an extremely slow rock slide at Bitchu-Matsuyama castle site (Japan). *Landslides*, 3(1), 22-38.
- Hoek, E., 2007. Practical Rock Slope Engineering. rocscience, http://www.rocscience.com/hoek/corner/Practical_Rock_Engineering.pdf.
- Hoek, E., Bray, J.W., 1981. *Rock Slope Engineering*. The Institution of Mining and Metallurgy, London.
- Iverson, R.M., 2000. Landslide triggering by rain infiltration. *Water Resour. Res.*, 36(7), 1897-1910.
- Krauskopf, K.B., Feitler, S., Griggs, A.B., Source:, 1939. Structural Features of a Landslide near Gilroy, California. *The Journal of Geology*, 47(6), 630-648.
- Lindenmaier, F., Zehe, E., Dittfurth, A., Ihringer, J., 2005. Process identification at a slow-moving landslide in the Vorarlberg Alps. *Hydrological Processes*, 19(8), 1635-1651.

- Malet, J.-P., Auzet, A.-V., Maquaire, O., Ambroise, B., Descroix, L., Esteves, M., Vandervaere, J.-P., Truchet, E., 2003. Soil surface characteristics influence on infiltration in black marls: application to the Super-Sauze earth flow (southern Alps, France). *Earth Surface Processes and Landforms*, 28(5), 547-564.
- Malet, J.P., van Asch, T.W.J., van Beek, R., Maquaire, O., 2005. Forecasting the behaviour of complex landslides with a spatially distributed hydrological model. *Nat. Hazards Earth Syst. Sci.*, 5(1), 71-85.
- Margielewski, W., Urban, J., 2003. Crevice-type caves as initial forms of rock landslide development in the Flysch Carpathians. *Geomorphology*, 54(3-4), 325-338.
- Meisina, C., 2006. Characterisation of weathered clayey soils responsible for shallow landslides. *Nat. Hazards Earth Syst. Sci.*, 6(5), 825-838.
- Moreno, F., Froese, C.R., 2007. Turtle Mountain Field Laboratory (TMFL): Part II - Review of trends 2005-2006, http://www.geo.mtu.edu/EHaz/VolcanoInstability_class/froese/pdf/Moreno%20and%20Froese%20NASL.pdf.
- Niethammer, U., James, M.R., Rothmund, S., Travelletti, J., Joswig, M., 2011. UAV-based remote sensing of the Super-Sauze landslide: Evaluation and results. *Engineering Geology*, In Press, Accepted Manuscript.
- Parise, M., 2003. Observation of surface features on an active landslide, and implications for understanding its history of movement. *Nat. Hazards Earth Syst. Sci.*, 3(6), 569-580.
- Pedrazzini, A., Froese, C.R., Jaboyedoff, M., Hungr, O., Humair, F., in press. Combining digital elevation model analysis and run-out modeling to characterize hazard posed by a potentially unstable rock slope at Turtle Mountain, Alberta, Canada. *Engineering Geology*(0).
- Petro, L., Vlcko, J., Ondrasik, R., Polascanova, E., 2004. Recent tectonics and slope failures in the Western Carpathians. *Engineering Geology*, 74(1-2), 103-112.
- Quinn, P.E., Diederichs, M.S., Rowe, R.K., Hutchinson, D.J., 2011. A new model for large landslides in sensitive clay using a fracture mechanics approach. *Canadian Geotechnical Journal*, 48(8), 1151-1162.
- Read, R.S., Langenberg, W., Cruden, D., Field, M., Stewart, R., Bland, H., Chen, Z., Froese, C.R., Cavers, D.S., Bidwell, A.K., Murray, C., Anderson, W.S., Jones, A., Chen, J., McIntyre, D., Kenway, D., Bingham, D.K., Weir-Jones, I., Seraphim, J., Freeman, J., Spratt, D., Lamb, M., Herd, E., Martin, D., McLellan, P., Pana, D., 2007. Frank Slide a Century Later: The Turtle Mountain Monitoring Project, Michigan Tech.
- Stumpf, A., Niethammer, U., Rothmund, S., Mathieu, A., Malet, J.-P., Kerle, N., Joswig, M., 2011. Advanced image analysis for automated mapping of landslide surface fissures, 2nd World Landslide Forum, Rome, Italy, pp. 6.
- Sturzenegger, M., Stead, D., Froese, C., Moreno, F., Jaboyedoff, M., 2007. Ground-based and airborne LiDAR for structural mapping of the Frank Slide, 1st Canada-US Rock Mechanics Symposium, Vancouver, Canada, pp. 925-932.
- Ter-Stephanian, G., 1946. On the landslide cracks classification. *Bulletin of the Academy of Sciences of the Armenian SSR*, 10, 65-80.
- van Asch, T.W.J., van Beek, L.P.H., Bogaard, T.A., 2009. The diversity in hydrological triggering systems of landslides., *The First Italian Workshop on Landslide*, Napoli, Italy pp. 151-156.
- van Beek, L., van Asch, T., 1999. A combined conceptual model for the effects of fissure-induced infiltration on slope stability. In: S. Hergarten, H. Neugebauer (Eds.), *Process Modelling and Landform Evolution. Lecture Notes in Earth Sciences*. Springer Berlin / Heidelberg, pp. 147-167.
- Youssef, A., Maerz, N., Hassan, A., 2009. Remote sensing applications to geological problems in Egypt: case study, slope instability investigation, Sharm El-Sheikh/Ras-Nasrani Area, Southern Sinai. *Landslides*, 6(4), 353-360.

2.1.5 MICRO SEISMICITY/ACOUSTIC EMISSIONS

Michael Roth

NORSAR, Norway

Alice Tonnellier & Jean-Philippe Malet

Centre National de la Recherche Scientifique, France

Small-scale shear failures, sudden and tiny movements on sliding planes and falling rocks generate elastic waves propagating in the subsurface. These microseismic signals, sometimes also called acoustic emissions (AE) since their frequency can reach the audible range, are an additional indicator on the state of an unstable slope, complementary to directly observable parameters. Mass movements of brittle material are generating microseismic events and an acceleration of the movement will result in an increase of strength and number of seismic events. The ambient seismic background noise (natural and manmade) and the rate of seismicity varies from site to site and also varies temporally. Microseismicity monitoring is a passive seismological method that can be used to continuously observe the varying dynamic processes during landslide movement in the pre-failure, failure and post-failure stage, according to the case studies. It is necessary to monitor a site over long-term periods in order to assess the natural variations, to optimize the monitoring parameters and to be able to identify significant changes in seismic activity.

The typical frequency range of the microseismic signals is between a few Hz up to several hundred Hz and the signal amplitudes are between micrometers down to nanometers, depending on the strength of the seismic source and its distance to the seismic sensors. Generally, the smaller the event is the higher the frequency content and the shorter the signal duration.

Seismic acquisition systems and real-time data display

A seismic acquisition system basically consists of a sensor or a small-scale network of sensors (accelerometer, geophone, seismometer), a digitizer (analog-to-digital converter) and a computer to store and process the data locally or to transmit the data for remote processing/storage. Because of the high-frequency content of the signal, it is necessary to use high sampling rates up to 1000 Hz adding up to a data volume of more than 10 MB per hour and channel. In case of a microseismic network it is advisable to record in triggered mode, i.e. short data segments of interest. This option is a standard implementation for modern digitizers.

The real-time display of microseismic waveform data is very useful and complementary to real-time data of other measurements. Generally, however, microseismic waveform data need

to be analysed automatically or manually with respect to event detection, event classification, and event source parameters, location and strength.

Examples of signals recorded on an unstable rock slope

The unstable rock slope at Åknes, Norway has been monitored seismically since October 2005. At that time a microseismic network consisting of eight 3-component geophones was installed in the uppermost part of the slope, and in 2009 a seismic 3-component broadband station was installed in the centre of the unstable area. The geophone network records in triggered mode, whereas the broadband instrument operates in continuous mode at a sampling rate of 200 Hz.

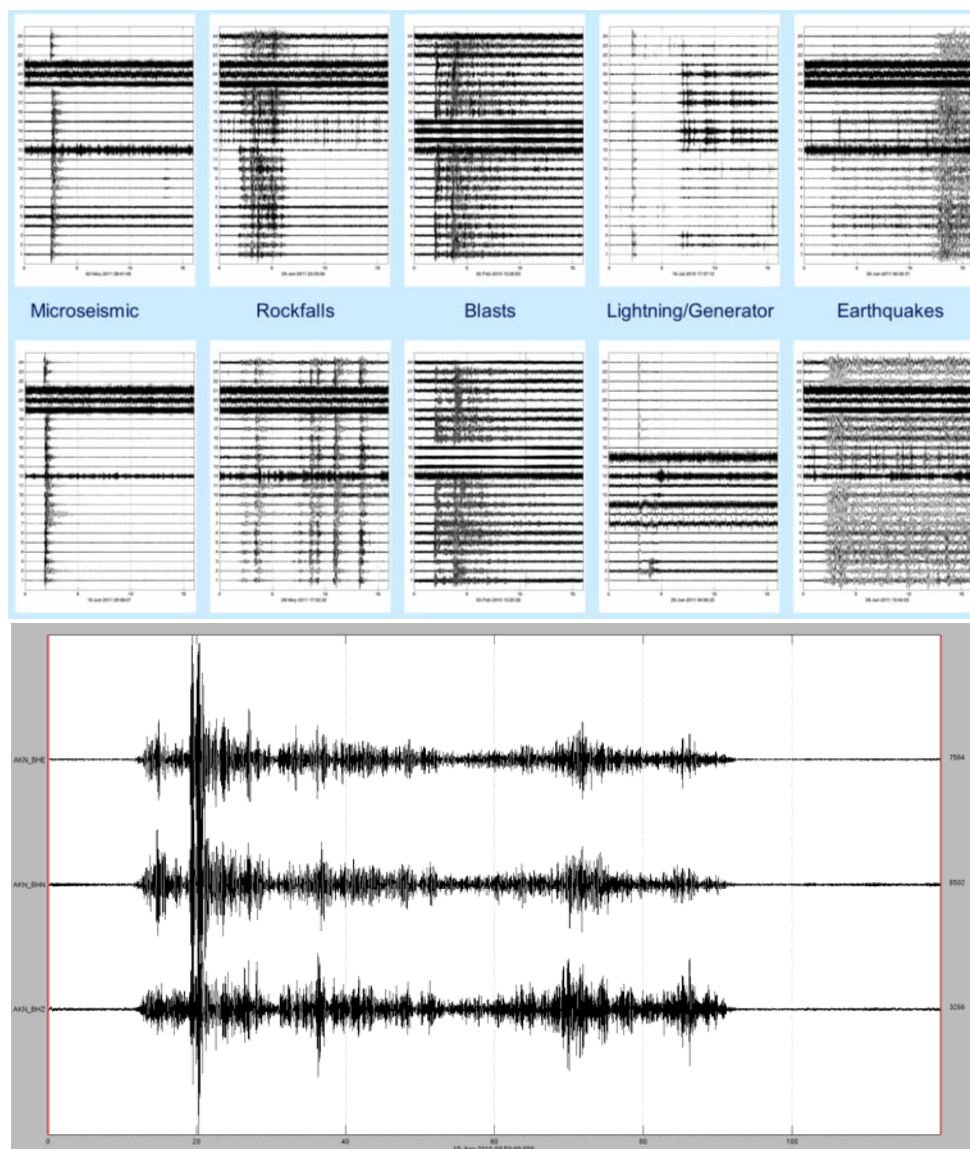


Figure 2.1.5-1. Seismic signals recorded with a microseismic network (top) and a seismic broadband station (bottom) at the unstable rock slope at Åknes, Norway. The panels for the geophone network (top) show the trace-normalized 24 channels for time segments of 16 seconds. The lower panel shows a small-scale rockslide/fall at Åknes with duration of about 80 seconds recorded with the broadband station.

The top part of Figure 2.1.5-1 shows examples of different seismic signals recorded with the 24 channels of the geophone network at the site. Besides microseismic events with a typical duration of a few seconds, one can observe seismic signals generated by rockfalls (multiple onsets caused by the impact of tumbling rocks); blasts from a nearby road tunnel construction (clear arrivals of compressional and shear waves); electronic spikes with very short duration caused by lightning and power generator upstarts; and regional earthquakes. The bottom part of Figure 2.1.5-1 displays the East-, North- and vertical component of the ground motion generated by a small-scale rockslide/fall at Åknes with duration of about 80 seconds.

Examples of signals and application on a soft-sediment landslide

This section presents the detection of landslide events and rockfall events within the large Super-Sauze mudslide (South French Alps, Figure 2.1.5-2). At Super-Sauze, from repeated campaigns started in June 2008, and from a permanent seismic monitoring station installed in October 2009, several seismic signals caused by varying dynamic processes were detected by applying the nanoseismic monitoring method. The nanoseismic monitoring acts as a seismic “microscope” for detecting small impulsive signals. The existence of such signals was not expected due to the lack of brittle material deformation that would generate impulsive fracture release within such weak sediments.

Accurate analysis of microseismic events requires detailed tomography information such as internal structure and velocity models to implement in the inversion algorithm. Two quite similar models are proposed for the landslide including a small surface layer of $v_p=[350-700] \text{ m.s}^{-1}$ sliding on the bedrock of $v_p=[2200-2300] \text{ m.s}^{-1}$, for the upper and the lower profile respectively. The dashed white line represented on the velocity profiles illustrates the discontinuity between sliding layer and bedrock. The sliding layer is 5-10 m thick in the central part of the profile, from the upper to the lower region respectively, where an accumulation of sediments is sensibly higher. In between a stable crest with $v_p=[1300-1700] \text{ m.s}^{-1}$ was identified, which is clearly seen on the global view picture between the unstable and the stable side of the landslide.

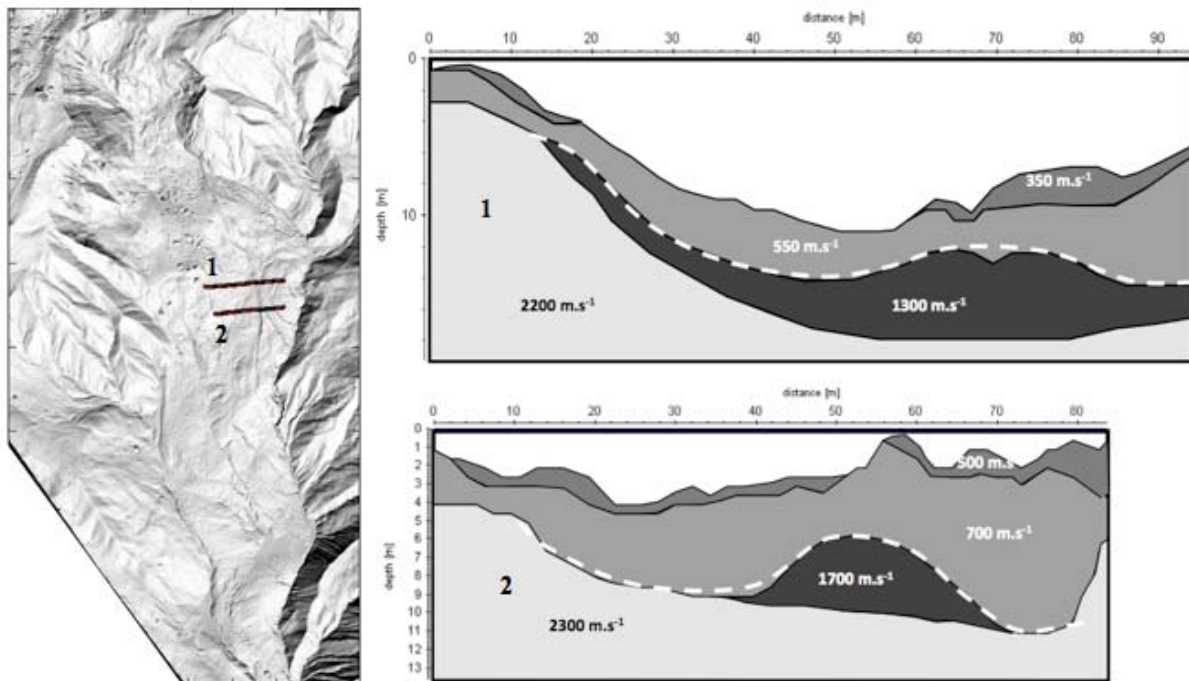


Figure 2.1.5-2. Tomography profile and v_p velocity models for both upper (1) and lower (2) profiles on the right. The darkest layer observed on the models corresponds to the crest between unstable and stable sides of the landslide, which is clearly seen on the global view picture on the left. The dashed white line represents the discontinuity between the sliding and the bedrock layers and was highlighted by previous studies.

Shots were made on 22 points (Figure 2.1.5-3) within the studied zone in strategic positions around the seismic monitoring array (less to very fractured zones, landslide unstable-stable boundary) in order to check the efficiency of the array geometry and to refine the velocity model (Figure 2.1.5-2). Acoustic emissions induced by the shots were recorded by the seismic permanent monitoring array, with the fixed sampling frequency at 400 Hz. Results simplified the tomography velocity model in two average 2D velocity models defined by only two layers and characterising the P and S waves' velocities too, to be easily used in the “nanoseismic” localisation algorithm. We decided to validate both of the models because the landslide is too heterogeneous and it would have been impossible to consider only one velocity model for the whole studied zone. The models are both characterised by $v_p=800 \text{ m.s}^{-1}$ in the sliding layer, 10 m thick, and $v_p=2300 \text{ m.s}^{-1}$ in the bedrock layer and differ by the v_p/v_s ratio that varies from 1.95 to 2.36 from the upper to the lower part suggesting that the S wave velocity decreases in the lower part. We can interpret this variation with the saturation, which might be higher in the lower part. Tomography suggested that the sliding layer is thicker in the lower part but varying the thickness parameter did not strongly influence the shot localisation test results. At last, we are not currently able to determine a precise localisation but a region of occurrence of the events with a 5-10 % precision in the best cases (according to the shot tests). The localisation might be worse in the lower part where the material is more fractured and diffraction is higher (Figure 2.1.5-3).

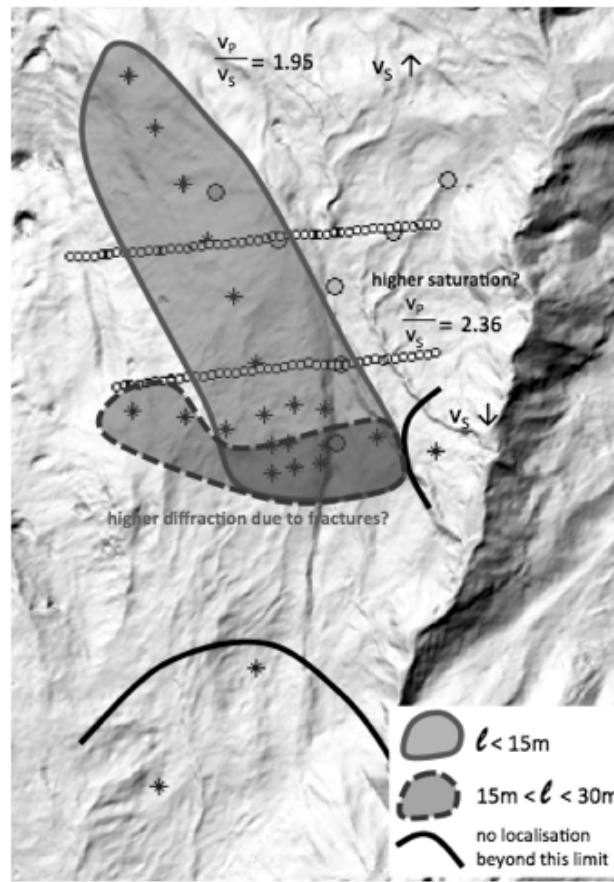


Figure 2.1.5-3. v_p/v_s ratio variation and localisation precision evaluation. Medium circles represent the seismic permanent monitoring sensors positions, circles lines are the tomography profiles and stars indicate the test shots positions. l is the distance between theoretic and inversed localisation.

Before trying to locate the sources of the events, preliminary observations were made and it was concluded that most of the observed seismic signals produced by mass movements have an average duration of 2 to 20s with a frequency content ranging from 10 to 150 Hz. One example of one potential signal is illustrated in Figure 2.1.5-4. Pointing the supposed first arrivals is subtle so that correlation options help in comparing the transients between each channel. Determining the sources' localisations happened to be very delicate due to the sensibility of the algorithms that depend on the sampling frequency (400 Hz) and on the precision in pointing the first arrivals. Clay material is very attenuating and heterogeneous indeed, so that the P and S waves' arrivals are often according to the distance from the sources and the characteristics of the travel distance (possible reflection and refractions).

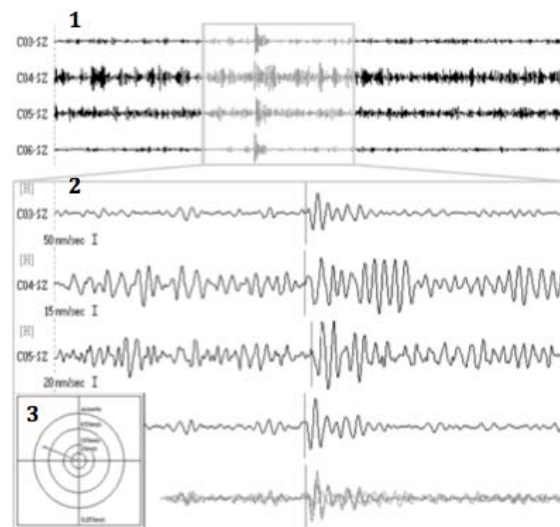





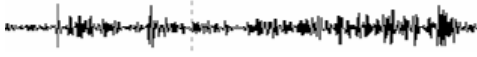
















Figure 2.1.5-4. Example of acoustic emission transient induced by the dynamics of landslide (1), six-second zoom window and arrival pointing (2), and direction of localisation through correlation (3).

The table 2.1.5-1 presents the different types of events that were detected during an active acceleration period in May 2010. They are categorised according to their time duration and frequency content. Amplitude can vary according to the distance between the source and the sensors because of the high attenuation of the medium, or the imminence of a higher event and thus cannot be used as a discrimination parameter.

Some of the events, like rockfalls or earthquakes, are not considered since we are only interested in the internal dynamics of the landslide. Some events are only observed around one or few sensors so that localisation can only be supposed to be near to these sensors. The occurrence of these last acoustic emissions is not common so we can neglect them, moreover because they are very weak on the spectrograms.

Table 2.1.5-1. Catalogue of the acoustic events identified by frequency analysis through their spectrogram patterns. Localisation is defined thanks to “nanoseismic monitoring” in cardinal directions (e.g. SE = South East) or with the names of the nearest sensors (e.g. C01). The events that may really be due to the internal dynamics and easy to localise are the ones whose localisation is grey-written (right column):

Spectrogram	Seismogram	Location
← 10s →	← 5s →	
		SE – C08
		C05 – C08
		SW – C07
		C04 – C07 only
		stable side
		C00 - NE
		C06
		crest – C03 noise? resampled 200Hz
		too weak SE rockfall, other velocities
		clear P, S waves arrivals local earthquake, other velocities

Recommended reading for a basic overview on principles of seismic sensors, recording, processing and analysis of seismic data:

Bormann, P. (Editor) 2002. *New Manual of Seismological Observatory Practice – NMSOP*, Volume 1&2, IASPEI, <http://www.iaspei.org/projects/NMSOP.html>

Stein, S. & Wysession, M. 2003. *An Introduction to Seismology, Earthquakes, and Earth Structure*. Blackwell Publishing

Mendecki, A. J. (Editor), 1997, *Seismic Monitoring in Mines*, Chapman & Hall, London, 262 pp.

2.1.6 ROCKFALL EVENT FREQUENCY

Federico Agliardi

Institution: UNIMIB

Rockfalls are among the most common landslide types in mountain areas, and are characterized by the failure and detachment of rock fragments (i.e. individual blocks, rock mass volumes) followed by a downward motion by free falling, bouncing, rolling, and sliding (Cruden and Varnes, 1996). Rockfalls originate from slopes of different sizes and natures and involve a wide range of volume scales. Preparatory conditions for rockfall occurrence include rock strength, the geometry, strength and hydraulic properties of discontinuities, rock mass weathering, as well as slope morphology and moisture availability. Rockfalls can be triggered by earthquakes (Kobayashi et al., 1990), rainfall or freeze-and thaw cycles (Matsuoka and Sakai, 1999). Nevertheless, large rockfall events often occur without clear triggers, due to the progressive weathering and damage of rock in suitable climatic conditions.

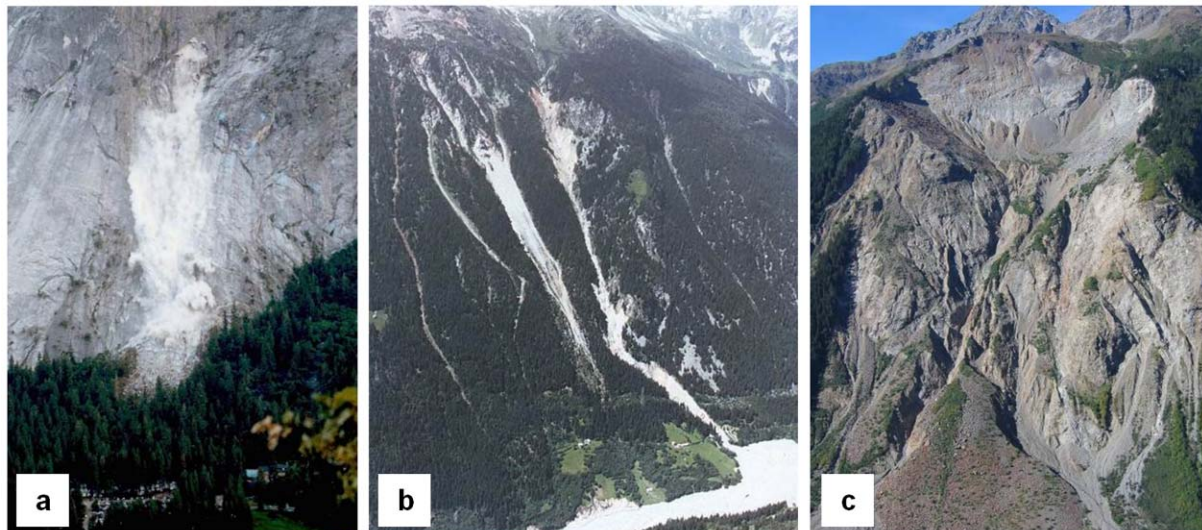


Figure 2.1.6-1. Rockfalls non-associated (a) and associated (b) to larger slope failures. a) 13 June 1999 rockfall above Camp Curry (Yosemite Valley, USA); b) the Val Pola slope (Valtellina, Italy) one day prior to 28 July 1987 and (c) after catastrophic collapse.

Deterministic approaches are rarely able to predict the location and timing of individual rockfall events. Instead, rockfalls as individual sources of hazard (i.e. independent on larger slope instabilities) are spatially-distributed phenomena with variable temporal frequency depending on environmental conditions and the considered event magnitude scenario. Therefore, despite few successful examples (Zvelebil and Moser, 2001), deterministic rockfall event forecasting is usually unfeasible, and the problem is dealt with in practice in terms of hazard, based on the statistical analysis of rockfall inventories and historical databases (Dussauge et al., 2003).

On the other hand, rockfalls have been also recognised to be among the precursory phenomena of larger rock slope failures undergoing accelerating creep prior to failure, due to rock mass damage and progressive failure (Voight, 1988). Suwa (1991) qualitatively reported increasing occurrence of rockfall and small landslides with time prior to a large failure event in a Japanese quarry. Azzoni et al. (1993) reported that, during the period preceding the catastrophic Val Pola rockslide/rock avalanche (Figure 2.1.6-1b,c), rockfall frequency

increased continuously (up to 100 events in the 24 hours before the slide), with a large rock pinnacle collapsing one hour before the main collapse. This behaviour has been commonly observed in a number of reported and unreported case studies on natural and engineered slopes, suggesting that change in rockfall activity may be potentially an early warning parameter. Nevertheless, literature dealing with the quantification of these phenomena remains scarce.

Rosser et al. (2008) characterised the spatial and temporal patterns of rockfall events in a small coastal cliff in the UK by periodic, high-resolution Terrestrial Laser Scanning (TLS) surveys. They demonstrated that the rate of rockfall activity (in terms of release volume per unit time and cliff area) undergoes non-linear increases prior to major failure events (Figure 2.1.6-2). This suggests that monitoring rockfall activity may allow successful prediction of rock slope failure provided that: 1) data are combined with reference models of failure mechanisms (Rosser et al., 2008), implying that mechanisms are not too complex; 2) rock face changes are characterised by TLS monitoring with sufficiently high survey frequency and sub-millimetric accuracy (Abellan et al., 2009).

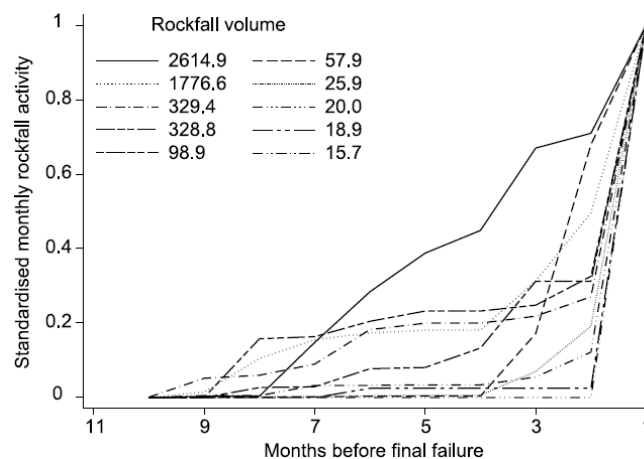


Figure 2.1.6-2. Increase in normalized rockfall activity (volume per month per square meter of rock face) prior to 10 major failure events (volumes in m³ in the legend), recorded by Rosser et al. (2008) by periodic, high-resolution TLS monitoring of a coastal cliff at Staithes (UK).

On the other hand, the practical use of precursory rockfall activity as an early warning parameter for large, complex rock slope failures remains very difficult despite widespread qualitative observations. Large rockslides usually expose wide, rapidly changing outcrops of disrupted rock masses, which can be prone to rockfalls also independently on the failure mechanisms of the main slope failure. Moreover, large rockslides are often characterised by spatially-variable failure mechanisms with complex temporal trends depending on seasonality and episodic external forcing (Crosta and Agliardi, 2003). All these effects are expected to bias the reliability of predictions, especially from an early warning perspective. Finally, monitoring rockfall activity on large natural slopes presents a number of practical difficulties. For example, for this application TLS data collected over large areas with very high accuracy and high survey frequency are needed, which may be hampered by logistical difficulties or unacceptable costs. Several attempts of correlating rockfall frequency and magnitude with seismic signals have also been made (Vilajosana et al., 2008). Nevertheless, this technique requires noise filtering and calibration through monitoring of multiple events, which may be practically unfeasible in large rockslide settings.

Available information suggests that monitoring rockfall frequency may provide very useful information on the evolution of rock slope failure, but its reliable application as an early warning parameter requires additional research.

References:

- Abellan, A., M. Jaboyedoff, T. Oppikofer, and J. M. Vilaplana (2009), Detection of millimetric deformation using a terrestrial laser scanner: experiment and application to a rockfall event, *Natural Hazards and Earth System Sciences*, 9, 365–372.
- Azzoni, A. S. Chiesa, A. Frassoni, and M. Govi (1992), The Valpola landslide, *Engineering Geology*, 33, 1, 59-70.
- Crosta, G., and F. Agliardi (2003), Failure forecast for large rock slides by surface displacement measurements, *Canadian Geotechnical Journal*, 40, 176– 191.
- Cruden, D.M., and D.J. Varnes, (1996), Landslides types and processes: chapter 3. In *Landslides: Investigation and Mitigation*, ed. A.K. Turner and R.L. Schuster. Transportation Research Board, 247, 36–71.
- Dussauge, C., J. R. Grasso, and A. Helmstetter (2003), Statistical analysis of rockfall volume distributions: implications for rockfall dynamics. *Journal of Geophysical Research*, 108(B6), 2286.
- Kobayashi, Y., E.L. Harp, T. Kagawa (1990), Simulation of rockfalls triggered by earthquakes. *Rock Mechanics & Rock Engineering*, 23,1–20.
- Matsuoka, N, H. Sakai (1999), Rockfall activity from an alpine cliff during thawing periods. *Geomorphology*, 28, 309–28.
- Rosser, N. J., M. Lim, D.N. Petley, S. Dunning, and R.J. Allison (2007), Patterns of precursory rockfall prior to slope failure, *Journal of Geophysical Research: Earth Surface.*, 112. F04014.
- Suwa, H. (1991), Visual observed failure of a rock slope in Japan, *Landslide News*, 5, 8–9.
- Vilajosana, L., E. Suriñach, A. Abellan, G. Khazaradze, D. Garcia, and J. Llosa (2008), Rockfall induced seismic signals: case study in Montserrat, Catalonia. *Natural Hazards and Earth System Sciences*, 8, 805–812.
- Voight, B. (1988), A method for prediction of volcanic eruption, *Nature*,332, 125– 130.
- Zvelebil, J., and M. Moser (2001), Monitoring Based Time-Prediction of Rock Falls: Three Case-Histories, *Physics and Chemistry of the Earth (B)*, 26, 2, 159-167.

2.2 HYDROLOGIC PROPERTIES

This section presents the parameters, which **directly describe the hydrological conditions** of the subsurface. The main goal is to detect changes in the hydrologic processes of the subsurface, **which might lead to an acceleration (or slowdown) of a mass movement, or could indirectly indicate it.** The parameters are, i.e.: groundwater level and pore-water pressure, soil suction, soil humidity, water balance (inflow and outflow, superficial flow), and surface and subsurface water quality.

2.2.1 GROUNDWATER LEVEL/PORE-WATER PRESSURE

Author: Anthony Lam and Håkon Heyerdahl
Institution: ICG

As the stability of soil and rock slopes could be significantly affected by groundwater level or pore-water pressure fluctuations within a slope, the establishment of the applicable groundwater conditions (i.e. thresholds) for early warning inevitably calls for slope instrumentation that monitors the groundwater levels and pore-water pressures. Groundwater level or pore-water pressure fluctuations could be used as input to a slope stability model to assess the temporal frequency of instability of landslides (Van Asch et al, 1997). Experience indicates that multiple standpipes and piezometers installed at different locations and depths are typically needed to adequately determine the groundwater regime and pore-water pressure distribution in order to resolve questions about landslide hydrology. Rock slope monitoring may be even more demanding, involving measurement of the pore-water pressures on discretely distributed joints.

Atmospheric pressure is usually taken as the zero pressure value and so a positive pore pressure zone exists below the water table. If there is no groundwater flow, the pore-water pressure is hydrostatic and the water level measured by a piezometer at any depth within the positive pore-pressure zone will coincide with the water table. Pore-water pressure inside a slope is normally not hydrostatic as groundwater flows under the influence of a hydraulic gradient. Hence, the groundwater levels measured by a piezometer in the positive pore-pressure zone will not coincide with the groundwater table, but normally will lie below it.

Depending on the local topography, artesian pressure instead of hydrostatic pore-water pressure distribution could be experienced. A typical situation for the development of artesian pressures could be due to the presence of hydraulic conductivity between the higher and the lower area of the hillsides. Some geological settings such as fine-grained sediments overlying bedrock, or coarse-grained sediments interbedded with layers of less impermeable sediments (colluvium or moraine) could be the sources of artesian pore-water pressures. Groundwater flowing through the permeable layers from the upper part of the slope could lead to artesian pore-water pressure in the fine-grained, less impermeable soil layers in the lower part of the slope.

Different aquifer systems demonstrate markedly different responses to rainfall depending on their storage characteristics. Aquifers may display rapid response to intense rainfall (storm response) or a gradual rise in groundwater level during the wet season (seasonal response). The storm component rises and falls in response to each significant storm. The seasonal component is generally lowest at the beginning of the wet season reaching a peak at some

time after the end of the wet season. Because of this variability in aquifer response, groundwater conditions for early warning should be based on groundwater levels or pore-water pressures measured in the field by appropriate standpipes and piezometers.

Groundwater levels and pore-water pressures must be recorded at sufficiently frequent intervals so that storm and seasonal responses could be distinguished. In situations where piezometers respond rapidly to storm events, monitoring would have to be continuous. Applying modern instrumentation technology, such continuous monitoring is readily available at a moderate cost. In the case of early warning observation, monitoring of groundwater conditions may focus on the basal shear zone to provide a direct measure of pore-water pressures that control landslide movement. If the location of the existing basal shear zone is known, sensors could be placed just above this zone to avoid being sheared or damaged.

Perched groundwater tables can exist above the main groundwater table where a localised reduction in strata permeability occurs in conjunction with recharge from above. It is quite common for the more permeable colluvium aquifers overlying the less permeable residual soils or deeply weathered rock to contain transient and permanent perched water tables, which could be of major importance for slope stability monitoring. Measurement of groundwater level or pore-water pressure in colluvium and deeply weathered rock profile could be difficult as conditions can vary rapidly with depth and areal extent. Perched water tables may be transient, developing rapidly in response to heavy rainfall and dissipating equally quickly.

Steep weathered rock slopes may also provide sufficient hydraulic gradient to initiate and develop pipes from naturally occurring voids and preferred flow paths. Hence, it could be difficult to adequately depict and confidently interpret the groundwater conditions, in particular when only limited number of piezometers without continuous monitoring capability have been adopted. There is also a need for prolonged monitoring, preferably over a number of years, in order to provide the basis for deriving the reference groundwater conditions.

For the complexity of the situation and the amount of data necessary to perform appropriate stability evaluations, financial constraints often constitute a limiting factor in the acquisition of sufficient pore-water pressure data. Boyle et al. (2009) reported that pore-water pressure records for a nine-year monitoring programme of a clayey slope in southeast Norway had concluded that several sensors in a vertical array improved the interpretation of the groundwater regime.

Early warning for slow-moving landslides

Monitoring the possible onset of landslide development at individual slopes would serve to provide information for slope stability assessment and the issue of early warning of landslides. It applies in particular to slopes showing signs of distress and prolonged deformation, and exhibiting signs of potentially large-scale failure that is difficult and costly to stabilize, e.g. the Canadian Turtle Mountain monitoring project (Read et al, 2005) and the continuous surveillance programme for the Åknes slide in Norway (Grøneng 2005, Blikra 2008).

Understanding the sensitivity of a slope to changes in pore-water pressure is useful in order to quantify the significance of the error in the pore-water pressure assumptions for the

assessment of slope stability. This was pointed out by Bishop (1955), as well as by Yucemen & Tang (1975) in their study of evaluation of uncertainties in the long-term stability of soil slopes. In addition, the monitoring of groundwater level and pore-water pressure could facilitate a better understanding of the hydrological conditions of individual slopes or catchments, and therefore establish a basis for the determination of applicable groundwater conditions or thresholds for early warning.

For slopes that are known to exhibit signs of distress and deformation (i.e. ductile failures), monitoring of groundwater level and pore-water pressure could facilitate the establishment of the linkages between pore pressure response at the basal shear zone and slope deformation. The basal shear zone should be monitored with piezometers isolated in that zone so that pore water pressures can be measured precisely where they are likely to have the greatest effect on slope deformation. These monitored pore-water pressures could be included in a deterministic slope stability model, being calibrated to determine what level of pore-water pressure is required for landslide movement. The correlation between the rate of landslide movement and the pore-pressure response could be useful for establishing conditions or thresholds for landslide early warning.

Long-term groundwater monitoring

Long-term groundwater monitoring could serve to provide information regarding the relationship between landslide deformations and pore-water pressure levels. Skempton et al. (1989) studied an ancient slow-moving landslide at Mam Tor, North Derbyshire in England. This landslide was known to be moving for centuries and the published data related to rainfall, piezometric levels, and displacements was dated back to 1965. The growing records of road damage on Mam Tor since 1909 have long demonstrated that slope movements occur during unusually wet winter months following wetter years. The study differentiates the storm response with the seasonal response by defining the slope movement owing to storm response as “the movement caused by a transient rise in piezometric level Δh above the level corresponding to a state of limiting equilibrium (F.S = 1.0) with the static residual strength” (see Figure 2.2.1-1).

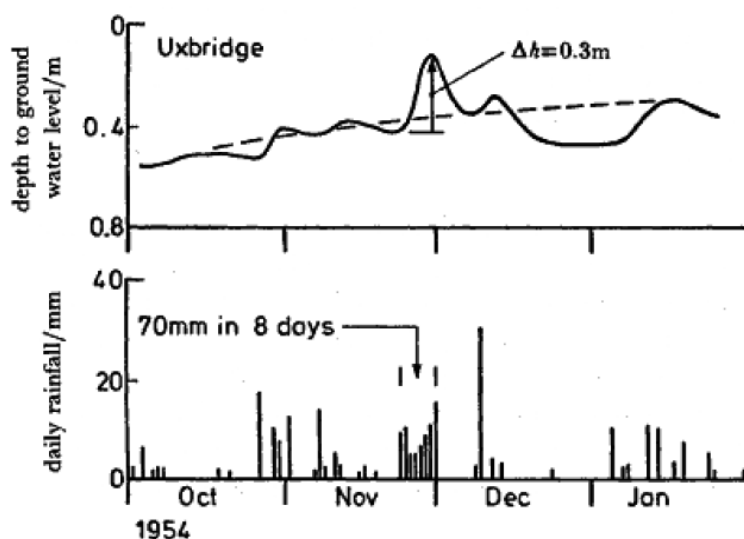


Figure 2.2.1-1. Relation between storm response and rainfall for Uxbridge, near the Mam Tor landslide in England (Skempton et al., 1989)

Calvello et al. (2007, 2009) studied the well-monitored slow-moving Porta Cassia Landslide in central Italy. They developed a numerical model to predict the movements along the pre-existing slip surface of this landslide from rainfall scenarios. All rainfall scenarios were based on the investigation of almost 20 years of continuous rainfall data. The model was also calibrated and validated using pore-water pressure and displacement data from a three-year monitoring period.

Simoni et al (2004) presented pore-water pressure monitoring results of an unstable clay slope in the Apennines. The measured transient pore-water pressure pulses generated by rainfall of relatively short duration tend to mimic pore-water pressure patterns that could trigger sliding, although no slope failures had occurred during the monitoring period.

Berti and Simoni (2011) measured pore-water pressures in clay shales that are prone to frequent sliding. They concluded that only seasonal fluctuations could be measured in the underlying shales, while response to a single rainfall resulted in clearly identifiable downward propagating pore-water pressure pulses in the soil /clay cover.

Reactivation of landslides

Pore-water pressure measurements may be especially important for reactivation of slow-moving landslides. Mansour (2009) reviewed the effect of pore-water pressure changes on the movement of reactivated slow-moving landslides based on an extensive field monitoring of pore-water pressures and slope displacements. The review concluded that the likely trigger of movement in slow-moving earth slides of moderate thickness is the seasonal changes in the boundary conditions that are affected by the hydrological variations over the year. He also defined the concept of critical pore-water pressure as “a certain pore water pressure threshold at which landslide displacement begins by loss of dynamic balance”.

Picarelli et al. (2004) investigated both first-time and reactivated slow-moving translational slides, which are common in the Italian Apennines. The continuous translational movements were triggered by seasonal fluctuations of piezometric levels (i.e. cyclic pore-water pressure changes) along the slip surfaces. Such changes had led to reduction of effective stresses, and consequently to a decrease of mobilized shear strength along slip surfaces.

Glastonbury and Fell (2008) studied 45 large slow-moving active or reactivated landslides and claimed that the landslide movements were predominantly controlled by fluctuations in piezometric pressures with varying levels of sensitivity. Mudslides with high silt, sand and gravel fractions displayed greater “storm response” (i.e. a higher groundwater level change for a given rainfall event) than those cases with lower coarse fractions. Furthermore, translational rock-debris slides showed reduced sensitivity to rainfall events as compared to mudslides. This is likely due to the much higher slide mass permeability in these slides.

Modelling landslide movements

Modelling of landslide movements taking into account pore-water pressure changes has been carried out for a number of cases. Corominas, et al (2005) studied the Vallcebre Landslide in the Eastern Pyrenees, Spain. The study indicated that the prediction of slope displacements

from the changes in groundwater levels was feasible, and a non-linear relationship between groundwater levels and landslide movements was also established. Further studies of the area were performed by Ferrari et al (2011) using a simple 2D model of two rigid blocks to numerically incorporate the effect of foot erosion, viscosity and pore-water pressures on the translational movement rate of the slope.

Cascini et al. (2010) stressed the importance of a reliable groundwater model to predict slow-moving landslides in clayey soils that exhibit continuous movements. They suggested that the main limitation of this type of model is the lack of reliable measurements of pore pressures along slip surfaces. Although it is possible to monitor the global changes in the groundwater level, it is mostly difficult to set up piezometers on the slip surface.

Effect of snowmelt

Blikra (2008) presented data for pore-water pressure response in a rock slope at Åknes, Norway, due to snowmelt. Rapid fluctuations up to 4.5 m/day were observed in one borehole (Figure 2.2.1-2). The observations coincided with increased displacements, measured by laser and extensometer sensors. Extensometers showed maximum movement of up to 0.25 mm/day, 1.3 mm/week, with a total movement of 22 mm/year.

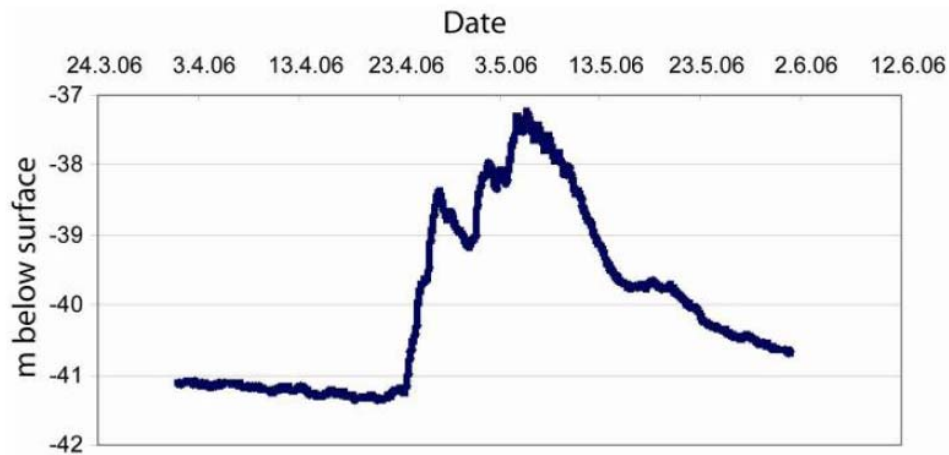


Figure 2.2.1-2. Water-level data during snowmelt in 2006 measured in a borehole at Åknes, Norway (Blikra 2008)

Francois et al (2007) studied the Triesenberg landslide located along the Rhine valley in the Principality of Liechtenstein, which covers an area of around 5 km². Variation in piezometric levels (i.e. pore-water pressures) in this large landslide is the major cause of movement. In the upper part of the slide, the piezometric behaviour is directly influenced by the inflow from the Valuna Valley. After snowmelt and storm events, more than 10 m high sharp piezometric peaks were recorded. In the lower part of the slide, the piezometric levels were smoothed by the landslide aquifer; hence, the peaks did not exceed 4 m.

Early warning for brittle slope failures

For slope failures which are brittle in nature, slope instrumentation and monitoring for the purpose of obtaining early warnings is a very difficult thing to do because the displacement leading up to a rain induced slope failure can be very small and the excess pore pressures in the individual slopes or catchments can be very localised both in plan and in elevation. Reliance on some kind of early warning observation could either lead to false alarms (giving rise to disillusion) or failure to detect instability because the instruments were not precisely located at the point of failure.

Relatively shallow landslides frequently occurred in tropically weathered rock slopes or hillsides, and they are normally triggered by short-duration, intense rainfall. The failure mechanism of these landslides is normally brittle in that they occur with little prior warning. The tropically-weathered rock profile is highly heterogeneous, in terms of the degree of weathering and hydrogeological conditions. Preferential flow paths exist in the ground, and the groundwater responses can be highly localized and very transient. In such circumstances, slope instrumentation would be of little use in monitoring the landslide development because there are few detectable signs of incipient slope failure.

Regional landslide warning

The need for regional landslides warning has been recognised in many places as an integral part of landslide risk management. For example, regional landslide warning systems have been implemented in Hong Kong (Chan et al 2003), San Francisco Bay Region (Keefer et al 1987; Wilson 1997), Rio de Janeiro (d'Orsi et al 2004), State of Oregon (Mills 2002), Lyme Regis UK (Cole and Davis 2002) and Washington (Baum 2005).

For slopes that are known to exhibit signs of distress and deformation, slope instrumentation applied to monitored landslide development would serve to provide information for slope stability assessment and the issue of early warning against landslides. However, it would be neither practical nor effective to monitor a large number of slopes or hillsides without any known distress and movement, for the purpose of providing landslide early warning.

Some regional landslide warning systems (e.g. the Hong Kong's Landslip Warning) are operated on the basis of recorded rainfall and the actual number of landslides reported during rainstorms. It is a general regional warning of possible landslide occurrence. It is not intended for predicting where and when a particular landslide would occur. The regional warning serves a number of useful purposes, such as triggering landslide emergency services in order to advise on emergency actions in the aftermath of landslides to mitigate the risk of possible further collapses, and alerting the general public to reduce their exposure to possible landslide danger.

References:

- Baum, R.L., Godt, J.W., Harop, E.L., McKenna, J.P. and McMullen, S.R. (2005). "Early warning of landslides for rail traffic between Seattle and Everett, Washington, USA". Proc., The International Conference on Landslide Risk Management, Vancouver, Canada, A.A. Balkema Publisher, 731-740.
- Berti, M. and Simoni, A. (2011). "Observation and analysis of near-surface pore-pressure measurements in clay-shales slopes". Hydrological processes, Wiley Online Library, DOI: 10.1002/hyp.7981.
- Bishop, A. W. (1955). The use of the slip circle in the stability analysis of slopes. *Geotechnique*, 5(1), 7-17.
- Blikra, L.H. (2008). "The Ånes rockslide; monitoring, threshold values and early warning". Proc.; 10th International Symposium on Landslides and Engineered Slopes, Xian, Peoples R. China, June 30-July

- 04, 2008 Landslides and engineered slopes: From the past to the future, Vols. 1 AND 2 , pp. 1089-1094
DOI: 10.1201/9780203885284-c143 2008
- Boyle, S., Karlsrud, K. and Høydal, Ø. (2009). "Pore-pressure response in a marine clay slope in southeast Norway". *Canadian Geotechnical Journal*, 46, 1391-1405.
- Calvello, M., Cascini, L., & Grimaldi, G. M. (2009). Displacement scenarios of a rainfall-controlled slow moving active slide in stiff clays. *Georisk: Assessment and Management of Risk for Engineered Systems and Geohazards*, 3(3), 116-125.
- Calvello, M., Cascini, L., & Sorbino, G. (2007). A numerical procedure for predicting rainfall-induced movements of active landslides along pre-existing slip surfaces. *Int. J. Numer. Anal. Meth. Geomech.*, 32, 327-351.
- Chan, R.K.S., Pang, P.L.R. and Pun, W.K. (2003). "Recent development in the Landslip Warning System in Hong Kong". *Proc., 14th Southeast Asian Geotechnical Conference, Hong Kong, Vol. 3*, 219-224.
- Cole, K. and Davis, G.M. (2002). "Landslide warning and emergency planning system in West Dorset, England". *Instability: Planning and Management*, Thomas Telford Publisher.
- Corsini, A., Pasuto, A., Soldati, M., & Zannoni, A. (2005). Field monitoring of the Corvara landslide (Dolomites, Italy) and its relevance for hazard assessment. *Geomorphology*, 66, 149-165.
- Corominas, J., Moya, J., Ledesma, A., Lloret, A., & Gili, J. A. (2005). Prediction of ground displacements and velocities from groundwater level changes at the Vallcebre landslide (East-ern Pyrenees, Spain). *Landslides*, 2, 83-96.
- d'Orsi, R.N., Feijó, R.L. and Paes, N.M. (2004). "2,500 operational days of Alerta Rio System: history and technical improvements of Rio de Janeiro Warning System for severe weather". *Proc., 9th International Symposium on Landslides, Rio de Janeiro, Vol. 1*, 831-836.
- Ferrari, A., Ledesa, A., Gonzales, D.A. and Corominas, J. (2011). "Effects of the foot evolution on the behaviour of slow-moving landslides". *Engineering Geology*, 117, 217-228.
- François, B., Tacher, L., Bonnard, C., Laloui, L., & Triguero, V. (2007). Numerical modelling of the hydrogeological and geomechanical behaviour of a large slope movement: The Triesenberg landslide (Liechtenstein). *Canadian Geotechnical Journal*, 44(7), 840-857.
- Glastonbury, J., & Fell, R. (2008). Geotechnical characteristics of large slow, very slow and extremely slow landslides. *Can. Geotech. J.*, 984-1005.
- Grøneng, G., Nilsen, B., Blikra, L.H. and Braathen, A. (2005). "The significance of climate on deformation in a rock-slope failure – the Åkerneset case study from Norway". *Proc., The International Conference on Landslide Risk Management, Vancouver, Canada, A.A. Balkema Publisher*, 725-729.
- Keefer, D.K., Wilson, R.C., Mark, R.K., Brabb, E.E., III, W.M.B., Ellen, S.D., Harp, E.L., Wiczorek, G.F., Alger, C.S. and Zatkan, R.S. (1987). "Real-time landslide warning during heavy rainfall". *Science* Vol. 238 No. 12, 921-925.
- Mansour, M. F. (2009). *Characteristic Behaviour of Slow Moving Slides*, PhD. Thesis. University of Alberta.
- Mills, K.A. (2002). "Oregon's debris flow warning system". *Geological Society of America Abstracts with Programs*, Vol. 34, No. 5, 25.
- National Research Council (2004). *Partnership*
- Picarelli, L., Urciuoli, G., & Russo, C. (2004). Effect of groundwater regime on the behaviour of clayey slopes. *Canadian Geotechnical Journal*(41), 467-484.
- Read, R.S., Langenberg, W., Cruden, D.M. Field, M., Stewart, R., Bland, H., Chen, Z., Froese, C.R., Cavers, D.S., Bidwell, A.K., Murray, C., Anderson, W.S., Jones, A., Chen, J., McIntyre, D., Kenway, D., Bingham, D.K., Weir-Jones, I., Seraphim, J., Spratt, D., Lamb, M., Herd, E., Martin, D., McLellan, P. and Pana, D. (2005). "Frank Slide a century later: the Turtle Mountain monitoring project". *Proc., The International Conference on Landslide Risk Management, Vancouver, Canada, A.A. Balkema Publisher*, 713-723.
- Simoni, A., Berti, M., Generali, M., Elmi, C. and Ghirotti, M. (2004). "Preliminary results from pore pressure monitoring on an unstable clay slope". *Engineering Geology*, 73, 118-128.
- Skempton, A. W., Leadbeater, A. D., & Chandler, R. J. (1989). *The Mam Tor Landslide, North Derbyshire*. *Phil. Trans. R. Soc. Lond. A*, 329, 503-547.
- Van Asch, T. J., & Buma, J. T. (1997). Modelling groundwater fluctuations and the frequency of movement of a landslide in the Terres Noires region of Barcelonnette (France). *Earth Surf. Processes Landforms*, 22, 131-141.
- Wilson, R.C. (1997). "Operation of a landslide warning system during the California storm sequence of January and February 1993". *Reviews in Engineering Geology*, Boulder, Geological Society of America.
- Yucemen, M. S., & Tang, W. H. (1975). Long term stability of soil slopes: a reliability approach. In Edgar Schutze (ed.). *Proceedings of the 2nd International Conference on Applications of Statistics and Probability in Soil and Structural Engineering*, (s. 215-229).

2.2.2 SOIL SUCTION

Author: Cascini Leonardo, Giuseppe Sorbino, Dario Peduto
Institution: UNISA

The behaviour of unsaturated soils on natural slopes and soil shear strength highly depends on water content change due to rainfall. The water content increase causes the decrease of soil suction and, as a consequence, the shear strength is decreased.

The reduction of suction values during infiltration may be a significant mechanism for shallow landslides on over steepened hillslopes or where soils or regolith are underlain by permeable substrates. In both environments, shallow slope failure may occur prior to the formation of positive pore pressures.

Whether shallow landslides commonly occur under partially saturated conditions is still controversial in part because of the lack of instrumental data on the hydrologic conditions within a naturally occurring shallow landslide (Godt et al., 2009).

In the following some details on soil suction and its measurement instruments are summarized referring to wider information which can be found in Lu and Likos (2004).

Total soil suction

Total soil suction measures the thermodynamic potential of soil pore water relative to a reference potential of free water. In particular, free water is the water containing no dissolved solutes, having no interactions with other phases that induce curvature at water interface, and having no external forces other than gravity. The physical and physicochemical mechanisms presiding over total soil suction are those that decrease the potential of the pore water relative to this reference state.

If temperature, gravity, and inertial effects are neglected, the primary mechanisms decreasing the potential of soil pore water can be associated with capillary effects, short-range adsorption (particle-pore water interaction) effects, and osmotic effects. The former mechanism characterizes only unsaturated soils whereas the latter two may occur under either saturated or unsaturated conditions.

Short-range adsorption effects derive from electrical and van der Waals force fields which occur in proximity of the solid-liquid (i.e. soil pore water) interface especially in fine grained soils.

Electrical and van der Waals fields decrease as the distance from the particle surface increases. As a consequence, the effects of short-range adsorption effects are higher at relatively low water content or degree of saturation since the adsorbed pore water appears as thin films surrounding the particles.

The osmotic effects result from solute dissolving in the pore water due to either externally introduced solutes or naturally occurring solutes adsorbed by the soil mineral surfaces. The chemical potential of the pore water can be reduced according to the concentration of dissolved solute.

The general term matric suction (measured in units of pressure as Ψ_m) stands for suction arising from the combined effects of capillarity and short-range adsorption. The term matric derives from the component of suction arising from interactions between the pore water and the soil particles, or soil matrix whereas the suction related to the presence of dissolved solutes can be referred to as osmotic suction, or Ψ_o .

Total soil suction Ψ_t corresponds to the algebraic sum of the matric and osmotic components:

$$\Psi_t = \Psi_m + \Psi_o$$

Units for soil suction

In geotechnical engineering practice the term *soil suction* refers to pore water potential in units of pressure. The International System of Units (SI) of suction pressure is pascal (Pa) and more often kilopascal (kPa) according to the more frequent range of magnitude among most practical unsaturated soil mechanics applications.

Brief overview of measurement techniques

Available experimental techniques suited for soil suction measurements and corresponding soilwater characteristic curves vary widely in terms of cost, complexity, and measurement range. Different typologies of techniques (laboratory or field methods) can measure different components of suction (matric or total). Laboratory techniques usually require undisturbed specimens so as to investigate the sensitivity of suction to soil fabric, especially for low-suction values where capillary effects tend to control the pore water retention behaviour. Disturbance effects can be less critical at higher suction values for highly expansive clays where particle surface adsorption or hydration mechanisms begin to dominate. Table 2.2.2-1 summarizes several common suction measurement techniques in terms of their applicable suction component, approximate measurement range as well as applicability in the laboratory or field (Lu and Likos, 2004).

Table 2.2.2-1. Summary of Common Laboratory and Field Techniques for Measuring Soil Suction (modified after Lu and Likos, 2004):

Suction Component measured	Technique/Sensor	Practical Suction Range (kPa)	Laboratory/Field
Matric suction	Tensiometers	0-100	Laboratory and field
	Axis translation techniques	0-1,500	Laboratory
	Electrical/thermal conductivity sensors	0-400	Laboratory/Field
Total suction	Contact filter paper method	Entire range	Laboratory and field
	Thermocouple psychrometers	100-8,000	Laboratory and field
	Chilled-mirror hygrometers	1,000-450,000	Laboratory
	Resistance/capacitance sensors	Entire range	Laboratory
	Isopiestic humidity control	4,000-400,000	Laboratory
	Two-pressure humidity control	10,000-600,000	Laboratory
	Noncontact filter paper method	1,000-500,000	Laboratory and field

Tensiometers are one of the most used techniques to directly measure negative pore-water pressure. They exploit the unique properties of high air-entry (HAE) materials which are characterized by microscopic pores of relatively uniform size and size distribution. When water saturates an HAE material, the surface tension at the gas-liquid interfaces formed

among the material's pores allows a pressure difference between gas and liquid phases located on either side. Surface tension acts as a membrane for separating the two phases, thus allowing negative water pressure to be directly measured, as in a tensiometer (Lu and Likos, 2004).

The expression "high air-entry" is associated with the fact that relatively high pressure is required for air to break through the membrane formed by surface tension.

The hydraulic conductivity decreases with increasing air entry pressure due to the increasingly smaller pore sizes of the material.

A comprehensive description of tensiometer measurement principles, construction guidelines, operating procedures, and applications is provided by Stannard (1992). A standard tensiometer consists of a water-filled tube with an HAE ceramic tip at one end and some type of sensor for measuring negative water pressure at the other. The ceramic tip usually has the shape of an inverted cup or small probe and it is able to create a saturated hydraulic connection between the soil pore water, the water in the tensiometer body, and the pressure sensor. The pressure sensor may be either a mechanical Bourdon-type gauge or an electronic diaphragm-type transducer (Lu and Likos, 2004).

A schematic diagram for a commonly used type of "small-tip" laboratory tensiometer is shown as Figure 2.2.2-1 (Lu and Likos, 2004).

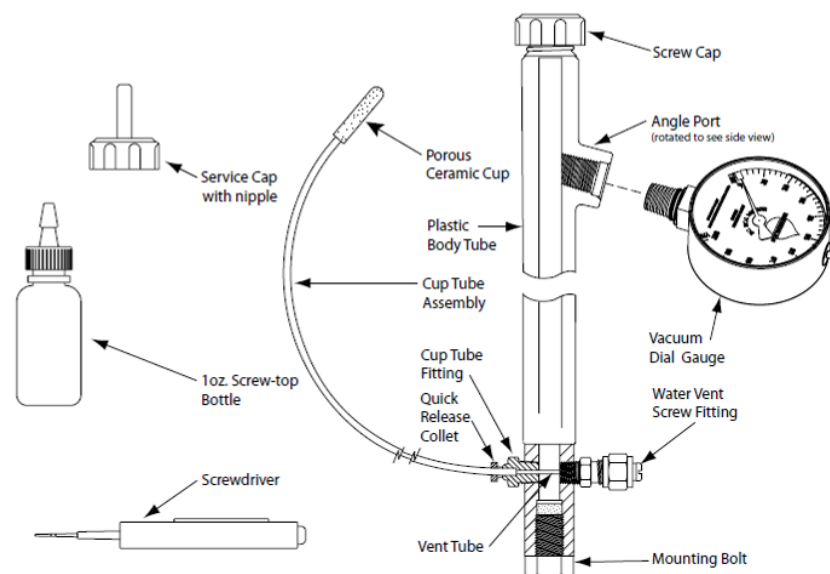


Figure 2.2.2-1. Schematic drawing of small-tip laboratory tensiometer (Soilmoisture Equipment Corp., 2003).

As for field measurements the used tensiometers (Figure 2.2.2-2) are similar in construction and identical in operating principle to those used for laboratory tests.

Negative pressure is transmitted through the saturated pores of the HAE ceramic tip such that water is withdrawn from the tensiometer until the internal pressure in the sensor body is equivalent to the matric potential of the soil water. If the soil is subsequently wetted, water flows in the opposite direction from the soil to the measurement system until a new equilibrium at a new pressure is attained (Lu and Likos, 2004).



Figure 2.2.2-2. Quick-draw field tensiometer (Soilmoisture Equipment Corp., 2003).

Since the sensor tip is permeable to dissolved solutes, the pore water osmotic potential does not influence the pressure measurement. The measurement, therefore, becomes a direct measurement of matric suction if gravitational potential is also considered (i.e. corrected for the difference in elevation between the sensor probe and the pressure gauge).

Tensiometer measurement has response time which is a function of the system compressibility, the hydraulic conductivity and thickness of the sensor tip, and the soil hydraulic conductivity. System compressibility is controlled by both the air bubbles in the system and liquid exchange volume necessary for the sensor to register an equilibrium pressure change. Most common response times are on the order of 1-10 minutes.

The tensiometer system is saturated with de-aired water before the test starts and temporary vacuum could be usefully applied for the removal of air bubbles from the system.

Whether measurements over prolonged testing periods are required the system must be periodically resaturated through the service port (Figure 2.2.2-1).

The values of matric suction obtainable using tensiometers are limited by the air-entry pressure of the porous ceramic tip and the capacity for water to sustain high negative pressures without cavitation occurring. Usually tensiometric standard testing measurements are limited to about 70 to 80 kPa.

Alternative types of “high-capacity” tensiometers incorporating extremely small, smooth-walled sensing reservoirs and relatively high air-entry pressure ceramics have been developed (e.g. Ridley and Burland, 1993; Guan and Fredlund, 1997; Tarantino and Mongiovi, 2001; Lu and Likos, 2004). In order to derive matric suction values approaching about 1500 kPa these types of sensors have been coupled with specialized operating procedures (e.g. cyclic prepressurization techniques). The approach associated with these types of sensors has been used to minimize potential sites for nucleation and thus fully realize the tensile strength of water, which although still largely uncertain has been shown experimentally and theoretically to be in the range of megapascals (e.g. Tabor, 1979; Zheng et al., 1991).

Peck and Rabbidge (1969) and Bocking and Fredlund (1979) focus on “osmotic” tensiometers using confined and prestressed (positively pressurized) aqueous solutions rather than free water for the transmission of negative pore pressure through the measurement system. To date, however, difficulties associated with drift and temperature sensitivity have largely precluded the use of osmotic tensiometers in practice (Lu and Likos, 2004).

References

- Bocking, K. A., and Fredlund, D. G., 1979, "Use of the osmotic tensiometer to measure negative pore water pressure," *Geotechnical Testing Journal*, **2**(1), 3–10.
- Guan, Y., and Fredlund, D. G., 1997, "Use of the tensile strength of water for the direct measurement of high soil suction," *Canadian Geotechnical Journal*, **34**, 604–614
- Godt, J. W., R. L. Baum, and N. Lu (2009), *Landsliding in partially saturated materials*, *Geophysical Research Letters*, **36**, L02403, doi:10.1029/2008GL035996.
- Lu N. and Likos W.J., 2004. *Unsaturated soil mechanics*. Published by John Wiley & Sons, Inc., Hoboken, New Jersey
- Peck, A. J., and Rabbidge, R. M., 1969, "Design and performance of an osmotic tensiometer for measuring capillary potential," *Soil Science Society of America Proceedings*, **33**, No. 2, 196–202
- Ridley, A. M., and Burland, J. B., 1993, "A new instrument for the measurement of soil moisture suction," *Getotechnique*, **43**(2), 321–324.
- Stannard, D. I., 1992, "Tensiometers—Theory, Construction, and Use," *Geotechnical Testing Journal*, **15**(1), 48–58.
- Tarantino, A., and Mongiovi, L., 2001, "Experimental procedures and cavitation mechanisms in tensiometer measurements," *Geotechnical and Geological Engineering*, **19**, 189–210.

2.2.3 SOIL HUMIDITY

Author: Emilia Damiano, Luciano Picarelli
Institution: AMRA

Slope stability is affected by pore pressure regime. In slopes where the groundwater table is very deep or absent, pore pressures are below the atmospheric pressure so any change in soil moisture due to rainwater infiltration or snowmelt can significantly modify suction and state of stress of the soil. In some cases, this can lead to slope failure. This is mainly true for granular soils which cover steep slopes (slope angle higher than friction angle of the soil in saturated conditions).

These kinds of covers, which may be the result of weathering (residual soils) or of air-fall deposition, are stable due to the beneficial effect of matric suction on soil shear strength. During wet periods, the change in the water content due to infiltration causes the increase of the weight of the soil cover (this is remarkable in the case of loose air-fall pyroclastic soils) and a significant decrease of matric suction. As a result, the additional shear strength provided by the matric suction can be reduced enough to trigger a shallow landslide (Fredlund and Rahardjo 1993). Moreover rainfall events may result in positive pore-water pressure development in the steep slopes as a result of the formation of a perched water table. During the dry phases between successive wet periods, the effects of rainwater infiltration are eventually balanced by downslope drainage and evapo-transpiration. This explains the substantial hydraulic equilibrium of the slope, which is characterised by transient fluctuations of the water content around a more or less constant average value; slope failure occurs only when such a balance is altered by intense rains which lead to excessive increases in the water content. However, such a process takes a period of time which depends on the initial water content, on the hydraulic and mechanical properties of the soil and on the length of water infiltration paths. In order to predict the time to failure, such factors should be considered jointly with the features of the expected precipitations.

The continuous monitoring of suction and/or of water content or of pore pressures, as indicators of stability conditions, can provide fundamental information for the assessment of the landslide hazard. A number of studies have focused on monitoring the pore-water pressures. However, sensors like piezometers and tensiometers have some limitations due to their maintenance, performance and reliability. Since pore-water pressure changes in unsaturated soils go hand in hand with changes in water content (through the Soil Water Retention Curve (SWRC)) an alternative method for the setup of an early warning system can be based on monitoring of soil moisture. Moisture content measuring devices such as ThetaProbe, Time Domain Reflectometer (TDR) waveguides and others overcome the disadvantages of pore-water pressure sensors. However, little data about actual slope monitoring during infiltration processes on steep slopes are available in literature. In most cases, the measurements were too infrequent to shed light on the dynamics of infiltration processes in the hours immediately before the failure. With respect to this, actual slope monitoring data has been supplemented with model slope experimental data, in which measurements of many hydrological and mechanical variables can be carried out with high temporal and spatial resolution until the slope failure is triggered (Eckersley, 1990; Take et al., 2004; Moriwacki et al., 2004; Olivares et al., 2009). Recent application in laboratory tests carried out by Tohari et al. (2007), Greco et al. (2010), Chae and Kim (2011) on small-scale

model slopes showed that monitoring of volumetric water content in the soil can be very useful for the prediction of slope failures.

In particular, Greco et al. (2010) showed that monitoring of soil volumetric water content seemed more useful than soil suction monitoring for early warning purposes, since water content grew smoothly during the entire infiltration processes, while soil suction showed abrupt steep fronts attaining its final value much before slope failure (Figure 2.2.3-1).

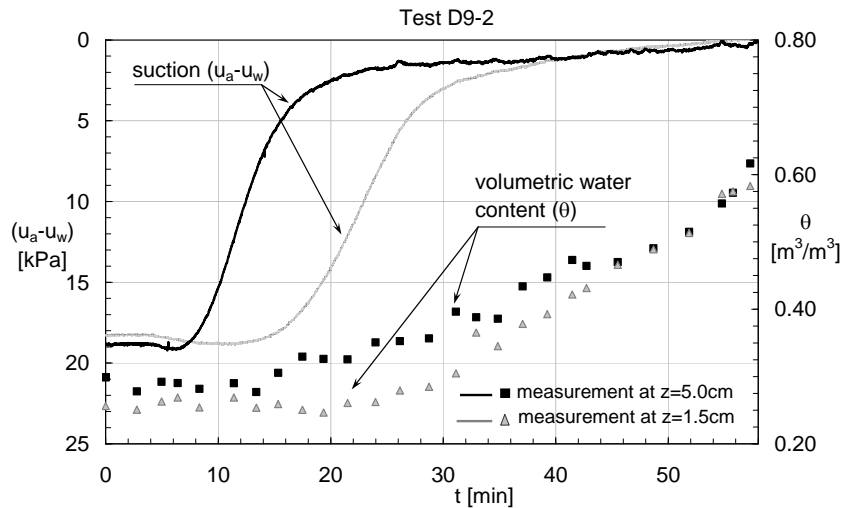


Figure 2.2.3-1. Matric suction and volumetric water content time histories during an infiltration test (Greco et al., 2010).

Tohari et al. (2007) proposed a warning algorithm based on volumetric water content measurements based on results of laboratory rainfall-induced slope failure (Figure 2.2.3-2). The authors define a critical time for evacuation as the time required for the wetting front to travel from the moisture content sensor head to the impervious layer or initial groundwater level (from t_1 to t_2). The initiation of the second stage of increase in the moisture content of the near surface soil represents the hydrologic condition in which the groundwater table starts to rise towards the slope surface. Thus, the corresponding time t_2 can be designated to trigger a final warning against the slope failure hazard. The extent of time for evacuation will depend on the depth of the sensor, with respect to the impervious layer or initial groundwater, as well as on the antecedent soil moisture condition. Consequently, the depth of the impermeable layer or groundwater level must also be determined through adequate subsurface investigations to determine an optimum depth for installation of the sensor for the effective prediction of failure initiation.

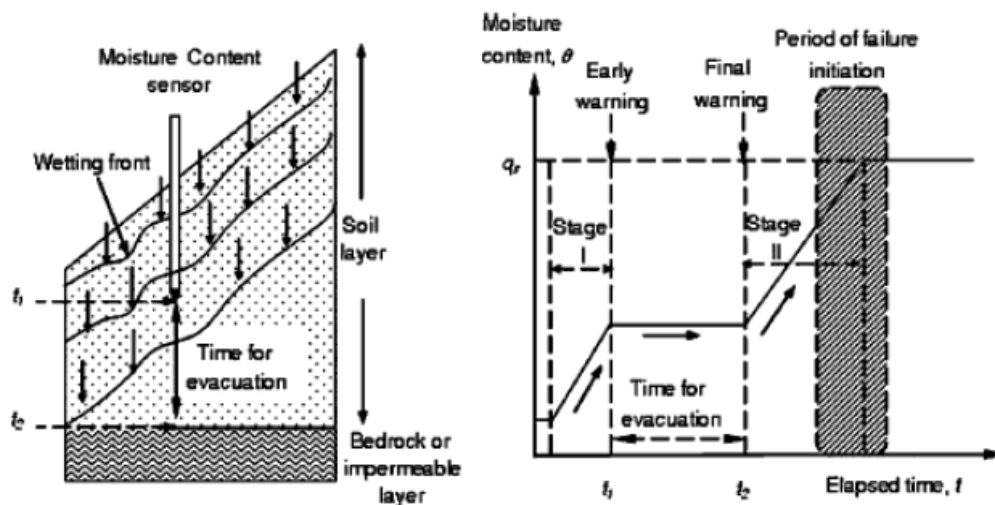


Figure 2.2.3-2. The conceptual prediction method for rainfall-induced landslide based on moisture content measurements (Tohari et al., 2007).

Recently, Chae and Kim (2011) installed an in situ real-time monitoring system. They evaluated the response of volumetric water content to rainfall events in steep slopes constituted by gneiss weathered soil in an area subjected to debris flows in Deoksan, Korea. The field monitoring showed that a direct proportional relationship exists between the effective cumulative rainfall and the gradient of volumetric water content per unit of time suggesting a threshold value of volumetric water content gradient which could serve as the basis of an early warning system for landslides in the monitored area.

However, all the experiences show it is crucial to understand the pre-failure and failure mechanism in order to recognize the characteristics of the evolution of soil moisture if it is to be used as an indicator of impending failure.

The Time Domain Reflectometer technique (TDR) is the most common application for monitoring soil moisture in shallow soil layers. It allows retrieving the mean value that volumetric water content assumes around a waveguide buried in the soil. The experimental device consists of an electromagnetic pulse generator connected, through a coaxial cable, to a metallic probe (waveguide) that is a few decimetres long. An electromagnetic pulse is sent through the soil, and the reflected signal is acquired. The speed of electromagnetic waves propagating through the soil depends on the bulk soil dielectric permittivity, ϵ_r , while the attenuation of the signal mainly depends on bulk soil electrical conductivity, σ . Both the variables are in turn related to soil volumetric water content, θ (Campbell, 1990). The $\epsilon_r(\theta)$ and $\sigma(\theta)$ relationships are usually experimentally determined in laboratory, by carrying out a series of coupled gravimetric and TDR water content measurements over undisturbed specimens. Usually, with a TDR acquisition only the travel time of an electromagnetic pulse through the soil is measured, providing the average bulk soil dielectric permittivity within the investigated soil volume. As a consequence, only the mean volumetric water content throughout the investigated volume is obtained (Topp et al., 1980).

Recently, a novel TDR measurement interpretation technique has been developed, which allows the inverse determination of the water content profile along the entire length of the

metallic probe buried in the soil. This technique is based upon the numerical integration of the transmission lines equations, which describe the electromagnetic transient along the metallic probe (Ramo et al., 1994). By minimizing the difference between the experimental TDR wave traces and the simulated wave traces, the distributions of bulk soil dielectric permittivity and electrical conductivity along the probe are obtained. The knowledge of the empirical relationships linking volumetric water content with bulk soil dielectric permittivity and electrical conductivity (which are obtained in the same way as with usual TDR measurements) allows the estimation of the volumetric water content distribution along the probe (Greco, 2006; Greco and Guida, 2008).

The acquisition of a TDR wave trace lasts a few seconds, while the elaborations for water content profile retrieval take a few minutes, thus real-time measurements can be easily carried out with high temporal frequency. Moreover, an increase in the length of the rods can lead to even more significant information providing data over greater depths. The same result could be obtained by installation of a series of TDR devices at different depths.

An application of such a technique has been performed in small-scale slope tests on granular soils (Greco et al., 2010), which shows the usefulness of monitoring the volumetric water content profiles in shallow soil layers for prediction of landslide triggering (Figure 2.2.3-3). Indeed, in loose sandy deposits subject to uniform rainfall, the retrieved water content profiles were characterised by the presence of steep water content vertical gradients during the initial phase of the infiltration process. This behaviour is typical of very coarse soils, for which hydraulic conductivity dramatically reduces at low water contents. Afterwards, the deepest part of the soil profile starts wetting as well, and the acquired profiles tend to smoothen until failure approaching the value of soil porosity. Therefore, a deep knowledge of the dynamics of the infiltration process can be achieved.

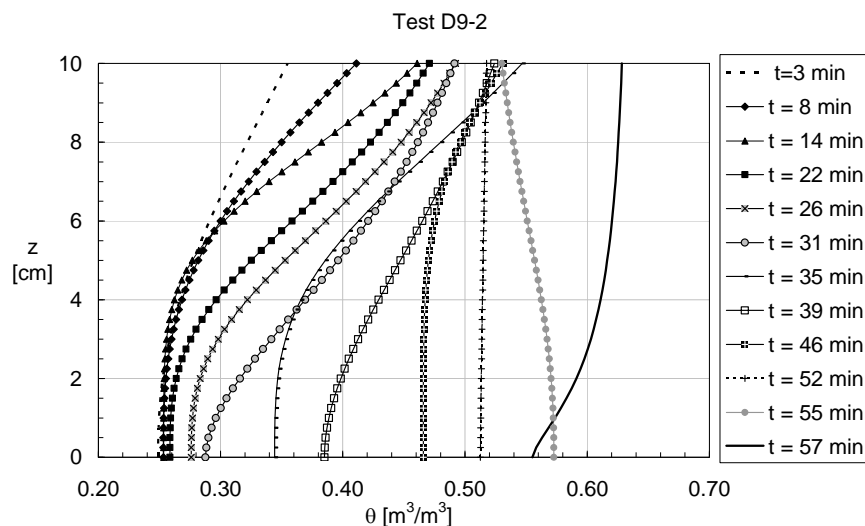


Figure 2.2.3-3. Volumetric water content profiles acquired by TDR probe at various stages of an infiltration test on small-scale slope (Greco et al., 2010).

The TDR device is not a novelty as such, since it has been used for a long time to measure the average water content of soil. However, obtaining complete vertical profiles of the volumetric water content along the entire rod length represents a significant improvement, contributing to the interpretation of the evolution of the infiltration process from the ground surface. In the near future, devices as TDR probes would represent fundamental tools for timely alerting of

landslide triggering by capturing a significant indicator of incoming slope failure. Due to their low cost and flexibility they can be extensively used, possibly coupled and/or used in conjunction with other devices and procedures for prediction of landslide triggering. This approach has already been adopted, for example in an area at risk located along the Seattle-Everett rail connection. The advisory signal corresponds to the reading of a critical volumetric water content, while warning is associated with an established rainfall intensity-duration threshold and warning is launched for assigned pore pressure values (Baum et al., 2005).

References

- Baum, R.L., Godt, J.W., Harp, E.L., McKenna, J.P., McMullen, S.R. (2005). "Early warning of landslides for rail traffic between Seattle and Everett, Washington, U.S.A." Proc. Int. Conf. on Landslide Risk Management, Vancouver: 731-740.
- Campbell, J.E. (1990). "Dielectric properties and influence of conductivity in soils at one to fifty megahertz". Soil Sci. Soc. Am. J. 54, 332-341.
- Chae, B-G, Kim, M-I (2011). "Suggestion of a method for landslide early warning using the change in volumetric water content gradient due to rainfall infiltration". Environ. Earth Sci.,
- Eckersely, J. (1990). "Instrumented laboratory flowslides". Geotechnique, 40 (3), 489-502.
- Fredlund, D.G., Rahardjo H. (1993). Soil mechanics for unsaturated soils. Wiley, New York, p 517.
- Greco, R. (2006). "Soil water content inverse profiling from single TDR waveforms". J. Hydrol. 317, 325-339.
- Greco, R., Guida, A. (2008). "Field measurements of topsoil moisture profiles by vertical TDR probes". Journal of Hydrology, 348, 442-451.
- Greco, R., Guida, A., Damiano, E., Olivares, L. (2010). "Soil water content and suction monitoring in model slopes for shallow flowslides early warning applications". Physics and Chemistry of the Earth, Elsevier Ltd., 35,127-136.
- Moriwacki, H., Inokuchi, T., Hattanji, T., Sassa, K., Ochiai, H., Wang, G. (2004). "Failure processes in a full-scale landslide experiment using a rainfall simulator". Landslides 1(4), 277-288.
- Olivares, L., Damiano, E., Greco, R., Zeni, L., Picarelli, L., Minardo, A., Guida, A., Bernini, R. (2009). "An instrumented flume to investigate the mechanics of rainfall-induced landslides in unsaturated granular soils". Geotech. Testing J., ASTM, 32(2), 1-11.
- Ramo, S., Whinnery, J., Van Duzer, T. (1994). "Fields and Waves in Communication Electronics". J. Wiley and Sons, New York.
- Take, W.A., Bolton, P., Wong, C.P., Yeung F.J. (2004). "Evaluation of landslide triggering mechanisms in model fill slopes". Landslides 1 (3), 173-184.
- Tohari, A., Nishigaki M., and Komatsu, M. (2007). "Laboratory rainfall-induced slope failure with moisture content measurement". Journal of Geotechnical and Geoenvironmental Engineering. 133 (5), 575-587.
- Topp, G.C., Davis, J.L., Annan, A.P. (1980). "Electromagnetic determination of soil water content: measurement in coaxial transmission lines". Water Resour. Res., 16, 574-582.

2.2.4 WATER BALANCE: INFLOW AND OUTFLOW, SURFACE FLOW

Anthony Lam and Håkon Heyerdahl

International Centre of Geohazards

The hydrological cycle

When moisture from the atmosphere falls to the Earth's surface it involves the movement of water along precipitation, evapotranspiration, surface flow (runoff), subsurface flow and groundwater pathways. In essence, water is evaporated from the land, oceans and vegetation to the atmosphere, using the radiant energy from the sun, and is recycled back in the form of rain, snow or hail. This constant movement of water above, on, and below the earth's surface is the hydrological cycle (see Figure 2.2.4-1).

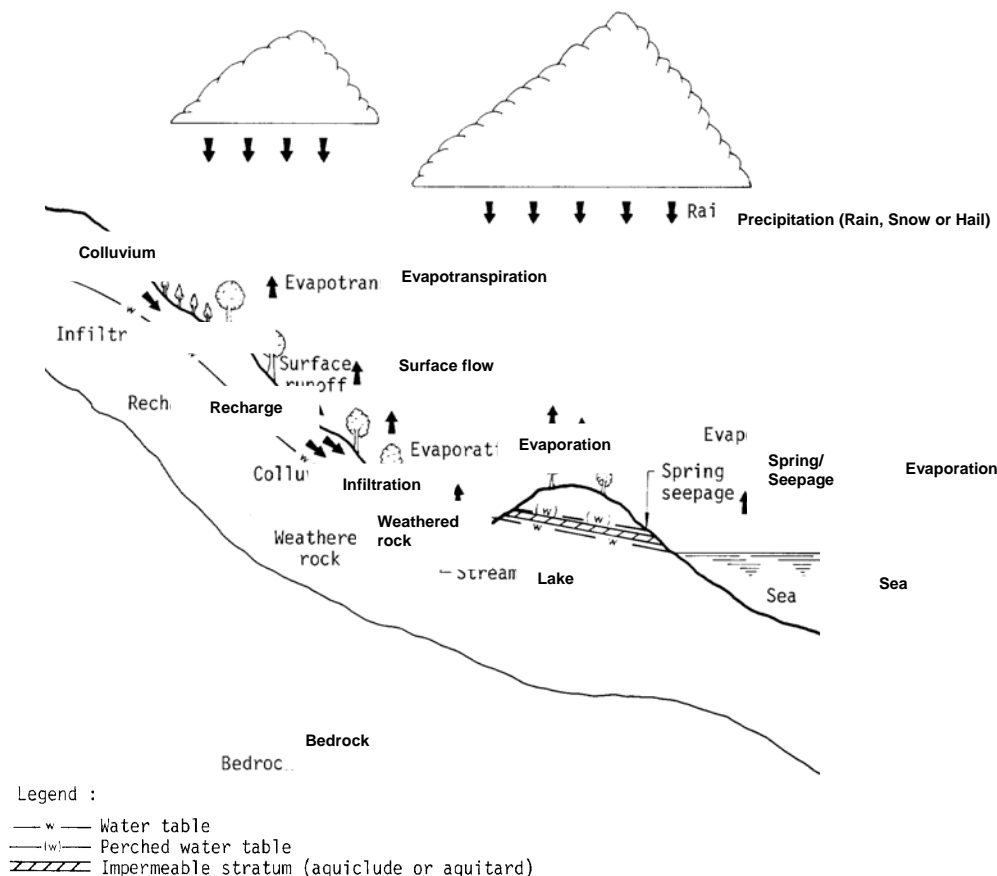


Figure 2.2.4-1. Simplified representation of the hydrological cycle

Precipitation (excluding snow and hail) wets vegetation, directly enters surface water bodies or begins to infiltrate the ground to replenish soil moisture. Excess water percolates to the zone of saturation, or groundwater, from where it moves downward and laterally to sites of groundwater discharge. The rate of infiltration varies with land use, soil characteristics and the duration and intensity of the rainfall event. If the rate of precipitation exceeds the rate of infiltration this leads to overland flow. Water reaching streams, both by surface flow and

subsurface flow eventually moves to the sea where it is again evaporated to perpetuate the hydrological cycle.

In terms of the stability of hillsides, the land-based portion of the hydrological cycle is of most interest. Inflow of water into catchment and landslide-prone areas may be derived from precipitation, lakes or rivers, and outflow from the system can be as evapotranspiration, surface flow (i.e. runoff) and subsurface flow. Changes in ground water (i.e. soil moisture and ground water storage) are the parts of the inflow which become incorporated into the ground water system. The above elements form the basis of the water balance within a catchment or a landslide body, which can be represented by the following equation:

$$\begin{array}{l} \text{Precipitation} \\ \text{and / or inflow} \\ \text{from lakes or} \\ \text{rivers} \end{array} = \text{Evapotranspiration} + \text{Surface flow (i.e. runoff)} + \text{Subsurface} \\ \text{flow} + \text{Change in soil moisture} + \text{Change in groundwater} \\ \text{storage (i.e. groundwater levels)}$$

Evapotranspiration is the combination of direct evaporation from the ground surface and transpiration through plant leaves. Surface flow (i.e. runoff) is that proportion of inflow (e.g. precipitation) that fails to penetrate the ground surface and flows from a catchment into streams, lakes and the sea. Subsurface flow is normally derived from precipitation that infiltrates the ground, down to the water table and then percolates into streams. Depending on the inflow and outflow elements of the water balance equation, changes in groundwater storage may be positive or negative. Where, for example, precipitation is low and evapotranspiration exceeds inflow, a loss of soil moisture will occur. This eventually results in a soil moisture deficit. Soil moisture deficit is the quantity of water in millimetres required to restore the soil to field capacity where field capacity is the maximum amount of water held by the soil before free drainage occurs. When precipitation exceeds outflow from the system, the soil moisture deficit is reduced until the soil becomes fully saturated. Thereafter, changes in groundwater storage become positive and recharge to groundwater occurs.

2.2.4.2 Water balance models

Water balance is not a landslide indicator; its role in early warning of landslides can be attributed to the knowledge concerning the interaction between the various elements of the water balance equation. The main elements in the water balance equation that have a direct impact on the stability of hillsides are the changes in soil moisture and groundwater storage (i.e. groundwater levels/pore-water pressures). Where the hillside has some groundwater storage capacity that must be filled before pore-water pressure can reach critical levels, the soil moisture condition at the onset of a storm event could be a significant precondition for triggering landslides. The reason that soil moisture plays a critical role in hillside stability is due to its ability to alter pore-water pressure within a slope, hence, the effective stresses and the shear strength of soils. The unsaturated soil properties play an important role in this picture, since the infiltration rate will be governed both by the suction in the soil and the unsaturated permeability, which also is a function of the soil moisture.

Although not constituting a direct landslide indicator, the water balance within a watershed may be an indicator for possible debris-flow initiation. Such events are strongly connected to water discharge and erosion in channels. Hence, the hydrologic balance and assessment of

resulting discharge may give guidance to early warning for such events. Many empirical models implicitly take this into account, by a long-term component for rainfall coupled with a short-term intense rainfall component as basis for early warning.

Berti and Simoni (2000, 2005) reported studies of debris flow initiation based on channel bed mobilization in mountainous areas in Italy. Channels incised in deep deposits, emerging from steep sloping basins with concentrated flow had higher likelihood of such initiation. The hydrological response of the initiation area to rainfall was used to model channel runoff, and the modelling was capable of predicting the observed hydrological response and giving a physical basis for a debris flow triggering threshold.

Whilst soil moisture and pore-water pressure could be determined using direct in-situ measurements, such measurements can be difficult and expensive to carry out on a regional scale. For this reason, water balance models are popular for predicting changes in soil moisture and pore-water pressure. Using the water balance approach, Barton & Thomson (1986) developed a model for predicting changes in soil moisture and groundwater levels due to meteorological changes. The model has been applied to a cliff site in Hampshire, England and the results show a good model fit to the observed data. Crozier (1999) used a water balance model and landslide data in Wellington City, New Zealand to develop an empirical correlation between soil moisture and landslide triggering. Wilson (2002) adopted a water balance model by Thornthwaite and Mather (1955) to assess the seasonal variation in soil moisture in the San Francisco Bay region.

Ponziani et al. (2011) defined a procedure for landslide warning by combining rainfall thresholds and estimates of soil moisture conditions derived from a water balance model calibrated and tested with local soil moisture and pore-water pressure observations. The procedure was developed by analyzing the most severe widespread landslide events that occurred in the Umbria Region of central Italy during the period 1991 to 2001, and documented in the AVI (Italian Vulnerable Areas) inventory.

Water balance models are semi-empirical in that they are derived on the basis of local knowledge of a specific site or area, hence, their use should be confined to that site/area. Whilst direct observation of soil moisture and pore-water pressure in existing landslide areas or landslide-susceptible areas can provide a more robust indicator of impending slope stability, water balance models that are properly tested and calibrated with actual soil moisture and pore-water pressure observations may still be useful tools for landslide early warning purposes. However, the inherent uncertainties in weather simulation, hydrological modelling, and geotechnical models mean that the predicted threshold value for a particular landslide indicator (e.g. soil moisture) can contain high degrees of uncertainties, in particular if the models are only verified on a local scale. The integration of in-situ measurements, remote sensing and simulation models may provide more reliable estimations of threshold values for landslide indicators (e.g. soil moisture) at the temporal and spatial resolutions required for operational activities related to landslide warning systems (Ray and Jacobs 2007; Capparelli and Versace 2010; Greco et al. 2010; Ray et al. 2010).

References:

- Barton, M.E. & Thomson, R.I. (1986). A model for predicting ground water level response to metrological changes. In Cripps, J.C. et al (Eds). *Groundwater in Engineering Geology*. Eng Geol.
- Berti, M., Genevois, R., LaHusen, R., Simoni, A. And Tecca, P.R. (2000). Debris flow monitoring in the Aquabona watershed on the Dolomites (Italian Alps). *Phys. Chem. Earth*, 25, 9, 707-715, Elsevier Science Ltd. 1464-1909/00/\$.
- Berti, M. and Simoni, A. (2005). Experimental evidences and numerical modelling of debris flow initiated by channel runoff. *Landslides*, 2, 171-182. doi: 10.1007/s10346-005-0062-4.
- Capparelli, G. & Versace, P. (2010) FLAIR and SUSHI: two mathematical models for early warning of landslides induced by rainfall. *Landslides*. doi:10.1007/s10346-010-0228-6.
- Crozier, M.J. (1999). Prediction of rainfall-triggered landslides: a test of the antecedent water status model. *Earth Surface Processes & Landforms* 24, 825-833.
- Greco, R., Guida, A., Damiano, E. & Olivares, L. (2010). Soil water content and suction monitoring in model slopes for shallow flowslides early warning applications. *Physics and Chemistry of the Earth* 35(3–5):127–136.
- Ponziani, F., Pandolfo, C., Stelluti, M., Berni, N., Brocca, L. & Moramarco, T., (2011). Assessment of rainfall thersholds and soil moisture modelling for operation hydrogeological risk prevention in the Umbria region (central Italy) *Landslides*. doi:10.1007/s10346-011-0287-3.
- Ray, R.L., Jacobs, J.M. & Cosh, M.H. (2010). Landslide susceptibility mapping using downscaled AMSR-E soil moisture: a case study from Cleveland Corral, California, US. *Remote Sens Environ* 114(11):2624–2636.
- Ray, R.L. & Jacobs, J.M, (2007). Relationships among remotely soil moisture, precipitation and landslide events. *Natural Hazards* 43(2):211–222.
- Thornthwaite, C.W. & Mather, J.R. (1955). *The water balance: Publications in climatology*, v. 8, no. 1, Laboratory of Climatology, Drexel Institute of Technology, Centerton, New Jersey, 104 pp.
- Wilson, R.C. (2002). Overture to a landslide – a seasonal moisture prerequisite. *Proceedings of the 19th Annual Pacific Climatic Workshop*, 149-157.

2.2.5 SURFACE AND SUBSURFACE WATER QUALITY

Jean-Philippe Malet, Thom Bogaard, Vincent Marc & Catherine Bertrand

Centre National de la Recherche Scientifique, France

This subsection is focused on the monitoring of water quality at the slope surface and subsurface as a possible forerunner of failure or acceleration of active landslides. Water quality is a term used to describe the chemical, physical, and biological characteristics of water, usually in respect to its suitability for a particular purpose. In the case of slope hydrology research, the use of water quality pertains to the possibility of unravelling the hydrological processes controlling landslide triggering or kinematics. The use of hydro(geo)chemical data in landslide research is mainly dedicated to instances where the slope hydrology is heterogeneous and difficult to measure.

This section first analyzes the impact of hydro(geo)chemical processes on physical properties of the soil material and rock slopes, i.e. the relation with deformation rate and the relation of pore fluid composition and residual shear strength of soil material. Second, the section describes the subsurface information that can be gained, i.e. the geological information of subsurface architecture and the hydrological information on origin of water, flow paths and travel times (using isotope analyses). Hydrochemical information used in both hard and soft rocks enables the display of clusters of water types, which is useful to identify the contribution of different aquifers to the landslide area. Kinetic-based modelling is shown to be very useful in the interpretation of hydro(geo)chemical information.

What can hydro(geo)chemistry do for landslide research, especially for early warning of imminent failure or acceleration?

Hydro(geo)chemistry is defined as, “the study of the chemical characteristics of ground and surface waters as related to areal and regional geology” (Dictionary of Earth Science, 2002). This definition is also suitable for engineering geology practice, as one relates the hydrochemical fingerprint to local lithology. Basically, information from hydro(geo)chemical studies is just another variable, which can be measured and taken into account in landslide research. Both water chemistry and geochemical measurements contain information about the subsurface reservoir properties and about subsurface flow processes. Moreover, chemical reactions can influence the physical properties of the subsurface, such as its permeability and its (residual) shear strength.

Clearly, hydro(geo)chemistry is not a new field in earth science. Many earth science disciplines have preceded the landslide researchers. A well-known example is the application of various hydrochemical techniques in catchment hydrology (Kendall & McDonnell, 2003). In catchment hydrology, tracer information was needed to better understand the process of discharge generation: from a lumped empirical approach towards a more distributed and

deterministic approach. This demand for increasingly detailed, process knowledge is also the motivation for performing hydro(geo)chemical research in landslide studies.

However, some differences exist between the application of tracer studies in catchment hydrological studies and in landslide studies. The latter focuses mainly on groundwater reaction at a specific location, often only part of a slope, and not in the overall catchment scale discharge generation. Also, the dynamic character of an unstable hillslope can make application and interpretation of hydro(geo)chemical investigations difficult. Lastly, in landslide research one is also interested in the strength properties of the soil material. Soil and rock properties can change because of hydro(geo)chemical processes.

The earth science information that can be gained in the subsurface is the geological information of subsurface architecture and the hydrological information on origin of water, flow paths and travel times. The chemical information that is used can be divided into information coming from water chemistry determined from standard water analyses, from isotope measurements, or from information of geochemical measurements.

The influence of pore-fluid composition on strength properties

Probably the most spectacular example of the influence of water chemistry on the physical properties of a soil is the sensitive (“quick”) clays. The definition for clay sensitivity is the ratio between undrained shear strength in undisturbed and remoulded clay > 30 or 50 and the remoulded shear strength < 0.4 or 0.5 kPa. The sensitive clays, derived from crystalline metamorphic rock flour deposited in marine and brackish environment, show a house-of-cards open structure and high porosity. Disturbance of the delicate structure results in collapse of the house-of-cards structure. However, the strength reduction is also caused by inter-particle repulsion, related to the electrical potential in the double layer, caused by leaching of salt pore water (Bjerrum, 1955, Eide & Bjerrum, 1955). In fresh water sediments, the post-depositional introduction of organic dispersing agents causes high sensitivity (Soderblöm, 1966).

There is a strong correlation between the pore water composition of sensitive clays and its geotechnical behaviour: high salinity results in high shear strength, low salinity in very low shear strength. However, leaching of salinity is not the only cause for an increase in sensitivity. Other factors influence the sensitivity of the clays, such as the mineral composition, weathering and total pore fluid concentration. Only a few percent of expandable clay (smectite) produced by in situ weathering increases the shear strength of a soil (Berry & Torrance, 1998). Weathering of the near-surface clays often results in higher strength and lower sensitivities. This is probably related to oxidation of the near-surface layer. The weathering processes and dissolution of Mg, Ca and K counterbalances the desalination of pore waters (Andersson-Sköld *et al.*, 2005, Berry & Torrance 1998, Torrance, 1990). The effects of Na, K, Mg and Ca and their ratios on the sensitivity of clays depend on the total concentration and on the mineralogy. The strength decreases caused by dilution is mainly coupled with rainwater infiltration.

Anson & Hawkins (1998) showed a raise in residual shear strength of sodium montmorillonite with increasing Ca concentration in the pore water. The same article shows that kaolinite is less sensitive to Ca concentration in pore water. Moore & Brunnsden (1996) showed the

influence of physico-chemical processes on a shallow coastal mudslide on the south coast of England. They reported that fluctuations in groundwater chemistry coincided with temporal movement patterns.

Di Maio *et al.* (1996, 2004) systematically analyze geotechnical properties of several Italian clays in relation to mineralogy, pore water composition and stress state. They hypothesized that the strength increase related to pore fluid composition depends on the lower void ratio of the clays prepared. Under the considered stress level, the void ratio of the clays, either dry or in cyclohexane (low dielectric fluid), is equal to or higher than that in the saturated salt solution. Di Maio *et al.* (2004) concluded that the increase in shear strength “reasonably depends on a particular particle aggregation or on shear resistance increase at the particles’ contact”. Furthermore, Di Maio *et al.* (2004) found that smectite fraction in the soil strongly influences the geotechnical behaviour of the soil as per Berry & Torrance (1998), but on the other hand that increasing stress reduces the influence of smectite fraction on compression and swelling.

The interaction between mineralogy, pore water chemistry and stress state should be considered more often in geotechnical research, in order to be potentially used for early warning.

The use of hydrochemical information for early warning of failures associated with hard-rock slopes

This section looks at the hydrogeology of hard-rock slopes in the narrow sense of bedrock flow, typically through fractures and fissures but also influenced by the unconsolidated topsoil or slope debris layer. Landslides, or more specifically rockslides, and rockfall in these environments are characterised by local water flow patterns, which are to a large extent determined by the secondary porosity of mountain slopes. Indeed, the hydrogeology of a rock slope depends on land surface topography, internal highly heterogeneous hydrogeological and mechanical properties, and infiltration of rainfall and melting snow.

The hydrological response of a fractured rock slope depends on the geometry and hydraulic connectivity of the network of discontinuities, individual discontinuity properties and on the intact rock properties (Tsang, 1999; Bonzanigo *et al.*, 2001). At the slope scale, a decrease in hydraulic permeability is commonly observed with depth because the increase of the state of stresses induces a closing of rock fractures. Close to the land surface, there is a low-stress decompression zone that can be 600 m thick where permeability may vary between 10^{-4} and 10^{-8} m.s⁻¹. Deeper in the high-stress zones of the massif, the permeability is between 10^{-9} and 10^{-11} m.s⁻¹ (Marechal, 1998; Marechal *et al.*, 1999).

At the discontinuities’ network scale, contrasts of a factor of 10^2 to 10^7 can be observed respectively between different discontinuities and between discontinuities and intact rock matrices (Cappa *et al.*, 2005; Guglielmi *et al.*, 2006). At the single discontinuity scale, a 50 % variability of the permeability and stiffness values is commonly observed (Rutqvist & Stephansson, 2003; Guglielmi *et al.*, 2006). Such heterogeneous hydraulic properties in a

slope induce a drainage concentration in 1 to 10 % of the fractures (Black *et al.*, 1991; Olsson *et al.*, 1998). As a result, it appears that landslides can be triggered by the presence of one open fissure diverting water towards a landslide region. Abundant observations of the local character of bedrock flow are available in literature. For example, Johnson & Sitar (1990) observed during their study of debris flow initiation by pore pressure buildup that, “scars with exposed bedrock continue to emit significant amounts of water from the bedrock for days or weeks following failure”.

Use of hydro(geo)chemical information for the analysis of the hard-rock slope failure of *La Clapière* is detailed below. Indirect methods based on the study of water-rock interactions (Compagnon *et al.*, 1997; Guglielmi *et al.*, 2000) and on artificial tracing experiments (Bonnard *et al.*, 1987) were developed in order to locate water flow paths through the rock mass and to estimate pore pressures at the scale of the large moving rock mass. Methods were based on the one hand on chemical and stable-isotopes analyses of spring waters and, on the other hand, on modelling different interface water-rock exchanges observed in the field. Chemical analyses of waters originating from springs outflowing from the slope aquifer were performed during different periods of the year. We defined a typology of existing water-types depending on in-situ hydrological conditions. The *La Clapière* landslide complex is a typical example of a large moving landslide occurring in highly fractured and altered gneissic rocks (Figure 2.2.5-1). The $60 \times 10^6 \text{ m}^3$ moving rock mass body displays a high internal brittle-ductile deformation and it is bounded by a multi-planar failure surface located at 100 - 200 m depth. For a quarter century, the *La Clapière* landslide has been monitored for slope deformation and hydrometeorological conditions. Follacci (1999) showed the correlation of local precipitation with the deformation rates. Indeed, seasonal accelerations of the landslide of 30 to 200 mm/day are clearly correlated to snowmelt and rainfall events on the slope. Unfortunately, the correlation was obviously highly nonlinear (because it did not take slope properties into consideration) and resulted in a poor estimate of hydrologic risk to trigger a catastrophic slope collapse.

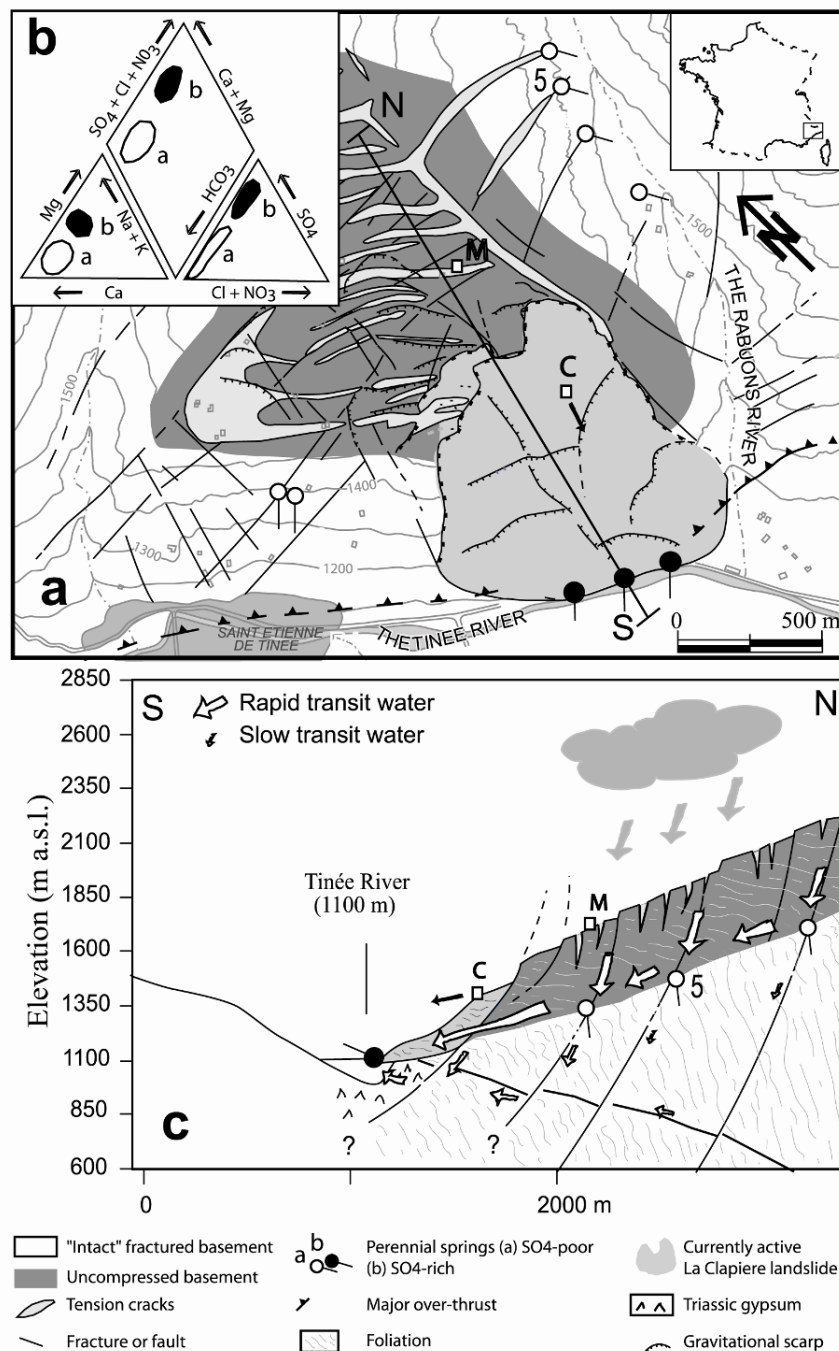


Figure 2.2.5-1. Hydrogeological model of La Clapière slope as inferred from hydro(geo)chemical data. Hydrogeological map (1a); Piper diagram of spring water chemical contents (1b); Conceptual hydrogeological cross-section of groundwater flow (1c).

Since 1995, a multi-scale field hydrogeological study was combined with a hydro(geo)chemical approach to improve knowledge of water flow through unstable hard rock slopes, using *La Clapière* as a reference site. Repeated sampling was performed of spring water chemistry in high and low water periods, both at the foot of the active landslide area and along the slope. $\delta^{18}\text{O}$ isotopes were also used to characterize the landslide recharge area.

Spatial chemical variations of spring chemistry were explored by plotting the water composition in a Piper diagram to distinguish water types of the springs mapped on the hillslope (Compagnon *et al.*, 1997; Figure 2.2.5-1a and 2.2.5-1b). A Ca-Mg-HCO₃ type of water exists at the higher located springs, whereas the springs at the foot of the slope showed a Mg-Ca-SO₄ water type. In order to explain the source of the high SO₄ concentrations, a hydro(geo)chemical modelling approach was followed by Guglielmi *et al.* (2000). The idea behind this methodology is that the calculation of the dissolution and precipitation of minerals due to water-rock interactions helps to interpret water chemistry information, or at least constrains the possible explanations for the sampled water chemistry. The thermodynamic- and kinetic-based model KINDIS (Madé *et al.*, 1990) can be used to simulate the observed water concentrations according to different water-rock interactions.

In case of the *La Clapière* study (Figure 2.2.5-2), acquisition of spring water chemistry was tested according to the chemical composition of the different expected input waters (snow-melt-type and rainfall-type waters) and the abundance of some minerals (Quartz, Plagioclase, Muscovite, Biotite and accessory minerals which are Feldspar, Calcite, Chlorite and Pyrite). On the gneissic slope of *La Clapière*, geochemical modelling explains sulphate concentration of waters from 0 to 130 mg/l by dissolution of sulphurous minerals, which exist in the basement as observed in the springs at the upper part of the slope (Figure 2.2.5-1C). The high concentrations (600 to 800 mg/l) cannot be explained by results from simulations (Figure 2.2.5-2, group b). At the top of the slope, groundwater directly flows through the uncompressed fissured basement with different flowpaths mainly guided by the high permeable gravitational features that correspond to interconnected tension cracks widely opened and more or less filled with colluvium that characterizes the structure of this part of the slope. A perched aquifer nested in those features is drained by the perennial springs located at the top of the slope. A basal aquifer is drained by springs at the lower part of the slope and at the landslide foot. The method strongly suggests existence of non-exposed rocks hidden under the studied slope (Figure 2.2.5-1C). In the local geological context, these rocks can only be Triassic gypsum likely to be trapped under a major thrust fault located at the foot of the slope.

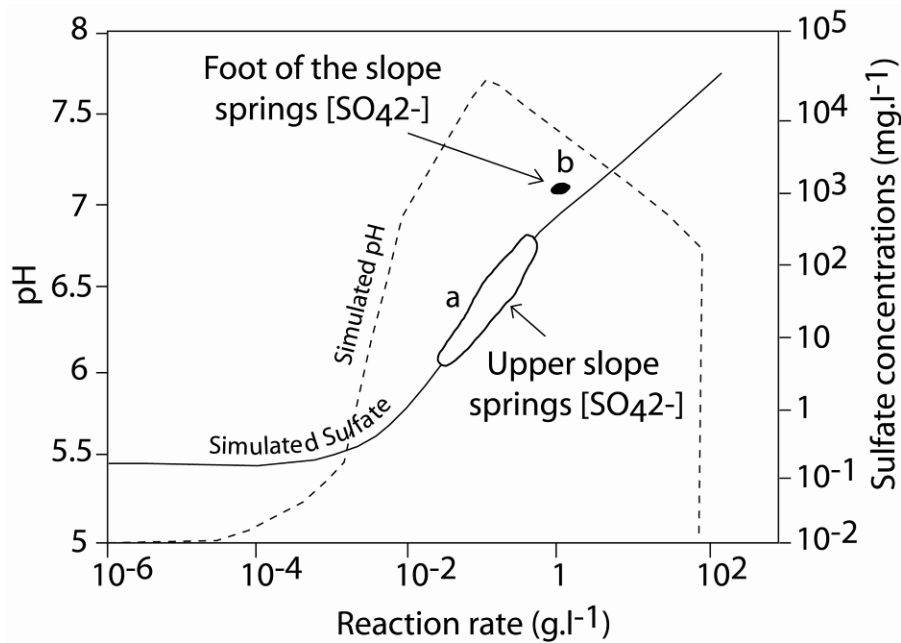


Figure 2.2.5-2. Simulation of water-rock interactions in the gneissic La Clapière slope. Plot of measured data on the simulating pH and sulphate versus reaction rate diagram (a and b groups refer to chemical facies measured in the field and plotted in the Piper diagram in Figure 2.2.5-1b).

Time evolution of spring water chemistry was characterized by SO_4^{2-} concentration decreases that occurred after precipitation events (Figure 2.2.5-3). When there is no precipitation (for example in August; Figure 2.2.5-3), the SO_4^{2-} concentration remains high and the variation is low. SO_4^{2-} transient variations appeared the opposite of NO_3^- transient variations. After a precipitation event, there is an increase of NO_3^- that is synchronous to a decrease in SO_4^{2-} content. The significant decrease in SO_4^{2-} means that, during precipitation periods, there are rapid infiltration fluxes through the reservoir corresponding to shallow waters, chemically far from equilibrium with the reservoir rock chemistry. Transient signals are in such cases interpreted as dilution inflows, linked to low concentration precipitation inflows, which mix with pre-event groundwater from the saturated zone that is chemically near equilibrium with the rock matrix primary minerals. Such hydrochemical variations with time can be well explained by a dual-permeability model. During periods of infiltration, a quick transit of fresh infiltrated water essentially flows through the very conductive fractures and a much delayed transit of those waters flows through the poorly conductive zones.

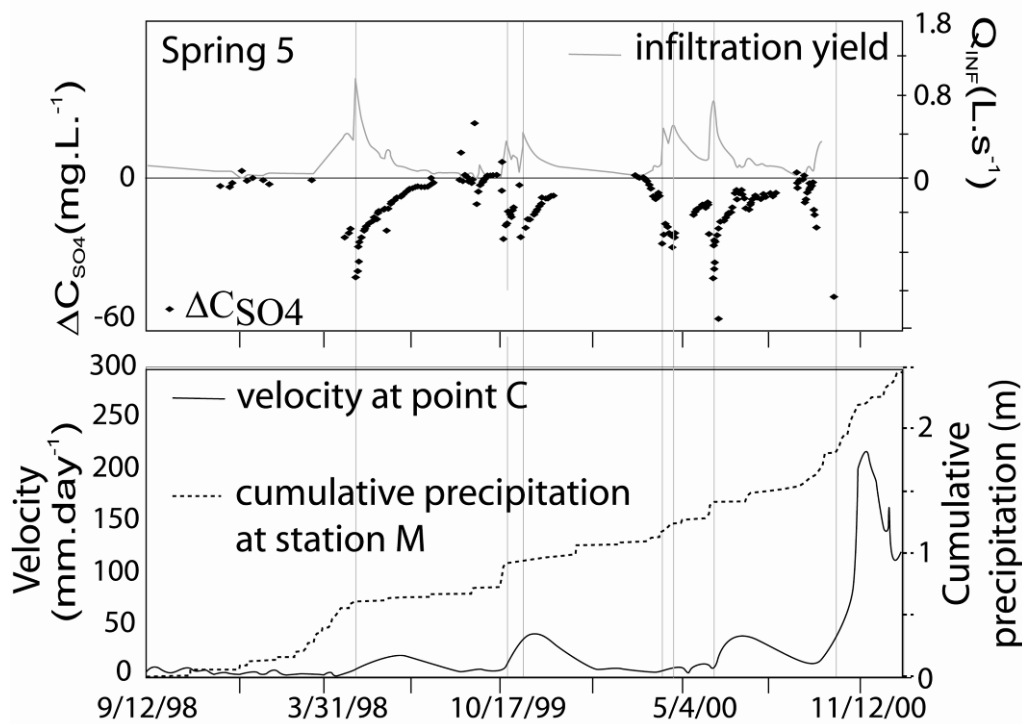


Figure 2.2.5-3. Typical comparison of chemical variations of spring 5 draining the upper part of the La Clapière slope and La Clapière landslide acceleration at Point C for 1999-2000 hydrologic period (Spring 5, Point C and Point M are located on the map of Figure 2.1.5-1a).

Landslide velocities of *La Clapière* are characterized by very slow periods with velocities of 1 to 5 mm.day⁻¹ and periods of acceleration of 0.02 and 0.25 m/day. These periods of acceleration are roughly synchronous and have the same duration as dilution periods of springs (Figure 2.2.5-4). Acceleration curves display an asymmetric shape with a rapid rise synchronous with the decreasing part of the spring water chemical content (dilution linked to main groundwater flood infiltration), and a slow decrease synchronous with the slow return to spring initial chemical content (slope drying up). Even if the correlation between estimated infiltration rate and landslide acceleration is far from being simple and linear, the main result is that a relatively small amount of water infiltrated (small infiltration rate over a short time period) triggers a general acceleration of the 60×10^6 m³ sliding volume. This means that the predominant effects of water in fractured hard rock are linked to the interstitial pressure increase located in a limited number of discontinuities within the slope, as was analyzed using various numerical codes by Guglielmi *et al.* (2006).

Similar results were obtained on the unstable *Séchilienne* rock slope near Grenoble where sedimentary layers located at the top of slope were responsible for a characteristic chemical content of infiltration waters in the landslide. This allowed Guglielmi *et al.* (2002) to perform a natural tracing of those waters through the landslide. The time variability of groundwater chemistry appeared closely correlated to slope movements. Indeed, the measured chemical variations are typical surficial waters, rapidly flowing into a limited number of highly

permeable and deformable discontinuities responsible for the destabilization of large fractured hard-rock slopes. This approach is based on three types of data: hydrogeological context that can be deduced from spring occurrence in the slope, rock petrography, and spring water chemistry and yields that are easily sampled in the field. The hydromechanical behaviour of the slope can then be analyzed using coupled numerical modelling of hydromechanical and chemical processes, both in the saturated and unsaturated parts of the slope.

The use of hydrochemical information for early warning of failures associated with soft-sediment slopes

Most landslides occur in non-consolidated, weathered materials like marls. The high clay content and the specific geomechanical characteristics of weathered marls make them prone to failure. The low permeability of the clayey matrix make hydrological analyses of the landslides difficult (Bogaard, 2001). Several pioneering studies have been performed on landslides using hydrochemical tracing in order to better understand the hydrological system (for example, Bogaard *et al.*, 1996, Sakai *et al.*, 1996, Bogaard *et al.*, 2000, Anson and Hawkins, 2002, Mikoš *et al.*, 2004, de Montety *et al.*, 2007).

To elucidate the potential of hydrogeochemistry in landslide research, the well documented *Super-Sauze* is described here in detail.

The *Super-Sauze* mudslide is one of the best studied landslides in weathered marls using hydrochemistry as a source of information for the hydrological behaviour of the site. The *Super-Sauze* landslide is a mudslide that was triggered in the 1970s at the interface between moraine and autochthonous black marls (Malet, 2003). It has been studied since 1996, and a spatio-temporal database is available on rainfall, temperature, capillary pressure head, soil moisture content, groundwater level and displacement (Malet, 2003; Malet *et al.*, 2005). The groundwater system has been described from a set of about twenty open standpipe piezometers evenly distributed over the landslide body. Accordingly, water chemistry has been surveyed at different strategic periods in 2003 and 2004 (end of winter and the snowmelt impact, spring, the low flow period of summer, autumn and the soil re-wetting), so that the hydrochemistry areal variations have been investigated according to the seasons. Continuous sampling over shorter periods has also been undertaken to examine the infiltration and recharge processes.

The characteristics and organisation of water chemistry over the *Super-Sauze* mudslide turned out to be stable throughout the year. There was a systematic increase of the water mineralization downwards while the proportion of Na decreased (30 % to 5 %) to the benefit of Ca and Mg (30 % to 50 % and 35 % to 60 % respectively). These evolutions have been readily explained by combined geochemical processes such as dilution (mixing of the landslide groundwater with the low mineralised moraine waters or meteoric waters), dissolution-precipitation of carbonate minerals, cation exchange and pyrite dissolution. This consistent areal distribution of the water chemistry is also an argument for the continuity of the groundwater system.

Locally, unexpected high concentrations of SO_4 , Mg and Na were observed. Typically, these chemical anomalies were shown to relate to topographical peculiarities and were explained as a contribution of deep waters moving along major discontinuities (faults, bedding and schistosity planes).

Long- and short-term variations of the hydrochemistry were surveyed to further investigate the conditions of subsurface water infiltration. Comparison between chemical variations and hydrologic observations enabled the authors to provide hypotheses about the distribution of rapid preferential vertical flows.

For example, the short-term chemical variations were investigated at the beginning of the snow-melt period. All the ions except NO_3 were characterised by the same temporal variation (Figure 2.2.5-4). The first part of increasing concentrations is explained by the contribution of the pre-event soil water which attained the groundwater via a piston flow mechanism. As soon as the low-mineralised new water has reached the water table, the concentrations decreased as a consequence of the dilution effect. The new water is enriched in nitrate compared with the pre-event water, in keeping with the cattle defecations or other animals' faeces lying on the ground surface. As melting and water sampling started at the same time, it was possible to assess the mean transit time of water infiltrating through the unsaturated zone. It took seven to eight days for the new water to reach the water table (starting the dilution process and NO_3 rising), proving the importance of the preferential vertical flows on the local recharge of the groundwater body.

The general hydrochemical features showed a very high ionic strength in keeping with the hydrochemical data from other landslides in marls of the South French Alps. But the water chemistry at *Super-Sauze* has its own peculiarity. The concentration in SO_4 was found to be up to twice that observed in the other studies while, unlike most landslides situated in black marls where Ca is usually the dominant cation, Mg has proved to be the major cation. Also, the specific character of the *Super-Sauze* mudslide lies in the very high Na concentrations (up to 35 meq/l). Further analyses have revealed unusually high concentrations in strontium. As suggested by Meybeck (1984), strontium anomalies may be a consequence of celestite dissolution, which is usually associated to gypsum. Yet, gypsum was not found in the mineralogical composition of the material.

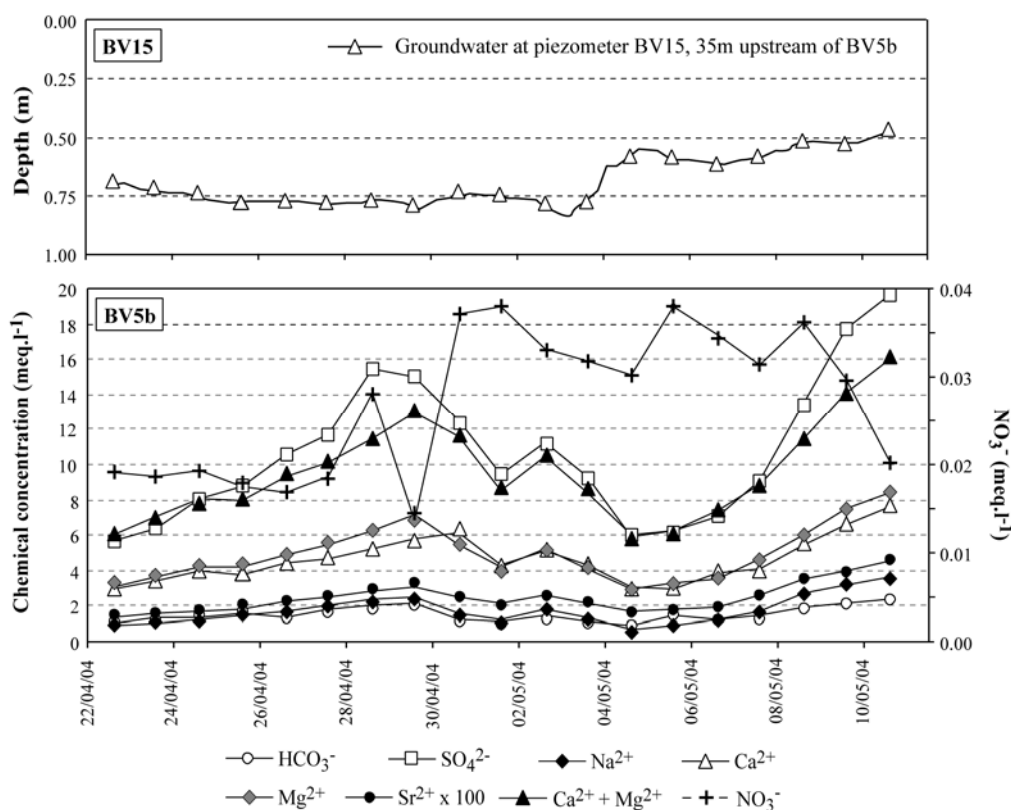


Figure 2.2.5-4. Example of short-term chemical variations compared with the water level variations (modified from de Montety *et al.*, 2007).

To tackle this problem, a geochemical modelling exercise has been undertaken and already applied with success at the *La Clapière* landslide (Guglielmi *et al.*, 2000). The thermodynamic- and kinetic-based model KINDIS (Madé *et al.*, 1990) has been used to simulate the observed water concentrations according to different water-rock interaction. The results of the simulations have shown that the mudslide water chemistry could not be explained by the dissolution of the constituent material. The groundwater clearly does not originate from direct rainfall or snow-melt with subsequent enrichment or from any other sources detected in the field. Evaporites, which are not present in the mudslide material, have been proved by de Montety *et al.* (2007) to be the main origin of the observed water chemistry. These results have pointed out the major impact of the gypsum and dolomite layer of the overthrust contact above the *Super-Sauze* mudslide. This is the only identified source of evaporite at a regional scale and accordingly they have identified a remote origin for the water. Finally, this hydrochemical investigation has contributed to the refinement of the conceptual hydrological model of the mudslide as proposed by Malet *et al.* (2005) (Figure 2.2.5-5).

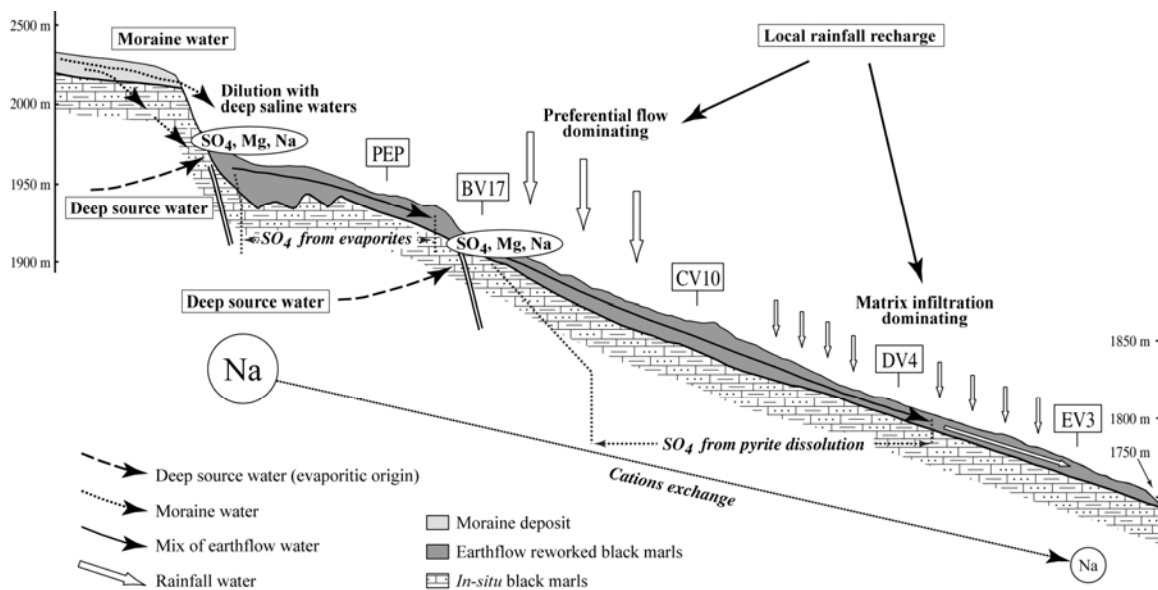


Figure 2.2.5-5. Synthetic cross section representing the hydrological concept of the Super-Sauze mudslide as interpreted from hydrochemical analyses, with indication of the mudslide velocities (modified from de Montety *et al.*, 2007).

The use of isotopic analysis in landslide analysis

Environmental isotopes are natural and anthropogenic isotopes whose wide distribution in the hydrosphere can assist in the solution of hydro(geo)chemical problems (Kendall & McDonnell, 2003). Tritium (^3H) analysis provides information on water transit times and the dynamics of deep-water percolation. The use of tritium to calculate recharge rate requires assessment of the temporal and spatial variation of the tritium content. If initial atmospheric concentrations are unknown, an alternative dating method is to use both ^3H and ^3He . The former decays into ^3He , which can be used as a quantitative tracer of the age of the water since precipitation (Kendall & Doctor, 2004).

In November 2000, Mikoš *et al.* (2004) studied the debris disaster at the *Stož* landslide in Log pod Mangartom, Slovenia, that occurred after an extreme rain event. A hydrological analysis showed a significant increase in runoff coefficients (the percentage of precipitation that appears as runoff (Dictionary of Earth Science, 2002)) in autumn 2000. They used tritium tracer to assess the travel time of sampled spring water, and oxygen-18 to assess the recharge area of the groundwater (see below).

The $\delta^{18}\text{O}$ composition (and $\delta^2\text{H}$, but that one is not considered here since $\delta^{18}\text{O}$ and $\delta^2\text{H}$ are strongly correlated) in precipitation depends on the temperature of the condensation of the precipitation and the rain out characteristics of an air mass. $\delta^{18}\text{O}$ is influenced by altitude (decrease in temperature) and distance from the sea and other local environmental conditions (e.g. humidity) (Kendall & Doctor, 2004). It is therefore of interest to know an interannual weighted average of the isotopic composition of the rainwater as a function of altitude. Ideally, this gradient is obtained in the field from rain gauges set up at different altitudes and requires a long-term isotopic database. If such a network is not available, spring water from local, limited,

altitude-ranged aquifers is sampled. Using this altitude-isotopic composition relationship, oxygen-18 information can contribute to understanding the origin and flow paths of water within a slope. Compagnon *et al.* (1997) used this $\delta^{18}\text{O}$ characteristic of springs on the *La Clapière* landslide complex to determine the altitude of the recharge. Guglielmi *et al.* (2002) also used $\delta^{18}\text{O}$ data for the *Séchilienne* landslide. Local isotopic $\delta^{18}\text{O}$ gradients were determined in the summer (*Séchilienne*) or both in the summer and winter (*La Clapière*) from springs for which the elevations of the source area are known.

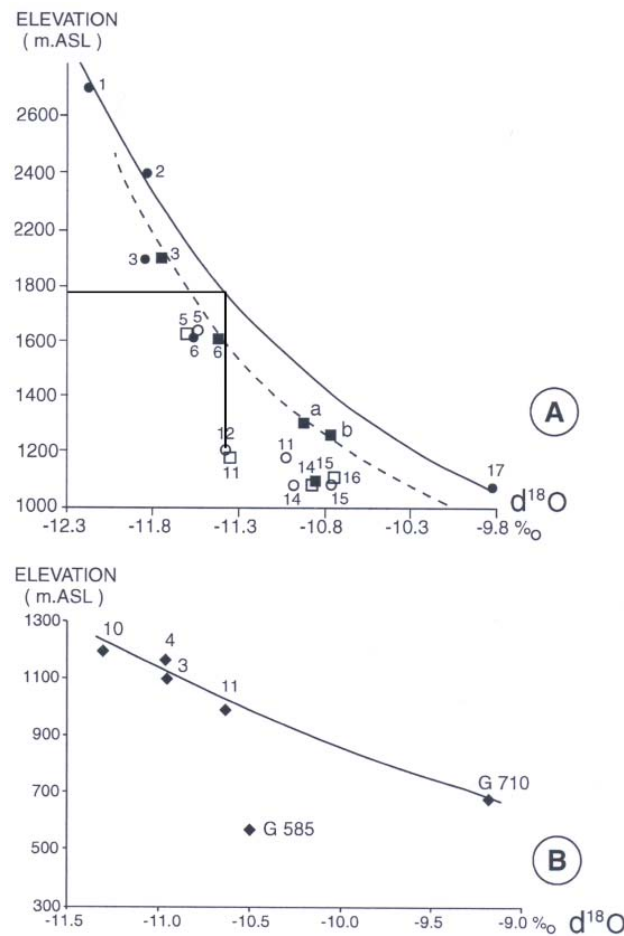


Figure 2.2.5-6. Isotopic gradients (values used to calculate the gradients are plotted in black, values of springs in the recharge area with mean elevation are plotted with open circles and squares). Squares a and b correspond to $\delta^{18}\text{O}$ values of springs located about 2 km from the La Clapière slope (June gradient dashed line with $\delta^{18}\text{O}$ values in squares; December gradient continuous line with $\delta^{18}\text{O}$ values plotted in circles, Figure 2.2.5-6a); B Séchilienne massif (Figure 2.2.5-6b) (modified from Guglielmi *et al.*, 2002).

Using this information the recharge areas of landslide springs could be deduced (Figure 2.2.5-6). The figure shows that most water samples (e.g. 11 through the 16 in A) have isotopic concentrations, which are depleted in $\delta^{18}\text{O}$ to a level normally found at higher altitudes than the sample location. This has important consequences for the hydrological analysis of a landslide area as the hydrological ‘catchment’ of the landslide reaches outside the landslide limits.

References

- ANDERSSON-SKÖLD Y., TORRRANCE J.K., LIND B., ODÉN K., STEVENS R.L. & RANKKA K. (2005). – Quick clay. A case study of chemical perspective in Southwest Sweden. – *Eng. Geol.*, 82, 107-118.
- ANSON R.W.W. & HAWKINS A.B. (1998). – The effect of calcium ions in pore water on the residual shear strength of kaolinite and sodium montmorillonite. – *Géotech.* 48, 787-800.
- ANSON R.W.W. & HAWKINS A.B. (2002). – Movement of the Soper's Wood landslide on the Jurassic Fuller's Earth, Bath, England. – *Bull. Eng. Geol. Environ.*, 61, 325-345.
- BERRY R.W. & TORRRANCE K. (1998). – Mineralogy, grain-size distribution and geotechnical behaviour of Champlain clay core samples, Québec. – *Can. Mineralogist*, 36, 1625-1636.
- BJERRUM L. (1955). – Stability of natural slopes in quick clays. – *Géotech.*, 5, 101-119.
- BLACK J., OLSSON J., GALE J. & HOLMES D. (1991). – Site characterization and validation. Preliminary assessment and detail prediction. – Stripa project, TR91-08, SKB, Report, Stockholm, Sweden, 1-38.
- BOGAARD T.A. & VAN ASCH TH.W.J. (1996). – Geophysical and hydrochemical investigation of a complex large-scale landslide in southern France. In: *Proc. 7th Int. Symp. on Landslides*, Trondheim, Norway. – Balkema, Rotterdam, 643-647.
- BOGAARD T.A., ANTOINE P., DESVARREUX P., GIRAUD A. & VAN ASCH, TH.W.J. (2000). – The slope movements within the Mondorès graben (Drôme, France): the interaction between geology, hydrology and typology. – *Eng. Geol.*, 55, 297-312.
- BOGAARD T.A. (2001). – Analysis of hydrological processes in unstable clayey slopes. – *Netherlands Geographical Studies*, 287, Utrecht, 191p.
- BONNARD C., NOVERRAZ F. & PARRIAUX A. (1987). – Origin of groundwater likely to affect a large landslide. In: *Proc. 9th European Conf. Soil Mech. and Found. Eng.* – Balkema, Rotterdam, 389-392.
- BONZANIGO L., EBERHARDT E. & LOEW S. (2001). – Hydromechanical factors controlling the creeping Campo Vallemaggia Landslide. – In: *Landslides: Causes, Impacts and Countermeasures*, Davos, Switzerland – Verlag Glückhauf, Essen, 13-22.
- CAPPA F., GUGLIELMI Y., FENART P., SOUKATCHOFF V. & THORAVAL A. (2005). – Hydromechanical interactions in a fractured carbonate reservoir inferred from hydraulic and mechanical measurements. – *Int. Journ. Rock Mech. and Mining Sc.*, 42, 287-306.
- COMPAGNON F., GUGLIELMI Y., MUDRY J., FOLLACCI J.-P. & IVALDI J.-P. (1997). – Approche chimique et isotopique de l'origine des eaux en transit dans un grand mouvement de terrain: exemple du glissement de La Clapière (Alpes Maritimes). – *C. R. Acad. Sci.*, 325, 8, 565-570.
- DE MONTETY V., MARC V., EMBLACH C., MALET J.-P., BERTRAND C., MAQUAIRE O. & BOGAARD T.A. (in press). – Identifying origin of groundwater and flow processes in complex landslides affecting black marls in southern French Alps: insights from an hydrochemical survey. – *Earth Surf. Proc. & Landforms*, 32: 32-48.
- DICTIONARY OF EARTH SCIENCE, 2002. 2nd Edition. McGraw-Hill.
- DI MAIO C. (1996). – The influence of pore fluid composition on the residual shear strength of some natural clayey soils. In: *Proc. 7th Int. Symp. on Landslides*, Trondheim, Norway. – Balkema, Rotterdam, 189-1194.
- DI MAIO C., SANTOLI L. & SCHIAVONE P. (2004). – Volume change behaviour of clays: the influence of mineral composition, pore fluid composition and stress state. – *Mech. of Materials*, 36, 435-451.
- EIDE O. & BJERRUM L. (1955). – The slide at Bekkelaget. – *Géotech.*, 5, 88-100.
- FOLLACCI J.-P. (1999). – Seize ans de surveillance du glissement de La Clapière (Alpes Maritimes). – *Bull. Liaison Lab. Ponts & Chaussées*, 220, 35-51.
- GUGLIELMI Y., BERTRAND C., COMPAGNON F., FOLLACCI J.-P. & MUDRY J. (2000). – Acquisition of water chemistry in a mobile fissured basement massif: its role in the hydrogeological knowledge of the La Clapière landslide (Mercantour massif, Southern Alps, France). – *J. Hyd.* 229, 138-148.
- GUGLIELMI Y., VENGEON J.-M., BERTRAND C., MUDRY J., FOLLACCI J.-P. & GIRAUD A. (2002). – Hydrogeochemistry: an investigation tool to evaluate infiltration into large moving rock masses (case study of La Clapière and Séchilienne alpine landslides). – *Bull. Eng. Geol. Env.*, 61, 311-324.

-
- GUGLIELMI Y., CAPPÀ F., RUTQVIST J., TSANG C.F. & THORAVAL A. (2006). – Coupled hydromechanical behaviour of a multi-permeability fractured rock slope subjected to a free-water surface movement: Field and numerical investigations. In: Coupled thermo-hydro-mechanical-chemical processes in geo-systems. – Fundamentals, Modelling, Experiments and Applications. Elsevier, Rotterdam (in press).
- JOHNSON K.A. & SITAR N. (1990). – Hydrologic conditions leading to debris-flow initiation. – *Can. Geotech. J.*, 27, 789-801.
- KENDALL C. & DOCTOR D.H. (2004). – Stable Isotope applications in hydrological studies. In: *Treatise on Geochemistry*, Volume 5. – Elsevier, Rotterdam.
- KENDALL C. & MCDONNELL J.J. (2003). – Isotope tracers in catchment hydrology – Elsevier, 3rd edition, 257p.
- MADÉ B., CLEMENT A. & FRITZ B. (1990). – Modélisation cinétique et thermodynamique de l'altération: le modèle géochimique KINDIS. – *C. R. Acad. Sc., IIA*, 310, 31-36.
- MALET J.-P. (2003). – Les “glissements de type écoulement” dans les marnes noires des Alpes du Sud. Morphologie, fonctionnement et modélisation hydro-mécanique. – PhD Thesis, Univ. Louis Pasteur, Strasbourg, France, 394p.
- MALET J.-P., VAN ASCH, TH.W.J., VAN BEEK, L.P.H. & MAQUAIRE O. (2005). – Forecasting the behaviour of complex landslides with a spatially distributed hydrological model. – *Nat. Haz. Earth Sys. Sc.*, 5, 71-85.
- MARÉCHAL J.-C. (1998). – Les circulations d'eau dans les massifs cristallins alpins et leurs relations avec les ouvrages souterrains. – Doctoral Thesis 1769, EPF, Lausanne, 298p.
- MARÉCHAL J.-C., PERROCHET P. & TACHER L. (1999). – Long-term simulations of thermal and hydraulic characteristics in a mountain massif: The Mont Blanc case study, French and Italian Alps. – *Hydrogeology J.*, 7, 341-354.
- MEYBECK M. (1984). – Les fleuves et le cycle géochimique des éléments. – Habilitation Doctoral Thesis, University Pierre et Marie Curie, Paris 6, 558p.
- MOORE R. & BRUNSDEN D. (1996). – Physico-chemical effects on the behaviour of a coastal mudslide. – *Géotech.*, 46, 259-278.
- MIKOS M., CETINA M. & BRILLY M. (2004). – Hydrologic conditions responsible for triggering the Stoze landslide, Slovenia. – *Eng. Geol.*, 73, 193-213.
- OLSSON O., BLACK J., GALE J. & HOLMES D. (1998). – Stripa project-site characterization and validation-stage 4. Preliminary assessment and detail prediction. – Stripa Project TR91-08, SKB, Stockholm, Sweden.
- RUTQVIST J. & STEPHANSSON O. (2003). – The role of hydromechanical coupling in fractured rock engineering. – *Hydrogeology J.*, 11, 7-40.
- SAKAI H., MARUTA O. & TARUMI H. (1996). – A variety of information obtainable from specific chemical contents of groundwater in landslide area. In: *Proc. 7th Int. Symp. on Landslides*, Trondheim, Norway. – Balkema, Rotterdam, 867-870.
- SÖDERBLOM A. (1966). – Chemical aspects of quick clay formation. – *Eng. Geol.*, 1, 415-431.
- TORRANCE J.K. (1990). – Oxide minerals in the sensitive post-glacial marine clays. – *Applied Clay Science*, 5, 307-323.
- TSANG C.F. (1999). – Linking thermal, hydrological, and mechanical processes in fractured rocks. – *Annu. Rev. Earth. Planet. Sci.*, 27, 359-384.

2.3 GROUND GEOPHYSICAL PROPERTIES

This section reviews the geophysical parameters whose **changes indirectly** (using model calculations or data inversion) **characterise changes of other parameters**, in most cases of hydrological properties. These parameters can/could be used to predict the activation of a mass movement. Such parameters are ground electrical resistivity (ER), self/spontaneous potential (SP) and induced polarisation (IP), seismic velocity, passive/pulse electromagnetic emissions (PEE) or proton magnetic resonance (PMR).

2.3.1 GEOELECTRICAL PARAMETERS

Robert Supper, Ivo Baroň, David Ottowitz
Geological Survey of Austria

Within recent years, geoelectric multi-electrode measurements have become the most routine and successful geophysical method to investigate subsurface geometry and structural patterns of landslide bodies, thus gaining the status of a state of the art method in civil engineering (Supper et al. 2000, 2001, 2002, 2008; Perrone, 2001; Mauritsch & Seiberl, 2000; Meric et. al., 2005; Jongmans & Garambois, 2007). Most of the European landslide events are intimately connected to precipitation and to the influence of underground water on slope stability (pore-water pressure, change of water flow regime, saturation). Since the electrical resistivity is mainly determined by the water content of the subsurface, observing the **temporal changes of electrical resistivity** seems to be a promising method for the monitoring of landslides (Supper et al., 2009).

Apart from electrical resistivity, other geoelectric parameters like **induced polarization** and **self-potential** could definitely have a potential for monitoring, but so far have hardly ever been investigated in detail.

Subsurface electrical resistivity

The electrical resistivity is a physical property of the substratum usually measured by multi-electrode resistivity surveys (also called electrical tomography). In most cases electrodes are set along straight profiles, however within recent years special 3D patterns of electrodes or borehole-to-surface configurations have also been applied. A multitude of potential differences is registered for current injections at several injection dipoles. For each measurement, the quotient of the registered potential difference and the injected current, multiplied with a geometrical factor which depends on the position of each of the electrodes, is calculated. The resulting physical quantity is called the **apparent resistivity**. This parameter represents the resistivity, which the subsurface would exhibit if it were homogenous. Since in most cases the subsurface is not homogenous at all (therefore called “apparent”), the value of this parameter is determined by the real resistivity distribution of the subsurface. In that case each part of the subsurface contributes to the total value according to a sensitivity function, which in turn depends on the electrode configuration. Consequently the

apparent resistivity is not only determined by the resistivity at a certain depth, but by the whole (three-dimensional) resistivity distribution of the subsurface up to a certain distance around the measurement electrodes.

From the entity of registered apparent resistivity values (usually several thousands of single measurements), the distribution of the (“real”) electrical resistivity of the subsurface can be calculated by applying delicate data inversion. Especially for monitoring data, time-lapse resistivity inversion can be applied (Loke, 1999; LaBrecque and Yang, 2001; Oldenborger et al., 2007; Kim, 2005; Kim et al., 2009) which is optimised to calculate resistivity changes. In the past ten years, several studies proved the applicability to monitor the temporal changes of **electrical resistivity** for a multitude of different applications (Supper et al., 2012).

Definitions and units

The electrical resistivity, a material property, is a measure of how strongly a material opposes the flow of electric current. The SI unit of electrical resistivity is the **ohm metre (Ωm)**. It is commonly represented by the Greek letter ρ (rho).

The basic formula for the electric resistivity is:

$$\rho = R \frac{A}{l},$$

where

R is the electrical resistance of a uniform specimen of the material (measured in ohms, Ω), a measured value, taken from a sample of material of certain size

l is the length of the piece of material (measured in metres, m)

A is the cross-sectional area of the specimen (measured in square metres, m^2).

Conductivity principles and dependencies

The most important mechanism, which is responsible for the conduction of electrical current in the subsurface, is the electrolytic conductivity. Electrical current is generated by a potential difference which forces ions in an electrolytic solution to move. Only under special geological settings (ore bodies) must consideration be given to the metallic conductivity due to fine spread metallic particles or massive ore veins, where the electrical conduction is caused by moving electrons.

Consequently the **resistivity** of the subsurface mainly depends on porosity, water saturation and conductivity of the pore fluid (e.g. Archie, 1942; Atkins 1961; Jackson, 1978; Schlumberger, 1987; Winsauer, 1952) and to a minor part on particle size, shape and packing. For rough calculations, the “Archie Equation” can be used to determine the subsurface bulk resistivity:

$$\rho_{\text{bulk}} = \rho_{\text{fluid}} * S^{-m} * \square^{-n}$$

where: ρ_{bulk} ...bulk resistivity
 ρ_{fluid} ...resistivity of the pore fluid
 \square ...Porosity, $n=1.5-3$
 S ...Saturation, $m=1.5-3$

Additionally, the clay content of the soil has a strong influence on the electrical conductivity and therefore must be considered in interpretation.

The resistivity of a particular rock can therefore vary within a very large range, since its value does not depend on the rock matrix but only on the quantity and property of the pore fluid comprised. For example the resistivity of a saturated sandy layer can vary from 35 to more than 100 Ohmm, depending on its porosity and the conductivity of the pore fluid. However in unsaturated or dry conditions such a layer can exhibit values up to several thousands of Ohmm. Therefore for precise interpretation of the results, additional information (e.g. about the general geological structure, the pore fluid conductivity, etc.) is necessary and results must be calibrated with drilling results from at least one drillhole in a similar geological environment. Otherwise, an exact assignment of resistivity ranges to geological layers is not possible. Figure 2.3.1–1 shows the possible ranges of electrical resistivity for different geological materials.

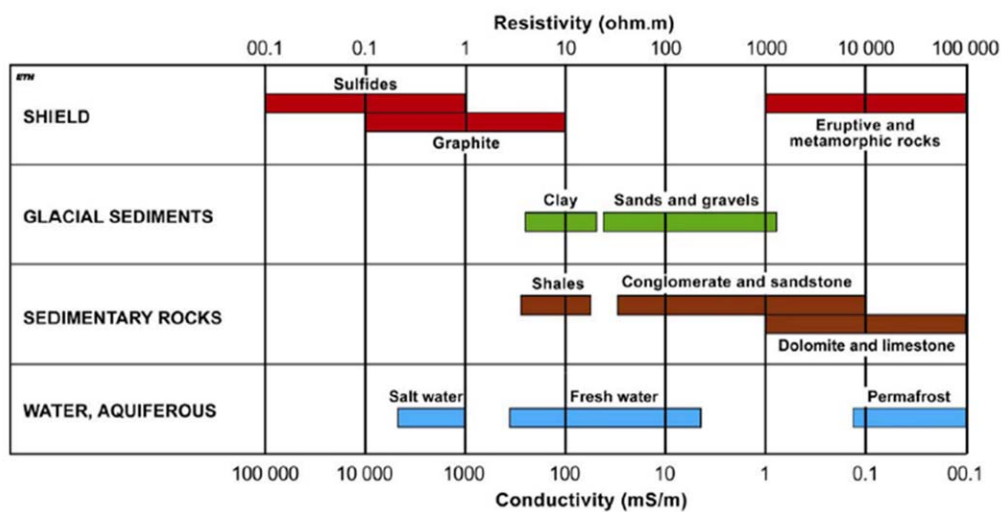


Figure 2.3.1–1. Chart of typical resistivity values of different materials (after L. Marescot: web Lectures on Electrical Surveying, Part I.)

Especially for long-term monitoring experiments the temperature dependency of the electrical resistivity must be considered. The equation below represents an approximation to calculate the influence of temperature on the resistivity.

$$\rho(t) = \frac{\rho(18)}{1 + \alpha(t - 18)}$$

- $\rho(t), \rho(18)$ is the resistivity at a particular temperature respectively at 18°C (in Ωm)
- t is the temperature (in °C)
- α is the temperature coefficient of resistivity with a value of 0.025/°C

Consequently for long-term resistivity measurements, corrections must be made to seasonal changes of the subsurface resistivity due to the temperature wave, which is generated by seasonal surface temperature variations and successively proceeds downwards with a time delay. However, since variable time shifts and thermal parameters of the subsurface are involved, which are basically not known, so far no precise correction algorithms are available.

Figure 2.3.1-2.3-1 shows typical seasonal variations of resistivity due to seasonal temperature variations at the Gschliefgraben test site.

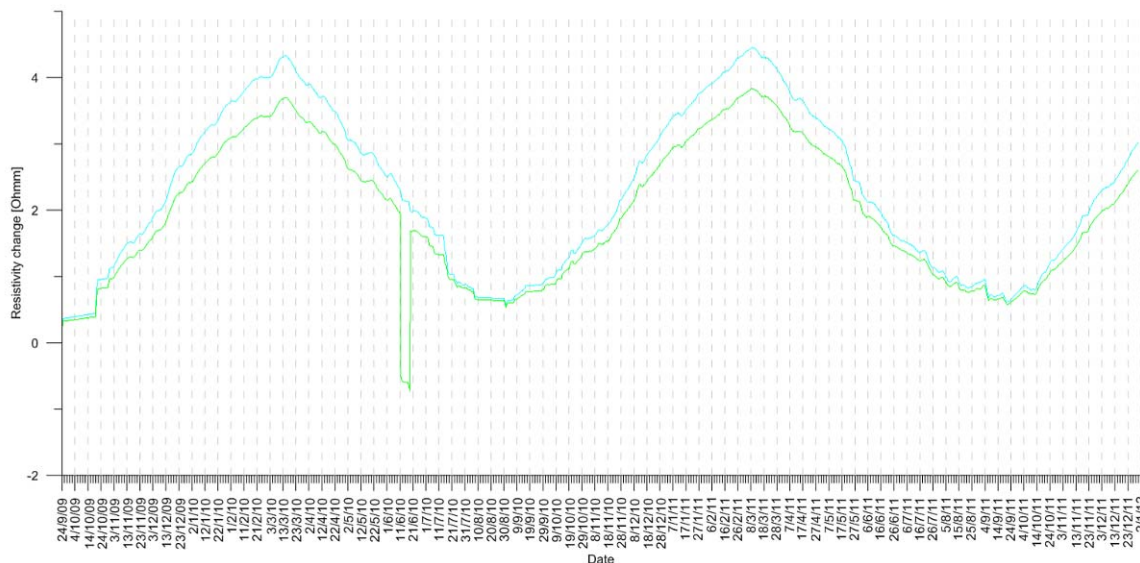


Figure 2.3.1-2.3-1. Seasonal resistivity variations at the Gschliefgraben test site

For temperatures below 0°C, the freezing of part of the pore fluid reduces the quantity of available electrolytes (which practically means a reduction of the effective porosity), resulting in an increase of resistivity. Permafrost monitoring experiments, however, have shown that even for a very long period of time with surface temperatures below zero degrees, a significant amount of free water is still available, thus allowing resistivity to be calculated based on ionic conductivity. Once all of the pore water is frozen, resistivity increases dramatically and alternative processes determine current conductivity (Petrenko, 1993). The detailed principles of electrical conductivity in totally frozen material and ice are still a field of research.

Application for landslide monitoring and early warning

Nowadays permanent geoelectrical monitoring of temporal **resistivity** changes of the substratum is widely used for many tasks, e.g. for detection of internal erosion and anomalous seepage in embankment dams (Sjödahl, 2006); leachate injection monitoring (Clément et al., 2010); wind-driven barotropic transports of marine water (Nilsson et al., 2007); exploration and monitoring in rock salt for the safety assessment of underground waste disposal sites (Yaramanci, 2000); monitoring of geological CO₂ storage sites (Kiessling et al., 2009); permafrost monitoring (Aaltonen, 2001; Hauck, 2001; Kneisel, 2004, 2006; Lambiel & Baroň, 2007; Noetzli et al., 2008; Supper et al., 2007); wetting and drying of masonry walls on historic stonework (Sass & Viles, 2010); and, in karst studies or for earthquake engineering (Kamshilin et al., 2008). Some sporadic studies have already been performed on repeated geoelectric surveying of landslides as a “monitoring” method (e.g. Niesner & Weidinger, 2008 and 2009), but the sampling frequency was low or rather sporadic and/or in operation only for a short period. Except for the pilot studies carried out by Supper et al. between 2002 and 2010 at the landslides of Sibratsgfall (Supper et al., 2000, 2002, 2008, 2009) and Gschliefgraben (Supper et al. 2010), only a few other attempts at long-term

experiments are known to the authors (Bell 2008; Chambers 2009, Krummel et al, 2012). Jongmans and Garambois (2007) concluded that the development of 2D and 3D imaging techniques as well as the installation of permanent monitoring systems constitute major advances for the future of landslide reconnaissance. However, they also highlight the necessity to calibrate and correlate results with geological and geotechnical data.

Although the monitoring of temporal **electrical resistivity** changes has undergone an intensive boom within the past few years, there is still a lack of application to landslides to allow for an evaluation of the methodology for monitoring and early warning. Therefore, within the SafeLand projects several sites (Ancona, Bagnaschino, Gschliefgraben, Ampflwang, Super-Sauze, Mölltal) were equipped with geoelectrical monitoring devices. There is still a demand for precise data inversion algorithms, especially for time lapse inversion, and data correction algorithms.

Induced polarization (IP)

Definitions and units

The **IP** is a geophysical effect of chargeability or voltage decay of the subsurface materials after introducing the electric current (Figure 2.3.1-3). The method is similar to electrical resistivity tomography; an electric current is induced into the subsurface through two electrodes, and a potential difference is observed at two other electrodes (Kearey & Brooks 1991).

Time domain IP methods measure the voltage decay or chargeability within a specified time interval after the applied potential difference is cut off. The totally integrated voltage or the voltage integrated within several time windows are usually used as the measurement. From these values, the “chargeability” of the subsurface can be calculated.

Frequency domain IP methods (also Spectral Induced Polarisation) use alternating electric currents (AC), which are induced in the subsurface, to measure the frequency dependency of the electrical resistivity for a range of low frequencies (Kearey & Brooks 1991).

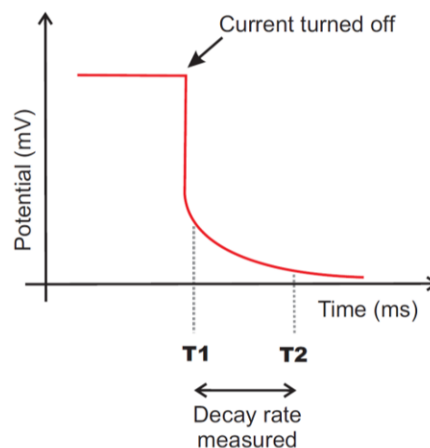


Figure 2.3.1-2.3-2. Principle of calculation of chargeability (after RSK STATS Geoconsult Ltd.)

Application for landslide monitoring and early warning

Applications of the IP method for landslide monitoring and early warning are very rare. In recent literature, just Maescot et al. (2008) carried out a combined ER and IP investigation in the Swiss Alps to delineate groundwater circulation within an unstable slope. Their results illustrated how low permeability clay/graphite units and permeable water-bearing units could be distinguished using a combined interpretation of resistivity and IP data in slope instability studies, and provided information on the main pathways for water transport within the slope. Monitoring of IP temporal changes within unstable slopes could, however, provide a new challenging approach for the understanding of landslide triggering processes in future.

Self-potential (SP)

Definitions and units

The **SP method** is a passive method based on the natural occurrence of electrical fields on the earth's surface or inside the subsurface (Jouniaux et al. 2009).

The SP parameter could be of (a) *electrokinetic* (i.e.: interaction between moving pore fluid and electric double layer at the pore surface), (b) *piezoelectric* (related to a crystal-lattice deformation), (c) *thermoelectric*, and (d) *electrochemical* (diffusion of ions due to a concentration gradient between two regions) origin, or caused by (e) "*Electro-redox*" potentials (Clint et al., 1999; Jouniaux et al., 2009; Zlotnicki & Nishida, 2003). However, the origin of self-potential in the subsurface is very complex, due to a wide range of processes which are so far not fully understood (Colangelo et al. 2008). Clint et al. (1999) proposed the SP as a potential earthquake prediction tool.

The SP is an electric potential difference naturally occurring in the subsurface. It is usually measured by voltmeters in millivolts (mV). Typical values of natural SP reach up to several hundreds of mV.

Application for landslide monitoring and early warning

Méric et al. (2005) investigated on the *Séchilienne* landslide that the SP amplitude appeared to be correlated with fracture density, and that interesting variations over time could be detected within the active zone. The same author noted that the SP data were able to detect and follow with depth an SP anomaly generated by a rainfall event (Meric et al. 2009) within the landslide. Hattori et al. (2008) and Kono et al. (2010) proved by indoor laboratory experiment that, within an artificial rainfall induced landslide, the SP anomalies occurred several minutes before the failure, demonstrating the possibility of establishing an early warning system of landslides using the self-potential method. This was also observed by Supper et al. (2010) on actual natural slopes.

Variations of electrical potential difference and acoustic emission change markedly with strain between the compaction and dilatancy phases of rock deformation, and show dependence on both effective pressure and strain rate (Clint et al. 1999). Clint et al. (1999) noted that differences between streaming potential and hydraulic permeability during deformation could be explained using a model of varying electrical and hydraulic tortuosity. Intergranular and intragranular cracking could be distinguished using the electrical potential generated from brine saturated rocks. The electrical and streaming potential signals occurring during deformation were found to reflect the accumulating and accelerating damage prior to fracture and the localisation of damage at dynamic fracture.

Wang et al. (2009) investigated the surface electric potential of coal samples during uniaxial compression. Tensile fracture and three-point bending performed that the SP can be produced

during coal deformation and rupture, and could be well correlated with the load. Particularly, the larger the load, the higher the surface potential and vice versa. This could be taken into account in landslide areas with deformed coal seams.

However, for landslide monitoring and early warning, mainly the electrokinetic effect, which could provide additional information on fluid flow and its variations within a landslide body, could be of interest. Although a few results for applications on real landslides exist (e.g. Lapenna et al., 2003, 2005; Meric et al., 2005, 2006), Garambois & Jongmans (2007) concluded in their review that there is a demand for further long-term monitoring experiments and improvements in processing techniques.

References:

- Aaltonen, J., 2001. Ground Monitoring using Resistivity Measurements in Glaciated terrains. MS. Dissertation, Department of Civil and Environmental Engineering, Royal Institute of Technology, Stockholm, 64 pp.
- Archie, G.E., 1942. The electrical resistivity log as an aid in determining some reservoir characteristics. *Trans. AIME*, 146, S. 54-62.
- Atkins, E.R., Smith, G.H., 1961. The significance of particle shape in formation factor-porosity relationships. *J. Petrol. Tech.*, v.13, S. 285-291.
- Bell, R., Thiebes, B., Glade, T., Becker, R., Kuhlmann, H., Schauerte, W., Burghaus, S., Krummel, H., Janik, M., Paulsen, H., 2008. The technical concept within the Integrative Landslide Early Warning System (ILEWS). In: *Geotechnologien - Science Report 14*.
- Chambers, J E, Wilkinson, P B, Kuras, O, Ford, J R, Gunn, D A, Meldrum, P I, Pennington, C V L, Weller, A L, Hobbs, P R N, and Ogilvy, R D. 2011. Three-dimensional geophysical anatomy of an active landslide in Lias Group mudrocks, Cleveland Basin, UK. *Geomorphology*, Vol. 125, 472-484
- Chambers, J E, Kuras, O, Meldrum, P I, Ogilvy, R D, and Hollands, J. 2006. Electrical resistivity tomography applied to geologic, hydrogeologic, and engineering investigations at a former waste-disposal site. *Geophysics*, Vol. 71, B231-B239
- Chambers, J E, Wilkinson, P B, Wealthall, G P, Loke, M H, Dearden, R, Wilkinson, R, Allen, D, and Ogilvy, R D. 2010. Hydrogeophysical imaging of deposit heterogeneity and groundwater chemistry changes during DNAPL source zone bioremediation. *Journal of Contaminant Hydrology*, Vol. 118, 43-61
- Chambers, J E, Wilkinson, P B, Weller, A L, Meldrum, P I, Gilvy, R D, and Caunt, S. 2007. Mineshaft imaging using surface and crosshole 3D electrical resistivity tomography: A case history from the East Pennine Coalfield, UK. *Journal of Applied Geophysics*, Vol. 62, 324-337
- Clément, R., Desclotres, M., Günther, T., Oxarango, L., Morra, C., Laurent, J.P., Gourc, J.P., 2010. Improvement of electrical resistivity tomography for leachate injection monitoring. *Waste Management 30* (2010) 452-464.
- Clint O.C., 1999: Electrical Potential Changes and Acoustic Emissions Generated by Fracture and Fluid Flow during Experimental Triaxial Rock Deformation. –MS. PhD. Thesis. Department of Geological Sciences, University College London, 237 pp.
- Colangelo G., Lapenna V., Perrone A., Piscitelli S., Telesca L., 2006: 2D Self-Potential tomographies for studying groundwater flows in the Varco d'Izzo landslide (Basilicata, southern Italy). - *Engineering Geology* 88 (2006) 274–286.
- Colangelo G., Lapenna V., Telesca L., 2008: Study of self-potential anomalous fluctuations in a seismic active zone of Lucano Apennine (southern Italy): recent results. - *Nat. Hazards Earth Syst. Sci.*, 8, 1099–1104.
- Hattori K., Kohno H., Tojo Y., Terajima T., Ochiai H., 2008: Early Warning of Landslides Based on Landslide Indoor Experiments. – *Proceedings of the First World Landslide Forum, ICL, 18-21 November 2008, United Nations University, Tokyo, Japan.*
- Hauck, C., 2001. Geophysical methods for detecting permafrost in high mountains. Ms. Swiss Federal Institute of Technology Zurich, Diss. ETH No. 14163.
- Jackson, P., Taylor-Smith, D., Stanford, P.N., 1978. Resistivity-porosity-particle shape relationships for marine sands, *Geophysics* 43, No. 6, p. 1250-1268.
- Jongmans, D., Garambois, S., 2007. Geophysical investigation of landslides: a review. *Bulletin de la Societe Geologique de France* 178(2), 101-112.

- Jouniaux, L., Mainault, A., Naudet, V., Pessel, M., Sailhac, P., 2009. Review of self-potential methods in hydrogeophysics. *Comptes Rendus Geosciences*, Volume 341, Issues 10-11, Hydrogeophysique, October-November 2009, Pages 928-936.
- Kamshilin, A., Volkova, E., Leontiev, V., Kuzichkin, O., 2008. On study of the geodynamic processes by geoelectrical Methods. *International Congress on Environmental Modelling and Software*, 8, Russia.
- Kearey, Philip; Michael Brooks, 1991. *An Introduction to Geophysical Exploration* (Second edition ed.). Blackwell Science, 254 pp. ISBN 0-632-02923-4.
- Kim, J.-H., 2005. Four dimensional inversion of dc resistivity monitoring data. *Proceedings of Near Surface 2005, the 11th European Meeting of Environmental and Engineering Geophysics*, A006.
- Kim, J.-H., Yi, M.-J., Park, S.-G., Kim, J.G., 2009. 4-D inversion of DC resistivity monitoring data acquired over a dynamically changing earth model. *Journal of Applied Geophysics* 68, 522-532.
- Kiessling, D., Schuett, H., Schoebel, B., Krueger, K., Schmidt-Hattenberger, C., Schilling, F., 2009. Geoelectric Monitoring of geological CO₂ storage at Ketzin, Germany (CO₂SINK project): Downhole and Surface-Downhole measurements. *EGU General Assembly 2009, Geophysical Research Abstracts*, Vol. 11, EGU2009-11041-1.
- Kneisel, C., 2004. New insights into mountain permafrost occurrence and characteristics in glacier forefields at high altitude through the application of 2D resistivity imaging. *Permafrost and Periglacial Processes* 15 (3), 221-227.
- Kneisel, C., 2006. Mapping and monitoring mountain permafrost using electrical resistivity tomography. *European Geosciences Union 2006, Geophysical Research Abstracts*, Vol. 8, 04181.
- Kono H., Yasunari T., Yabe S., Hattori K., Ochiai H., 2010: Monitoring of the rain-induced landslide process with use of self-potential method. – *Japan Geoscience Union Meeting 2010, May 23-28 at Makuhari, Chiba, Japan.*
- Krummel H., Janik M., Wiebe H., Holland R. 2012. Resistivity monitoring of a landslide in the Swabian Alb, Germany, 1st Workshop on Geoelectrical Monitoring, extended abstracts, Vienna.
- LaBrecque, D.J., Yang, X., 2001. Difference inversion of ERT data: a fast inversion method for 3-D in situ monitoring. *Journal of Environmental and Engineering Geophysics* 6, 83-89.
- Lapenna, V., Lorenzo, P., Perrone, A., Piscitelli, S., Rizzo, E., Sdao, F., 2003. High-resolution geoelectrical tomographies in the study of the Giarrossa landslide (Potenza, Basilicata). *Bull. Eng. Geol. Env.* 62, 259-68.
- Lapenna, V., Lorenzo, P., Perrone, A., Piscitelli, S., Rizzo, E., Sdao, F., 2005. 2D electrical resistivity imaging of some complex landslides in Lucanian Apennine chain, southern, Italy. *Geophysics* 70.
- Lambiel, C., Baroň, L., 2008. Two-dimensional geoelectrical monitoring in an alpine frozen moraine. *Proceedings of the 9th International Conference on Permafrost, Fairbanks, Alaska, June 2008, Extended Abstracts volume.*
- Loke, M.H., 1999. Time lapse resistivity imaging inversion. *Proceedings of the 5th Meeting of the Environmental and Engineering European Society, Em1.*
- Jouniaux L., Mainault A., Naudet V., Pessel M., Sailhac P., 2009: Review of self-potential methods in hydrogeophysics. – *Internal geophysics (Applied geophysics), C. R. Geoscience*, 341 (2009): 928–936.
- Marescot L., Monnet R., Chapellier D., 2008: Resistivity and induced polarization surveys for slope instability studies in the SWISS Alps. – *Engineering Geology*, 98 (2008): 18-28. Elsevier.
- Mauritsch, H.J., Seiberl, W., Arndt, R., Römer, A., Schneiderbauer, K., Sendlhofer, G.P., 2000. Geophysical investigations of a large landslide in the Carnic Region (case study). *Engineering Geology* 56, 373-388.
- Meric, O., Garambois, S., Jongmans, D., Wathélet, M., Chatelain, J.-L., Vengeon, J.-M., 2005. Application of geophysical methods for the investigation of the large gravitational mass movement of Séchilienne, France. *Canadian Geotechnical Journal* 42, 1105-1115.
- Meric O., Garambois S., Orenge Y., 2006: Large Gravitational Movement Monitoring Using a Spontaneous Potential Network. – *Conference Proceedings. SAGEEP 2006, April 2-6, 2006, Seattle, Washington, USA, 7 pp.*
- Nilsson, J.N.U., Sigray, P., Tyler, R.H., 2007. Geoelectric Monitoring of Wind-Driven Barotropic Transports in the Baltic Sea. *Journal of Atmospheric and Oceanic Technology* 24, 1655-1664.
- Niesner, E., Weidinger, J.T., 2008. Results of a continuous geoelectrical monitoring in the forefront of the large landslide event of 2007/2008 in the Gschlifgraben (Gmunden, Upper Austria). *EGU General Assembly 2008, Geophysical Research Abstracts*, Vol. 10.

- Niesner, E., Weidinger, J.T., 2009. The potential of geoelectrics for landslide forecasting. EGU General Assembly 2009, Geophysical Research Abstracts, Vol. 11.
- Noetzli, J., Hilbich, C., Hauck, C., Hoelzle, M., Gruber, S., 2008. Comparison of Simulated 2D Temperature Profiles with Time-Lapse Electrical Resistivity Data at the Schilthorn Crest, Switzerland. 9th International Conference on Permafrost, Book of published papers: 1293-1298.
- Oldenborger, G.A., Knoll, M.D., Routh, P.S., LaBrecque, D.J., 2007. Time-lapse ERT monitoring of an injection/withdrawal experiment in a shallow unconfined aquifer. *Geophysics* 72, F177-F187.
- Perrone, A., 2001. Electrical and Self-Potential tomographic techniques for landslide monitoring: first results on Southern Apennine Chain (Italy). II international Workshop on Geo-Electro-Magnetism / Abstract, *Memorie dell'Accademia Lunigianese di Scienze "G. Capellini"* Vol. LXXI (2001), Scienze Matematiche, Fisiche e Naturali, La Spezia.
- Petrenko V.: Electrical Properties of Ice, Special Report 93-20, U.S.Army Cold Regions Research, New Hampshire, 1993.
- RSK STATS Geoconsult Ltd, http://www.environmental-geophysics.co.uk/tech_ip.htm
- Sass, O., Viles, H.A., 2010. Wetting and drying of masonry walls: 2D-resistivity monitoring of driving rain experiments on historic stonework in Oxford, UK. *Journal of Applied Geophysics* 70, 72–83.
- Schlumberger, 1987. Log Interpretation Charts, Houston, Schlumberger Educational Services.
- Sjödahl, P., 2006. Resistivity investigation and monitoring for detection of internal erosion and anomalous seepage in embankment dams. MS. Doctoral Thesis, Lund University, 96 pp.
- Supper, R., Jochum, B., Seiberl, W., Arndt, R., 2000. Geoelectrical multielectrode measurements for surveying and monitoring of landslide areas. Proceedings of the "Workshop on Advanced Techniques for the Assessment of Natural Hazards in Mountain Areas", p.99, Igls, Austria.
- Supper, R., Seiberl, W., Hübl, G., 2001. Combined Airborne Electromagnetics and Ground Geoelectrics for Landslide Investigations. II international Workshop on Geo-Electro-Magnetism / Abstract, *Memorie dell'Accademia Lunigianese di Scienze "G. Capellini"* Vol. LXXI (2001), Scienze Matematiche, Fisiche e Naturali, La Spezia.
- Supper, R., Hübl, G., Jaritz, W., 2002. Geophysical Surveys for the investigation and monitoring of landslide areas. Proceedings of the Environmental and Engineering Geophysical Society, 8th Meeting Aveiro, Portugal.
- Supper, R., Römer, A., Avian, M., Kellerer-Pirklbauer, A., 2007. Geoelectrical measurements for permafrost monitoring at the Hoher Sonnblick, Salzburg, Austria. EGU General Assembly 2007, Geophysical Research Abstracts, Vol. 9.
- Supper, R., Ahl, A., Römer, A., Jochum, B., Bieber, G., 2008. A complex geo-scientific strategy for landslide hazard mitigation – from airborne mapping to ground monitoring. *Advances in Geosciences* 14, 1-6.
- Supper, R., Römer, A., Jochum, B., 2009. Geoelectrical measurements for natural hazard monitoring. SEGJ 9th International Symposium, Extended Abstracts, Sapporo.
- Supper R., Jung-Ho Kim, Baroň I., 2010: Temporal changes of geoelectrical properties as possible indicator of future failure of high risk landslides: Assessment and improvements of the geoelectrical technology for integrated early warning – TEMPEL. – Project proposal
- Supper R, Jochum B., Kim J.H., Ottowitz D., Pfeiler S., Baroň I., Römer A., Vecchiotti F., Lovisololo M., Cardellini S., Moser G., 2012. The TEMPEL geoelectrical monitoring network for landslides: highlights of recent monitoring result, 1st Workshop on Geoelectrical Monitoring, extended abstracts, Vienna.
- Wang E.-Y., Li Z.-H., Liu Z.-T., Li Y.-N., Song X.-Y., 2009: An Experimental Study on Surface Electric Potential of Loaded Coal. – *CHINESE Journal of Geophysics*, 52 (3): 641-649.
- WILKINSON, P B, CHAMBERS, J E, MELDRUM, P I, GUNN, D A, OGILVY, R D, and KURAS, O. 2010. Predicting the movements of permanently installed electrodes on an active landslide using time-lapse geoelectrical resistivity data only. *Geophysical Journal International*, Vol. 183, 543-556
- Winsauer, W.O., Shearin, H.M., Jr., Masson, P.H., Williams, M., 1952. Resistivity of brine saturated sands in relation to pore geometry. *AAPG Bull.*, v. 36, p. 253-277.
- Yaramanci, U., 2000. Geoelectric exploration and monitoring in rock salt for the safety assessment of underground waste disposal sites. *Journal of Applied Geophysics* 44, 181-196.
- Zlotnicki, J., Nishida, Y., 2003. Review on Morphological Insights of Self-Potential Anomalies on Volcanoes. *Surveys in Geophysics* 24, 291-338.

2.3.2 SEISMIC VELOCITY

Magda Čarman, Špela Kumelj
Geological Survey of Slovenia

Seismic wave velocity reflects the elastic properties of the medium, which are in turn dependant, among other factors, on water content and porosity. Seismic P-wave velocity depends on the bulk modulus of the medium, the shear modulus of the medium and the density of the medium; seismic S-wave velocity depends on the shear modulus and density only. In general, seismic wave velocity is inversely proportional to porosity; increased porosity produces lower seismic velocities. Assuming air-filled porosity, seismic wave velocity is lowest in a dry porous material. Seismic velocity increases as the material becomes partially water saturated and is highest when the material becomes water saturated. Variation depends on porosity but is also proportional to the ratio between air and water density (Mavko et al., 1998). In principle, seismic velocity change may be indicative of change in water content, however, geoelectric methods are more effective in this respect.

Methods in landslide investigation using seismic waves are usually employed to study the subsurface structure of the landslide and include: high-resolution seismic reflection (limited use due to complex topography and attenuation problems, e.g. Bichler et al., 2004; Jongmans and Grambois, 2007; Sass et al., 2008); seismic refraction (Glade et al., 2005); seismic noise measurement - H/V method (Méric et al., 2007); and inversion of shear waves – MASW (Socco and Jongmans, 2004; Méric et al., 2007). Seismic wave velocity variation due to changing subsurface structure, such as a change in lithology, is larger than the variation due to variation of water (Mavko et al., 1998). Typically, both S- and P-wave velocities are significantly lower in landslide bodies than in unaffected ground. The most routinely used seismic methods in landslide studies are seismic refraction studies of landslides (GRM – Generalized Reciprocal Method and seismic tomography) and lately in MASW studies. In practice, seismic refraction surveys are effective at discerning changes in material inside the landslide mass as well as detecting the outer limits of the landslide. Seismic velocity is lower inside the landslide mass due to reduced elastic and shear properties of the material. Seismic P-wave velocities are in the range between around 200 m/s for highly porous, dry landslide masses, through the typical 500 – 1000 m/s for landslide bodies, to up and above 2500-4000 m/s for solid bedrock. S-wave velocities are lower (Caris and Van Asch, 1991; Glade et al., 2005). A shortcoming of the refraction GRM method is the failure in detecting the so-called hidden layers where seismic velocity inversion occurs (where a lower-velocity layer underlies a higher-velocity layer). Refraction methods are also usually limited to depths of about 50 meters. Geophysical methods utilizing shear waves (MASW and H/V) are especially suitable for detection of shear planes such as the main slip plane, as there may be a marked shear-wave velocity contrast along it.

Geophysical methods utilizing seismic waves offer strong tools for landslide analysis, however, due to described shortcomings they are best used in conjunction with other methods.

Used on multiple occasions they may be able to detect changes in the landslide body, structure and geometry.

References:

- Bichler, A., Bobrovsky, P., Best, M., Douma, M., Hunter, J., Calvert, T., Burns, R. 2004. Three-dimensional mapping of a landslide using a multi-geophysical approach: the Quesnel Forks landslide. *Landslides* (2004) 1: 29–40 DOI 10.1007/s10346-003-0008-7
- Caris, J.P.T. and Van Asch, Th.W.J. 1991. Geophysical, geotechnical and hydrological investigations of a small landslide in the French Alps. *Engineering Geology* 31: 249 – 276.
- Glade, T., Stark, P., Dikau, R. 2005. Determination of potential landslide shear plane depth using seismic refraction—a case study in Rheinhessen, Germany. *Bull Eng Geol Environ* (2005) 64: 151–158 DOI 10.1007/s10064-004-0258-1
- Mavko, G., Mukerji, T., Dvorkin, J. 1998. *The Rock Physics Handbook. Tools for seismic analysis and porous media*. Cambridge university press. 329 pp.
- Méric, O., Grambois, S., Malet J-P, Cadet, H., Guéguen P., Jongmans, D. 2007. Seismic noise-based methods for soft-rock landslide characterization. *Bulletin Société Géologique de France* 178, 2 (2007) 137-148 DOI : 10.2113/gssgfbull.178.2.137
- Jongmans, D. and Grambois, D. 2007. Geophysical investigation of landslides: a review. *Bulletin Société Géologique de France* 178, 2 (2007) 101-112" DOI : 10.2113/gssgfbull.178.2.101
- Sass, O., Bell, R., Glade, T. 2008. Comparison of GPR, 2D-resistivity and traditional techniques for the subsurface exploration of the Öschingen landslide, Swabian Alb (Germany). *Geomorphology* 93 (2008) 89–103
- Socco, V. and Jongmans, D. 2004. Special issue on Seismic Surface Waves. *Near surface geophysics*, 2, 163 – 258.

2.3.3 PASSIVE ELECTROMAGNETIC EMISSION

Ivo Baroň

Geological Survey of Austria

In recent literature, several authors refer to new promising monitoring parameters of landslides: the *passive (pulse) electromagnetic emissions* – *PEE* (Aitmanov et al. 1997, Burdakova et al. 2005, Kharkhalis 1996, Wagner et al. 2002) or also called *natural pulsed electromagnetic field of earth* – *NPEMFE* (Lauterbach 2005). When the substrate undergoes a change of strain and displacement within different material blocks, passive electromagnetic radiation occurs; this phenomenon could occur at different scales from forming of microfissures up to dislocations separating major landslide blocks (Aitmanov et al. 1997). The method is being applied also for earthquake monitoring (Gershenzon and Bambakidis 2001), for stress field identification in tunnelling engineering (Lichtenberger 2006), or for investigating soil suffosion and collapses of subcutaneous caverns (Liebermann 2009).

As summarized by Gershenzon and Bambakidis (2001), the origin of the passive EM pulses could be the *piezomagnetic effect* (deformation of the minerals with residual magnetism due to ferromagnetic inclusions, e.g. titano-magnetite, when the orientation of the inclusions change); the *piezoelectric effect* of quartz; the *electrokinetic effect* (pore water causes an electric double layer at the pore boundary due to the difference in the electrochemical potentials of water and rock); and an *induction effect* (large-scale movement of material in the geomagnetic field gives rise to an induced electric field and current).

The most important parameters of PEE for landslide monitoring and early warning are the *pulse duration, separation, emission activity - quantity of impulses in time, impulses energy* and *radiation spectrum structure* (Aitmanov 1997). The PEE could be recorded by specific antennas, both in boreholes and on the ground surface. The borehole measuring equipment could be constructed non-serially by any producer of industrial electronic devices after development based on the customer's specification (e.g. Sensor Enterprise, Bratislava; Peter Wagner, Geological Survey of Slovakia, pers comm.). Lauterbach (2005) used a portable commercial instrument called “Cereskop” (Ceres GmbH, Staffort) for landslide investigation in Germany.

Kharkhalis (1996) presented a case about the natural electromagnetic pulse field in an experimental area of a landslide-prone slope in the river Uzh valley (Carpathians). Electromagnetic emission was observed in the 2-50 kHz range. They demonstrated that anisotropy of the electromagnetic pulse field was of a deformation nature and that it reflected the intensity of stresses developed in the slope. The data were interpreted on the basis of an electromagnetic model.

However, the PEE measurements are often influenced by electromagnetic noise (Linderbach 2006), and it is sometimes very difficult to discriminate the useful signal from this noise from various origins (atmospheric, artificial, etc.). For that reason, the use of acoustic emissions could be a more useful parameter for landslide monitoring at present (Oleg Kozlov & Alexander Strom, pers. comm.).

References:

- Aitmanov I.T., Torgoyev I.A., Alioshin Yu.G. (1997): Monitoring of Dangerous Geodynamical Processes in Highland Areas. –In.: Zhang et al.: Proceedings of the 30th International Geological Congress, vol. 2&3
- Burdakova E.V., Glinskaya N.V., Palamarchuk V.K. (2005): Short-term prediction of the landslides initiated activity in studies of the steep slopes. – Geophysical Research Abstracts, Vol. 7, 09955, 2005. SRef-ID: 1607-7962/gra/EGU05-A-09955
- Gershenson N., Bambakidis G. (2001): Modeling of seismo-electromagnetic phenomena. - Russian Journal of Earth Sciences 3 (4).
- Kharkhalis N.R. (1996): Manifestation of natural electromagnetic pulse emission on landslide slopes. - International Journal of Rock Mechanics and Mining Sciences and Geomechanics Abstracts 33 (6): 242.
- Liebermann Ch. (2009): Geologisches Strukturmodell im Weiteren Umfeld des Erdfalls „Northeimer Bergbad“. – MS. Bachelor thesis. Georg-August Universität, Göttingen, 72 pp.
- Lauterbach M. (2005): Beurteilung der Eignung der NPEMFE-Methode (Natural Pulsed Electromagnetic Field of Earth) mit dem "Cereskop" in Rutschungen und in Lockerund Festgesteinen mit Spannungsänderungen im Mittel- und Hochgebirge. - Dissertation.Univ. Mainz, 1-174.
- Wagner P., Scherer S, Jadron D., Mokra M., Vybiral V. (2002): Analysis of landslide monitoring results. – In.: Rybář J., Stemberk J., Wagner P. (eds.): Landslides – Proceedings of the 1st European Conference on Landslides, Prague, Czech Republic, June 24-26, 2002. – Swets & Zeitlinger, Lisse, 471-476.
- Lichtenberger M. (2006): Underground Measurements of Electromagnetic Radiation Related to Stress-induced Fractures in the Odenwald Mountains (Germany). - Pure and Applied Geophysics, 163 (8): 1661-1677.

2.3.4 PROTON MAGNETIC RESONANCE (PMR)

Robert Supper

Geological Survey of Austria

Introduction/Definition

Protons in subsurface water possess a nonzero magnetic moment. In equilibrium condition they are oriented towards magnetic north. If an alternating magnetic field pulse is applied using the proton resonance frequency (which depends on the earth's magnetic field) perpendicular to the earth's magnetic field, a magnetic resonance signal is generated, caused by the precession of the spin magnetization around the geomagnetic field.

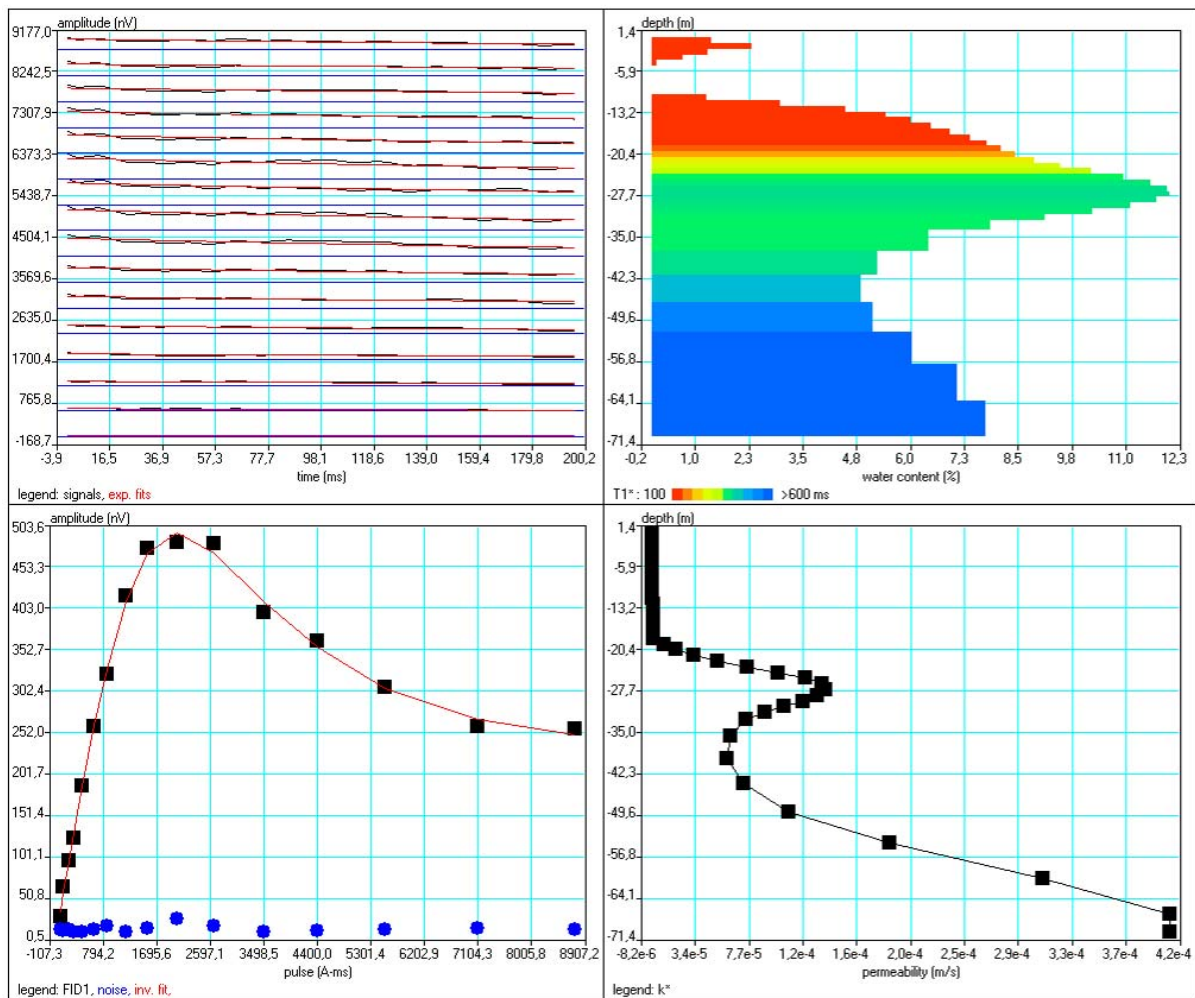


Figure 2.3.4-1. Results of MRS soundings in Austria. Top left: relaxation curves for different pulse moments; bottom left: MRS sounding curve; top right: calculated water content depending on depth; bottom right: calculated permeability/transmissivity with depth.

Dependency on subsurface parameters

As a major advantage compared to other geophysical methods, the PMR signal directly depends on the quantity of water in the subsurface. Due to advanced data acquisition technologies, water content (amplitude of signal) as well as hydraulic transmissivity (relaxation time) can be estimated for the model of a horizontally- (multi-) layered subsurface (Figure 2.3.4-1; see further details at: Legschenko et al. 2004).

Technologies of acquisition: magnetic resonance sounding (MRS)

The PMR signal is generated by an alternating current pulse (using the resonance frequency of the protons) energizing a large loop lying on the surface. After cut off of the injection current, the signal injected in the loop by preceding protons and the relaxation time of the signal T_2^* are measured. Various pulse magnitudes are used to achieve depth resolution.

The saturation recovery method (application of two pulses with a certain delay) can be used to measure the longitudinal relaxation time T_1 , which is proportional to the mean pore size (Figure 2.3.4-2).

MRS is a large-scale method, which means that the investigated volume is approximately equal to a cube width of 1.5 times the size of the injection loop.

Units

The PMR signal, which is injected in the surface loop is measured in nV, whereas the amplitude of the signal varies from approximately 100 nV to 1000 nV depending on water content.

Magnetic Properties of Rocks and MRS Relaxation Times					
Rock Type	Magnetization (A/m)	Susceptibility (SIU)	T_2^* (msec)	T_1 (msec)	Comments
Reef limestone (Cyprus)	1×10^{-4}	-9.1×10^{-6}	80	220	Unsaturated zone
Fractured limestone (Cyprus)	2.8×10^{-4}	-8.5×10^{-6}	130	430	Aquifer
Highly fractured limestone (France)	8.1×10^{-3}	1.5×10^{-3}	280	800	Aquifer
Karst limestone (Cyprus)	4.5×10^{-5}	-7.2×10^{-6}	460	1000	Aquifer
Clay and fine sand	1.4×10^{-3}	1.4×10^{-4}	70	310	Aquifer
Medium sand (France)	3.9×10^{-4}	2.9×10^{-5}	120	420	Aquifer
Gravel and coarse sand (France)	7.5×10^{-4}	4.4×10^{-4}	330	600	Aquifer
Sandstone (USA)	3.2×10^{-4}	2×10^{-4}	80	—	Aquifer
Basaltic gravel	1.3×10^{-1}	4.8×10^{-3}	10	—	Aquifer

Figure 2.3.4-2. Typical values of relaxation times for different rocks (from Legschenko et al., 2004)

Natural background

The major disadvantage of MRS is its sensitivity to noise (Figure 2.3.4-3.). In most cases the expected signal is below 500 nV (approximately <30 % of water content) whereas in inhabited regions of Europe the electromagnetic noise (mostly 50 Hz and multiples) can reach levels of several thousands of nV. Signal stacking and the use of reference loops or eight-shape loops can improve signal quality significantly. However, measurements are in many cases still not possible near settlements.

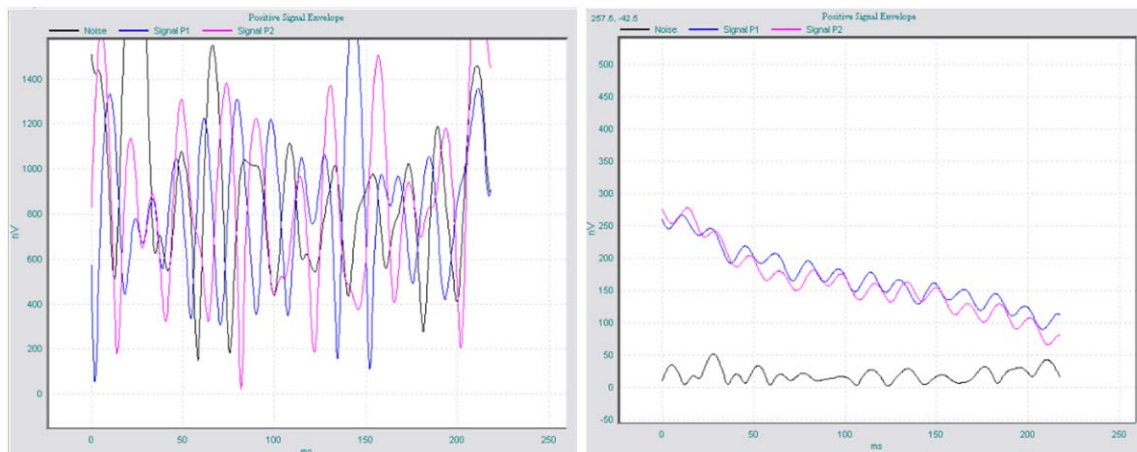


Figure 2.3.4-3. PMR decay curves in environment with high (left) and low (right) background noise; data taken from a test survey in Austria in October 2011.

Potential as monitoring or early warning parameter

The MRS method has so far not been used for monitoring purposes. Due to the high costs of the equipment (100-200k€) an application for standard early warning purposes cannot be expected in the near future. However since the method provides a direct measure of the subsurface water content, especially for scientific applications to improve the understanding of subsurface processes, an interesting potential for application of this method can be expected. Yet, several technical improvements are necessary to use this method for monitoring purposes.

References:

- Bernard J. (2004): MRS: Step-by-step operation of NUMIS systems. – IRIS Instruments document.
- Bernard J., Legchenko A. (2003): Groundwater exploration with the Magnetic Resonance Sounding method. – Proc. of the 16th ASEG Geophysical Conference and Exhibition, Adelaide, February 2003, and Invited Paper at the 65th EAGE Conference & Exhibition, Stavanger, June 2003.
- Braun M., Hertrich M. & Yaramanci U. (2005): Complex inversion of MRS data. – *Near Surface Geophysics*, **3**, 155-164.
- Hertrich M., Braun M. & Yaramanci U. (2005): Magnetic Resonance Soundings with separated transmitter and receiver loops. – *Near Surface Geophysics*, **3**, 141-154.
- Lachassagne P., Baltassat J., Legchenko A. & De Gramot H.M. (2005): The links between MRS parameters and the hydrogeological parameters. – *Near Surface Geophysics*, **3**, 259-266.
- Legchenko A., Beauce A., Guillen A., Valla P. & Bernard J. (1997): Natural variations in the magnetic resonance signal used in PMR groundwater prospecting from the surface. – *European Journal of Environmental and Engineering geophysics*, **2**, 173-190.
- Legchenko V., Baltassat J. M., Beauce A. & Bernard J. (2002): Nuclear magnetic resonance as a geophysical tool for hydrogeologists. – *Journal of Applied Geophysics*, **50**, 21-46.
- Legchenko V., Baltassat J. M., Bobachev A., Martin C., Robain H. & Vouillamoz J.-M. (2004): Magnetic resonance soundings applied to the characterization of aquifers. – *Groundwater*, **42**, 436-473.

- Legchenko A. & Valla P. (2002): A review of the basic principles for proton magnetic resonance sounding measurements. – *Journal of Applied Geophysics*, **50**, 3-19.
- Lubczynski, M., Roy, J. (2003): Hydrogeological interpretation and potential of the new magnetic resonance sounding (MRS) method. – *Journal of Hydrology*, 283
- Semenov, A.G. (1987): NMR Hydroscope for water prospecting. – Proceedings of the seminar on Geotomography: Indian Geophysical Union, Hyderabad
- Valla, P., Yaramanci, U., 2002, Surface Nuclear Magnetic Resonance : What is possible? – Special issue of the *Journal of Applied Geophysics*, volume 50
- Vermeersch F. (2000): NUMIS Plus equipment operating manual. – IRIS Instruments document.
- Yaramanci, U., Lange, G., Knodel, K., 1999, Surface NMR within a geophysical study of an aquifer at Haldensleben (Germany). – *Geophysical Prospecting*, 47.

2.4 EXTERNAL TRIGGERS

This part deals with **external processes, which have an effect on the mass movement body** and which are able to activate or accelerate it. Those parameters could be monitored in order to predict or just detect the reactivation or critical acceleration of mass movement. The text reviews those processes, presents how they are monitored and how this data must be processed/provided (e.g. direct information from other warning centres) to be used in early warning platforms.

2.4.1 METEOROLOGICAL CONDITIONS

Paola Mercogliano

Centro Euro-Mediterraneo per i Cambiamenti Climatici

Slope failures are caused by a combination of several factors including atmospherical conditions. The most important landslide triggering atmospheric factors are:

- precipitations (rain),
- air temperature and wind,
- snowmelt and freeze-thaw.

The landslide triggering mechanisms are very heterogeneous even if only atmosphere-related triggers are considered.

The reason precipitation, snowmelt, and freeze-thaw have an effect on the slope stability is that an addition of water from rainfall or snowmelt reduces the effective strength parameters of the substrate and adds weight to the slope. Water can seep into the soil or rock and replace the air in the pore space or fractures. Since water is heavier than air, this increases the weight of the soil. Weight determines increasing stress in the soil and this can lead to slope instability. Water also has the ability to change the angle of repose (the slope angle which is the stable angle for the slope). Snowmelt events, more frequent during the spring season, can increase pore pressures in the soil thereby increasing the risk of slope failures. Freeze-thaw events, which usually happen during spring and fall but also during warm winters, can increase the potential for slope failure by expanding and contracting the water within the soil.

As reported by some authors (Collison, 1996; van Asch, 1997) precipitation can represent a triggering factor for different types of landslides:

1. deep-seated landslides with shear planes at depth greater than 10 m,
2. shallow landslides with shear planes at 1–10 m depth,
3. landslides with superficial shear planes, e.g. debris flow.

For these three cases, different hydrologic systems and, hence, rainfall characteristics must be considered as triggering factors. For example, debris flows have a strong correlation with the short-term rainfall events (duration of few hours, more frequent during summer and fall season) while deep-seated landslides are related to yearly and/or monthly precipitation. In other words, (Terzaghi, 1950) precipitations might have a different influence based on the examined landslide. This aspect is well highlighted in following picture (Figure 2.4.1–1),

which reports the cumulated annual precipitation and the frequencies of different types of soil movements in a single area of California, USA, during a 45-year period.

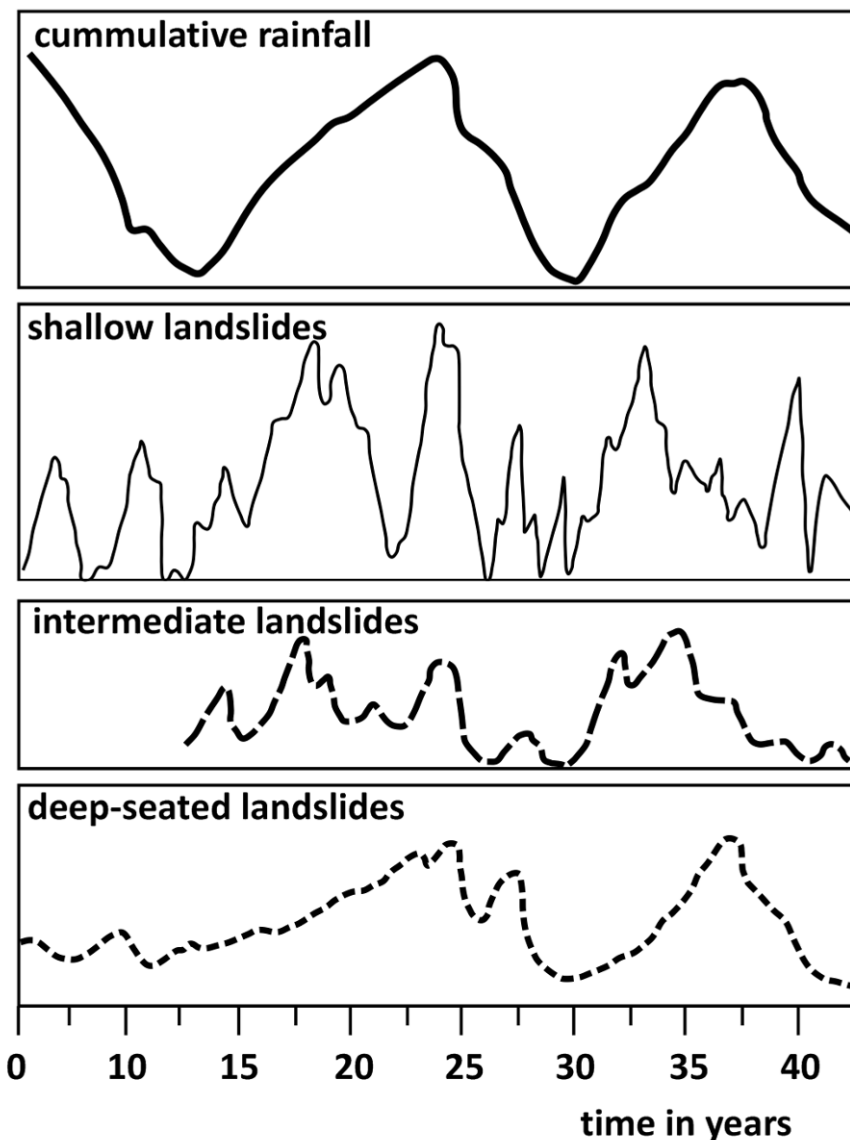


Figure 2.4.1–1. Cumulated annual precipitation and frequency of different types of landslides (after Sangrey et al., 1984). The upper figure shows the cumulated rainfall, the second figure the frequency of the shallow landslides (frane corticali); the third figure shows the frequency of the landslide at intermediate depth while the last figure shows the frequency of the deep landslide. On the horizontal axis the time is reported (measured in years).

The annual precipitation can only be correlated with deep movements. The frequencies of the shallow landslides are independent from the annual precipitation, but more dependent on precipitation in shorter periods. The latter is the case for the unsaturated pyroclastic deposits of the Campania Region (Damiano, et al, 2011, Mercogliano et al. 2011) in which the soil stability shows a dependence on the rainfall over, approximately, a three-month period.

On multiple sites, rainfall thresholds have been identified based on empirical correlations between rainfall characteristics (usually intensity and duration of the rainfall events) and landslide (usually surface landslide) occurrences. These thresholds are very specific for the

geomorphological characteristics of the area and they can further depend on daily, hourly, or general rainfall that precedes the landslide events. These methods can be developed only when a large dataset of rainfall and landslide observations is available for the area. The term “threshold” can be defined as the critical level of some quantity needed for a process to take place (Reinchenbach et al. 1998). Based on the knowledge of this relationship it is possible to say that landslides are very likely to occur when rainfall intensity/duration characteristics are above the empirical threshold. (An example of this approach is available on <http://landslides.usgs.gov/monitoring/seattle/rtd/plot.php>.) This threshold can be used as a warning signal for personnel who manage the monitoring system (Bacchini and Zannoni 2003).

Other important factors are air temperature and wind, mainly for the dependence of evapotranspiration on these parameters. The evapotranspiration determines the water loss at the soil-air boundary, and this loss has an influence on the soil-water balance on which soil stability depends. The water loss, in particular, takes place through the phenomenon of evaporation and transpiration. Since, in practice, it is extremely difficult to separately measure the evaporation from plant surfaces and the evaporation from the soil surface, puddles, ditches, etc. surrounding the plant, it is common practice to amalgamate all of the evaporative surfaces in the evapotranspiration phenomenon. The transpiration element is due to vegetation (loss of water as vapour through stomata in leaves) while evaporation that happens on the soil-air boundary is directly due to atmospheric conditions. The evaporation factor can further be broken down into a combination of vaporisation and vapour removal, where vaporisation is directly driven by applied energy (for instance the near-soil atmospheric temperature) and vapour removal happens because of wind or convection of dry air.

If some input atmospheric parameters can increase the frequency of landslides, some other factors related to climate change, like material availability, changes in the soil properties, etc., can decrease it. As an example, in the case of debris slides or debris flows, even the heaviest rainfall cannot trigger a mobilization if debris is not available. On the contrary, if debris availability increases due to melting glaciers and permafrost (one of the main consequences of global warming), as outlined in Zimmermann and Haeberli (1992) and Dikau et al. (1996), this is a sufficient condition for an increased frequency of debris flows.

Moreover, other factors related to the climate might be important:

- changing land use, induced by human activities or due to climate change,
- vegetation succession due to climate change,
- changing weathering regime due to climate change.

All these factors can play an important role in changing the overall susceptibility of a slope to climatic factors.

References:

- Bacchini M. and Zannoni A. (2003): Relations between rainfall and triggering of debris-flow: case study of Cancia (Dolomites, North-eastern Italy). – *Natural Hazards and Earth System Sciences*, 3: 71–79.
- Collison A., Wade S., Griffiths J., Dehn M. (2006). Modelling the impact of predicted climate change on landslide frequency and magnitude in SE England. *Engineering Geology* 55 (2000), pp. 205–218.
- Damiano E., Mercogliano P., “A study on forecasting of shallow landslides in pyroclastic soils due to climatic changes in the Mediterranean area” keynote lecture for “The Second World Landslide forum” , Rome 3-8 October 2011.
- Dikau R., Schrott L., Dehn M., Hennrich K., Ibsen M. L., Rasemann S., Eds. (1996). The temporal stability and activity of landslides in Europe with respect to climatic change. – MS. TESLEC. Final Report, Summary Report. European Community CEC Environment Program, Contract No. EV5VCT940454, Brussels.
- Mercogliano P., Damiano E., Bucchignani E., Olivares L., “Prediction of shallow landslides in pyroclastic soils due to climatic changes in the Mediterranean area” accepted for the oral session NH9.8 of EGU General Assembly 2011 “Risk management in a changing world considering spatio-temporal variability”.
- Reichenbach P., Cardinali M., De Vita P., Guzzetti F. (1998): Regional hydrological thresholds for landslides and floods in the Tiber River Basin (central Italy). – *Environmental Geology*, 35 (2– 3): 146–159.
- Sangrey D.A., Harrop-Williams K.O., Klaiber J.A. (1984). Predicting ground-water response to precipitation. *Journal of the Geotechnical Eng. ASCE*, vol. 110, 7
- Terzaghi K. (1950). Mechanisms of landslides. *Application of Geology to Engineering Practice*, Berkey volume, Sidney Paige, Geol. Soc. America.
- van Asch T.W.J. (1997). The temporal activity of landslides and its climatological signals. In: Matthews, J.A., Brunsdon, D., Frenzel, B., Gläser, B., Weiβ, M.M. (Eds.), *Rapid Mass Movement as a Source of Climatic Evidence for the Holocene*. *Palaeoclimate Research*, vol. 19. Gustav Fischer, Stuttgart, pp. 7-16.
- Zimmermann M., Haerberli W. (1992). Climatic change and debris flow activity in high-mountain areas - a case study in the Swiss Alps. *Catena Suppl.* 22, pp. 59-72.

2.4.2 SEISMICITY/EARTHQUAKES

Magda Čarman, Špela Kumelj
Geological Survey of Slovenia

Earthquakes with magnitude greater than ~4.0 produce landslides on very susceptible slopes, and larger earthquakes produce widespread landsliding (Keeper 1984; Malamud et al., 2004). The passage of a seismic wave changes the vertical and shear loading of the landslide mass. Vertical stress is changed by vertical acceleration and movement of the mass during the seismic wave's passage, with increasing tensile stress during upward movement and increasing compressive stress during downward movement; cyclic shear stress is produced by lateral movement of the mass during the seismic wave's passage. Stress depends on seismic wave amplitude, while effects also depend on the duration of the seismic wave action. Also, topographic amplification of seismic waves may occur in some areas (Meunier et al., 2008; Delgado et al., 2011). Any geological material with low geomechanical strength may be affected (soil or rock). Low strength may be produced by intense weathering and fracturing, weak cementation, high water saturation and/or poor compaction. Under high water saturation, seismic wave action may lead to a complete loss of material cohesion, leading into material liquefaction.

Earthquakes/seismic events may affect landslides in a direct or indirect manner. Direct effects are mobilizations of landslides during earthquakes. This may occur from failure of the sliding plane(s) due to shear stress and/or a landslide mass' partial or complete liquefaction. The result may be a slowly moving landslide mass or a fast moving debris flow. Rockfalls may occur on unstable steep rock slopes, especially under favourable orientation of bedding and/or cracks. This effect may be further enhanced by topographic amplification of seismic waves (Meunier et al., 2008).

Indirect effects are changes in the landslide mass that may lead to eventual activation of the landslide. These effects may include appearance, and expansion and multiplication of tension cracks and shear zones. This would increase water percolation in the landslide mass, in turn increasing pore pressure and reducing landslide material cohesion. In hard rock, the formation of new cracks and expansion of existing ones may subject the rock to increased effects from frost and insolation, increasing the probability of future failure.

Observations show that seismic landslide occurrence is strongly dependent on the proximity of the fault rupture (Sassa, 1996). Vertically convex slopes appear to be slightly more susceptible to seismically induced failures than vertically concave slopes. Steep rock slopes are susceptible, as well as gentle slopes in soft sediments. Thus, the combined effect of the slope and geology must be taken into account (Sato et al., 2007).

To assess an earthquake-induced landslide hazard, multiscale surveys integrated in GIS are most suitable. Geological mapping should be conducted on slopes that are potentially failure-prone during seismic events: soft sediment slopes with lithology that is more landslide-prone, rock slopes with existing fracture systems, and fossil landslides. Mapping results should be combined with remote sensing data. Also, an earthquake hazard map should be included to properly weigh the increased probability of earthquake-induced slope failure, to produce a map of earthquake-induced landslide hazards (Chigira et al., 2003; Metternicht et al., 2005; Haneberg et al., 2009; Jaboyedoff et al., 2010).

Post-earthquake, new unstable slope areas may have formed. Pre-existing landslides and heavily fractured rock areas that were not mobilized during the earthquake may have been further weakened, increasing the landslide hazard. These areas need to be found immediately post-earthquake and properly surveyed. Areas of increased hazard, such as pre-existing landslides and unstable, heavily pre-fractured rock masses may be closely monitored by geological mapping, remote sensing, seismic monitoring techniques and repeated geodetic surveys. Inspections for new tension cracks and fractures can be made with field observations/mapping and remote sensing techniques capable of detecting cracks, such as airborne LiDAR and terrestrial laser scanners (e.g. Abellán et al., 2006; Abellán et al., 2010). Geodetic measurements and small- to large-scale remote sensing can be used to determine changes in landslide morphology and movement before and after the seismic event, for instance GPS, digital photogrammetry, airborne LiDAR, and ground-based, airborne and spaceborne radar interferometry (Gill et al., 2000; Tarchi et al., 2003; Mora et al., 2003; Chang et al., 2005; Colesanti and Wasowski, 2006; Chen et al., 2006; Glenn et al., 2006; Cardenal et al., 2008; Ventura et al., 2011).

Seismic monitoring techniques for audible and subaudible noise activity – including infrasound, micro-seismic and nano-seismic monitoring – combined with signal analysis can be used to determine changes in landslide motion parameters. They can also identify potential forerunners (noise activity prior to failure) and activations of landslides (Kogelnig et al., 2011). Such techniques may provide early warning and event-warning capabilities (Arattano, 1999; Arattano and Marchi, 2008). Combined with topography analysis and landslide motion simulations, probable landslide paths can be evaluated and proper hazard mitigation measures taken, such as evacuations and road blocks (e.g. Hungr et al., 2005).

Existing and new landslides must also be monitored for increased water percolation due to the formation of new cracks and shear zones. This may be done in boreholes.

References:

- Abellán, A., Vilaplana, J. M., Martínez, J. 2006. Application of long-range Terrestrial Laser Scanner to a detailed rockfall study at Val de Núria (Eastern Pyrenees, Spain). *Engineering geology* 88, 3-4: 136 – 148.
- Abellán, A., Calvet, J., Vilaplana, J. M., Blanchard, J. 2010. Detection and spatial prediction of rockfalls by means of terrestrial laser scanner monitoring. *Geomorphology* 119: 162 – 171.
- Arattano, M. 1999. On the use of seismic detectors as monitoring and warning systems for debris flows. *Natural hazards* 20: 197 - 213.
- Arattano, M., Marchi, L. 2008. Systems and Sensors for Debris-flow Monitoring and Warning. *Sensors* 8: 2436 – 2452.
- Cardenal, J., Mata, E., Perez-Garcia, J. L., Delgado, J., Hernandez, M. A., Gonzalez, A., Diaz-de-Teran, J. R. 2008. Close range digital photogrammetry techniques applied to landslides monitoring. In: *The International Archives of the Photogrammetry, Remote Sensing and Spatial Information Sciences*. Vol. XXXVII. Part B8. Beijing 2008 235 – 240.
- Chang, K.-J., Taboada, A., Chan, Y.-C. 2005. Geological and morphological study of the Jiufengshan landslide triggered by the Chi-Chi Taiwan earthquake. *Geomorphology* 71, 3-4: 293 – 309.
- Chen, R.-F., Chang, K.-J., Angelier, J., Chan, Y.-C., Deffontaines, B., Lee, C.-T., Lin, M.-L. 2006. Topographical changes revealed by high-resolution airborne LIDAR data: The 1999 Tsaoiling landslide induced by the Chi-Chi earthquake. *Engineering geology* 88, 3-4: 160 – 172.
- Chigira, M., Wang, W.-N., Furuya, T., Kamai, T. 2003. Geological causes and geomorphological precursors of the Tsaoiling landslide triggered by the 1999 Chi-Chi earthquake. *Engineering geology* 68: 259 – 273.
- Colesanti, C., Wasowski, J. 2006. Investigating landslides with space-borne Synthetic Aperture Radar (SAR) interferometry. *Engineering geology* 88: 173 – 199.
- Delgado, J., Garrido, J., López-Casado, C., Martino, S., Peláez. 2011. On far field occurrence of seismically induced landslides. *Engineering geology* 123: 204 – 213.
- Gili, J. A., Corominas, J., Rius, J. 2000. Using Global Positioning System techniques in landslide monitoring. *Engineering geology* 55: 167 – 192.

-
- Glenn, N. F., Streutker, D. R., Chadwick, D. J., Thackray, G. D., Dorsch, S. J. 2006. Analysis of LIDAR-derived topographic information for characterizing and differentiating landslide morphology and activity. *Geomorphology* 73: 131 – 148.
- Haneberg, W. C., Cole, W. F., Kasali, G. 2009. High-resolution lidar-based landslide hazard mapping and modeling, UCSF Parnassus Campus, San Francisco, USA. *Bull Eng Geol Environ* 68: 263–276 DOI 10.1007/s10064-009-0204-3
- Hungr, O., Corominas, J., and Eberhardt, E. 2005. Estimating landslide motion mechanism, travel distance and velocity. In: *Landslide Risk Management: Proceedings of the International Conference on Landslide Risk Management*, Vancouver. 99 – 128.
- Jaboyenoff, M., Oppikofer, T., Abellán, A., Derron, M.-H., Loye, A., Metzger, R., Pedrazzini, A. 2010. Use of LIDAR in landslide investigations: a review. *Natural Hazards*, DOI 10.1007/s11069-010-9634-2
- Keeper, D. K. 1984. Landslides Caused by Earthquakes. *Geological Society of America Bulletin*, 95: 406 – 421.
- Kogelnig, A., Hübl, J., Surinach, E., Vilajosana, I., McArdell, B. W. 2011. Infrasound produced by debris flow: propagation and frequency content evolution. *Natural Hazards*, DOI 10.1007/s11069-011-9741-8
- Malamud, B. D., Turcotte, D. L., Guzzetti, F., Reichenbach, P. 2004. Landslides, earthquakes, and erosion. *Earth and Planetary Science Letters* 229 (2004) 45– 59.
- Metternicht, G., Hurni, L., Gogu, R. 2005. Remote sensing of landslides: An analysis of the potential contribution to geo-spatial systems for hazard assesment in mountainous environments. *Remote sensing of Environment* 98, 2-3: 284 – 303.
- Meunier, P., Hovius, N., Haines, J. H. 2008. Topographic site effects and the location of earthquake induced landslides. *Earth and Planetary Science Letter* 275: 221 – 232.
- Mora, P., Baldi, P., Casula, G., Fabris, M., Ghirotti, M., Mazzini, E., Pesci, A. 2003. Global Positioning Systems and digital photogrammetry for the monitoring of mass movements: application the the Ca' di Malta landslide (northern Apennines, Italy). *Engineering geology* 68: 103 – 121.
- Sassa, K. 1996. Prediction of earthquake induced landslides. In *Proc. Landslides*, Senneset (ed.), 115 – 131.
- Sato, H.P., Hasegawa, H., Fujiwara, S., Tobita, M., Koarai, M., Une, H., Iwahashi, J. 2007. Interpretation of landslide distribution triggered by the 2005 Northern Pakistan earthquake using SPOT5 imagery. *Landslides* 4: 113 – 122.
- Tarchi, D., Casagli, N., Fantì, R., Leva, D. D., Luzi, G., Pasuto, A., Pieraccini, M., Silvano, S. 2003. Landslide monitoring by using ground-based SAR interferometry: an example of application to the Tessina landslide in Italy. *Engineering geology* 68: 15 – 30.
- Ventura, G., Villardo, G., Terranova, C., Bellucci Sessa, E. 2011. Tracking and evolution of complex active landslides by multi-temporal airborne LIDAR data: The Montaguto landslide (Southern Italy). *Remote Sensing of Environment* 115: 3237 – 3248.

2.4.3 VOLCANIC ACTIVITY

Stefano Morelli, Samuele Segoni, and Veronica Tofani

Università degli Studi di Firenze (UNIFI)

The slope instability in active volcanoes represents the attainment of a degree of structural weakness, which increases the probability of failures of all or part of the edifice (Mc Guire, 1966). This condition may result from the combination of processes usually operating in non-volcanic landslides and from mechanisms typically active in volcanic environments (Figure 2.4.3-1). These two factors tend to differently destabilize volcanoes and their combined action makes these slopes more prone to collapse than other elevated terrains (McGuire, 2003; Morelli et al., 2010).

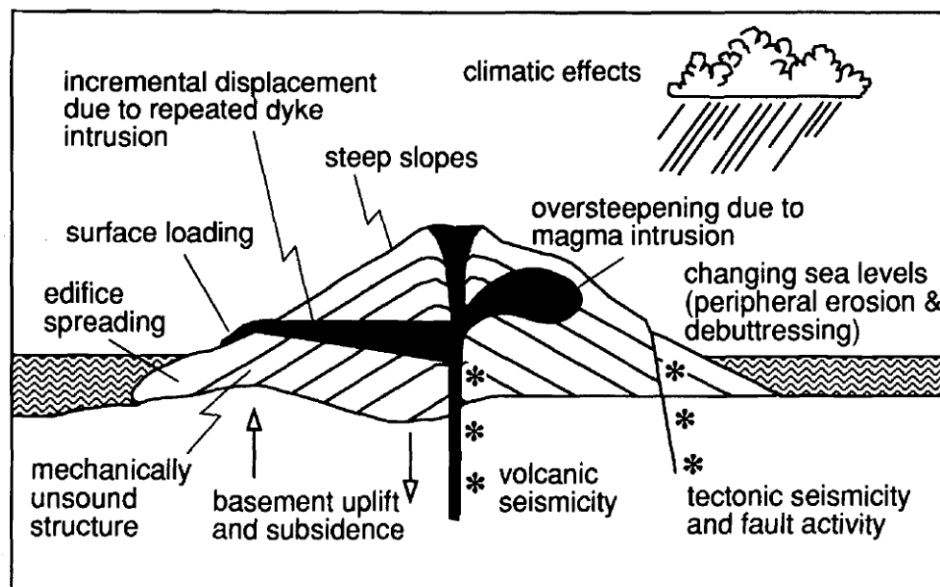


Figure 2.4.3-1. Sketch of the most important contributions to the development of instability in the active volcanic environment (McGuire, 1996).

Volcanoes are highly dynamic structures that change their morphology mainly in response to both intrusive and extrusive phenomena. The magma emplacement may influence the stability of the flanks through the periodic filling and tapping of the magma reservoirs which lead to bulging and contracting cycles. The replenishment modalities are related to activities inside the volcano: the emplacement of a magmatic body in the shape of intrusive dome (cryptodome) (McGuire, 2002) or minor intrusion along preferential rift zones (dykes) (Figure 2.4.3-2) in which elevated pore fluid pressures are mechanically and thermally generated (Elsworth & Voight, 1996). These mechanisms produce a cyclical slope increase that can turn into destabilization and collapse in quite different amounts of time. In fact, a few months may elapse before a significant intrusive event triggers the formation of a landslide (the time varies according to the growth rate), while thousands of years are usually necessary to trigger collapses caused by progressive dyke-induced rifting (McGuire, 2003). The first case occurred, for example, on Mount Saint Helens in 1980 with the emplacement of a dacite cryptodome only a few months before the failure of the north flank (Christiansen & Peterson, 1981; Glicken, 1991). The second case is typical on the flanks of the Hawaiian volcanoes and

on the edifices belonging to the Canary and Cape Verde Archipelagoes in which the pore pressure generation acts on potential basal failure planes, decreasing effective stresses and consequently decreasing frictional resistance to failure (McGuire, 2002; Elswonh & Day 1999).

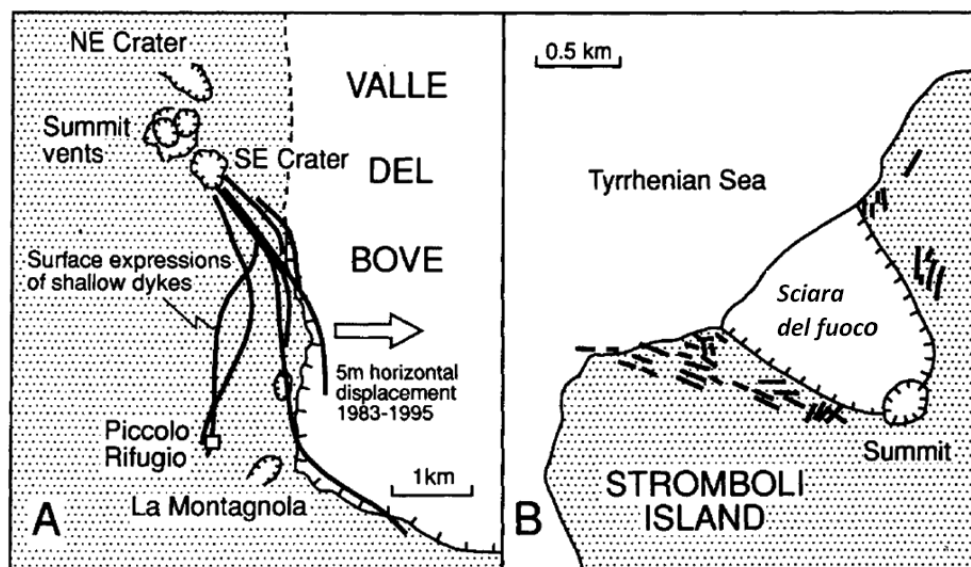


Figure 2.4.3-2. Example of creating large sector-collapse structures in response to dyke-induced rifting. Such behaviour is illustrated by the orientation of post-lateral collapse dykes at both Etna (A) and Stromboli (B) (Italy) (McGuire, 1996).

Destabilization also results from extrusive activity which may give rise to syn-eruptive (primary) or post-eruptive (secondary) mass movements, or mass movements unrelated to eruptions (Vallance, 2005). However, in the first case, landslides and volcanic effusive events are so closely related that in some circumstances it is very difficult to separate one from the other. In any case the instability is related to the progressive loading of a steep slope by the products (tephra and lava) of successive eruptive events (Le Friant et al., 2003), or to the expansion and the oversteepening of an active lava dome (Begè & Kienle, 1992). As such, both the extrusion and intrusion occurrences may trigger critical ruptures through the gravity loading, mechanical push, or temperature-related modifications in pore pressure. In addition to the direct actions of the magma, several external factors related to volcanic activity may contribute to the destabilization of the edifices, reflecting the dynamic geological settings in which volcanoes are located. In volcanoes positioned on oceanic crust (or close to it), the main external factors are large and rapid variations in sea level (McGuire, 2003), the spreading of basaltic shields on weak horizons of oceanic sediment (Nakamura, 1980; Walter & Troll, 2003), and the response to seaward-creeping bodies of olivine cumulate (Clague & Denlinger, 1994). Also, in continental volcanoes, significant vertical movements of the basement due to the growth of a volcanic edifice on a weak substrate (e.g. clay-rich material) (McGuire, 2003) or on a bedrock highly crossed by active faults (Morelli et al., 2010) can represent a predisposing factor leading to the detachment of the down-slope sectors.

As previously described, the interaction of magma with the volcanic structure is the prime mover for creating instability in volcanoes, but also water plays an important role in the destabilization. It may be superficially achieved through the bulking and the debulking of rain-triggered mudflows (called lahars) (Hudson-Doyle et al., 2011), or internally produced

through significant interactions between rocks and fluids. The latter may derive from phenomena originating outside the volcanic context such as precipitations and percolation from snowmelt or sea intrusion, or sometimes they have a direct volcanic origin. The meteoric and marine water circulation can induce a reduction in rock strength within the edifices, as in non-volcanic slopes. Once the circulating fluid meets the volcanism (e.g. degassing of intrusions or direct contact with the magmatic mass) it may become hydrothermal, and chemical alteration processes are activated. Sometimes these types of fluids arise directly from the magmatic composition causing hydrothermal alteration in its surroundings. The main factors controlling the processes of hydrothermal alteration are the nature of the wall rock, the composition of fluids in terms of concentration, activity and chemical potential of components dissolved in the solution (H⁺, CO₂, O₂, K⁺, etc.), and the interior temperature. As such, the hydrothermal alteration plays an important role in reducing the rock mass strength (Concha-Dimas & Watters, 2003; Siebert et al., 1987) while the dehydration of active hydrothermal systems during the magma emplacement can increase the pore pressures to a significant level of instability (Reid, 2004). Moreover, the more the volcanic apparatus is charged of water when an internal modification of the volcano structure occurs (such as the aforementioned hydrothermal alteration, the movement of a fault system, or the intrusion or the extrusion of magma), the more the pore pressure increases due to mechanical and/or thermal modifications.

The sensitivity of pore fluid pressures to perturbation is also highly dependent upon the rock permeability, which may be subject to rapid changes by fracturing, faulting and other processes. The pore pressure changes may be considerable even in quite highly permeable rocks since most of the mechanisms for pressurization (e.g. temperature changes) in volcanic edifices are very rapid. However, some authors indicate that the effects are unpredictable in such cases (Day, 1996). The detection of high pore pressures' development and spreading within active volcanoes may, however, be possible by a sensible monitoring of seismicity patterns. It has been highlighted that volcanogenic landslides are triggered more often by those destabilizing factors than by ground accelerations associated with strong volcanogenic or tectonic earthquakes (Keefer, 1984; McGuire, 2003).

In general, triggering factors acting inside the volcanic edifices (e.g. the aforementioned circulation of fluids) can cause instability phenomena at much greater depths (e.g. collapse of an entire flank) than superficial triggering factors. In these circumstances, very deep sliding surfaces can be shaped (common in huge rock/debris avalanches) and the mass movement can induce high depressurization to such a point that large eruptions occur even if the volcano was not predisposed for it (at most only small intrusive activities are present). This can give rise to Bezymianny-type eruptions (magmatic or phreatomagmatic eruptions preceded by eruptive and seismic precursors) or Bandai-type eruptions (only phreatic eruptions without emission of juvenile materials and with only seismic precursors, which are often short-lived). This can influence the movement of the previous event (Siebert et al., 1987; Tadahide et al., 2000). Besides the presence or the absence of magma, the two cases also differ in intensity and in duration of the eruptive activity. In general terms the type of eruption is determined by the position of the magma inside the volcano in the moments preceding the landslide. If the magma is at the top of the edifice, the landslide creates a weakness zone that promotes the emission of juvenile products through violent lateral explosions. When the magma is deeper, the depressurization effects are less immediate and the explosion can occur along the main conduit exposed by the landslide, with magmatic Plinian eruptions and without any lateral blasts. Finally, when the magma is not within the volcanic edifice, but more in depth, only phreatic explosions (not magmatic) occur, involving only the hydrothermal system. In

addition, in a dormant volcano the development of massive landslides is not accompanied by any volcanic activity. This phenomenon represents a third case of occurrence, called an Unzen-type, which derives from the event that occurred at Unzen volcano in Japan in 1792 (Siebert et al., 1987; Tadahide et al., 2000).

Furthermore, the relationship between the landslide volume and event frequency must be considered in any estimation of landslide risk in a volcanic environment. While low-volume events such as minor rockfalls usually occur every few days or weeks, the largest events, such as huge mega slides in ocean-island volcanoes, have a repetition time of hundreds of thousands of years (McGuire, 2003). In any case the development of instability culminating in the landslide generation may be cyclical if the destabilization causes persist. When the volcanism regenerates the lost morphologies the same type of mass movement occurs in the same location. For instance, repetitive lava-dome growth at Augustine volcano terminated each time with collapse due to oversteepening (Begét & Kienle, 1992), and highly recurring Strombolian activity associated with the intrusion of striking dikes caused frequent superficial deformation patterns in the Stromboli volcano, resulting in several flank collapses (Casagli et al., 2009). However, large-scale structural instability development is invariably confined to major polygenic volcanoes, located either on continental volcanoes (stratovolcanoes) or oceanic crust volcanoes (basaltic shield volcanoes). In both cases the weakness distribution, governed by the tectonic field, definitely influences the source area and the landslide volume (Figure 2.4.3-3 and 2.4.3-4) (Siebert, 1984, Tibaldi et al., 2003, Morelli et al., 2010).

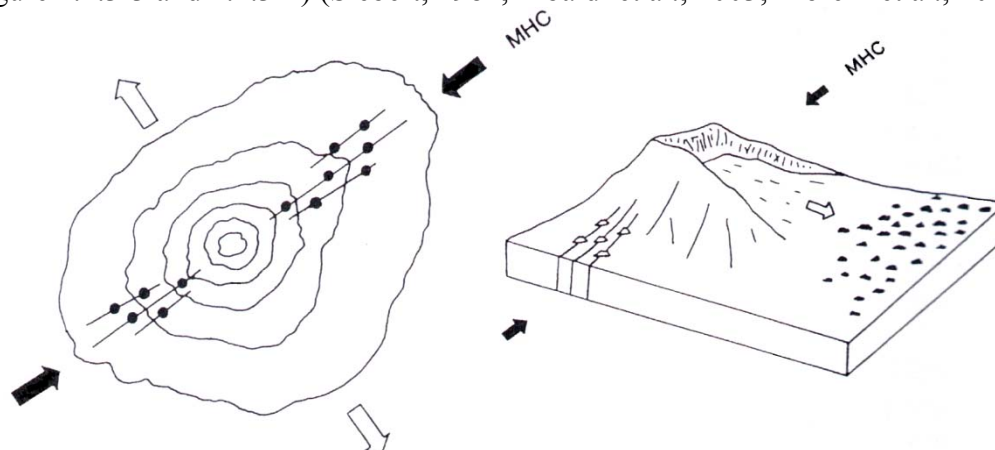


Figure 2.4.3-3. Schematic representation of the emplacement of radial dikes and parasitic vents parallel to the maximum horizontal compression (MHC) favoring the collapse normal to it (right figure) (Siebert, 1984).

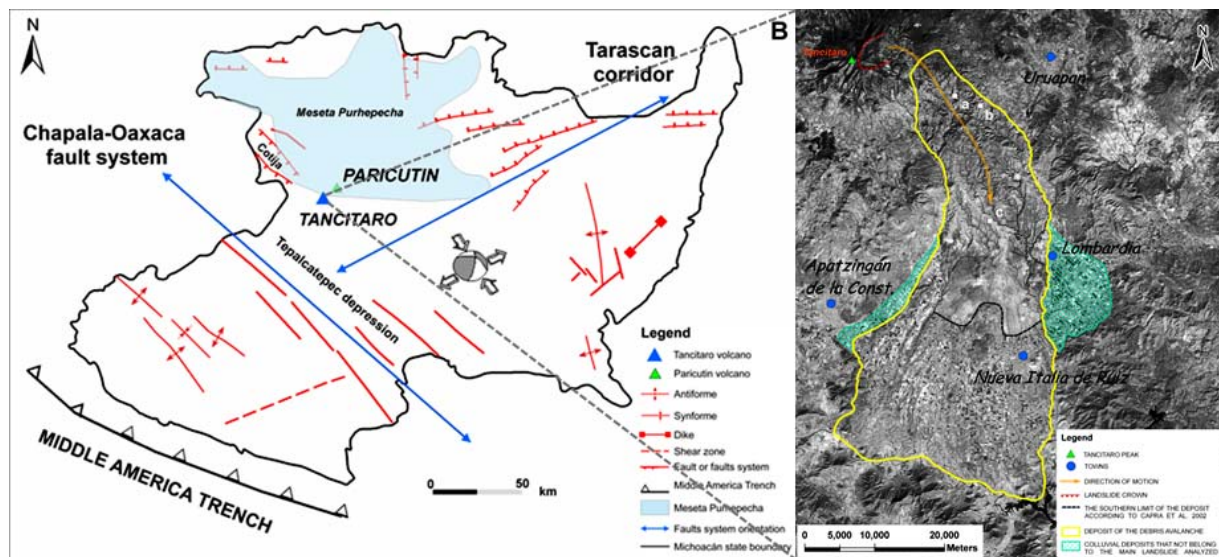


Figure 2.4.3-4. Simplified tectonic overview of Michoacán state (Mexico) (A) and high-resolution Landsat satellite image of the Tancitaro debris avalanche including the source area, which is tightly influenced by the regional tectonic, and the spatial distribution of the deposit (Morelli et al., 2010).

The maximum amount of the collapsing volume usually corresponds to no more than the 20 % of the entire edifice. This upper limit can be explained as a consequence of a macroscopic stress distribution characterized by conjugate shear planes that always have an angle smaller than 90° (McGuire et al., 2002). Moreover, an important and not uncommon source of hazard occurrence is associated with significant marine events which are able to generate tsunami waves (Tinti et al., 2003; Whelan & Kelleter, 2003). An example is Stromboli in the Tyrrhenian Sea (north of Sicily), which is destabilized by the continuous intrusion of fresh magma and by the weight of the erupted material. For these reasons it experienced at least seven episodes of incremental collapses over the past 100,000 years, some of which are associated with damaging tsunamis (the last was during the 2002 event) (Tibaldi, 2001; Antonello et al., 2004; Casagli et al., 2009).

References:

- Antonello G., Casagli N., Farina P., Leva D., Nico G., Sieber A. J., Tarchi D. (2004): Ground-based SAR interferometry for monitoring mass movements. *Landslides*, 1: 21-28.
- Begét J.E. & Kienle J. (1992): Cyclic formation of debris avalanches at Mount St. Augustine volcano. – *Nature*, 356, 6371: 701-704.
- Casagli N., Tibaldi A., Merri A., Del Ventisette C., Apuani T., Guerri L., Fortuny-Guasch J., Tarchi D. (2009): Deformation of Stromboli Volcano (Italy) during the 2007 eruption revealed by radar interferometry, numerical modelling and structural geological field data. – *Journal of Volcanology and Geothermal Research*, 182(3-4): 182-200.
- Christiansen R.I. & Peterson D.W. (1981): Chronology of the 1980 eruptive activity. – In: Lipman, P.W. & Mullineaux, D.R. (Eds.): *The 1980 eruptions of Mount St. Helens*. – U. S. Geol. Surv. Prof. Paper, 1250: 17-30.
- Clague D.A. & Denlinger R.P. (1994): Role of olivine cumulates in destabilizing the flanks of Hawaiian volcanoes. – *Bull. Volcanol.*, 56: 425– 434.
- Concha-Dimas A. & Watters, R.J. (2003): Preliminary evaluation of volcanic flank stability using finite difference modeling: Citlaltépetl volcano, Mexico. – 12th Panamerican Conference on Soil Mechanics and Geotechnical Engineering, Soil Rock America 2003, June 22–26, Boston Massachusetts, 2003.
- Day S.J. (1996): Hydrothermal pore fluid pressure and the stability of porous, permeable volcanoes. – In: McGuire W.J., Neuberg J. & Jones A. (Eds.): *Volcano instability on the Earth and terrestrial planets*. – *Geol. Soc. Lond. Spec. Publ.*, 110: 77-93.

- Elsworth D. & Voight B. (1996): Evaluation of volcano flank instability triggered by dyke intrusion. – In: McGuire WJ, Jones AP, Neuberg J (eds), *Volcano instability on the Earth and other planets*. Geological Society of London Special Publications, 110: 45-53.
- Elswohn D. & Day, S.J. (1999): Flank collapse- triggered by intrusion: The Canary and Cape Verde archipelagoes. – *Journal of Volcanology and Geothermal Research*, 94: 323-340.
- Glicken H. (1991): Sedimentary architecture of large volcanic debris avalanches. – *SEPM spec. publ.*, 45 *Sedimentation in volcanic settings*: 99–106.
- Hudson-Doyle E., Cronin S. & Thouret, J. (2011): Defining conditions for bulking and debulking in lahars. – *Geological Society of America Bulletin*, 123 (7/8), 1234-1246.
- Keefer, D.K. (1984): Landslides caused by earthquakes. – *Bulletin of the Geological Society of America*, 95: 406-421.
- Le Friant A., Boudon G., Deplus C. & Villemant B. (2003): Large scale flank collapse events during the activity of Montagne Pelée, Martinique, Lesser Antilles. – *J. Geophys. Res.*, 108 (B1): 2055.
- McGuire W.J. (1996): Volcano instability: a review of contemporary themes. In: McGuire. W. J., Jones, A. P. & Neuberg J. (Eds): *Volcano instability on the Earth and Other Planets*. – Geological Society of London Special Publications, vol. 110: 1-23. Bath, UK: Geological Society Publishing House.
- McGuire W.J., Day S.J. & Kilburn C.R.J. (2002): Volcanogenic landslides. *Landslide Risk Mitigation and Protection of Cultural and Natural Heritage*. – UNESCO/Tokyo University: 691–750.
- McGuire W.J. (2003): Volcano instability and lateral collapse. – *Revista Vulcànica*, 1: 33 45.
- Morelli S., Garduño-Monroy V.H., Gigli G., Falorni G., Arreygue E. & Casagli N. (2010): The Tancitaro debris avalanche: characterization, propagation and modeling. – *J. Volcanol Geotherm Res*, 193: 93-105.
- Nakamura K. (1980): Why do long rift zones develop in Hawaiian volcanoes: a possible role of thick oceanic sediments. – *Bull. Volcanol. Soc. Japan*. 25: 255-269.
- Reid M.E. (2004): Massive collapse of volcano edifices triggered by hydrothermal pressurization. – *Geology*, 32: 373–376.
- Siebert L. (1984): Large volcanic debris avalanches: characteristics of source areas, deposits, and associated eruptions. – *Journal of Volcanology and Geothermal Research*, 22: 163–197.
- Siebert L., Glicken H. & Ui T. (1987): Volcanic hazards from Bezymianny- and Bandai-type eruptions. – *Bull. Volcanol.* 49: 435-459.
- Tadahide U., Shinji T. & Mitsuhiro Y. (2000): Debris Avalanches. – In: Haraldur Sigurdsson (Eds): *Encyclopedia of Volcanoes*. Academic Press: 617-626, San Diego.
- Tibaldi A. (2001): Multiple sector collapses at Stromboli volcano, Italy: How they work. – *Bull. Volcanol.*, 63: 112 – 125.
- Tibaldi A., Corazzato C., Apuani T. & Cancelli A. (2003): Deformation at Stromboli volcano (Italy) revealed by rock mechanics and structural geology. – *Tectonoph.*, 361 (3-4): 187-204.
- Tinti S., Pagnoni G., Zaniboni F. & Bortolucci E. (2003): Tsunami generation in Stromboli island and impact on the south-east Tyrrhenian coasts. – *Nat. Hazards Earth Syst. Sci.*, 3: 299–309.
- Vallance J.W. (2005): Volcanic debris flows. – In: M. Jakob, O. Hungr, (Eds): *Debris-flow Hazards and Related Phenomena*, Praxis, Chichester: 247–274.
- Walter T.R. & Troll V.R. (2003): Experiments on rift zone evolution in unstable volcanic edifices. – *J Volcanol Geoth Res*, 127: 107-120.
- Whelan F. & Kelletat D. (2003) Submarine slides on volcanic islands: A source for megatsunamis in the Quaternary. – *Progress in Physical Geography* 27: 198-216.

2.4.4 TIDES

Anna Zöchbauer

Geological Survey of Austria

Another possible trigger for landslides can be the tides. The forces, generated from the sun and the moon, are possible factors that lead to shear sliding processes, like earthquakes or glacier movements (Cochran et al. 2004, Gudmundsson 2006).

In particular, the atmospheric tides can be responsible for movements of landslides that are nearly at failure. Solid earth tides are too small to change the stability in this shear sliding process (Schulz et al. 2009).

The atmospheric tides are mainly generated by gravitational forces of the moon and the sun as well as the heating of the atmosphere from the sun's activity (Chapman & Lindzen 1970). Those oscillations are regularly indicated by changes in the (ground surface) pressure in periods of 12 and 24 hours.

In general, it is observed that changes in air pressure can cause only minimal changes in tilt or extensometric measurements in tectonically active areas compared to the effect of precipitation, which is about an order of magnitude higher. But this observation was made with tidal-filtered pressure and deformation data, so it does not implicate the tidal forces (Dal Moro & Zadro 1998).

The interrelation of landslide movements and the atmospheric tides have not been frequently investigated to date. However, Schulz et al. (2009) showed in their research that there is a correlation between the two phenomena. Their theory gives an insight to this field.

A promising hint to the understanding of landslide movements is the frictional stress that can be influenced by atmospheric tides. Even though the influence is rather small and difficult to detect, atmospheric tides can change those stresses. According to the Mohr-Coulomb failure criterion, landslides occur if the frictional stress of the shear surface is decreasing, as is demonstrated below (Zepp, 2004; Schulz et al, 2009):

$$\tau = c' + (\sigma - u) \tan \varphi'$$

where:

τ =shear stress

c' =soil cohesion

σ =total normal stress

u =pore-water pressure

φ' =angle of internal friction for effective stress

The frictional stress depends on the pore-water pressure and the total normal stress. The theory assumes that changing air pressure goes through soil into groundwater and the fluids flow from high pressure to low pressure. However, these moving fluids are responsible for the change in frictional stress. On the one hand, increasing air pressure can be responsible for the downward movement of fluids, thereby generating a downward-directed force which increases the frictional stress. On the other hand, decreasing air pressure causes fluids to move upward, leading to a decrease in the frictional stress and an increase in the possibility of landslide movement.

The thickness of the landslide, groundwater depth, and soil and fluid properties are factors that change the frictional stress. In the case of narrow pore throats and long distances to the shear surface at the base of the landslide, pressure changes can pass through the soil which results in great stress changes.

The pressure at the shear surface at the base of the landslide is smaller than the atmospheric pressure because those pressure fluctuations are damped and delayed during their descent through the soil. As such, the measured pressure changes at the shear surface (P_1) and at the ground surface (P_a) change the normal stress, therefore the Mohr-Coulomb criterion is:

$$\tau = c' + (\sigma - u + P_a - P_1) \tan \phi'$$

In impermeable media, like glacial ice, atmospheric pressure changes do not propagate. Consequently, the fluctuations directly change the frictional strength at the shear surface. The worldwide variation of pressure changes from atmospheric tides is quite small in relation to the thicknesses of the landslides, so the effect of atmospheric tides on the landslides depends on their thickness and on the pressure damping properties (Schulz et al. 2009).

References:

- Cochran, E.S., Vidale, J.E., Tanaka, S. (2004): Earth tides can trigger shallow thrust fault earthquakes. Scienceexpress, 2004
- Gudmundsson, G. H. (2006): Fortnightly variations in the flow velocity of Rutford Ice Stream, West Antarctica. Nature 441, 2006
- Schulz, W. H., Kean, J.W., Wang, G. (2009): Landslide movement in southwest Colorado triggered by atmospheric tides. Nature Geoscience,
- Chapman, S., Lindzen, R.S. (1970): Atmospheric Tides, thermal and Gravitational. Gordon and Breach, 1970
- Dal Moro, G., Zadro, M. (1998): Subsurface deformation induced by rainfall and atmospheric pressure: tilt/strain measurements in the NE-Italy seismic area. Earth and planetary science letter 164, 1998.
- Zepp, H. (2004): Geomorphologie: eine Einführung. UTB, 2004.

3 GENERAL EVALUATION OF MONITORING PARAMETERS

Ivo Baroň

Geological Survey of Austria

For landslide early warning, different techniques and sensors provide different kinds of information with different data reliability. We tried to provide a kind of quantitative comparison of those methods. Therefore a “Questionnaire on National State of Landslide Site Investigation and Monitoring” was disseminated among different worldwide institutes and representatives within the frame of the SafeLand project. The forms were completed by local experts responsible for the respective sites, so the results are based on the practical experience from the field. The main goal of the study was (i) Assessing general state of the slope-instability investigation and monitoring in different countries, (ii) Assessing effectiveness/reliability of each method for slope instability investigation and monitoring, and (iii) Evaluating applicability of the monitoring techniques for early warning. Some results of the questionnaire were already presented in D4.5 (Baroň 2010a, 2010b). Here, we focus on the evaluation of monitoring parameters’ EW potential, and in the case of displacement, the techniques. For this purpose, slope-related ground-based methods only were evaluated.

The questionnaire was focused on landslides that have been investigated with at least two independent methods and monitored for longer than one year. A Word-doc application was prepared in a comprehensive and user-friendly way (for a detailed description of the forms, see D4.5). Answers were provided by ticking and filling in active fields, and the answers were statistically assessed.

The monitored parameters were expressed relative to the total number of monitored sites included in the study, called *relative occurrence (RO [%])*. The applicability of the monitoring method for early warning – called the *early warning potential (EWP [%])* – was determined by the number of positive answers to the possibility of using the method for early warning relative to the total number of collected sites. In the latter questionnaire (D4.8) it was evaluated directly in numerical way by the respondents.

The information was received from 89 monitored sites from Andorra, Austria, Switzerland, Czech Republic, France, Great Britain, Italy, Japan, Kyrgyzstan, Martinique, Norway, Russian Federation, Slovenia, Slovak Republic and Spain (Table 3-1).

Table 3-1: List of the monitored sites and countries.

No.	Country	Site	Author	No.	Country	Site	Author
1	AD	Canillo	J. Corominas	46	IT	Tessina	A. Passuto
2	AT	Kerschbaumsiedlung	gbl.minntal@die-wildbach.at	47	IT	Magliatica	G. Truffelli
3	AT	Blaubach	V. Kaufmann	48	IT	Bosmato-Stadette	M. Broccolato, J. Blanc
4	AT	Murenbach	Ch. Ihrenberger	49	IT	Vollein	M. Broccolato, J. Blanc
5	AT	Sibratsgöl / Rindberg	M. Wöhler-Alge	50	IT	Letze-Bosmato	M. Broccolato, J. Blanc
6	AT	Gschliefgraben	W. Gasperl	51	IT	Becca di Nona	M. Broccolato, J. Blanc
7	AT	Maesstobel	WLW	52	IT	Pitigliano	N. Casagli
8	AT	Wagrainer Ache	WLW	53	IT	SanMiniato	N. Casagli
9	CH	Gruben	S. Springman	54	KG	Gulcha-Basar LS	I. Torgoev
10	CH	Ruedlingen	S. Springman	55	KG	Kambar-Ata LS	I. Torgoev
11	CH	Tössegg	S. Springman	56	KG	Kok-Jangak, Kapitalnja LS	I. Torgoev
12	CZ	Pustevny	J.Klimes	57	KG	Min-Kush LS	I. Torgoev
13	CZ	Halenkovice	M. Bil	58	KG	M-Suu Izolit LS	I. Torgoev
14	CZ	Holstejn	V. Hanzl	59	KG	M-Suu Tektonik LS	I. Torgoev
15	CZ	Přihrazý	J. Rybar, J. Klimes	60	KG	M-Suu, Koy-Tash LS	I. Torgoev
16	CZ	Třebenice	J. Rybar, J. Klimes	61	KG	Taran-Basar LS	I. Torgoev
17	CZ	Čeraniště	J. Rybar, J. Klimes	62	NO	Aaknes, Western Norway	L.H. Bliakra
18	CZ	Ondřejník	J. Rybar, J. Klimes	63	NO	Hegguraksla	L.H. Bliakra
19	CZ	Karolinka	P. Blaha	64	NO	Jettan Nordnes	L.H. Bliakra
20	CZ	Ujala	P. Blaha	65	NO	Mannen Romsdalens	L.H. Bliakra
21	CZ	Obří Hrad	F. Hartvich	66	RU	Zagorsk	M.M. Ilyin
22	CZ	Pravčická brana	Z. Varilova	67	SI	Macesnik	M. Carman, S. Kumelj
23	ES	Vallcebre	J. Corominas	68	SI	SlanoBlato	M. Carman, S. Kumelj
24	FR	Mas d'Avignonet	D. Jongmans	69	SI	Stože	M. Carman, S. Kumelj
25	FR	Super Sauze	J.-P. Malet	70	SK	Banska Stiavnica	P. Wagner
26	FR	Villerville	J.-P. Malet	71	SK	SK_Bojnice	P. Wagner
27	FR	La Valette	J.-P. Malet	72	SK	Demjata	P. Wagner
28	FR	Precheur Rier (Martinique)	V. Clouard	73	SK	Dolna Micina	P. Wagner
29	FR	Séchilienne	S. Garambois, A. Helmstetter	74	SK	Fintice	P. Wagner
30	GB	Hollin Hill	C. Foster	75	SK	Handlova_1960	P. Wagner
31	IT	Cervinara site	L. Picarelli	76	SK	Handlova - Kunesov road	P. Wagner
32	IT	Castagnola	N. Casagli	77	SK	Hlohovec	P. Wagner
33	IT	Masseria Marino mudslide	G. Urciuoli	78	SK	K Klecenov	P. Wagner
34	IT	Torgiovanetto	N. Casagli	79	SK	Liptovska Mara	P. Wagner
35	IT	Santo_Stefano_d'Aveto	N. Casagli	80	SK	Morovno Estate	P. Wagner
36	IT	Monteforte Irpino area	G. Urciuoli	81	SK	Okolicne	P. Wagner
37	IT	Ponti	M. Lovisolo	82	SK	Slanec	P. Wagner
38	IT	Ruinon	M. Lovisolo	83	SK	Velka Izra	P. Wagner
39	IT	Idro	M. Lovisolo	84	SK	Velka Causa	P. Wagner
40	IT	Bagnaschino	M. Lovisolo	85	SK	Vistuk	P. Wagner
41	IT	Ancona	S. Cardellini	86	JP	Kuchisakamoto	G. Furuya
42	IT	Chervaz	M. Broccolato, J. Blanc	87	JP	Aratosawa	S. Tosa
43	IT	Comba Citrin	M. Broccolato, J. Blanc	88	JP	Yui	S. Tosa
44	IT	Cherz	A. Passuto	89	JP	Takisaka	H. Marui
45	IT	Passo della Morte	A. Passuto				

Monitoring parameters related to displacement and deformation

It is no surprise that the displacement and its derivatives – the velocity and the acceleration – were considered as the most relevant monitoring parameters. The early warning potential values exceeded 50 % for several techniques. The results for different ground-based sensors of displacement and deformation are presented in Figure 3-1, displaying their relative occurrence within all 89 monitoring sites and ordered by their relative early warning potential. Classical and automated inclinometers, wire extensometers, dGPS, optical images and total stations are the most reliable sensors of displacement and deformation monitoring with the highest early warning potential.

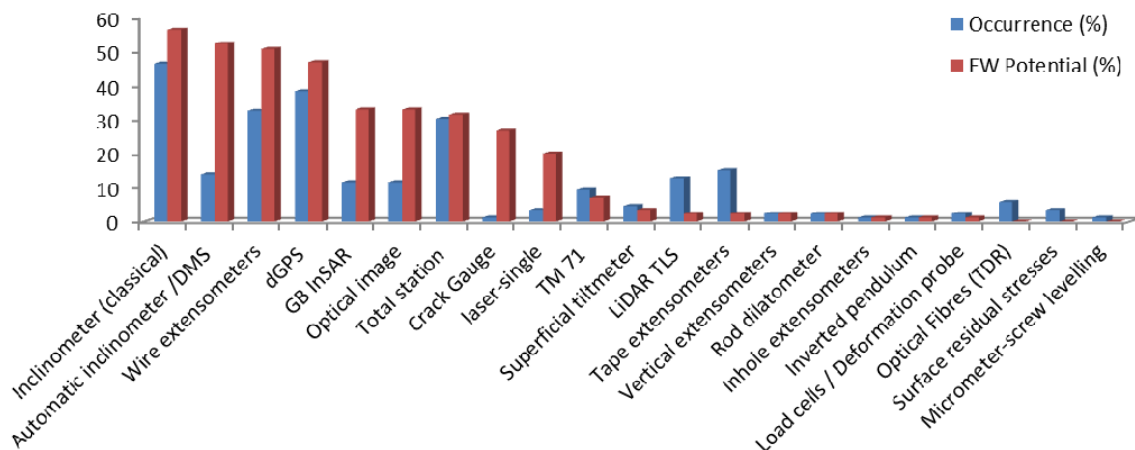


Figure 3-1. Review of sensors of displacement and deformation monitoring, presenting their relative occurrence within all 89 collected monitoring sites and ordered by their relative early warning potential.

Hydro-meteorological monitoring parameters

About 16 different hydro-meteorological monitoring parameters have been observed in the listed landslide sites; the **precipitation amount**, **pore-water pressure** and **air temperature** were the most abundant ones (Figure 3-2). They have been monitored at more than 55 % of the test sites. Pore-water pressure and precipitation amount have the highest EW potential.

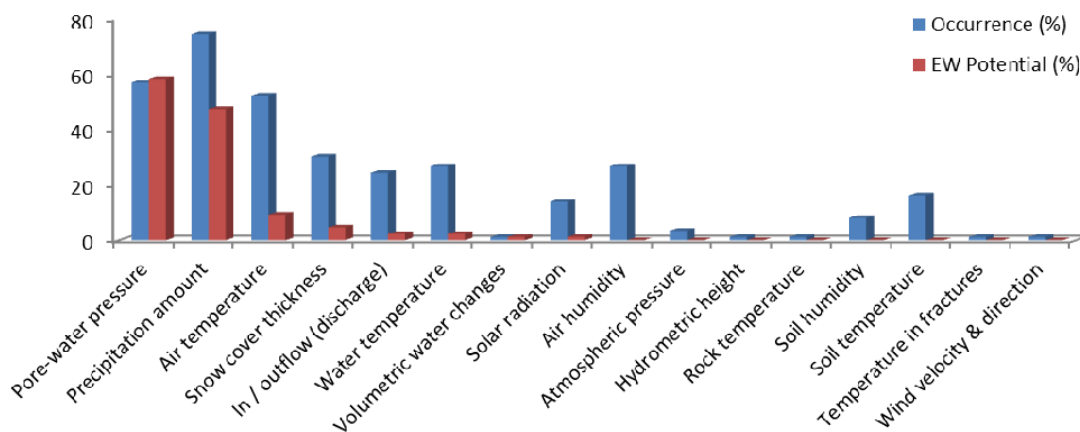


Figure 3-2. Review of hydro-meteorological monitoring parameters presenting their relative occurrence within all 89 collected monitoring sites ordered by their relative early warning potential.

Geophysical monitoring parameters

Most of the geophysical parameters are far from their routine application for landslide monitoring. Their relative abundance is generally below 20 %. Being the most reliable geophysical parameters for EW, passive seismic/acoustic emissions, electromagnetic emission and DC resistivity were evaluated by the questioned experts (Figure 3-3). However, only passive seismic/acoustic emissions exceeded an EWP of 30 %. Other geophysical parameters are of rather academic importance at the moment.

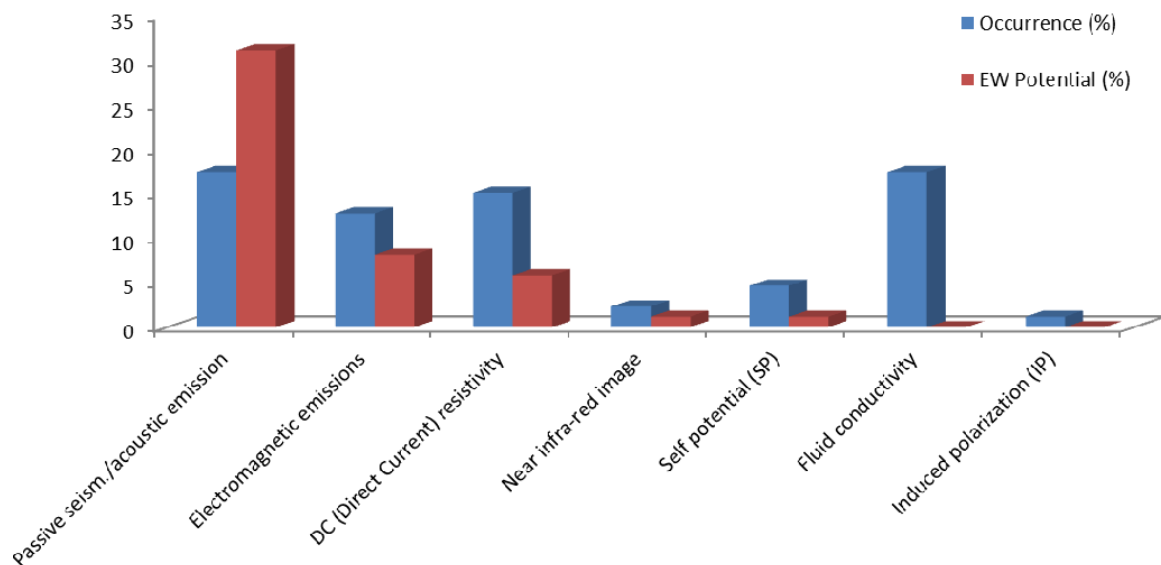


Figure 3-3. Review of geophysical monitoring parameters presenting their relative occurrence within all 89 collected monitoring sites ordered by their relative early warning potential.

References:

- Baroň I. & Supper R. (2010a): Questionnaire on Landslide Site Investigation and Monitoring in Europe. – In.: Tofani V., Segoni S., Catani F., Casagli N., Intrieri E.: Evaluation report on innovative monitoring and remote sensing methods and future technology, Deliverable D4.5. Report of the 7th FP Project SafeLand, <http://www.safeland-fp7.eu/>
- Baroň I. & Supper R. (2010b): State-of-the-Art of Landslide Monitoring in Europe: Preliminary Results of the SafeLand Questionnaire. – In.: Supper R. & Baroň I. (Eds.): Landslide Monitoring Technologies & Early Warning Systems, Current Research and Perspectives for the Future, Book of extended abstracts. Open Workshop within the frame of the EU FP7 “SafeLand” Project, February 24th, 2010, Vienna. Berichte der Geologischen Bundesanstalt 82: 17-23. ISSN 1017-8880

4 CASE HISTORIES – ANALYSIS OF REAL MONITORING DATA

The practical issue of how to find the indicators of impending activation of mass movements is a crucial task for any landslide early warning system. The critical values of those EW indicators, i.e. monitoring parameters with very close relation to a landslide's physical conditions and deformation state, are difficult to find due to site-specific and regional differences in topography, lithology, climatic and other factors.

This core chapter of the deliverable presents the examples of real data collection and analysis from the SafeLand test sites obtained mainly during the project period from 2009 to 2011. The analysis of the monitored parameters is described with a focus on investigating the correlation between the parameters. The goal was finding their critical values (alerts/thresholds) on the background of their geological settings.

The chapter presents the results from three test sites in Austria (*Ampflwang in Hausruck, Gschlifgraben, Sonnblick & Mölltaler Glacier*), two in France (*Super-Sauze, Villerville*), six in Italy (*Ancona, Bagnaschino, Bindo, Casella, Rosano, Ruinon*), three in Norway (*Åknes, Mannen, Jettan – Nordnes*), and one test site in Spain (*Vallcebre*) (see Figure 4-1).

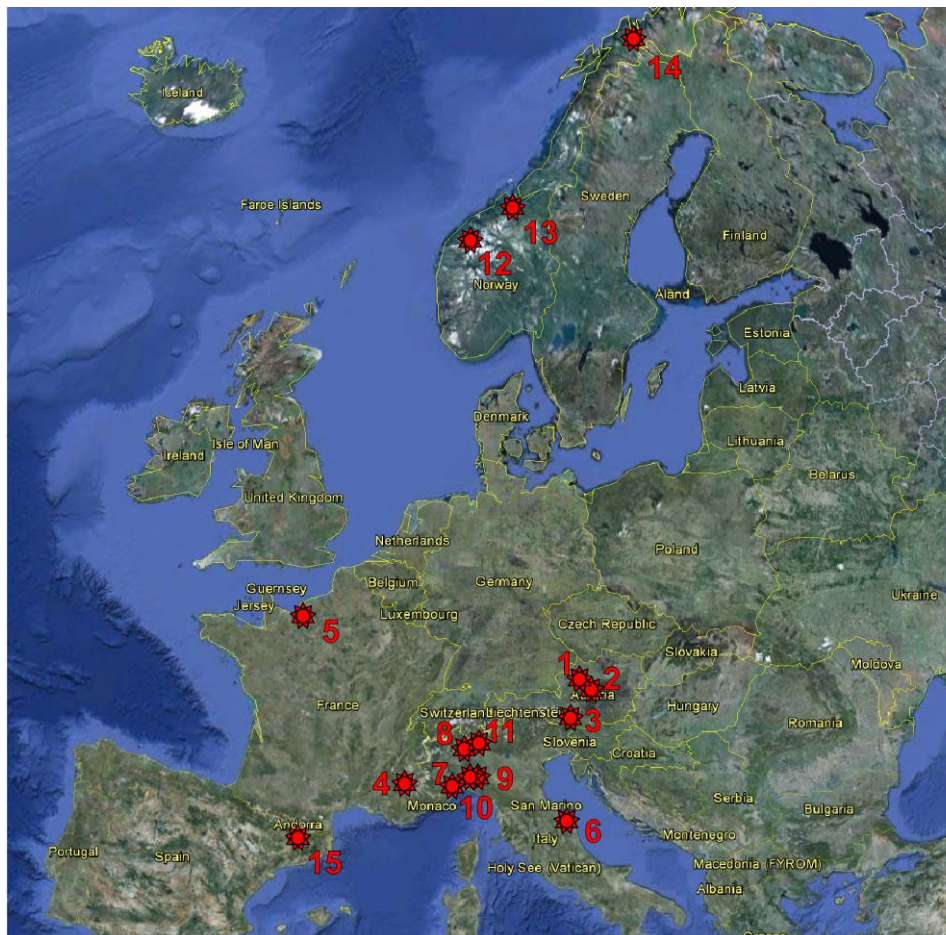


Figure 4-1. Review of test sites presented in this report. Austria: 1 – Ampflwang in Hausruck, 2 – Gschlifgraben, 3 – Sonnblick & Mölltaler Glacier; France: 4 – Super-Sauze, 5 – Villerville; Italy: 6 – Ancona, 7 – Bagnaschino, 8 – Bindo, 9 – Casella, 10 – Rosano, 11 – Ruinon; Norway: 12 – Åknes, 13 – Mannen, 14 – Jettan; Spain: 15 – Vallcebre (Source of the map: GoogleEarth).

These test sites represent a variety of different types of slope failures of different volumes and recent velocities; they have been monitored for different periods. Such different test sites enable us to present a variety of approaches applicable for different types of mass movement. Table 1-1 reviews the test sites and their location and presents their main characteristics, such as the type of slope failure, volume, present mean velocity and the monitoring period.

Table 1–1: Review of the presented test sites and their main characteristics.

Test site	Country	Entire slope failure	Monitored Instability	Volume [Mm3]	Present Mean Velocity [m/year]	Permanently operated since
Aknes	NO	Complex	Rockslide+Rockfall	54	0.08	2004
Ampflwang	AT	Simple	Shallow rotational slide	0.01	0.05	2010
Ancona	IT	Compound	Deep-seated rotational slide	180	0.01 to 0.02	2002
Bagnaschino	IT	Complex	Roto-translational slide	1.2	0.08 to 0.6	2008
Casella	IT	Complex	Roto-translational slide	30	0.006 to 0.013	2010
Bindo	IT	Simple	Translational slide/Earthflow	1.5	1.2	2003
Gschliefgraben	AT	Complex	Translational slide/Earthflow	3.8	0.07	2009
Jettan	NO	Complex	Rockslide+Rockfall	17	0.05	2003
Mannen	NO	Complex	Rockslide+Rockfall/Rock Avalanche	17 - 23	0.05	2004
Rosano	IT	Composite	Roto-translational slide	3.6	0.022	2010
Ruinon	IT	Complex	Roto-translational rockslide+secondary rockslides+debris slides	13 - 20	0.88	1997
Sonblick/Möltaller Glacier	AT	PERMAFROST	PERMAFROST	PERMAFROST	PERMAFROST	PERMAFROST
Super-Sauze	FR	Complex	Translational slide/Earthflow	0.7	0.5 to 5	1995
Vallcebre	ES	Compound	Translational slide	13	0.2 to 0.8	1987 (intensively since 1996)
Villerville	FR	Compound	Roto-translational slide	2.4	0.005 to 0.10	2007

All of the monitoring parameters to be described in the report are reviewed in the Table 1-2. The most important parameter was displacement, which was observed by means of a variety of different sensors. DMS and differential GPS monitoring was conducted in 53 % of the test sites. Other sensors, such as inclinometers (47 %), crack/extensometers (33 %), GB InSAR (27 %), total stations (27 %), terrestrial laser scans (20 %), and tiltmeters (20 %) were presented.

Deformation was observed by means of microseismicity (only at one site, i.e. 7 %) and crack spatio-temporal evolution (7 %).

The monitored and presented hydro(geo)meteorological parameters were air temperature and precipitation (both in 93 % of the test sites), ground-water level and pore-water pressure (80 %), and discharge (7 %).

And finally, the monitored and here-analyzed geophysical parameters were resistivity (abundance at 40 % of the test sites), self-potential (33 %), and soil temperature (33 %).

We hope that this study well illustrates the complexity of landslide EW systems, the state of the art in Europe and the outlook towards the future.

Table 1–2: Review of the test sites and the monitoring parameters to be described in the report

Test site	Displacement & Deformation									Hydro(geo)meteorological parameters				Geophysical parameters			
	DGPS	Total station	TLS	GB InSAR	Crack- / extension-meter	Crack spatio-temporal evolution	Tilt-meter	Inclinometer	Seismic emissions	DMS	GWL & Porewater pressure	Dis-charge	Temperature	Precipitation	Resistivity	Self potential	Soil temperature
Aknes (Norway)	X	X	X	X	X		X		X	X	X		X	X			
Ampflwang (Austria)									X	X	X		X	X	X	X	X
Ancona (Italy)	X	X					X			X	X		X	X	X		
Bagnaschino (Italy)							X			X	X		X	X	X		X
Bindo Rockslide (Italy)		X								X	X		X	X			
Casella site (Italy)										X	X		X	X			
Gschliefgraben (Austria)					X				X	X	X		X	X	X	X	X
Jettan (Norway)	X		X		X		X						X	X			
Mannen (Norway)	X		X	X	X					X	X		X	X			
Rosano (Italy)										X	X		X	X			
Ruinon Rockslide (Italy)	X			X	X			X			X		X	X			
Sonnblick & Möltaler Glacier (Austria)													X	X	X		X
Super Sauze (France)	X					X									X		
Vallcebre (Spain)	X			X							X		X	X			
Villerville (France)	X	X					X				X		X	X			X

4.1 ÅKNES (NORWAY)

L.H. Blikra & L. Kristensen

Åknes/Tafjord Early Warning Centre, Norway

ABSTRACT

The Åknes rockslide is a large, slow-moving landslide in Precambrian gneiss in Sunnlyvsfjorden in western Norway. It has a volume of more than 50 million m³ and parts are moving at velocities of 2-8 cm/year. If the sliding mass were to fall into the fjord, it would generate large tsunami waves. Given the hazard, a major site investigation was conducted and a monitoring program was established in cooperation with a number of national and international groups. The monitoring program integrated a variety of surface and subsurface instruments, including extensometers, crackmeters, tiltmeters, single lasers, GPS, total station, ground-based radar, geophones, climate station, and borehole inclinometers and piezometers. Reliable power and communications systems operate the instruments and transmit data. Movement data collected to date demonstrate continuous movement throughout the year, but with significant seasonal differences. During spring snowmelt and heavy precipitation events, the rate of movement can increase to 1 mm/day, which is ten times the annual mean. Preliminary early warning levels and associated actions have been implemented based on data from the Åknes rockslide and information on historical rockslides elsewhere in coastal Norway.

Presented parameters: displacement, velocity, microseismicity, groundwater level, precipitation, air temperature.

4.1.1 GENERAL DESCRIPTION OF THE TEST SITE

The Åknes rockslide is located on the northwest flank of Sunnlyvsfjorden in western Norway (Figure 4.1-1). It has an estimated volume of up to 54 Mm³ and is moving at a velocity of up to 8 cm/year. Catastrophic failure of the rock mass would trigger a devastating tsunami in the fjord (Blikra, 2008; Glimsdal and Harbitz, 2011). Because of the size of the moving rock mass, remedial engineering measures are not feasible and the risk must be managed by implementing an effective warning system. A major investigation, monitoring, and early warning program were begun at Åknes in 2004. The operational monitoring and early warning system is now administered by the Åknes/Tafjord Early Warning Centre on a permanent basis.

Geological and geomorphic settings

The Åknes rockslide is located in the Western Gneiss Region and is seated in medium-grained granitic and granodiorite gneisses of Proterozoic age (Braathen *et al.*, 2004; Ganerød *et al.*, 2008). The gneisses contain bands and lenses of mafic material. They have well developed foliation and mineral banding (Braathen *et al.*, 2004) and numerous centimetres to decametre-scale, close to tight folds. At Åknes, biotite-rich layers up to 20 cm thick coincide with zones of high fracture frequency (Ganerød *et al.*, 2008). The sliding surfaces are likely located within these mica-rich layers. The foliation generally slopes parallel to the surface. Well defined, very steep, sharp folds are related to the tension cracks at the top of the landslide (Ganerød *et al.*, 2008; Jaboyedoff *et al.*, 2011).

The morphology of the rockslide show several characteristic features (Figure 4.1-1), including a prominent upper fracture system that can be followed for more than 500 m. The slope-

parallel foliation and weak biotite-rich layers control the large-scale displacement dynamics. A large depression or graben has developed in the upper west corner of the rockslide (Figure 4.1-1, detail). The total vertical displacement measured here is 20-30 m. Tension fractures are also present in the upper and the middle parts of the slope. Prominent slide scarps characterize the east side of the deep canyon that defines the west boundary of the landslide. Historical data indicate that slides occurred on the upper part of the slope in the late 1800s, 1940, and 1960. Small slide scars also characterize the lower part of the rockslide. Large blocks have been pushed or squeezed out of the slope in two areas, one in the middle and the other on the lowermost part of the rockslide (Figure 4.1-1). Springs discharge water on the lowermost part of the slope at about 100 m a.s.l., and there are also smaller springs in the middle part of the landslide (Frei, 2008).

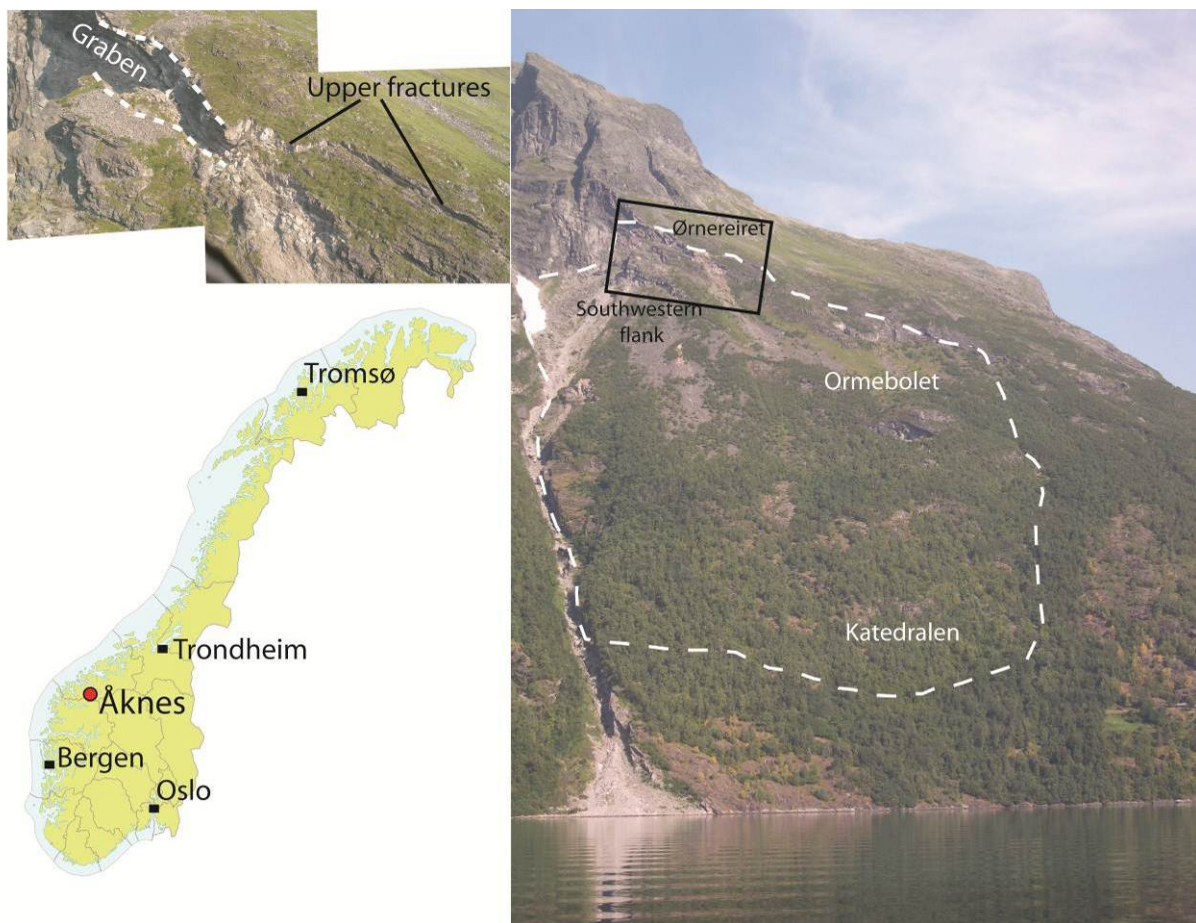


Figure 4.1-1. The Åknes rockslide and its location in western Norway

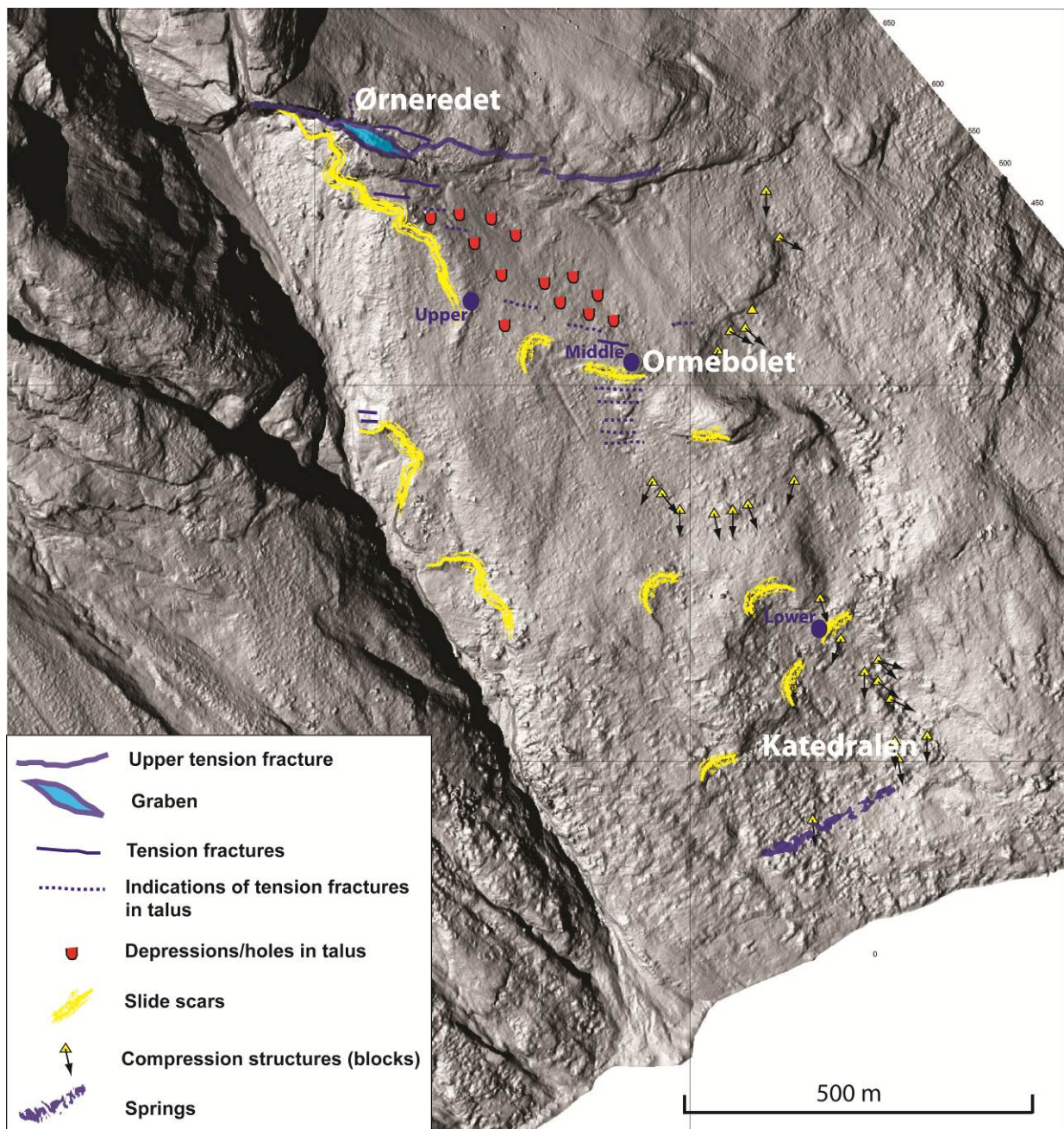


Figure 4.1-2. The morphology of the Åknes rockslide. Historical events are concentrated to smaller rockslides in the western flank. See the slide scars to the left.

Characterization of the site

Numerous geological, geophysical, and geotechnical studies have been completed on the Åknes rockslide to better understand the movement mechanism and to locate sliding surfaces (Blikra, 2008; Ganerød *et al.*, 2008; Kveldevik, 2008; Oppikofer, 2009; Grøneng, 2010; Kristensen *et al.*, 2010). The mode of deformation and displacement is not yet fully understood, but the instability is clearly controlled by the structure of the gneissic rocks, with the steep back scarp following near-vertical folds and the sliding zones parallel to the foliation farther down the slope. The rockslide is defined as complex or translational rockslide, characterized by extension in the upper part, but with two zones of compression in lower half (Figure 4.1-3). However, the geometry and subsurface deformation are much more complex

(Jaboyedoff *et al.*, 2011). The rockslide is composed of several semi-independent blocks with different surface movement directions and different rates of movement at depth.

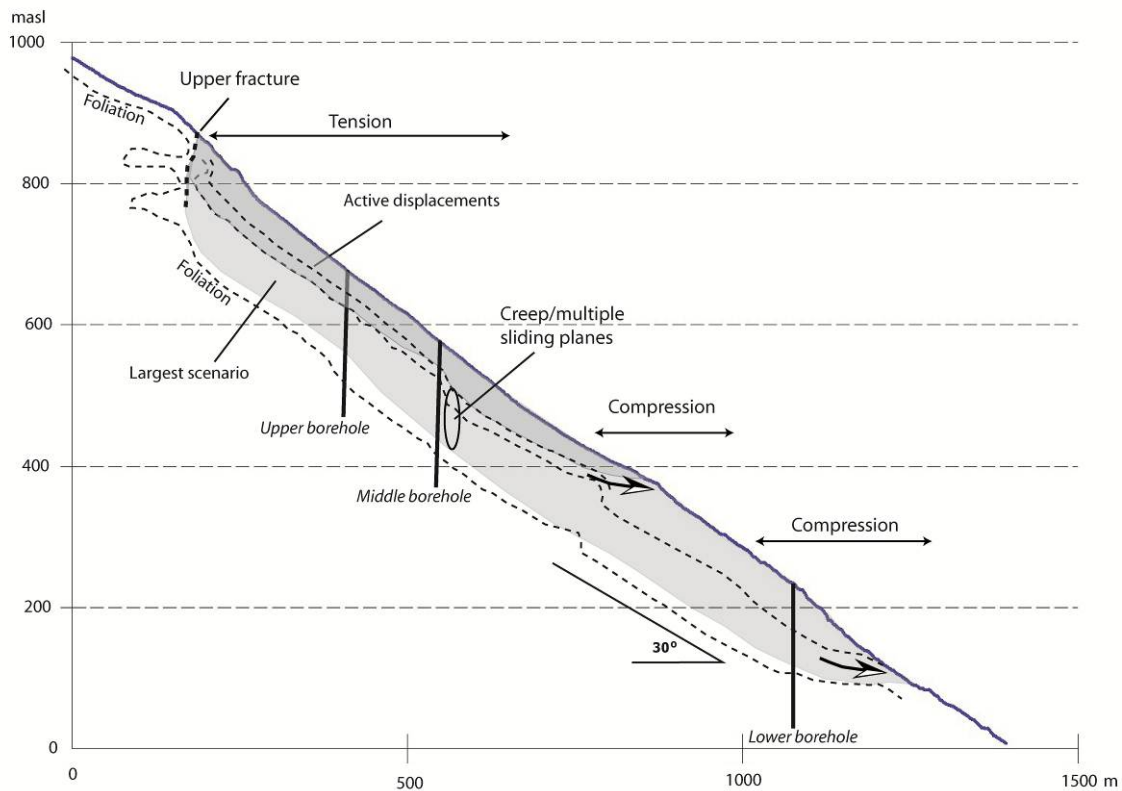


Figure 4.1-3. Schematic 2D deformation model.

The largest scenario has been estimated to be up to 54 Mm³. This includes both the active area and the inactive lower part of the rockslide. The average annual displacement rate ranges from 6-8 cm/year on the upper southwest flank to about 2 cm/year in the middle and east sector. The boreholes show that the upper sliding plane is situated between 25 and 55 m depth, but sliding also occurs deeper than 100 m (Rønning *et al.*, 2006). The drill cores show several brecciated and crushed zones along some of the foliation planes. The borehole logging results and borehole deformation data also show that deformation is occurring at considerable depths (Figure 4.1-3).

Long-term movement rates are roughly constant, but there are shorter-term seasonal fluctuations (Braathen *et al.*, 2004; Kveldsvik, 2008; Blikra, 2008; Kristensen *et al.*, 2010; Grøneng *et al.* 2011). Velocities are lowest in mid-winter and mid-summer. Rates increase during periods of heavy precipitation and snowmelt. In May 2006 movement rates increased about ten times above the background rate in the upper area of the landslide (Figure 4.1-4). The increase was preceded by an increase in temperature from below 0°C to 10°C, accompanied by rapid snowmelt. Water infiltrated open fractures on the slope, evidenced by a 4 m increase in water level in the middle borehole. The higher velocity persisted for more than one week. The change was also evidenced in data from the level of the sliding plane in the upper borehole at 49-50 m depth.

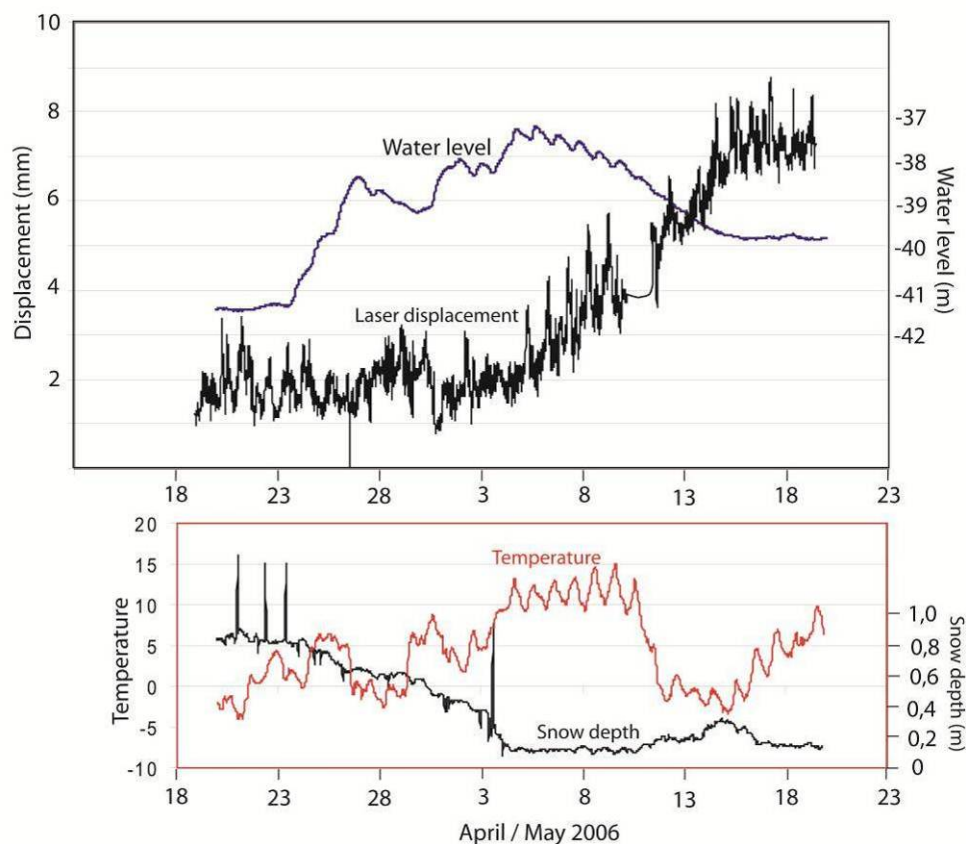


Figure 4.1-4. Increased movement of the Åknes rockslide in April and May 2006, shown by data from a single laser. Also shown are water level measurements in the middle borehole and temperature and snow-depth data from the meteorological station.

Elements of risk and scenarios

Definition of hazard zones at Åknes is based on extensive work on landslide and tsunami modeling (Glimsdal and Harbitz, 2011). Probabilities for different scenarios have been evaluated on the basis of the actual deformation on the slope and historical and geological documentation of rockslide events in the fjord. The largest modeled landslide at Åknes is 54 Mm³ and is estimated to have an annual probability of >1/5000. A scenario involving a failure of 18 Mm³ is estimated to have an annual probability of >1/1000. The largest rockslide would have dramatic consequences – the tsunami triggered by such a landslide would affect a large number of communities along the fjord (Figure 4.1-5), with an estimated run-up of 85 m at Hellesylt and 70 m in Geiranger.

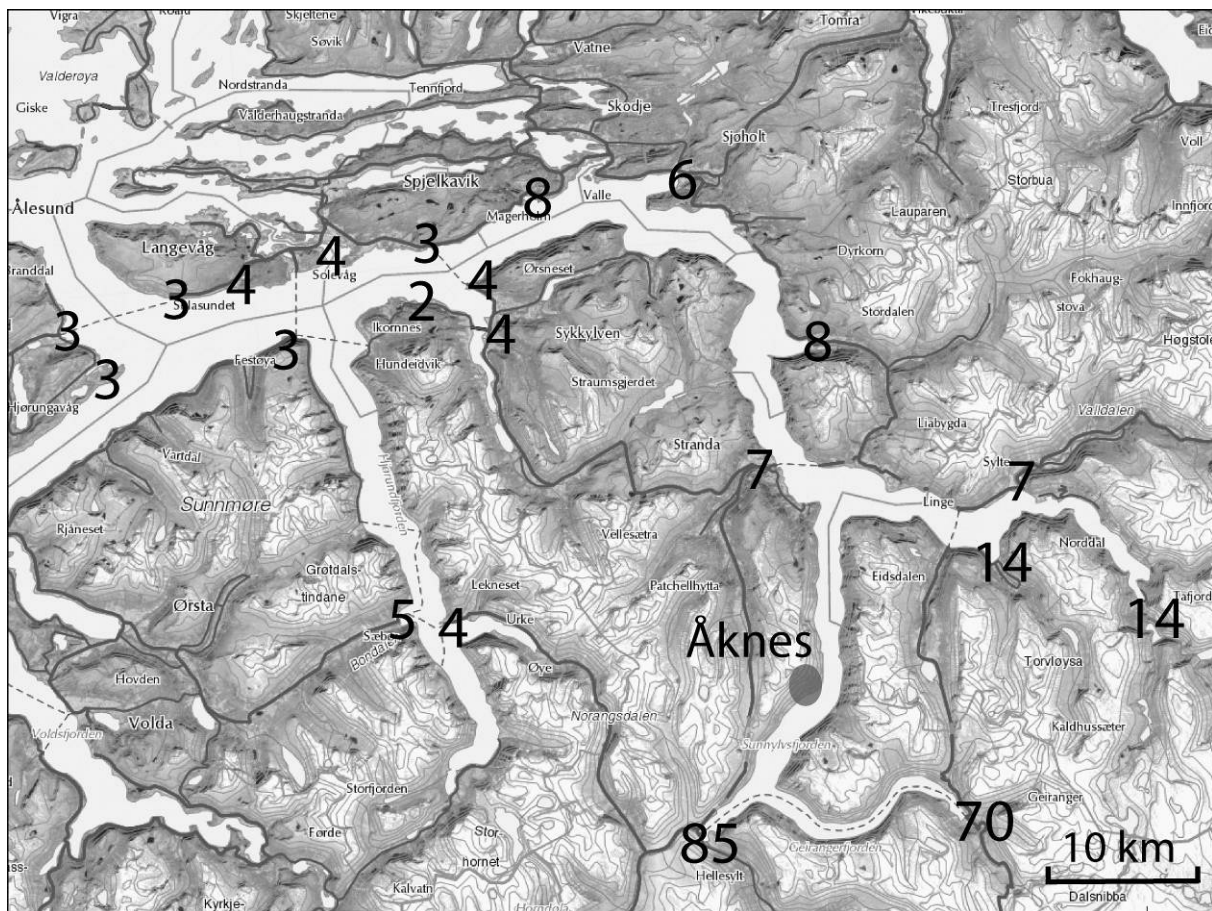


Figure 4.1-5. Estimated tsunami run-up heights (m) for the largest landslide scenario at Åknes (54 Mm³).

Description of the history of the mass movement

Three historical rockslides are known in the Åknes rockslope, all of them from the western flank; see slide scars in Figure 4.1-2. The approximate dating of these events is 1850-1900 (uppermost), 1940, and 1960.

In the fjord region there are several large events that have caused destructive tsunamis. The Tafjord event in 1934 generated a tsunami with run-up height of up to 60 m and 41 people were killed. More than 60 rockslide events have been mapped in this fjord system, demonstrating that large rockslide failures are relatively frequent events (Blikra et al., 2005).

4.1.2 DESIGN OF THE MONITORING NETWORK

The principles of the investigation program and selected monitoring data are presented here. The methods described have proven to be important in evaluating the geometry and volume of the moving rock mass and in designing the monitoring system.

Investigation program

The investigation program was important for several reasons. First, we need to define rockslide scenarios in order to model possible tsunamis. Realistic volume estimates and failure scenarios are essential for risk management planning for numerous municipalities along the fjord. Second, we need to know the location and extent of the unstable area and the

displacement pattern in order to design and implement an effective monitoring program. Third, we need an extensive knowledge base to conduct reliable and real-time monitoring and to provide early warning if required. A thorough understanding of deformation dynamics is especially important during critical events, when decisions regarding alarm levels and evacuation have to be made on short notice. There are no guidelines or handbooks defining the specific requirements for the type and level of investigations needed to perform reliable monitoring and to provide early warning of large landslides. Because of the high risk related to large rockslides and tsunamis, our requirements are demanding. It must be stressed however, that the investigations need to be based on the local conditions.

Surface investigations

We required high-resolution topographic data and thus carried out an airborne LiDAR campaign by helicopter. Based on this survey, we produced topographic maps with 1 m contour intervals. Detailed geological data were also required, including structural geology, geomorphology, and hydrology. Surface displacements were investigated in great detail using satellite-based and ground-based radar (Figure 4.1-6), ground-based LiDAR, and periodic measurements using GPS and total station. The surface investigations allowed us to define the distribution of the unstable zones and provided an overview of the deformation in different sectors of the landslide.

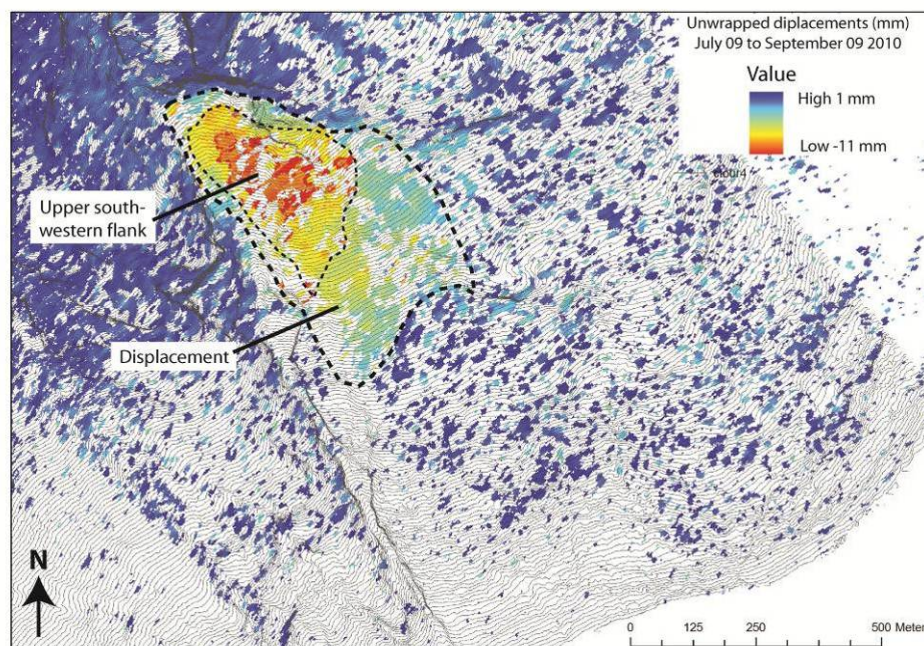


Figure 4.1-6. Data from the ground-based radar campaign at Åknes in 2010.

Subsurface investigations

We also required subsurface geological data, including the depth of the sliding zones and the related deformation, in order to obtain a realistic 3D geometric model of the instability. These data were acquired by drilling and geophysical surveys. Extensive 2D resistivity measurements were made at Åknes and supplemented with refraction and reflection seismic surveys (Rønning *et al.*, 2006, 2007). Boreholes were drilled and near-continuous core acquired at three sites on the landslide. In-hole geophysical measurements were made in the three boreholes (Ganerød *et al.*, 2007). Televiwer logging of boreholes provides additional

information on subsurface rock structure, including fractures and foliation, but it was only performed in the upper part of one of the boreholes.

Laboratory analysis and modeling

To perform stability modeling, we collected rock samples from the surface and from drill cores for analysis of shear strength and other input parameters. Although a stability model cannot conclusively demonstrate that a slope will ultimately fail, it does provide an understanding of the critical parameters for failure (sensitivity analysis). Modeling of landslide run-out must be performed as part of the investigation program. At Åknes, we linked several Ph.D. research projects to the investigation program, and laboratory analysis and stability modeling were done as part of these projects (Kveldsvik *et al.*, 2008; Grøneng, 2010; Grøneng *et al.*, 2010). Codes such as 2D UDEC and 3D FLAC were used to model stability. Another project focused on slide and tsunami modeling and included laboratory experiments (Glomsdal and Harbitz, 2011).

Monitoring network, instrumentation and infrastructure

The unstable rock slope at Åknes is extensively and continuously monitored (Figure 4.1-7 and 8). The concepts and design are described briefly below. The monitoring system was designed to be robust and redundant, while providing the range of data required for stability analysis and decision-making during periods of accelerated movement. The system includes surface and subsurface sensors designed to provide a full understanding of deformation and the controlling mechanisms. The sensors monitor all important sectors or parts of the unstable area on the surface and in boreholes and measure both local deformations across individual fractures and total displacements. They include pore-pressure sensors and a full climate station. The system includes redundant, or back-up, instruments for all critical areas. The infrastructure includes a back-up power supply and data communication capabilities. An overview of the monitoring system is provided below (Figs. 7 and Figure 4.1-8).

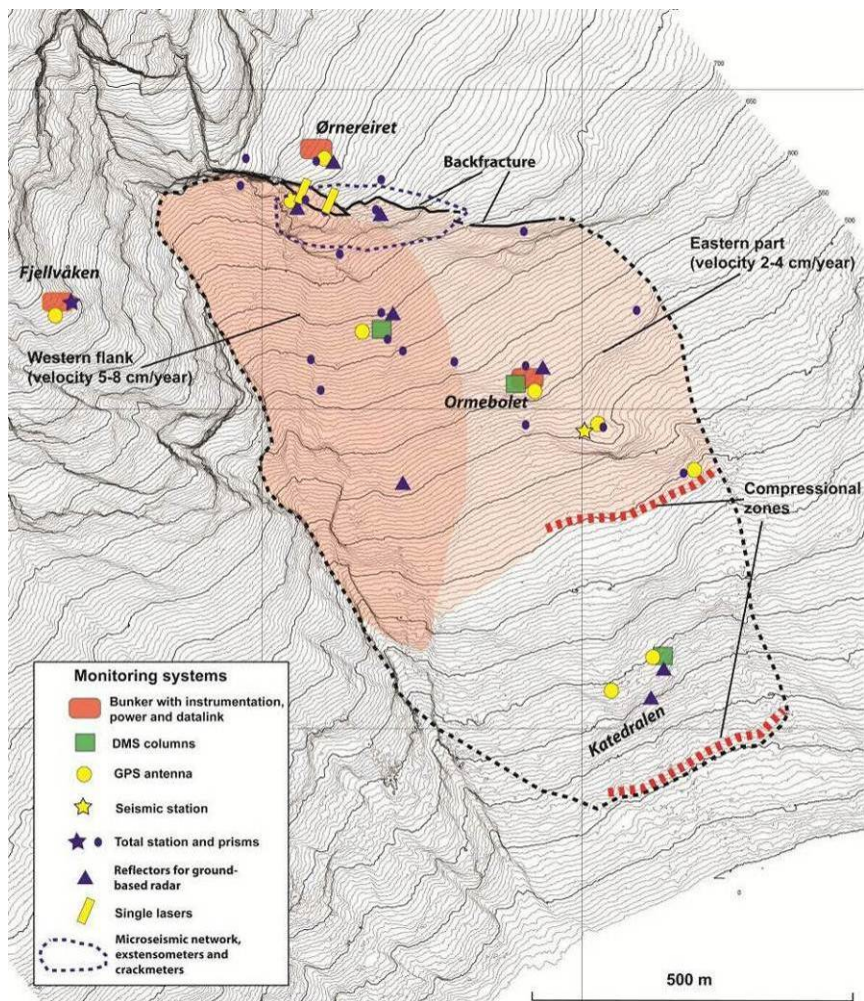


Figure 4.1-7. Overview of the monitoring systems at Åknes. The main deformation sectors of the rockslide are also shown.



Figure 4.1-8. Selected monitoring systems at Åknes. A) GPS antenna B) Total station C) Single laser at the deep upper fracture D) Borehole DMS instrumentation.

Surface monitoring

Monitoring to assess total displacements includes a permanent GPS network with eight antennas (Figure 4.1-7 and Figure 4.1-8A), a total station measuring distances to 30 prisms (Figure 4.1-8B), and a ground-based radar located on the opposite side of the fjord to measure distances to eight reflectors. Due to large atmospheric changes and relatively long distances, it has been difficult to obtain reliable measurements from the total station, especially during the winter (Nordvik and Nyrnes, 2009). The data from the ground-based radar suffer similar problems, and reliable results depend on reference reflectors being located nearby and at the same elevations as the monitoring points.

A series of small crackmeters and a microseismic network of eight 3-component geophones were installed in the upper landslide area (Figure 4.1-7). The microseismic sensors are stable and give reliable data. A series of surface 2D tiltmeters were placed throughout the landslide area.

Local measurements across the fractures were made using three large extensometers and two single lasers (Figure 4.1-8C). The extensometers give excellent data with limited noise. The single lasers are relatively stable, but data acquired during bad weather, especially during periods of snow and fog, are unreliable.

Subsurface monitoring

The three boreholes are instrumented with DMS columns (Figure 4.1-8D), which are linked to a real-time operational early warning system (Figure 4.1-7). Biaxial inclinometers and temperature sensors are spaced at 1 m intervals on the columns. Additional piezometer sensors and digital compasses are placed in selected metre modules. The system is stable and gives high-resolution continuous data, as can be seen in Figure 4.1-9.

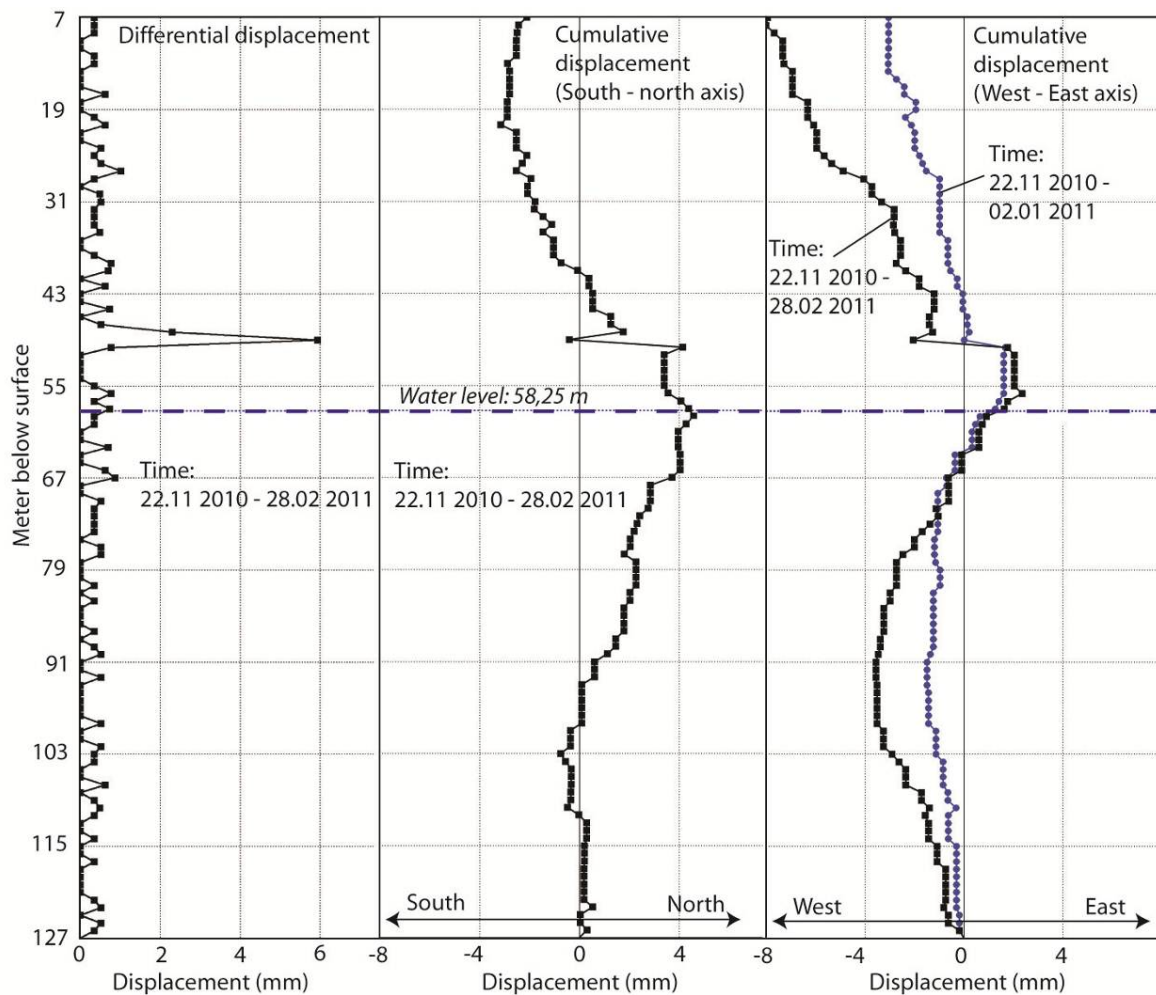


Figure 4.1-9. Data from the DMS column (Differential Monitoring of Stability) in the upper borehole, acquired from 22 November 2010 to 28 February 2011. The 120 m long column extends from 7 m to 127 m depth. The left curve shows the differential displacements of each sensor, and the middle and the right curves show cumulative displacements along two different axes. The right curve also shows the displacement over a shorter time span. The three-month measuring period is sufficient to define the main sliding surface at 50 m depth. There also appears to be movement deeper in the slope, but the displacements of individual sensors are too small to confirm this over the short period of measurement.

Management of data acquisition and maintenance of the systems

The bunkers for power supply, communication system and instrumentation are connected to the internet by a radio link. Thus, the generator control system, dataloggers, routers and other equipment in the bunkers are accessible from everywhere via VPN. The data is transferred to a database and this database has a web interface that allows display of the measurements of flexible intervals.

All sensors are checked daily in order to identify failure of instrument or communication as well as unusual movement. Online cameras often provide a first indication of the cause of a problem; it could be fog, obscuring the view from the lasers, ice placed on the reflectors or snow that distorts the total station measurements. In the case of a bigger problem, such as broken cable from a rockfall or an avalanche, it is repaired as fast as possible. However, access to several sensors on the slope is difficult and dangerous during the winter, and at any

rate it may be impossible to find and fix an instrument or cable below a very thick snow cover. The generators are maintained according to schedule.

4.1.3 ANALYSIS OF MONITORING DATA

4.1.3.1 DGPS network

A permanent GPS (GNSS) network has been in place since 2007. It consists now of nine antennas, of which two are placed on assumed stable positions. Data is processed using a RTK (Real Time Kinematic) technique every 15 minutes, and it is postprocessed from between 4 and 12 hours on average.

Five of the antennas located in the active part show movements between 1.5 and 6 cm/year. The 12 hours post-processing are more precise than the RTK processing, with fluctuations of about 3 mm in the north and east directions and 15 mm in the z direction.

The GPS data also demonstrate the seasonal fluctuations, with the increased velocity starting in the beginning of April 2011 (Figure 4.1-10 and Figure 4.1-11).

The established GPS system has shown to be very robust and reliable, also contributing to near real-time data.

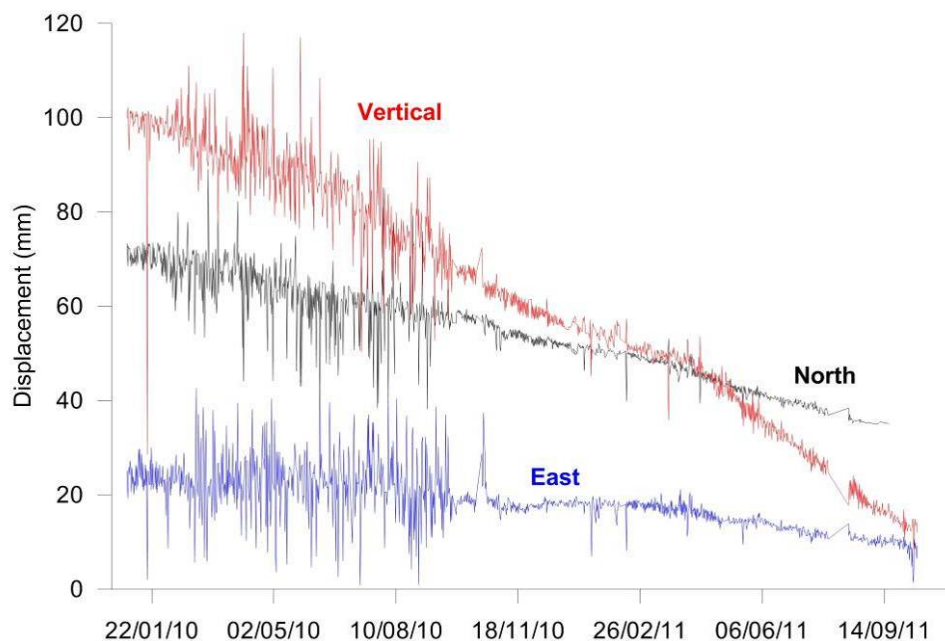


Figure 4.1-10. Movement in three directions of GPS 3 in the upper part (graben) of the rockslide between January 1 2010 and October 11 2011.

4.1.3.2 Lasers

Two lasers measure the distance across the main back crack (location: Figure 4.1-7) and have been operating since 2005. Once every five minutes, 10 measurements are taken, the data quality checked and the average value logged. The lasers use visible light and depend on free sight to the reflectors, therefore fog or heavy precipitation can disturb the measurements.

They measure in the Line Of Sight (LOS) which may underrepresent the true displacement vector. In most cases the values fluctuate within a couple of mm, but regularly meteorological conditions create fluctuations of >20 mm. Some noise is removed by using daily averages when plotting a longer time series.

Both lasers show an easily identifiable trend with many outliers. They seem to have about the same amount of outliers that are >50 mm from the trend, while the upper laser has more small-scale noise than the lower laser.

The lasers have measured displacements in the order of 5 to 7 cm/year, and they show significant seasonal fluctuations (Figure 4.1-11). Generally they show increased velocities during the snowmelt in April/May, and also during heavy precipitation in the fall. The velocity is normally at its minimum during mid-winter and mid-summer. The data further show that snowmelt and/or heavy precipitation rapidly increase the water level in fracture. The water pressure and/or water-saturated sliding planes are thought to be the main reason for the increased displacements at Åknes. Figure 4.1-11 shows this effect very nicely. Temperature increase and snowmelt in the beginning of April 2011 led to a sudden increase in the water level. The high water level continued in the second half of 2011, and the general velocity increased compared to earlier years (Figure 4.1-11).

The lasers directly measure displacement and thus mass movement. They are important parts of the early warning system, due to their frequent measurements across the main back scarp. However, setting SMS messages on the laser measurements is a bit difficult as the number of outliers is quite large, and we receive too many messages from the sensors.

As the sensors are placed at stable ground, and the reflectors are passive, no cables are required inside the instability (except some heating during winter). If the reflectors move out of sight from the lasers, they can be easily adjusted from the top.

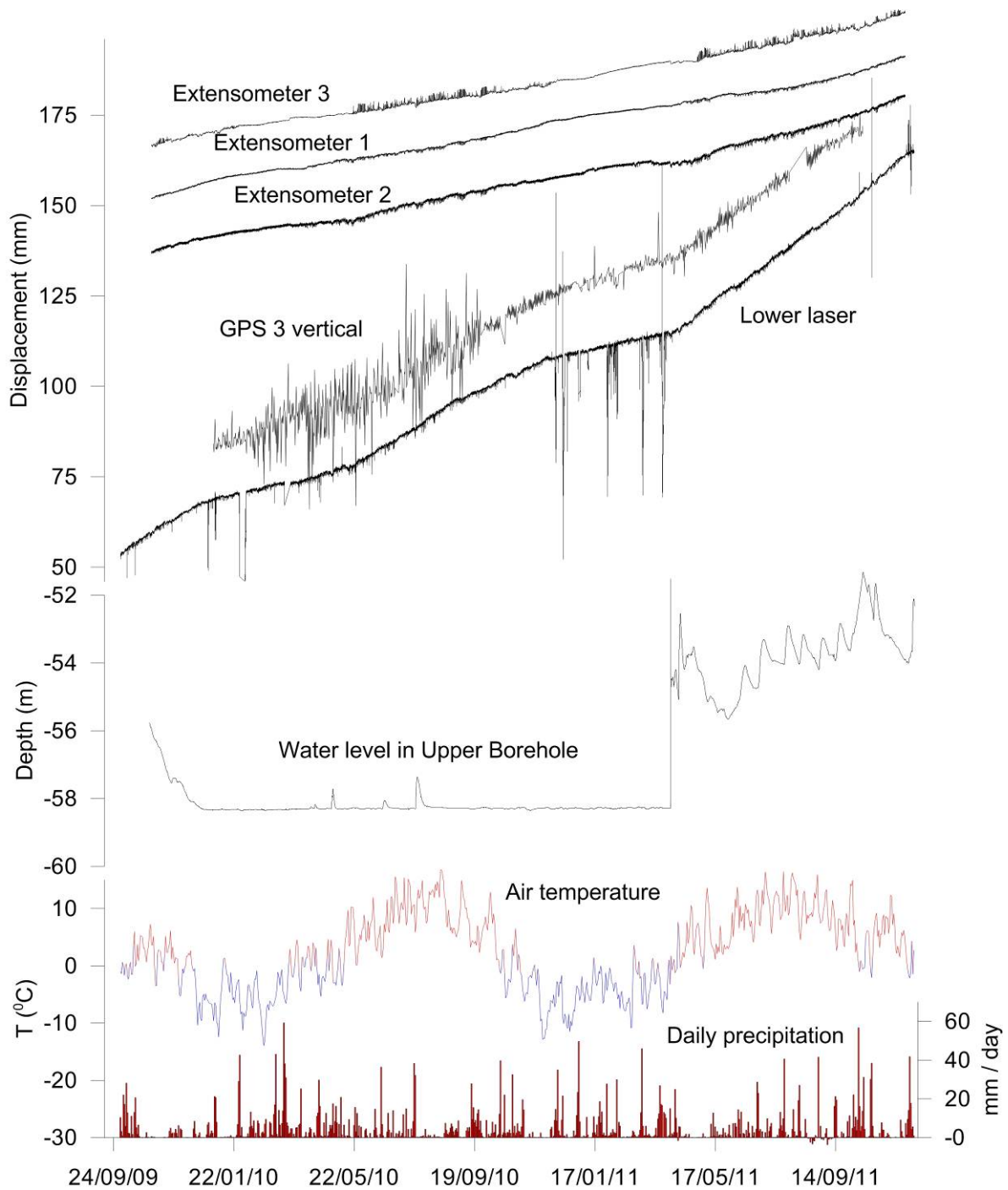


Figure 4.1-11. Displacements from extensometers and lasers. Water level in upper borehole, air temperature and daily precipitation are also shown.

4.1.3.3 Extensometers

Three extensometers have been measuring movement across different cracks in the upper part of the instability since 1992 (see location in Figure 4.1-7). The attempt was to place the instruments parallel to the direction of movement. The displacement recorded by the extensometers is logged every five minutes. The last two years are shown in Figure 4.1-11.

The yearly displacements are from 1.5 to 2.5 cm/year. It is clear from the comparison with other sensors that the extensometers do not capture the entire movement of the rockslide. Extensometers only capture local displacement within the landslide body, and in periods there are also movements backwards due to back-rotation of individual blocks.

As can be seen from the curves (Figure 4.1-11), all three extensometers record a continuous widening of the crack. There are small daily fluctuations that may be due to changes in the temperature of the sensor, but they are at maximum in the order of 3 mm and usually less than 1 mm.

When acceleration of the landslide initiates, the extensometers will most likely supply frequent and reliable information of the movement, unless new crevasses are responsible for most of the movement. The extensometers are only able to expand up to some maximum level and beyond that they will fail, so they are not suited for monitoring the landslide in the latest stages of acceleration. However, the reliability of the sensors makes them very well suited for automatic messages/alarms.

4.1.3.4 Total station

An automatic robotic total station was installed together with c. 25 prisms in 2007. Due to various technical problems, there are several gaps in the time series. However, it has been relatively reliable over the last half year. Most of the prisms shown significant movements in the south direction (downslope) in the order of 2 – 7 cm/year (see example in Figure 4.1-12).

The measurements are relative depending on the weather conditions, and data is normally missing during bad weather conditions (rain, fog, snow). There are also major problems with ice and snow in the prisms. We must expect that the robot will be unable to find the prisms when a large enough displacement of the landslide has occurred. However, it should be able to find the prisms even if they have moved a couple of meters if the mirror is still turned towards the total station. Another advantage is that there are no electric cables on the landslide itself, which could break during accelerated movement. In summary, the total station is probably not the most reliable instrument during an accelerated phase of the landslide, but it provides details of differential displacement that are otherwise difficult to obtain.

No readings were more than 40 mm from the mean, and this may indicate that an SMS message could be set on the prisms, but we need to investigate the reliability further before implementing automatic alarm functions.

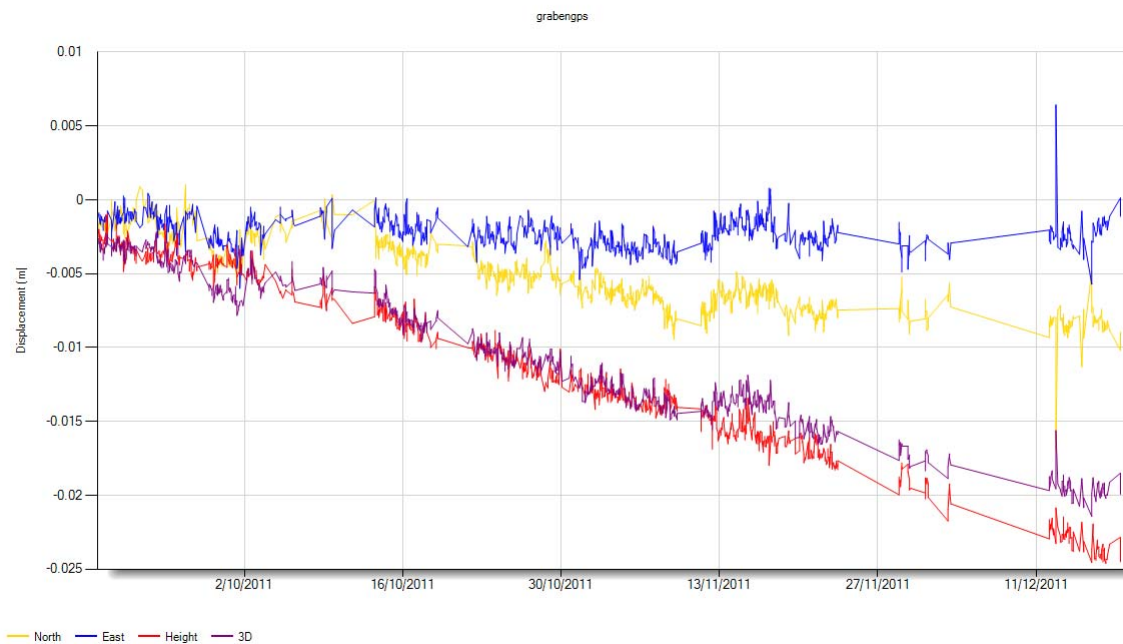


Figure 4.1-12. Three months of data from the total station (prism in the graben area). Time period: September 18 to December 21.

4.1.3.5 Crackmeters

Four crackmeters (small extensometers) were installed in the upper parts of the Åknes landslide in 2009 to measure movement across small cracks. Their position is shown in Figure 4.1-7. Crackmeters 2 and 3 are at the same location but measure in different directions. A measuring period of 14 months is shown in Figure 4.1-13 (January 2009 – March 2010).

The crackmeters only measure across small extensional features and therefore do not capture the total displacement of the landslide. Crackmeters 3 and 4 measured up to 3 mm contraction while Crackmeter 2 measured about the same amount of extension. Crackmeter 1 measured a very small extension. The contraction took place primarily in the spring and summer 2009, while the extension seems most pronounced during the autumn. During the winter all the sensors measured only minor changes. The measurements show that the cracks are active, but without a clear trend of expansion or contraction.

The crackmeters have the potential of recording spreading activity in smaller cracks, which may be important for the landslide dynamics. Although they record very small amounts of the total movement, they are suited for automatic SMS messages and alarms. Due to the fact that they only capture local movements and that the movement can be larger than they can expand, they will be difficult to use in the late stages of an event. The crackmeters are small and not robust, so we have experienced problems in the winter.

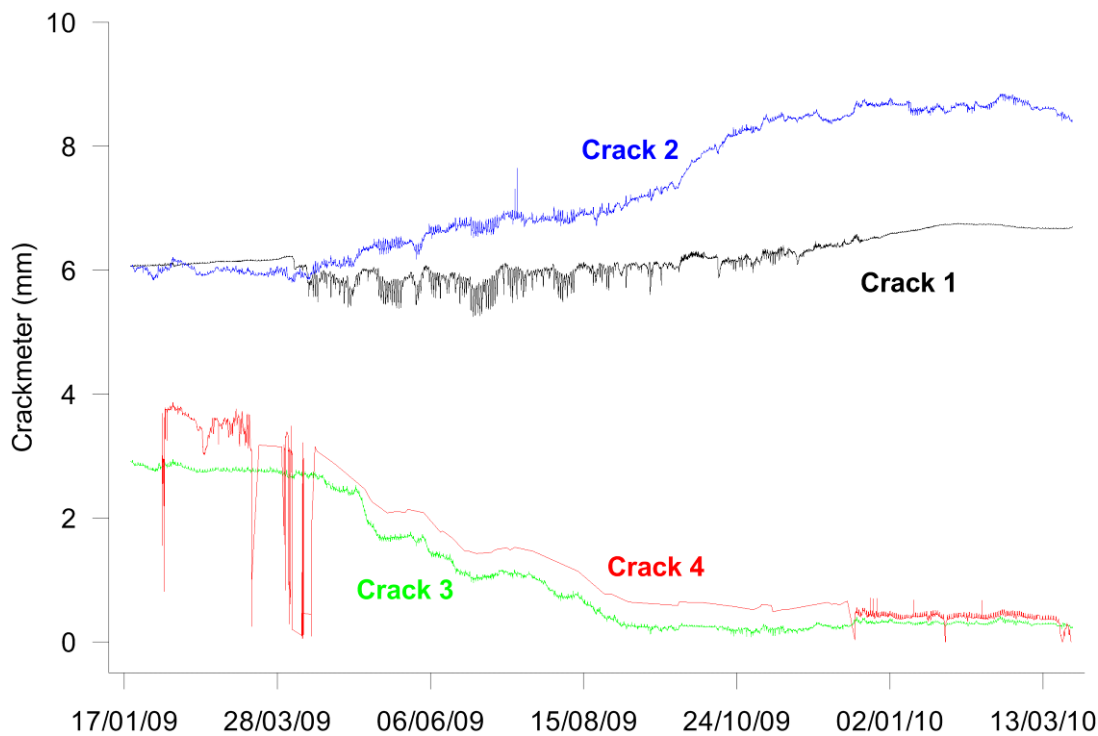


Figure 4.1-13. Measurements of the four crackmeters during a 14-month period.

4.1.3.6 Tiltmeters

Several tiltmeters have been placed on the Åknes rockslide. It is not evaluated here as we need more time to evaluate the use of the tiltmeters in terms of studying the dynamics of the rockslide and the potential use for SMS messages.

4.1.3.7 DMS column - displacements

Three 200 m deep core boreholes were performed at Åknes. DMS columns of different length have been used for the investigation of subsurface displacements and later for continuous monitoring. Figure 4.1-11 and Figure 4.1-14 show some of the data from the upper borehole. It now consists of 120 m long columns in the upper and middle sites and a 100 m long system at the lower site (location in Figure 4.1-7). The system measures displacement or tilt for every meter, in addition to water pressure and temperature. The DMS instrumentation is important in the investigations, as it provides information about sliding planes in depth.

Figure 4.1-14 shows the differential south-north displacement measured over the last year. The main sliding plane is clearly defined to 49 m depth, with a southward displacement of 25 mm/year. The total 2D displacement (south-southwest) is 35 mm/year.

The DMS instrumentation is very important to the early warning system as it is connected to real-time alarm functions. The signal to noise ratio is very low, with noise in the order of 0.3 to 0.5 mm.

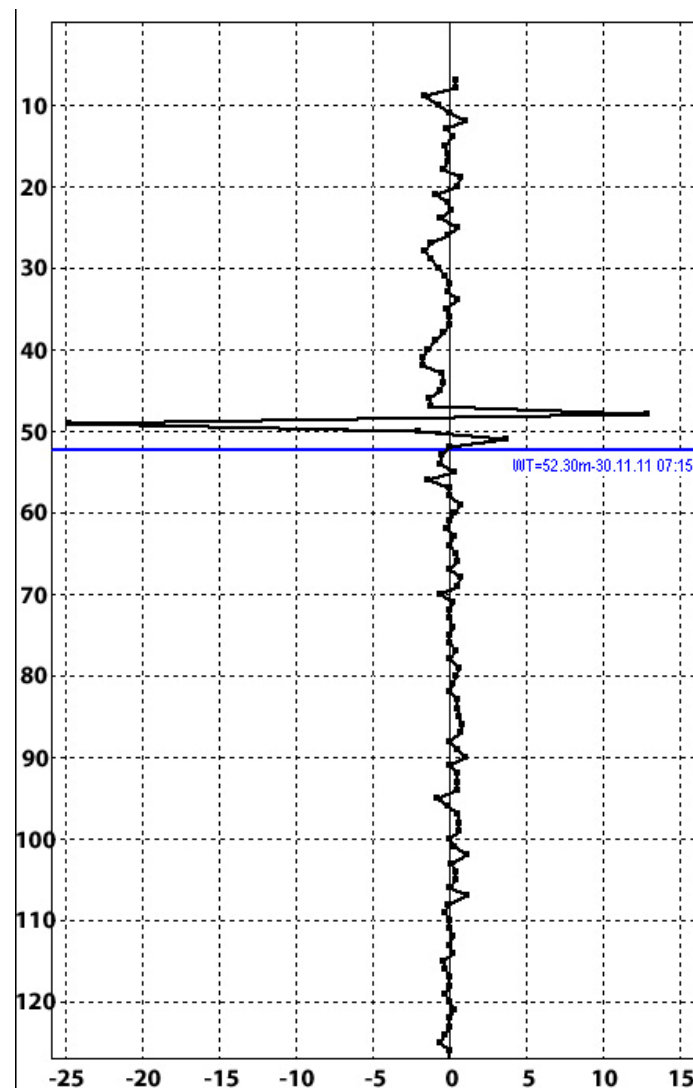


Figure 4.1-14. Differential displacement in south-north direction in mm (south: main downhill direction) measured in the DMS column in the period: 30th November 2010 to 30th November 2011. The blue line shows the water level the 30th of November 2011.

4.1.3.8 DMS column – water level

The water level data is an important part of the monitoring system, and piezometers are placed in all DMS columns. The water level in the upper borehole is shown in Figure 4.1-11. It demonstrates the close relationship between the water level and displacements.

The piezometer data are used in the early warning system as we move to blue alarm level, with a water level increase of 1 m/day or 4 m/week.

4.1.3.9 Meteorological station

A meteorological station is located in the upper part at the upper bunker (Figure 4.1-7). It records air temperature, wind speed and direction, precipitation, humidity and snow depth. Average daily temperatures and daily precipitation can be seen in Figure 4.1-11. High precipitation or snowmelt events lead to an almost immediate increase in water level that affects the displacement.

The data are used in the early warning system as we move to blue alarm level when precipitation exceeds 70 mm/day or 200 mm/week.

4.1.3.10 Microseismic network

A small microseismic network composed of eight 3-component geophones are located in the upper part of the Åknes rockslide (see location in Figure 4.1-7). The system has been operational since 2005, with real-time data transfer and processing. Also, a broadband station (seismograph) is located in the middle part of the slope. Microseismic events on the slope are associated with rockfalls, small-scale rockslides and the general movement of the entire instability. An acceleration of the slope will increase the microseismic activity.

The data is published on an open webpage (see example of one-month plot in Figure 4.1-15). The cumulative amplitudes of the events are thought to be associated with an increase in the number of and/or the magnitude of seismic events. The data shows the increase of event magnitude in the spring very nicely (Figure 4.1-16).

The implemented seismic system has shown to be robust and of high reliability. The data gives supplementary information that is important during increased displacements.

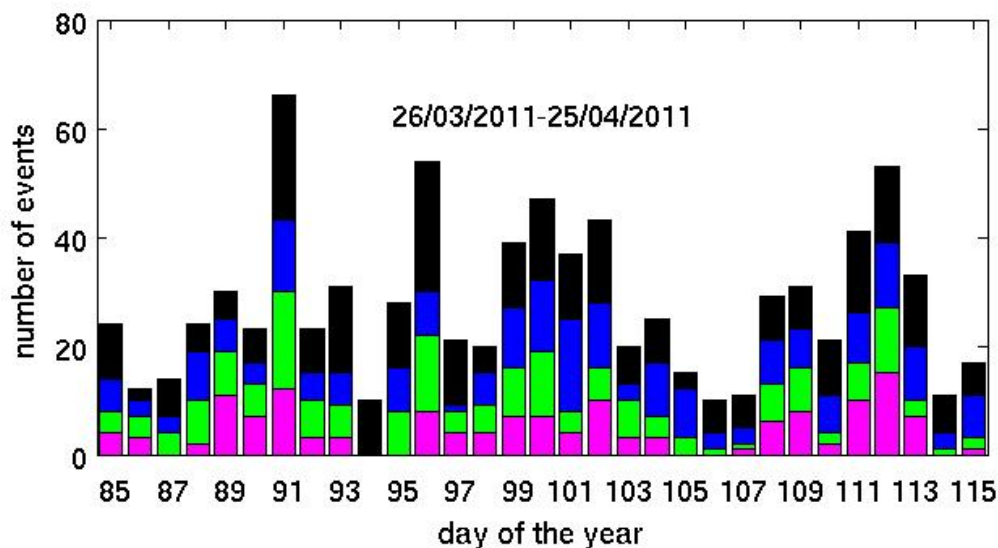


Figure 4.1-15. Plot of the daily number of microseismic events during 1 month.

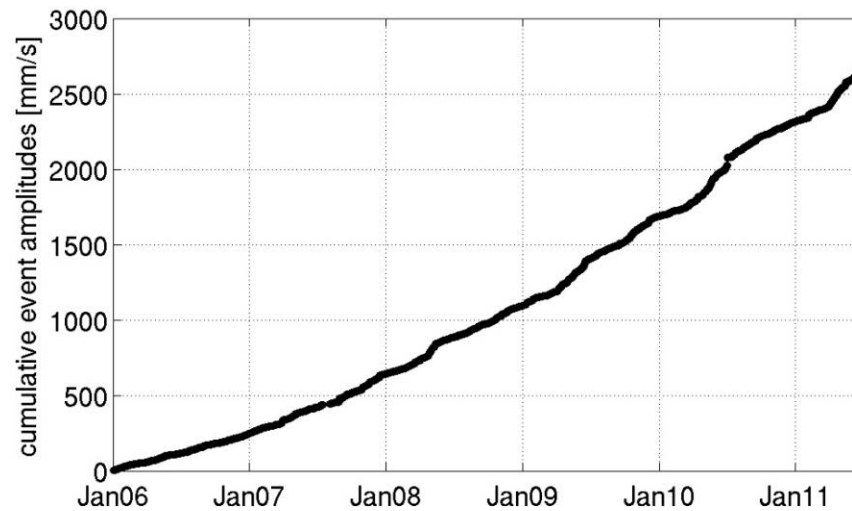


Figure 4.1-16. Cumulative amplitude of reviewed events in the period January 2006 to July 2011.

4.1.4 END-USER INVOLVEMENT AND ALARM CHAIN

The total early warning system for the Åknes rockslide and other monitored rockslides in Norway involves all responsible partners or end-users that may be affected by the potential rockslide and tsunami. A systematic end-user involvement includes local, regional and national levels, the police, and all other sectors like road authorities, health authorities, the coast guard, power companies, etc. A national emergency plan is being implemented to secure the communication chains and quality of the system. National tests have been organized, including both table-top and field-based.

The early warning levels are based on the velocity level and the stability situation at the monitored sites (Figure 4.1-17). The normal situation at Åknes is the green level, with movements typically about 0.1-0.2 mm/day (Figure 4.1-17). The next higher level (blue) comes into effect when the velocity increases substantially due to seasonally wet weather. The yellow level is reached when the velocity increases beyond the seasonal fluctuations. The orange level comes into effect when movements accelerate, and the red level is reached when a catastrophic failure is imminent, at which time an evacuation is ordered. Specific actions are implemented for the different warning levels and involve the Early Warning Centre, police, county governor, municipalities, road authorities, coast guard, and power companies.

The operational system is based on the following routines: (1) daily check of all sensors and data by the geologist on duty; (2) daily technical checks by the technical person on duty; (3) mobile phone text messages (SMS) on data acquired from selected sensors and technical system failures; and (4) long-term contracts with monitoring companies that have different operational responsibilities.

The use of the SMS and e-mail messages is difficult due to the different types of noise in the data. It is important to use thresholds that do not result in too many false alarms but rather provide warning of real events. SMS messages are never used alone to change warning levels, but provide important support for the people on duty. One of the challenges is that sensors with large noise levels, for example the single lasers, create a large number of messages and cannot be used alone to raise the warning level.

The detailed communication chain structure between the Early Warning Centre, the responsible organizations, and all involved partners is written in detailed documents and plans. The Early Warning Centre has the responsibility to inform the responsible organization when the early warning level is changed. The county governor has the responsibility for the coordination during the yellow and orange levels, while the police take over this role during the red level. The implementation of warnings and evacuation is done by the police. Two different methods are used to issue warnings. First, a system of phone messages is generated based on a continuously updated database, in addition to automatic SMS messages based on regional coverage from the mobile network companies. Second, an electronic warning siren in all the villages situated in the tsunami hazard zone can be activated.

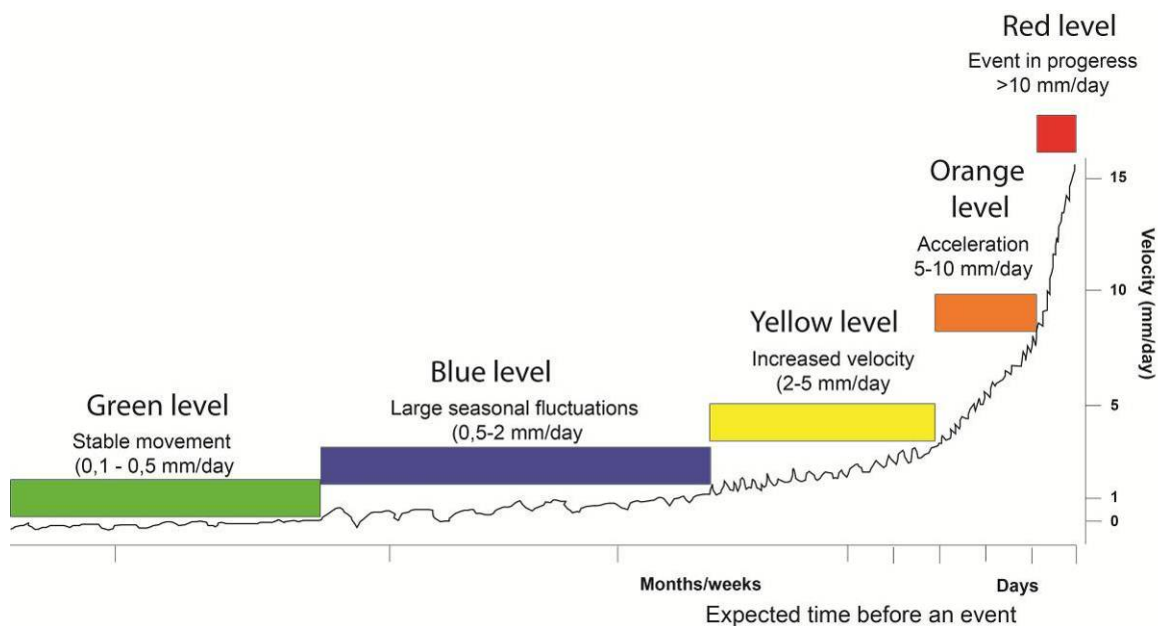


Figure 4.1-17. Early warning levels for the Åknes rockslide and tsunami.

4.1.5 SUMMARIZED EVALUATION OF PARAMETERS

The total design and implementation for the monitoring system and related early warning issues are complete for the Åknes rockslide. It is our opinion that the system is operating well, has reduced the risk to an acceptable level, and fulfills the requirements of national codes.

It has shown to be a near-coupling between the different monitored parameters, like meteorological data (precipitation/snowmelt), different surface displacement data (GPS, total station, laser, extensometers), seismic events (microseismic network), subsurface displacements (DMS column) and water level (piezometers). The seasonal fluctuations are evident in the dataset, with increased surface and subsurface displacements during heavy rainfall and/or snowmelt producing higher water levels (Figure 4.1-11).

The change in alarm levels are always based on data from a combination of sensor types, and includes an overall evaluation of the stability. The geoindicators used for this purpose are grouped under “primary” and “supplementary”.

Primary indicators:

- Surface displacements (velocity and acceleration): GPS, total station, extensometers, lasers, crackmeters
- Subsurface displacements: DMS columns (inclinometers)

Supplementary indicators – sensors:

- Water level: piezometers in DMS column
- Precipitation and snowmelt: meteorological station
- Seismic events: seismograph and a microseismic network

The velocity thresholds for defining alarm levels are different from instrument to instrument, and also differ according to the time period over which the data are evaluated. Extensometer data over a period as short as one hour can serve as the basis for a warning, whereas data from the total station and GPS are assessed over a longer period due to larger fluctuations and noise.

In conclusion, the most reliable and important data for evaluating alarm levels are the GPS network, robust extensometers, and DMS columns.

Considerable effort has been put into the instrumentation of the Åknes rockslide. It has been a challenge to instrument with the risk of rockfall and snow avalanches. Parts of the slope are also inaccessible during the winter. All the instrument sensors are working and give the monitoring centre continuous data, however bad weather is a major problem for getting good quality data from the laser systems and the total station.

Future outlook includes building a more complete model of the rockslide, which combines all new measurements of displacement with structural information, geophysical measurements and borehole data. This will improve our understanding of processes and mechanisms of failure, which will give us better confidence in forecasting a rockslide event. Furthermore, a significant task for the monitoring centre is to maintain all instruments and systems in good working order, to ensure timely early warnings can be given. Due to problems with the upper borehole, a new borehole will be performed in 2012.

References

- Blikra, L.H. (2008). The Åknes rockslide; monitoring, threshold values and early-warning. In *Landslides and Engineered Slopes*, ed. Z. Chen, J.-M. Zhang, K. Ho, F.-Q. Wu and Z.-K. Li . Proceedings of the 10th International Symposium on Landslides and Engineered Slopes, 30 June - 4 July 2008, Xi'an, China. Taylor and Francis. ISBN: 978-0-415-41196-7. 6 p.
- Blikra, L.H., Longva, O., Harbitz, C. & Løvholt, F. (2005): Quantification of rock-avalanche and tsunami hazard in Storfjorden, western Norway, 57-64. *I. Senneset, K., Flaate, K. & Larsen, J.O. (eds.) Landslides and Avalanches ICFL 2005 Norway.* Taylor & Francis Group, London.
- Braathen, A., Blikra, L.H., Berg, S.S. and Karlsen, F. (2004). Rock-slope failures of Norway; type, geometry, deformation mechanisms and stability. *Norwegian Journal of Geology*, **84**, 67-88.
- Crosta, G.C. and Agliardi, F. (2003). Failure forecast for large rock slides by surface displacement measurements. *Canadian Geotechnical Journal* **40**, 176-191.
- Frei, C. (2008). *Groundwater Flow at the Åknes Rockslide Site (Norway). Results of Multi-tracer Test.* M.Sc. thesis, ETH Zurich, Zurich, Switzerland.
- Froese, CR. and Moreno, F. (2011). Structure and components for the emergency response and warning system on Turtle Mountain, Alberta, Canada. *Natural Hazards*, doi 10.1007/s11069-011-9714-y.

-
- Ganerød, G.V., Grøneng, G., Aardal, I.B. and Kveldsvik, V. (2007). *Core Logging of Seven Boreholes from Åknes, Stranda Municipality, Møre and Romsdal County*. Geological Survey of Norway Report, **2007.020**.
- Ganerød, G., Grøneng, G., Rønning, J.S. *et al.* (2008). Geological model of the Åknes rockslide, western Norway. *Engineering Geology*, **102**, 1-18.
- Glimsdal, S. and Harbitz, C.B. (2011). *Numerical Simulations of Tsunamis from Potential and Historical Rock Slides in Storfjorden; Hazard Zoning and Comparison with 3D Laboratory Experiments*. Norwegian Geotechnical Institute Report, **20051018**.
- Grøneng, G. (2010). *Stability Analyses of the Åknes Rock Slope, Western Norway*. Ph.D. thesis, Norwegian University of Science and Technology, Trondheim.
- Grøneng, G., Christiansen, H.H., Nilsen, B. and Blikra, L.H. (2011). Meteorological effects on seasonal displacements of the Åknes rockslide, western Norway. *Landslides*, **8**, 1-15.
- Grøneng, G., Lu, M., Nilsen, B. and Jenssen, A.K. (2010). Modelling of time-dependent behaviour of the basal sliding surface of the Åknes rock slide area in western Norway. *Engineering Geology*, **114**, 414-422.
- Jaboyedoff, M., Oppikofer, T., Derron, M-H., Böhme, M., Blikra, L.H. and Saintot, A. (2011). Complex landslide behavior and structural control: A 3D conceptual model of Åknes rockslide, Norway. In *Slope Tectonics*, ed. M. Jaboyedoff. *Geological Society of London Special Publication*, **351**, 147-161.
- Kristensen, L., Blikra, L.H. and Hole, J. (2010). *Åknes: State of Instrumentation and Data Analysis*. Åknes Report no **02.2010**, 43 p.
- Kveldsvik, V. (2008). *Static and Dynamic Stability Analyses of the 800 m High Åknes Rock Slope, Western Norway*. Ph.D. thesis, Norwegian University of Science and Technology, Trondheim.
- Kveldsvik, V., Einstein, H.H., Nilsen, B. and Blikra, L.H. (2008). Numerical analysis of the 650,000 m² Åknes rock slope based on measured displacements and geotechnical data. *Rock Mechanics and Rock Engineering*, **22**, 689-728.
- Lovisolò, M., Ghirotto, S., Scardia, G. and Battaglio, M. (2003). The use of Differential Monitoring Stability (D.M.S.) for remote monitoring of excavation and landslide movements. In *Proceedings of the Sixth International Symposium on Field Measurements in Geomechanics*, ed. I. Myrvoll Oslo: Balkema, pp. 519-524.
- Nordvik, T. and Nyrnes, E. (2009). Statistical analysis of surface displacements – An example from the Åknes rockslide, western Norway. *Natural Hazards and Earth System Sciences*, **9**, 713-724.
- Oppikofer, T. (2009). *Detection, Analysis and Monitoring of Slope Movements by High-resolution Digital Elevation Models*. Ph.D. thesis, University of Lausanne, Lausanne, Switzerland.
- Rønning, J.S., Dalsegg, E., Elvebakk, H., Ganerød, G. and Tønnesen, J.F. (2006). *Geofysiske Målinger Åknes og Tafford, Stranda og Nordal Kommuner, Møre og Romsdal*. Geological Survey of Norway Report, **2006.002** (in Norwegian).
- Rønning, J.S., Dalsegg, E., Heincke, B.H. and Tønnesen, J.F. (2007). *Geofysiske Målinger på Bakken og ved Hegguraksla, Stranda og Norddal Kommuner, Møre og Romsdal*. Geological Survey of Norway Report, **2007.023** (in Norwegian).
- Thöny, R. (2008). *Dynamic Fluid Electric Conductivity Logging for Identification and Characterization of Preferential Groundwater Flow in the Åknes Rockslide (Norway)*. M.Sc. thesis, ETH Zurich, Zurich, Switzerland.

4.2 AMPFLWANG – HAUSRUCK (AUSTRIA)

R. Supper, B. Jochum, I. Baroň, D. Ottowitz, S. Pfeiler, A. Römer
Geological Survey of Austria

M. Lovisolo
C.S.G., Italy

G. Moser
ZT-Moser-Jaritz, Austria

ABSTRACT

Monitoring results from the Ampflwang test site are presented. This site is an active shallow landslide, activated in spring 2010 within an older deep-seated rotational landslide. During a period from December 2010 to September 2011, displacement and soil temperature, measured by means of a DMS system, compared to resistivity and self-potential monitoring (GEOMON^{4D}), and air temperature are presented. High-resolution displacement monitoring has proven to be an efficient way to monitor displacements and to issue early warnings. The results showed that the availability of at least hourly data is a necessity. However, to derive information about related triggering processes, correlation with other data is necessary. For this purpose precipitation and resistivity monitoring proved to be supplementary and very efficient in this case. After half of the survey period, this landslide obviously stabilised. To derive a more detailed understanding of the behaviour of this landslide and to decide if the stabilisation is permanent, a longer survey period would have been necessary.

Presented parameters: displacement, velocity, groundwater level, precipitation, air temperature, soil temperature, resistivity, self-potential.

4.2.1 GENERAL DESCRIPTION OF THE TEST SITE

The Ampflwang monitoring site represents a recent landslide formed after a house construction within the area of an old deep-seated landslide. It is situated at the limit of Ampflwang town in the Hausruck Hills in northwest Austria.

Geological and geomorphic settings

The deep-seated landslide developed mostly in quaternary colluvium (slope and old landslide deposits) and anthropogenic deposits situated above the underlying Upper Tertiary rocks, i.e. fluvial gravels of Hausruck formation (HF) at the top, limnic to fluvial coal-rich clay with brown coal beds of Ampflwang formation (AF) in the middle, and in marine silty-sandy marl to silty sand of Ottwang formation (OF) at the base. The slope deposits originated from those Tertiary host rocks.

The surrounding area of the monitored active landslide is comprised of a deep-seated rotational landslide. This dormant landslide is about 650 m long and 900 m wide, with an estimated depth of failure about 20-30 m b.g.l. The typical geomorphic features are a head scarp up to 10-15 m high, back-tilted flats with some pseudokarst dolines, and

smooth pressure ridges and other hummocks. The area was influenced by brown coal mining, thus some of the dolines could have originated from undermining and suffusion.

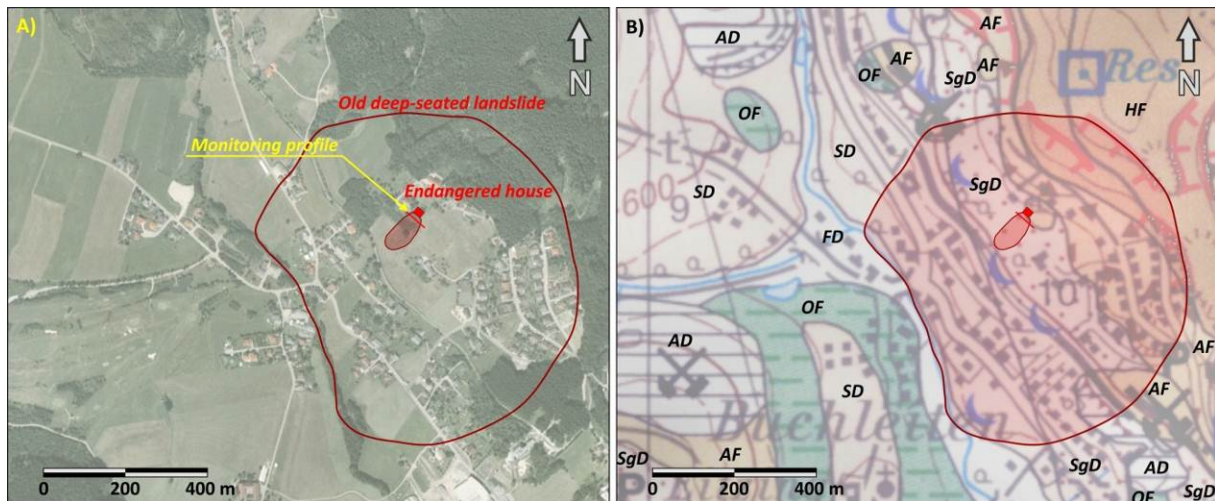


Figure 4.2-1. Situation at the Ampflwang monitoring site: (A) Orthophoto with the marked landslides and geoelectric monitoring profile, and (B) Geological map of the site: AD – Anthropogenic deposit, SD – Slope deposit due to solifluction (Würm to postglacial), SgD – Mostly gravel slope deposit due to solifluction (Würm to postglacial), HF – Hausruck formation (fine to coarse gravel in coarse to fine sandy matrix, fluvial), AF – Ampflwang formation (clay, coal-rich clay, brown coal beds, sand, occasionally with gravel, limnic to fluvial), OF – Otttang formation (silty-sandy marl to silty sand, massive or indistinctly bedded, marine). Source of maps: Application GoogleEarth and Geological Survey of Austria

Characterization of the site

The reactivated part, as recognized by topographic changes and inclinometric data, is about 110 m long, 40 m wide and about 4 m thick. It is a shallow rotational-translational landslide of an elliptic shape and has quite smooth topography. It is in the initial evolution stage. However, a newly constructed family house was partly damaged by the crown of the landslide in 2010. The monitoring of the reactivated landslide involves fully remotely-controlled continuous DMS and GEOMON^{4D} techniques.

Description of the history of the mass movement

The entire area north of the town of Ampflwang was affected by a deep-seated landslide in the Holocene. However, there is no information available about other distinct past activity and historical events. Despite a quite high landslide hazard, new houses were built within the area of this old deep-seated landslide in past decades.

In March 2010, following snow melting and heavy rainfalls, a shallow landslide was triggered in the vicinity of a newly constructed house in the central part of the old landslide (Figure 4.2-1 and Figure 4.2-2). It significantly damaged the surrounding of the house, i.e.: parking lot, terrace, water and power supply, waste pipe, and endangered the entire house by retrogressive reactivations. Therefore, a monitoring system was implemented in cooperation with the geotechnical bureau of Moser/Jaritz, C.S.G. and the Geological Survey of Austria in order to investigate the behaviour of the landslide and its triggering in more detail, and to develop an optimized strategy for site-specific remediation measures. Due to the ongoing

displacement, this site was selected as one of the test sites for the SafeLand and Temple projects.



Figure 4.2-2. Damage of a newly constructed house caused by the shallow landslide in March 2010. The landslide has been monitored since then for displacement and geoelectric parameters (Foto: J. Gaisbauer)

4.2.2 DESIGN OF THE MONITORING NETWORK

The monitoring system at Ampflwang site consists of two DMS monitoring columns and a GEOMON^{4D} resistivity and self-potential monitoring instrumentation. Immediately after the event in March 2010, five core drillings were performed. Due to the high hazard (directly endangered family house), a simple manual inclinometric monitoring was started soon after the first event. In December 2010 a permanent, fully automated monitoring system consisting of two DMS columns and a geoelectric monitoring device were installed. One of the DMS columns was installed upslope of the house (column 1) where previously no displacements could be detected, whereas the other one was positioned close to the expected crown of the landslide downslope of the building (column 2). The geoelectrical profile was installed inside a shallow drainage trench downslope of the house and close to the second DMS column. Later on, geoelectrical measurements were performed along two profiles to investigate the surrounding area of the landslide.



Figure 4.2-3. Situation at the Ampflwang monitoring site: DMS column located below the orange box and the trench with the GEOLMON^{4D} cables (left) and part of the cable situated on the ground surface (Photo: Ivo Baroň).

The DMS columns consisted of tilt/displacement, temperature and piezometric sensor modules and they registered displacement data on an hourly basis down to the depth of 5 and 7 m b.g.l. respectively. The transversal geoelectric GEOMON^{4D} profile comprised 60 electrodes at a spacing of one meter. The precipitation data was taken from the weather station of Wolfsegg, courtesy of the Central Institute for Meteorology and Geodynamics (ZAMG) under the cooperation contract between GSA and ZAMG.

The monitoring data are sent via GPRS to the GSA and C.S.G. office in order to be analysed and interpreted.

4.2.3 ANALYSIS OF MONITORING DATA

4.2.3.1 Displacement (GSA)

Measureable displacements were only registered in the borehole situated below the building in the upper part of the landslide (Figure 4.2-3). The inclinometric record of cumulative displacement along the N-S plane is presented in Figure 4.2-4. A quite sharp slip surface was registered between a depth of 3 and 4 m b.g.l. with a general direction of movement towards SSW (Figure 4.2-5). The converse movement below is most probably due to the fact that the inclinometer module (1 m long each) between 3 and 4 m b.g.l. is rotated around a pivot between these depths, and the deeper part of the module is forced to move against the slope movement inside the tube with some effect on the module below. However, based on these inclinometric measurements the slope could be considered as stable below the depth of 4 m.

Figure 4.2-6 shows the time series of the total displacement over the whole monitoring period. The one major event occurred from January 13th, 01:16 h (CET) to January 15th 2011, 10:16 h (CET) after a period of snowmelt and intense rainfalls (labelled as the **“January 2011 event”** or **“Event 1”** in Figure 4.2-6). The total displacement reached 18.48 mm in 58 hours, the maximum velocity was up to 0.88 mm/h, and the average velocity was about 0.32 mm/h. The graph of cumulative displacement, velocity and acceleration from hourly DMS measurements and their eight-hour running averages are presented in Figure 4.2-7. Generally, evaluating from the eight-hour running averages, the acceleration rose in the first part then in the middle of the event the mass decelerated immediately. After this short event, the mass showed a small and quite constant displacement, except during four other relatively small events (Figure 4.2-6) of increased acceleration. Most of them (except event 2) were related to rainfalls. After mid-July the velocity decreased to almost zero. It is worth mentioning that most events (except event 5) happened during the winter and were preceded by longer periods of positive temperatures, most probably related to increased water inflow into the landslide body due to snow melting. Although the spring and summer brought quite frequent and intense rainfalls, neither of these events triggered a comparable acceleration to that of event 1. Consequently, from the data available from the survey period, we could either conclude that the landslide finally mostly stabilised after event 4, or that pre-loading of the mass by snow melting prior to rainfalls is necessary for the triggering of this slide. Only a longer survey period could decide between those possibilities. However the monitoring device had to be removed due to remediation measures at the location of the system.

DMS GSA02A-010-1210: North displacement - Cumulative Report

Contractor: Geological Survey of Austria
 Site: Ampflwang - KB1
 Project: 11MT+1IUT30+8IT
 Monitoring interval: 0-9mbgl
 Installation date: 03/12/2010
 Calibration date: 06/12/2010 08.44
 Data alignment: 07 December 2010 01:00
 Notes: Borehole depth = 12m
 Inclometric pipe $\varnothing = 60\text{mm}$

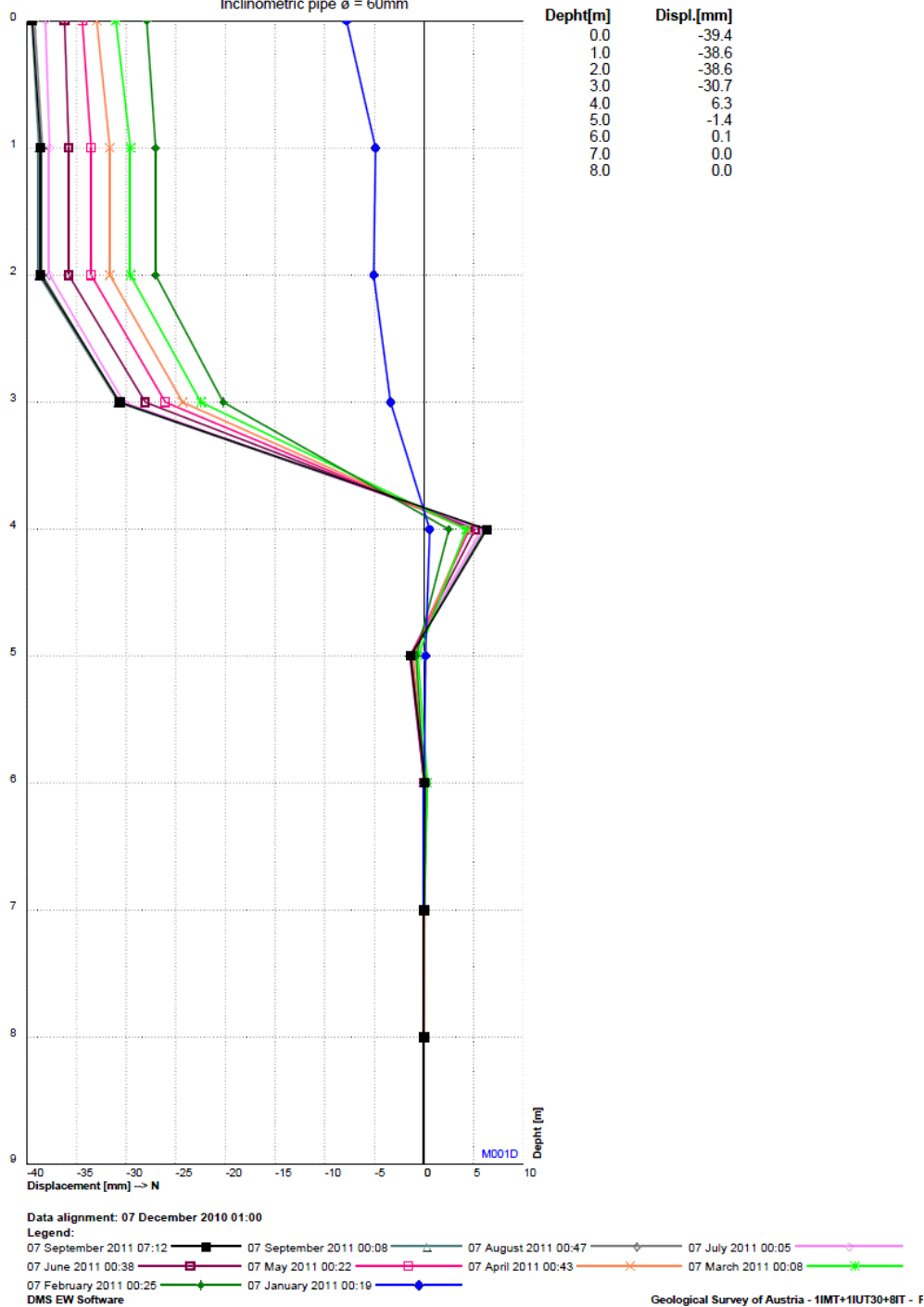


Figure 4.2-4. Inclinometric record of cumulative displacement along the N-S plane in the DMS borehole at the Ampflwang site registered from December 2010 to September 2011.

DMS GSA02A-010-1210: Polar diagram - Cumulative Report

Contractor: Geological Survey of Austria
 Site: Ampflwang - KB1
 Project: 1IMT+1IUT30+8IT
 Monitoring interval: 0-9mbgl
 Installation date: 03/12/2010
 Calibration date: 06/12/2010 08.44
 Data alignment: 07 December 2010 01:00
 Notes: Borehole depth = 12m
 Inclinometric pipe \varnothing = 60mm

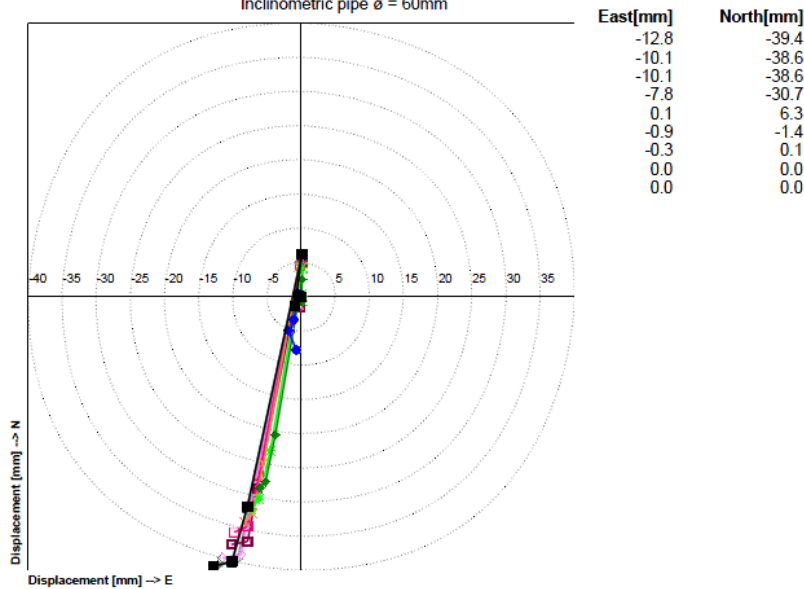


Figure 4.2-5: Polar diagram of the inclinometric record of cumulative displacement in the DMS column below the building at the Ampflwang site registered from December 2010 to September 2011.

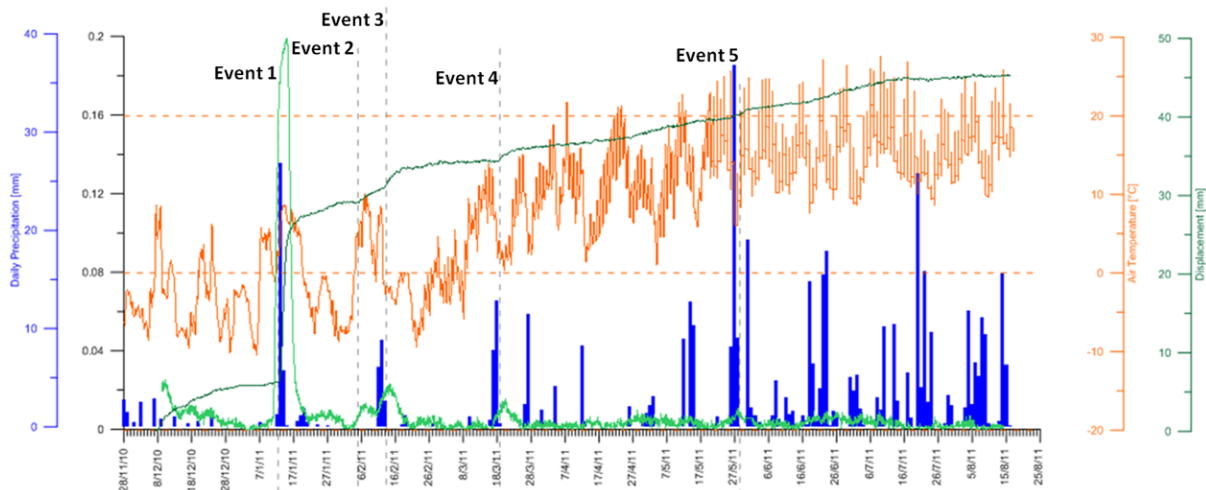


Figure 4.2-6. Graph of cumulative displacement (dark green), compared to total daily precipitation (blue, courtesy of the Central Institute for Meteorology and Geodynamics (ZAMG)), to calculate acceleration (wood green, absolute value [mm/h²]), and air temperature (orange) registered at the Ampflwang site between December 2010 to September 2011.

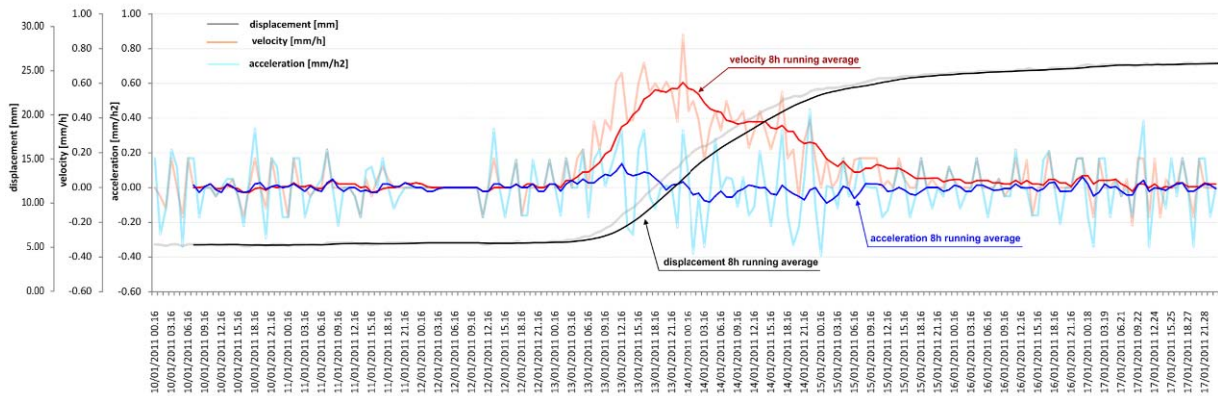


Figure 4.2-7. The “January 2011 event”: Graph of cumulative displacement, velocity and acceleration from hourly DMS measurements (transparent colours) and their eight-hour running averages (in full colour).

4.2.3.2 Soil temperature

Figure 4.2-8 shows the results of temperature monitoring at different depths. The results show no relevance to the movement of the landslide below the depth of 1 m. Only seasonal variations can be recognised. The minimum temperature can be detected in early March at a depth of 1 m and is delayed to mid-July at a depth of 7 m. However no anomalous events can be identified. In any case, recording of temperature variations is important for the interpretation of resistivity measurements since they depend significantly on that value. The available results from this test site suggest that for depths below 4-5 meters the influence of temperature on resistivity is negligible.

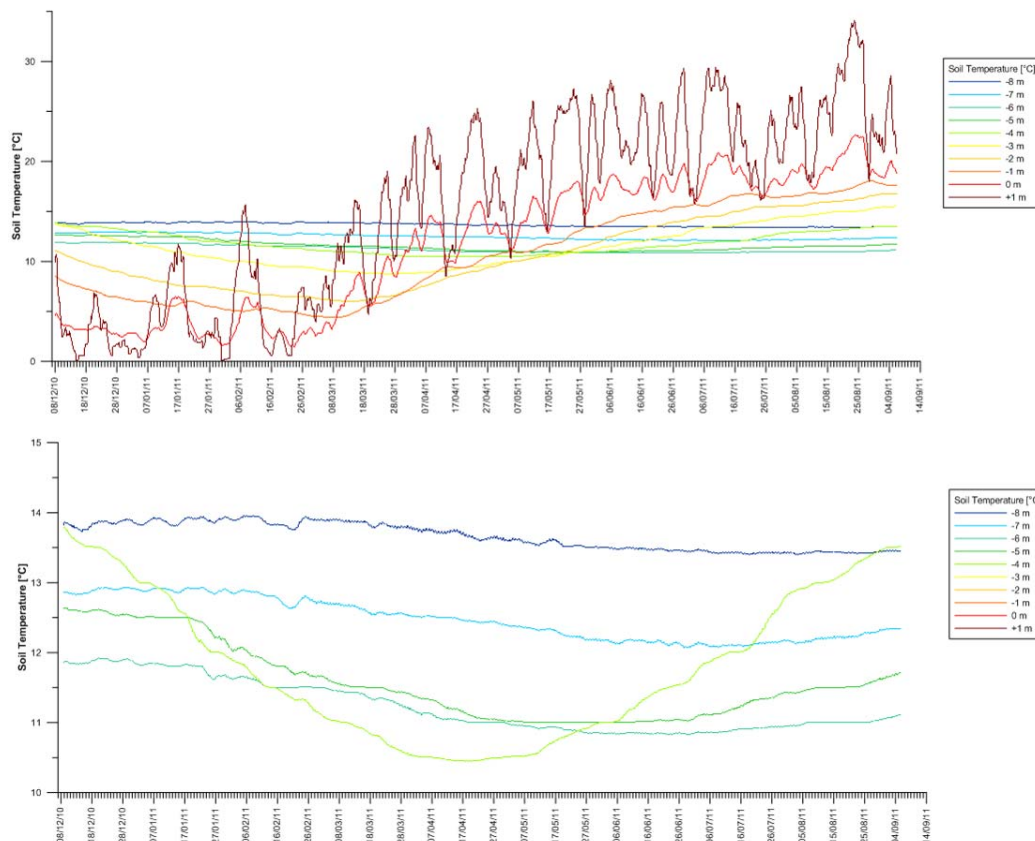


Figure 4.2-8. Measurements of temperature at different depths measured inside the DMS column, upper graph showing all depths and lower graph only displaying results from deeper levels (different scales for better resolution used)

4.2.3.3 Resistivity

Resistivity measurements were performed along one profile close to the DMS column 2. One set of data comprising around 4000 gradient-type measurements was taken every four hours. For the power supply, a connection to the local power grid was installed. The data was sent every day to the GSA office, where the results were checked for quality and time sequences of apparent resistivity and inversions were automatically generated each day. Figure 4.2-9 shows the display of all performed measurements for the entire survey period. This general plot is used to observe the performance of the system and to detect general tendencies and dependencies on precipitation (plotted at the left side of the Figure 4.2-9). Colours indicate normalised variations to the starting value of apparent resistivity. It very clearly indicates a general decrease of resistivity reflected in almost all measurements after major rain events. In displacement events 1 and 3, a decrease of resistivity can be recognised even some time before the rainfall event, most probably due to increased water infiltration because of snowmelt and/or thawing of the top soil layers. Additionally, seasonal variations (increase of resistivity in spring and decrease of resistivity in summer) can clearly be observed.

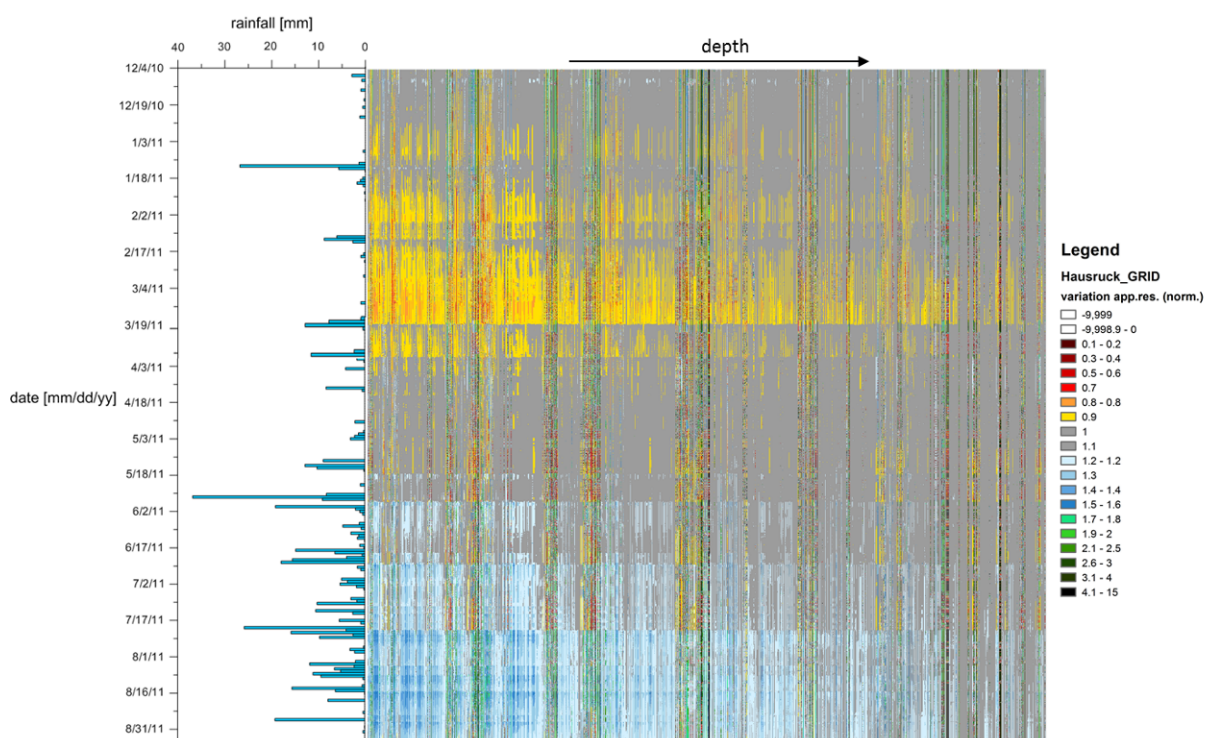


Figure 4.2-9. Display of all performed measurements for the entire survey period; colours indicate normalised variations to the starting value of apparent resistivity.

Figure 4.2-10 shows the time series of selected apparent resistivity values in correlation with precipitation and displacement whereas Figure 4.2-11 gives a close up look at the winter and spring period, during which all major displacement events took place. From these figures it is obvious that most of the major rain events were accompanied by a resistivity decrease. To investigate the dependencies in more detail, we will focus on the data from selected periods. Figure 4.2-12 and Figure 4.2-13 show details of the period of the major displacement event that took place on January 13th 2011. Resistivity values already start to decrease around

January 8th, most probably due to additional inflow of water from snow melting. This trend continues until a first short rainfall on January 12th after which the decrease accelerated. Following the start of an intense rainfall after midnight on January 12th, apparent resistivity decreased further until around 4 o'clock when the landslide started to move again with increased speed. At around 16 o'clock, after the main acceleration phase, resistivity started to increase rapidly although precipitation continued with less intensity for almost one day.

Data from events 2 and 3 in February (Figure 4.2-14 and Figure 4.2-15) show quite similar behaviour. Resistivity started to decrease in the afternoon of February 4th and 5th, thus starting to speed up the landslide on the 5th without any influence from the rainfall. Again, the reason could be snow melting. The resistivity decrease took place before and during the acceleration phase. During the period of constant (but increased) speed of the landslide, resistivity also became constant on an average until after the first rainfall took place in the morning of February 11th. Interestingly, during the first hours of rainfall on the 12th the landslide slowed down, indicated also by a short increase of resistivity. After that, resistivity started to decrease significantly until 14 o'clock when the landslide started to speed up again. During the acceleration phase, resistivity values became almost constant and started to increase again after the major acceleration phase on February 13th.

Figure 4.2-16 and Figure 4.2-17 show the results from event 4 in March 2011. No additional influence from snow melting can be assumed for this period. However, apparent resistivity values started to decrease several days before the event on March 10th which eventually correlated with a small rainfall. A sharp decrease in resistivity started at 18 o'clock on the 17th for surface values, and at 6 o'clock on the 18th for deeper soil layers. The decrease continued until the acceleration of the landslide, when a smooth increase of resistivity started.

Figure 4.2-18 shows the time lapse inversion results of the resistivity data measured between the 11th and 16th of January. For reference, compare the results with Figure 4.2-13. Hardly any resistivity change took place until 4 o'clock in the morning of January 12th. Until 8 o'clock on the same day, however, a very local resistivity decrease could be determined around profile distances 18 and 30 which disappeared again until intense precipitation started after midnight. The results at 4 o'clock in the morning of the 13th show a general decrease of resistivity in the very shallow part of the subsurface. The wetting front successively penetrated to greater depths until 16 o'clock (to the depth of the sliding plain at four meters, as determined by the DMS system) and the largest decrease of resistivity was reached. This period of maximum decrease in resistivity very well correlates with the period of maximum acceleration of the landslide. After that the subsurface resistivity increased again until 4 o'clock on the 14th, when only an isolated anomaly was left, eventually correlating with the position of a drainage pipe. Also, in that period the speed of the landslide first decreased smoothly and then rapidly after the morning of the 15th. However, this final rapid decrease of speed was not visible in the resistivity data.

Based on the results described above, we can conclude that decreasing values in the time series of apparent resistivity definitely correlate with the penetration of wetting fronts into the subsurface due to rainfall or snowmelt events. However, no information could be derived about landslide movements triggered by rainfalls, since no acceleration event was monitored in the late spring and summer when even more intense rainfalls took place. The reason could be that the landslide generally stabilised during that period. Further facts to understand this behaviour could only be derived if the monitoring were to continue for another year, which in this case is not possible.

In any case, it can be concluded that resistivity monitoring can help to map the subsurface processes that accompany the triggering of a landslide. Thus resistivity monitoring very efficiently supplements automatic displacement measurements (which provide only point information) by providing additional facts about ongoing subsurface processes, and therefore it could support decision-making nicely in the case of emergencies. Finally, one observation must be made which may bring about ideas for better interpretation in future; in the above case, movements were only triggered during periods of general resistivity increases (correlated with a temperature decrease equal to thawing between low temperature periods). In the spring and summer when resistivity showed a general decreasing trend, no movements were triggered.

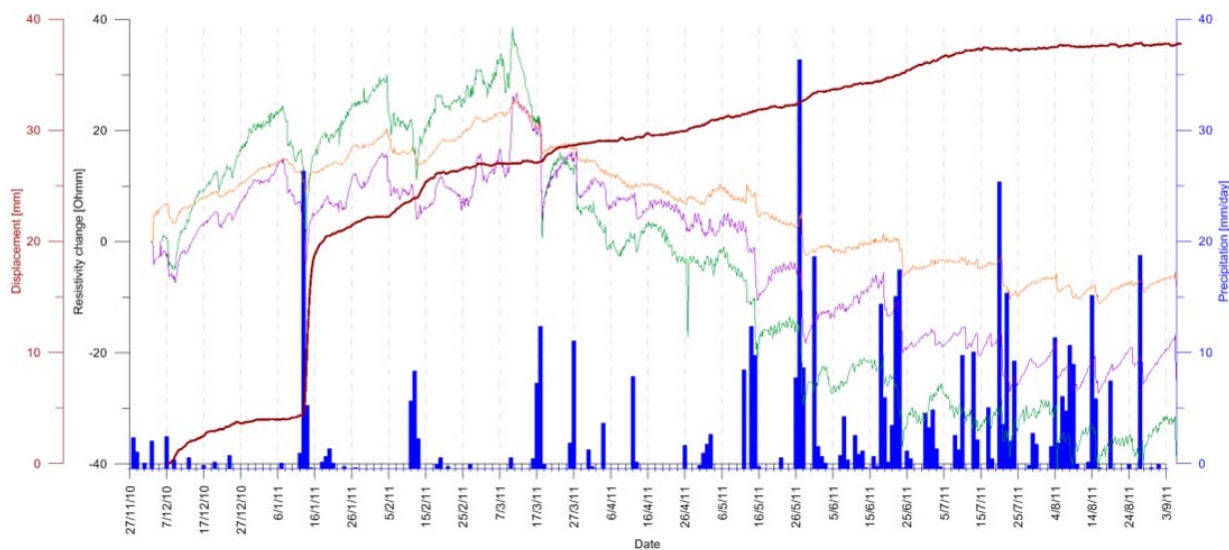


Figure 4.2-10. Display of displacement (red), precipitation (blue; courtesy of the Central Institute for Meteorology and Geodynamics (ZAMG)) and apparent resistivity at different relative apparent depths (green: 1 m; purple: 2 m; orange: 4 m) for the whole survey period.

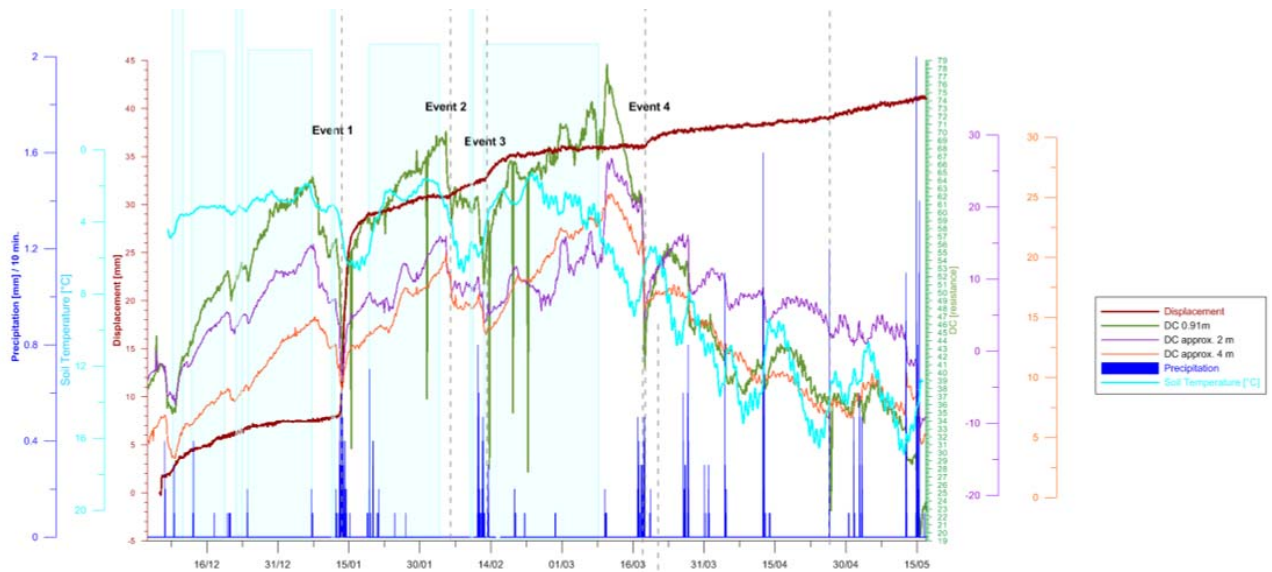


Figure 4.2-11. Display of displacement (red), precipitation (blue; courtesy of the Central Institute for Meteorology and Geodynamics (ZAMG)) and apparent resistivity at different relative apparent depths (green: 1 m; purple: 2 m; orange: 4 m) in the winter/spring period.

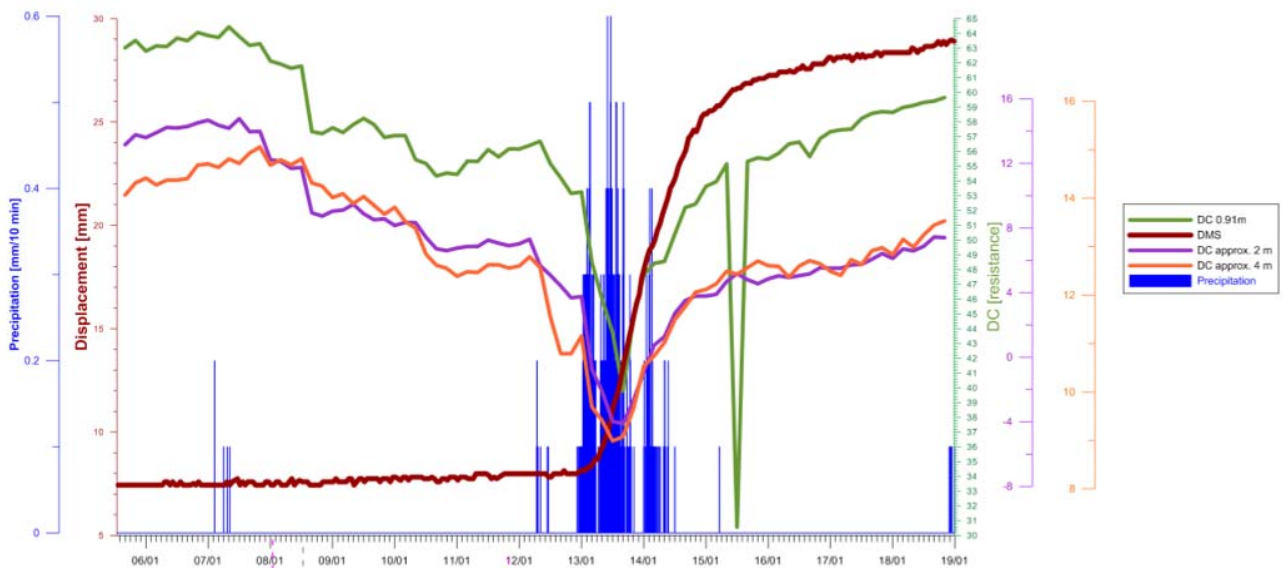


Figure 4.2-12. Display of displacement (red), precipitation (blue; courtesy of the Central Institute for Meteorology and Geodynamics (ZAMG)) and apparent resistivity at different relative apparent depths (green: 1 m; purple: 2 m; orange: 4 m) for the time around the major displacement event (event 1) in January 2011.

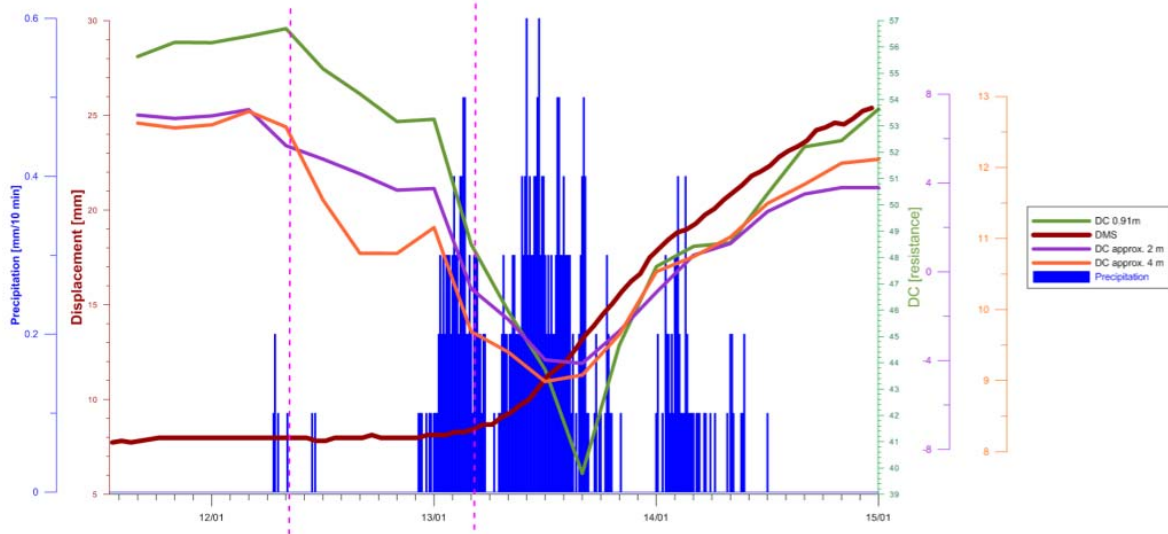


Figure 4.2-13. Display of displacement (red), precipitation (blue; courtesy of the Central Institute for Meteorology and Geodynamics (ZAMG)) and apparent resistivity at different relative apparent depths (green: 1 m; purple: 2 m; orange: 4 m) for the time around the major displacement event (event 1) in January 2011; close-up detail of the major event.

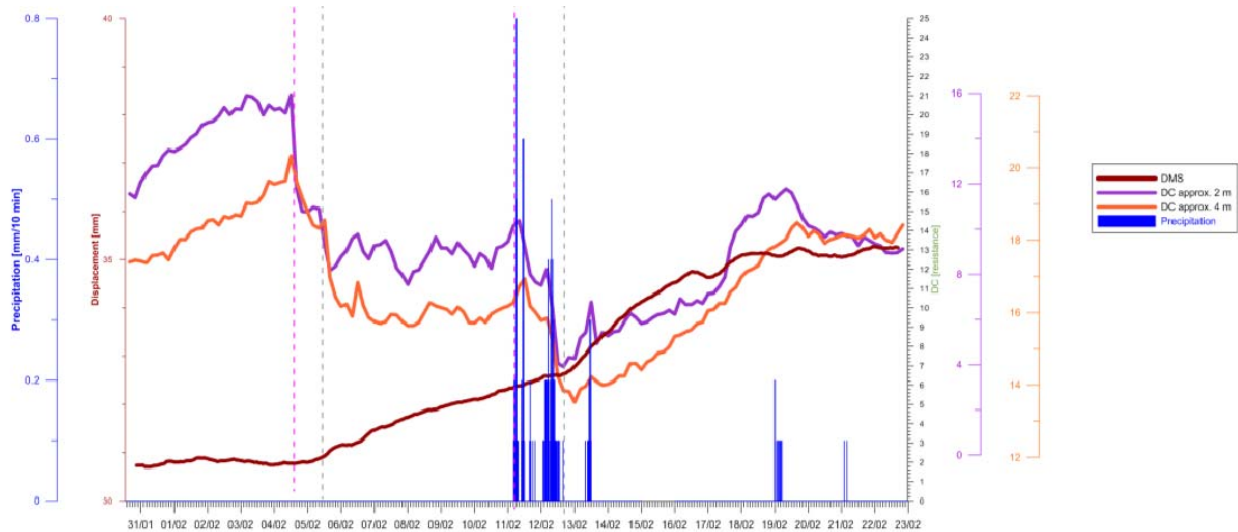


Figure 4.2-14. Display of displacement (red), precipitation (blue; courtesy of the Central Institute for Meteorology and Geodynamics (ZAMG)) and apparent resistivity at different relative apparent depths (green: 1 m; purple: 2 m; orange: 4 m) for the time around event 2 and 3 in February 2011.

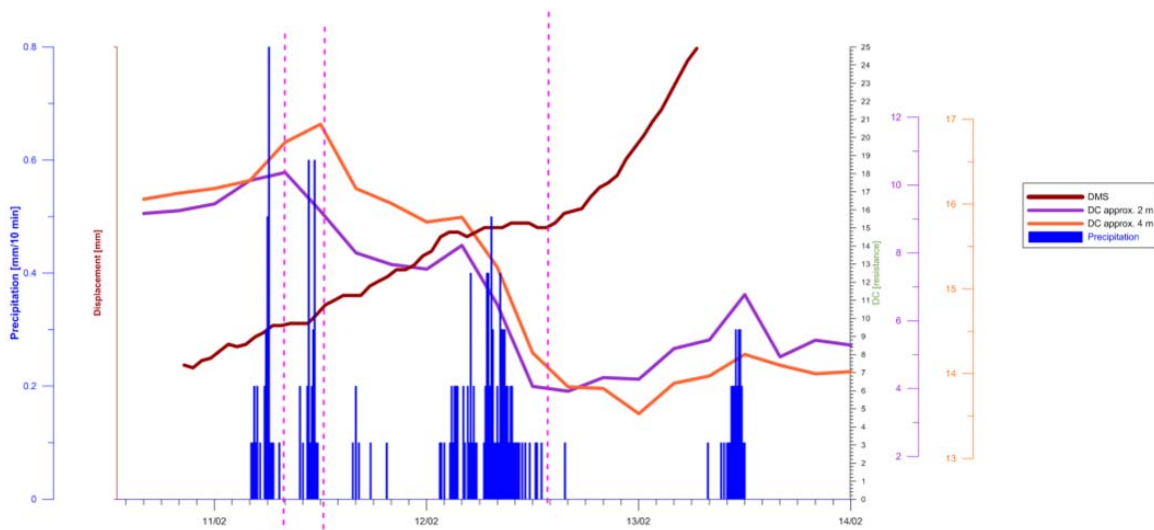


Figure 4.2-15. Display of displacement (red), precipitation (blue; courtesy of the Central Institute for Meteorology and Geodynamics (ZAMG)) and apparent resistivity at different relative apparent depths (green: 1 m; purple: 2 m; orange: 4 m) for the time around event 3 in February 2011; close-up detail.

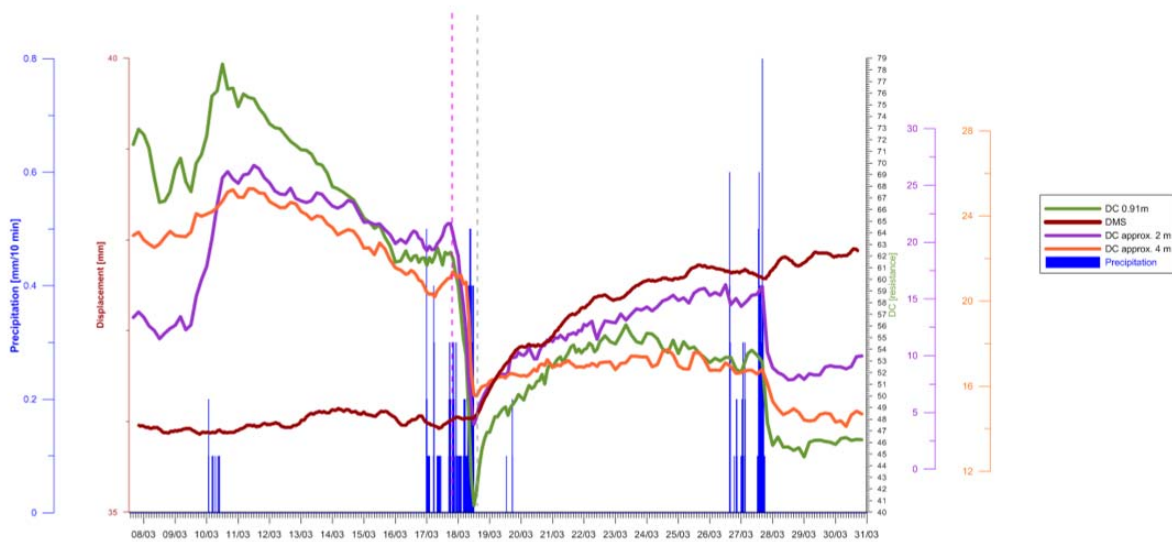


Figure 4.2-16. Display of displacement (red), precipitation (blue; courtesy of the Central Institute for Meteorology and Geodynamics (ZAMG)) and apparent resistivity at different relative apparent depths (green: 1 m; purple: 2 m; orange: 4 m) for the time around event 4 in March 2011.

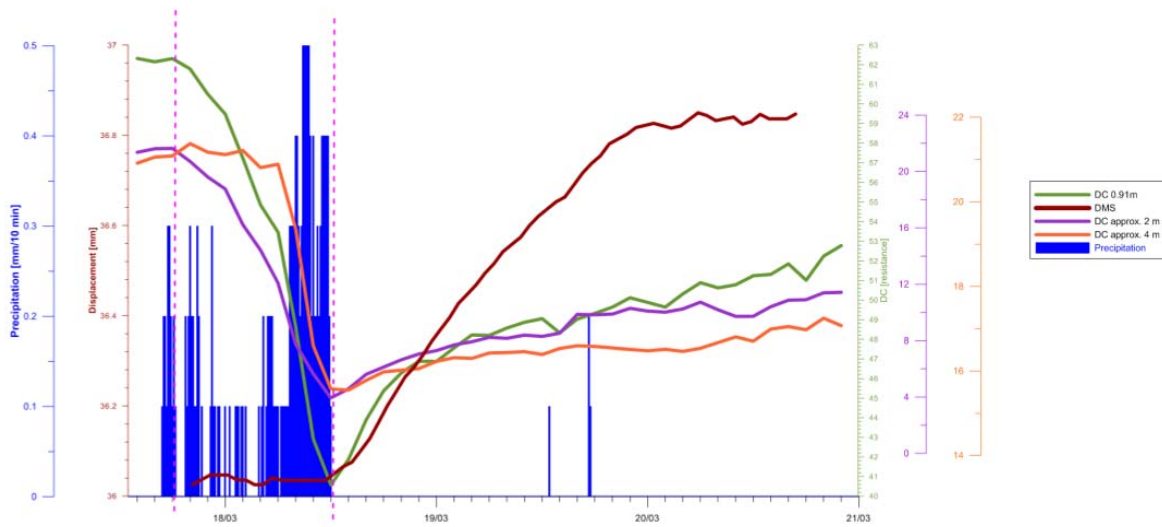
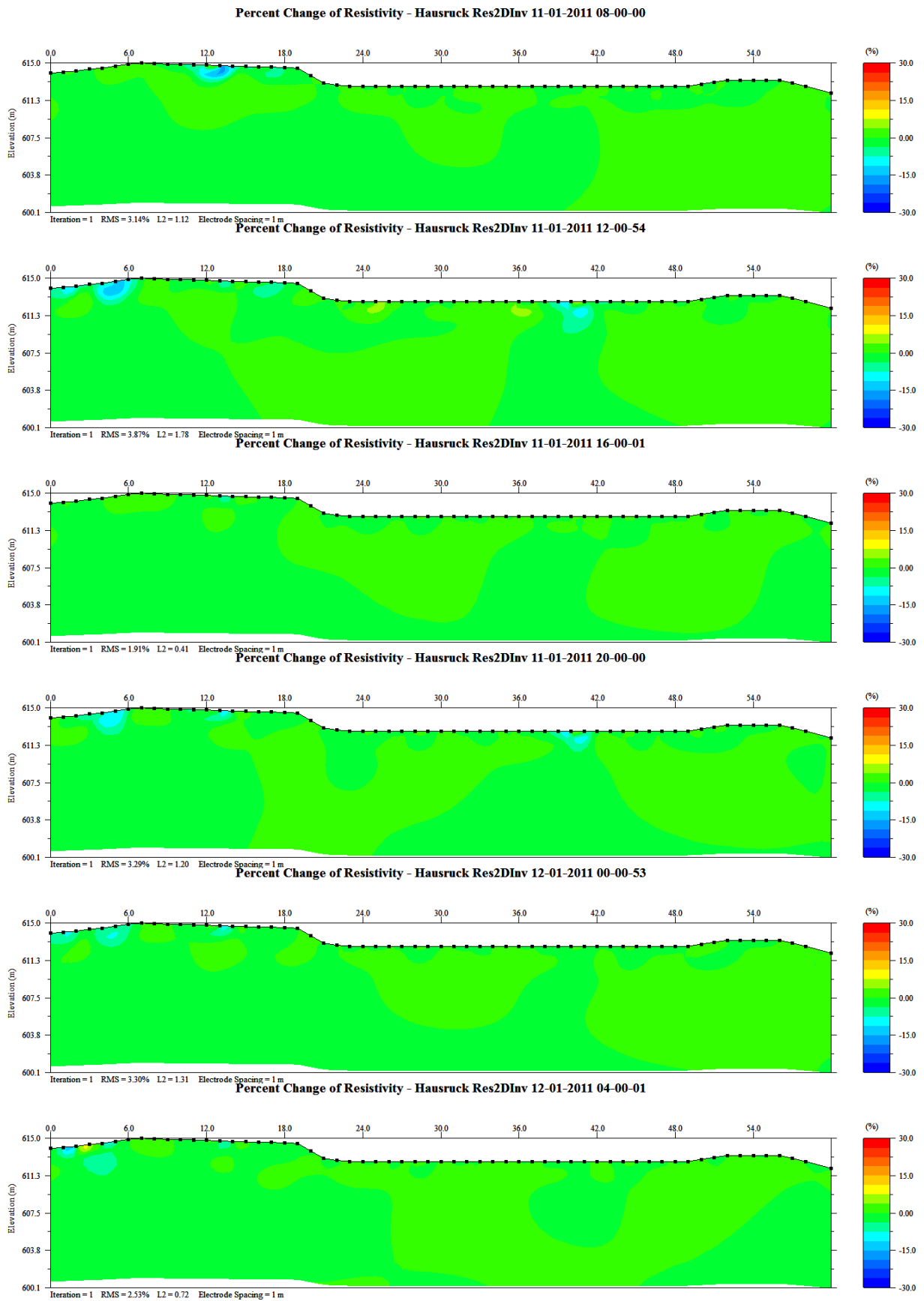
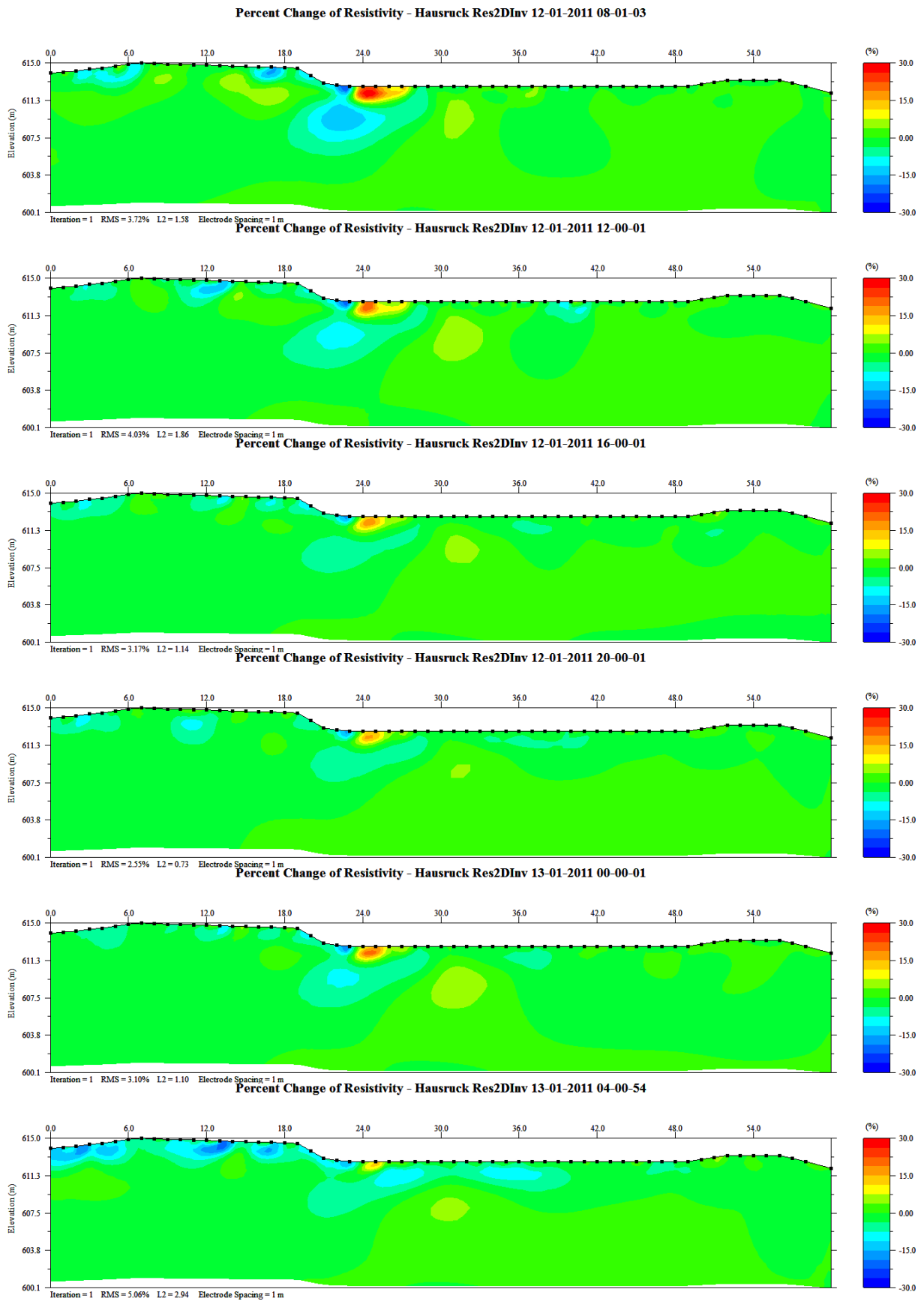
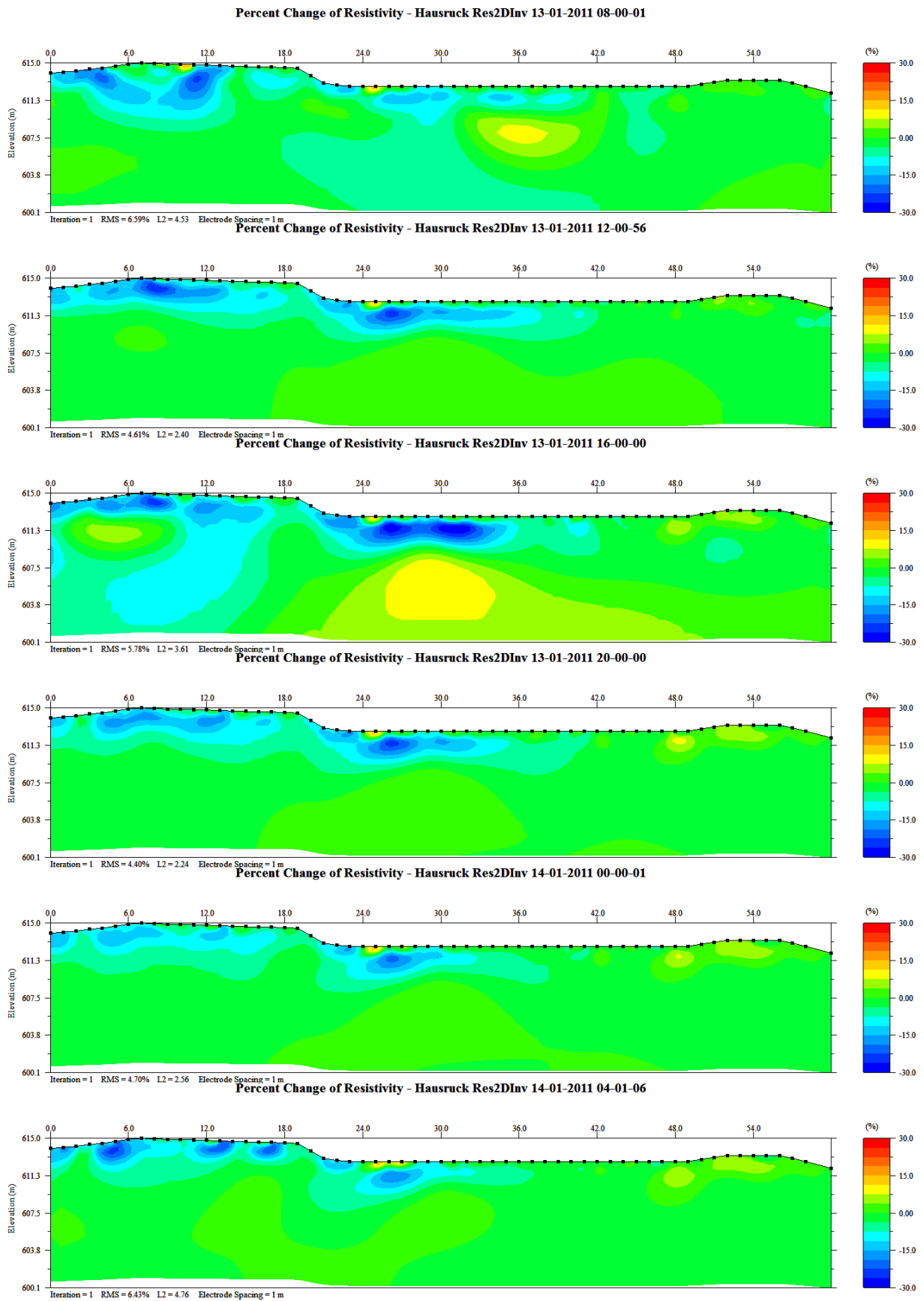
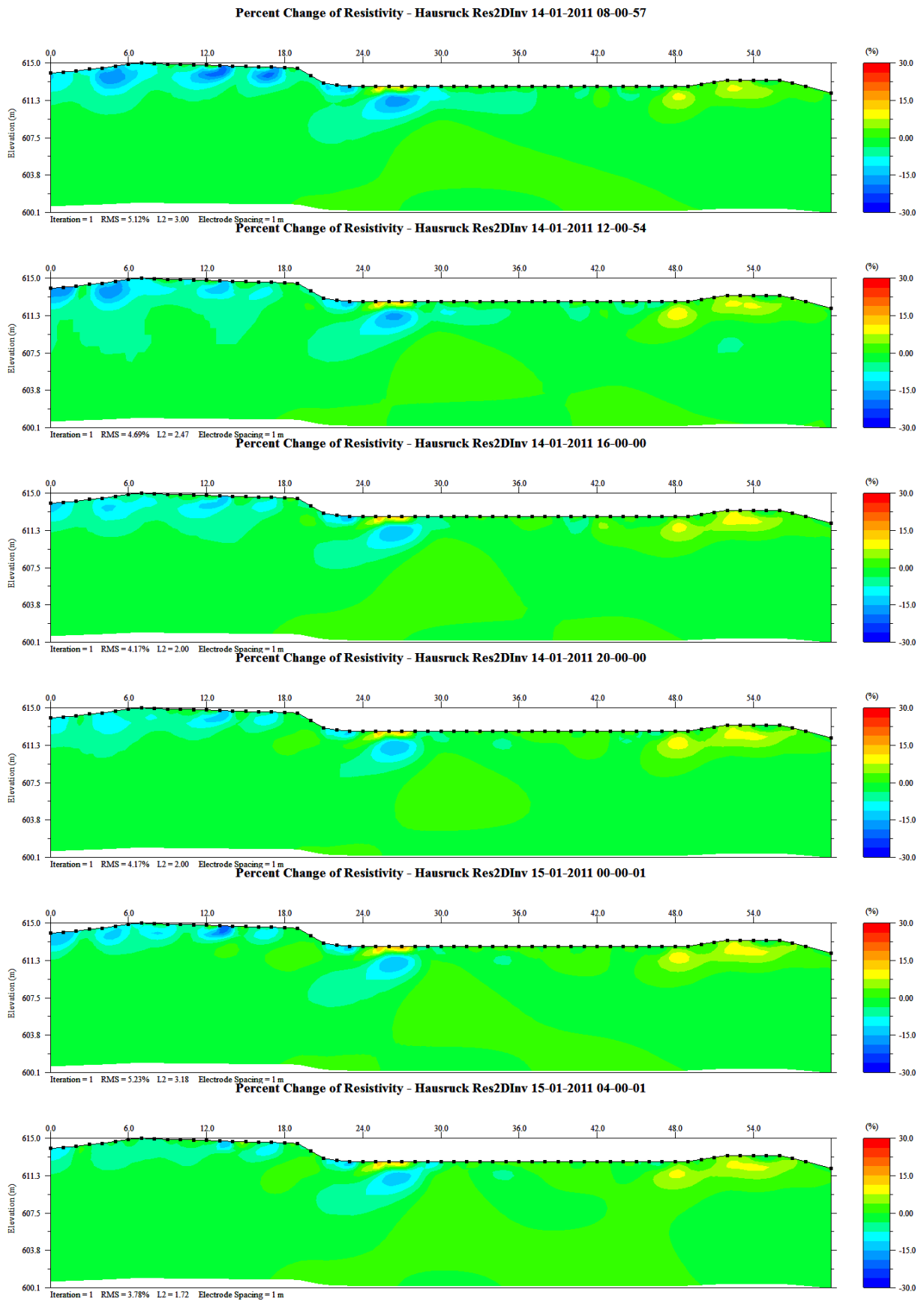


Figure 4.2-17. Display of displacement (red), precipitation (blue; courtesy of the Central Institute for Meteorology and Geodynamics (ZAMG)) and apparent resistivity at different relative apparent depths (green: 1 m; purple: 2 m; orange: 4 m) for the time around event 3 in March 2011; close-up detail.









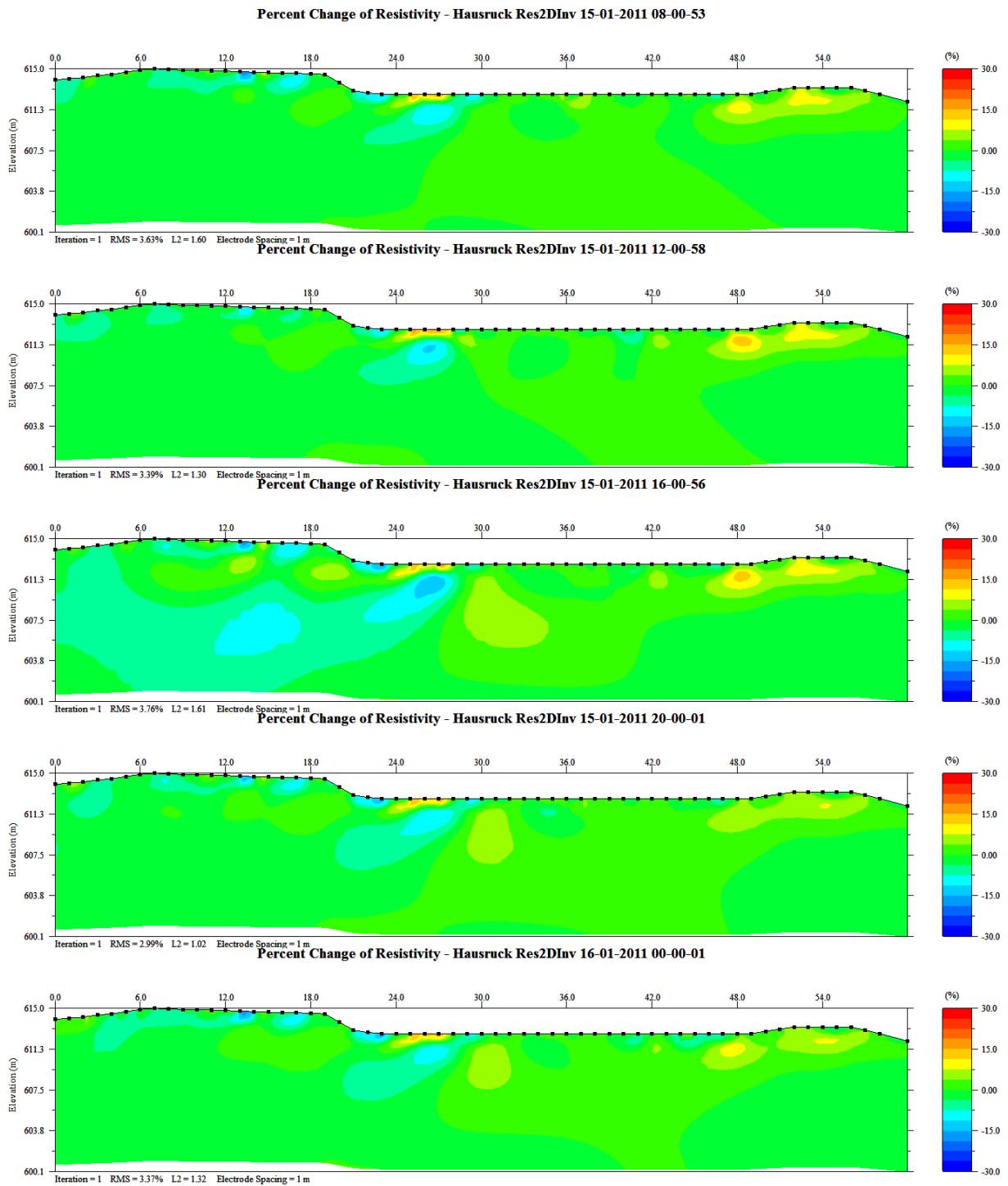


Figure 4.2-18. Time lapse inversion result of resistivity measurements for the period between January 11th and 16th. Resistivity changes are calculated to a reference measurement on January 11th at 4 o'clock.

4.2.3.4 Self-potential

Figure 4.2-19 shows the results of a selected self-potential time series over the whole survey period. It shows a quite obvious correlation of SP anomalies with rainfall events until the end of May 2011. After that period the correlation could no longer be detected. Moreover, the major displacement event in January is correlated with a very large SP event, which is more than five times larger than every other anomaly. Figure 4.2-20 shows the results of that period in more detail. The sharp decrease of SP in the morning of January 12th exactly correlates with the appearance of the resistivity decrease that is an isolated anomaly, visible in the inversion results after January 12th at 8 o'clock (Figure 4.2-18) – almost one day before the triggering of the landslide.

Event 2 and 3 in February are both correlated with a small decrease in SP immediately before the triggering, which is accompanied by an increase in SP during the major acceleration phase (Figure 4.2-21). The results of event 4 (March, Figure 4.2-22) again show an increase in SP before triggering time.

To conclude, it is obvious that a major SP anomaly was correlated with the only significant triggering event. However this anomaly developed in correlation with a very local resistivity anomaly and could only be detected in that area. Since one of the drainage pipes is located close to this location, the SP as well as the resistivity anomaly might be correlated with an inflow of water along this drainage pipe.

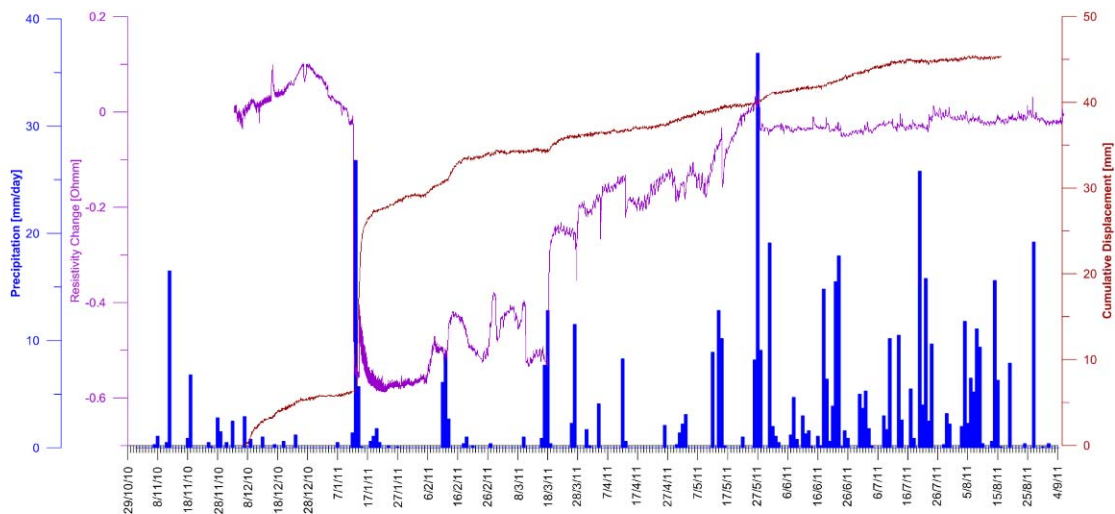


Figure 4.2-19. Results of inclinometric and self-potential monitoring and precipitation (courtesy of the Central Institute for Meteorology and Geodynamics (ZAMG)) for the whole survey period.

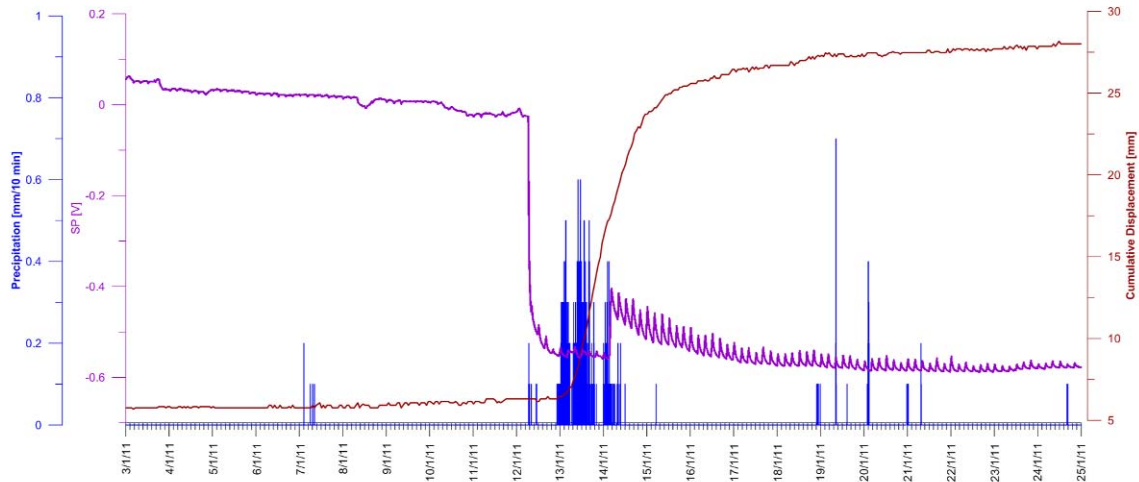


Figure 4.2-20. Results of inclinometric and self-potential monitoring and precipitation (courtesy of the Central Institute for Meteorology and Geodynamics (ZAMG)) for the event in January 2011.

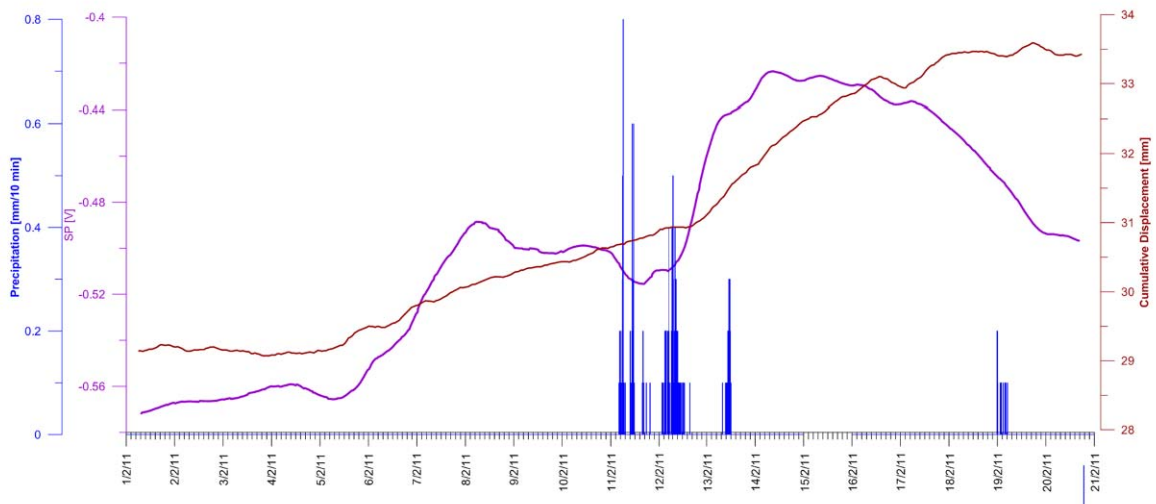


Figure 4.2-21. Results of inclinometric and self-potential monitoring and precipitation (courtesy of the Central Institute for Meteorology and Geodynamics (ZAMG)) for the event in February 2011.

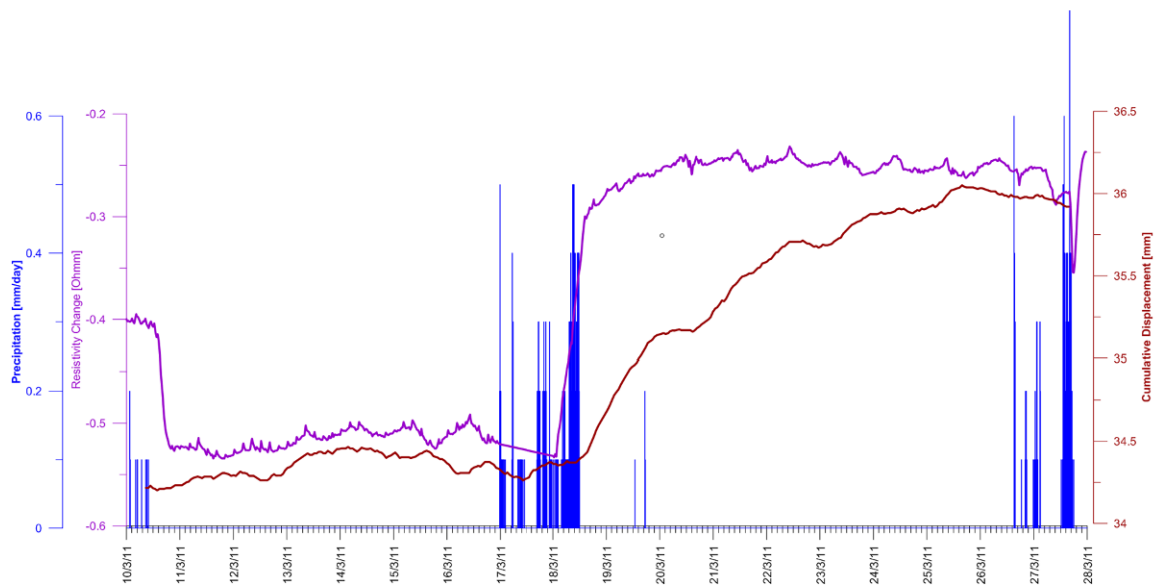


Figure 4.2-22. Results of inclinometric and self-potential monitoring and precipitation (courtesy of the Central Institute for Meteorology and Geodynamics (ZAMG)) for the event in March 2011.

4.2.4 END-USER INVOLVEMENT AND ALARM CHAIN

In this case, although automatic warning messages were sent to GSA personnel, only a manual communication by phone was set up with the owners of the house and the responsible civil engineering company as this monitoring was not set up for early warning purposes, but rather for scientific research and to plan future remediation measures in detail. However, this kind of alarm chain proved to be sufficient in this case. The end-user additionally supported GSA during the installation of the system, provided manually measured data (outflow of drainage system), and performed some maintenance tasks.

4.2.5 SUMMARIZED EVALUATION OF PARAMETERS

High-resolution displacement monitoring has proven to be an efficient way to monitor displacements and to issue early warnings. The results showed that the availability of at least hourly data is a necessity. However, to derive information about related triggering processes, correlation with other data is necessary. For this purpose, precipitation and resistivity monitoring proved to be supplementary and very efficient.

4.3 ANCONA (ITALY)

Robert Supper, Filippo Vecchiotti, Ivo Baroň, Birgit Jochum
Geological Survey of Austria

Mario Lovisolo
Centro Servizi di Geoingegneria, Italy

Stefano Cardellini
Municipality of Ancona, Italy

ABSTRACT

The Ancona site represents a large and deep landslide, which affected the city of Ancona on December 13th, 1982, ten years after a distinct earthquake in this area. The landslide occurred in the lower and middle Pliocene clays of the Tavernelle sincline. The early warning system and an Emergency Plan of the Ancona City were established in 2008 after a regional law was issued in 2002. The core of the monitoring system consists of seven Automatic Robotic Stations with 230 reflector points; 26 geodetic GPS; eight geodetic GPS (dual frequency); and seven high-precision clinometric sensors, complemented with the automated inclinometers, thermometers and piezometers of DMS in three boreholes up to 100 metres deep, and with the GEOMON^{4D} situated in the lower central portion of the landslide installed in April 14th, 2011. This report summarizes the analysis of the DMS, GEOMON^{4D}, and hydrological monitoring results from 2011 and 2012. In order to understand the link between rainfall, water table and displacements, an analysis on the delay time between them was performed. A major rainfall occurred from 27/02/2011 to 03/03/2011 with a cumulative precipitation of 161.8 mm. The groundwater level started to rise about 30 and 31 hours later, and a micro-reactivation occurred about one month later in the depth of 67-68 m b.g.l., and about 2.7 months later in the depth of 91 to 92 m b.g.l. The latest displacement event could be delayed after the rainfall event due to greater volume of the mass, or caused by settlement. The study of geoelectric parameters was significantly influenced by external noise and the analysis of this effect is presented.

Presented parameters: displacement, velocity, groundwater level, precipitation, resistivity, self-potential.

4.3.1 GENERAL DESCRIPTION OF THE TEST SITE

The Ancona site represents a large and deep landslide, which affected the city of Ancona located on the east coast of the Adriatic Sea on December 13th, 1982 (Cardellini and Osimani 2010). The northern part of the city at the Montagnolo Hill slid towards the sea (Figure 4.3-1). The 1982 landslide caused extensive damage to structures and infrastructure, such as the University Medical Faculty, the local hospital, main road, and the railway line running parallel to the coast (Anon, Cotecchia; both in Cotecchia 2006). About 3000 people were evacuated, gas and water supplies were interrupted and the city was without elementary services for days (Cardellini and Osimani 2010).

Geological and geomorphic settings

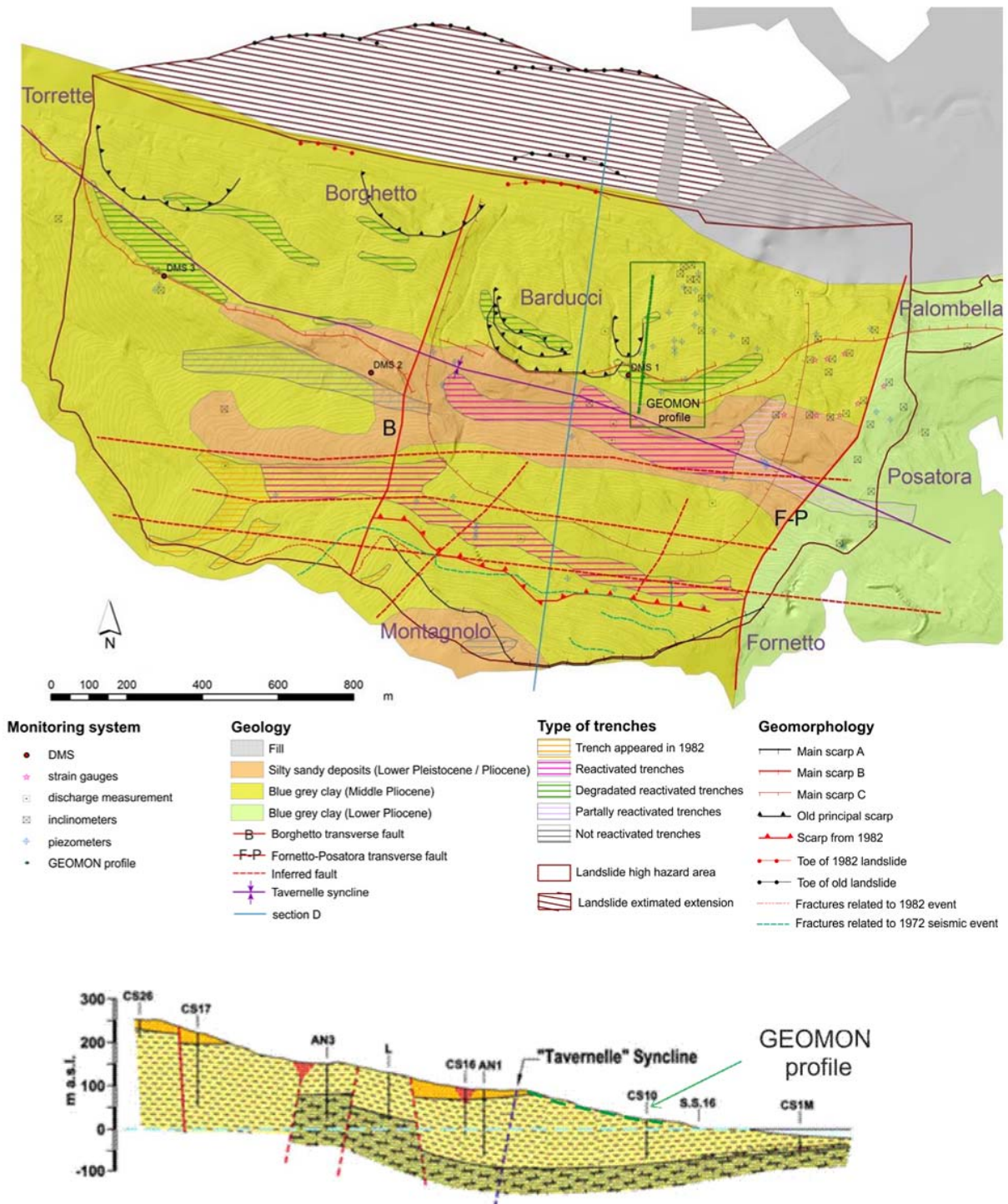
The town of Ancona is situated between two major geological structures: the Tavernelle sincline and the Conero anticline, both related to the tectonic compressive evolution of the Adriatic Foredeep. The NE-SW transverse faults (Borghetto and Posatora faults) and the EW normal faults with an anti-Appennine strike have been activated since the lower Pleistocene.

These faults form the contact between the lower and middle Pliocene clays (Cotecchia 2006) in Ancona.



Figure 4.3-1. General view of the Ancona monitoring site.

The area is tectonically active and it has been affected by several earthquakes since 1972. In particular, the earthquake of June 14th 1972 caused deep jointing of the clayey rock; natural trenches originated on the north slopes of the Montagnolo Hill (Cotecchia 2006). The joints and trenches were probably the main factor in subsequent water infiltration and sinking to deep parts of the host clayey rock, and thus could be considered the main controlling factor of the landslide event that occurred 10 years later.



Characterization of the site

The 1982 landslide involved about 180 million m³ of Lower and Middle Pliocene homogenous and well-stratified marly clays and clayey marls with a high silt content, and rarely with the presence of thin sandy beds, and covered an estimated area of $2.2 \cdot 10^4$ m² (Cotecchia 2006) in a slightly elliptical shape (Figure 4.3-3). It is a rotational-translational very deep-seated landslide with the maximum depth of the sliding zone down to 120 m b.g.l. (Cotecchia 2006). The head scarp of the entire original slope failure is about 80 m high. The upper part of the landslide body is comprised of several blocks separated by trenches and scarps. The lower part of the body is relatively steep and it was affected by subsequent rotational landslides. The landslide toe is not distinct because it is situated below the level of the Adriatic Sea.

Description of the history of the mass movement

The first records of cracks and jointing occurrence were recorded in 1773, in the area of the future landslide. Another documented event happened in 1858, when a landslide occurred in the eastern portion of the future landslide. In 1919, both the Montagnolo Hill and the Barducci superficial slides were seen to share a common deep-seated sliding surface (Crescenti et al. 1983).

On June 14th, 1972 at 18:55 p.m. (GMT), the city of Ancona was hit by a particularly strong earthquake (magnitude $M = 4.7$) with a focal depth of 15 km (UNESCO 1974). As a direct consequence of the earthquake, a deep-seated jointing and bedrock separation into blocks occurred in a major portion of the future landslide area.

On December 13th, 1982 the stronger event took place. The main triggering factor was a period of six days of uninterrupted rainfall.

In 2000, the geological and geotechnical surveys related to the landslide concluded that the most effective solution for slope remediation would be a massive consolidation of the slope. However, the consolidation was considered not feasible because of the relevant environmental impact and high costs (Cardellini and Osimani 2010).

Aiming at reducing the risk for inhabitants, the local authority of the Marche Region carried out a series of alternative remedial works consisting of bulkhead reinforcement and a superficial and subsurface drainage system. The authority made a special law for the people still living in the landslide area, giving the local administration the responsibility of creating an early warning system and an emergency plan.

In early March 2011, a heavy rainfall event occurred over several days in the whole Marche Region. A landslide isolated 20 families in the local village of Sappanico near Ancona, and another slide invaded the local road from Ancona to Portonovo, resulting in its closure (Boccanera et al. 2011). The local meteorological station of Ancona registered a cumulative rainfall of 161.8 mm in about five days (between February 27th and March 3rd). Since the DMS columns are multi-parametric, it was possible to compare the rise of the water table with the micromovements registered in depth. In column DMS 1 a delay of 30 hours was calculated between the start of the rainfall and the water table's rise to 4 m. Finally a micromovement of 5 mm occurred a month later (between March 29th and April 5th) at 67-68 m b.g.l. The same happened on column DMS 2, where the water table's rise (of 2.5 m) occurred 31 hours after the rainfall event, and three displacement events of about 5-7 mm were registered a month later (from February 26th until March 4th) at 80-81 m, 61-63 m and 36-37 b.g.l. This data

allow the implementation of a forecasting model and the evaluation of the hazard level in function of a multi-parametric instrument like the DMS.

4.3.2 DESIGN OF THE MONITORING NETWORK

The early warning system and the Emergency Plan of the Ancona City were established in 2008. The core of the monitoring system consists of seven Automatic Robotic Stations; 230 reflector points (installed in part on the 64 inhabited houses and on the structures and infrastructures); 26 geodetic GPS; eight geodetic GPS (dual frequency); and seven high-precision clinometric sensors, complemented with the automated inclinometers, thermometers and piezometers of DMS (Differential Monitoring of Stability; patent and trademark CSG-Italy) that have been installed inside three boreholes up to 100 m deep (Cardellini and Osimani 2010, 2011).

The geoelectric monitoring system was installed on April 14th, 2011 (Figure 4.3-4/Figure 4.3-5). The electrode spacing of the S–N oriented profile is 4 m. The profile is measured five times a day, and the electrical self-potential (SP) is measured every hour. Electricity is provided by a 230V power cable. The profile was set up close to the DMS 1 installation site (Figure 4.3-3). Cables were dug at an approximate depth of 40 cm (Figure 4.3-5). The profile was planned to monitor variations in the hydrological conditions of the subsurface, since no major accelerations are expected on this site in near future. The inversion results of geoelectrical measurements collected along this profile using gradient configuration generally show very low resistivity values (below 25 Ohmm) (Figure 4.3-6). Only one anomalous region with a high resistivity of up to 150 Ohmm (most probable an artificial lateral fill) could be found, marking the edge of the steepest slope. Additional borehole inductivity measurements proved the existence of very low resistivity values down to a depth of 130 m. The borehole is located approximately 200 m aside from the geoelectrical profile around profile distance 212 (approximately 50 m a.s.l.). The log shows relatively high resistivity values (6-10 Ohmm) from the surface down to 40 m b.g.l. Below 65-70 and 75-85 m, values decrease to 4.5 Ohmm. Below 90 m, a successive increase up to 7 Ohmm was detected. A fluid conductivity log could not be measured since the sensor was too lightweight to enter the fluid-clay mixture in the hole. The logging results fully agree with the outcome of the geoelectric inversion, as they show few high values within the top layers and low values at the bottom. Based on the generally low resistivity values we can conclude that the majority of the volume monitored consists of clay layers with a variable content of sand. The lower resistivity values below 50 m might be due to the influence of saline water infiltrating from the sea. Due to the high clay content, groundwater flow will only be possible in more sandy layers along slipping plains. Therefore, resistivity variations on the monitoring profile are expected to be small. Assuming a background resistivity of the pore fluid (rainwater) of approximately 20 Ohmm, the impact of precipitation could result in a decrease of subsurface resistivity. At a certain depth the infiltration of seawater will be dominant, however no direct proof exists.



Figure 4.3-4. Location of the geoelectric monitoring in Ancona (Source of map: GoogleEarth).



Figure 4.3-5. Installation trench of the monitoring profile.

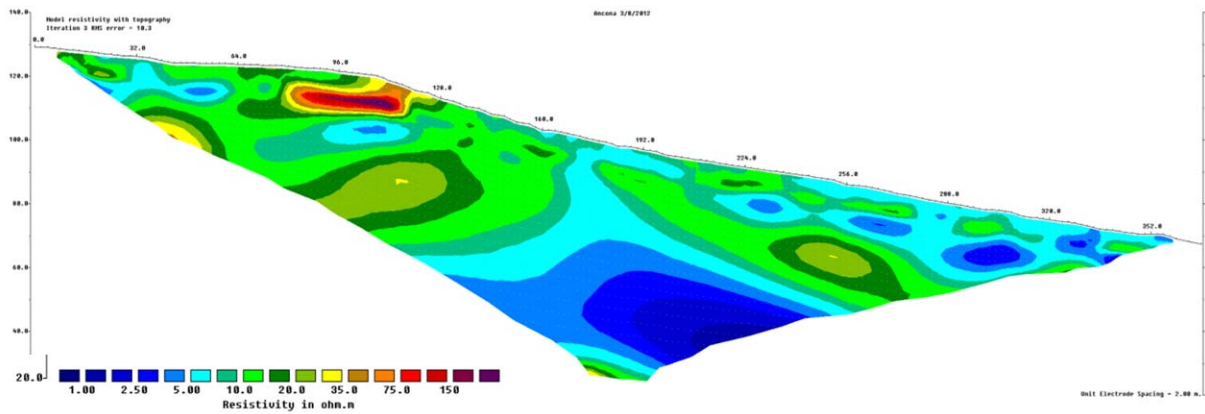


Figure 4.3-6. Results of geoelectrical inversion along the monitoring profile Ancona.

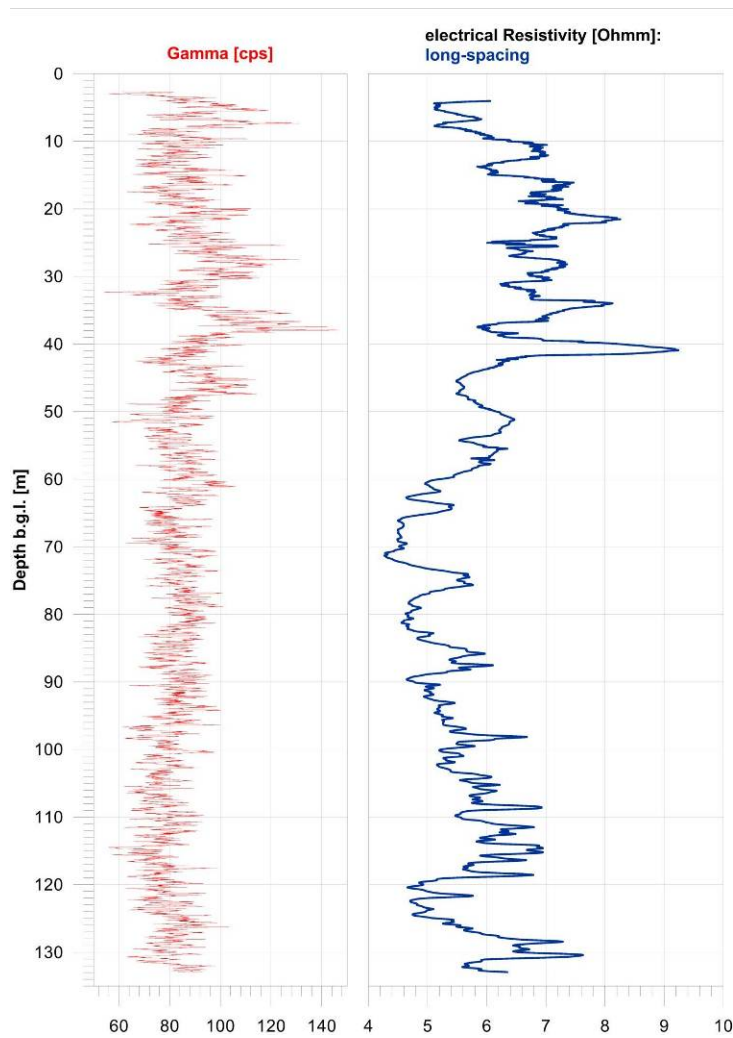


Figure 4.3-7. Results of borehole geophysical measurements: gamma log (red), inductivity log (blue), altitude of top of the hole: 50 m above sea level.

4.3.3 ANALYSIS OF MONITORING DATA

4.3.3.1 Displacement

In order to understand how rainfall, water table and displacements are linked, an analysis on the delay time was performed.

Analyzing rainfall events that occurred in Ancona and data from the DMS system, the delay time between the rainfall events, the rising of the water table level, and the beginning of micromovements were calculated.

The three largest rainfall events in Ancona since 2008 occurred at the following periods:

From 27/02/2011 at 17:00 to 03/03/2011 at 6:00 with a cumulative rainfall of 161.8 mm

From 27/09/2010 at 15:00 to 01/10/2011 at 9:00 with a cumulative rainfall of 134.1 mm

From 03/03/2008 at 10:00 to 08/03/2008 at 16:00 with a cumulative rainfall of 109.2 mm

For a detailed analysis, the first event, which happened in 2011, was chosen (Figure 4.3-8).

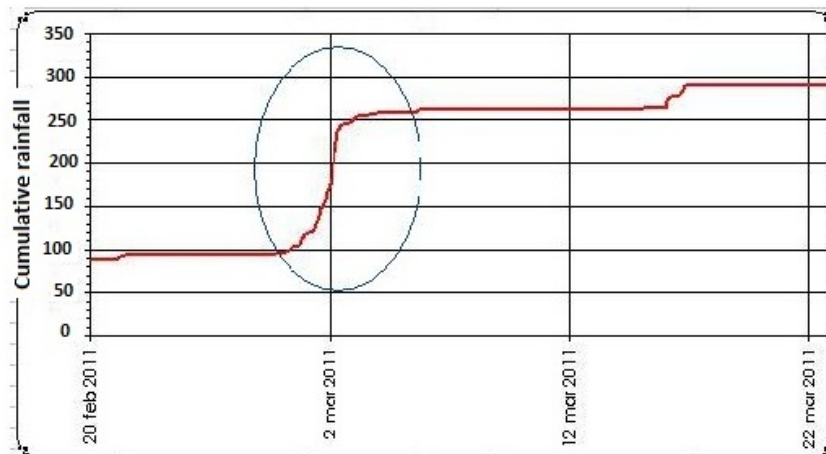


Figure 4.3-8. Cumulative rainfall in March 2011

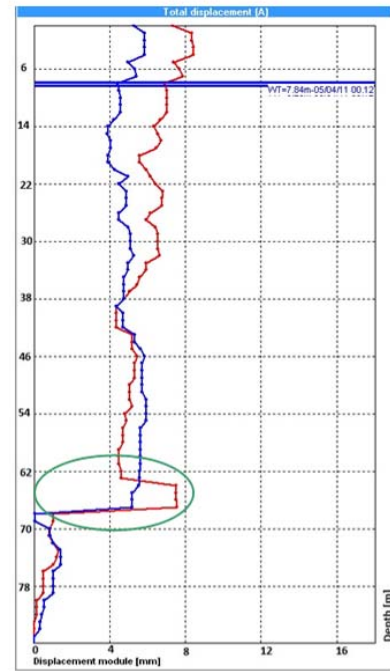
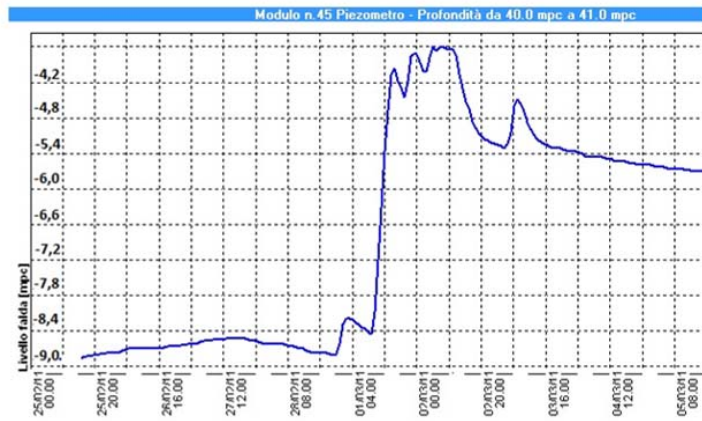
The delay time between the precipitation event and the rising of the water table was calculated from measurements from each of the three DMS columns, and it was evaluated whether there were displacements soon after the events.

For the first column, called **DMS Ancona1**, the water level started to rise on February 27th at 23:00, 30 hours after the onset of the precipitation event (Figure 4.3-9).

By aligning the column to February 27th (the starting date of the event), it was possible to detect some micro movements (Figure 4.3-9):

On module 18, depth 67-68 m, from 29/03/11 to 05/04/11, (blue line)

On module 22, depth 63-64 m, from 05/04/11 to 09/04/11, (red line)



DMS Ancona1_2011: Displacement - Module No.18
Period: 27/02/2011 - 16/04/2011
On axis (334° N)

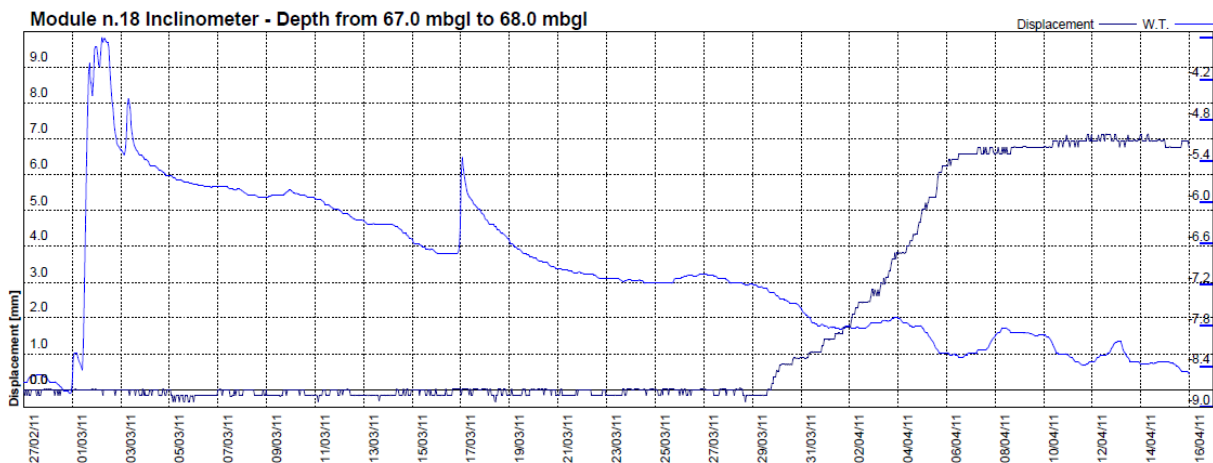


Figure 4.3-9. Water table level and total displacements of DMS_Ancona1

As such, it was possible to detect a triggering event between 63 and 68 m b.g.l., appearing one month after the start of the precipitation event.

On the second column, **Ancona2**, the water table level rose on March 1st at 00:00, 31 hours after the onset of the rainfall (Figure 4.3-10).

The column detected some micromovements occurring after that (Figure 4.3-10):

On module 14, depth 80-81 m, from 26/03/11 to 09/04/11

On module 32 and 33, depth 61-63 m, from 26/03/11 to 09/04/11

On module 58, depth 36-37 m, from 26/03/11 to 09/04/11

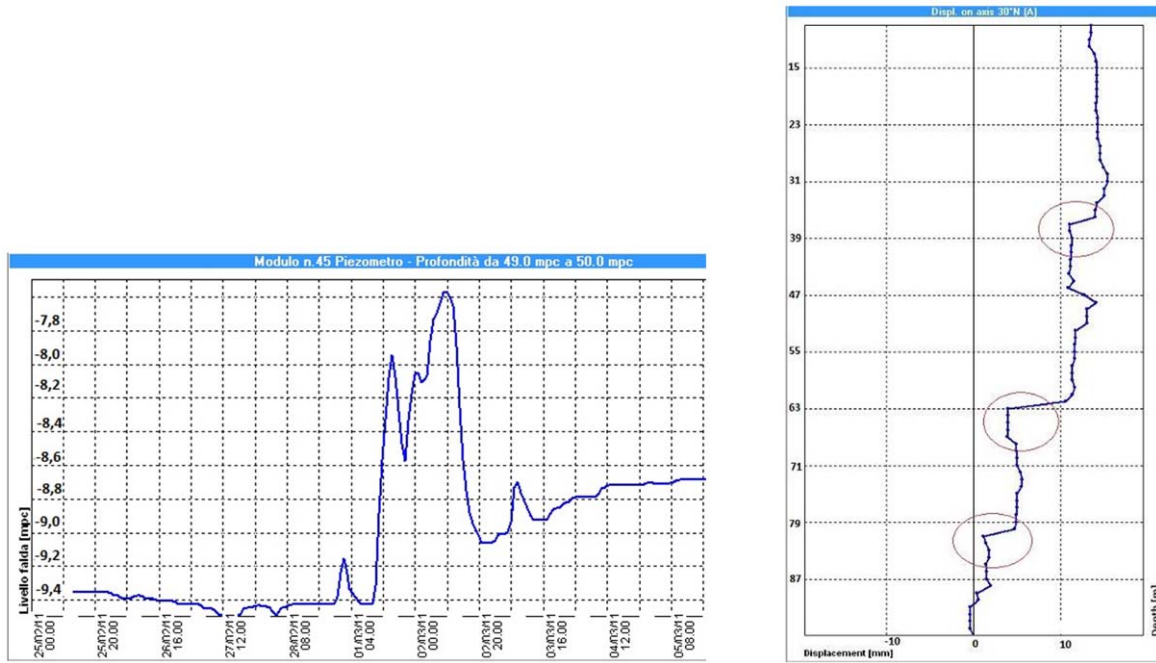


Figure 4.3-10. Water table level and total displacements of DMS_Ancona2

Figure 4.3-10 presents three triggering events that originated with a delay, like the previous one.

The same procedure was implemented on the third column, **Ancona3**. The water level rose on February 29th at 23:00, with a delay of 30 hours (Figure 4.3-11).

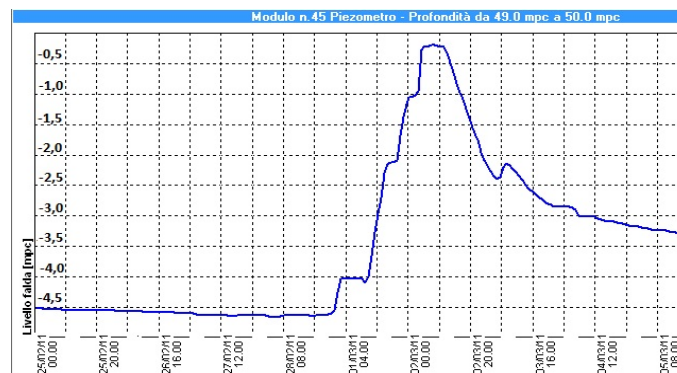


Figure 4.3-11. Water level at DMS_Ancona3 site

Within the analysed period no sensible displacements were detected. Only a very small micro-event is shown by module 3, between 91 and 92 m b.g.l., from 19/05/11 to 21/05/11. This displacement could have been triggered by the rainfall event with a very large delay or caused by settlement.

In general the analysis of DMS data shows a delay of about 30 hours between the beginning of the rainfall and the effect on the water table level, and one month of delay on the occurrence of displacement phenomena.

This data permits the implementation of a forecasting model and the evaluation of the risk level in function of more parameters, unlike traditional instruments.

It is important to notice that this analysis could not be achieved with only surface systems, because it was developed based on micro-movements occurring at important depths.

4.3.3.2 Hydrological parameter

Figure 4.3-12 shows the location of sensors of the hydrological measurement network around the geoelectrical monitoring profile. In 2011 three piezometers (PZCL3, PZBA1 and DMS 1) and four sensors for discharge measurements (MP4, MP5, MP3, and MP1) were still active (yellow rectangle).

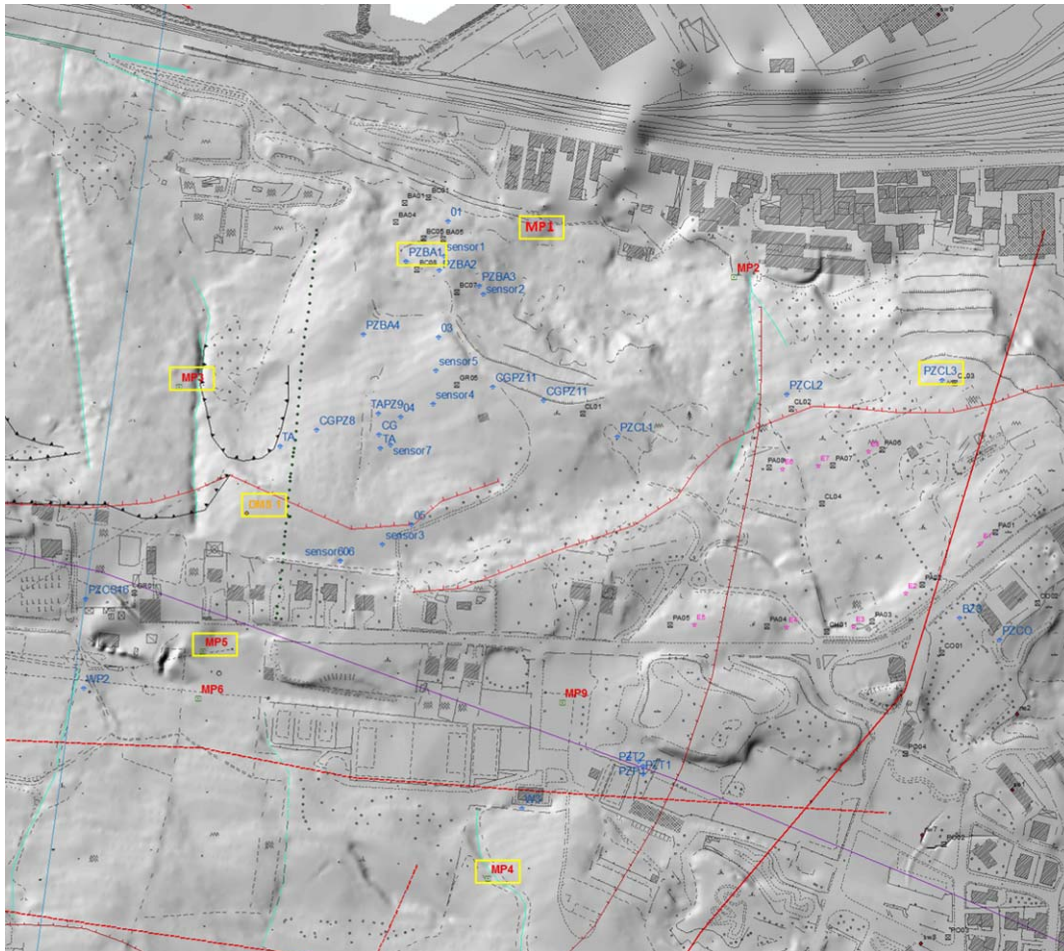


Figure 4.3-12. Location map of monitoring instrumentation used for interpretation (red: points of discharge measurements; blue: piezometers; orange: DMS (displacement and piezometer)).

Figure 4.3-13 and Figure 4.3-14 show a compilation of all hydrological results for the survey period 1.1.2011 to 25.2.2012. As the curve of cumulative precipitation shows, two major rainfall events took place, one at the beginning of March 2011 with a cumulative value of more than 160 mm, the other at the beginning of February 2012 with around 80 mm. All piezometers show an increase of water levels during the time of the first major event and

during most of the minor events during the winter and spring period. Within April 2011 only PZBA1 shows an increase in water level correlated with minor rainfalls. After April 2011 until February 2012 no correlation between precipitation events and water levels could be detected at all. No data is available so far for the February 2012 event. Interestingly, data from PZBA1 show a significant and abrupt decrease of values before each of the events not following the general trend of decay at this location. The values of discharge (Figure 4.3-14) correlate well with almost all precipitation events, even during the summer to winter period, when piezometers show no anomalies. After the precipitation events, values decay rapidly. The only anomalous behaviour is shown by the values of MP3 after the major event in March 2011. After a sharp increase during the rainfall, a steady increase of the outflow follows until the time of the recorded displacement event at DMS 1 (shaded rectangle) when values soon start to decrease. Since MP3 is located quite close to DMS 1, a correlation between the triggering of the micro-movements and the increased outflow in MP3 seems to be obvious. One reason could be the continuous opening of micro-cracks and consequent activation of sliding planes due to the increased water pressure and correlated larger outflow rates. However the reservoir seems to be different to that monitored by DMS 1, since the water level in this hole decays rapidly after the event and no change of its behaviour is detectable after the displacement event. For events later in 2011, MP3 reacts again in the usual way, i.e. rapid decay after an event (Figure 4.3-15).

Therefore we can conclude that an anomalous behaviour of MP3 (Figure 4.3-15) after a precipitation event could be an indication of an impending (micro-) movement.

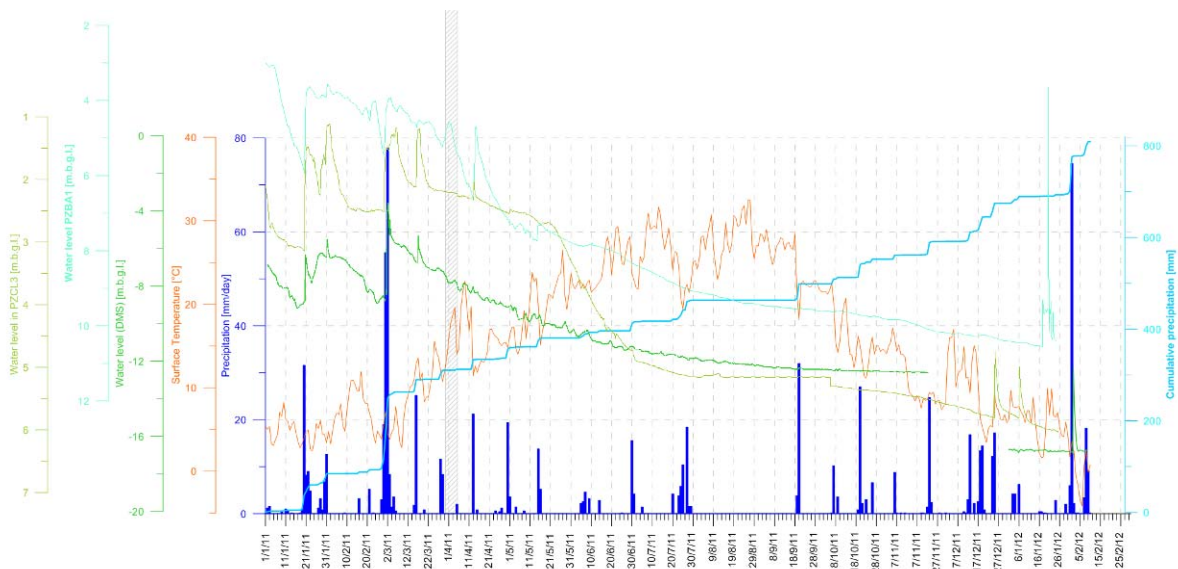


Figure 4.3-13. Overview of hydrological parameter 1: precipitation, water levels and temperature; grey rectangle shows period of increased displacement rates.

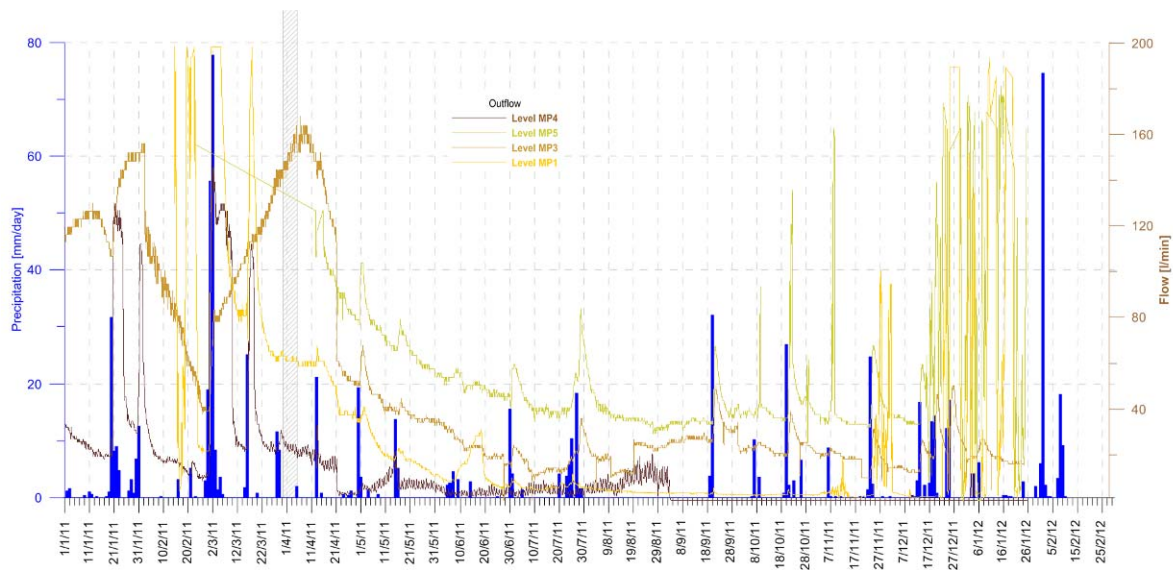


Figure 4.3-14. Overview of hydrological parameter 2: precipitation, discharge.

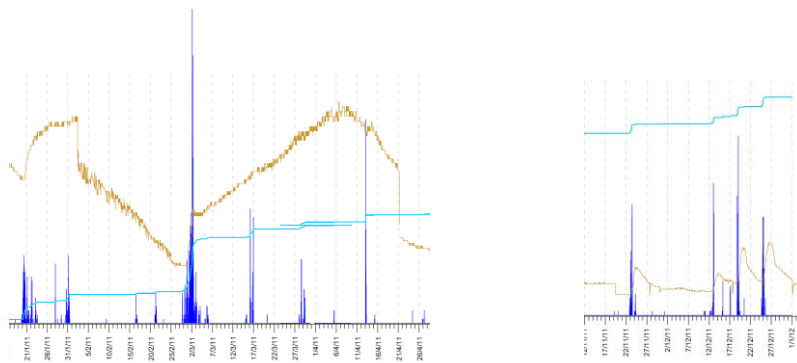


Figure 4.3-15: abnormal (left) and "normal" (right) behaviour of outflow at MP3

When we look on the more detailed display of curves (Figure 4.3-16 and Figure 4.3-17), we see that water levels in PZCL3 and PZBA1 react almost immediately after the first precipitation events and reach the value of saturation even before the major phase of precipitation. On the other hand, MP4 and MP3 react with a delay of 10 h and DMS 1 and MP1 with a delay of more than 24 h. Therefore, we could conclude that PZCL3 and PZBA1 are more directly influenced by raining water, whereas DMS 1 and MP1, MP4 and MP3 monitor the subsurface water flow.

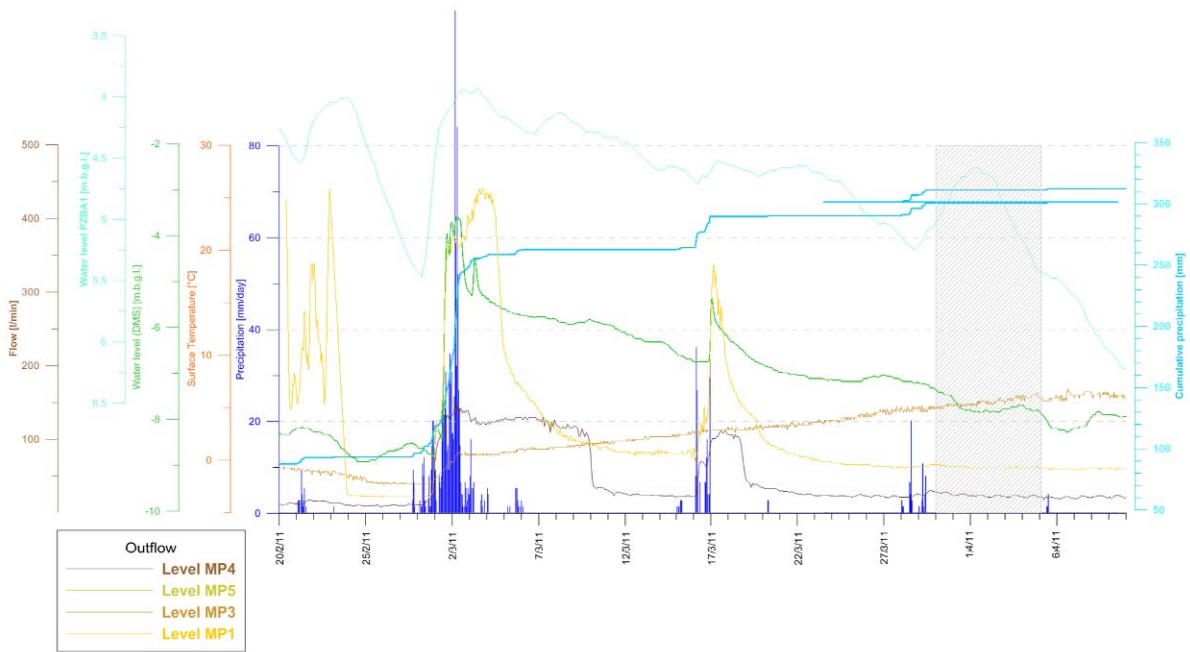


Figure 4.3-16. Hydrological parameters: details for the period 20.2.-10.4.2011.

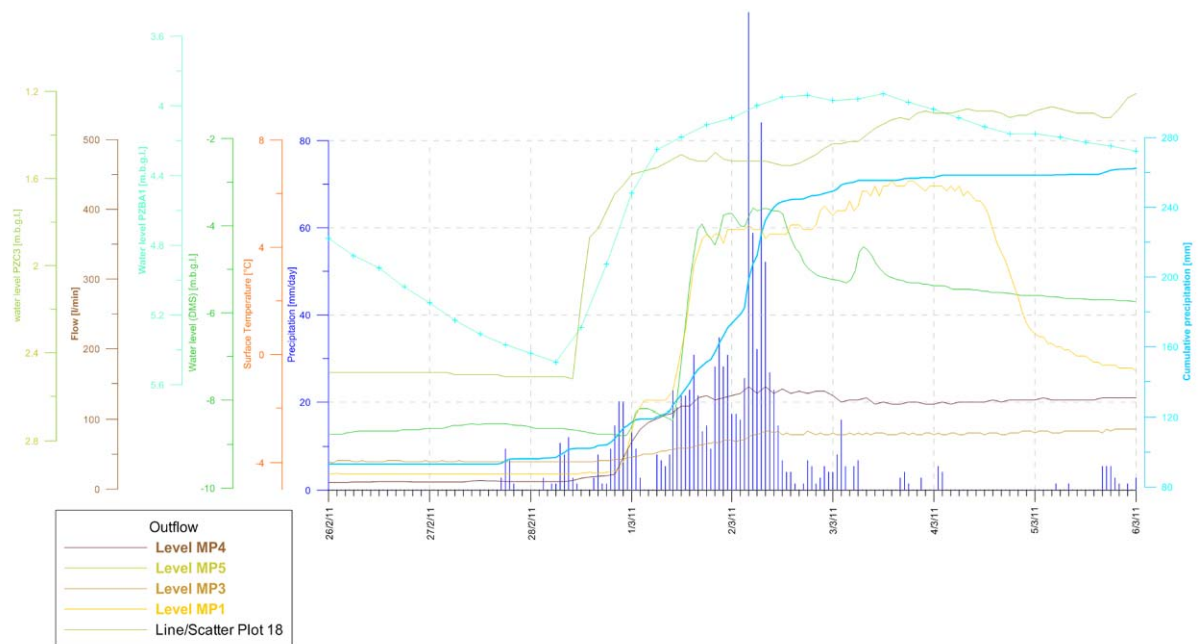


Figure 4.3-17. Hydrological parameters: details for the period 26.2.-6.3.2011.

4.3.3.3 Resistivity

Monitoring results from the first year showed that due to the low background resistivity and the high background noise (very low signal to noise ratio), no stable results (inversion error without clipping of low quality data > 40 %) could be monitored. Filtering over time improved the stability of the inversion results; however any reasonable interpretation of changes remained difficult. Figure 4.3-18 clearly shows that the variations of monitoring values have increased with drying of the surface soil during the hot summer period. Amazingly, after an intense rainfall at the beginning of February 2012 data quality improved significantly (Figure 4.3-19). The inversion error without cutting of values came down below 12 % after the first iteration, a result which was never achieved before on this profile (not even at the beginning of the monitoring).

Analysis of raw data values (Figure 4.3-20 and Figure 4.3-21) showed that the background noise remained at the same level (around 50mV), but at many injection dipoles, a much higher amount of current could be injected which significantly improved the signal to noise ratio. Therefore we can conclude that for monitoring in a low resistive environment within urban areas (high noise level), more than 400 mA must be injected to derive a reasonable result.

For the interpretation of the results we conclude that geoelectric monitoring at Ancona site proved to be very difficult due to the low signal to noise ratio (high noise level in a very low resistive environment). For a detailed interpretation, a longer observation period is necessary and special noise-filtering algorithms must be developed. Both are planned within a follow-up project after the termination of SafeLand.

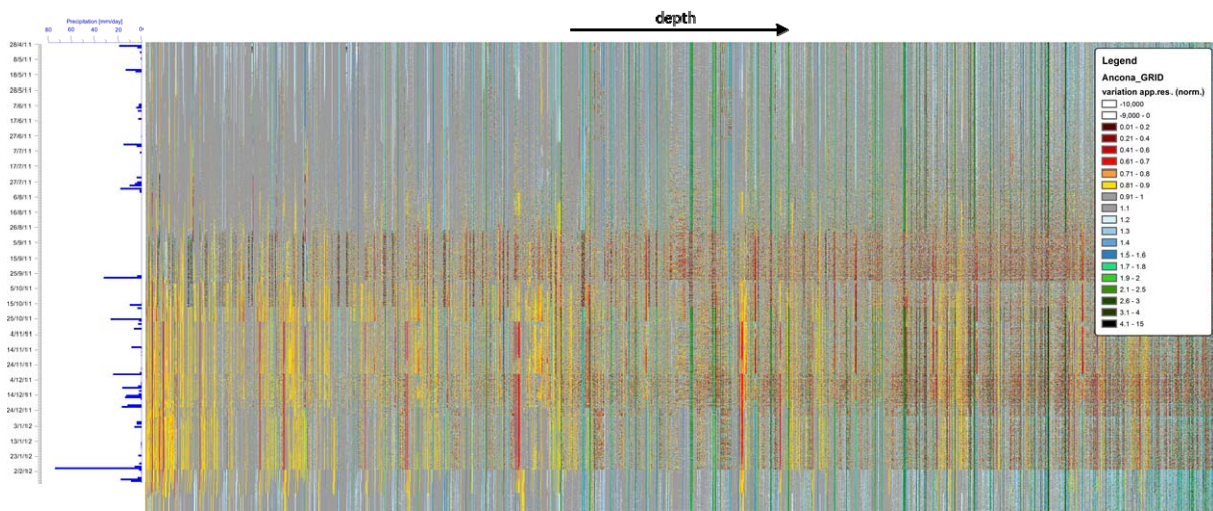


Figure 4.3-18. Grid of measured resistivity variations (normalised) with time.

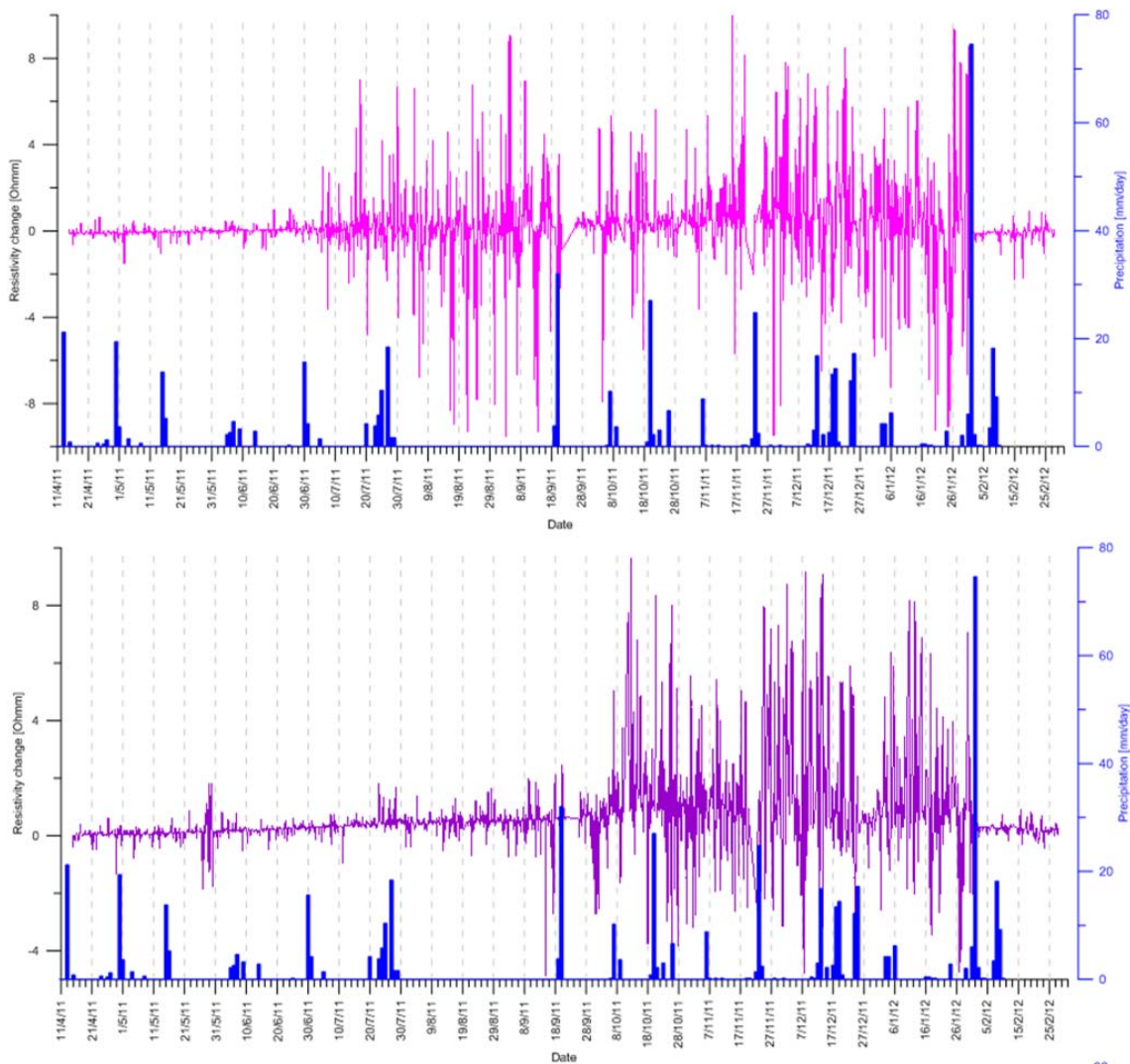


Figure 4.3-19. Variation of resistivity values (purple, pink, [Ohmm]) with time of selected configurations correlated with rainfall events.

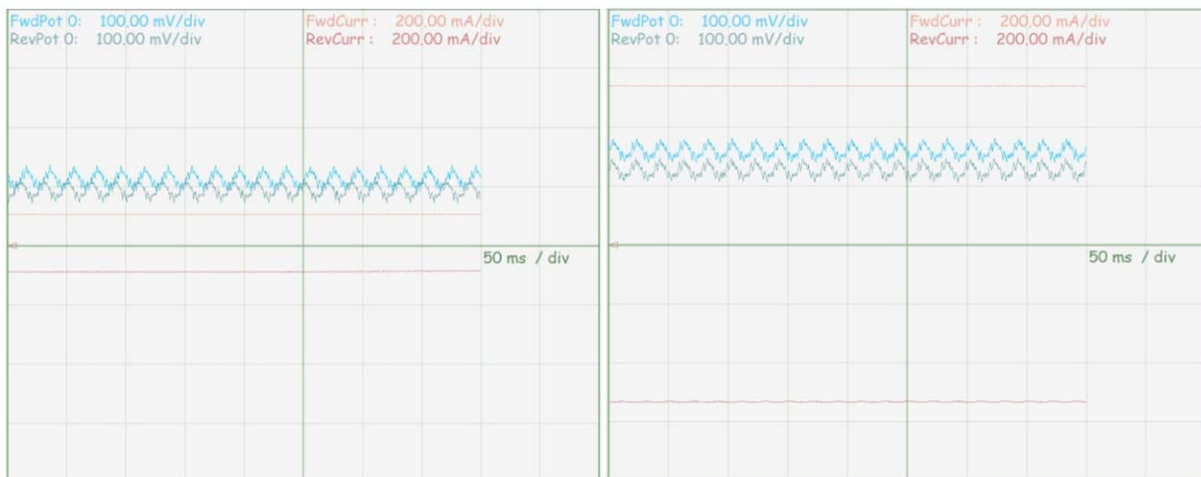


Figure 4.3-20. Data samples for one single measurement before (left) and after (right) the intense rainfall at the beginning of February.

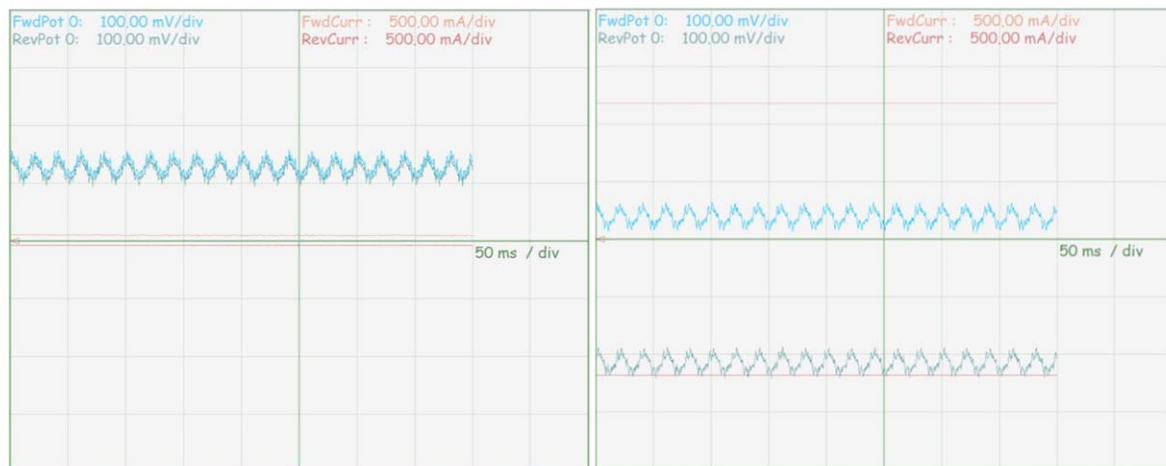


Figure 4.3-21. Data samples for one single measurement before (left) and after (right) the intense rainfall at the beginning of February.

4.3.4 SUMMARIZED EVALUATION OF PARAMETERS

The monitoring data have demonstrated a general dormancy of the landslide since 2008, both on the ground surface and in the subsurface. Only micromovements have been recorded in particular by DMS.

The rain event of March 2011 showed significant variations of the water table increasing at the same date and time in all three DMS columns.

In future, particular attention will be dedicated to the evaluation of the landslide's natural and artificial drainage systems to define in the model the rain events capable of triggering the overall landslide body.

References:

- Boccanera F., Iocca F., Lazzeri M., Sofia S. (2011): RAPPORTO DI EVENTO 1-3 marzo 2011, Area meteo. Report in Italian. – REGIONE MARCHE, Dipartimento per le Politiche Integrate di Sicurezza e per la Protezione Civile, Centro Funzionale per la Meteorologia, l'Idrologia e la Sismologia, 75 pp.
- Cardellini S. and Osimani M. (2010): Living with Landslides: the Ancona Case History and Early Warning System. – In.: Supper R. Baroň I. (Eds.): Landslide Monitoring Technologies & Early Warning Systems. - Ber. Geol. B.-A., 82: 61-66. ISSN 1017-8880
- Cardellini S. and Osimani M. (2011): The Ancona early warning centre, instrumentation and continuous monitoring of the landslide. – The Second World Landslide Forum Abstracts, WLF2 - 2011– 0169, Rome: p. 202.
- Cotecchia V. (2006): The Second Hans Cloos Lecture. Experience drawn from the great Ancona Landslide of 1982 landslide. – Bull. Eng. Geol. Env., 65: 1-41
- Crescenti U., Ciancetti G.F., Coltrorti M. et al. (1983): La Grande Frana di Ancona del 1982. – Collana Problemi del Territorio. Università di Ancona e Comune di Ancona, 51 pp.
- Unesco (1974): Annual Summary of Information on Natural Disasters in 1972. Earthquakes, Tsunamis, Volcanic Eruptions, Landslides, Avalanches. – The Unesco Press, Paris, 101 pp.

4.4 BAGNASCHINO (ITALY)

R. Supper, B. Jochum, D. Ottowitz, I. Baroň, F. Vecchiotti, S. Pfeiler, A. Römer
Geological Survey of Austria

M. Lovisolo
Centro Servizi di Geingegneria S.r.l., Italy

J.-H. Kim
KIGAM, Republic of Korea and Geological Survey of Austria

ABSTRACT

At the Bagnaschino landslide an early warning system comprised of automatic displacement measurements in combination with geoelectrical and water level monitoring was installed. Within two survey periods, several events could be detected and analyzed. The results showed an obvious correlation between heavy precipitation and the reactivation of the landslide. A correlation between instability and quantity and duration of rainfall could be derived. The results of geoelectric time lapse inversion and water level monitoring helped to refine the conception of ongoing subsurface processes. The results highlight the necessity of installing multi-parameter monitoring networks to support efficient early warning procedures.

Presented parameters: displacement, velocity, groundwater level, precipitation, air temperature, soil temperature, resistivity.

4.4.1 GENERAL DESCRIPTION OF THE TEST SITE

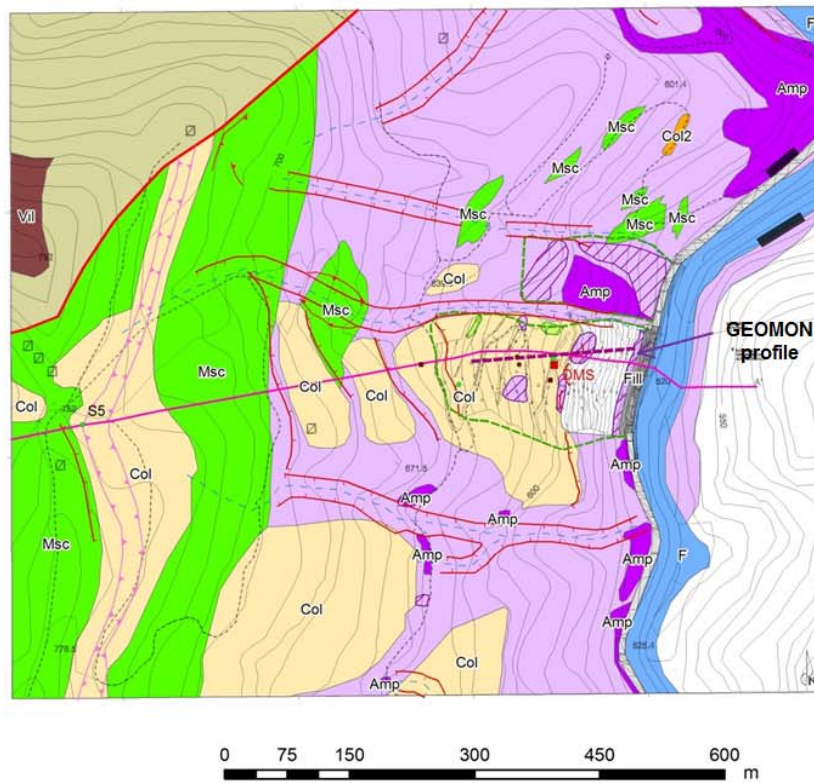
The Bagnaschino site represents a complex landslide reactivated within an old deep-seated gravitational slope deformation mass. The main event occurred in November 1994 destroying part of the provincial road in the Casotto valley.

Geological and geomorphic settings

The old landslide is located on the east slopes of the Casotto valley about 4 km SE of Torre Mondovì (NW Italy; Figure 4.4-1) and developed in a tectonically densely jointed calcareous-mica schist and diamictic colluvium superimposed on altered amphibolite and prasinites. Evident indications of deep-seated gravitational deformation (crowns and scarps, zone of accumulation of large paleoslides, etc.) suggest that the current slopes are in a condition of limit-equilibrium and are predisposed to slow instability, triggered most probably by rain and/or snow melting and river erosion at the foot.



Figure 4.4-1. Location of the Bagnaschino monitoring site (Photo by: Corrado Faletto, Province of Cuneo).



- | | |
|--|--|
| <p>Monitoring system</p> <ul style="list-style-type: none"> ■ DMS ● Boreholes (stratigraphic) ■ Inclinometers ● Piezometers --- GEOMON installation <p>Geomorphology</p> <ul style="list-style-type: none"> → Gravitative scarp → Morphologic scarp --- Rapid superficial incision water runoff → Trench --- Extent of previous remedial works → Geologic profile AA' | <p>Geology</p> <ul style="list-style-type: none"> ■ Detrital filling ■ Fluvial deposits of Casotto creek ■ Colluvial deposits: sandy silt and clay ■ Deposits clay and silty clay intensively altered ■ Detrital deposits made of Amphibolite clasts ■ Detrital deposits made of Mica schist clasts ■ Villanova unit outcrop: Limestone and dolomite ■ Villanova unit inferred: Limestone and dolomite ■ Bagnaschino Unit outcrop: Amphibolite and gneiss ■ Bagnaschino Unit inferred: Amphibolite and gneiss ■ Bagnaschino Unit fractured: Amphibolite ■ Bagnaschino Unit outcrop: Mica schist → Thrust fault |
|--|--|

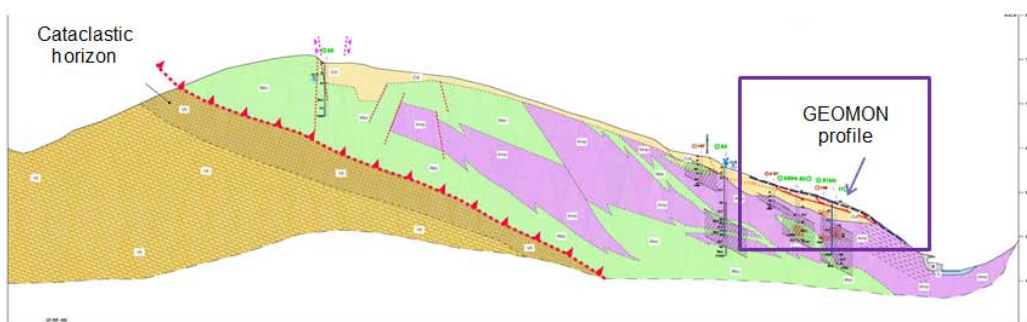


Figure 4.4-2. Geomorphic and geological sketch of the Bagnaschino landslide and related geological cross section (Peisino et al. 2009).

The unit of Bagnaschino, eradicated from the Brianzonese domain (portion of the crystalline basement) was thrust over the Villanova formation belonging to the Piedimont domain. Following this event, a series of brittle tectonic elements was superimposed over the two formations. The geological structure was studied by several core boreholes. The main rocks, recognized underneath the colluvium clastic deposit, were intense fractured mica schist and amphibolite. These rocks reached a high level of metamorphism (green schist). The Villanova formation lying below is composed of limestone and dolomites characterised by diffuse karstification (Giuliani et al. 2010).

Characterization of the site

The studied active landslide from 1994 covers an estimated area of 150,000 m² and comprises a displaced material of 1.2 million m³ (only the flow part). It is a rotational-translational landslide of an elliptical shape and with a depth of failure at about 8 m b.g.l. It affected mainly colluvium deposit and mica-schist rocks. The maximum observed velocity of the slide was about 1 m/year in 2009. The crown of the landslide is situated at an altitude of 637 m a.s.l., whilst the toe is about 540 m a.s.l. A perched groundwater level was registered at a depth of about 6.5 m b.g.l., which is probably the main triggering factor of the active sliding zone. The displacement has performed in distinct relation to rainfall events or snow melting.

The active landslide is part of an older deep-seated gravitational slope deformation (DSGSD), situated on the east slopes of the mountain ridge elevated about 778 m a.s.l. The DSGSD is most probably structurally controlled and its base and upper trench follow the probably active regional thrust fault (Figure 4.4-2). Deep creep movement of the DSGSD has been recognized about 30-44 m b.g.l.

Description of the history of the mass movement

The entire Bagnaschino DSGSD was recognised and mapped in the frame of the Inventario dei Fenomeni Franosi in Italia (IFFI) project in 1979. Debris and small boulder falls affected the road called SP n. 164. However, the main recent event related to the active landslide occurred in November 1994 after a distinct heavy rainfall event. It caused an interruption of the SP n. 164 road and also partly dammed the Casotto creek.

Since another reactivation took place in October 1996, a geologic survey began in 1997 in order to study the behaviour of the slope failure. The road, which was affected by the landslide, was rebuilt and a protective tunnel was realised.

Later on, the DMS column registered five displacement events, which occurred between the fall of 2008 and the spring of 2009. These events were clearly triggered by snow melting and/or heavy rainfalls.

The active landslide endangers a provincial road. The other hazard is related to the formation of a potential dam.

4.4.2 DESIGN OF THE MONITORING NETWORK

A 60-meter long DMS monitoring column was installed in October 2008. It allowed for the investigation of several displacement events and GWL variations. The column was removed

in July 2009, when a maximum displacement of 60 cm was reached, since its operation on larger displacements could not be guaranteed (Figure 4.4-3). The excavation of the column made it possible to exactly verify the results of the DMS readings. The whole column could be recovered and was taken to CSG for repair. A new monitoring strategy was developed so the system could accommodate the specific local conditions of a fast-moving first layer and slowly creeping deeper structures, and so the installation would hold for a longer observation period. The column was separated in two parts. The first column, 20 m in length, was installed in a separate hole to monitor the shallow and fast displacements. For the second column, 40 m in length, a hole with a diameter of 1 m was excavated to a depth of 20 m. This was followed by the usual inclinometric drilling on the downhill side of the 1 m hole, thus allowing the exact monitoring of the deeper displacements and in case of larger shallow movements. This second installation was in operation from June 2010. Subsequently, in October 2010 a geoelectrical monitoring system with variable electrode distances was installed using the GEOMON technique. The main aim of the monitoring is early warning for civil protection. Additionally, precipitation data is available from the weather stations Viola and Pamparato, operated by the Province of Cuneo, and piezometric data is available from the deep DMS column (although the casing is not perforated) and one automatic station near the end of the geoelectric profile.

4.4.3 ANALYSIS OF MONITORING DATA

Observation period November 2008-April 2009



Figure 4.4-3. DMS column installation (October 28th 2008) and removal (July 13th 2009) - Bagnaschino site (Photo: C.S.G.).

4.4.3.1 Displacement and precipitation

Correlations between the DMS column and weather data permitted the identification of critical events that have reactivated the landslide on the sliding surface at 7 m b.g.l., with 30° NE direction. During the observation period it was possible to continuously monitor different kinematics and weather conditions (Figure 4.4-4). The DMS column permitted the investigation of five triggering events and their relative period of stasis, with a clear delay time after rain events or snow melting. The characteristics of each event are described in what follows:

- *First event:* On November 28th 2008 there was the first snowfall (one of the most intense of the last century in the area) that was followed by some rainy days and finally by another snowfall on the 13-19th of December. Over the same days there was a temperature rise that caused partial snow melting and subsequently, the first movement read by the DMS column.
- *Second event:* On March 1st 2009 there was a light rainfall followed by a strong temperature rise (thermal zero moved to 1500 m a.s.l) that caused the second landslide activation on March 2nd 2009 at 20:03, 37 hours after the rainfall began.
- *Third event:* On March 31st 2009 at 06:00 a strong rainfall began and lasted for a few days. After 30 hours, the landslide started to move.
- *Fourth event:* This event is linked to several rainfalls that occurred on April 16-22nd 2009 and differs from the previous events because of a lower movement velocity (displacement of about 10 mm).
- *Fifth event:* On April 26th 2009 the strongest spring rainfall started and after about 29 hours (on April 27th at 08:00) the landslide moved. This heavy rainfall lasted for a few days; the cumulative displacement was 299.7 mm in only two days. The roll axis on the involved DMS module reached its saturation angle (tilt>20°), and the further displacement is calculated with the interpolation of its pitch axis, still active.

In the following diagram and table each triggering event has been described in detail considering also rain, cumulative rain, snow events and temperature.

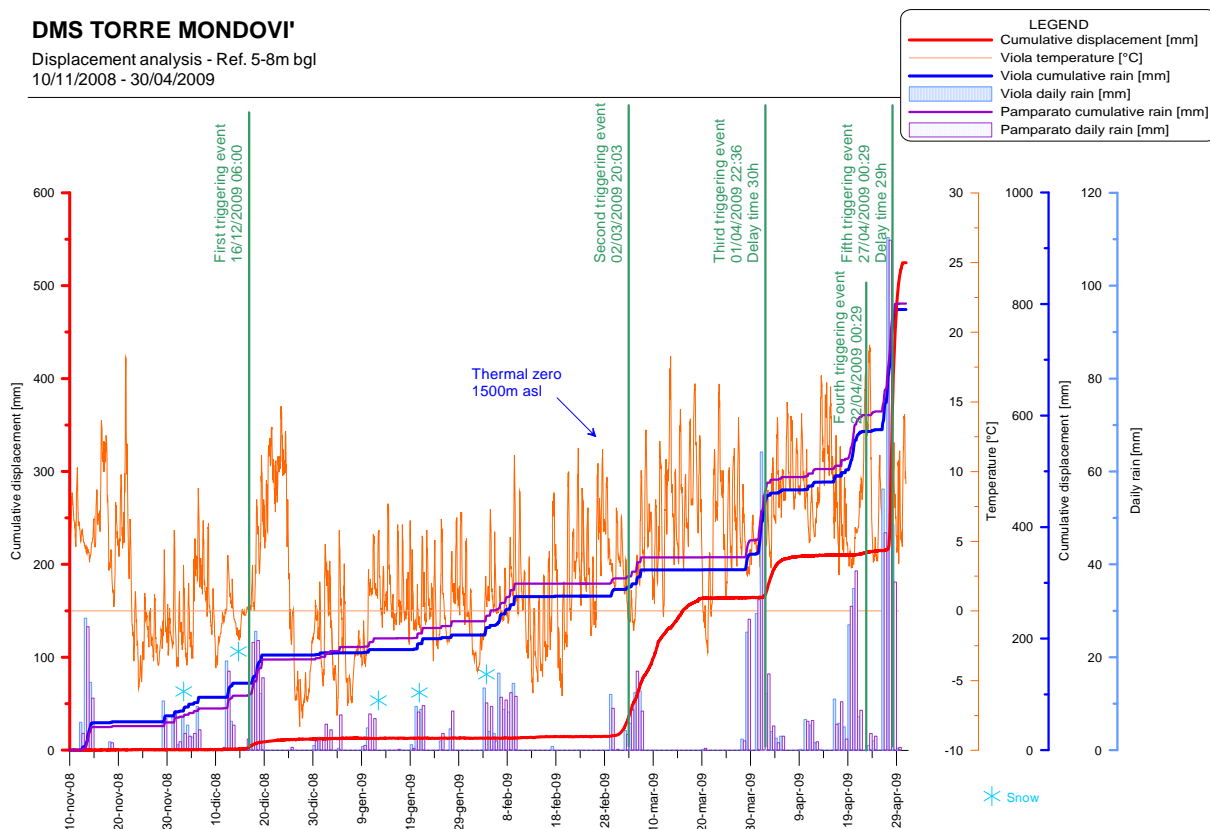


Figure 4.4-4. Chart of displacement events at the depth of 5-8 m b.g.l. (thick red line) compared to air temperature (thin red line), and rainfall data from the Viola and Pamparato meteorological stations.

Table1: Triggering events:

	1 st EVENT	2 nd EVENT	3 rd EVENT	4 th EVENT	5 th EVENT
Rainfall start	12/12/2008 0.00	01/03/2009 6.00	31/03/2009 6.00	16/04/2009 6.00	26/04/2009 3.00
Displacement start	16/12/2008 6.00	02/03/2009 20.00	01/04/2009 12.00	22/04/2009 0.00	27/04/2009 8.00
Rainfall type	Snow	Rain/snow	Rain	Rain	Rain
Snow at ground	Yes	Yes	Yes	No	No
Temperature rise	Yes	Yes	No	No	No
Concomitant factors	Snow melting 90 mm	Snow melting 120 mm	-	-	-
Rainfall [mm]	70	44	63	160	77.6
Rainfall duration [h]	84	96	30	138	29
Critical intensity [mm/h]	1.786	1.708	2.100	1.159	2.676
Total cumulative rainfall [mm]	190	354	480	590	800
Cumulative rainfall event [mm]	150	164	180	110	220
Total cumulative displacement [mm]	11.5	160.6	209.0	225.0	524.7
Cumulative displacement event [mm]	11.5	149.1	48.4	10.0	299.7

For each event, a particular value – the *critical intensity* – was calculated that corresponds to the ratio between precipitation quantity (calculated in millimeters) that caused triggering movement and its duration (calculated in hours).

The interpolated line in the bi-logarithmic plot can be considered a site-specific deterministic approach to the limit equilibrium threshold that separates the stability and instability field.

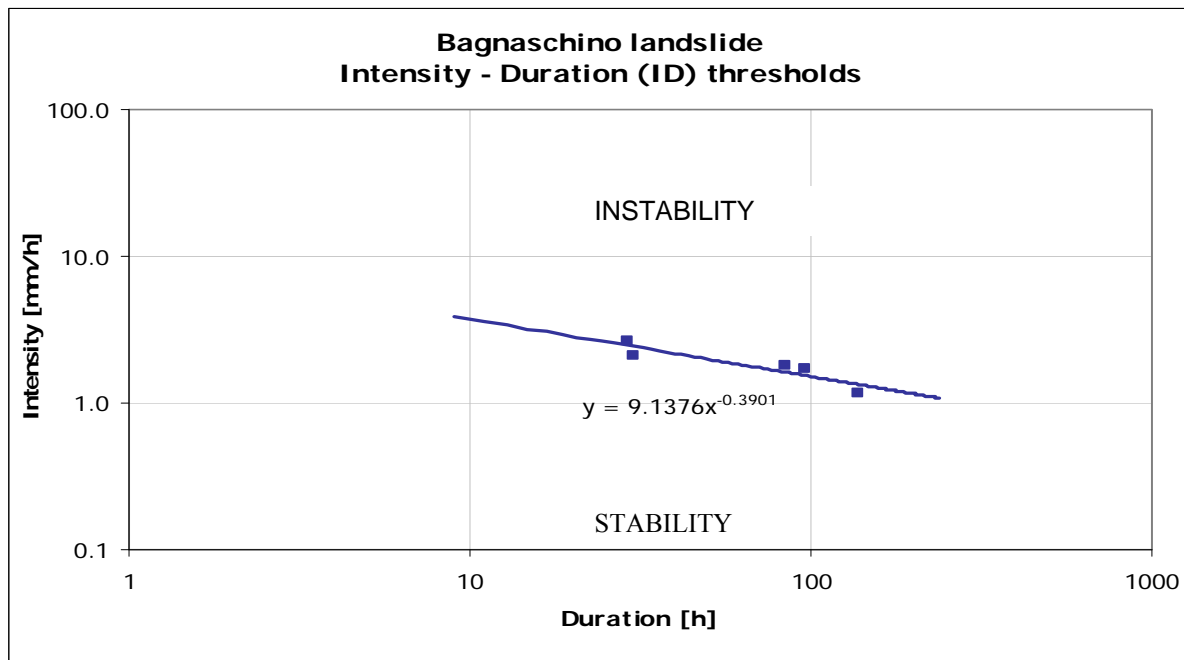


Figure 4.4-5. Rain intensity-duration graph for the reactivation events at the Bagnaschino site in the period 2008-2009.

The DMS column was removed on July 13th 2009 (Figure 4.4-2). The DMS column allowed the kinematics of the landslide in action – not only limited to the initial stages of trigger but also during the evolution up to achievement of stasis conditions – to be obtained with continuity.

The integrity of the DMS column was preserved in spite of a displacement of 60 cm; the excavation to release the column confirmed depth, direction and extent of the displacement, allowing the complete recovery of the instrumentation and the repair of the inclinometric pipe that is replaced and protected by another pipe with a large diameter.

Continuous monitoring of the landslide allowed for weak deep creep to be noticed in the interval 30-44 m b.g.l., in addition to the considerable shallow movements. The activation of deep movements is delayed in respect to shallow movements, with well-defined behaviour.

Observing period June 2010-November 2011

4.4.3.2 Displacement

Two new DMS columns were installed in June 2010 for early warning purposes as described above, active in the interval depths of 20-60 m and 0-20 m b.g.l. In the following chapter, the results obtained within the observation period from June 2010 to November 2011 are presented.

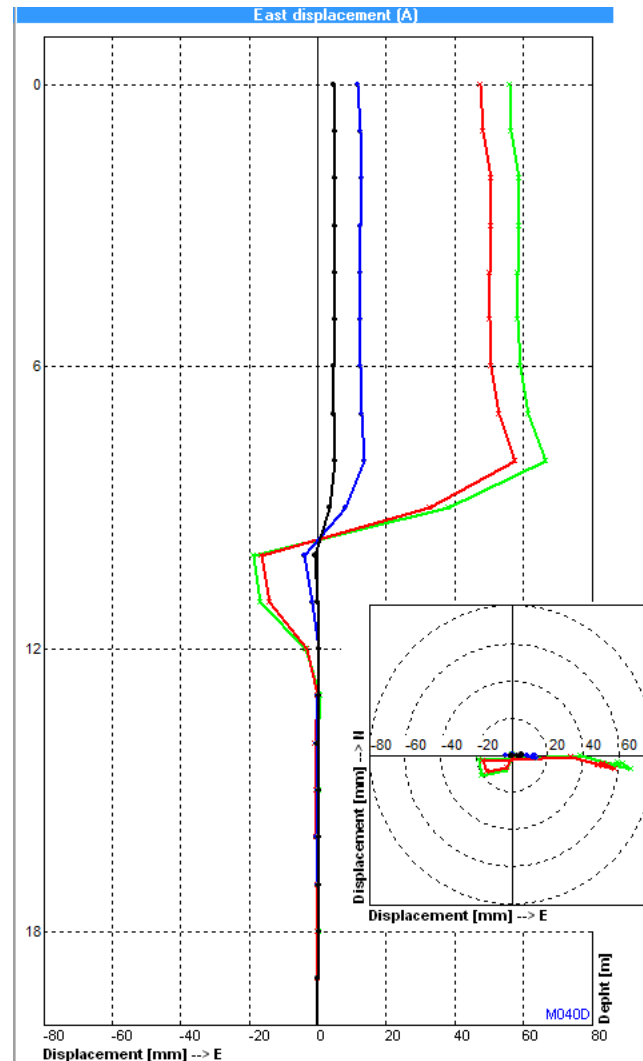


Figure 4.4-6. Inclinometric record of E cumulative displacement in the shallow DMS column at the Bagnaschino (March 2011 event).

The displacement registered by the DMS column *at shallow depth (0-20 m b.g.l.)* represents the behaviour of the shallow active landslide, which generally moves towards the east. The inclinometric results of the mass movement fit well with the geomorphic and engineering-geological observations of the local topography and the slope orientation. A slip zone was identified at the depth of 8-10 m b.g.l. (Figure 4.4-6). A triggering event occurred starting on

12th March; cumulative displacement reached 63.3 mm at a depth of 8 m b.g.l. on 17th March, and the event stopped after 9 days on 21st March with cumulative displacement of 71.5 mm oriented eastwards (Figure 4.4-6 and polar detail 4.4-7).

In July 2009, the previous DMS column was excavated and removed. Inside the hole, a 1 m pipe for the deep column was installed and the hole filled up again. The colluvial mass that was excavated and then again deposited has probably undergone settlement since then. This settlement could still influence the local observations at shallow depth, although the new drillhole for the shallow DMS was performed several meters away.

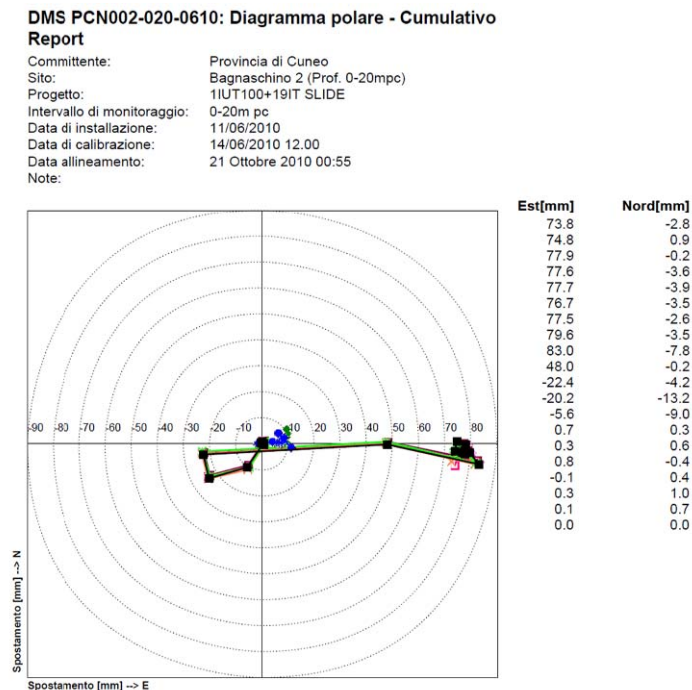


Figure 4.4-7. Polar diagram of the inclinometric record of cumulative displacement in the shallow DMS column at the Bagnaschino site registered from December 2010 to November 2011 (alignment October 21st, 2010).

The inclinometric results of the *displacement in deeper part (20-60 m b.g.l.)* display slow and small displacements of about 2 cm along the monitoring column during the observation period (Figure 4.4-8). The results do not show any distinct sliding surface or a stable (not moving) base. The vectors of the deep movements differ: the deepest parts move towards north (perpendicular to the slope dip), and the movement vector in the more shallow part (-33 m b.g.l. and less) then turns towards east respecting the slope dip (Figure 4.4-9).

The deepest movements, which are oriented towards north, could be due to two possible reasons: (i) the aluminium inclinometric pipe has bended laterally within the borehole due to loading by the weight of the modules, or (ii) due to neotectonic activity. The site is located in a tectonically active area and the regional thrust fault is situated very close to the base of the DSGSD (Figure 4.4-2). The absence of a distinct sliding zone could either indicate that the entire slope undergoes a creep deformation and/or that the base of the inclinometer was not fixed in stable ground. However, for any final interpretation, a much longer observation period is needed.

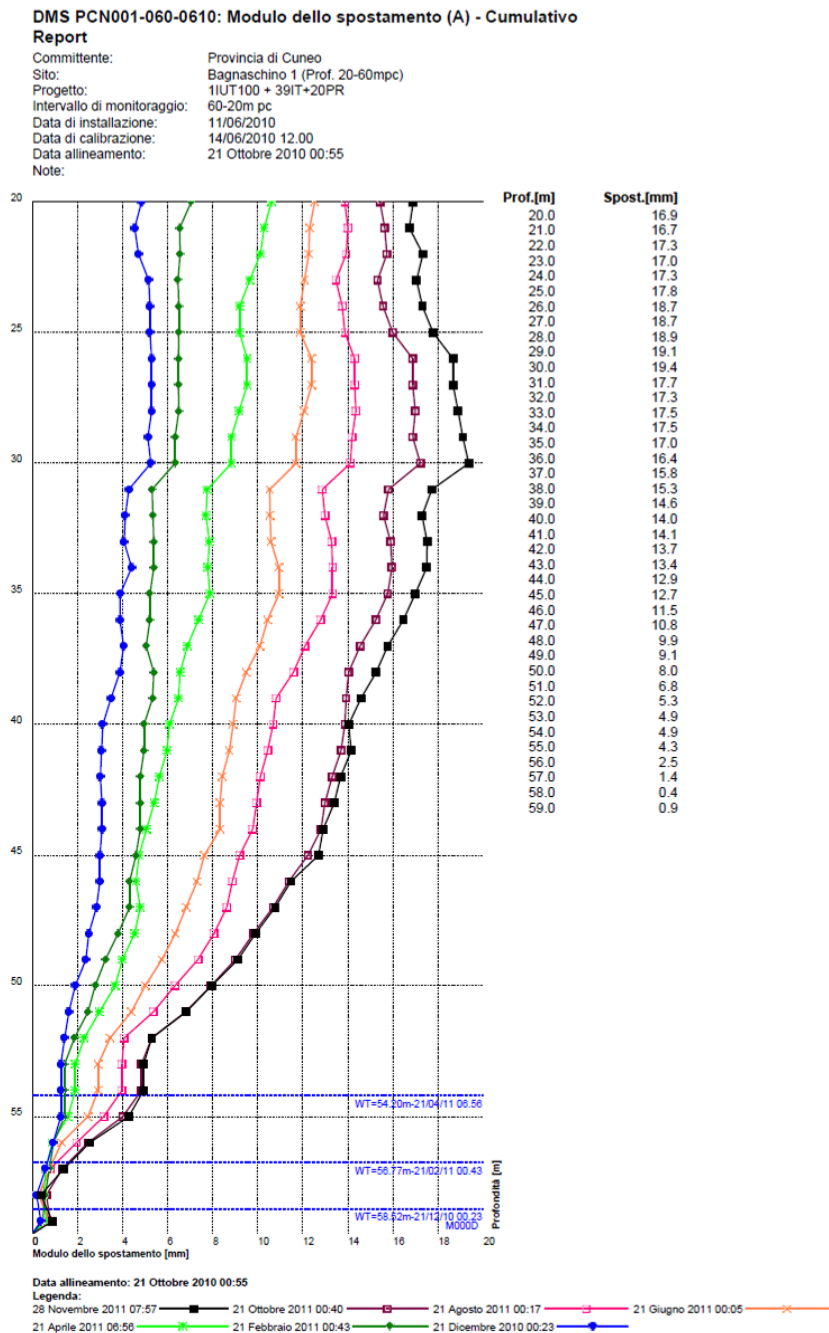


Figure 4.4-8. Inclinometric record of total cumulative displacement in the deeper DMS column at the Bagnaschino site registered from December 2010 to November 2011 (alignment October 21st, 2010).

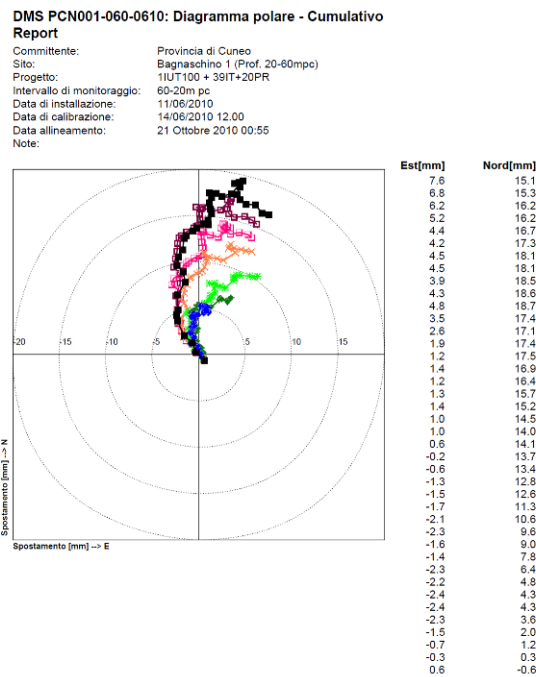


Figure 4.4-9. Polar diagram of the inclinometric record of cumulative displacement in the deeper DMS column at the Bagnaschino site registered from December 2010 to November 2011 (alignment October 21st, 2010).

The temporal evolution of displacement exhibits quite stable behaviour except for one distinct and several indistinct reactivation events (Figure 4.4-10). The first two months of observation were characterized by two small events with a maximum displacement of about 0.5 mm within two days. They occurred in October 2010, several months after the DMS installation. A question that arises is whether they are related to mass movement itself or rather reflect the settlement of the substrate and the DMS instrument. Yet, they were also related to rainfall (Figure 4.4-10).

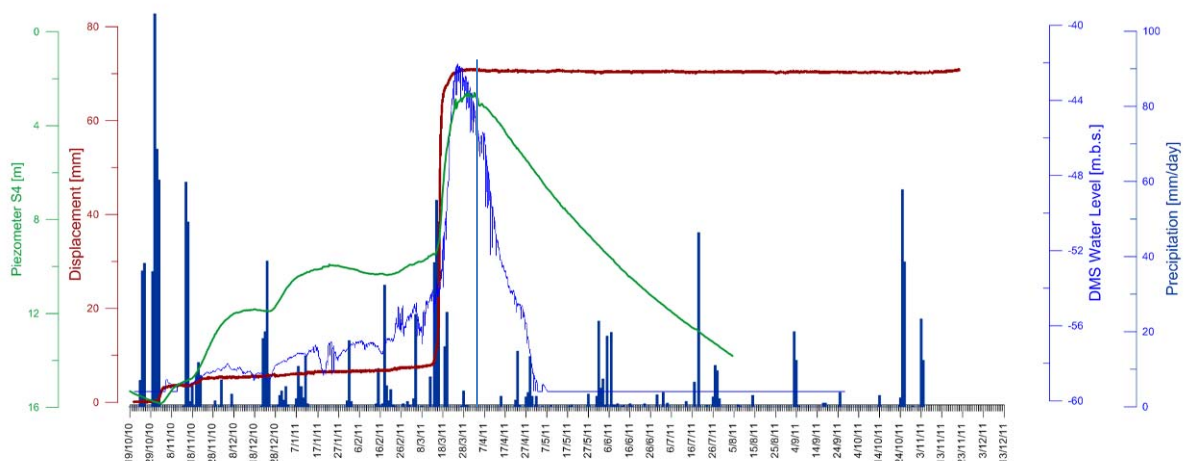


Figure 4.4-10. Graph of cumulative displacement (purple), compared to total daily precipitation (dark blue), to groundwater level in DMS column (blue), and to pore-water pressure (green) registered in the shallow depth from October 19th 2010 to December 13th 2011.

During the whole observation period only one significant reactivation event occurred between March 15th 2011 at 09:41 (CET) and March 18th 2011 at 11:08 (CET), called the “**March 2011 event**” (Figure 4.4-11). The total displacement reached about 70 mm in 73 h 27 min, the maximum velocity was up to 1.3 mm/h, and the average velocity was about 0.25 mm/h. The graph of cumulative displacement, velocity and acceleration from hourly DMS measurements and their eight-hour running averages are presented in Figure 4.4-11. Generally, evaluating from the eight-hour running averages, this event is characteristic with an acceleration phase lasting for almost 14 hours, correlated with the period of the highest precipitation rates during the first third of its duration. Then the velocity was constant and terminated with a peak of acceleration at the end of the second third of the event duration. This was followed by a period of distinct deceleration until the end of the event (Figure 4.4-11).

In any case, this event provided essential information on how the slope reacts to precipitation.

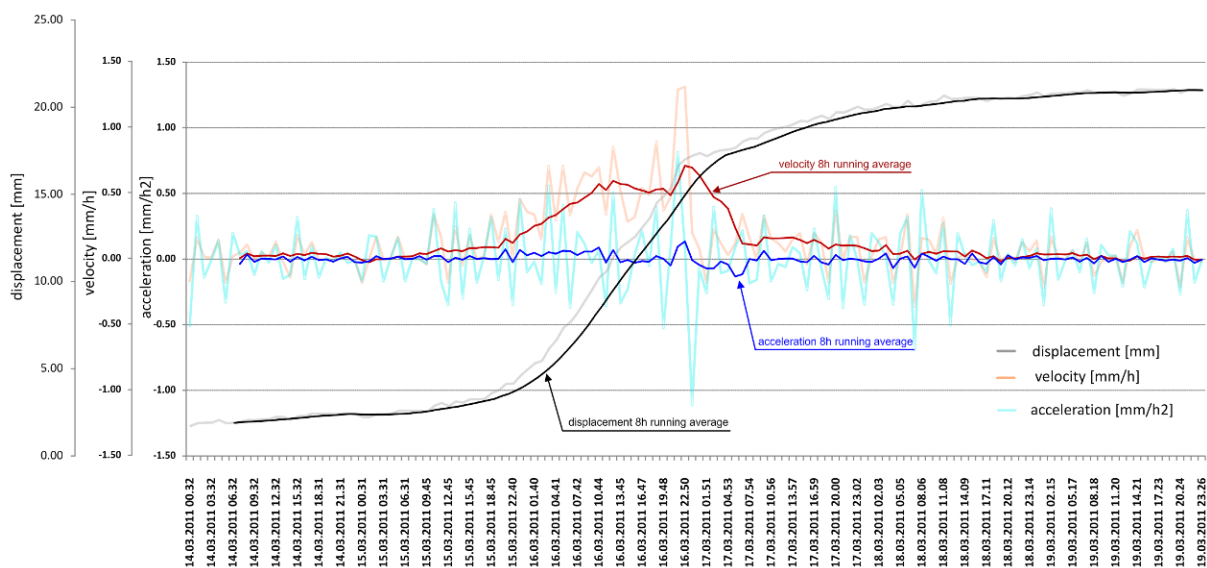


Figure 4.4-11. The “March 2011 event”: Graph of cumulative displacement, velocity and acceleration from hourly DMS measurements (transparent colours) and their eight-hour running averages (in full colour) for the period from March 14-19th 2011.

4.4.3.3 Groundwater level and precipitation

At this test site, water levels were continuously recorded within the deep DMS pipe and inside one drillhole (S4) located at the end of the geoelectric profile close to the supposed scarp of the landslide. Figure 4.4-10 displays the results acquired during the whole observation period whereas Figure 4.4-12 focuses on the March event. The water table of S4 is generally increasing before the March event, whereas successive rising periods are “triggered” by major rain events above 20 mm/day and smaller rainfalls show no obvious effect. After a rising phase of approximately 20 days, a kind of “relaxation” period usually took place, characterised by a constant or even slowly falling water table until the next rise is induced by heavy rainfalls. It is remarkable that in the period before the event, hardly any decrease of the water table took place. The same behaviour during that period was also detected inside the DMS column. However, immediately after the event, water levels in both holes started to drop rapidly. Within the DMS column no water level could be detected after

the 27th of April, whereas in S4 the water level dropped continuously until August (last data available). In that period, no influence on the water level due to rainfalls could be observed, although heavy rainfall events did take place. It must be noted that the decrease of the water levels started almost 10 days later in S4 than in the DMS hole. Within this observation period there is no obvious correlation between the intensity of the rainfalls and the quantity of the movement. However the water level data suggest that continuous filling of the pore space of the subsurface took place, which eventually could have reached the sliding plane, reduced shear strength there, and triggered a movement.

Looking at the detailed plot of the March event (Figure 4.4-12) it can be noted that the acceleration of the landslide started more than 32 hours after the onset of the rainfalls, lasting only eight hours and ending before the rainfalls did. During the time of the acceleration the DMS water level did not show any reaction to the rainfall, whereas the water level in S4 was smoothly increasing and reached the level of 9 m b.g.l. at the time of the landslide's reactivation. However, in both cases the major rise took place after the major displacement occurred.

To sum up, the situation is not quite clear. There seems to be a correlation between the successive saturation of the subsurface and the triggering of movements. However it is quite difficult to understand why the water level at the DMS site reacted only with delay after the main acceleration phase. Perhaps the movement was triggered upslope at first, and continued downslope as a chain reaction by increasing the force on the substratum. Due to the opening of cracks an additional inflow of groundwater to the DMS pipe was caused. This interpretation is however very speculative and somehow contrary to the outcome of the geoelectric monitoring.

Consequently, to derive distinct early warning parameters for this site, analysis of other future events seems to be necessary to solve some open-ended questions.

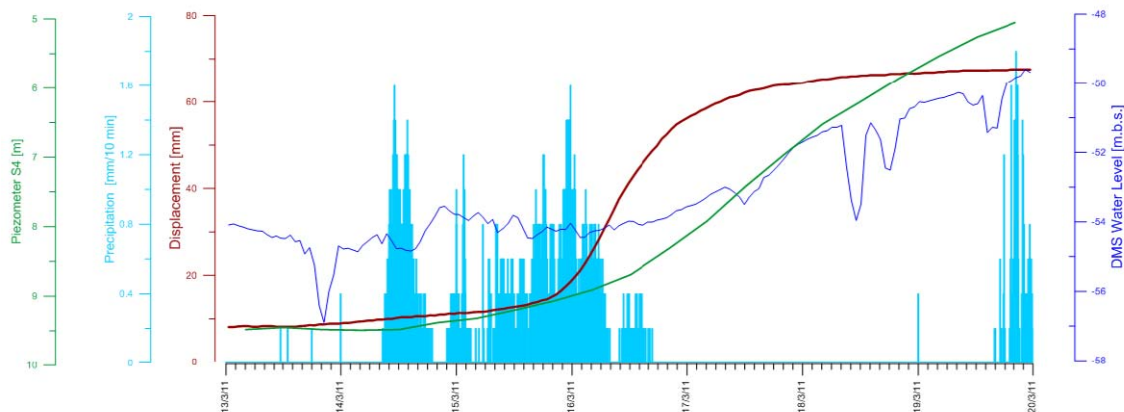


Figure 4.4-12. The “March 2011 event”: Graph of cumulative displacement (red), compared total 10 minutes precipitation (light blue), to groundwater level in DMS column (blue), and to water level registered at piezometer S4 (green) from March 13th-20th 2011.

4.4.3.4 Resistivity

The electrical monitoring (GEOMON^{4D}) system was installed in October 2010 along a west-east line downslope of the landslide (Figure 4.4-13). In the upper part, starting almost at drillhole S4 until 40 m after the midpoint of the array which was positioned close to the DMS system, the monitoring cables could be buried in a trench. However in the deeper parts down to the protection tunnel, the cables had to be fixed at the surface due to slope steepness. For power supply a combination of fuel cell and solar power is used. The profile consists of 93 electrodes at different spacing, varying from 1 m in the central part of the profile to 8 m in the outside sections, to derive high-resolution data in the middle around the DMS system without losing depth resolution. Every day, two datasets of high-resolution data from just the inner electrodes with a spacing of 1 m and two datasets involving all electrodes were measured. During the time of the March event, the measurement interval was increased to six measurements per day. Self-potential was measured hourly.

Figure 4.4-14 shows the correlation of resistivity layers with the dynamic pattern of the landslide. Layers with diverse displacement patterns are well delineated by bodies with different electrical properties. The shallow surface layer (thickness of approximately 10 m), which exhibits the highest displacement rate, shows a relatively low electrical resistivity below 250 Ohmm (colluvial and detrital deposits). It slides on a highly resistive, partly fractured Amphibolite body (500-5000 Ohmm), which exhibits an almost constant (with depth) creeping behaviour. At around 45 m of depth a layer with lower resistivity (below 350 Ohmm) can be detected, which might correlate with schist. This layer shows increasing displacements with altitude between 60 and 45 m. The low resistivity anomaly at depth in the middle of the profile is most probably an artefact produced by the steel casing of the DMS drillhole.

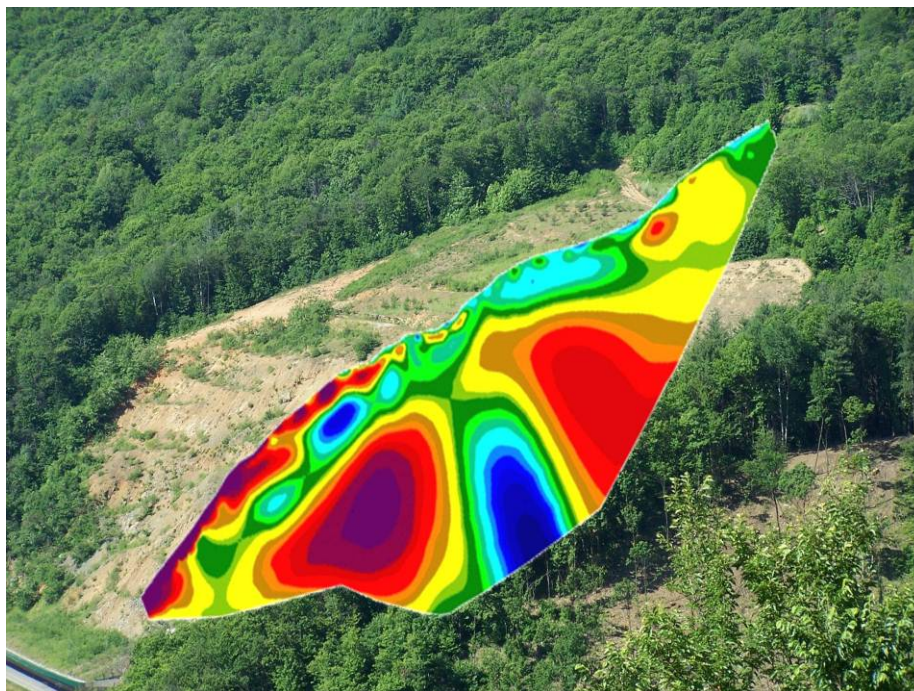


Figure 4.4-13. Position of the geoelectric monitoring line along the slope of the landslide of Bagnaschino.

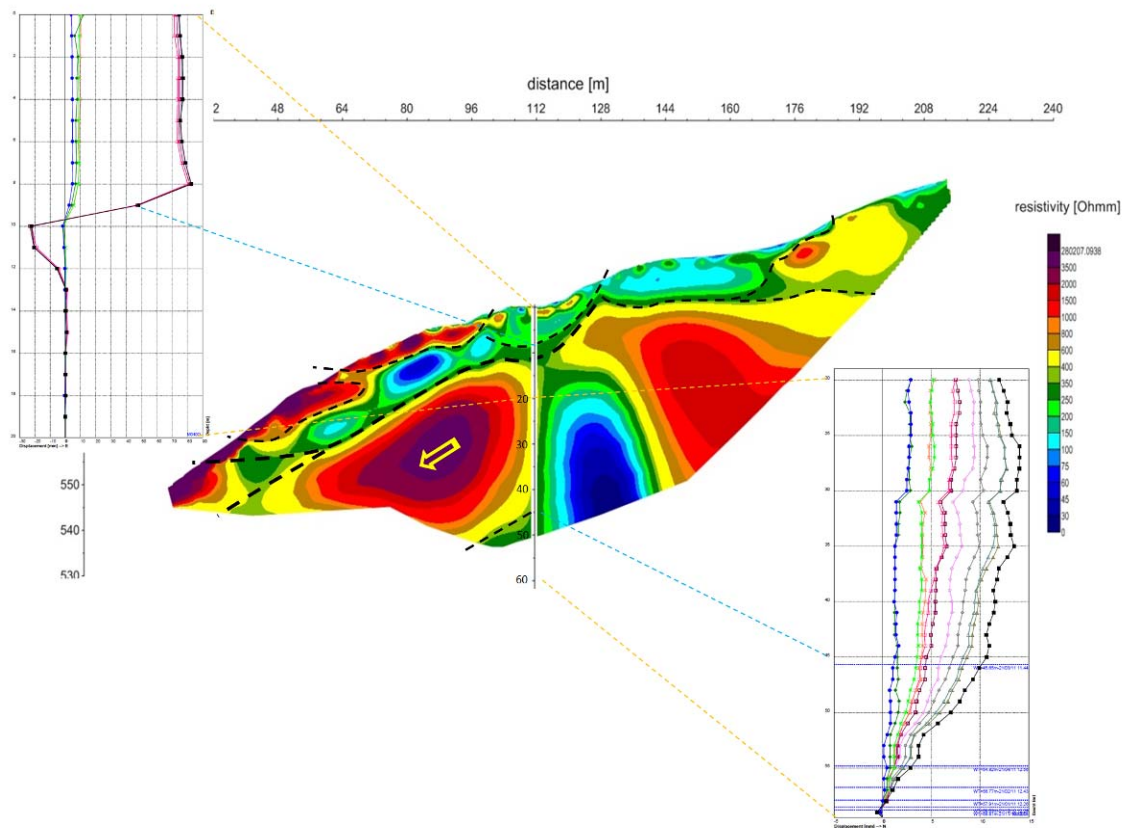


Figure 4.4-14. Correlation of resistivity layers with results of inclinometric monitoring

Figure 4.4-15 shows the results of the time lapse inversion of the geoelectrical data in the central section of the profile. At first a small isolated resistivity anomaly developed during the night between the 14th and 15th of March, most probably related to the first intense rainfall. The following night the major resistivity decrease took place in an area downslope of the DMS system, which well correlates with the period of the major acceleration phase. After that period no more significant resistivity changes took place. These results suggest that the area affected was mostly restricted to a region close to the DMS system, where the pore space of part of the subsurface colluvial and detrital deposits (Figure 4.4-16, Figure 4.4-2) was filled with water and consequently triggered a shallow landslide.

Therefore, the results of the geoelectric monitoring could contribute nicely to the understanding of the event since the DMS data provides only point data, which cannot be used to evaluate the general scenario of the event and its lateral impacts without supplementary information.

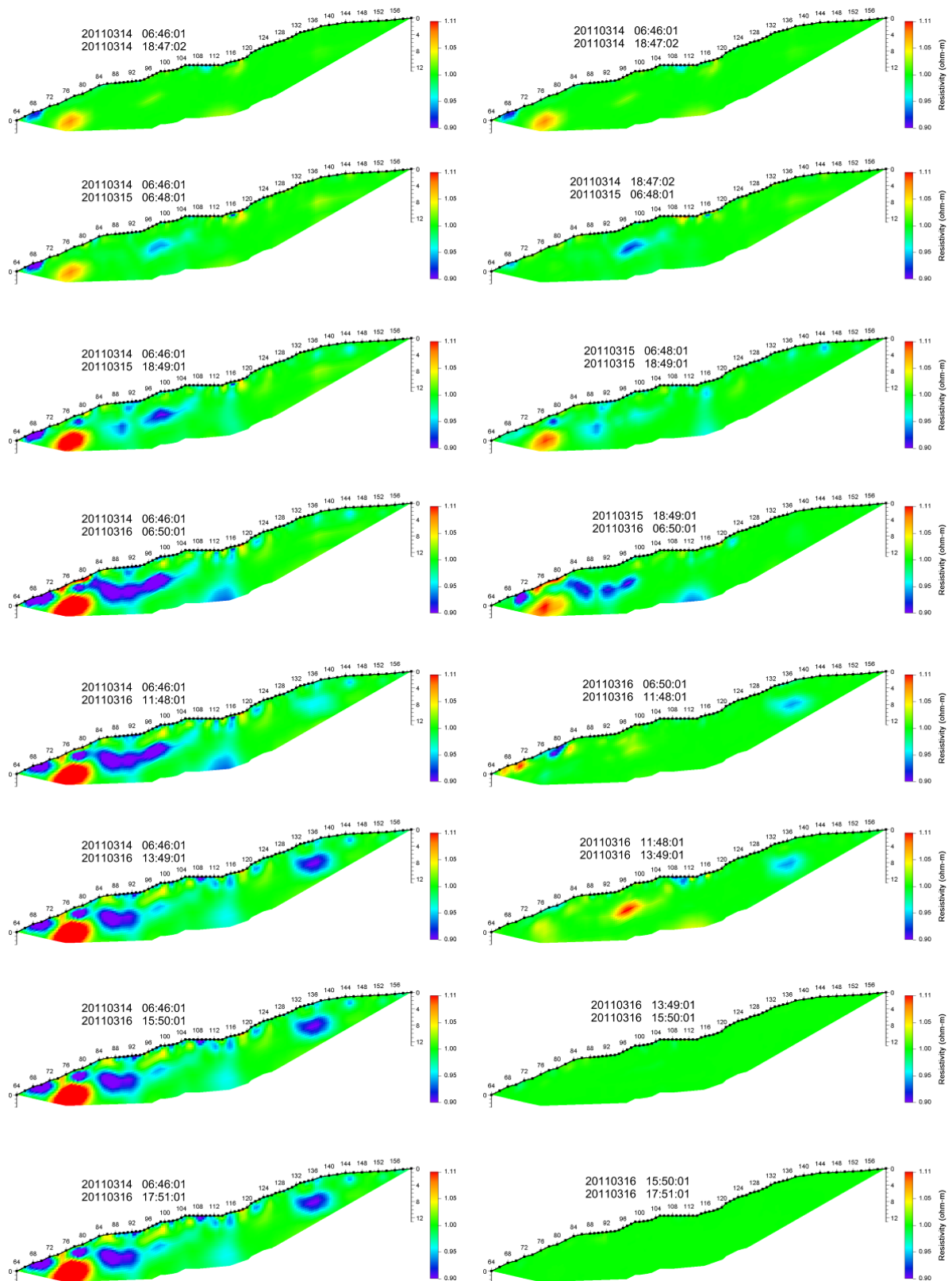


Figure 4.15. Results of time lapse inversion of geoelectrical data for the March 2011 event (left column: differences to one reference measurement; right column: incremental differences).

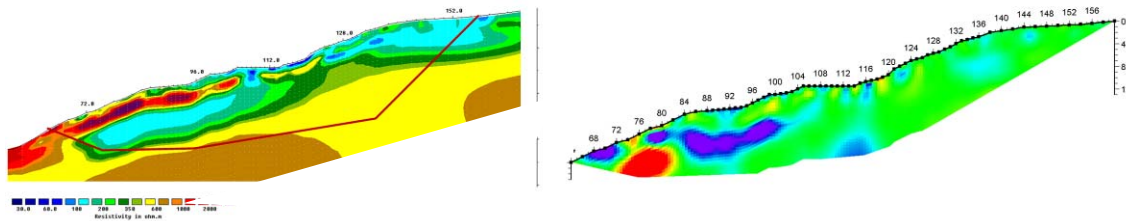


Figure 4.4-16. Comparison of results of geoelectric inversion (left) and time lapse inversion (right).

4.4.3.5 Soil temperature

Figure 4.4-17, Figure 4.4-18 and Figure 4.4-19 show the results of temperature monitoring over the entire survey period at different depths. From the upper part down to 8 m b.g.l. (Figure 4.4-17), mostly seasonal variation can be recognised, and the upper part (e.g. 2 m) in particular shows a sudden increase in temperature at the time the March event was detected. However, deeper recordings (below 9 m, Figure 4.4-18) show a slight decrease in temperature during the March event, suggesting an inflow of groundwater to the inclinometric pipe. Unfortunately no piezometer is available in this hole. Recordings of the deep DMS column (Figure 4.4-19) exhibit a very constant behaviour over time. Recorded variations are beyond the resolution of the sensors.

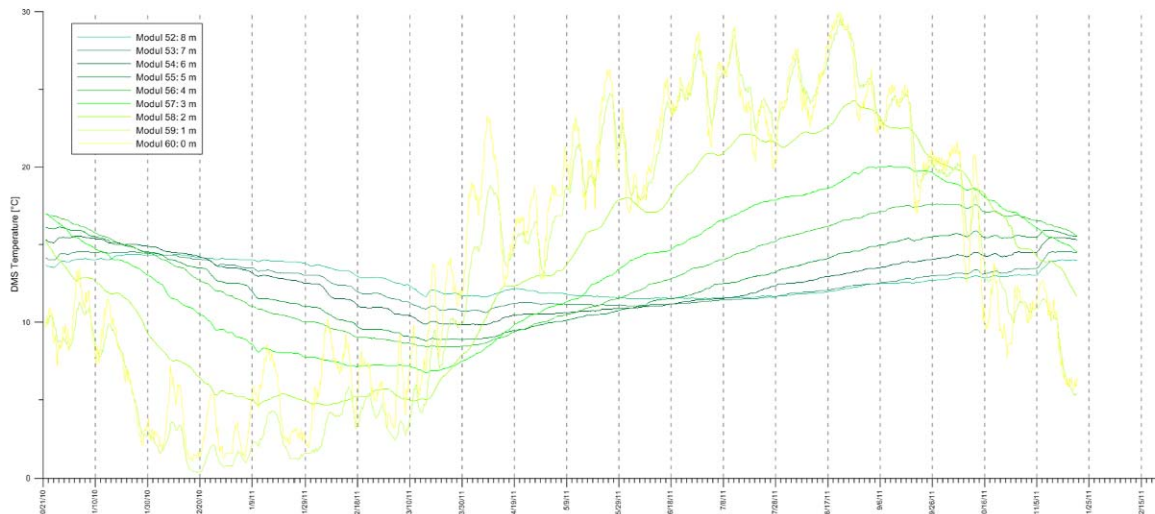


Figure 4.4-17. Results of temperature monitoring inside the DMS casing (shallow system, shallow depths).

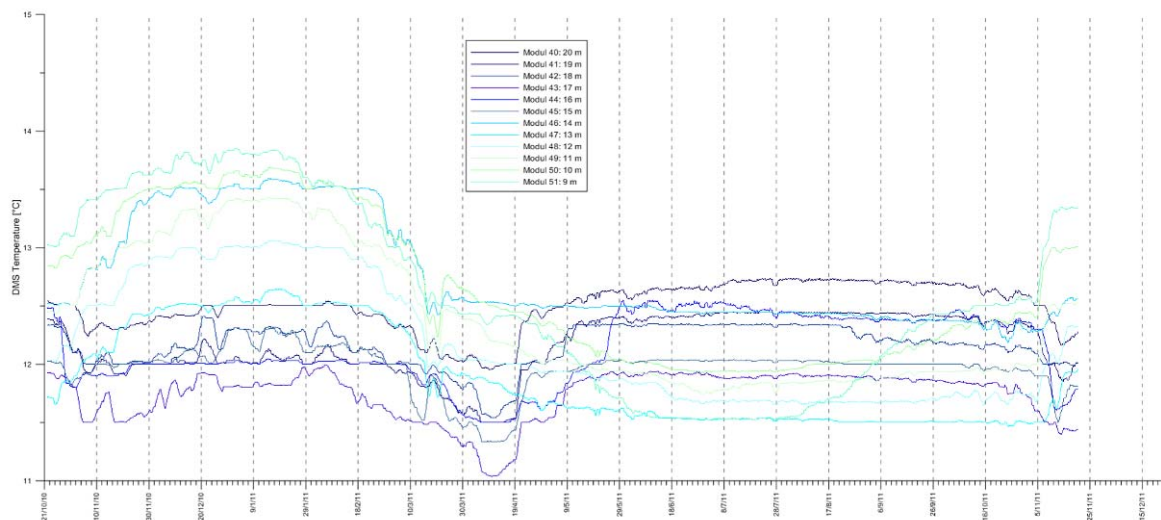


Figure 4.4-18. Results of temperature monitoring inside the DMS casing (shallow system, deeper depths).

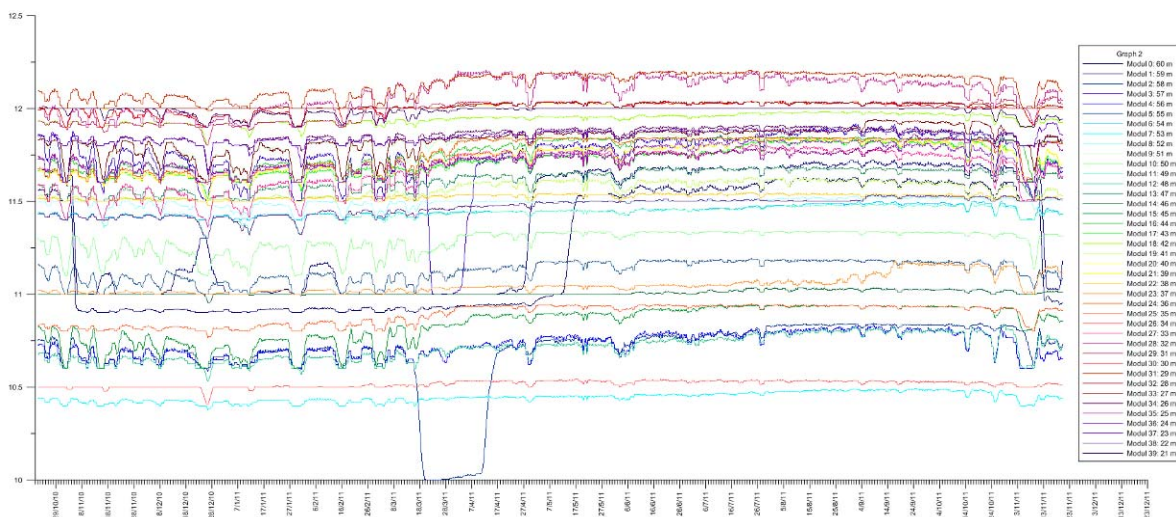


Figure 4.4-19. Results of temperature monitoring inside the DMS casing (deep system, all depths).

4.4.4 END-USER INVOLVEMENT AND ALARM CHAIN

Thanks to real time monitoring, detecting of displacements and their triggering events was possible, linking them to the rainfall events and evaluating the delay times. Moreover it was possible to calculate a site specific equation of rainfall thresholds for the initiation of the landslide.

The monitoring system significantly improved security of the traffic on the road at the landslide's toe and the Civil Protection interventions. E.g., based on the prompt monitoring results, the Province of Cuneo closed the road no. 164 on the day 13 /03/2011 with reopening the day 21 /03/2011, when the displacement stopped.

4.4.5 SUMMARIZED EVALUATION OF PARAMETERS

The analysis of data proved that all recorded events at this landslide were triggered by rainfalls. For the observation period 2008/2009 a correlation between instability and duration and quantity of rainfall could be seen. However, the quantity of displacement could not be explained by this relation. Subsequently, an analysis of the data from the survey period 2010/2011 suggested that the pre-wetting of the subsurface, evidenced by an increase in the groundwater table, also played an important role in triggering the landslide. However, no final conclusion could be derived since only one major event was recorded in the whole survey period. In any case the results highlight the necessity of displacement measurements being accompanied by the monitoring of other parameters (especially water level and geoelectrics). Otherwise, a reliable interpretation of the results and an estimation of possible further impacts, especially for early warning purposes, is very difficult. Geoelectrical monitoring definitely helped to extrapolate the results of local displacement monitoring to the larger area and to detect the processes involved.

References:

- Giuliani A., Bonetto S., Castagna S., Comina C. and Mandrone G. (2010): A Monitoring System for Mitigation Planning: The Case of “Bagnaschino” Landslide in Northern Italy. – *American Journal of Environmental Sciences* 6 (6): 516-522.
- Peisino V., Brunamonte F., Lampone F. (2009): Valutazione geologica e geotecnica del movimento franoso Sp 164 e definizione a livello di studio di fattibilità degli interventi tecnici da adottare: Fase 1 – Step Conoscitivo Generale. (geological Map, Geological Profile, Report) – MS. IG Ingegneria geotecnica, Final Report, Torino, Cuneo, Italy.

4.5 BINDO-CORTENOVA ROCKSLIDE (ITALY)

Giovanni B. Crosta, Federico Agliardi, Rosanna Sosio

University of Milano-Bicocca, Italy

ABSTRACT

A debris avalanche involving about 1.2 million m³ occurred in the Italian Prealps from the accumulation of a paleo-landslide. After the failure occurrence a monitoring network was installed, consisting of a series of optical targets, monitored every two hours through two total stations (Bindo, Val Rossiga) Leica TCA2003, three inclinometers and TDR cables, and three open-pipe piezometers instrumented with pressure transducers. In addition, a series of hydro-geophysical investigations including slug tests, electrical resistivity tomography (ERT) and tracing tests were performed on the landslide.

Field surveys and monitoring revealed that the upper part of the slope above the largest recent landslide is unstable with a possible failure volume of between 1 and 1.5 million m³.

The motion during the 2005-2009 period on the Bindo-CortenoVA slope has been modelled numerically by means of a 1D pseudo-dynamic visco-plastic approach, based on Perzyna's theory. The viscous nucleus in the 1D block model is assumed to be linear or non-linear, and the parameters are calibrated and compared to laboratory-determined properties. Geo-mechanical, geo-morphologic and piezometric data have been used as input data. Ground-based displacements have been used to calibrate and validate the model on a long temporal series (2004-2010) and it demonstrated a high reliability.

Presented parameters: displacement, velocity, groundwater level, precipitation, temperature, resistivity.

4.5.1 GENERAL DESCRIPTION OF THE TEST SITE

The Bindo-CortenoVA landslide is a 1.2 km wide translational landslide situated east of Lake Como (Valsassina, Lecco, Lombardy region, Italy). The site is characterized by a large and active slope failure occurring in a Permian conglomerate formation (Crosta et al., 2004). The sliding material is formed by very large conglomeratic rock blocks, up to 100 metres in size, immersed in a gravely sand matrix.

The area is characterised by a pre-alpine landscape with a maximum elevation of 3000 m a.s.l. The study area lies within the Monte Muggio tectono-metamorphic unit (greenschists), which is unconformably overlain by the sedimentary cover represented by the terrigenous Permian-Anisic rocks (Verrucano Lombardo). Basement rocks are meta-pelites (paragneiss, mica schist, phyllites) and orthogneiss (Gneiss Chiari del Corno Stella) pertaining to the Gneiss di Morbegno unit. These basement rocks are intruded by a series of quartz-dioritic bodies (Val Biandino Granodiorite, Cortabbio Diorite) whereas a granitic mass outcrops close to the landslide site in CortenoVA (Val Biagio Granite). The Verrucano Lombardo (Upper Permian) formation is formed by reddish conglomerates and coarse-grained sandstones. It forms a 100 m thick unit in the CortenoVA area with a slight eastward increase in thickness. From a structural point of view the study area has peculiar features, being at the western closure of the E-W trending Orobic Anticline, locally oriented to the NW (Figure 4.5-1) and placed to the S of the Orobic thrust, and separated from the Grigna unit (Triassic) to the west by the N-W trending Valsassina fault.

Fieldwork revealed that the entire slope above the Bindo Cortenova village is unstable and has the potential to fail in the future (Figure 4.5–2). The possible failure volume may reach as high as 1.5 million m³. The unstable area covers 1.2 km² and extends between 450 and 1200 m a.s.l., where a large subvertical rocky scarp up to 80 m high is visible (Ambrosi and Crosta, 2003).

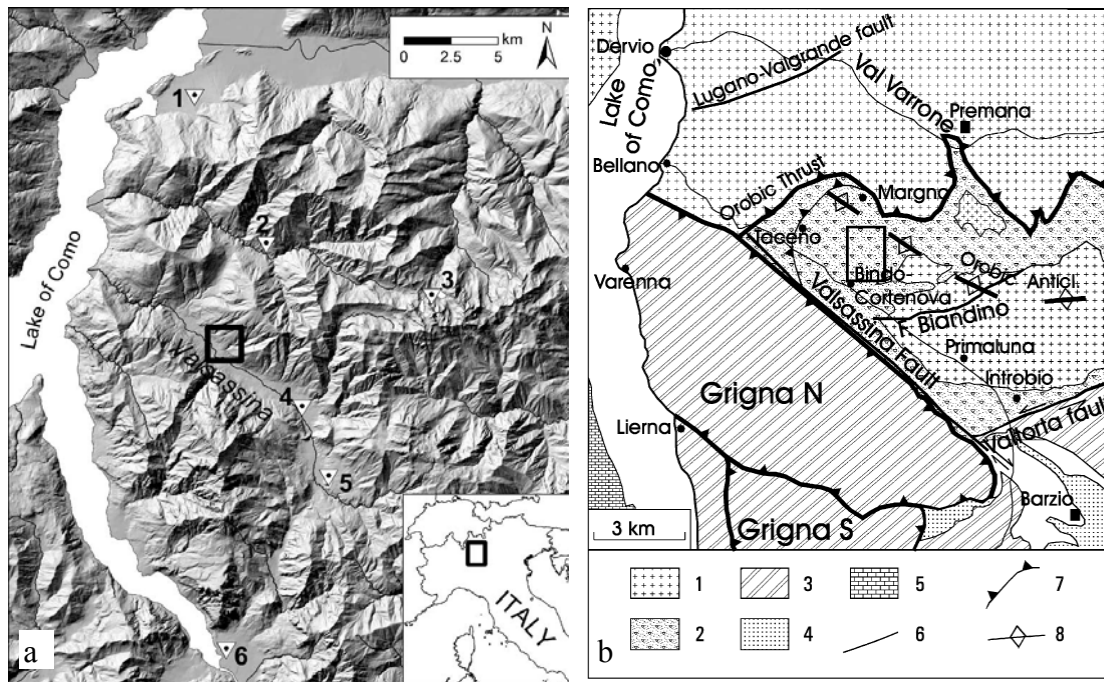


Figure 4.5–1. a) Location map and b) geological sketch of the Cortenova rockslide.

Some major landslide scarps have been mapped within the old landslide accumulation at about 700, 800, 975 and 1100 m a.s.l. with an estimated dip slip displacement of 10 to 20 m along each of them. The old landslide accumulation is limited on two sides by secondary NE–SW trending valleys (S. Biagio and Rossiga valleys) incised into the bedrock. The accumulation presents large blocks of Verrucano Lombardo, opened by NW–SE trending deep and large fractures, immersed in a sandy gravel matrix. The geological controls on the landslide complex include the lithological contact between the metamorphic–igneous rocks and the Permian conglomerates (Verrucano Lombardo, Figure 4.5–1B), the fracture intensity in the conglomerate, and the dip slope attitude of the tectonic contact at an average angle of 17° to the SW. The average thickness of the conglomerate debris ranges locally between 35 and 65 m and the piezometric levels lie above these depths. Groundwater was collected into an aqueduct at different points along the toe of the slope at elevations between 460 and 500 m a.s.l. Various small landslide activations (on June 1987, November 2000, and May 2001) of 1000 m³ of material took place at the slope toe.

The toe of the slope underwent a catastrophic failure (Crosta et al., 2004) in December 2002 after a long period of extremely heavy rainfall (up to 850 mm in 14 days while the annual rainfall is 1500–2000 mm/year). The landslide involved about 1 to 1.2 million m³ of debris and disconnected rock mass from the toe of the relict landslide, covering a slope sector of about 85,000 m². The mass spreads over an area of about 65,000 m² beyond the slope toe with a thickness of about 5–20 m. The maximum runout distance is estimated as 260 m away from the original slide toe.

The instability evolution has been monitored since 2003. Slow sliding movements (about 200 mm/year on average) are still affecting the slope (about 1 km in length, from the 2004 event crown to the main scarp at 1250 m a.s.l. Le Gronde in Figure 4.5–1; mean slope angle $\alpha = 28^\circ$) on a 30 to 50 m deep slip surface. In May 2004, a second event caused a new collapse ($0.2 \cdot 10^6 \text{ m}^3$) that involved the crown of the previous rockslide and stepped over the 2002 deposit. It affected part of the installed monitoring network. The failure was triggered by a period of heavy rainfall (175 mm in seven days).

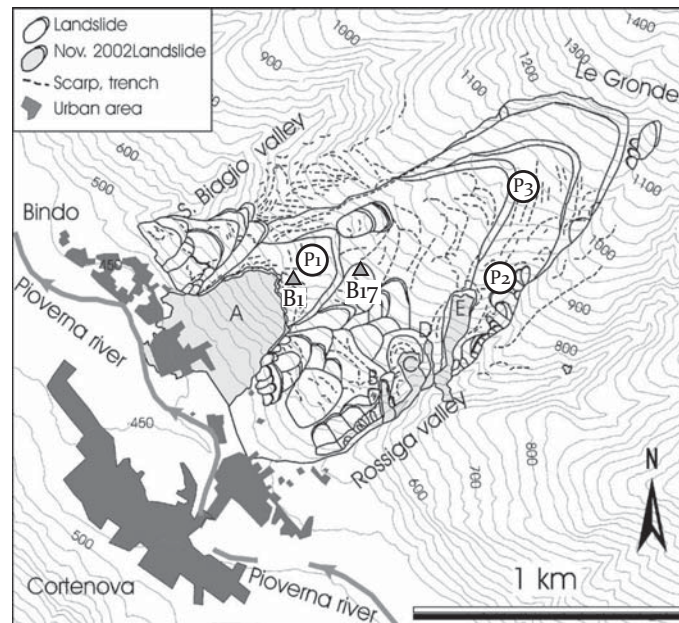


Figure 4.5–2. Bindo-CortenoVA failure (2004 event, Zone A) and unstable area (black lines, up to Le Gronde). Piezometers are specified by the points P1, P2, P3 while the two considered optic devices by B1 and B17.

4.5.2 DESIGN OF THE MONITORING NETWORK

An in-situ monitoring system has been in operation since May 2003. Figure 4.5–3 shows the location of the instruments, consisting of a series of optical targets monitored every two hours through two total stations (Bindo, Val Rossiga) Leica TCA2003, three inclinometers and TDR cables, and three open-pipe piezometers instrumented with pressure transducers.

- The optical targets are sited all along the crown of the previous failures and in the slope, which remains unstable.
- The piezometers are located (1) at the crown of the 2002 rockslide event, (2) in the unstable slope, at an altitude of 950 m and (3) in a sector sloping toward the Rossiga Valley, which has already been intersected with diffuse instability of the debris cover. They provide data every four to six hours.
- The inclinometers are close to the piezometers and their records have been considered to determine the depth and thickness of the sliding surface (on average 38 m and 0.3 m, respectively).
- Four GPS stations which are not operating anymore due to problems in data transmission.



Figure 4.5–3. Aerial view of the Bindo-Cortanova rockslide, showing the main failure occurring in December 2002 and the location of optical targets.

Daily rainfall data are available from two rain gauge stations situated at the toe of the slope and 10 km southeast.

4.5.3 ANALYSIS OF MONITORING DATA

4.5.3.1 Rainfall

The average annual precipitation in the study area can be considered relevant, ranging between 1300 and 2100 mm with most of the amount (40-50 %) recorded during the summer season. On average, the most intensive rainfall season is in May with the average monthly precipitations between 160 and 190 mm. Nevertheless, November 2002 was one of the higher precipitation periods with 493 up to 875 mm of measured cumulative rainfall. The maximum daily rainfall reached 200 mm along the Orobian divide and 140 mm at the rain gauge closest to the Bindo–Cortanova area. Two major rainfall events occurred in 15 days with a short interval of lower precipitations, and only one day without precipitation. Return times range from 100 to 200 years for seven to 15 days of rainfall.

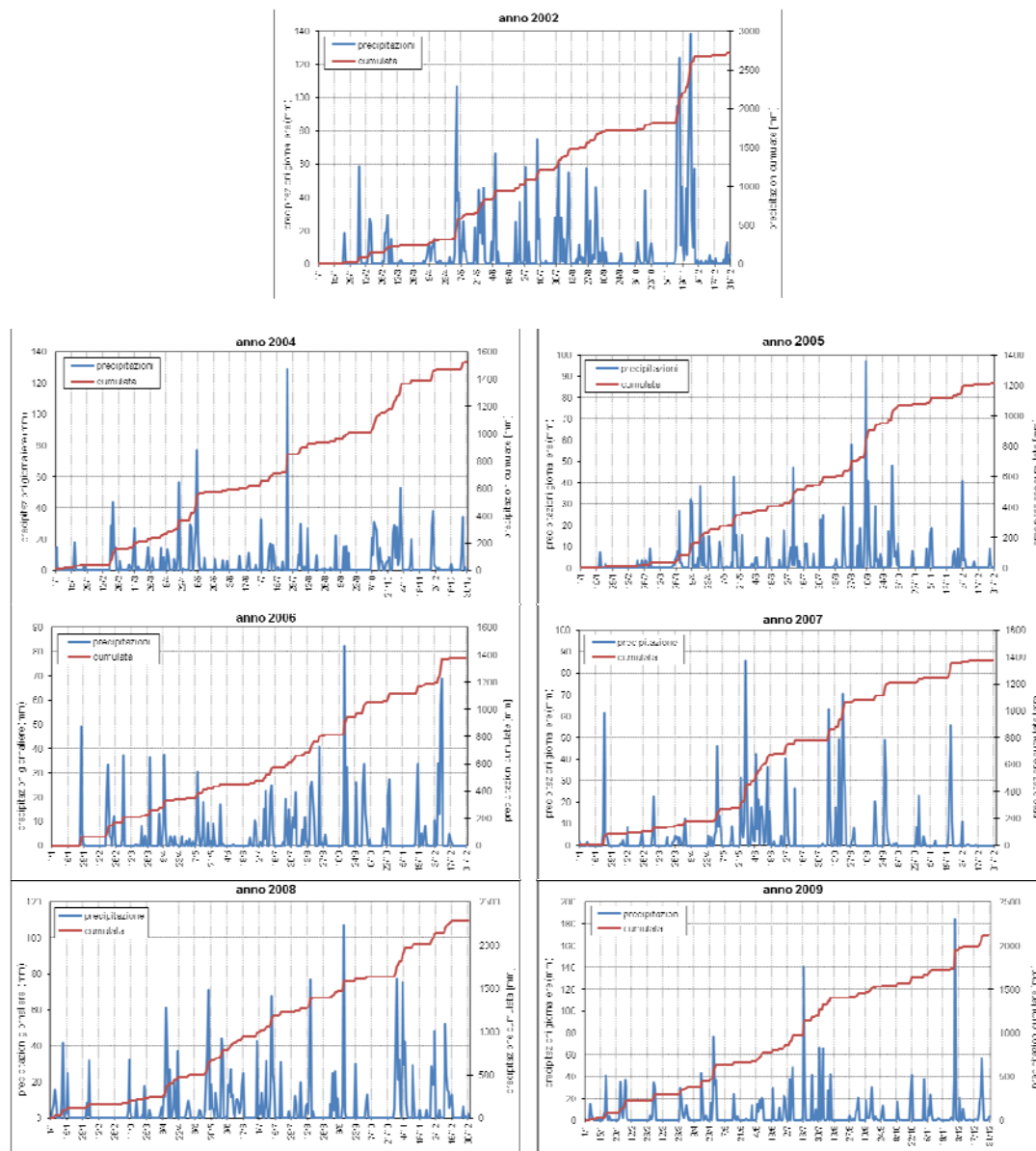


Figure 4.5-4. Rainfall records for different years. Note the exceptional rainy period that occurred in November 2002, which preceded the Bindo-Cortenova landslide.

4.5.3.2 Water table

The water level follows the rainfall trend, and the melting and evapotranspiration processes, showing minimum values during the winter period. The water level rises during the spring and then it decreases during summer. The water table level ranges between 4.0-5.0 (winter) and 4.7-7.0 (spring and autumn).

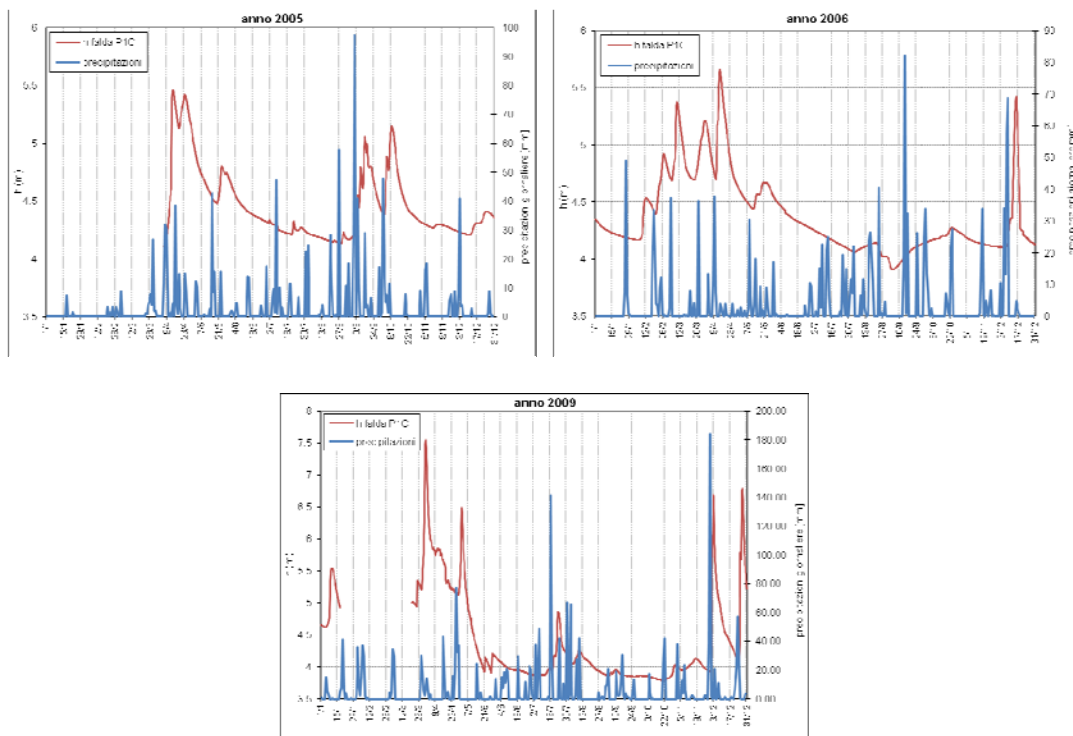


Figure 4.5–5. Water table records for different years. Note that the maximum levels are recorded during the spring season.

4.5.3.3 Geophysical investigations

A series of hydro-geophysical investigations including slug tests, electrical resistivity tomography (ERT) and tracing tests were performed on the Bindo landslide. Time lapse ERT surveys were carried out (over 40 days) during a 15-day water infiltration test (100 m³) along two longitudinal downhill profiles of different lengths (approximately 72 m and 212 m), and at different resolutions (48 channels, 1.5 m and 4.5 m electrodes offset). The freshwater and tracer injections (fluorescein) lasted seven days each. One borehole fluorometer was installed 600 m downhill from the injection point, and measurements have been done periodically at 13 springs at the slope toe.

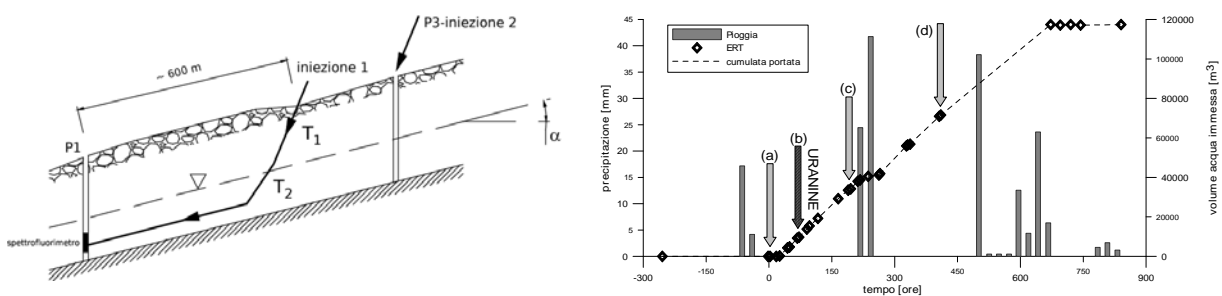


Figure 4.5–6. (A) Spectrofluorimeter monitoring scheme and (A) Plot of the main investigations (infiltration, tracer tests, ERT) performed on the Bindo-Cortenoia landslide.

Permeability values have been obtained, heterogeneities (e.g. large blocks or voids) have been recognized at different scales, flow paths identified and the change in moisture content mapped both during the saturation/infiltration and the draining phase (Figure 4.5–6).

Seismic refraction and electrical tomography surveys were carried out to define the 3D contact between the landslide material and the igneous-metamorphic bedrock, to follow infiltration and tracer tests (Figure 4.5–7) aimed at analyzing groundwater recharge and flow within the landslide, and to understand the correlation between measured displacements and rainfall.

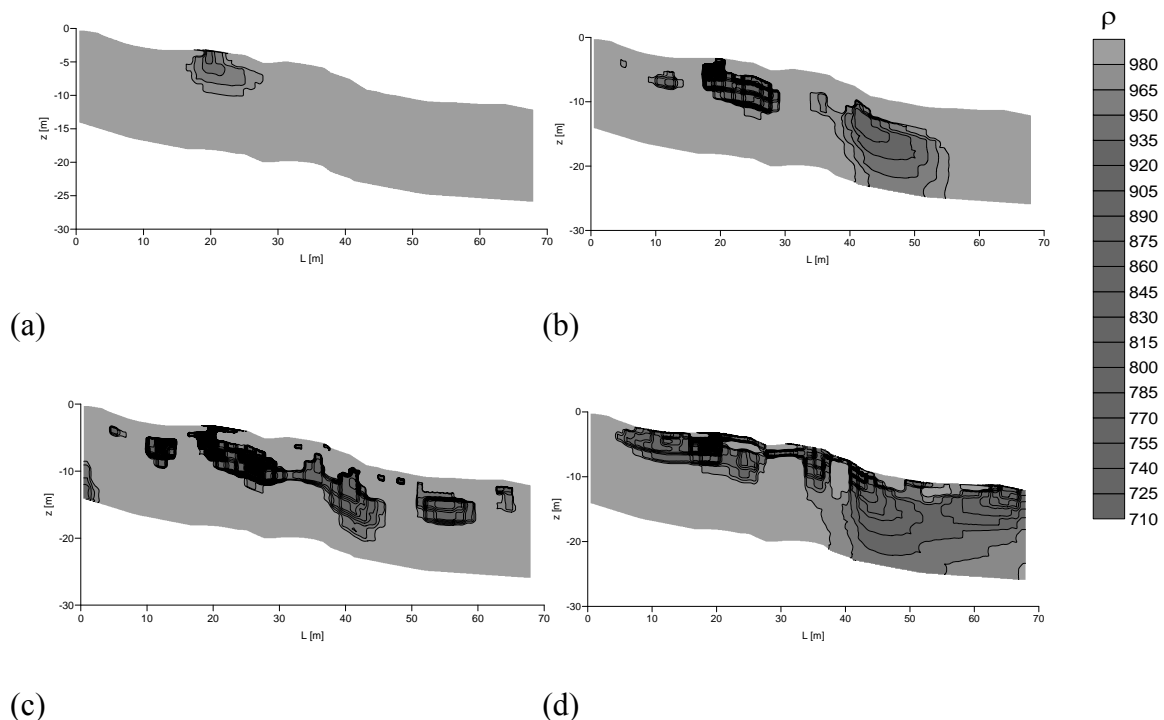


Figure 4.5–7. (A) and (B) resistivity sections ($[\rho]=\Omega\cdot m$) at different timings, with punctual injection of known water amounts; (C) and (D) after the tracer injection.

4.5.3.4 Displacements

The on-site displacement data show that the system is characterised by time-dependent behaviour and it is dominated both by dynamic/inertial and viscous effects. This means that the beginning of slope movements and the stress increment are not simultaneous but are described by different time intervals (dynamic/inertial effect). The slope movements evolve after the end of the load increment (viscous effect). Thus, a visco-plastic constitutive model is needed to simulate the visco-plasticity and a pseudo-dynamic contribute must also be introduced. Figure 4.5–8 illustrates a typical event where it is possible to verify both the dynamic-inertial effects and the highly viscous mechanical response of the slope. The slope motion starts six days after the increase in water table elevation, and the system continues to accelerate after the peak in water level. This suggests that the deformative reaction is delayed in time and is not instantaneous.

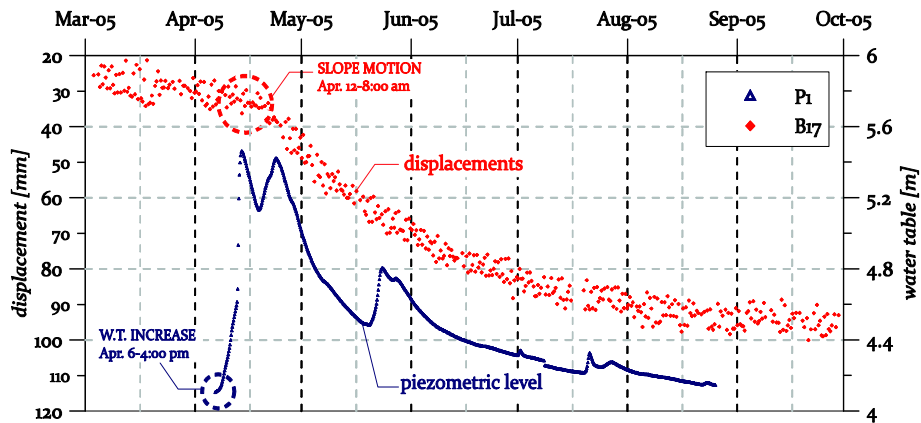


Figure 4.5–8. The landslide (red) starts accelerating six days after the water table rise (blue), and the slope motion continues after the piezometric level has reached the asymptotic level.

Figure 4.5–9 presents a comparison between the variation of the water table at P1 since 2005 and the displacements recorded by two optical targets located close to P1. The data show displacements which are periodical and follow every increase in the water table that induce the process of slope failure. The maximum cumulative displacement recorded since 2003 is about 2 mm (optical targets DB5 e DB11).

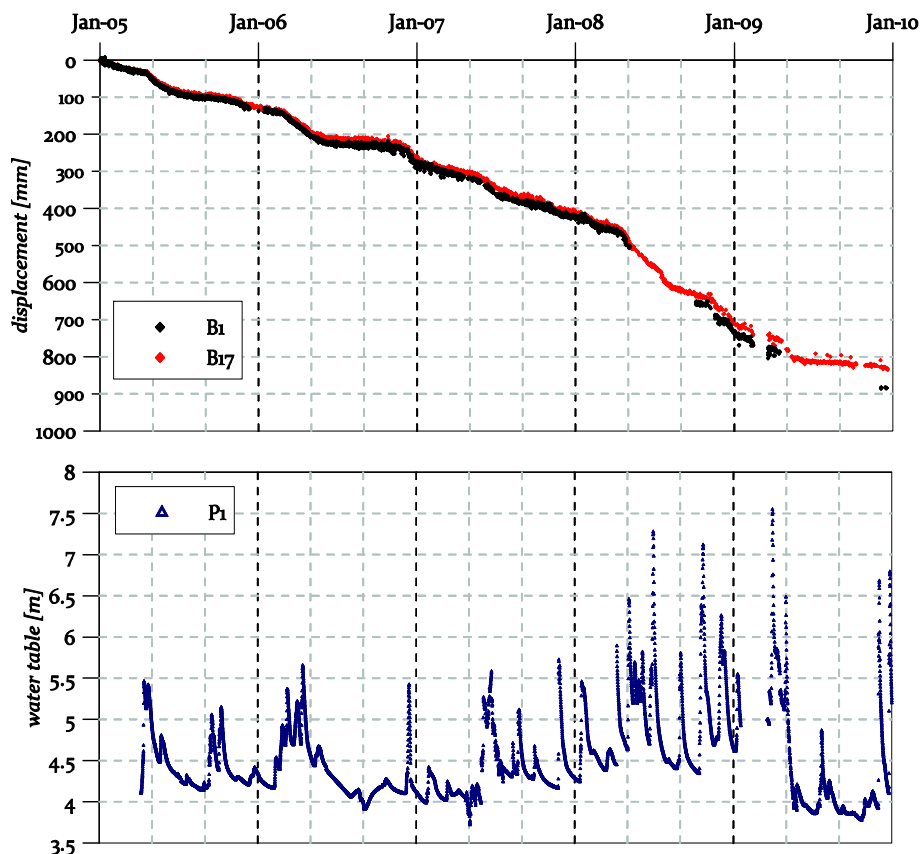


Figure 4.5–9. Displacements at B1 and B17 and groundwater level oscillation at P1 (see Figure 4.5–1), from January 2005 to December 2009.

The Newmark approach (Newmark, 1965) is adopted to determine the displacements for the Bindo-Cortanova landslide. It allows (i) to model a pseudo-dynamic system, taking into account the "time" factor by introducing the acceleration term in the expression of the mobilising shear resistance and (ii) to introduce a visco-plastic deformation by means of constitutive modelling (Perzyna, 1963). Moreover, the Mohr-Coulomb failure criteria is adopted to determine shear resistance.

According to the Newmark theory, the standard plastic flow rule is modified and the consistency condition abolished. Therefore, the visco-plastic strain rate tensor $\dot{\varepsilon}_{ij}^{vp}$ is defined as follows:

$$\dot{\varepsilon}_{ij}^{vp} = \gamma \cdot \phi(f) \cdot \frac{\partial g}{\partial \sigma'_{ij}} \quad 1$$

where f is the yield function, g the plastic potential, γ a constitutive parameter, σ'_{ij} the effective stress tensor and $\phi(f)$ the viscous nucleus. To evaluate the rate of visco-plastic deformations and, hence, the displacements, many different analytic expressions for the viscous nucleus can be naturally introduced. In order to reproduce the monitored deformations of a translational landslide, we present hereafter a 1D visco-plastic pseudo-dynamic model based on the Perzyna's constitutive relationship (Secondi et al., 2011).

For the case of the Bindo-Cortanova landslide the elastic deformation can be neglected, and the rate in angular deformation $\dot{\gamma}$ is assumed to be sufficient for describing the slope mechanical behaviour, reducing the problem to 1D. Dilatancy is also neglected as a residual strength condition is considered for the slope (the shear band is assumed at a steady state). Hence, no displacements normal to the sliding surface have to be taken into account and the system can be modelled as 1D. Eq.1 becomes:

$$\dot{\gamma}_{ij}^{vp} = \frac{\tilde{\gamma}}{p'} \cdot \phi(f) \quad 2$$

where $\tilde{\gamma}$ is a viscous constitutive parameter (calibrated on experimental data or by means of back analyses), $\dot{\gamma}$ a function of the axial deformation rate \dot{x} and of the shear band thickness Δs , and p' the isotropic pressure:

$$\dot{\gamma} = \frac{\dot{x}}{\Delta s} ; p' = \frac{\sigma'_v + 2\sigma'_h}{3} \quad 3$$

The $\phi(f)$ function directly governs the modulus of $\dot{\gamma}^{vp}$, thus no consistency law is needed and the stress state can violate condition $f \leq 0$. Irreversible deformations can evolve for any value of the f function. As described by Eq. 3, visco-plastic deformations can occur even without any load increment. The $\tilde{\gamma}$ constitutive parameter represents the velocity through which the system evolves and reaches the asymptotic value of deformation. In Eq.3 hardening or softening are neglected. Either the shape or the dimension of the yield surface is constant during the irreversible visco-plastic deformation.

To evaluate the rate of visco-plastic deformations and, hence, of the slope displacements, an analytic expression for the viscous nucleus $\phi(f)$ must be assigned. The $\phi(f)$ function describes the evolution of visco-plastic deformation; it always satisfies the following condition:

$$\frac{d\phi}{df} \geq 0 \quad 4$$

A simple formulation for the viscous nucleus is the bi-linear: the deformative behaviour of the slope is different if the stress state lies inside or outside the plastic surface (Figure 4.5–10).

Two parameters $\tilde{\gamma}_1$ ($f > 0$) and $\tilde{\gamma}_2$ ($f \leq 0$) must be introduced:

$$\begin{aligned} \dot{\gamma}_{ij}^{vp} &= y' + \frac{\tilde{\gamma}_1}{p'} \cdot f \text{ if } f > 0 \\ \dot{\gamma}_{ij}^{vp} &= y' + \frac{\tilde{\gamma}_2}{p'} \cdot f \text{ if } f \leq 0 \end{aligned} \quad 5$$

where the $\tilde{\gamma}_i$ replaces $\tilde{\gamma}$ of Eq. 3 and y' is a new constant parameter. The latter identifies the velocity value in x-direction when $f=0$.

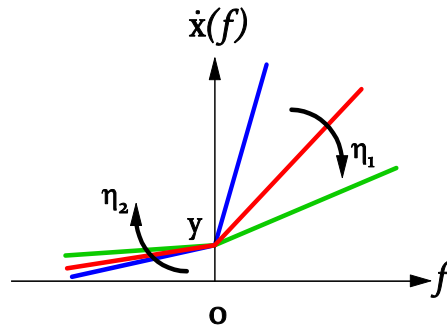


Figure 4.5–10. Rate of axial deformation as a function of the parameters of viscosity η_1 and η_2 .

The f function can be put in an explicit form:

$$f = \tau - \tau_{res} \quad 6$$

where τ represents the effective shear stress and τ_{res} the yield threshold (depending on the failure criterion adopted). As dynamic and inertial effects must be taken into account, the effective shear stress is composed both by the static term τ_{stat} (weight of the masses acting on the system), and a dynamic one (depending on the acceleration in the x-direction and on the masses per unit area m^*):

$$\tau = \tau_{stat} - m^* \ddot{x} \quad 7$$

By substituting Eq.4, 6 and 7 into Eq. 5 and by introducing the parameters in Eq.8:

$$\begin{cases} y = y' \cdot \Delta s \\ \eta_i = \frac{p'}{\Delta s \cdot \gamma_i} \quad i = 1, 2 \end{cases} \quad 8$$

the following expression for x-acceleration can be obtained (where $i=1$ if $f > 0$, or $i=2$ if $f \leq 0$):

$$10^{-3} \cdot m^* \ddot{x} + \eta_i \dot{x} = \eta_i y + (\tau_{stat} - \tau_{res}) \quad 9$$

As is shown in Figure 4.5–10, when the stress state lies outside the plastic surface ($f > 0$), an increase in η_1 brings a decrease in the visco-plastic deformations. The opposite occurs when $f \leq 0$.

The limit equilibrium approaches usually suppose a rigid perfectly plastic behaviour for the slope. This leads to the conclusion that the deformations start only after the failure condition is reached. If the failure criterion is satisfied, the shear resistance can be considered as constant and not depending on the accumulated displacements. Then, in a limit equilibrium condition, the resistance on the shear band is not influenced by the slope movements and can be considered as constant (and equal to shear resistance).

Within the same framework, in order to introduce a dependence on the time factor, the Newmark pseudo-dynamic approach (Newmark, 1965) can be used. This model allows introducing the acceleration term as shown in Eq.6. By means of a finite difference method, Eq.9 can be solved in terms of both velocity and displacements for the landslide considered. The slope is still considered as a non-deformable mass subjected to a translational motion on a stable-rigid layer. In contrast with a classical limit equilibrium approach, the acting forces can be either higher or smaller than the constant resisting forces, depending on the magnitude of load increment (e.g. water table oscillations). The higher the difference between acting and resisting forces, the higher the velocity of the system. As pseudo-ductile mechanical behaviour is introduced when the limit equilibrium conditions are reached, irreversible deformations can always occur.

The Newmark approach considers the slope as a rigid block placed in the centre of mass. When applying the approach to the Bindo-Cortanova landslide, as the available monitoring system data are referred to the toe of the landslide (zone A in Figure 4.5–1), the equations of the model must be modified and an active force S_A (divided by the total contact area) must be added.

$$\tau_{stat} = W' [h(t)] \cdot \sin \alpha + J + S_A \quad 10$$

where W' is the immersed weight divided by the total contact area, J the seepage force divided by the total contact area, and $h(t)$ the water table level (as a function of time t).

In order to solve Eq.9, a Mohr-Coulomb failure criterion is introduced. As the slope considered is characterised by slow movements inducing irreversible deformations due to post-failure conditions, a residual friction angle ϕ'_{res} is used:

$$\tau_{res} = N'^* \tan \phi'_{res} \quad 11$$

where N'^* is the effective force normal to the sliding plane divided by the total contact area.

By substituting Eqs.10 and 11 into Eq.9, and by means of a classical finite difference integration scheme (both for $f > 0$ and $f \leq 0$), it is possible to simulate the displacements for the slope.

The motion acting during the 2005-2009 period on the Bindo-Cortanova slope has been modelled numerically. Geo-mechanical (residual friction angle, dry and saturated unit weights), geo-morphologic (slope angle, landslide length, shear band width and depth) and piezometric data (historical series of water table oscillations) have been used as input data. Ground-based displacements have been used to calibrate/validate the set of viscous constitutive parameters (η_1 , η_2 and γ).

Laboratory tests, carried out on samples recovered at the failure surface, provided the following geomechanical parameters: saturated unit weight $g_{sat} = 19.01 \text{ kN/m}^3$, cohesion $c' = 0$

kPa, residual and peak friction angles $\phi'_{res}=33.9^\circ$ and $\phi'=36^\circ$. Friction angle values were obtained by means of load and displacement controlled triaxial creep tests. The pressure p' , acting at the depth of the sliding surface (38 m), has been evaluated considering a value of the mean piezometric level of 4.47 m (2005-2009 period) above the failure surface. Rheometer tests were also carried out to investigate the viscous mechanical behaviour of the material involved at different water contents.

Optical targets B1 and B17 (Figure 4.5–1) were used to calibrate and validate the model presented, since they are located close to piezometer P1 and thus their data can be directly correlated to water table level data. The used dataset consists of six to twelve daily readings on a five-year time span (from January 2005 to December 2009) for which both groundwater level and displacements are available.

Various calibrations of the viscous parameters (γ , η_1 and η_2), based on different yearly datasets have been compared. Here we present the best results in terms of modelled displacements.

The slope behaviour must be defined under three different mechanical conditions (stress state outside, $f>0$, inside $f<0$, or on the f surface, $f=0$), leading to the necessity for three different calibrations.

The same event has been also used to calibrate the η_2 parameter (Table). As the displacement velocity $\dot{x}(f)$ is always linear (Figure 4.5–10), it is not necessary to define how much the stress state exceeds condition $f=0$. The η_1 ($f>0$) parameter has been evaluated using the data available between April and September 2005. During this time period an extremely regular oscillation in the water table has been observed (Figure 4.5–11-green rectangle). The piezometric level always exceeds its equilibrium level (4.47 m). Hence τ always exceeds τ_{res} and then $f>0$.

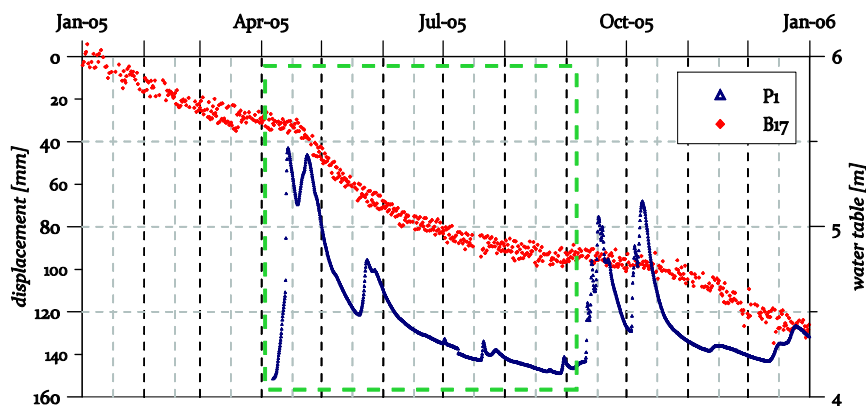


Figure 4.5–11. 2005 dataset and (green rectangle) 6/04 – 10/09 event, used to calibrate η_1 parameter.

The γ parameter (corresponding to the velocity in a limit equilibrium condition, $f=0$) has been calibrated by means of the event illustrated in Figure 4.5–12 (green dashed box), characterised by a piezometric level equal to the equilibrium level. The value of the rate of displacement in this condition corresponds to the γ parameter.

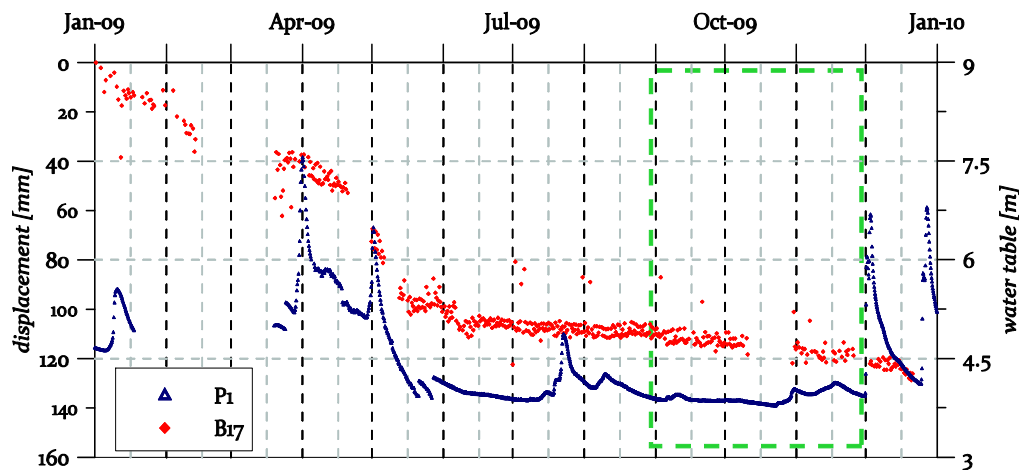


Figure 4.5–12. 2009 dataset and (green rectangle) 27/08 – 30/11 event, used to calibrate γ parameter.

Table 4.5–1 - Viscous nucleus parameters.

Calibrated viscous nucleus parameters			
γ [m/s]	$1.44 \cdot 10^{-9}$	γ' [1/s]	$7.79 \cdot 10^{-9}$
η_1 [kPa·s/m]	$5.06 \cdot 10^8$	$\tilde{\gamma}_1$ [1/s]	$2.05 \cdot 10^{-6}$
η_2 [kPa·s/m]	$4.00 \cdot 10^9$	$\tilde{\gamma}_2$ [1/s]	$3.17 \cdot 10^{-7}$

Figure 4.5–13 illustrates a comparison between predicted and measured displacements at point B17, using the pseudo-linear viscous nucleus. The model predictions fit the monitored data quite well. Note that the adopted residual friction angle was not calibrated by means of back analysis, but measured by means of standard triaxial compression tests. The viscosity parameters were calibrated on small-scale rheometer tests (Frigerio, 2010) and only the shear band thickness (0.3 m) was derived by back analysis.

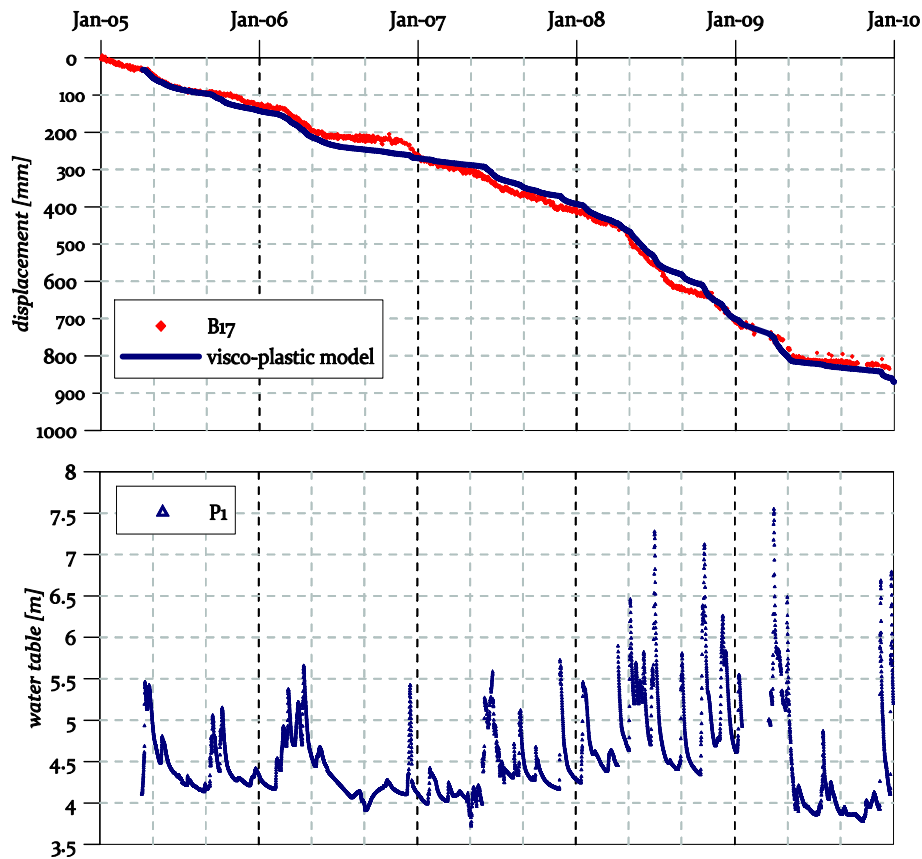


Figure 4.5–13. Measured and predicted displacements obtained by using the previously discussed approach.

4.5.4 SUMMARIZED EVALUATION OF PARAMETERS

The 2002 Bindo-Cortanova landslide is among the most hazardous slope failure events that have recently occurred in Italy. Field surveys and monitoring revealed that the upper part of the slope above the largest recent landslide is unstable with a possible failure volume between 1 and 1.5 million m³. The unstable paleo-landslide has been monitored since 2003, while geophysical and hydrological analyses provided permeability and heterogeneities (e.g. large blocks or voids) at different scales and flow paths. The recorded data have been used to numerically reproduce the slow motion of slides. A visco-plastic constitutive modelling approach has been adopted and was coupled with a pseudo-dynamic Newmark model, to take into account the inertial effects. A pseudo-linear formulation for the viscous nucleus has been adopted. The proposed model is capable of reproducing quite satisfactorily the dataset of displacements concerning the Bindo-Cortanova case study over a long period of time (about five years).

Future efforts are directed at developing the method to include the effects of multiple sliding blocks to simulate the progressive acceleration and/or deceleration of different landslide sectors as influenced by groundwater pressures changing along the slope, or their inertial effects. The development of a simplified hydrological model to simulate the groundwater response to rainfall or snow melting events could be implemented for improving the forecasting capabilities and use for civil protection and emergency actions.

References

- Ambrosi and G.B. Crosta, Rilevamento, modellazione e valutazione della pericolosità di grandi frane nel bacino del Pioverna, Lecco, *Atti I° Convegno Nazionale AIGA* (2003), pp. 31–45 (in Italian).
- Crosta G. B., Chen H., Frattini P., (2006) Forecasting hazard scenarios and implications for the evaluation of countermeasure efficiency for large debris avalanches. *Eng. Geol.* 83 (1-3):236-253.
- Frigerio G., (2010) Evoluzione di movimenti franosi lenti: interpretazione dei dati mediante modellazione numerica semplificata. Master Thesis (in Italian), Politecnico di Milano.
- Newmark, N. M., (1965). Effects of earthquakes on dams and embankments. *Geotechnique*, 15(2):139-160.
- Perzyna P., (1963) The constitutive equations for rate sensitive plastic materials. *Quart. Appl. Math.* 20:321-332.
- Secondi M., Crosta G. B., di Prisco C., Frigerio G., Frattini P., Agliardi F. (2011) Forecasting landslide motion by a dynamic elasto-visco-plastic model. *Geophysical Research Abstract* 13, EGU2011-13850, European Hazards Session NH3.8, Wien, Austria, 3-8 April 2011.

4.6 CASELLA (ITALY)

Mario Lovisolo

Centro Servizi di Geingegneria, Italy

ABSTRACT

The test site Casella is situated in a Cabella hamlet in the Piedmont region, Italy, where a dormant landslide body incorporates some active landslides in its lower portion; the landslide area is 1.2 km² with a total volume of 30 Mm³. The area was historically affected by landslide movements that often correlated with heavy rainfall, e.g. events occurring in 1993, 1994, 2000 and 2002. The monitoring system began in 2004 and was renewed on April 16th, 2010 within a frame of the Safeland project; it is composed of one DMS column of a total active length of 29 meters including 28 IT modules (inclinometer and thermometer) and one IUT module (inclinometer, thermometer and piezometer). The report is an analysis coupling rainfall, groundwater level and displacement. Only one distinct reactivation event has been registered in the monitoring period at a depth of 23 m b.g.l. A total displacement of about 4.2 mm occurred on May 23rd 2005, with a trigger at approximately 14:00 and a stop in the evening of the same day. It was well correlated with the water table rising and the intense rainfall that occurred starting the 17th of May, six days in advance of the reactivation.

Presented parameters: displacement, velocity, groundwater level, precipitation.

4.6.1 GENERAL DESCRIPTION OF THE TEST SITE

Description of the location and geological background

The monitoring area is a Cabella hamlet, Alessandria province, Piedmont region, Italy. The inhabited area of Casella is located along a dormant landslide body incorporating active lower landslides; the landslide area is 1.2 km² for a total volume of 30 Mm³ (Figure 4.6-1). The sliding direction is 235°N and the height difference between crown and foot is about 680 m. The landslide type is complex translational - rotational with deep creep. The elements at risk are the inhabited areas affected by the landslide, the regional highway called Serravalle-Carrega, and the development of a landslide dam in Borbera Torrent.



Figure 4.6-1. Casella landslide area.

The stratigraphy of the area shows between 0 to -2 m clayey and silty overburden. Between -2 and -23.5 m it shows landslide debris made by heterometric clayey and calcareous clastic in silty and clayey matrix, and beyond -23.5 m is bedrock made by an alternation of overconsolidated clays and silts and limestone rocks all locally fractured (See Figure 4.6-2).

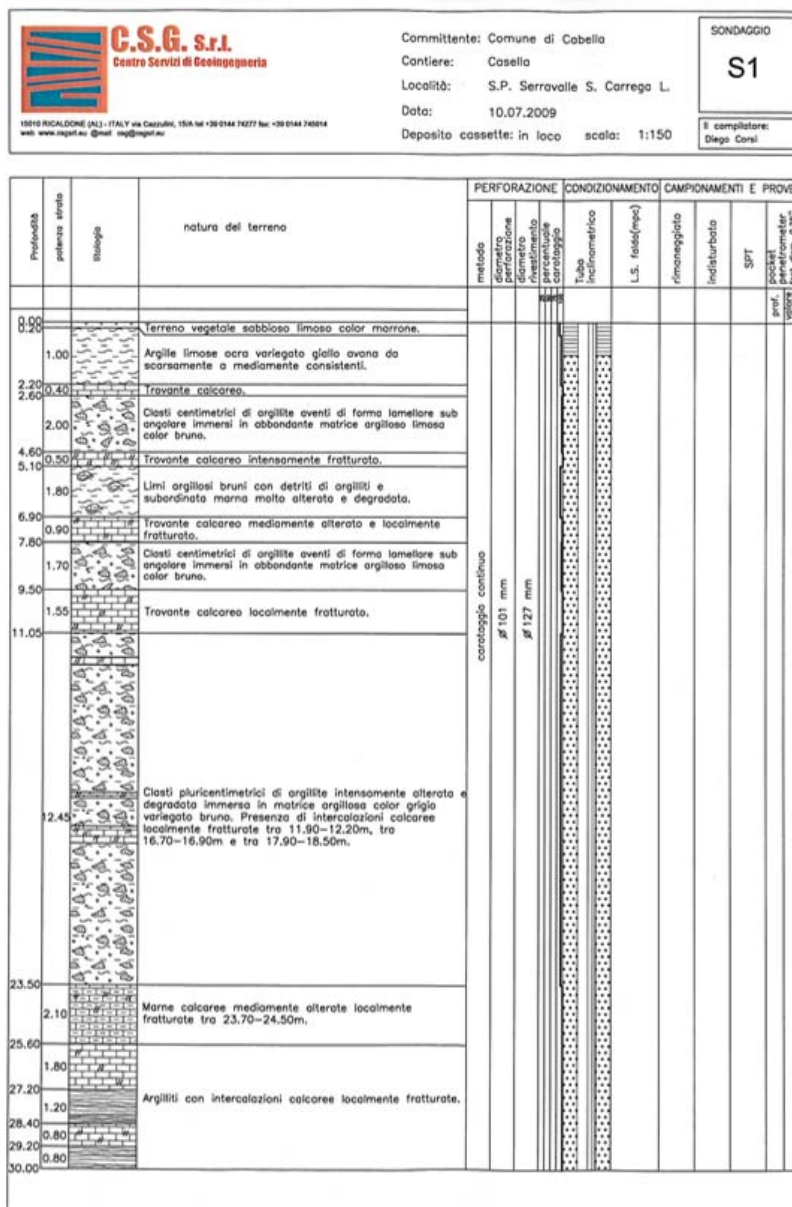


Figure 4.6-2. Stratigraphy sketch and coring of Casella S1/2009 borehole.

The Municipality of Cabella, which includes Casella, was historically affected by landslide movements that often correlated with high rainfall such as in events that took place in 1993, 1994, 2000 and 2002.

Table 4.6-1. Historical events in the Cabella area

Date	Area	Event	Damages
January 1873	Cabella Ligure	Settlement	Damaged the inhabited area of Dova Soprana and Dova Sottana
16 – 17 November 1940	Cabella	Torrent Borbera flooding	Tree arch of the bridge destroyed
29 – 31 October 1976	Cabella	Landslides	Same roads blocked ; a landslide over 1.500 m ³ damaged the road for Dova a bit after Rosano
October 1979	Cabella	Flood event	Damage to Case Bianche road.
December 1986	Cosola	Landslide	Landslide
22 – 26 November 2002	Cabella and other areas	Heavy rainfall	Landslides on different roads interrupted the viability between Casella Pobbio, Costa Piuzzo, Aie and Montaldo di Cosola, Centrassi, Cremonte, Rosano, Dova and Dovanelli

4.6.2 DESIGN OF THE MONITORING NETWORK

Instrumentation characteristics

The monitoring system is composed of one DMS column installed April 16th 2010. The column has a total active length of 29 meters and includes 28 IT modules (inclinometer and thermometer) and one IUT module (inclinometer, thermometer and piezometer).

The system was brought to the site on a bobbin and was installed by a DMS Reeler.

The municipality of Cabella and the monitoring area are covered by the European research project SafeLand 2009-2012.



Figure 4.6-3. DMS system during and after installation.

After the installation, the functionality of the whole column was tested in direct connection using the RS485 protocol.

The control unit for the data processing and transmission was installed on the same day. This control unit is made up of one IP66 box containing the control unit for the management of data, the GSM module, and an electronic board for the temperature and voltage checks. The UPS unit for power backup lasting for seven days was also installed and linked to the control unit.

Once the connection and GSM transmission were completed using a rugged notebook, the functionality of the installation was verified and the "0 reading" of the casing was carried out. This activity took place on the date of April 19th 2010.



Figure 4.6-4. DMS installation sites

During the night of September 12th, the control unit and the solar panel were stolen. For this reason, the instrumentation is now supplied by the power network thanks to collaboration with the Cabella Municipality.

Management and maintenance

The Guardian software downloads data by GSM to the monitoring room at a time interval set by the user. The control unit compares data in real-time, and if the value exceeds thresholds, it automatically sends an SMS or a direct call to the geological staff. Data processing is carried out using DMS EW full software.

Regarding maintenance, the stainless steel structure of the modules makes the instrument very robust, and because of the high quality of the sensors, ordinary maintenance work is not required.

4.6.3 ANALYSIS OF MONITORING DATA

Instrumentation data analysis

A preliminary investigation about the kinematic conditions of the Casella landslide was begun in 2004 when a DMS column was installed in the central area of the landslide.

During that period, the results showed a principal sliding surface between 27 and 30 m b.g.l., and a secondary one at a depth of 19 m b.g.l. In both cases the direction was S-SE, consistent with the maximum slope direction, for a total displacement of 13.3 mm.

The principal sliding surface caused a displacement of 8.6 mm, and the second one caused a displacement of 4.7 mm.

The graph below shows the cumulative displacement of the whole column related to the calibration date: June 24th 2004.

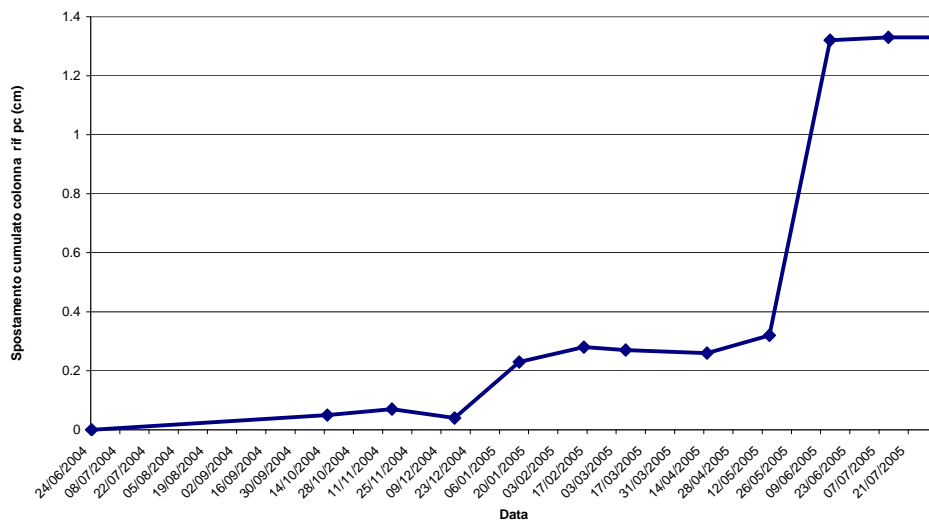


Figure 4.6-5. Cumulative displacement of DMS column.

A displacement occurred on May 23rd, 2005 with a trigger at approximately 14:00 and a stop in the evening of the same day. Displacement along the principal sliding surface was 4.2 mm. The phenomena was correlated with the water table rising and intense rainfall that occurred starting on May 17th.

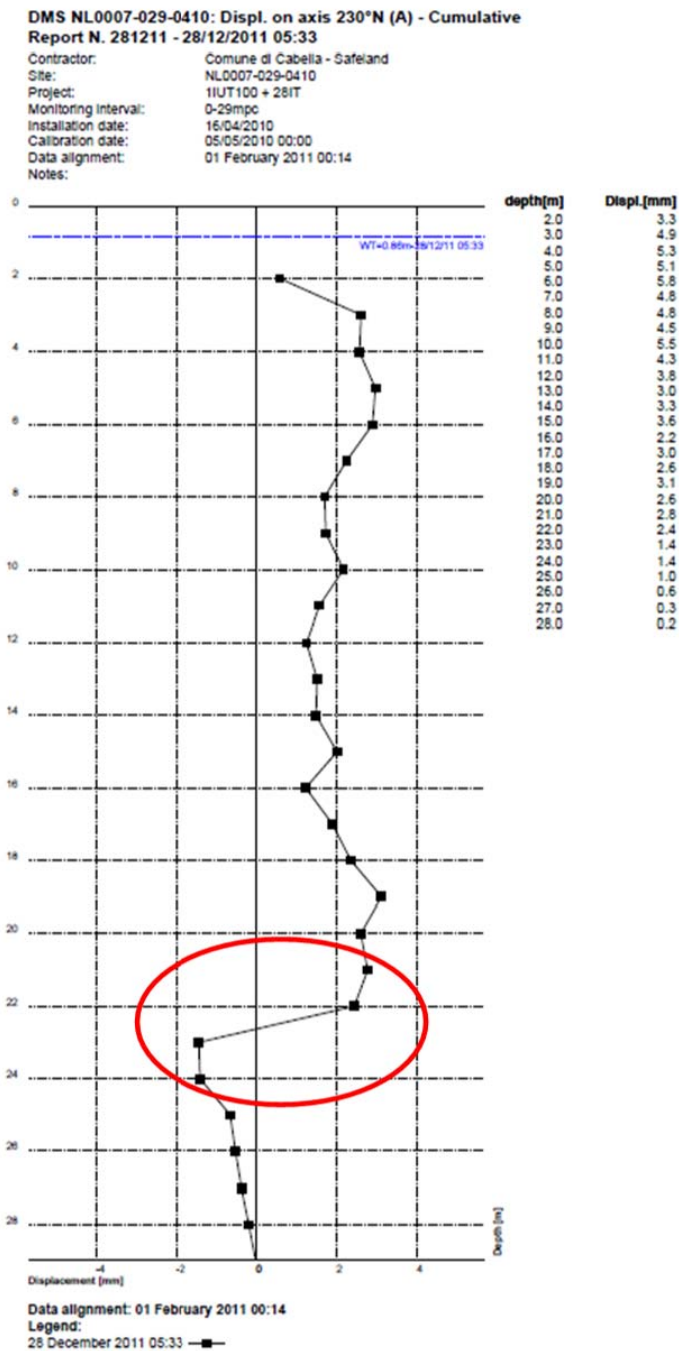


Figure 4.6-6. DMS 2011 displacement.

The new system installed on the toe of the landslide, in the frame of the SafeLand project, is still detecting a slow displacement in the direction of 230°N, which is consistent with landslide morphology. The last monitoring data available (December 28th 2011) show a clear sliding zone with a cumulative displacement of 5.8 mm in 2011.

The sliding surface is located at a depth of 23 m b.g.l., coinciding perfectly with the base of the landslide body (see stratigraphy Figure 4.6-2). The water table level changes in the interval between ground level and 1 m b.g.l.

4.6.4 ROLE AS EW PARAMETER

DMS columns are able to contextually detect displacements and water table level changes, and correlations between these two parameters can be found. Warning thresholds were set for both parameters, and on the basis of the time delay analysis, it is possible to define a forecast model to improve the efficiency of the EW system.

4.6.5 END-USER ROLE

Considering the high-risk context of the area, the Municipality of Cabella planned the installation of DMS monitoring and data transmission instruments in order to gain information on local displacement triggering factors (critical rainfall thresholds), displacements and instantaneous velocities, and sliding zones depths.

In this way, it will be possible to manage public safety procedures and to verify that the mitigation works.

4.6.6 SUMMARIZED EVALUATION OF PARAMETERS

Monitoring platform strength and lack

The system installed is able to detect data in real-time and to advise on-duty staff with a warning SMS or direct call in the event of displacements or water table levels exceeding the set thresholds. Moreover, the possibility of detecting displacements and water table levels in the same borehole improves the correlation analysis accuracy, guaranteeing cost savings at the same time.

The correlation between rainfall events and displacements should be improved with the installation of a weather station on site, directly linked to the existing DMS control unit. In this way it will be possible to directly link rainfall, water table and displacement data, improving the correlation analysis and the landslide model.

Further activities

Deeper knowledge about local kinematic conditions will allow future activities or a potential project for an EW system to be defined, considering the high risk conditions of the area.

4.7 GSCHLIEFGRABEN (AUSTRIA)

R. Supper, I. Baroň, B. Jochum, D. Ottowitz, S. Pfeiler, S. Kauer, A. Römer, A. Ita
Geological Survey of Austria

G. Moser
ZT-Moser-Jaritz, Austria

M. Lovisolo
Centro Servizi di Geoingegneria S.r.l., Italy

J.-H. Kim
KIGAM, Korea and Geological Survey of Austria

ABSTRACT

This contribution presents monitoring results from Gschliefgraben, which is one of the most prominent and recently studied slope failures in Central Europe. During a period from September 2009 to November 2011, a complex set of monitoring parameters were measured, including displacement – measured by means of an automatic inclinometer system (DMS) – resistivity, self-potential (GEOMON^{4D}), in- and outflow, as well as meteorological parameters like precipitation and air temperature. The results of 26 months of permanent monitoring are presented and the role of applied technologies to provide possible monitoring and early warning parameters is discussed.

Presented parameters: displacement, velocity, groundwater level, precipitation, soil temperature, resistivity, self-potential, in/outflow.

4.7.1 GENERAL DESCRIPTION OF THE TEST SITE

The Gschliefgraben site is one of the most prominent and recently studied slope failures in Central Europe. It comprises a large complex of geologically controlled landslides, earth flows, topples, rockfalls and deep-seated gravitational deformations in the Gschliefgraben valley and along the slopes of the Northern Calcareous Alps.

Geological and geomorphic settings

The area of Gschliefgraben is a 2.85 km long and 0.85 km wide valley along the foot of the Northern Calcareous Alps (Figure 4.7-1A, B) south of the town of Gmunden in northwest Austria. At the front of the Northern Calcareous Alps there is a steep cuesta, with the summit at Mt. Traunstein (1,691 m a.s.l.). The valley floor is divided into small sub-parallel catchments; its topography is strongly controlled by complicated tectonic structure and a very complex lithology, as well as by mass wasting that has been active here since the end of the last glacial period. The surveyed area of Gschliefgraben covered three main geological units with completely different lithologies and geological structures (Figure 4.7-1C): (i) **Northern Calcareous Alps and the “Marginal Nappe”** (NCA) – mostly densely fractured, diversely stratified, steeply dipping and frequently faulted competent brittle dolomite and limestone; (ii)

Ultrahelveticum (UHV) – tectonically strongly deformed variegated marl, claystone, nummulitic limestone, sandstone, arkose etc.; (iii) the **Rhenodanubian Flysch Zone (RFZ)** – slate, shale, cemented marl and sandstone of different thicknesses.



Figure 4.7-1. General setting of the Gschlifgraben site: (A) Position within Austria, (B) Airborne photo of the Gschlifgraben valley and Mt. Traunstein from the west (Photo: R. Supper, 2009), and (C) Geological map of the area of Gschlifgraben. The blue contours indicate the Deep-seated gravitational deformations. Legend: Quaternary deposits: 8 - Alluvial Fan, 9 - Slope Scree, 11 - Block Fields, 13 - Landslide Deposits, 20 - Glacilacustrine deposits, 22 - Slope Breccia, 35 - Moraine deposit; UHV: 50 - Buntmergel Fm., 52 - Greisten Fm.; RFZ: 53 - Altliengbach Fm., 57 - Perneck Fm., 58 - Zementmergel Fm., 59 - Seiesenburg Fm., 60 - Rieselsberg Fm., 62 - Gaultflysch Fm.; NCA: 66 - Schrambach Fm., 69 - Ruhpolding Fm., 71 - Calcarenite Fm., 75 - Koessen Fm., 76 - Koessen Fm., 77 - Koessen Fm., 79 - Plattenkalk Fm., 80 - Hauptdolomit Fm.; the major tectonic faults are as dot-and-dashed lines (modified after Egger et al. 1996, Egger et al. 2007 and Moser et al. 2009).

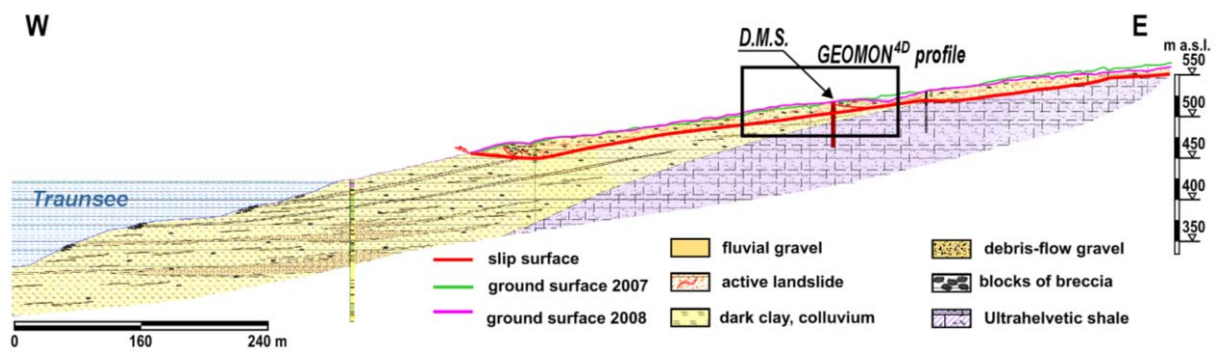


Figure 4.7-2. Schematic lithological profile of the lower part of the Gschliefgraben site with marked position of the DMS column and GEOMON^{4D} longitudinal profile (section modified after Moser et al. 2009).

Characterization of the site

The main mass wasting processes are represented by sliding and flowing in the central part, which is built up mostly of the UHV unit. The UHV emerge here in the form of a tectonic window between the RFZ and the NCA. On the other hand, falling, toppling, and spreading are the most characteristic types of mass movement in the eastern and southern marginal areas of the Gschliefgraben valley along NCA, where hard rock dominates (dolomite, limestone, cemented Pleistocene breccia). At some places, great portions of the NCA and the RFZ and UHV units situated below are subject to deep-seated gravitational deformations in a rather initial evolution stage.

In late November 2007, a landslide of about 3.8 million m³ of colluvial mass was reactivated in the central and western parts of the valley within old earthflow and other deposits (Figure 4.7-1C and Figure 4.7-2). Displacement velocity was up to 4.7 m/day at the beginning and 55 buildings had to be evacuated. Recently, the Gschliefgraben landslide is a test site of the European FP7 project SafeLand, where the new techniques have been tested for an effective early warning consisting of airborne and ground-based geophysical surveys, the GEOMON^{4D} system and the DMS (Differential Monitoring of Stability) including automated in-place inclinometer, piezometer and thermometer sensors.

Description of the history of the mass movement

The Gschliefgraben site has been known for centuries for its repeated landslide activity. In the winter of 2007/2008 it was reactivated (Figure 4.7-3 and Figure 4.7-4A). This reactivation caused damage to property, despite a hazard zone map having been set up in 1974, giving rise to a complete prohibition on construction in this area. Hundreds of people had still been living on the alluvial fan close to the lake. Other geological descriptions and previous preliminary monitoring results appear also in the deliverables D 4.3 and D 4.5.

Within the **first phase** of mitigation in 2008, major measures were focused on property and infrastructure protection and were coordinated by the Austrian Service for Torrent and Avalanche Control. About 220 wells and one deep channel were implemented to drain the sliding mass. Additionally a big quantity of sliding material was removed close to the inhabited areas (Figure 4.7-4B). Differential GPS and water level measurements were performed to evaluate the effectiveness of the measures, which led to a significant slowdown of the movement. During the **second phase** (soon after the suspension of the evacuation), multi-disciplinary investigations including drilling, borehole logging and complex geophysical measurements (e.g., geoelectric, seismic and ground-penetrating radar (GPR) surveys), were performed to investigate the structure of the landslide area in order to evaluate maximum hazard scenarios as a basis for planning further measures. Based on these results,

monitoring techniques for an early warning system were tested within the **third phase** in the frame of the SafeLand project. The final early warning system should enable local stakeholders to provide an appropriate response in the event of further landslide reactivation. Several innovative approaches were applied, such as the airborne multi-parameter geophysical mapping, differential airborne laser scanning (ALS), automated inclinometers (DMS), time-to-main reflectometry (TDR), discharge monitoring and differential Global Positioning System (dGPS) surveys.

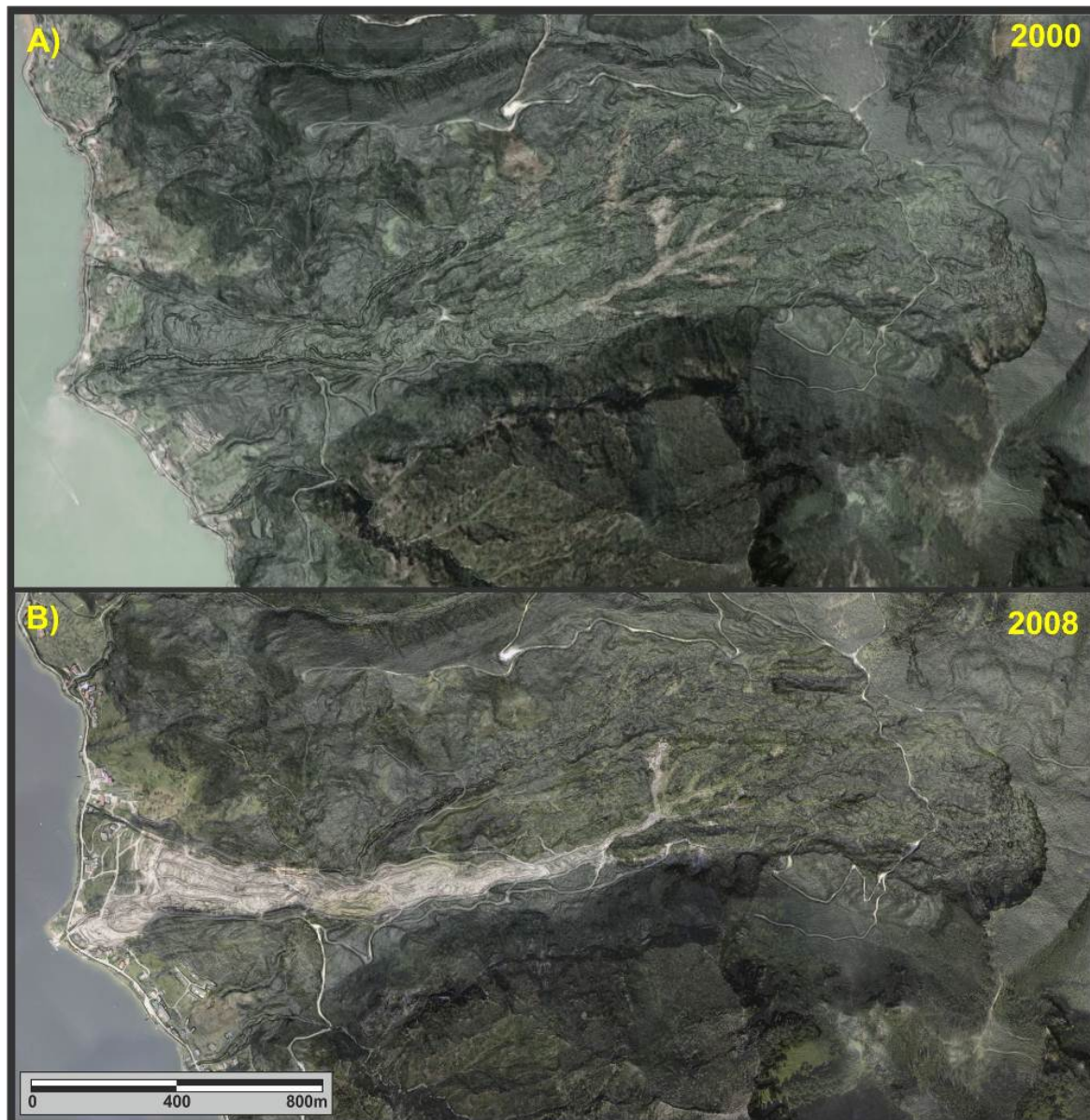


Figure 4.7-3. The activity of the earthflow complex between 2000 and 2008 was assessed based on the identification of bare surfaces on a set of orthophotos. The orthophotos are superimposed on the ALS pseudo-hillshade.

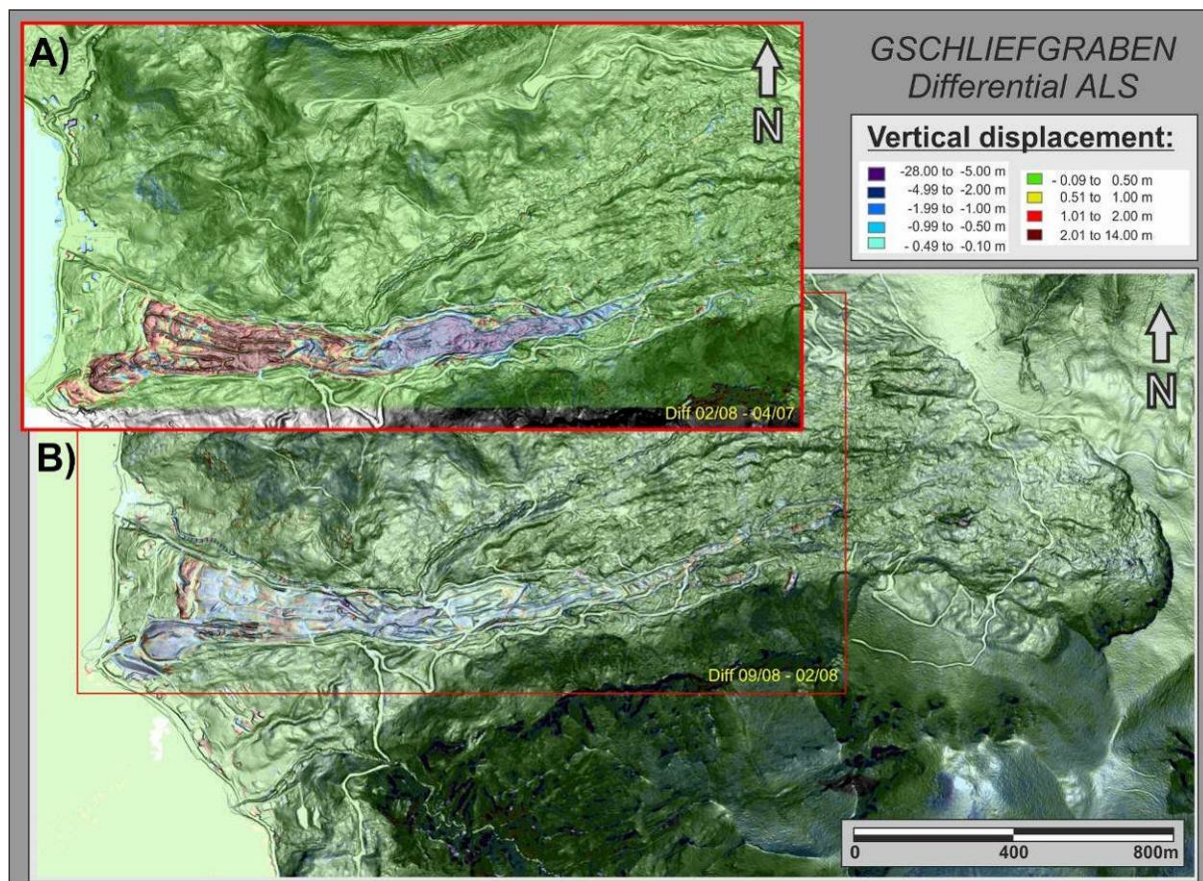


Figure 4.7-4. Two differential ALS scenes highlight mass transport due to (A) the major recent landslide event in winter 2007/08 and (B) later remedial works comprising of distinct material removal (in blue colours) in the active earthflow (below). The presented individual ALS surveys took place in April 2007, February 2008 and September 2008.

4.7.2 DESIGN OF THE MONITORING NETWORK

This report will focus mainly on geoelectrical and displacement monitoring results which will be compared to hydro-meteorological data. The monitoring system in Gschliefgraben is one of the first known cases in which geoelectric monitoring was coupled with high-resolution displacement monitoring for several years. The monitoring started in September 2009 and the system has been operating since that time, with only one short interruption due to a torrential rain event that flooded the retention channels and damaged the geoelectrical cables.

Before the installation of the monitoring equipment at the Gschliefgraben site, airborne geophysical mapping followed by a multi-electrode geoelectrical survey were performed in a broader area of the active earthflow to verify the subsurface structure and to optimise the location for a geoelectric and displacement monitoring system. Figure 4.7-5 clearly highlights the correlation between the geoelectric pattern along one of the monitoring profiles, closely passing by the inclinometric borehole, and areas of different displacement characteristics. The low resistivity structure at the top correlates with the most active top layer, whereas the region with higher resistivity below exhibits only a slow creeping behaviour. The sliding plains detected by the DMS inclinometer are clearly marked by high gradients of resistivity.

Based on these promising results, a geoelectric monitoring system of the type GEOMON^{4D} was installed in the upper central part of the active earthflow of Gschliefgraben in September 2009 (Figure 4.7-6) as part of the early warning approach at the Gschliefgraben test site.

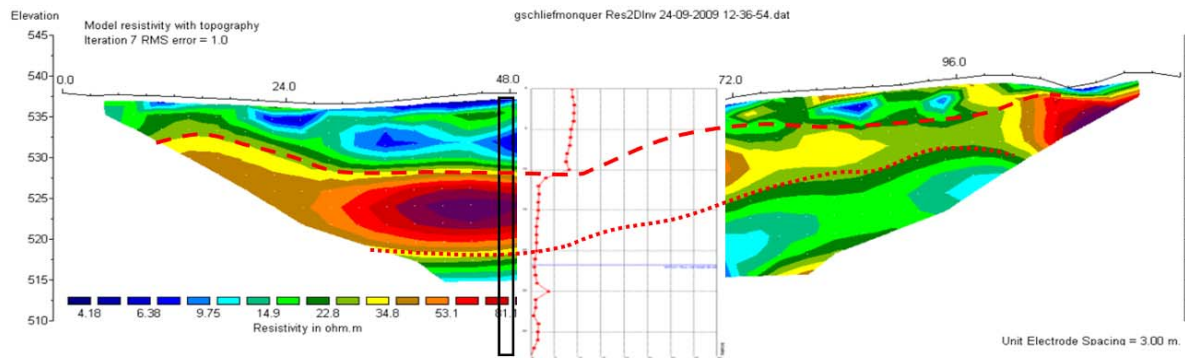


Figure 4.7-5. Correlation of resistivity layers with sliding surfaces determined by a permanent inclinometer (red curve) in the area of Gsschlieflonquer.

The GEOMON^{4D} was specifically developed for monitoring applications by the Geological Survey of Austria (Supper et al. 2003, 2009, and 2010). The completely open architecture of the instrument allows installation of any number of current or potential electrodes by adding parallel or serial cards. Furthermore, data acquisition at a speed of about 3000 measurements/hour in single-channel mode, and usually 1000 samples per single configuration including recording of the full signal, enable effective noise analysis and filtering. The GPRS (General Packet Radio Service) data transfer allows the maintenance to be fully remote controlled. Data, such as measurement results, test sequences, and log files containing information about system and GPRS connection status are sent automatically via email to the data processing centre at GSA. Consequently, immediate availability of information for local stakeholders could be guaranteed. For power supply, a 500 m long cable was installed to connect to the local power grid. The length of the two perpendicular profiles (for location see Figure 4.7-1C) is 120 m (electrode separation 3 m, 41 electrodes) and 192 m (electrode separation 4 m, 49 electrodes).

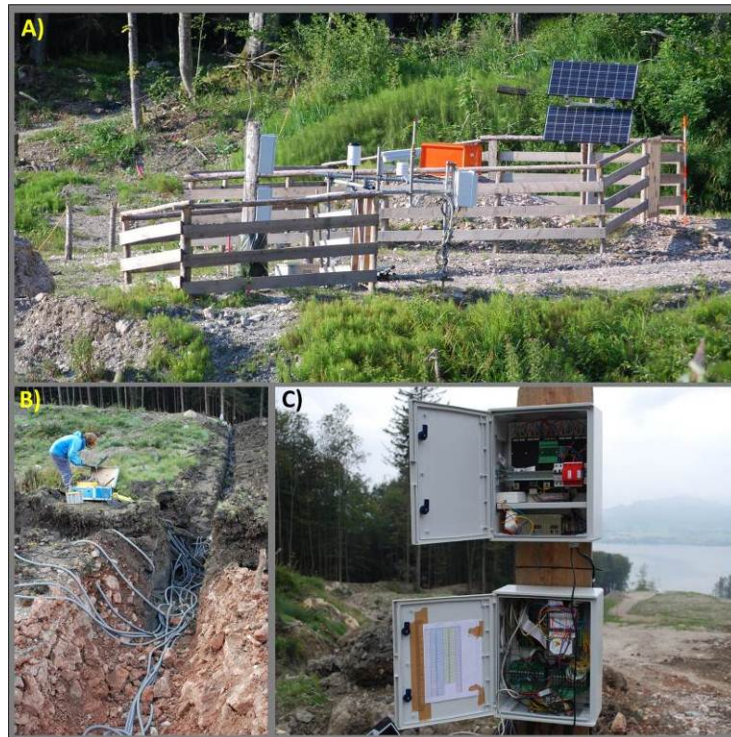


Figure 4.7-6. GEOMON^{4D} instrument at the Gschlifgraben site: A) the control panel and the central unit were placed near the crossing of both monitoring profiles and near the DMS automatic inclinometer (the orange casing); B) the electrodes and cables were buried up to 1 m below the ground surface to protect them against major meteorological and mechanical influences; C) general appearance of the control unit (Photo by: Ivo Baroň 2009 and 2010).

4.7.3 ANALYSIS OF MONITORING DATA

4.7.3.1 Displacement

The displacement was measured by a DMS column placed in the central part of the active landslide (see Figure 4.7-2), near the crossing point of the geoelectric profiles. A distinct basal sliding surface was registered at a depth between 10 and 11 m below the top of the casing pipe (equal to 9-10 m b.g.l., Figure 4.7-7). The sliding zone correlates with a very thin sandy layer documented by the borehole log. The total cumulative displacement along this sliding zone reached almost 14 cm during the observation period from September 2009 to November 2011. The displacement vector is constant and is oriented towards WNW (Figure 4.7-8).

DMS GSA01A-033-0909: Total displacement (A) - Cumulative Report

Contractor: Geological Survey of Austria - Wildbach und Lawinenverbauung
 Site: Gschliefgraben (Gmunden)
 Project: DMS 11MT+11UT+31IT
 Monitoring interval: 0-33m bgl
 Installation date: 22/09/2009
 Calibration date: 23/09/2009
 Data alignment: 24 September 2009 12:11
 Notes: Borehole depth 55 m.
 I-pipe depth 44 m.

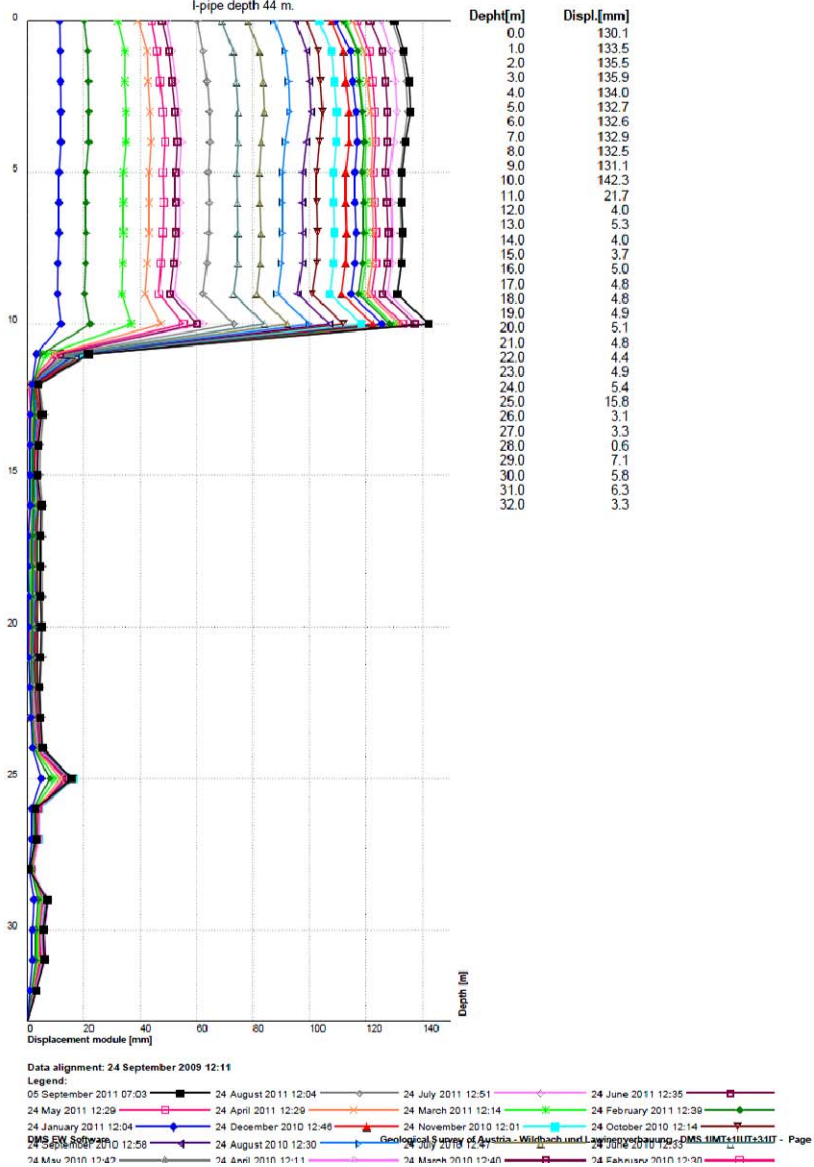


Figure 4.7-7. Inclinometric record of total cumulative displacement in the DMS borehole at the Gschliefgraben site registered from September 2009 to November 2011 (depths are below the top of the inclinometric pipe, situated 1 m above the ground surface).

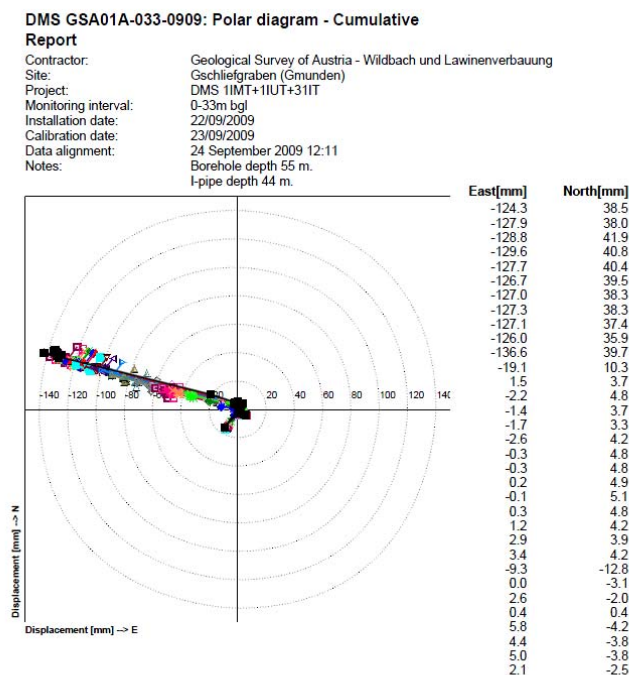


Figure 4.7-8. Polar diagram of the inclinometric record of cumulative displacement in the DMS borehole at the Gschliefgraben site registered from September 2009 to November 2011.

Within the deeper parts of the inclinometric column, only minor displacements have been registered. The maximum values are below 0.8 cm except for one peak in the depth of about 25 m (24 m b.g.l., Figure 4.7-7). This isolated movement reached about 1.8 cm and correlates with a sandy layer. The displacement vector is SE-oriented (Figure 4.7-8) and is probably related to lateral escape of the monitoring column at the base of the soft material due to loading by the instrument.

Figure 4.7-9 shows the evolution of displacement during the whole survey period. In general the movement rates were comparably low compared to other SafeLand test sites. The total cumulative displacement during the whole survey period (26 months) was around 14 cm. Major periods of quasi-constant velocity were interpreted in Figure 10. It is obvious, that, apart from some very small events of acceleration, only one significant “event” on May 1st is visible that correlates with intense rainfalls, flooding of the retention basin upslope of the site, and earthflows close to the main street. In 2009 several short periods of acceleration took place until the end of November, when a sudden acceleration took place with no obvious correlation with precipitation. After that event, the velocity reached approximately 18.3 cm/year, which is the highest speed detected during the monitoring period. The high velocity continued until almost the end of the year, when the velocity started to decrease (major deceleration periods are 23.12.09-2.1.10 and 1.2.-3.3.10). Around the beginning of March the landslide reached a speed of approximately 4.3 cm/year, which stayed constant until May 1st when a torrential rainfall triggered a sudden acceleration reaching again the maximum speed of 18.3 cm/year. After May 20th velocity started to decrease again (with two short-term accelerations that did not have any significant influence on the general behaviour), reaching an almost constant velocity of 7.3 cm/year in August and September. At the end of September, velocity again decreased to 6.2 cm/year, remaining constant until the end of 2010.

In the first two week of January 2011 the landslide slowed down again (interestingly, correlated with a rain/snowfall event of 38 mm/day) to a constant velocity of 2.5 cm/year. At the beginning of April a further deceleration took place after which the landslide reached the lowest recorded velocity of 0.9 cm/year until the month of May, during which a small acceleration to 2.9 cm/year took place, due to several heavy rainfall events. From the end of May until the end of October, velocity stayed almost constant at the low level of 2.9 cm/year. In early November another decrease of velocity to 1.2 cm/year took place.

Comparing the results of calculated cumulative precipitation and displacement, a correlation between periods of increased precipitation and periods of change in the displacement velocity could be derived, however the type of correlation is undefined since periods of increased precipitation were either correlated with acceleration or deceleration of the landslide.

The clear fact is that the major event on May 1st, 2010 can be correlated with a sudden heavy rainfall after a longer dry period. However it can be assumed that rainfall alone was perhaps not the only triggering cause (later more intense rainfalls did not have a similar effect). A blocking of the drainage system (which was not fully completed and operational at that time) and an increased inflow of surface water caused by the blockage might have had an additional determining influence on the acceleration. This result highlights the importance of proper maintenance of the drainage system in future, and definitely supports the remediation strategy of the Torrent and Avalanche Control of Lower Austria. For a future early warning system, inclusion of sensors that check the proper operation of the drainage system is of high importance.

To conclude, contrary to other test sites monitored by GSA and C.S.G., no larger distinct reactivation events have been registered during the entire survey period since September 2009. However, for any more precise interpretation and evaluation of EW indicators, several more distinct reactivation events must be monitored and analyzed.

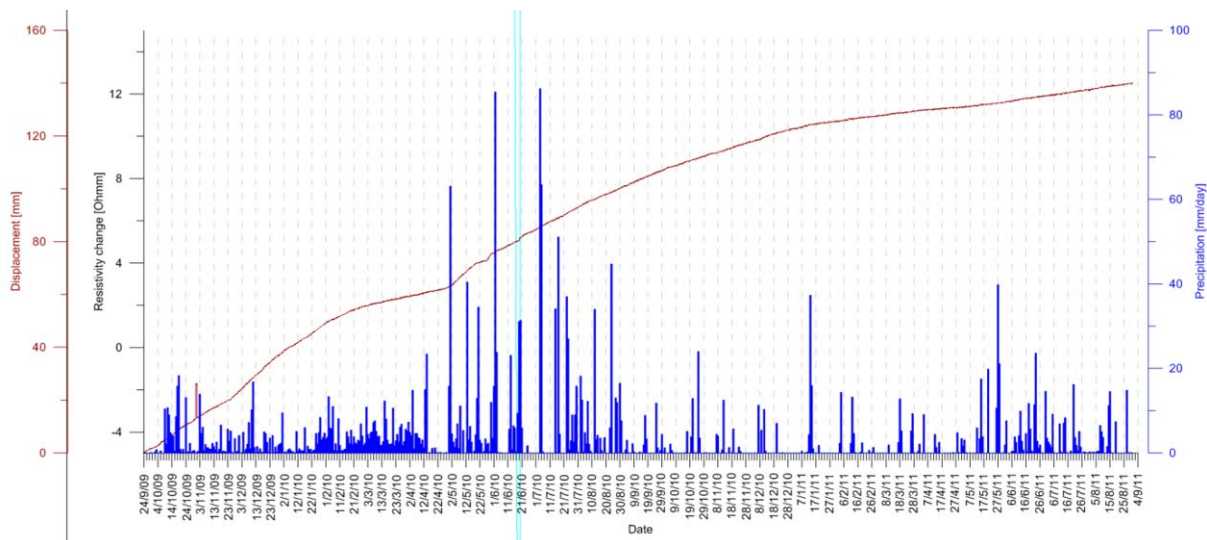


Figure 4.7-9. Correlation between cumulative displacement (DMS) along the slip surface at 10-11 m b.g.l. and daily precipitation registered from September 2009 to November 2011.

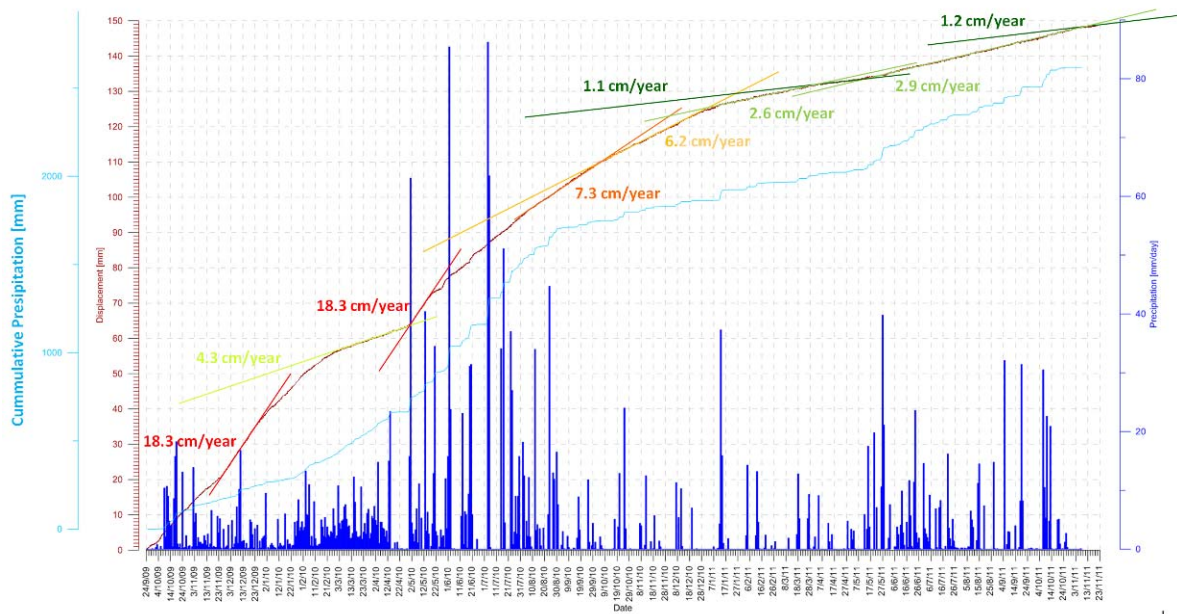


Figure 4.7-10. Interpretation of displacement monitoring: average mean velocities for different phases.

4.7.3.2 Soil temperature

Temperature was monitored at certain depths inside the DMS casing. Figure 4.7-11 shows the results within the first 8 m of depth. The graphs mainly represent the seasonal variations of temperature. The time shift between the seasonal temperature wave at surface and at 8 m depth is approximately six months. For recordings of deeper sensors, hardly any changes above the resolution of the sensors could be detected. No significant anomalies related to a sudden inflow of groundwater could be detected. However, the results are important for the interpretation of geoelectrical monitoring results since subsurface resistivity depends on this parameter, among others. In a case such as Gschliefergraben, in which hardly any changes in resistivity could be observed, temperature is the dominant factor of seasonality for several measurement configurations as shown in Figure 4.7-12.

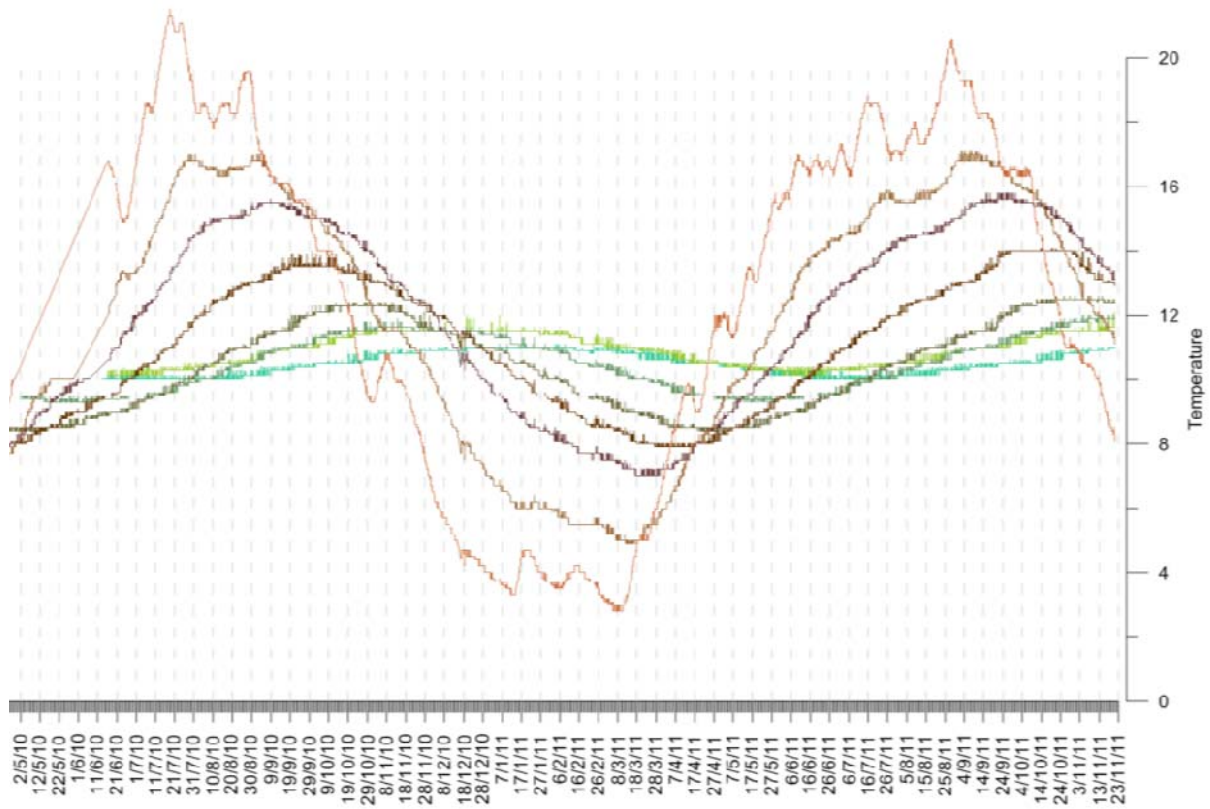


Figure 4.7-11. Record of ground temperature at different depths between May 2010 and November 2011.

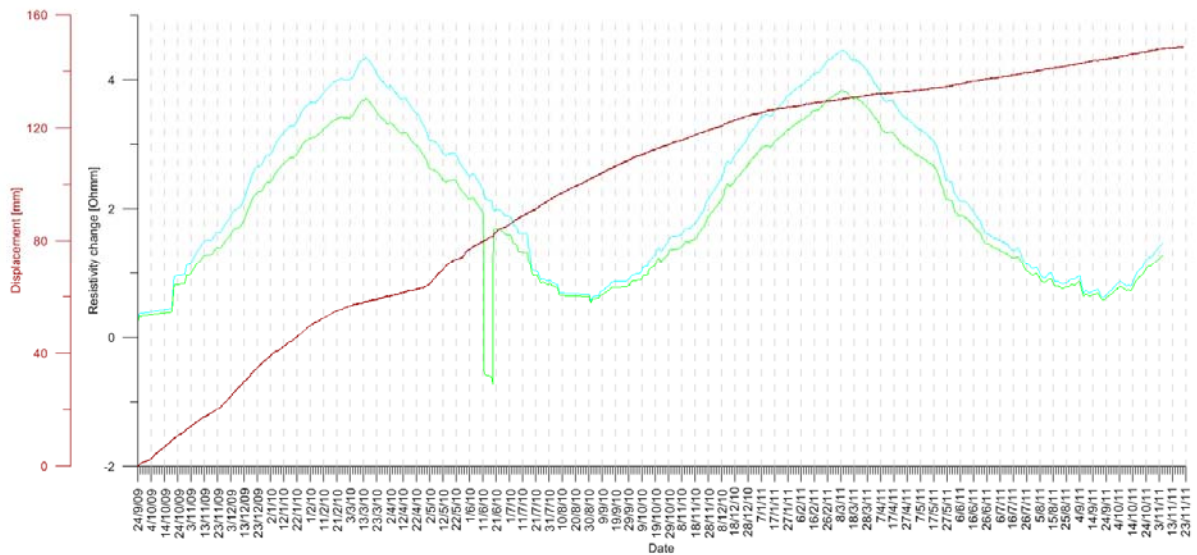


Figure 4.7-12: Correlation of selected apparent resistivity data (green, blue) with displacement for the entire survey period.

4.7.3.3 In/Outflow

The major inflow creeks of the area were captured into two strings of pipes upslope of the major part of the landslide and discharged to the Traunsee Lake. The sensors measure the total flow through the pipe at points close behind the inflow point and in the middle of the landslide. This monitoring system was installed by the University of Natural Resources and Life Sciences in Vienna, which also provided the precipitation data.

Although these values are measurements of the extracted water, not the inflow inside the landslide body, they represent an important monitoring parameter in two respects:

- 1) Since, of course, not all incoming water could be captured, the remaining surface inflow inside the landslide body might be proportional to this value;
- 2) The difference of the upper and lower values on each string provides a value on the functionality of the drainage system. If the upper and lower values differ significantly, the pipes might be losing water through a hole or might be blocked. Both situations could have a severe impact on the behaviour of the landslide and require immediate action in case of heavy precipitation. Therefore, a warning is sent to the responsible stakeholder in such a case. In fact, the only small “event” that was recorded within the survey period was most probably caused by such a blocking of the pipes and related increased inflow to the landslide. However, the effect on the landslide was quite small and could only be detected due to the high resolution of the DMS system.

Figure 4.7-13 shows the results of measurements taken from March to November 2011. Due to some failure of the sensors (freezing, power failure) data are not available for the whole survey period. The results clearly show the response due to major rainfalls and the times of increased flow after these events (five to seven days for a normal precipitation event, and a maximum of 12 days for extreme events). Figure 4.7-14 zooms in on two precipitation events: one in the spring and the other in the autumn of 2011. A comparison of results shows that in the spring, both the upper and lower sensors could detect almost the same flow, whereas in the autumn an almost constant shift between both datasets could be recognised. This is also true for some other events. Consequently, this suggests some kind of leakage along the string.

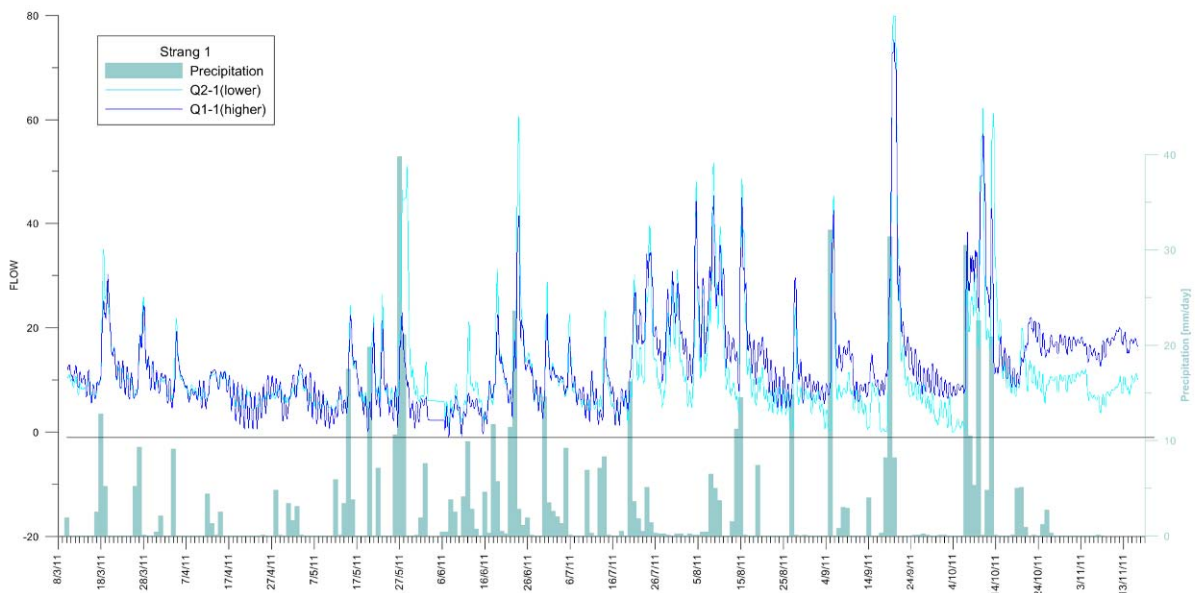


Figure 4.7-13. Correlation between precipitation and in/outflow: drainage channel 1 (flow and precipitation data courtesy of University of Natural Resources and Life Sciences, Vienna).

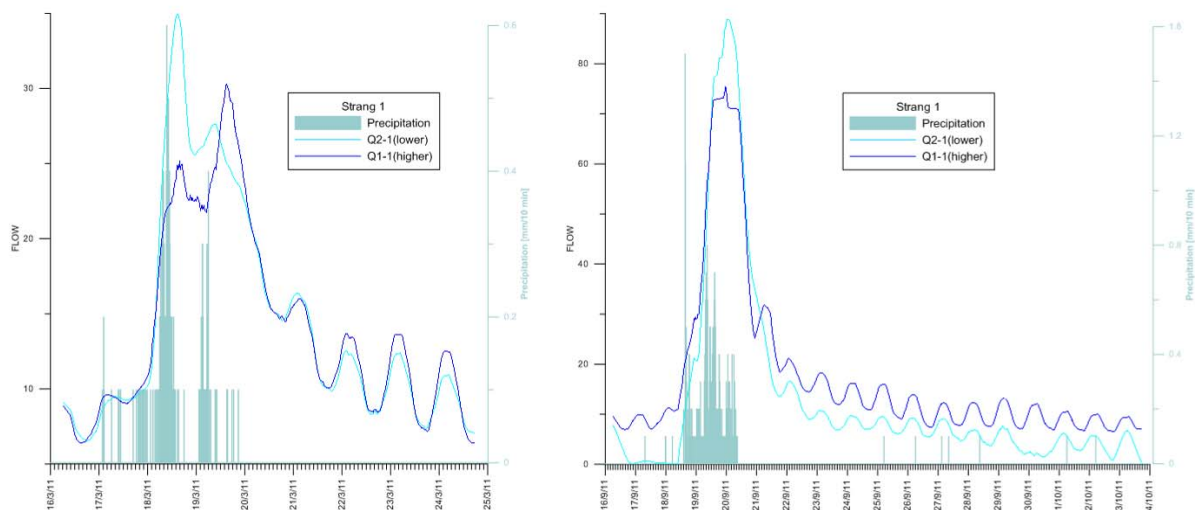


Figure 4.7-14. Correlation between precipitation and in/outflow: single events in spring and autumn (flow and precipitation data courtesy of University of Natural Resources and Life Sciences, Vienna).

4.7.3.4 Resistivity

A multi-electrode monitoring system was installed in the centre of the landslide close to the DMS displacement monitoring site. It comprises two profiles, one inline of the slope (49 electrodes, 4 m constant spacing), the other one perpendicular (41 electrodes, 3 m constant spacing) to the major flow direction. For power supply, a strong 500 m long cable was installed to connect to the local power grid. However, this solution proved to be unreliable, especially during summer thunderstorms when the power supply was interrupted for several times due to overvoltage. Therefore a fuel cell system was installed in addition, to guarantee permanent power supply. As mentioned above, during the whole survey only one small triggering event (May 1st 2010; acceleration from approx. 2 mm/12 days to 6 mm/12 days) with longer lasting aftermaths could be detected.

Consequently a correlation of resistivity anomalies with landslide acceleration is not possible and we can only focus on a correlation with very small changes in displacement velocity, which in fact are not relevant for early warning purposes. Yet, this might help to understand the dynamics of the landslide under “normal” conditions, and to derive information on the background variations of subsurface resistivity.

Figure 4.7-15 and Figure 4.7-16 show the variation of some selected values of apparent resistivity over the whole survey period. It can be seen that the major variations of resistivity, which are very small (± 3 Ohmm), are due to seasonal temperature variations. In some cases sudden resistivity changes (increase or decrease) correlated with major rainfalls, depending on the sensitivity of the respective array and on the absolute apparent resistivity value. Figure 4.7-17 to Figure 4.7-20 zoom in on the May 1st event. In all presented cases the rainfall event and the connected acceleration of the landslide was correlated with a (very small but detectable) decrease in apparent resistivity (below 2 Ohmm!). The response times are difficult to calculate, since the starting time of acceleration cannot be determined exactly and only daily values for precipitation are available for this period. However, the results suggest a delay between 6-24 hours between the onset of the resistivity decrease and the initiation of the acceleration. On the other hand, Figure 4.7-17, Figure 4.7-24 and Figure 4.7-26 prove that precipitation events with no correlated acceleration are also often associated with a resistivity decrease. In Figure 4.7-21 and Figure 4.7-23 results of time lapse inversion calculated with two different codes are presented. Both results are quite similar, although the EarthImager inversion result is less detailed. On the morning of May 1st, a small superficial anomaly with decreasing resistivity develops between profile distances 100 and 110, which is the location of that the profile crosses the street. This street was constructed by digging out landslide material to a depth of at least one meter and filling it up with coarse gravel or stones. Therefore, this area exhibits a much higher resistivity, and wetting of the material through rainfall is expected to produce a much larger resistivity decrease than in the surrounding area. In the afternoon (13-19h) of the same day, resistivity decreases in a broader area. Of special interest is an elongated anomaly, parallel to the surface between profile distances 125 and 170. This anomaly most probably reflects the flow of water downslope towards the deep drainage system, which might have been responsible for accelerating the landslide.

We can conclude that resistivity monitoring (especially the inversion results) helped to understand the process that led to a minor acceleration of the landslide in May 2010. However, apart from that, no significant changes of subsurface resistivity took place over the whole survey period. Most variations can be associated with seasonal temperature changes or short-term precipitation events. Since no major triggering event occurred during the entire

survey period, no detailed correlation between resistivity and displacement could be investigated. Longer survey periods must be envisaged.

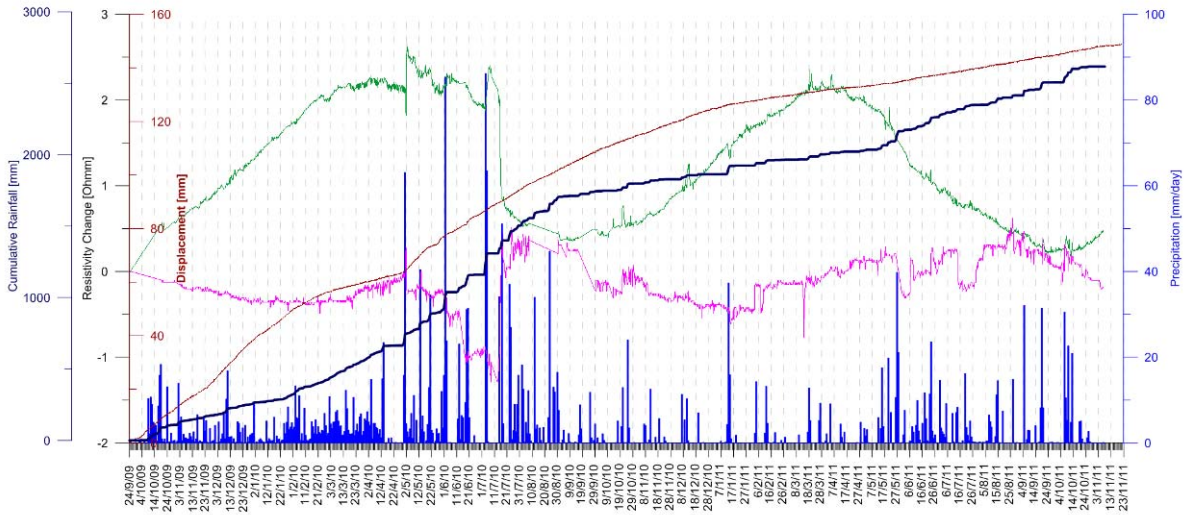


Figure 4.7-15. Correlation of selected apparent resistivity data (normalised to 20 Ohmm) with displacement and precipitation for the entire survey period.

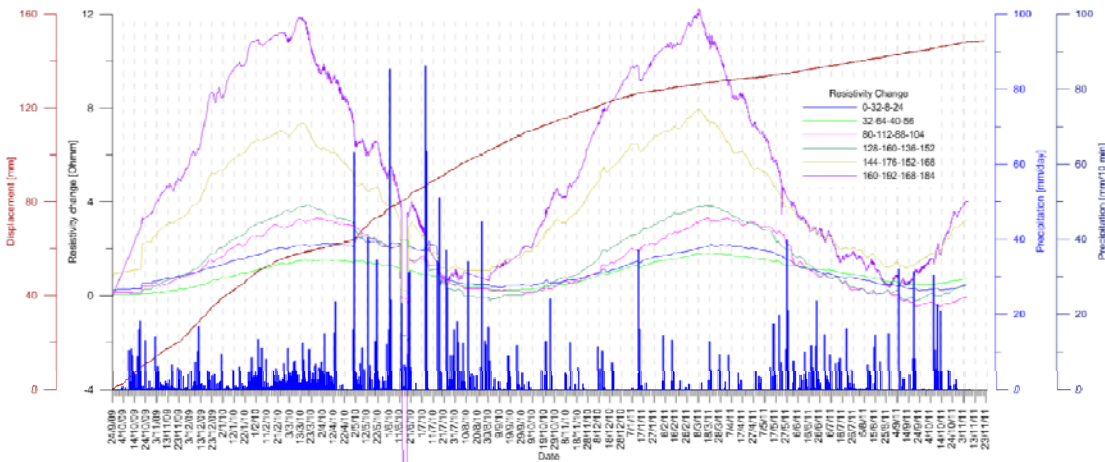


Figure 4.7-16. Correlation of selected apparent resistivity data (green, purple) with displacement and precipitation for the entire survey period.

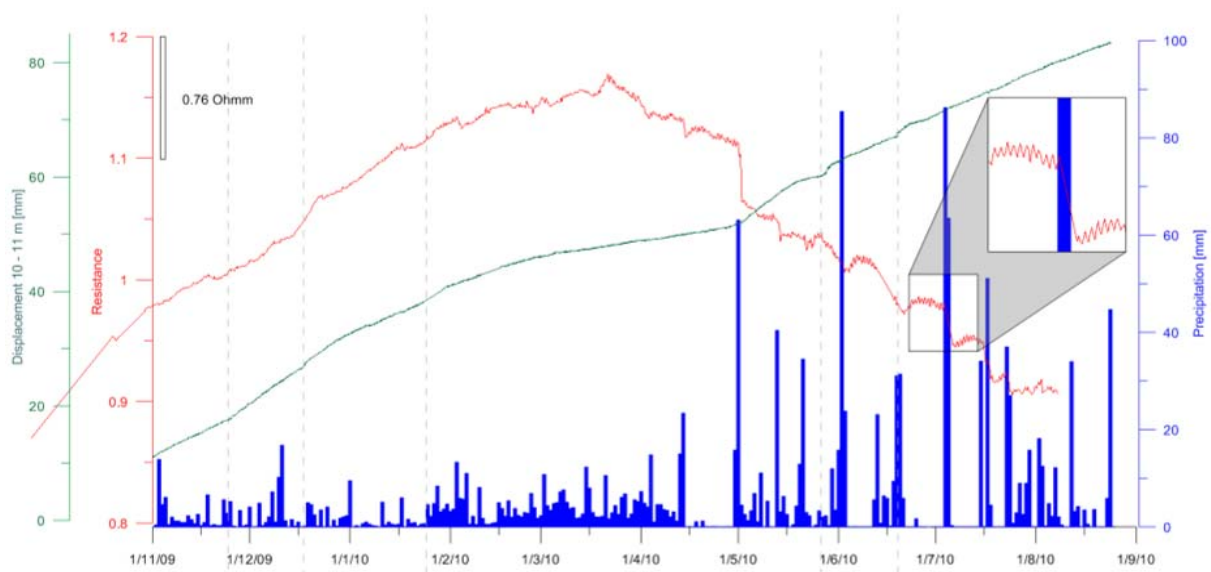


Figure 4.7-17. Correlation of selected apparent resistivity data (red) with displacement and precipitation for the period from November 2009 to September 2010.

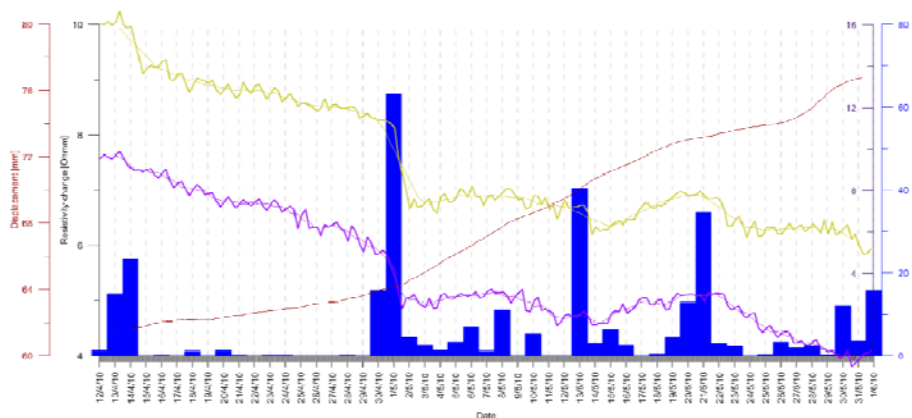


Figure 4.7-18. Correlation of selected apparent resistivity data (yellow, purple) with displacement and precipitation for the event on May 1st, 2010.

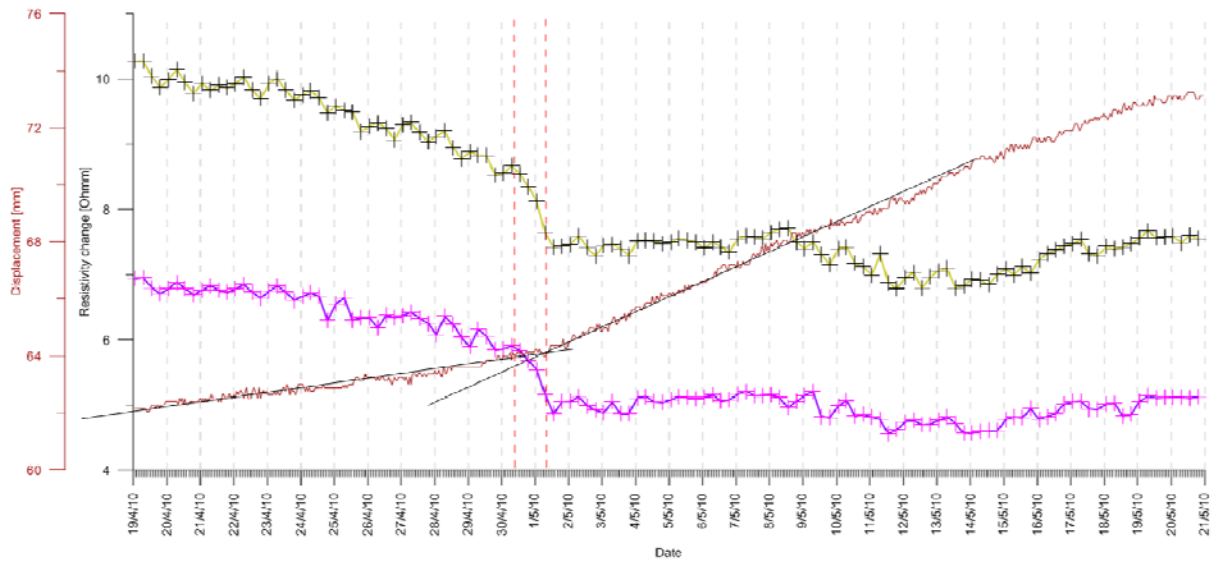


Figure 4.7-19. Correlation of selected apparent resistivity data (yellow, purple) with displacement and precipitation for the event on May 1st.

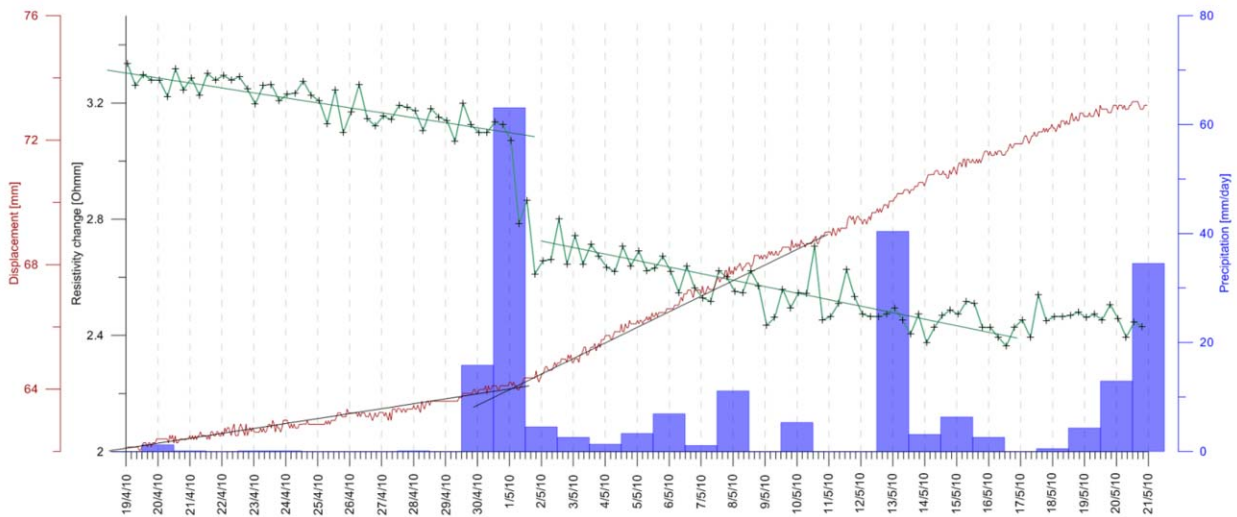


Figure 4.7-20. Correlation of selected apparent resistivity data (yellow, purple) with displacement and precipitation for the event on May 1st.

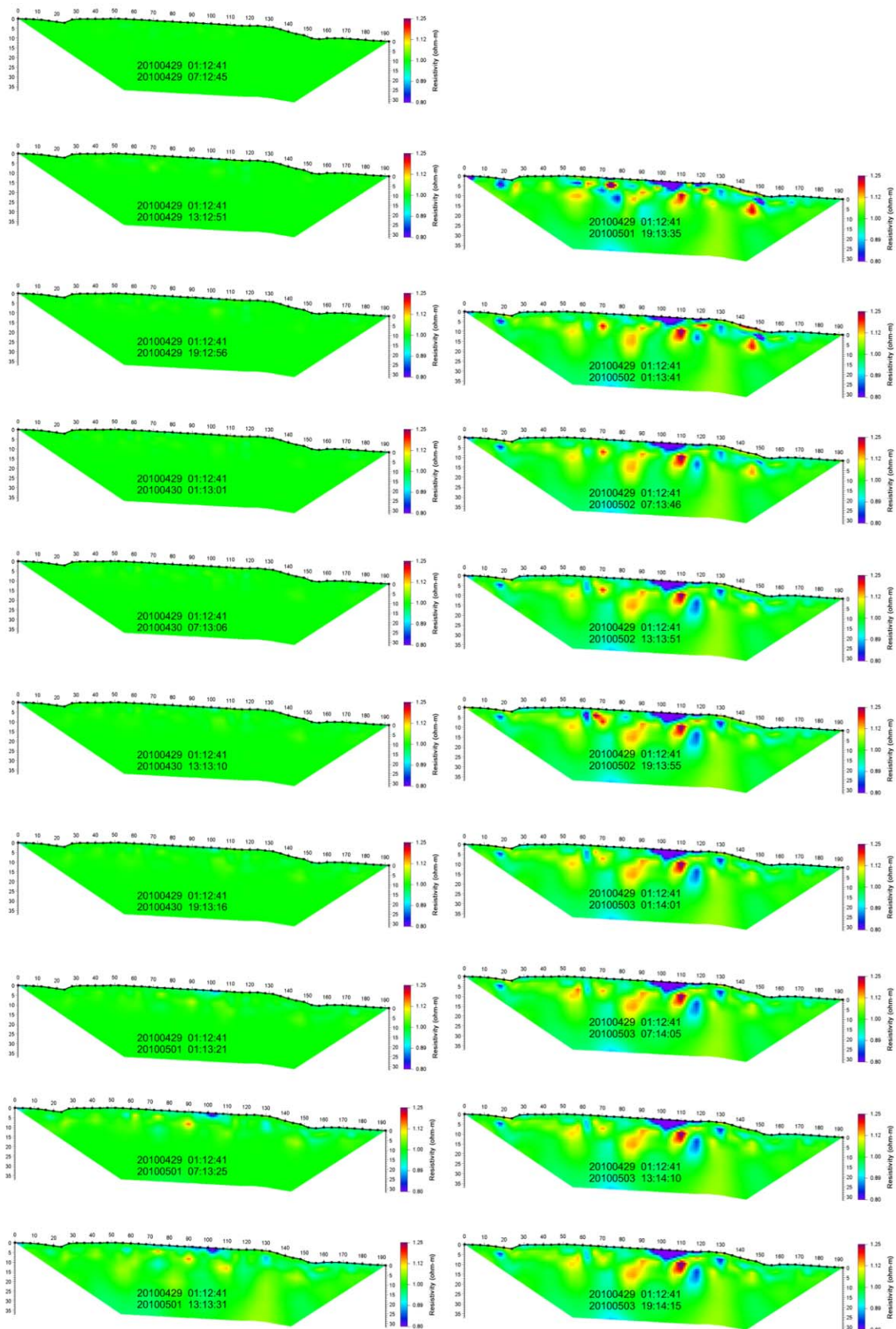


Figure 4.7-21. Time lapse inversion difference to the first measurement.

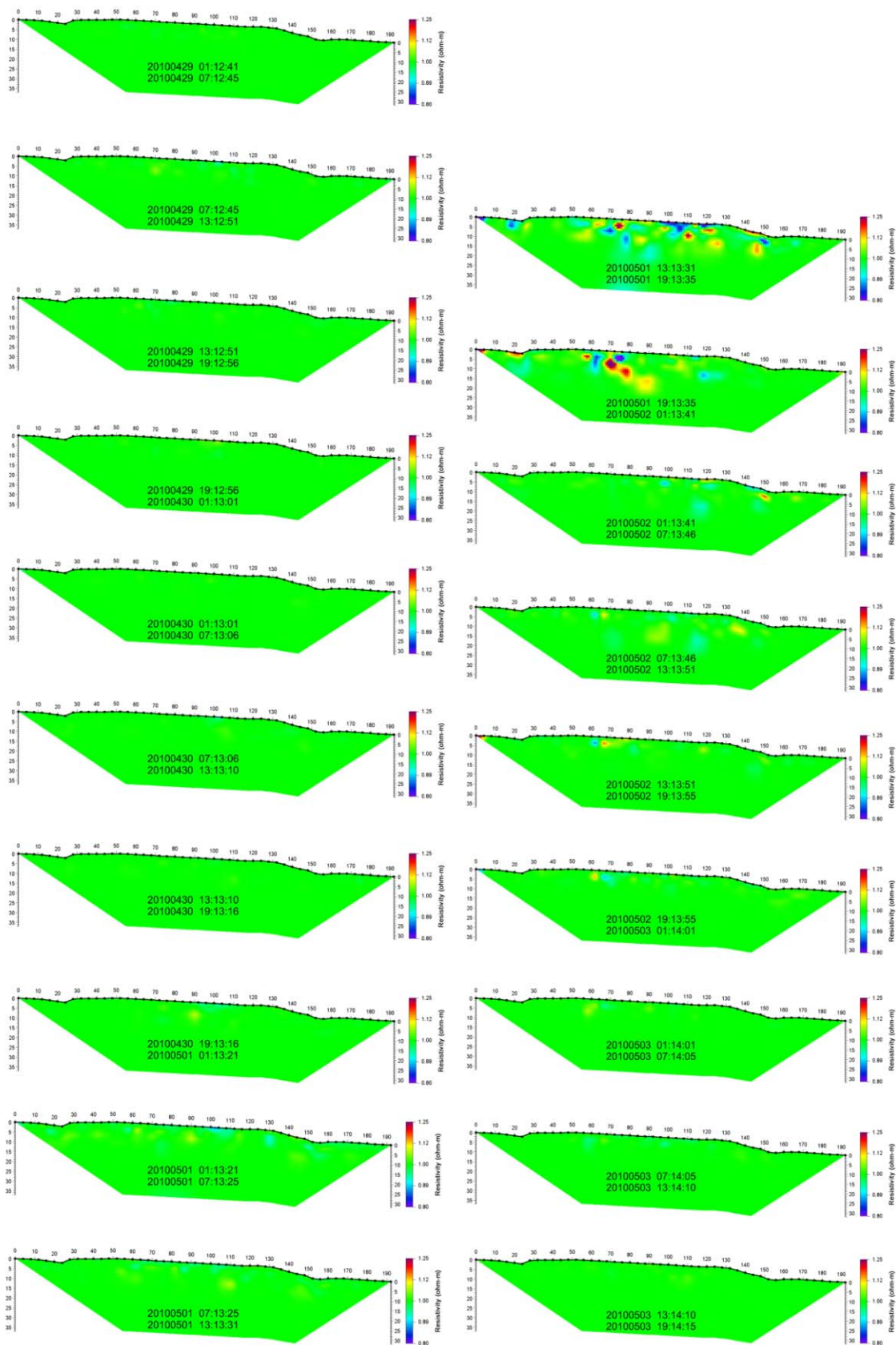


Figure 4.7-22. Time lapse inversion difference to the previous measurement.

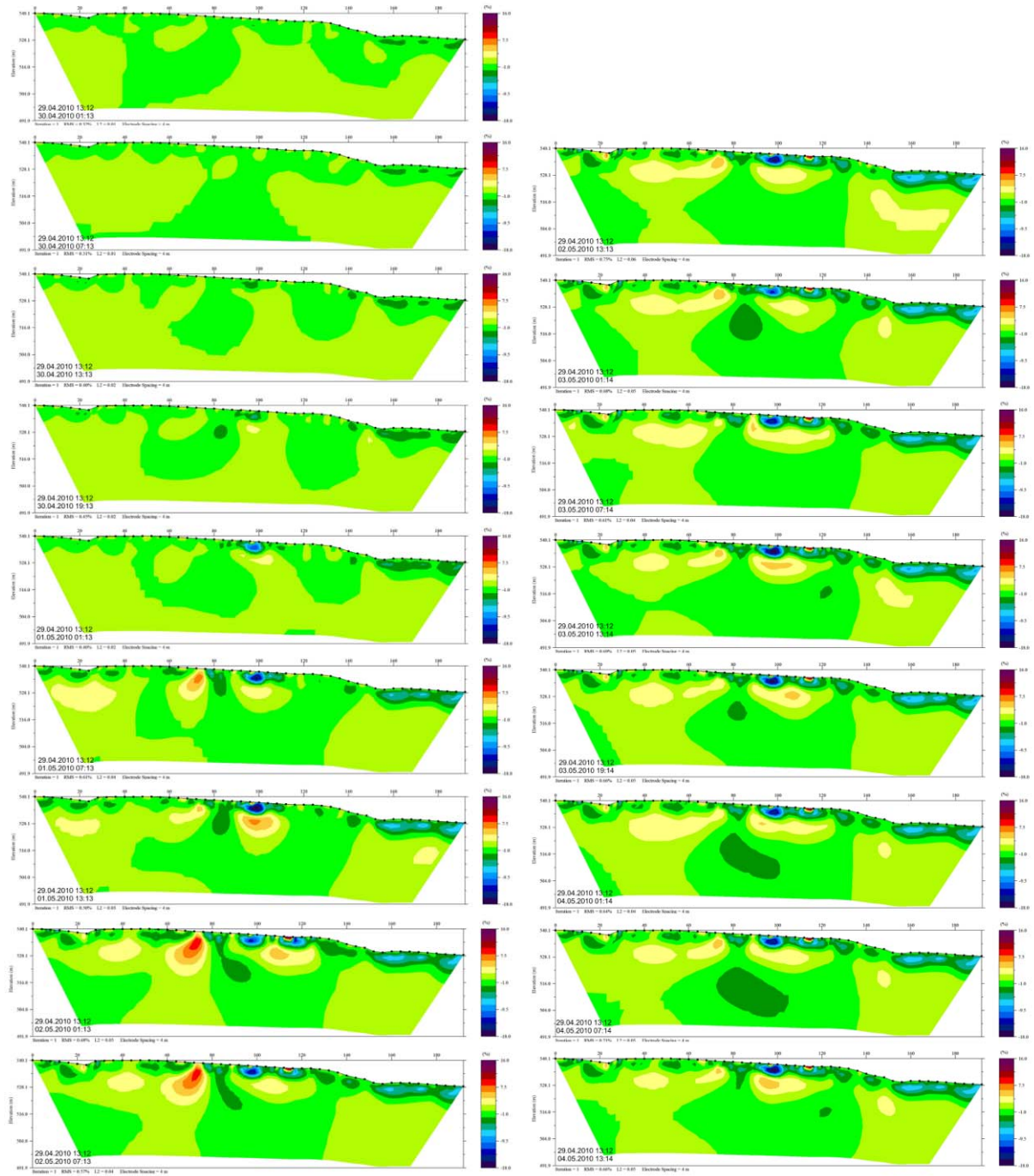


Figure 4.7-23. Time lapse inversion results using the EarthImager code (AGI, EarthImager), differences to the first measurement.

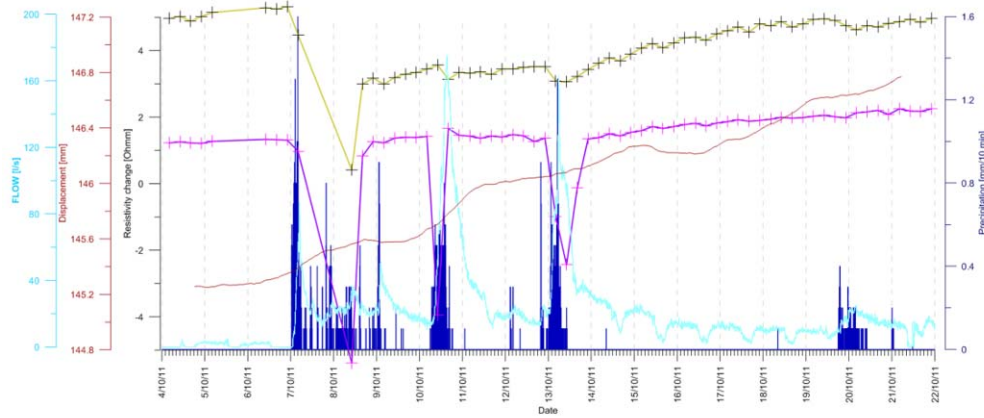


Figure 4.7-24. Correlation of selected apparent resistivity data (yellow, purple) with displacement and precipitation for singular rain events.

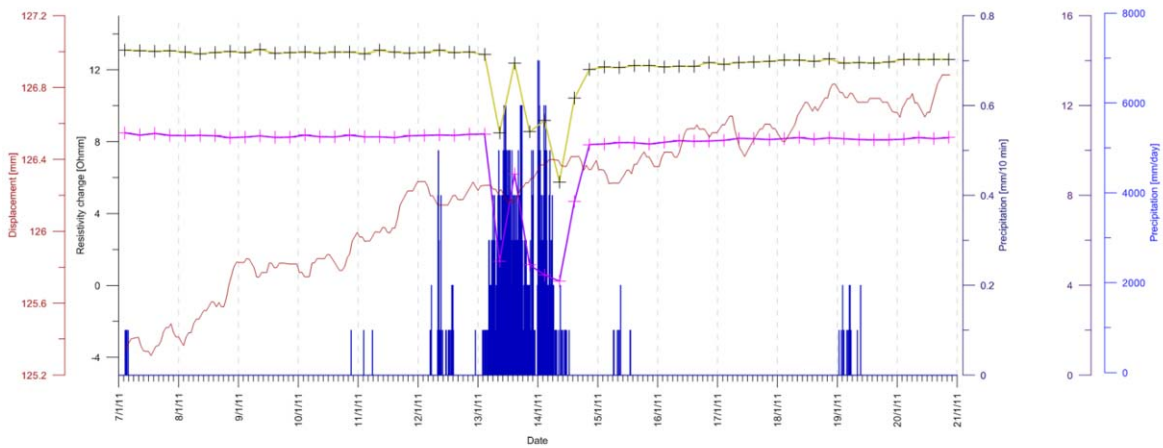


Figure 4.7-25. Correlation of selected apparent resistivity data (yellow, purple) with displacement and precipitation for singular rain events.

4.7.3.5 Self-potential

Along the geoelectric profiles, self-potential (SP) measurements were additionally performed using stainless steel electrodes. The dataset, which was measured hourly, includes gradient-type measurements. It also includes measurements to a reference electrode and to six borehole electrodes which were fixed outside the inclinometric casing of the central DMS drillhole.

Figure 4.7-26 and Figure 4.7-27 present selected results of SP measurements for the whole survey period. The general good correlation of SP anomalies with rainfall is obvious, which is somehow better expressed within the first 19 months of the survey. Figure 4.7-27 shows the results of measurements taken near the drainage river. Periods of a probable increased inflow to the subsurface caused by high flow rates in the river during the spring of 2010 and at the end of May 2011 are marked by a significant decrease of SP values. Figure 4.7-28 allows a closer look of events in the spring of 2011. The location of the electrodes was near the deep drainage system. The figure shows that not all rainfall events were correlated with SP anomalies, however those which were correlated exhibited a very pronounced anomaly lasting several days longer than the rainfall. Figure 4.7-29, Figure 4.7-30 and Figure 4.7-31 show selected events in more detail. With all three events, the SP anomaly started with a sudden increase of the SP value of almost 0.4 V, which happened several hours after the onset of the precipitation and in two cases even after the precipitation. The delay was 20 hours in case 1 (Figure 4.7-29) and six hours in the other cases (Figure 4.7-30, Figure 4.7-31). After a short period (half a day to one day) of continuous increase between 0.2 and 0.3 V, a long-lasting (three- to five-day) decrease to near-original values took place.

Figure 4.7-32 and Figure 4.7-33 display values of precipitation, SP and flow for different survey periods. Although the flow parameter is measured inside the drainage strings, it can be assumed that this parameter might be correlated with time-dependency of the general inflow of surface water to the landslide body. This could explain the almost perfect correlation of the flow data with SP anomalies (including shape and duration of the major phase; see detailed graph Figure 4.7-34). Therefore, we can conclude that in this case SP anomalies represent a parameter which can be used to monitor the inflow of water to the landslide. Time delays of response might define the arrival time of the major water front. However, further analysis must be performed to investigate this correlation in detail.

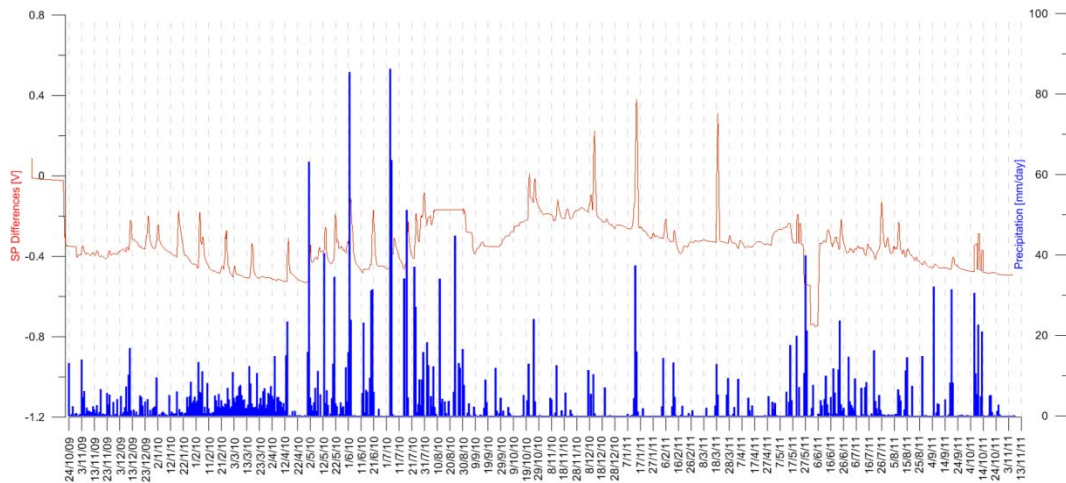


Figure 4.7-26. Self-potential monitoring over the whole survey period.

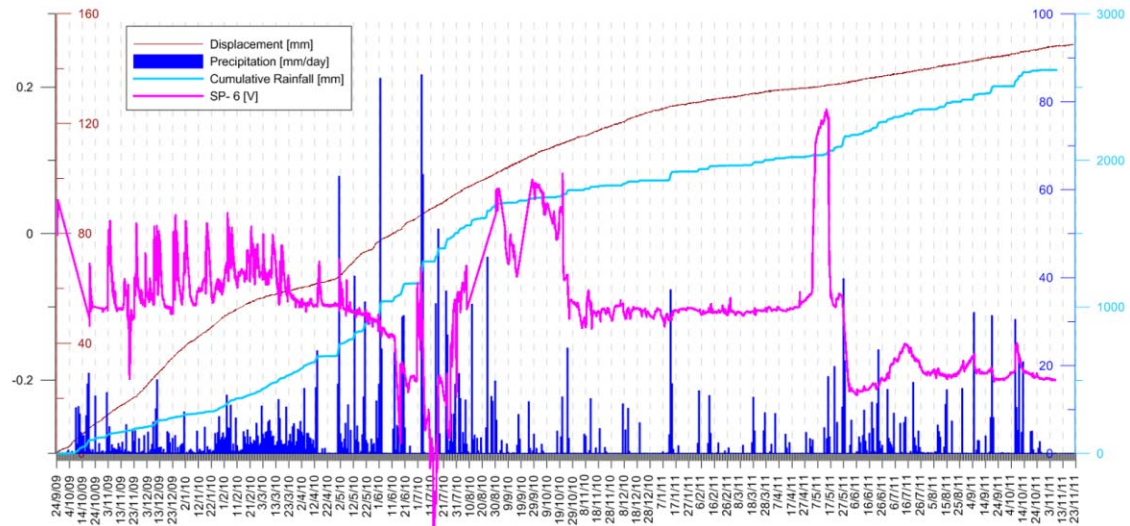


Figure 4.7-27. Self-potential monitoring near the drainage river.

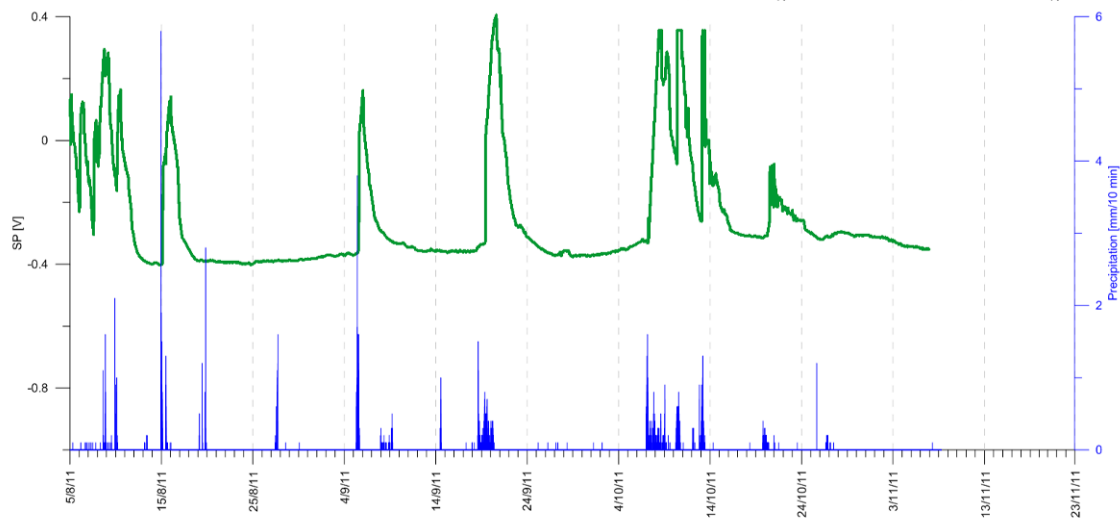


Figure 4.7-28. Correlation of SP anomalies with rainfall in autumn 2011.

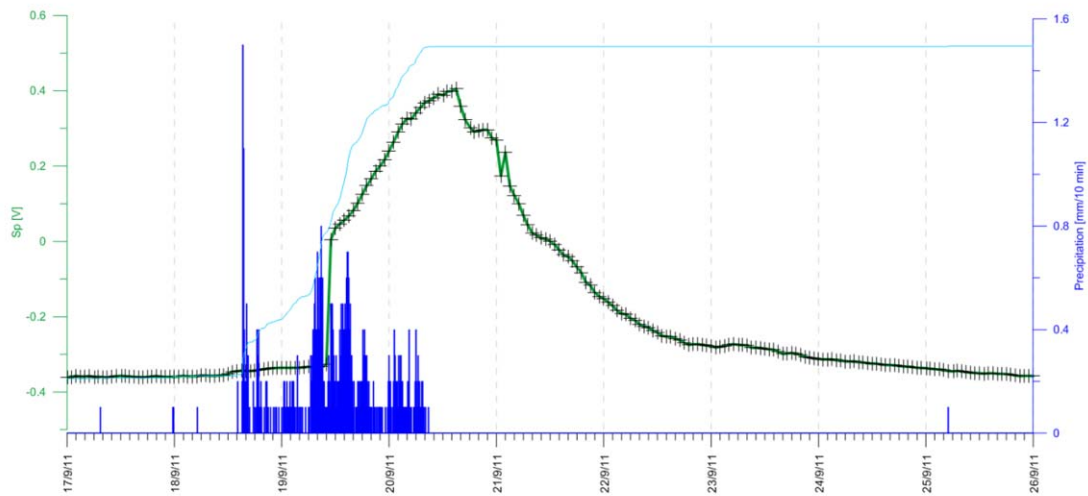


Figure 4.7-29. Detailed graph of a SP anomaly correlated with a rainfall event from 18-20.9.2011.

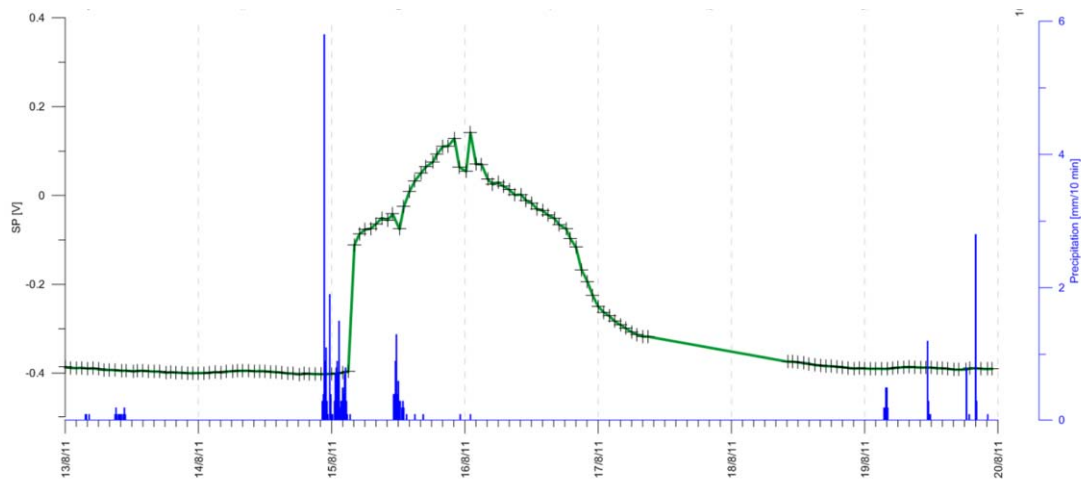


Figure 4.7-30. Detailed graph of a SP anomaly correlated with a rainfall event on 15.8.2011.

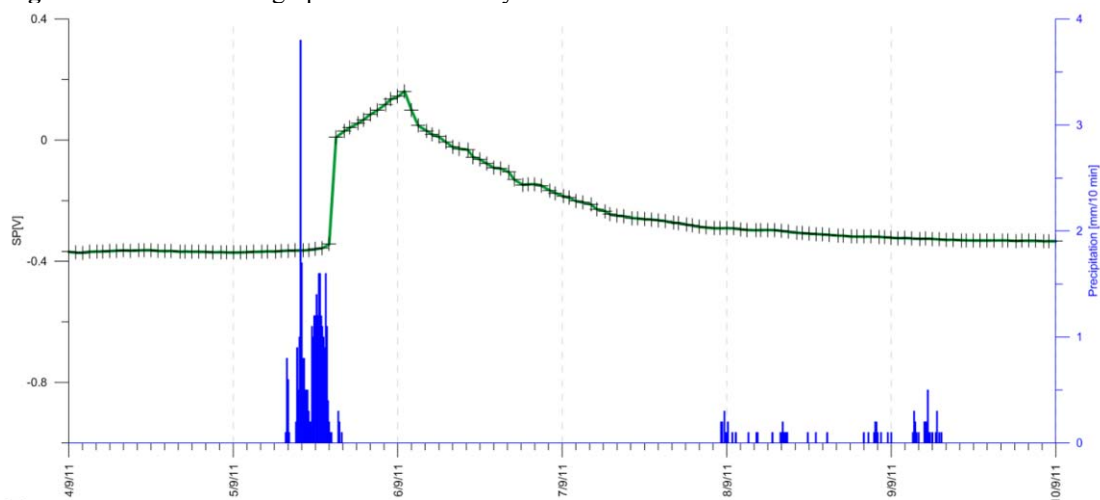


Figure 4.7-31. Detailed graph of a SP anomaly correlated with a rainfall event on 5.9.2011.

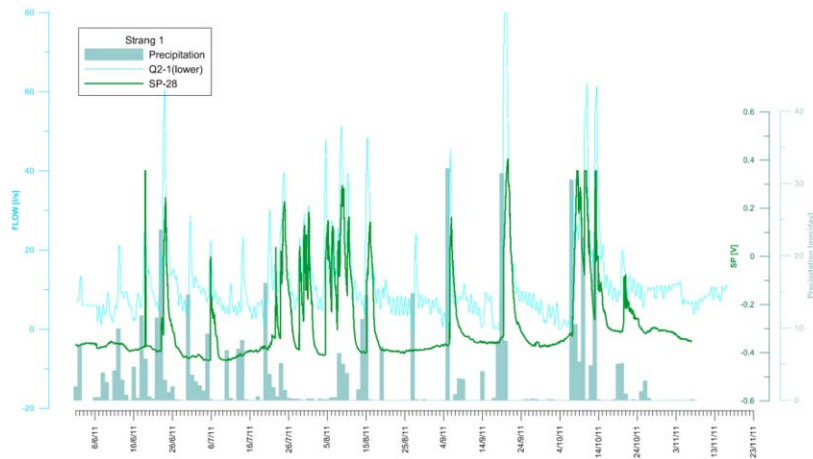


Figure 4.7-32. Correlation of SP anomalies with precipitation and inflow: survey period 2011.

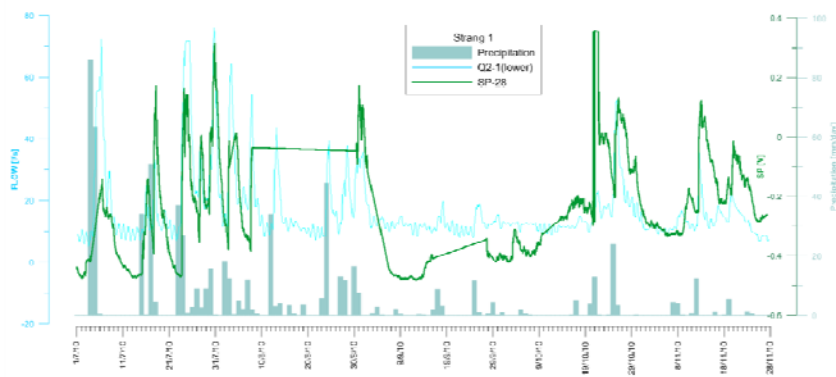


Figure 4.7-33. Correlation of SP anomalies with precipitation and inflow: survey period 2010.

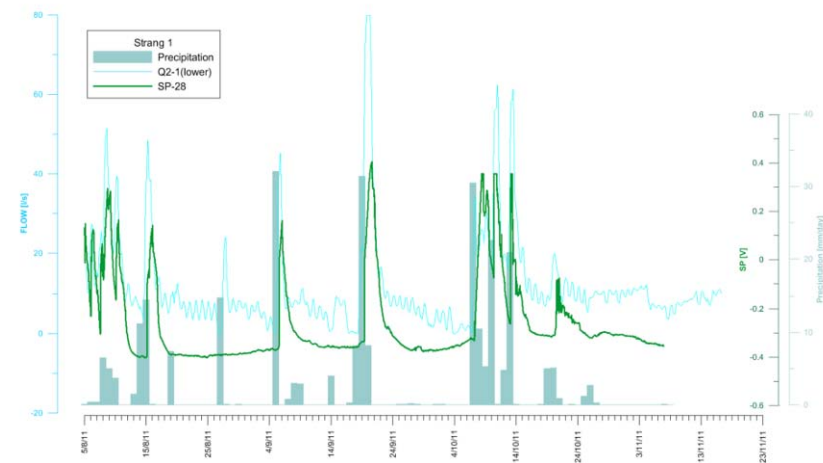


Figure 4.7-34. Graph showing the correlation of SP anomalies with precipitation and inflow in detail.

4.7.4 SUMMARIZED EVALUATION OF PARAMETERS

The case study has so far proven the reliability of the applied methods for long-term monitoring. It clearly shows the long-term stability of geoelectrical parameters and their response to changes in the hydrological system of the subsurface, and proved the high resolution of the DMS system, also allowing the monitoring of very small displacement tendencies. The results showed that intense rainfalls had a direct impact (positive and negative) on the displacement and resistivity pattern causing very small but clearly identifiable changes in both parameters. Moreover, they highlight the necessity of applying a complex monitoring approach, comprising displacement, hydrological parameters (mainly precipitation, water level, inflow) and geophysical parameters, to assess ongoing processes in detail. It also can be concluded that a high time-resolution of monitored data is very important to change small tendencies in the development of parameters, which might allow recognition of system changes far enough ahead of catastrophic consequences. Therefore we can conclude that only permanent monitoring and automatic data broadcasting can provide the data necessary for early warning purposes. For displacement monitoring, we suggest an increase in time resolution from one measurement per hour to one measurement every 10 minutes. Only then can reliable values for velocity automatically be calculated, since data averaging is necessary for small velocities.

However, given that no major changes in the displacement pattern took place in that area during the observation period, a direct evaluation could not be performed of the applied methods' ability to provide early warning parameters. For the same reason, no early warning thresholds for this site could be derived so far and longer observation periods are necessary.

References:

- Egger H. et al. (1996): Geologische Karte der Republik Österreich 1:50 000 – 66 Gmunden. Geologische Bundesanstalt, Wien.
- Egger H. et al. (2007): Geologische Karte der Republik Österreich 1:50 000 – 67 Grünau im Almtal. Geologische Bundesanstalt, Wien.
- Fogliano L., Lovisolo M., Della Giusta A., 2006, Contribution of DMS monitoring systems in the analysis of slide micro-movements for early warning management, risk assesment and evaluation of mitigating actions, Geophysical Research Abstracts, Vol. 8, 06122.
- Hübl, J., Scharf, M., Zott, F. (2010): Gschlifegraben – Gemeinde Gmunden. Band 2: Entwicklung und Aufbau eines Prototyps zur Erfassung hydrologischer Parameter am Gschlifegraben; IAN Report 124, Band 2; Institut für Alpine Naturgefahren, Universität für Bodenkultur, Wien
- Moser G., et .a. (2009): Großhangbewegung Gschlifegraben: Fachübergreifender Synthese-Berich. – MS. Moser/Jaritz Ingenieurbüro für Geologie, Hydrogeologie und Geotechnik, Gmunden. Final report in German with maps, CD.
- Niesner, E., Weidinger, J.T., 2008. Results of a continuous geoelectrical monitoring in the forefront of the large landslide event of 2007/2008 in the Gschlifegraben (Gmunden, Upper Austria). EGU General Assembly 2008, Geophysical Research Abstracts, Vol. 10.
- Supper, R., Römer, A., 2003. New Achievements in Developing a High Speed Geoelectrical Monitoring System for Landslide Monitoring. Proceedings of the Environmental and Engineering Geophysical Society, 9th Meeting Prag, Prag.
- Supper, R., Römer, A., Jochum,B., 2009. Geoelectrical measurements for natural hazard monitoring. SEGJ 9th International Symposium, Extended Abstracts, Sapporo.
- Supper, R., Baroň, I., Jochum, B., Ita, A., Winkler, E., Motschka, K., Moser, G., 2010. From structural investigation towards multi-parameter early warning systems: geophysical contributions to hazard mitigation at the landslide of Gschlifegraben (Gmunden, Upper Austria), Terra Abstracts, European Geosciences Union 2010.

4.8 JETTAN - NORDNES (NORWAY)

L.H. Blikra & L. Kristensen

Åknes/Tafjord Early Warning Centre, Norway

Based on manuscript: Blikra, L.H., Christiansen, H., Kristensen, L. & Dehls, J. (in press): Displacements and the influence of permafrost on rockslides in northern Norway; Implications for driving mechanisms and hazards. 11th International Symposium on Landslides, Banff Canada June 3 -8 2012. ISL 2012

ABSTRACT

Here we present a study of one of the most active rockslides in northern Norway: the Jettan rockslide. An extensive monitoring system has been implemented, in addition to a systematic study of the temperature regimes to understand the influence of seasonal frost and permafrost. An area of up to 17 Mm³ is being displaced today. This area is the topmost northern part of a larger failure system. Displacement varies from about 1 to more than 5 cm/year. Increased velocity starts in May during snowmelt, when air temperature increases. This continues during the entire summer and does not stabilize before late autumn or mid-winter. Movement is not affected by rainfall, and cannot be controlled only by snowmelt. The controlling process for the systematic seasonal deformation pattern is interpreted to be caused by the melting and refreezing of snow and ice in deep fractures. The understanding of the relation between temperature conditions and the displacement pattern at the Jettan slide will have major consequences for the specific handling of the rockslide, but also for the overall hazard evaluation in the region.

Presented parameters: displacement, velocity, air temperature.

4.8.1 GENERAL DESCRIPTION OF THE TEST SITE

In recent years, a large focus has been placed on mapping and detecting large rock slope instabilities due to their potential large risk of initiating destructive tsunamis. Particular attention has been on steep fjord landscapes where several coastal settlements exist. Recent data from differential synthetic aperture radar interferometry (InSAR) have detected a large number of active rockslides in the Troms county of northern Norway (Figure 4.8-1).

One of the main challenges has been analyzing, evaluating and classifying the risk of these active rockslides. Traditionally we are very concerned about the risk linked to large instabilities with active movement. The main controlling parameter for large-scale landslides is normally increased water pressure due to increased precipitation or snowmelt. However, the area under discussion is located in the Arctic portion of the periglacial mountain landscape of northern Norway at 69°30'N, where permafrost exists in the upper parts of the mountains (Christiansen et al., 2010). Processes linked to melting, refreezing and temperature changes in ice can thus be important driving mechanisms for the observed displacements.

The results presented here are based on a study of one of most active rockslides in northern Norway: the Jettan rockslide in Kåfjord municipality (Figure 4.8-1 and Figure 4.8-2). An extensive monitoring system has been implemented in addition to systematic studies of the ground thermal regime to understand seasonal freezing and permafrost conditions (Christiansen et al., 2010). The data are being compiled and discussed in more detail in Blikra & Christiansen (in prep.).

Geological and geomorphic settings

The first geological studies of the Jettan rockslide were started by NGU in 1999 (Blikra & Longva, 2000; Braathen et al., 2004), and a program of periodic GPS measurements was initiated in 2003. Documentation of active movement was provided by NGU in 2004 (Blikra et al., 2006). The Jettan rockslide is part of several large instabilities on a steep mountain slope along the fjord called Storjfjorden, extending from about 900 m amsl. (Figure 4.8-3). The Jettan rockslide consists of a volume possibly up to 17 million m³, and parts are moving with velocities of more than 50 mm/yr (Blikra et al., 2009; Nordvik et al., 2010; Kristensen & Blikra, 2011) (Figure 4.8-3 and Figure 4.8-44). The geomorphology shows that the instabilities are composed of large-scale frontal lobes extending almost down to the fjord (Figs. 3 and 4). However, only a small part of this structure has active displacement. The steep frontal lobes are characterized by heavily fractured rocks and smaller slide scars (Figure 4.8-4).

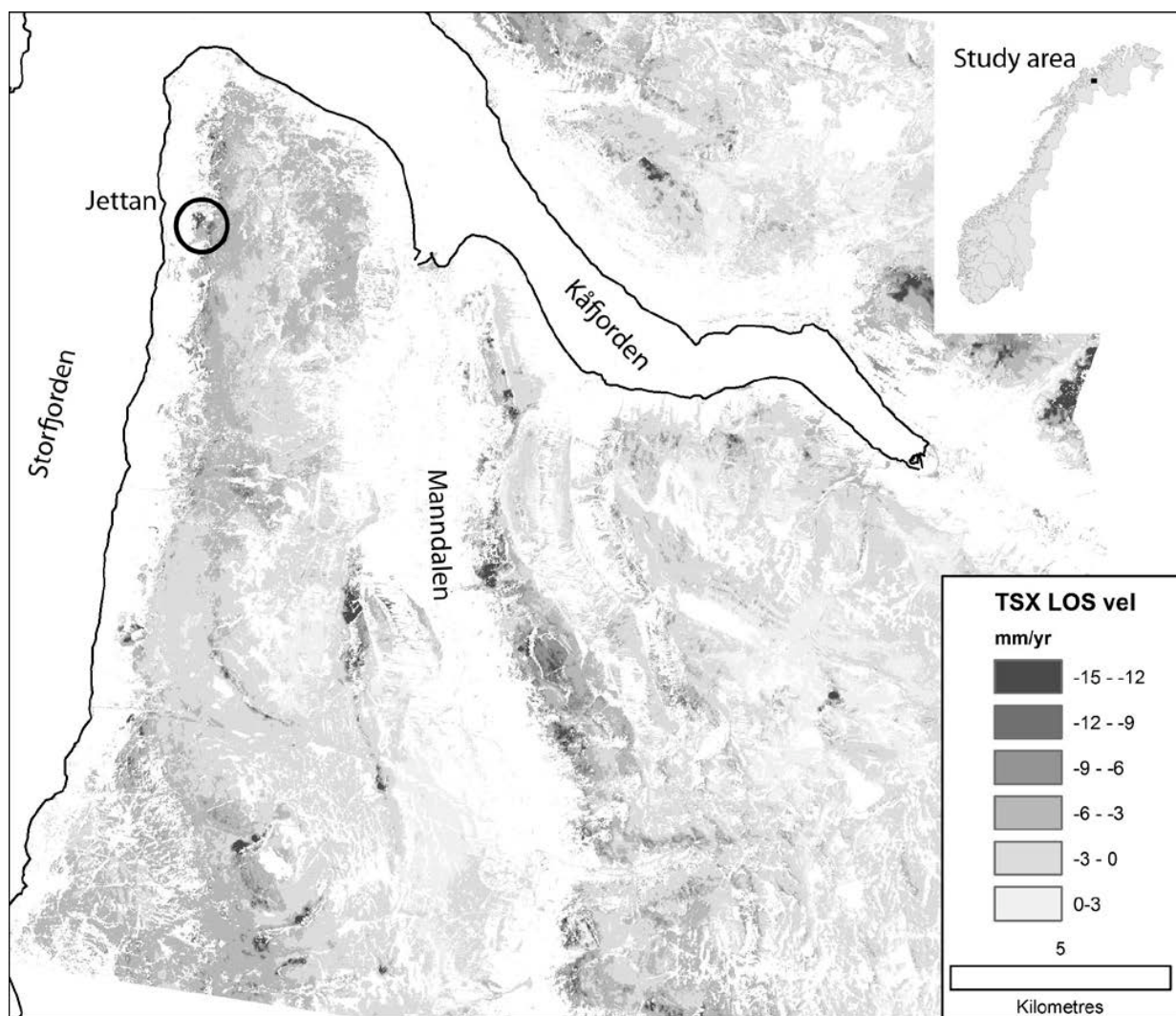


Figure 4.8-1. Overview of the Storjfjorden-Kåfjord study area in Troms county, northern Norway. Annual displacement (line of sight, LOI) recorded from InSAR results based on TerraSAR-X SAR data, provided by DLR, are shown (unpublished, NORUT and NGU). The location of the Jettan rockslide is shown.



Figure 4.8-2. The uppermost chaotic part of the active Jettan rockslide. The instruments in the middle left part are a GPS antenna and reflectors for a single laser and for InSAR (3 m high).

The bedrock consists of different types of marble and schist, with foliation dipping generally towards the west (downslope, Figure 4.8-4). Data from Carrera et al. (2010) and NGU (2004) shows that the foliation generally dips towards southwest and south within the range of 200 and 278°, with a dip in the range of 5 to 30°.

The unstable area is detached from the intact bedrock at its rear by large normal faults, and internally this area is characterized by a series of extensional fractures. Some can be traced up to 300 m long surface depressions. The large back-fracture, bounding the active area (Figure 4.8-4), is about 300 m long, up to 10 m wide and deeper than 25 m. Closer to the steep cliff in the north, the deformation of the surface is more chaotic and intense (Figure 4.8-2). The geometry and basal sliding plane(s) of the complex rockslide are not well understood due to limited information about the deeper structures. The foliation has relatively gentle gradients in many areas, indicating that the sliding plane(s) probably have several steps with destruction of rock bridges. Geophysical measurements (electric and seismic) indicate fractured bedrock deeper than 100 m below the ground's surface (Rønning et al., 2008), but drilling, coring and subsurface deformation data are needed before further conclusions can be made. With an approximate depth of 70 to 120 m of the sliding planes, the total volume of the active area can be as large as between 5 and 17 million m³ (Kristensen & Blikra, 2011).

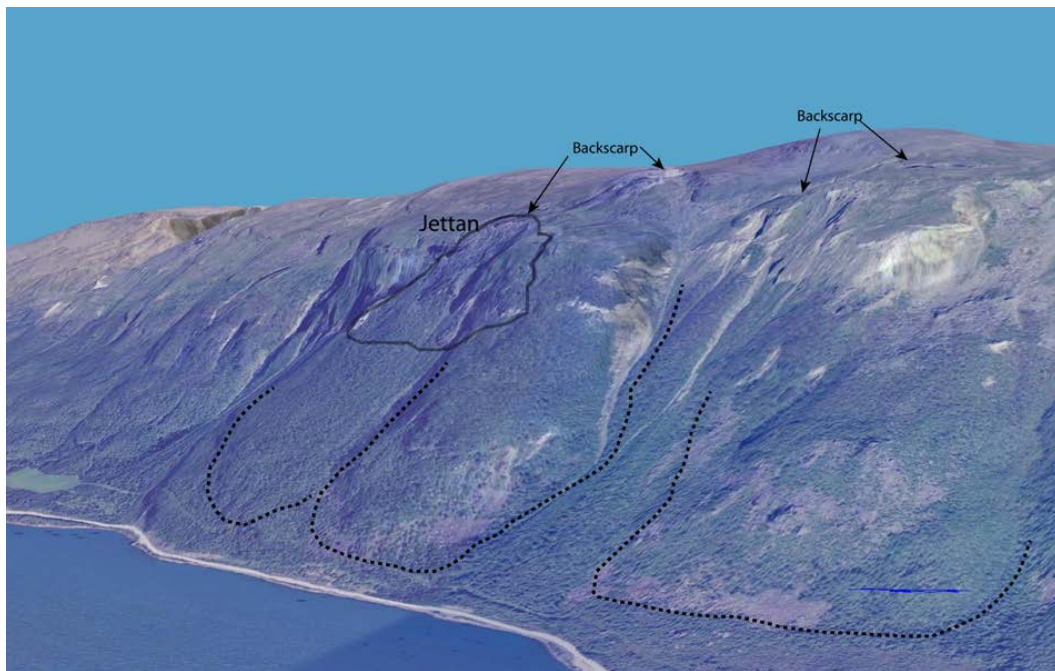


Figure 4.8-3. A seaward view towards NE of the instabilities at Nordnes with the Jettan to the left. Note the extent of the large frontal “lobes” of the instabilities consisting of highly fractured bedrock (stippled lines). The active moving area at Jettan is encircled in the top part. From www.norgei3d.

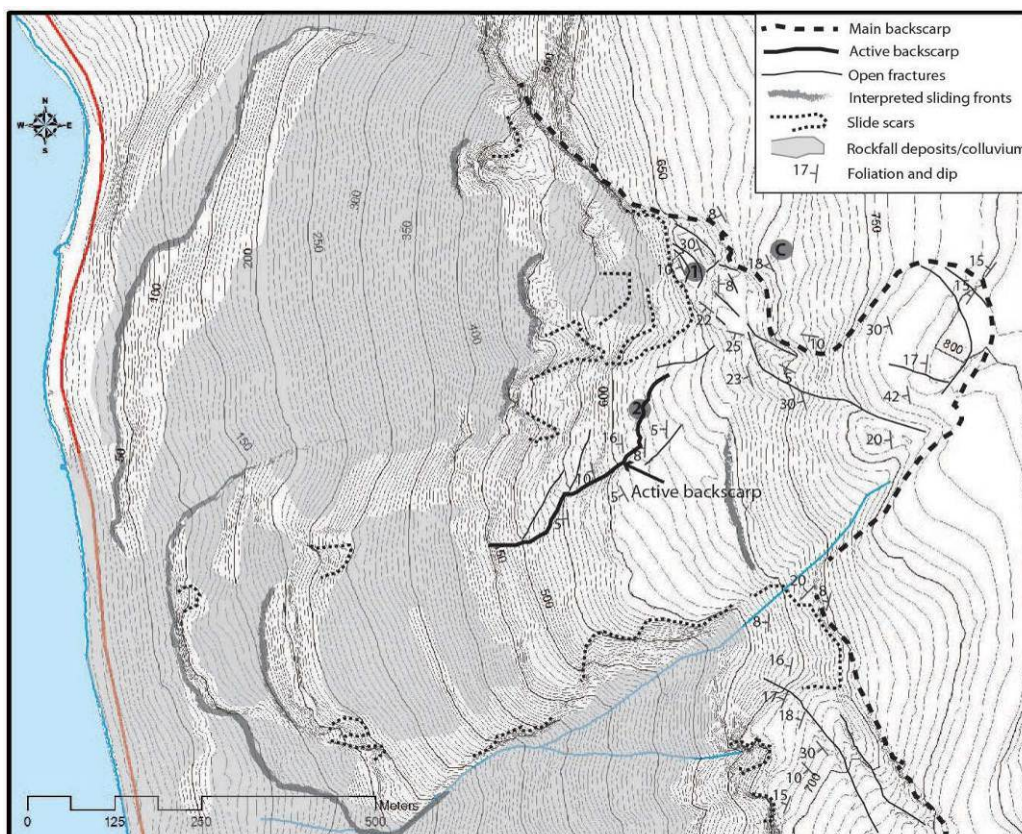


Figure 4.8-4. Topographical and geomorphological map of the Jettan rockslide with foliation measurements. Point 1 is the location of laser 1 and GPS YN3 and point 2 is the location of extensometer 2 and crackmeter 3 shown in figure 5 and 6. Point c is the meteorological station.

4.8.2 DESIGN OF THE MONITORING NETWORK

A monitoring program focusing on surface displacements was initiated in 2007. The present system includes a large sensor network of GPS, single lasers, extensometers, crackmeters and tiltmeters (Blikra et al., 2009; Nordvik et al., 2010).

4.8.3 ANALYSIS OF MONITORING DATA

4.8.3.1 Displacement

The results of the continuous GPS records showing displacement vectors and an overview of the area with active deformations are shown in Figure 4.8-5. It can be seen that the active back scarp is responsible for the main part of the movement. By far the greatest displacement takes place in the chaotic northern part (52 mm/yr), with a vector towards the west.

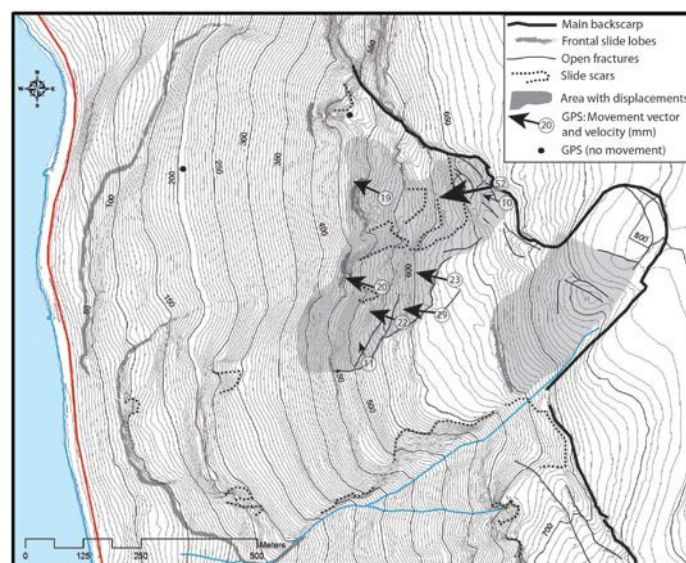


Figure 4.8-5. The geomorphic map of Jettan with documented GPS displacements and overview of the active areas.

Most of the GPS points show a distinct seasonal variation, with significantly increased displacement during the snowmelt as of May. This slows down again in late autumn (Figure 4.8-6). The lasers, extensometers and crackmeters also show characteristic seasonal trends (Figure 4.8-7); the laser and extensometer show the same trend as the GPS with a very well-defined onset of increased velocity in May and a velocity reduction in November. This seasonal trend has been documented during the entire measuring period of more than four years (Kristensen & Blikra 2011). The crackmeters record movement of local minor cracks, and they show a different trend with extension during the winter and contraction during the summer (Figure 4.8-7). The onset of the displacement is well defined in all the crackmeters in active fractures, starting at the beginning of August and ending in late-autumn/early winter along with the lasers and extensometers.

The extensometer in Figure 4.8-7 is located in the large active back scarp and shows displacement of close to 2 cm/year (Figure 4.8-5 and Figure 4.8-7). This indicates that displacement across the large fracture is responsible for most of the total movement recorded by the GPS in this area; see point 2 in Figure 4.8-4.

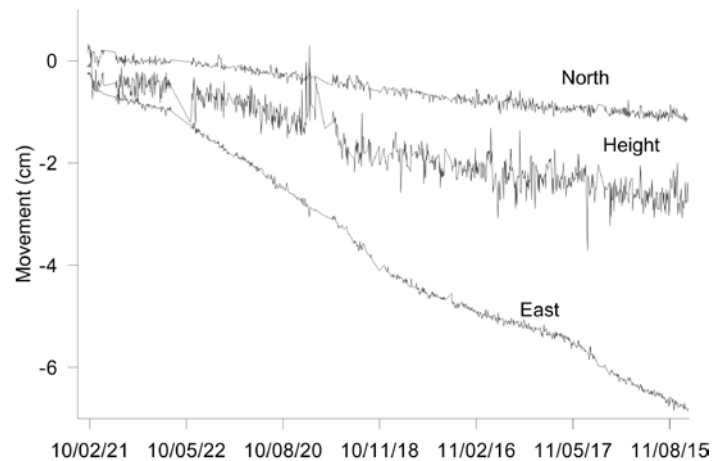


Figure 4.8-6. Movement of GPS antenna in the northern part of Jettan. Note the seasonal variation with high displacement from May to late November in the eastern component (movement towards west).

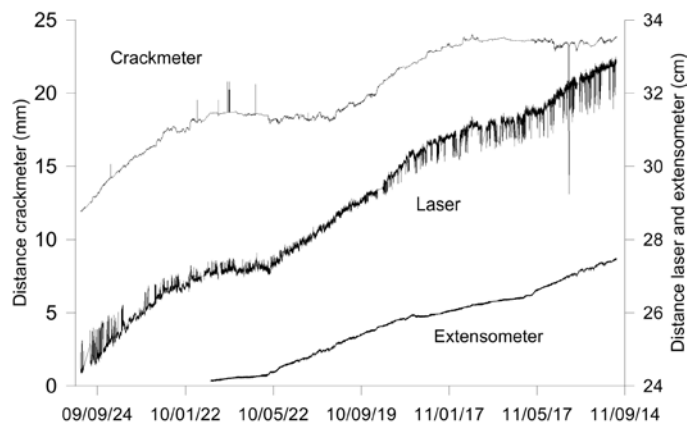


Figure 4.8-7. Displacement of the laser at point 2 (Figure 4.8-4) and from the crackmeter and the extensometer at the active backscarp at point 2 (Figure 4.8-4).

4.8.3.2 Temperature

The ground thermal regime has been recorded in different parts of the Jettan rockslide and its surroundings to study how ground freezing and thawing might affect the seasonal deformation pattern in this location just below the regional permafrost level (Blikra & Christiansen, in prep.).

The mean annual air temperature for the study period of September 1st 2009 to September 1st 2011 is, respectively, -1°C and -0.3°C. The air temperature is largely negative from October to April, and reaching 15-20°C in the summer (Figure 4.8-8, upper panel). Correspondingly, the air temperature of the active back scarp (Figure 4.8-8 lower) follows the air temperature variation at the beginning of the winter until enough snow has accumulated into the back scarp to isolate the crack air temperature from the atmosphere. From that point, the air temperatures in the crack remain between 0 and -2°C. (At the end of summer 2010, a thermistor was installed in the deepest accessible part of the back scarp directly into the ice body identified there (Figure 4.8-8 lower panel and Figure 4.8-9). This part of the crack experienced significant early-winter cooling before enough snow filled the crack to prevent further cooling. A relatively stable winter temperature of around -2°C is then reached.) In May, when snow melting starts, the ice temperature increases to around 0°C. This

temperature remains stable through the summer until early autumn, when (most likely) meltwater erosion has increased the temperature further and melted the ice around the sensor. Field inspection at the end of summer 2011 was not possible, as new ice had formed on top of where the sensor was located.

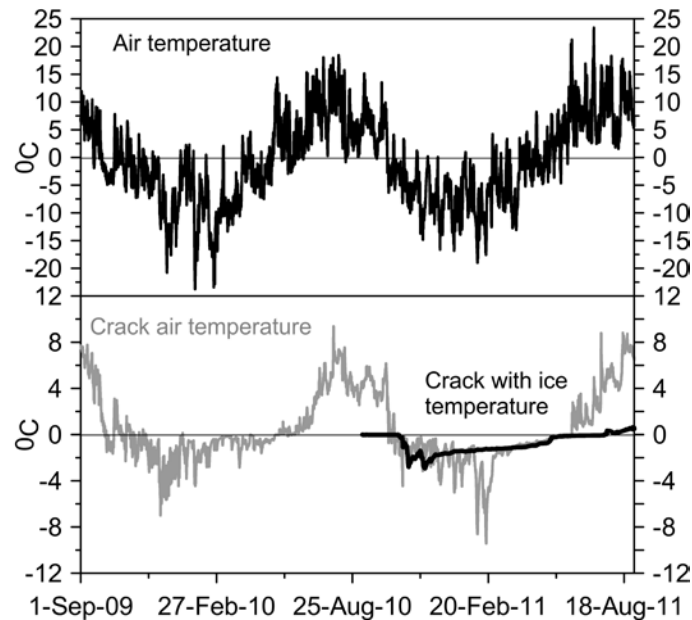


Figure 4.8-8. The air temperature (2 m) from the Nordnes meteorological station (upper panel) (see location in Figure 4.9-4). Crack air temperature measured approx. 10 m below the terrain surface and the temperature recorded in the ice in the lower part of the active backscarp (lower panel). Observe difference in scale on the y-axes.



Figure 4.8-9. The ice caves at 20 to 25 m depth in the active backscarp. View upwards.

4.8.4 SUMMARIZED EVALUATION OF PARAMETERS

The work done at Nordnes during the TSP IPY project demonstrated the occurrence of discontinuous permafrost conditions in this area (Christiansen et al., 2010), and permanent ice is also found below 25 m depth in the active back scarp. A more detailed study and interpretation of these conditions is being published by Blikra & Christiansen (in prep).

The displacement data demonstrate a very systematic seasonal displacement pattern that has been identified over several years. The onset of the increased velocity is initiated in May during snowmelt, when air temperature becomes positive. It continues through the entire summer and into the autumn and only stabilizes in late autumn or mid-winter (see Figure 4.8-6 and Figure 4.8-7). Thus, the displacement pattern cannot be caused only by snowmelt. Moreover, the displacement shows no correlation with precipitation. The controlling process for this characteristic pattern is interpreted to be melting and refreezing of ice in deep fractures.

Thus, the driving mechanisms for the Jettan rockslide seem to be controlled by processes linked to the occurrence and changing characteristics of permafrost in the unstable rocks. The shear strength of the detachment plane(s) are largely controlled by thermal conditions, and characteristics of the ice in the permafrost are due to several processes:

1. Increased ice temperature during snowmelt in the spring as meltwater drains into the fractures and later refreezes in lower and still colder parts. This produces heat, which will increase the ice temperature from several degrees below freezing up to near the melting point (Figure 4.8-8). This temperature increase will drastically reduce the shear strength if ice occurs along the sliding planes.

2. Summer meltwater eroding its way downwards causes refreezing in the permafrost thermal regime of the back scarp's lower parts, forming ice in the deep fractures. This can lead to volume increase, and thus a pushing effect along the active back scarp.

3. Spring meltwater can lead to the total melting of cold ice in the sliding planes, causing possible reduced shear strength.

The shear strength of the sliding plane(s) will be largest with the occurrence of cold ice, and smallest with the occurrence of warm ice just below 0°C. The largest displacements should thus be experienced during stages in which warm ice is present in these areas, which should initiate during maximum snowmelt in late spring and early summer.

4.8.5 IMPLICATIONS FOR HAZARD

The evaluation and classification of a rockslide hazard is a very difficult task. In practice, most large landslides with active movements and large consequences are monitored with the implementation of an early warning system. In Norway, an attempt was made at a systematic risk classification of large unstable rockslopes. This hazard classification is based on the following criteria (Dahle et al. 2011; Hermanns et al. 2011): 1) displacement rates; 2) structural and kinematic conditions; and 3) frequency of failures in similar geological settings both regionally and locally. The most important factor for the risk evaluation will be the displacement rates, and the understanding of the driving mechanisms will thus be critical for the risk classification and handling.

The displacement characteristics documented from the satellite InSAR analysis show a large number of rockslide areas in this region (Figure 4.8-1). As the displacement rate is the most important factor for evaluating the risk of large landslides, a large number of sites will probably be considered as high-risk. This may lead to the initiation of monitoring and early

warning systems at a large number of sites, requiring significant economic and personal resources.

The analysis of the seasonal temperature regime and the displacement pattern at the Jettan site, and also several observations of permafrost with high ice content in fractures at other rockslide sites in the region, show that processes linked to ice formation and erosion in permafrost environments are most likely very critical to driving mechanisms. It seems that the occurrence of ice in fractures and in detachment zones is needed to reduce the shear strength and thus drive the rockslide movements. This is also indicated by the relatively gentle gradient of foliation planes seen at the Jettan site; the gravitational forces along relatively gentle sliding planes may be too small to drive a rockslide without processes linked to ice. However, these conditions will vary locally, controlled by the local slope conditions.

In conclusion, an increased understanding of the coupling of the permafrost thermal regime and displacements of the Jettan rockslide in the Arctic landscape in northern Norway enables the identification of important questions related to the evaluation of hazards, and thus how society will cope with these processes. It is clear that future research must be focused on obtaining more knowledge of temperature conditions and their influence on the driving mechanisms behind large rockslides in northern Norway.

ACKNOWLEDGMENTS

The data presented are part of the monitoring project established by the monitoring center Nordnorsk Fjellovervåking in Kåfjord. We especially thank Roald Elvenes, Bernt Lyngstad and Henning Hansen. The InSAR analysis is performed by NORUT and NGU.

References

- Blikra, L.H. & Christiansen et al. (in prep.): Permafrost influence on rockslide deformations, Nordnes, northern Norway. In preparation.
- Blikra, L.H., Eiken, T., Henderson, I. & Ganerød, G.V. 2006: Forprosjekt fjellskred i Troms–Status: 2005. Norges geologiske undersøkelse Rapport 2006.040.
- Blikra, L.H., Henderson, I. & Nordvik, T. 2009: Faren for fjellskred fra Nordnesfjellet i Lyngenfjorden, Troms (in Norwegian). Geological Survey of Norway Report 2009.026, pp 29.
- Blikra, L.H. & Longva, O. 2000: Gravitational-slope failures in Troms: Indications of palaeoseismic activity? Pp 31-40. In: Dehls, J. & Olesen, O. (red.): Neotectonics in Norway. Annual Technical Report. NGU Report 2000.01.
- Braathen, A., Blikra, L.H., Berg, S.S., Karlsen, F., 2004. Rock-slope failures in Norway; type, geometry, deformation mechanisms and stability, Norwegian Journal of Geology, 84, 67-88.
- Bunholt, H., Osmundsen, P.T., Tedfield, T., Oppikofer, T., Eiken, T., L'Heureux, J-S., Hermanns, R. & Lauknes, T.M. 2011: ROS Fjellskred i Troms: status og analyser etter feltarbeid 2010. NGU Report 3011.031.
- Carrea, D., Derron, M.-H., Lévy, S., Nichoud, C., Oppikofer, T. & Jaboyedoff, M. 2010: Analysis of groundbased Lidar data from Troms County (Norway). Report IGAR2010-N01.
- Christiansen, H.H., Eitzelmüller, B., Isaksen, K., Juliussen, H., Farbrøt, H., Humlum, O., Johansson, M., Ingeman-Nielsen, T., Kristensen, L., Hjort, J., Holmlund, P., Sannel, A.B.K., Sigsgaard, C., Åkerman, H.J., Foged, N., Blikra, L.H., Perenosky, M.A. & Ødegård, R. (2010) The Thermal State of Permafrost in the Nordic area during the International Polar Year 2007-2009. Permafrost and Periglacial Processes, 21, 156-181.
- Dahle, H., Anda, E., Sætre S., Saintot, A., Böhme M., Hermanns, R., Oppikofer T., Dalsegg E., Rønning, J.S. & Deron, M. H. 2011. Risiko og sårbarhetsanalyse for fjellskred i Møre og Romsdal. 105 p.
- Henderson, I.H.C., Saintot, A., Venvik-Ganerød, G., Blikra, L.H., 2007. Fjellskredkartlegging i Troms, NGU Rapport 2007.041, Norwegian Geological Survey (in Norwegian), 1-37.
- Hermanns, R., Blikra, L.H., Anda, E., Saintot, A., Dahle, H., Oppikofer, T., Fisher, L., Bunholt, H., Böhme, M., Dehls, J., Lauknes, T.R., Redfield, T., Osmundsen, P.T. & Eiken, T. 2011: Systematic mapping of large unstable rock slopes in Norway. Proceedings of the 2nd world landslide forum, 3-7 October 2011.

- Kristensen, L. & Blikra, L.H. 2011: The unstable rockslopes at Nordnesfjellet in Troms: Displacements, revised scenarios and early-warning levels. Åknes report 06.2011. NGU, 2004: Detailed structural map of the Jettan and Indre Nordnes rockslope failures. Unpublished
- Nordvik, T., Blikra, L.H., Nyrrnes, E. & Derron, M.H. 2010: Statistical analysis of seasonal displacements at the Nordnes rockslide, northern Norway. *Engineering Geology* 114, 228-237.
- Rønning, J.S., Dalsegg, E., Heincke, B.H., Juliussen, H., Tønnesen, J.F., 2008. Geofysiske målinger på Nordnesfjellet sommeren 2007. NGU Rapport 2008.024, Norwegian Geological Survey (in Norwegian), 1-28.

4.9 MANNEN (NORWAY)

L.H. Blikra & L. Kristensen

Åknes/Tafjord Early Warning Centre, Norway

ABSTRACT

Mannen is one of only four high-risk rock instabilities in Norway. It has the potential of creating a rock avalanche of 2 - 20 million m³ with catastrophic consequences for houses and infrastructure in the valley, in particular as a landslide dam may be formed. An early warning system has been established, which is based on measurements of displacement in the instability and a well-defined alarm chain. The monitoring sensors are a GPS network, lasers, extensometers, a ground-based radar system and a borehole instrument; all data are checked daily. Construction of the early warning system was nearly complete in 2010 and over one year's worth of measurements are reported here. During this time the velocity in the upper part of the instability was about 2 cm/year. A seasonal trend with increased velocities during the snowmelt and summertime is seen. The active rockslide body is highly fractured and has no groundwater, and the increased movement is interpreted to be an effect of water coming into the fine-grained and brecciated detachment zones. This will saturate the sliding planes and reduce their shear strength.

Presented parameters: displacement, velocity, precipitation, air temperature.

4.9.1 GENERAL DESCRIPTION OF THE TEST SITE

Geological and geomorphic settings

The Mannen rock slope instability is located in Møre and Romsdal County in western Norway (Figure 4.9-1). The instability is developed at the edge of a 1295 m elevated plateau southwest of the steep, glacially eroded valley called Romsdalen.

The bedrock consists of Proterozoic sillimanite-bearing gneisses with inherited structural weaknesses from the tectonic deformation. Specifically, the metamorphic foliation surfaces are prone to be reactivated where favorable orientation occurs in regards to the gravitational forces (Saintot et al. 2011).

At the top, where the main backcrack is developed, foliation is near-vertical. In the upper part of the moving area, a borehole showed foliation dipping about 30° to the north and downslope, but further down the pattern is more complex as the gneisses are intensely folded. Inside the instability the bedrock is extremely fractured and weathering products of soil cover much of the surface. The morphology is characterized by the well-defined backscarp and numerous smaller slide scars (Figure 4.9-1). The scars bear witness to multiple recent rockfalls or smaller rock avalanches on the slope; the latest occurred on November 7, 2011, which destroyed a cable to one of the GPS antennas.

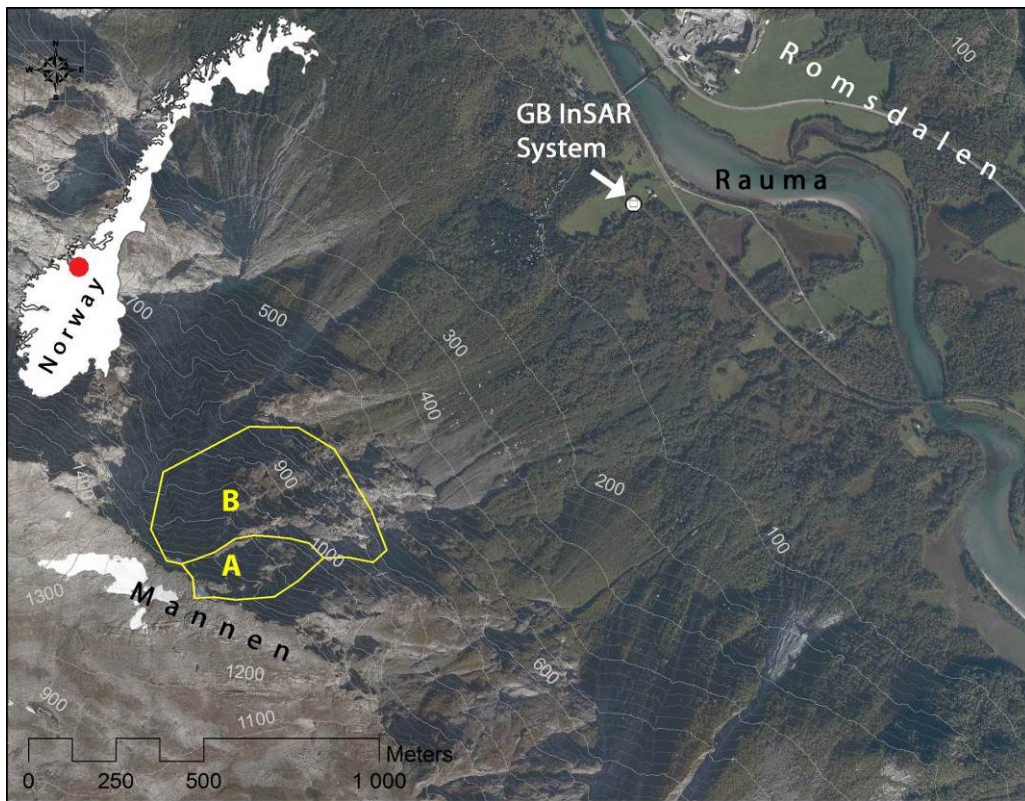


Figure 4.9-1. The location of Mannen and the mapped scenarios, with estimated annual likelihood of A: 1/100 and B: 1/1000.

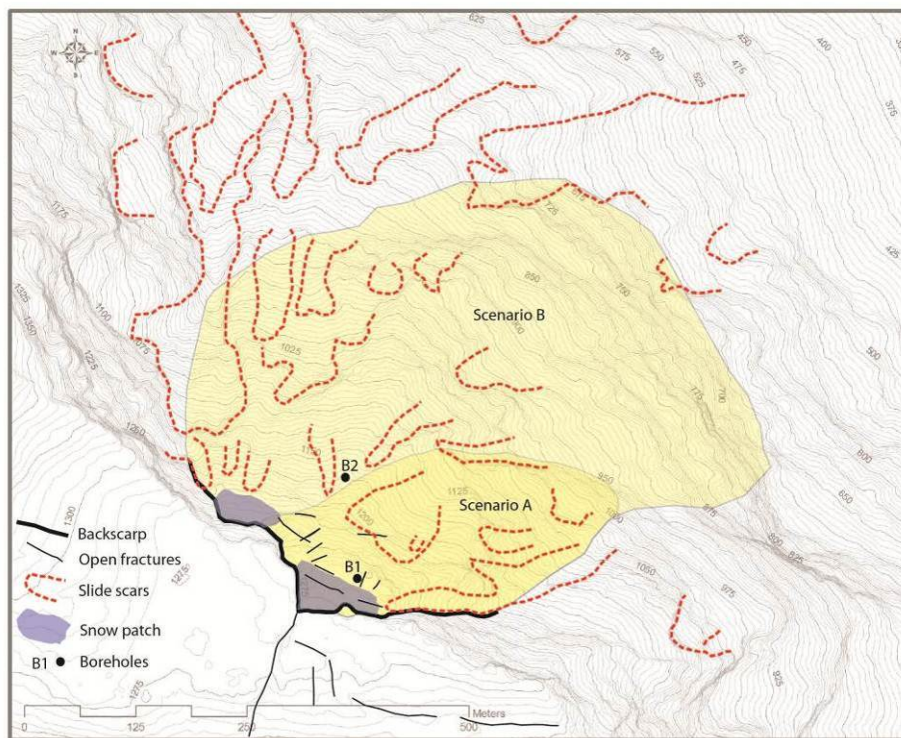


Figure 4.9-2. Morphological map of the Mannen rockslide.

Characterization of the site

A part of the plateau towards the valley (100 million m³) is bounded by deep clefts indicating past movement, but most of this appears inactive today (Figure 4.9-2). A block of possibly 15-20 million m³ has been lowered 15-20 m from the plateau (Figure 4.9-2 and Figure 4.9-3), and a block in its upper part (of 2-3 million m³) has been measured periodically with DGPS, showing a yearly movement of 4-5 cm dipping 45-50° against ENE. These two blocks are the basis of scenarios (A & B) drawn in Figure 4.9-1 and Figure 4.9-2. The Norwegian Geological Survey and the county governor have estimated that the annual probability of a rock avalanche of scenario A is about 1/100. Following structural and geological analysis of the surrounding areas, Henderson and Saintot (2007) deduced a translational sliding as a mechanism of deformation of the rock slope instability.

Modelling work shows that a rock avalanche of a magnitude of either scenarios A or B would destroy the road and railroad at the valley bottom as well as several houses. Furthermore, the rock debris may dam the river Rauma, with a subsequent risk of dam collapse and flooding downstream of the river.

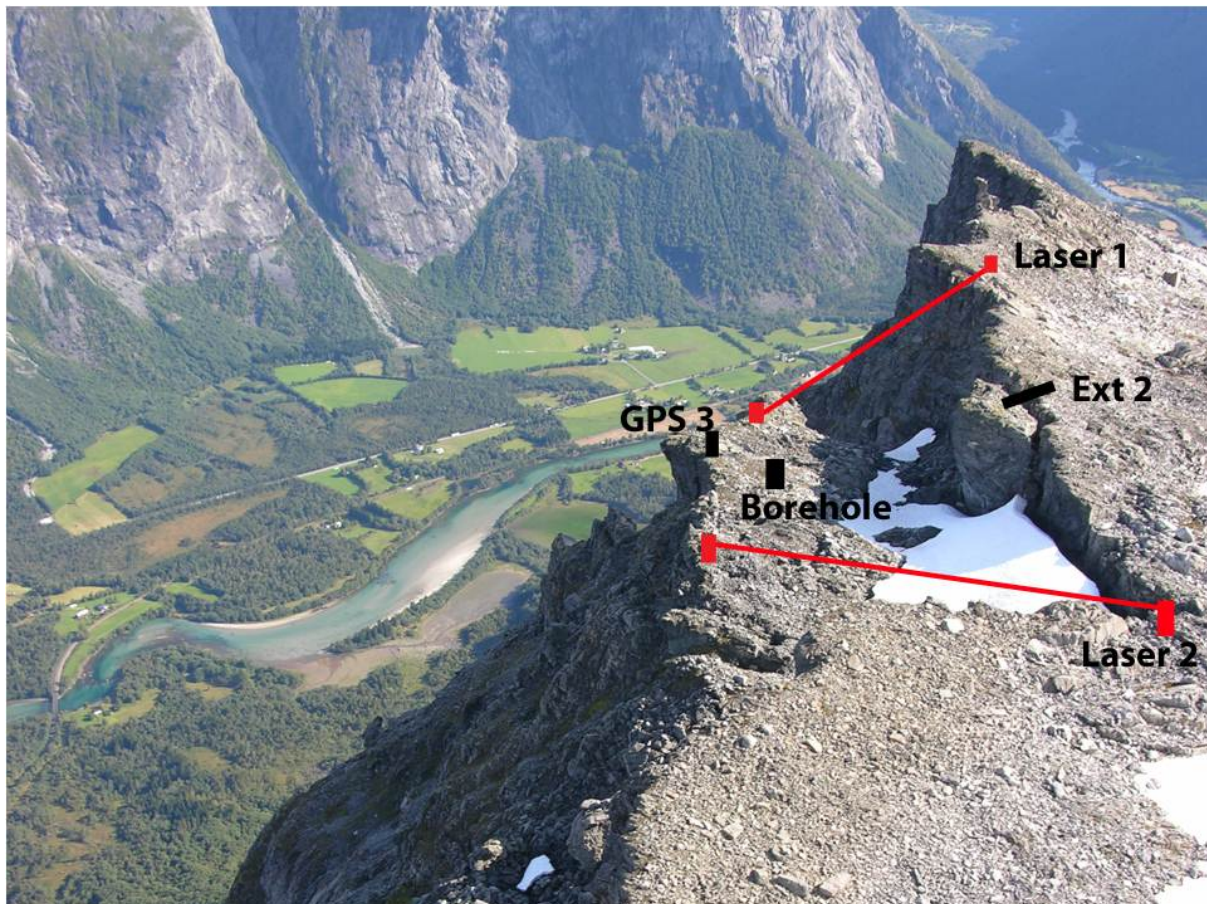


Figure 4.9-3. Photo of the upper part of Mannen, showing the block that has been lowered from the plateau. Some instruments from the upper part of the rock slope instability are shown.

Description of the history of the mass movement

Deposits of more than 15 large rock avalanches postdating deglaciation have been mapped over a 25 km stretch in Romsdalen. In historic times, numerous rockfalls and smaller rock avalanches have occurred in the valley, many of which cost human lives. Most appear to have

occurred during spring and summer time (www.skrednett.no), but a possible correlation to precipitation or other environmental factors has not been tested. A rockfall event inside the instability occurred on November 7, 2011 after several days of fine weather, though unusually high temperatures probably led to some snowmelt. Large active talus fans (Figure 4.9-1) bear evidence of high slope activity.

4.9.2 DESIGN OF THE MONITORING NETWORK

Investigations at the site were initiated in 2004 by annual measurements of fixed points using differential GPS, and more points were added in 2006. The measurements showed a total displacement of 4-5 cm/yr with a dip of 45° towards ENE in the most active block (Dahle et al 2008). Detailed geological mapping followed in 2006. Based on the high displacement rate, the past slope displacement, and the large potential consequences of a rock avalanche, the instability was classified as a high-risk object in 2009 (Dahle et al., 2008; Saintot et al., 2011) and the construction of an early warning system was initiated the same year by Åknes Tafjord Early Warning Centre. Meanwhile, investigations continued in 2010 with the core-drilling of a 139 m deep borehole (location Figure 4.9-2 and Figure 4.9-3). The core was carefully logged for rock type and deformation structures, and the borehole was photographed using a televiewer that makes it possible to see all fractures and breccias inside the borehole in detail and study their relation to foliation (Saintot et al 2011). Afterwards, the borehole was instrumented with a DMS column that both identifies sliding planes and is used in the early warning system to monitor displacement. In 2011, another borehole was drilled further down the slope (Figure 4.9-2) which will also be instrumented with a DMS column. Also in 2011, a 800 m long 2D resistivity profile was surveyed across the upper part of the instability, in an attempt to find slope parallel sliding structures to better delineate the depth of the instability.

Investigations are now more or less complete, though a model that better links the structural information with observed patterns of displacement is yet to be constructed. The day to day monitoring data works both to provide information to be used for early warning and to be included in the rock instability investigation.

Instrumentation at the Mannen instability consists of two lasers, seven extensometers, eight GPS antennas, one DMS borehole instrument, and a meteorological station. At the valley bottom, a ground-based radar system is in place that measures displacement of the entire slope and provides the only information we obtain from the lower, inaccessible part of the rock instability. A diesel generator inside a bunker at the top provides power to the sensors, and the data signals are collected in dataloggers in the bunker as well.

The bunker is connected to the internet by a radio link to the valley. Thus, the generator control system, dataloggers, routers and other equipment in the bunker are accessible from everywhere via VPN. The data is transferred to a database and this database has a web-interface that permits a display of the measurements of flexible intervals.

All sensors are checked daily in order to identify failure of instrument or communication as well as unusual movement. An online steerable camera at the top often provides a first indication of the cause of a problem – it could be fog, obscuring the view from the lasers, ice placed on the reflectors, or snow that distorts the GB InSAR measurements. In the event of a bigger problem, such as a broken cable from a rockfall or an avalanche, it is repaired as fast as possible. However, access to several sensors on the slope is difficult and dangerous during the

winter, and it may be impossible to find and fix an instrument or cable below a very thick snow cover in any case. The generator is maintained according to schedule.

4.9.3 ANALYSIS OF MONITORING DATA

4.9.3.1 Surface displacement: DGPS network

A permanent GPS (GNSS) network has been in place since November 3, 2010. It consists of eight antennas, of which two are placed at assumed stable locations as references (Figure 4.9-4). Data is processed using a RTK (Real Time Kinematic) technique every 15 minutes and post-processed for 12-hour averages.

The six antennas in the active part of the instability have moved between 0 and 22 mm in 3D within one year of measurement. The fastest antenna is GPS 3 and a plot of the recordings in north, east and height (z) directions is seen in Figure 4.9-5. On Figure 4.9-4, a summary of all antennas and their velocity and direction is shown.

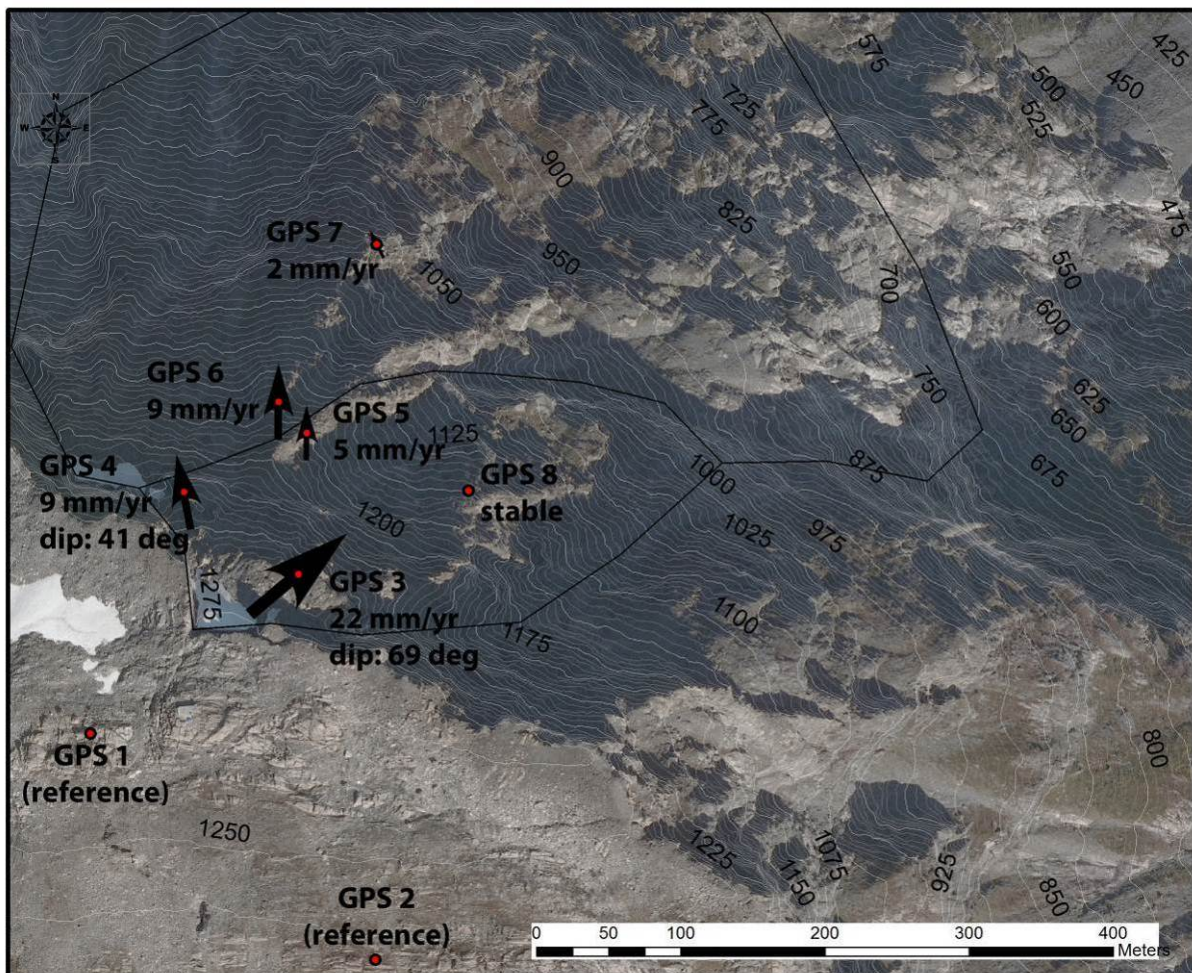


Figure 4.9-4. The location of the GPS antennas and an overview of their velocities and directions.

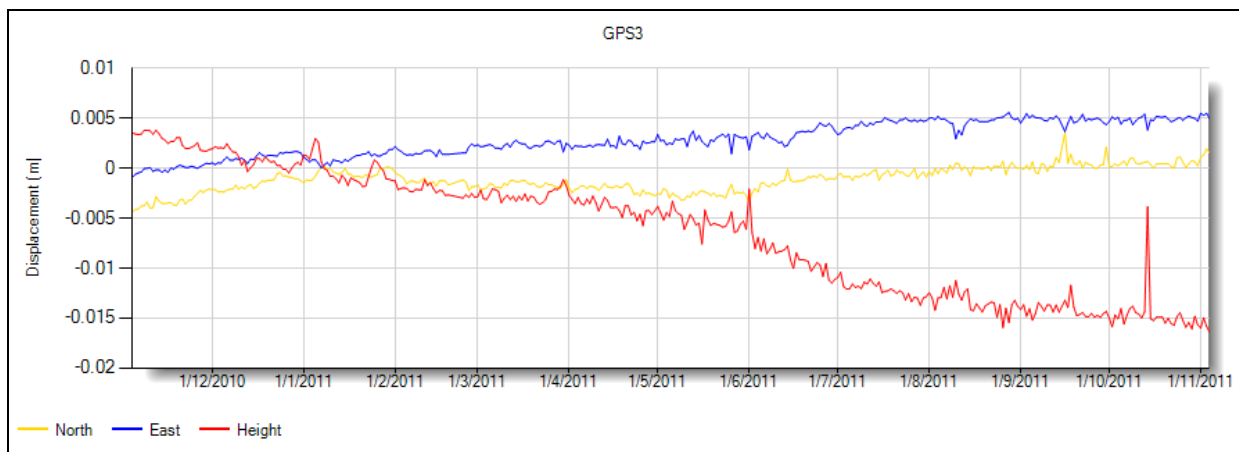


Figure 4.9-5. Movement in three directions of GPS 3 between November 3, 2010 and November 3, 2011.

The 12-hour post-processing are more precise than the RTK processing, with fluctuations of about 2 mm in the north and east directions and 10 mm in the z direction. The RTK data fluctuate about 10 mm in the north and east directions and 30 mm in the z direction. No automatic filtering is applied.

The GPSs provide reliable data, but apart from GPS 3, the recorded movement is not much bigger than the level of random fluctuations so far. GPS 3 was fastest in the summer from June to August (Figure 4.9-3), in particular in the z direction.

The GPSs directly show the magnitude of surface displacement and thus mass movement. As they are distributed in the upper part of the instability they may also help delineate zones moving with different velocities and stable areas.

The GPS antennas are very important parts of the EW system. They will provide reliable data in an acceleration phase up to a certain level; however, they are dependant on cables to the bunker both for power and data transmission, and the cables will probably fail in the last stages before a rock avalanche.

4.9.3.2 Surface displacement: lasers

Two lasers measure the distance across the main back crack (location: Figure 4.9-2) and have been operational since October 21 2009. Once every five minutes, 10 measurements are taken, the data quality checked, and the average value logged. The lasers use visible light and depend on free sight to the reflectors, therefore fog or heavy precipitation can disturb the measurements. They measure in the Line Of Sight (LOS) which may underrepresent the true displacement vector. In most cases the values fluctuate within a couple of millimeters, but regularly meteorological conditions create fluctuations of >20 mm. Some noise is removed by using daily averages when plotting a longer time series.

The lasers have measured about 40 mm displacement in their two years of operation (Figure 4.9-6), corresponding to 20 mm/yr. Some fluctuations in velocity are present in the data and probably linked to seasonal variation, but the variation is slightly different between the two lasers.

The lasers directly measure displacement and thus mass movement. They are important parts of the early warning system, due to their frequent and reliable measurements across the main back scarp. As the sensors are placed at stable ground, and the reflectors are passive, no

cables are required inside the instability (except some heating during winter). In case the reflectors move out of sight from the lasers, they are easy to adjust from the top.

4.9.3.3 Displacement: extensometers

Seven extensometers measure movement across different cracks in the upper part of the instability. Apart from extensometer 2, they have all measured less than 2 mm displacement since since August 25, 2010. Extensometer 2 is placed behind a block with the highest rate of displacement in the instability (Figure 4.9-3). When this block fails, it will fall onto the main block instability, but it is probably too small to trigger a larger rock avalanche.

Extensometer 2 has recorded displacement in the crack of a total of 56 mm in 14 months (Figure 4.9-6), which is more than twice the velocity of the lasers and GPS 3. The movement of extensometer 2 displays a strong seasonality, with high rates of displacement in summer and autumn, and a marked slowdown in winter (Figure 4.9-6). The other extensometers are not catching significant crack openings, and seem to be placed across more or less passive fractures on the moving block.

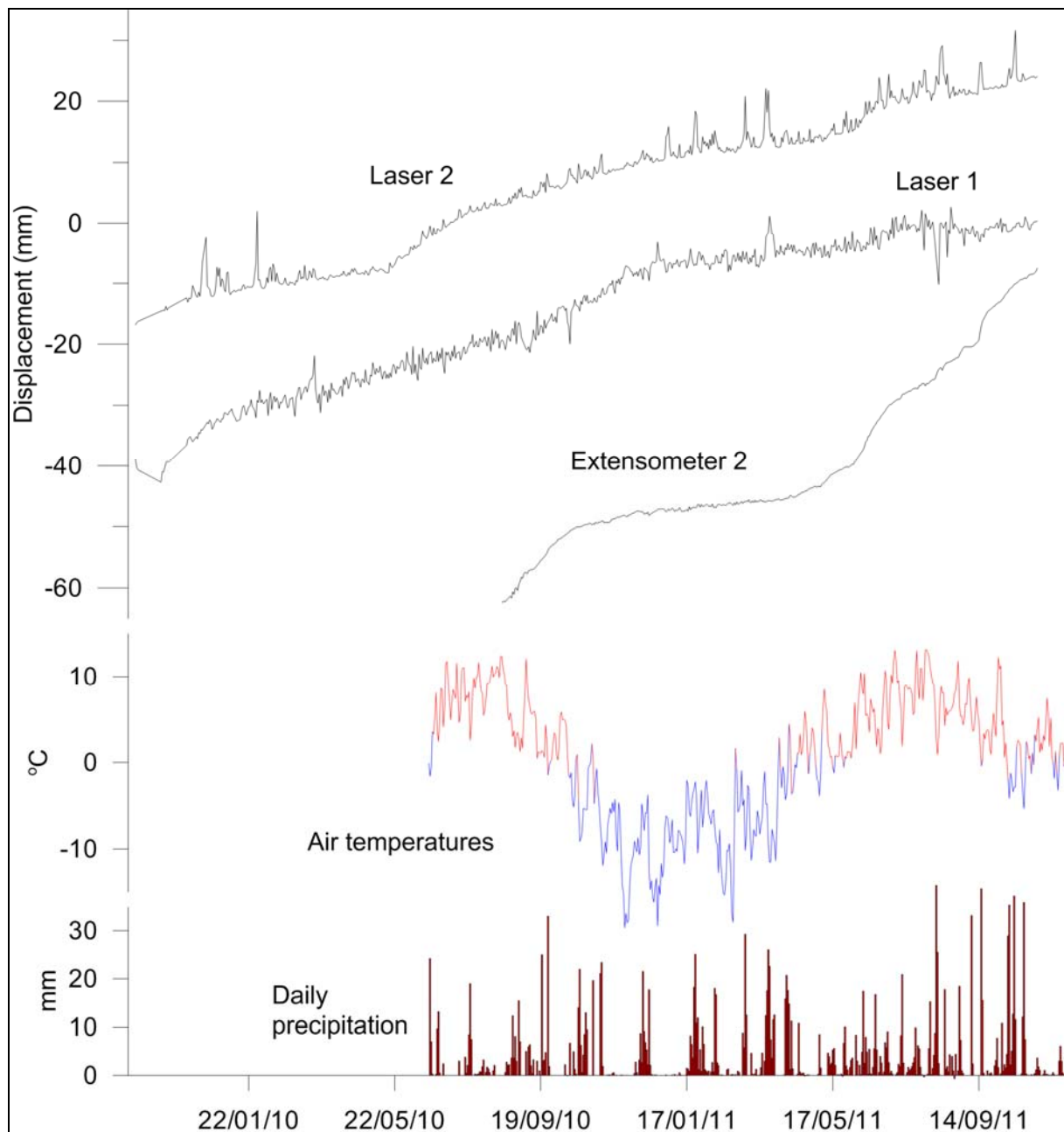


Figure 4.9-6. Displacement of lasers and extensometer 2. Air temperature and daily precipitation is also shown.

4.9.3.4 Displacement: Ground-based Interferometric Synthetic Aperture Radar System (GB InSAR)

A GB InSAR system is placed at the valley bottom (location: Figure 4.9-1), measuring distributed displacement of the entire mountainside on a continuous basis. Movement is measured in the Line of Sight (LOS) to the radar, which is often smaller than the real movement. Measurements from August 2010 to August 2011 are georeferenced and plotted on Figure 4.9-7. The velocity is quite well defined to the upper part of scenario A and compares well to the measurements by the GPS antennas (also drawn). The northern

movement shown by GPS 4 to 7 is difficult to pick up by the radar system due to the LOS (Figure 4.9-7).

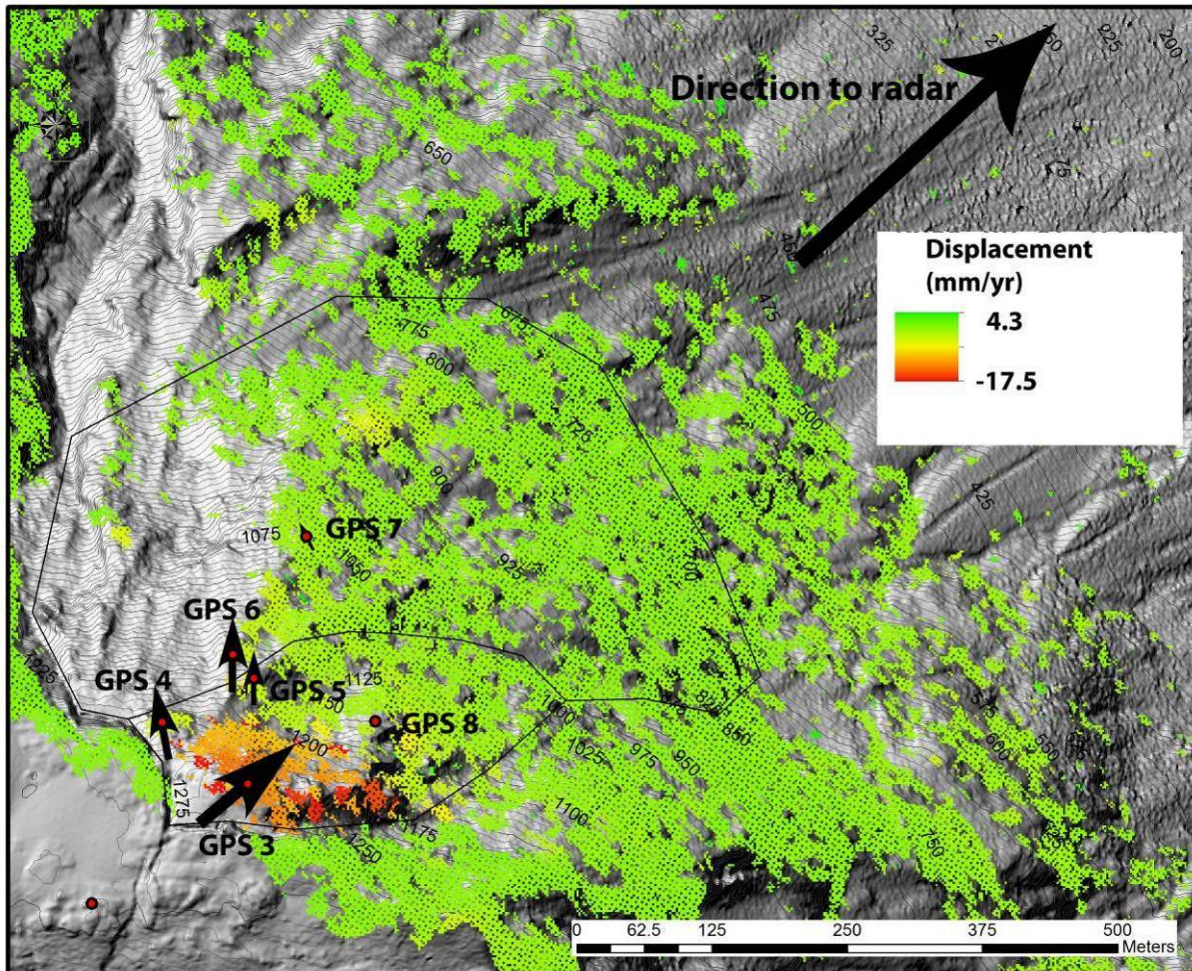


Figure 4.9-7. Displacement measured by the radar in from August 2010 to August 2011. Negative values are displacement towards the radar. Arrows show displacement vectors from the GPS antennas.

4.9.3.5 Displacement: DMS

A 139 m deep borehole was drilled in the upper part of the instability (see Figure 4.9-2 and Figure 4.9-3). It was instrumented with a 120 m long DMS column, measuring displacement or tilt for every meter. The DMS instrumentation is important in the investigations as it provides information of sliding planes in depth. It is also very important in the early warning system, as we obtain hourly updates of movement inside the instability. Figure 4.9-8 (left) shows the northward displacement measured during a 2.5 month period. The main sliding plane is clearly defined to 24 m depth (6.5 mm in 2.5 months), where the recovered borehole core and the televiewer revealed a thick breccia (Figure 4.9-8 right). A secondary sliding plane with a northern component is located at 86-89 m depth (2.1 and 1.2 mm movement in

2.5 months). Piezometers are placed in the DMS instrument, but no water is present in the borehole at Mannen.

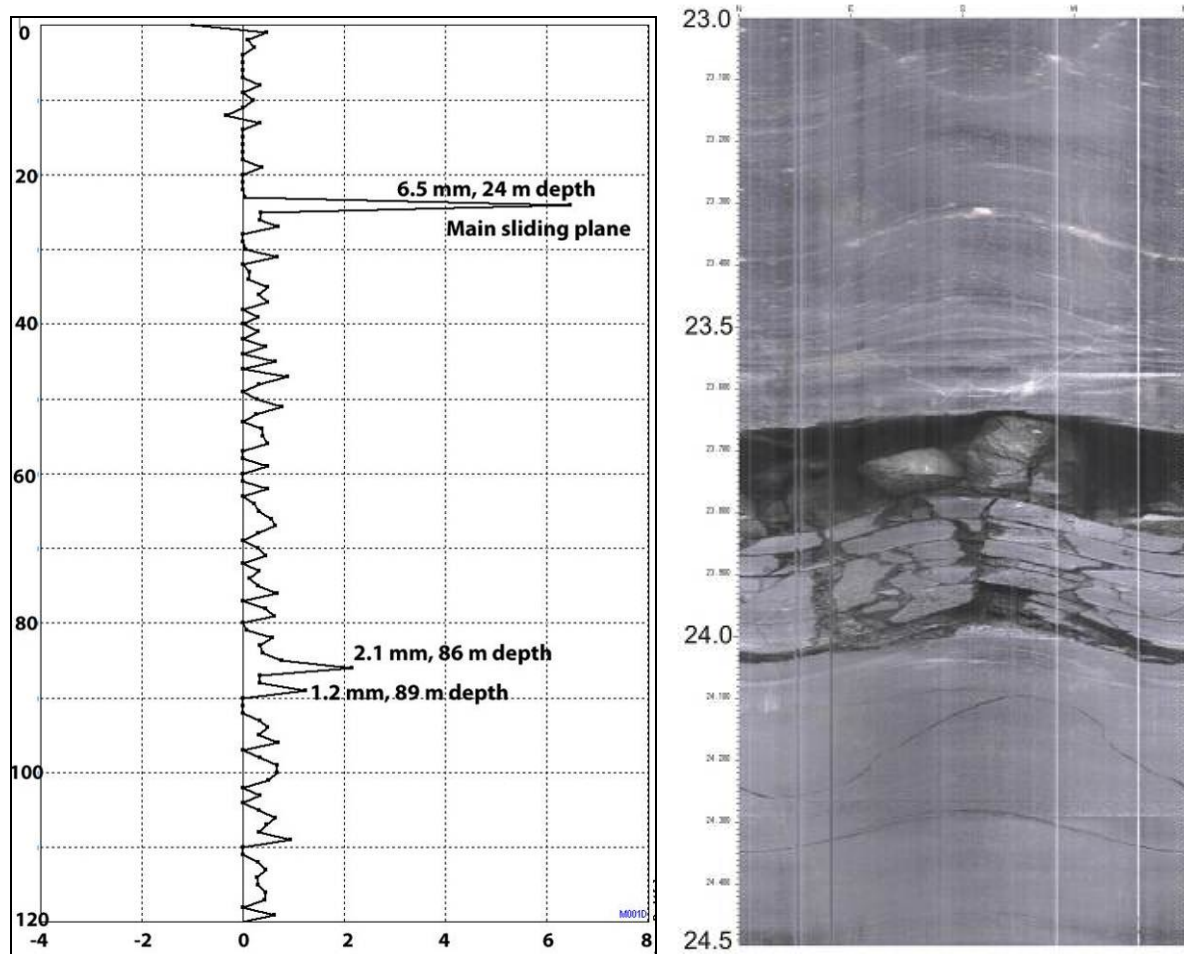


Figure 4.9-8. Left: Displacement in north direction in mm (main downhill direction) measured in the DMS column in the period: September 2 to November 25, 2011. Right: Televiwer image of the main sliding plane, found at 24 m depth. A 35 cm thick silty to gravelly breccia was recovered in this zone.

4.9.3.6 Meteorological station

A meteorological station is located at the plateau near the bunker, outside the instability. It records air temperature, wind speed and direction, precipitation, humidity and snow depth. Average daily temperatures and daily precipitation can be seen in Figure 4.9-6. Events of high precipitation or snowmelt are known to be linked to landslides of various types, but for the Mannen instability, we have not observed a clear pattern between precipitation and displacement rate. However, we move to blue alarm level when precipitation exceeds 70 mm/day or 200 mm/week.

4.9.4 END-USER INVOLVEMENT AND ALARM CHAIN

The total early warning system for the Mannen rockslide and other monitored rockslides in Norway involves all responsible partners or end-users that may be affected by the potential rockslide and tsunami. A systematic end-user involvement includes local, regional and

national official levels, police, and all other sectors like road authorities, health authorities, the coast guard, power companies, etc. A national emergency plan is being implemented to secure the communication chains and quality of the system. National tests have been organized, including both table-top and field-based.

The early warning levels are based on the velocity level and the stability situation at the monitored sites (Figure 4.9-9). The normal situation at Mannen is the green level, with movements typically about $0.1-0.25 \text{ mm/day}^{-1}$ (Figure 4.9-9). The next level (blue) is in effect when the velocity increases substantially due to seasonally wet weather, and the yellow level is reached when the velocity increases beyond the seasonal fluctuations. The orange level is reached when movements accelerate, and the red level is reached when a catastrophic failure is imminent, at which time an evacuation is ordered. Specific actions are implemented for the different warning levels and involve the Early Warning Center, police, county governor, municipalities, road authorities, coast guard, and power companies.

The operational system is based on the following routines: (1) daily check of all sensors and data by the geologist on duty; (2) daily technical checks by the technical person on duty; (3) mobile phone text messages (SMS) on data acquired from selected sensors and technical system failures; and (4) long-term contracts with monitoring companies that have different operational responsibilities. The use of the SMS and e-mail messages is difficult due to the different types of noise in the data. It is important to use thresholds that do not result in too many false alarms, but rather provide warning of real events. SMS messages alone are never used to change warning levels, but provide important support for the people on duty. One of the challenges is that sensors with large noise levels, for example the single lasers, create a large number of messages and cannot be used alone to raise the warning level.

The structure of the communication chain between the Early Warning Centre, the responsible organizations, and all involved partners are written in detailed documents and plans. The Early Warning Centre has the responsibility to inform the responsible organization when the early warning level is changed. The county governor has the responsibility for the coordination during the yellow level, while the police take over this role during orange and red level. The implementation of warnings and evacuation is done by the police. Two different methods are used to issue warnings; first, a system of phone messages is generated based on a continuously updated database, in addition to automatic SMS messages based on regional coverage from the mobile network companies. Second, an electronic warning siren in all the villages situated in the hazard zone can be activated.

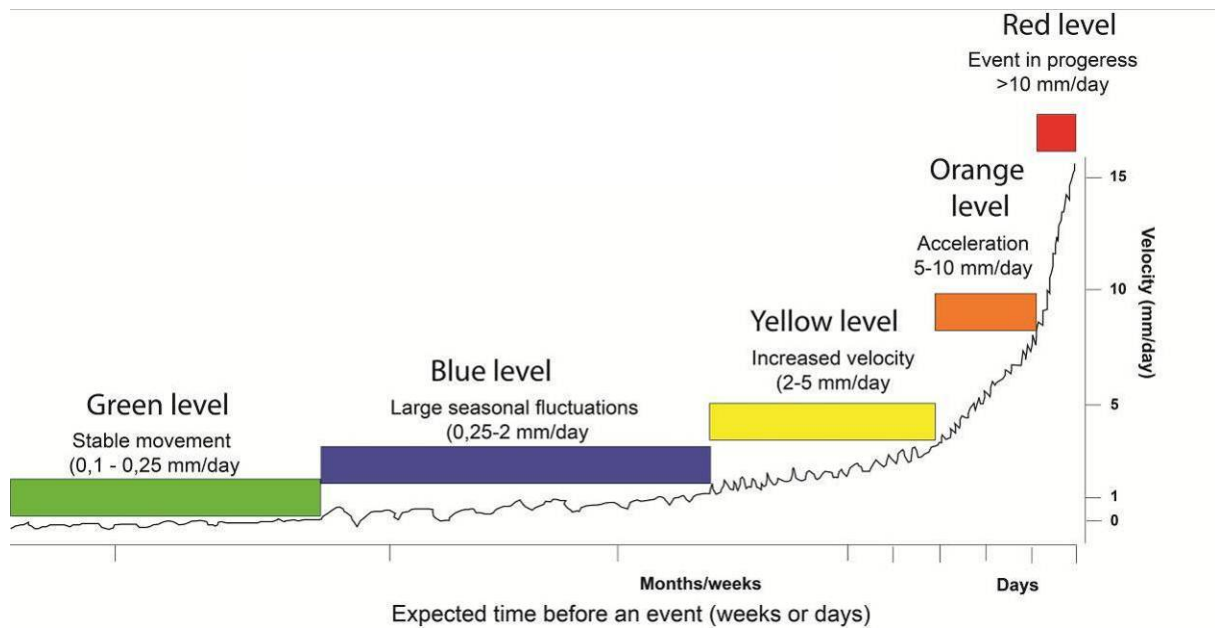


Figure 4.9-9. Early-warning levels for the Mannen rockslide

4.9.5 SUMMARIZED EVALUATION OF PARAMETERS

All sensors (GPS 3, Laser 1 & 2 and the GB radar) show movement of the upper part of the instability of about 2 cm/yr. The GPS indicates the displacement vector to be dipping 69° NE, close to the direction of the radar but much steeper. Further north, the GPS antennas show a smaller velocity and movement towards the north, which also corresponds well to the GB radar measurements. The movement in the upper block is smaller than what was measured by periodic (annual) fixed-point measurements. However, these were also varying considerably from year to year, and we assume the smaller movement can be caused by variations from year to year. Both measurements from the GB radar and the GPS antennas suggest that the area of biggest displacement is smaller than the mapped scenario A, and the scenarios should be redrawn on the basis of this information.

A seasonal trend with increased velocities during the snowmelt and summertime is seen, in particular at extensometer 2. The active rockslide body is highly fractured and has no groundwater, and the increased movement is interpreted to be an effect of water coming into the fine-grained and brecciated detachment zones. This will saturate the sliding planes and reduce their shear strength.

The threshold values that increase the alarm level from green to blue are about 1 mm/week for the upper block in the instability (excluding extensometer 2). Several instruments must be evaluated in combination, as 1 mm is less than the noise level for the lasers and GPS.

The depth of the main sliding plane is 24 m while a secondary zone of movement is found at 86-89 m depth. Some movement is seen throughout the borehole, which can be due to the highly fractured bedrock at all depths and subsidence in the main back crack which forms a graben-like structure.

A considerable effort has been put into the instrumentation of the Mannen instability, and we will consider the instrumentation to be more or less complete once the lower borehole has been instrumented with a DMS column. It has been a challenge to instrument the lower parts of the instability, and the lowermost GPS antennas and in particular as their cable connections

are at risk of snow avalanches and rockfalls. The lowermost part of the slope is inaccessible and only monitored with the GB radar.

All the instrument sensors are working fine and give the monitoring centre continuous data. However, bad weather is a major problem for getting good quality data from the laser systems and the ground-based radar.

The future outlook includes building a more complete model of the instability, which combines measurements of displacement with structural information and geophysical measurements. This will improve our understanding of processes and mechanisms of failure, which will give us better confidence in forecasting a rockslide event. Furthermore, a significant task for the monitoring centre is to maintain all instruments and systems in good working order, to ensure timely early warnings can be given.

References

Dahle et al. 2008. Faren for fjellskred fra fjellet Mannen i Romsdalen. NGU rapport nr: 2008.087

Henderson & Saintot, 2007. Fjellskredundersøkelser i Møre og Romsdal. NGU rapport nr: 2007.043

Saintot et al. 2011. Mannen unstable rock slope (Møre & Romsdal): Logging of borehole and drill core KH-01-10, geomorphologic digital elevation model interpretation & displacement analysis by terrestrial laser scanning. NGU report no. 2011.026.

www.skrednett.no: National skreddatabase på internett. (National database of avalanches, landslides, rock avalanches and rockfall). NVE & NGU.

4.10 ROSANO (ITALY)

Mario Lovisolo

Centro Servizi di Geoingegneria, Italy

ABSTRACT

The test site Rosano is situated in a hamlet of Cabella in the Piedmont region, Italy. The landslide has a length of about 700 m, an elevation of about 170 m and an estimated volume of 3.6 Mm³, and consists of a clayey and silty overburden, landslide debris and below lying calcareous rocks. The monitoring system was installed there from May 28th to October 22nd, 2010, containing a 17 m long column with 16 IT modules (inclinometer and thermometer) and one IUT module (inclinometer, thermometer and piezometer). The total cumulative displacement was 11.1 mm in the north direction. During the monitoring period, one distinct event was recorded: from November 4th to 8th, 2011, heavy rainfall occurred on Cabella with a cumulative precipitation of 435 mm. During this event, the DMS column detected a cumulative displacement over 5 mm at a depth of 2-5 m b.g.l. The water table started to rise about 18h after the rainfall event, and the difference of the GWL was about 7 m reaching the ground surface. Two reactivations followed the rainfall event with a delay of 11 hours (the minor reactivation) and 47 hours (the major reactivation), thus proving that setting up the critical thresholds of precipitation could serve as an EW parameter at a particular landslide.

Presented parameters: displacement, velocity, groundwater level, precipitation.

4.10.1 GENERAL DESCRIPTION OF THE TEST SITE

Description of location and geological background

The Rosano site is a Cabella hamlet, Alessandria province, Piedmont Region, Italy. The area is placed southeast of Cabella's centre, orographically left of the Borbera Torrent, in the lower portion of the slope. The geomorphological hazard of the area is particularly relevant to the potential implications of even a partial reactivation of the Rosano landslide, both for the direct effects on the homonymous village and damage arising from actions that could affect the Borbera riverbed. A composite landslide of considerable size (about 18 ha) is potentially active because continued reports by residents indicate an increase in conditions of structural instability of some buildings located along the north sector. The landslide has a longitudinal development of about 700 m, a height difference between the foot and crown of about 170 m, and an estimated volume of 3.6 Mm³.

The village, organized into two main groups at different levels, is located in areas related to real morphological scarps of the landslide. The elements at risk are the inhabited areas affected by the landslide itself and the development of a landslide dam in the Borbera Torrent. The Municipality of Cabella, which includes Rosano, was historically affected by landslide movements that often correlated with high rainfall events, such as in 1873, 1940, 1976, 1986, and 2002. In December 2004 landslide reactivations were detected in Rosano that affected rural buildings.

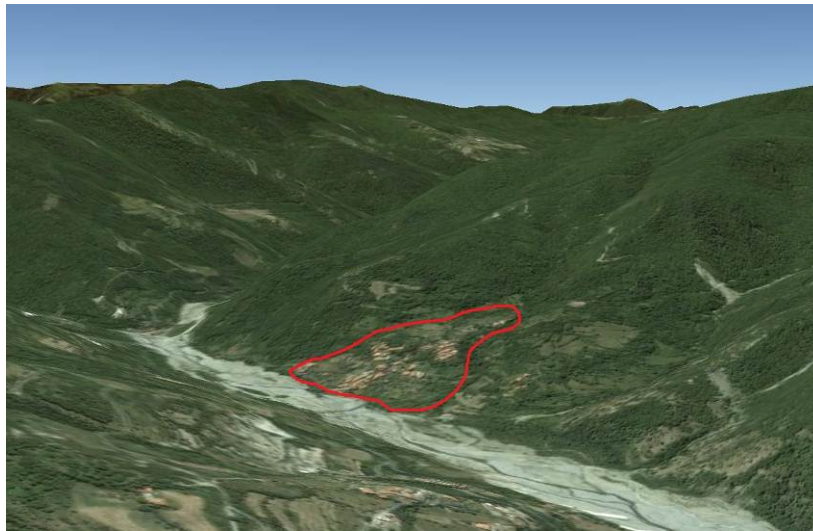


Figure 4.10-1. Rosano landslide area.

Table 4.11-1. Historical events on Cabella area:

Date	Area	Event	Damages
January 1873	Cabella Ligure	Landslide	Damaged the inhabited area of Dova Soprana and Dova Sottana
16 – 17 November 1940	Rosano	Torrent Borbera flooding	Tree arch of the bridge destroyed
3 October 1976	Cabella	Various instabilities	Damaged road and interruption of viability between Dova sup. and San Clemente
29 – 31 October 1976	Cabella	Landslides	Same roads blocked ; a landslide over 1.500 m ³ damaged the road for Dova a bit after Rosano
December 1986	Cosola	Landslide	Landslide
22 – 26 November 2002	Cabella and other areas	Heavy rainfall	Landslides on different roads interrupted the viability between Casella Pobbio, Costa Piuzzo, Aie and Montaldo di Cosola, Centrassi, Cremona, Rosano, Dova and Dovanelli
December 2004	Rosano	Heavy rainfall	Landslide reactivation in the inhabited area.

4.10.2 DESIGN OF THE MONITORING NETWORK

Technologic analysis pre-installation

A first geotechnical campaign began in 2007 in the centre of the village. The stratigraphy of the area, ref. the borehole S1/07, showed in particular between 0 to -3.5 m clayey and silty overburden; between -3.5 and -17 m it showed landslide debris made by heterogeneous clastic rocks inside a silty and clayey matrix, with a presence of calcareous blocks. Over 17 m a bedrock made by calcareous rocks, a little fractured, was found.

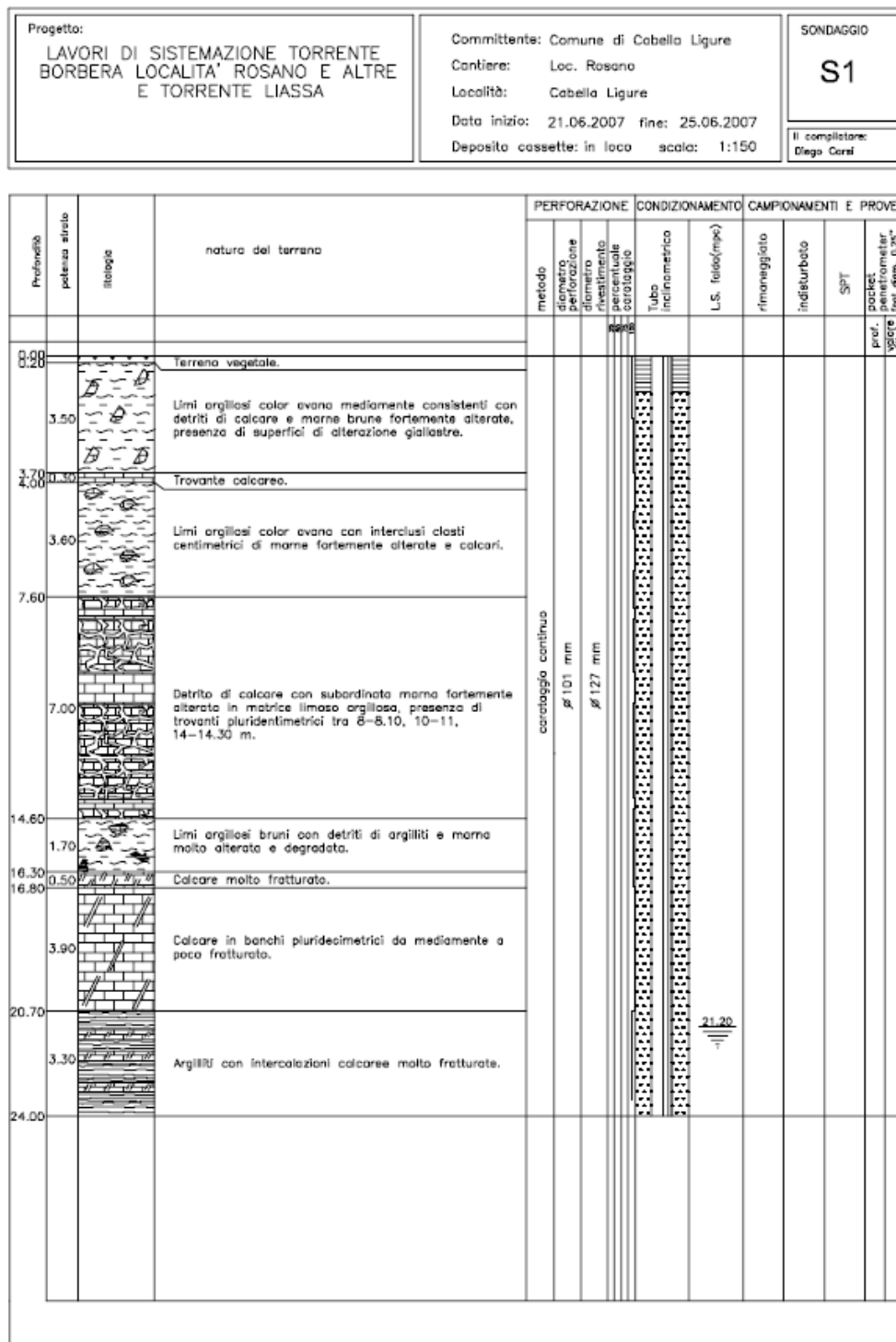


Figure 4.10-2. Stratigraphy sketch S1/2007 campaign.

After the preliminary investigation in 2010 a deep high-resolution ERT campaign (GSA) was commissioned by the Cabella municipality and a second geotechnical investigation was performed in the same year (see S1/10).

Progetto: LAVORI DI SISTEMAZIONE TORRENTE BORBERA LOCALITA' ROSANO E ALTRE E TORRENTE LIASSA	Committente: Comune di Cabella Ligure Località: Rosano Ditta esecutrice: Ecofond S.r.l. - Genova Inizio perforazione: 28.07.10 Fine perforazione: 03.08.10 Deposito cassette: in loco scala: 1:200	SONDAGGIO S1/10 Il compilatore: Diego Corsi
---	--	---

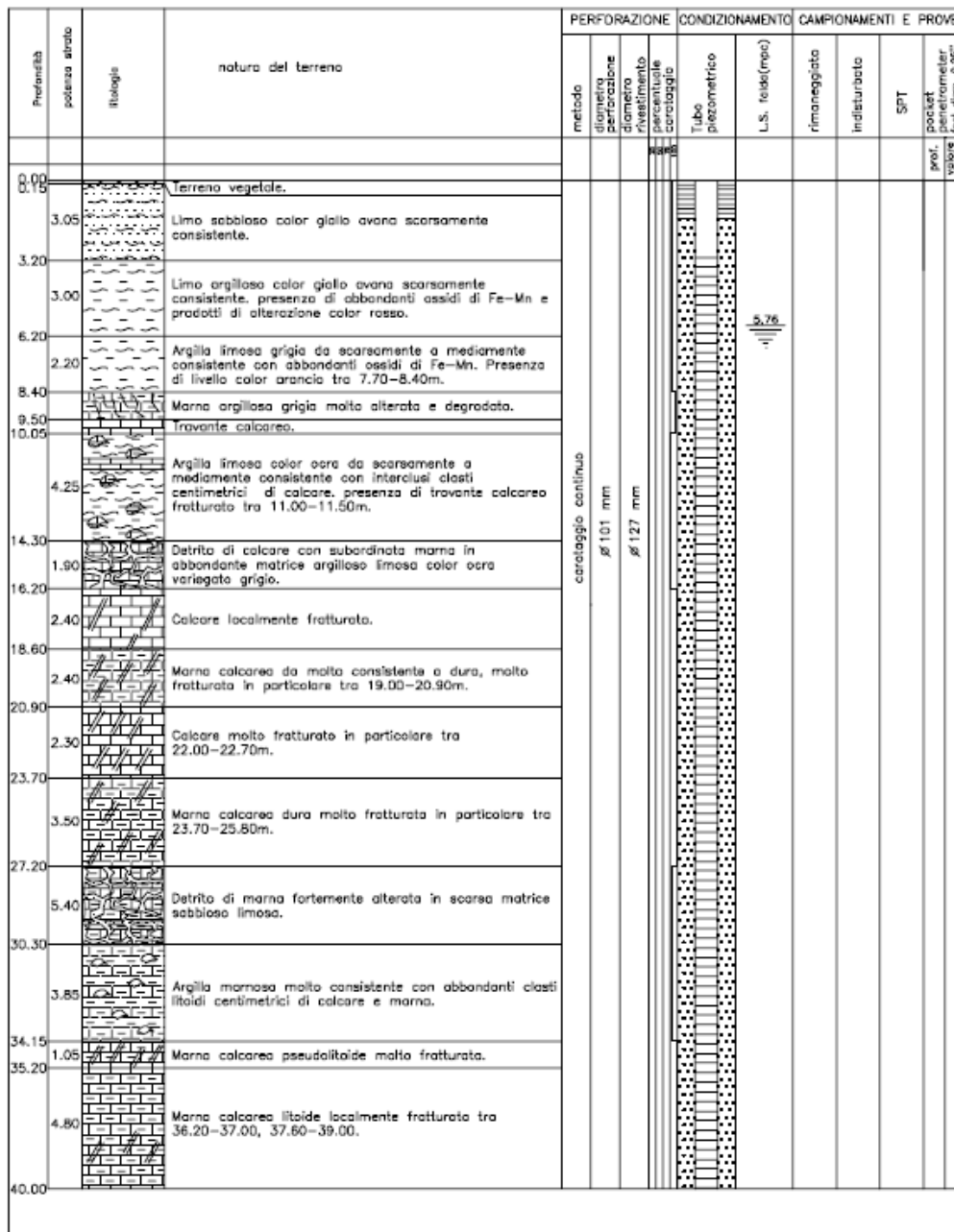


Figure 4.10-3. Stratigraphy sketch S1/2010 campaign.

Instrumentation characteristics

In 2010, considering the geomorphological hazard of the area and the European research project SafeLand 2009-2012, GSA installed a DMS multiparametric column inside S1/07 for landslide monitoring, intending to use this instrumentation to complete the geophysical survey and provide a preliminary contribution for continuous monitoring of slope stability.

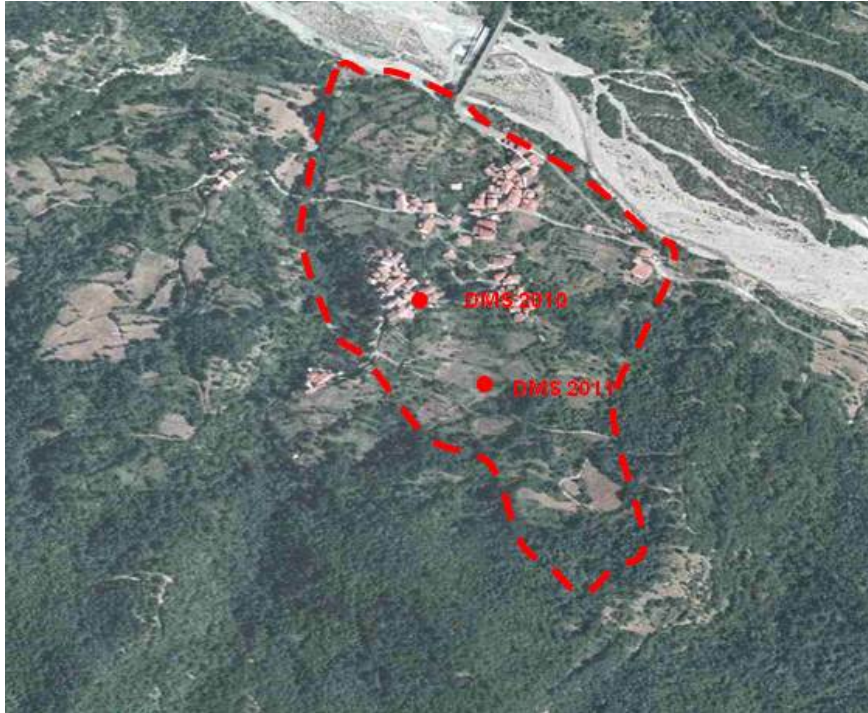


Figure 4.10-4. DMS 2010 and 2011 sites.

The instrumentation was installed on May 28th, 2010 and removed on November 22nd, 2010 to be reinstalled in a new early warning monitoring project in Austria. The column was 17 m long, comprised of 16 IT modules (inclinometer and thermometer) and one IUT module (inclinometer, thermometer and piezometer). The last available record, from November 22nd, 2010, showed a cumulative displacement of 11.1 mm in the north direction.

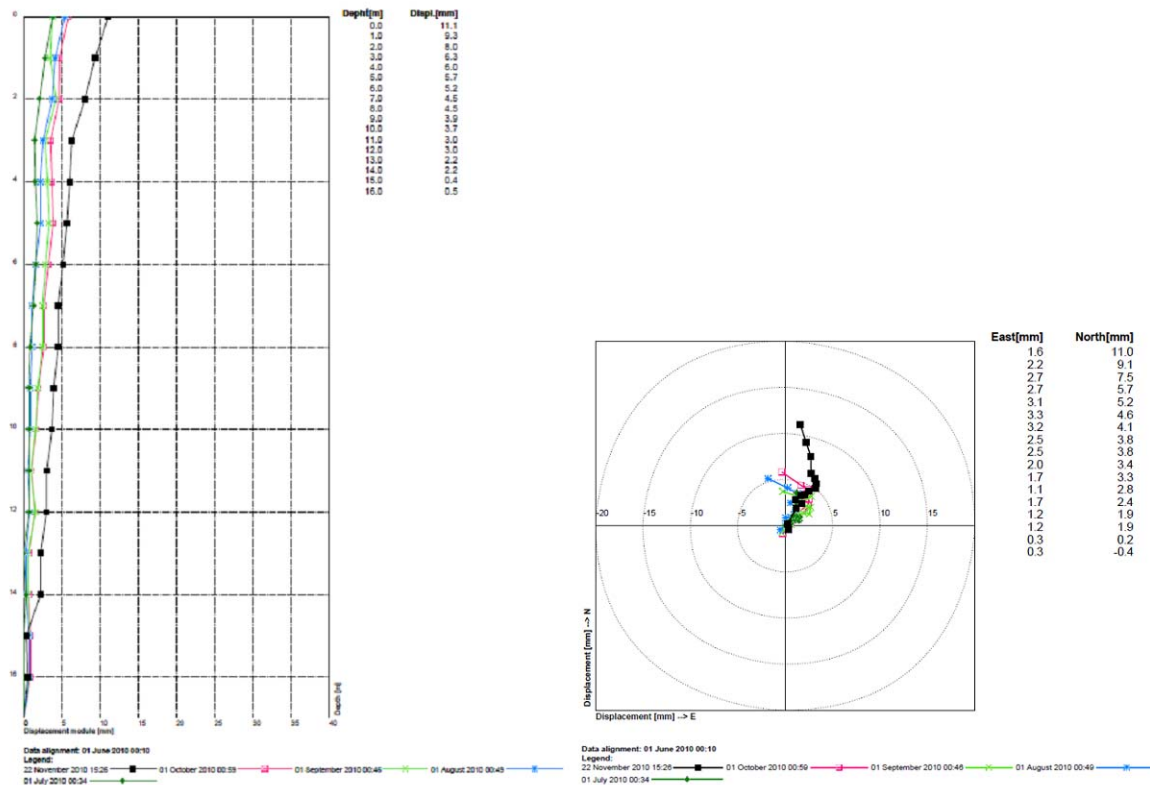


Figure 4.10-5. Displacement graph and polar diagram DMS 2010.

After the result of the investigation, a DMS system was installed in the deeper borehole S1/2010 in January 2011.

The column has a total active length of 38 m and includes 37 IT modules (inclinometer and thermometer) and one IUT module (inclinometer, thermometer and piezometer).

The column is connected to a control unit that takes care to continuously detect, then store and transmit data to the monitoring room.

The data download is performed by GSM or directly on site through RS232 connection.

The power is supplied by one solar panel and backup batteries to guarantee the functionality of the system for at least seven days in the event there is no sun.



Figure 4.10-6. DMS 2011 during and after installation.

Management and maintenance

Management of DMS column data is taken directly by the Guardian software, which downloads data by GSM to the monitoring room at a time interval set by the user. The control unit compares data in real-time to set alarm thresholds, and if the value exceeds thresholds, it automatically sends an SMS or a direct call to the geological staff. Data processing is carried out using DMS EW full software inside the monitoring room.

The stainless steel structure of the system makes the instrument very robust, and because of the high quality of the sensors specifically built for EW, ordinary maintenance work is not required.

Analysis of monitoring data

4.10.2.1 Instrumentation data analysis

Between November 4th and 8th, 2011 an intense rainfall event occurred on Cabella with a cumulative value of 435 mm (ARPA Piemonte “EVENTO METEOROLOGICO DEL 4-8 NOVEMBRE 2011”).

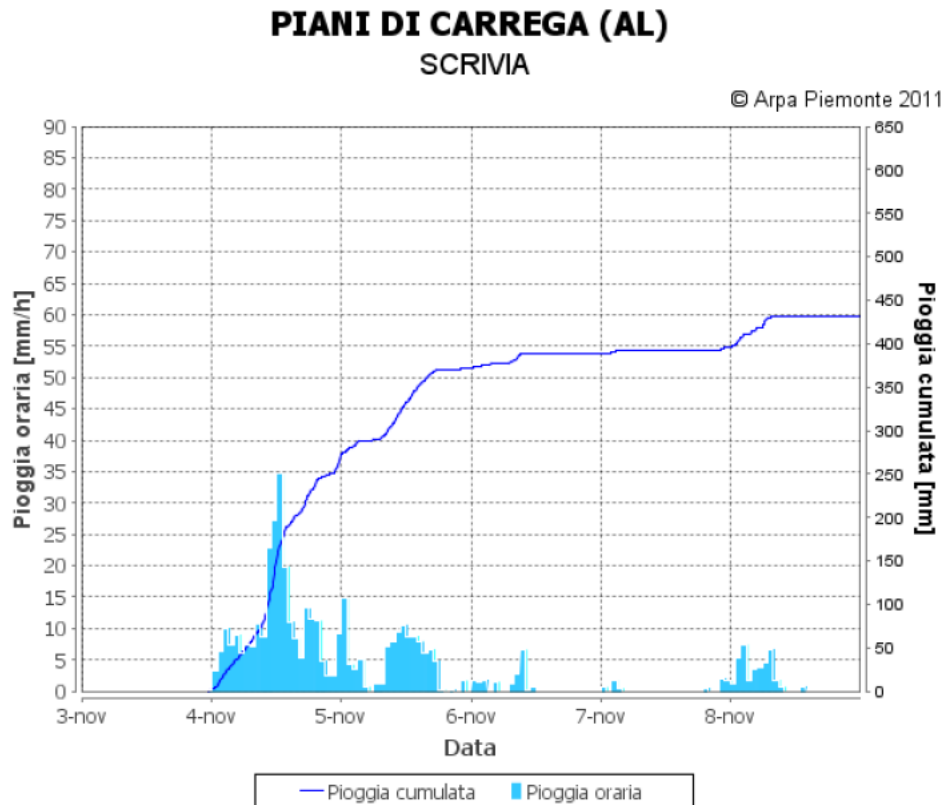


Figure 4.10-7. Rainfall event November 03-08, 2011 (Arpa Piemonte).

During this event, the DMS column detected a cumulative displacement of over 5 mm, direction 45° N, between 2-5 m b.g.l. Moreover, a sensible rising of the water table level (7 m) was detected, reaching the ground surface and flowing outside the borehole. The aquifer is semi-confined.

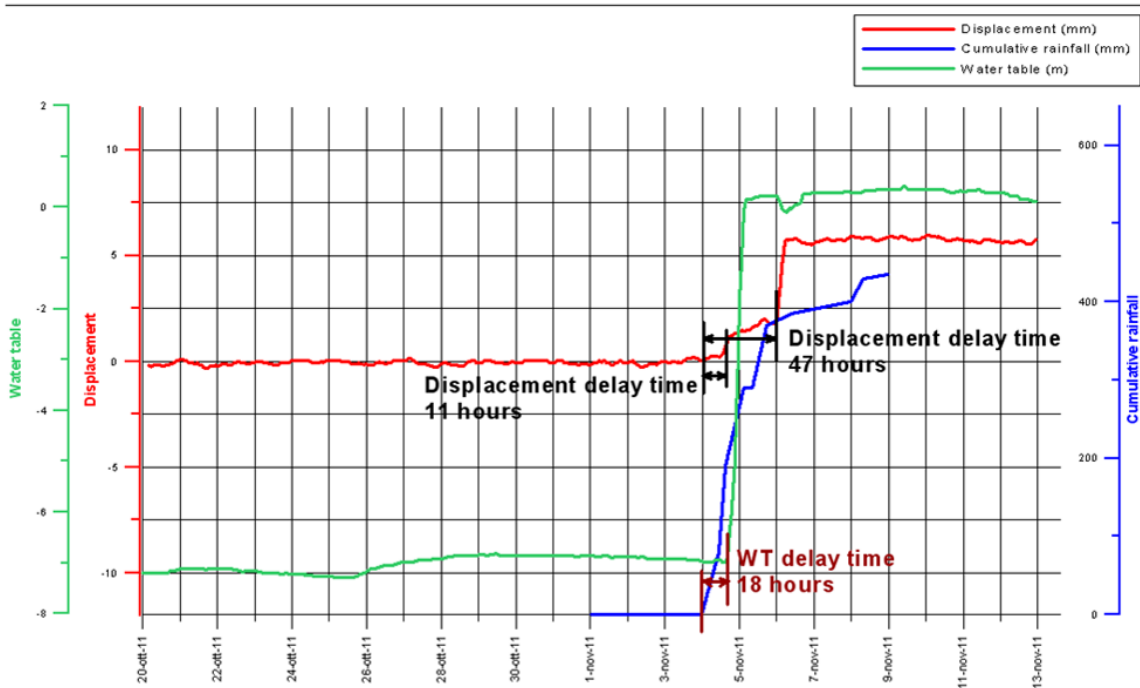
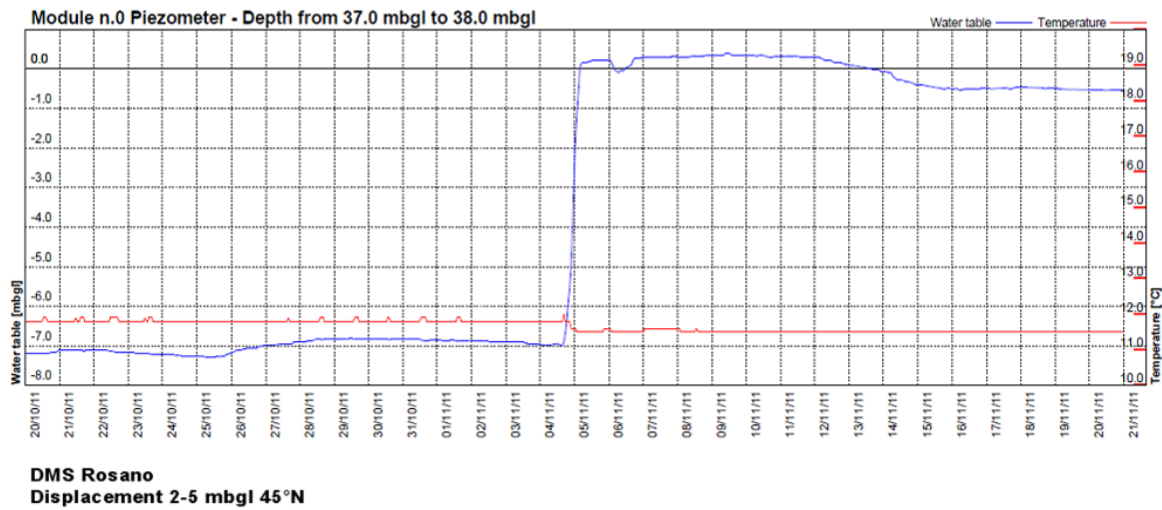


Figure 4.10-8. Delay time analysis between rainfall, water table and displacement

The rainfall event starts at 00:00 on November 4th and after 18h, the water table level starts to rise. After the rainfall event two triggering events were detected, the first one starting at 11:00 on the 4th with a value of 1.9 mm, and the second one starting at 23:10 on the 5th with a value of 5.85 mm.

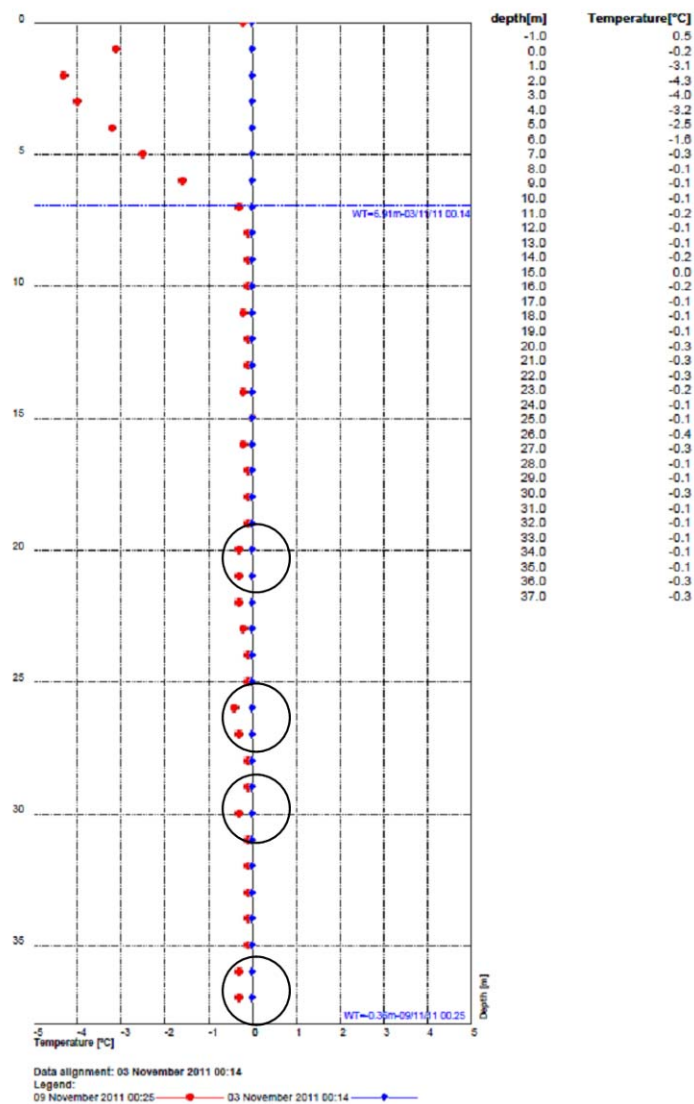


Figure 4.10-9. Temperature graph with in-flow areas.

Thanks to the possibility of monitoring the temperature on each modular zone of the column, it was possible to moreover detect different outflow zones along the vertical. The temperature of the fresh water infiltrating after the rain event (November 4-8, 2011) caused a lower temperature to be detected by the column compared to the mean value of 11.5°C; four main inflow zones were detected inside the fractured body at depth 20-21 m, 26-27 m, 30 m and 36-37 m. The red diagram shows the difference in temperature (-0.5° max) recorded November 9th, with an alignment to November 3rd.

4.10.3 ROLE AS PARAMETER AND EW

DMS columns are able to contextually detect displacements and water table level changes, and correlations between these two parameters can be found. Warning thresholds were set for both parameters, and on the basis of the time delay analysis, it is possible to define a forecast model to improve the efficiency of the EW system.

4.10.4 END-USER ROLE

Considering the high-risk context of the area, the Municipality of Cabella planned the installation of DMS monitoring and data transmission instruments in order to gain information on local displacement triggering factors (critical rainfall thresholds), displacements and instantaneous velocities, and sliding zones depths.

In this way, it will be possible to manage public safety procedures and to verify that the mitigation works.

4.10.5 SUMMARIZED EVALUATION OF PARAMETERS

Monitoring platform strength and lack

The system installed is able to detect data in real-time and to advise on-duty staff with a warning SMS or direct call in the event of displacements or water table levels exceeding the set thresholds. Moreover, the possibility of detecting displacements and water table levels in the same borehole improves the correlation analysis accuracy, guaranteeing cost savings at the same time.

The correlation between rainfall events and displacements should be improved with the installation of a weather station on site, directly linked to the existing DMS control unit. In this way it will be possible to directly link rainfall, water table and displacement data, improving the correlation analysis and the landslide model.

Further activities

Deeper knowledge about local kinematic and water table conditions of the Rosano landslide, in particular after heavy rain events, will moreover allow the definition of the first results of the structural intervention.

4.11 RUINON ROCKSLIDE (ITALY)

Federico Agliardi, Giovanni B. Crosta, Rosanna Sosio
University of Milano-Bicocca, Italy

ABSTRACT

We analyze a long-term monitoring dataset collected for a deep-seated rockslide (Ruinon, Lombardy, Italy), whose activity has been documented by ground-based and remote sensing data since 1997. The monitoring data allowed to set up and update the geological model, to identify rockslide complexities (e.g. uncertain geometry, composite failure mechanisms, and seasonal behavior) and their impact on the reliability and early warning potential of monitoring data. GB InSAR data permitted the identification of different behaviours for sectors characterized by outcropping bedrock, thick debris cover, or close to major structures, and to set up a “virtual monitoring network” by a posteriori selection of critical locations. Displacement time series extracted from GB InSAR provides a large amount of data even in debris-covered areas when ground-based instrumentation fails. Such spatially-distributed, improved information, validated by selected ground-based measurements, allowed the establishment of new velocity and displacement thresholds for early warning purposes.

Presented parameters: displacement, velocity, acceleration, precipitation.

4.11.1 GENERAL DESCRIPTION OF THE TEST SITE

The Ruinon rockslide is located in the Upper Valtellina (Italian Central Alps, Figure 4.11-1), which is characterized by typical continental-alpine rainfall regime (i.e. rainy summer and autumn) with an annual average, maximum, and minimum rainfall of 750, 1300, and 300 mm, respectively. Slope instability involves pre-Permian phyllites of the Austroalpine Campo Nappe (Agliardi et al., 2001).

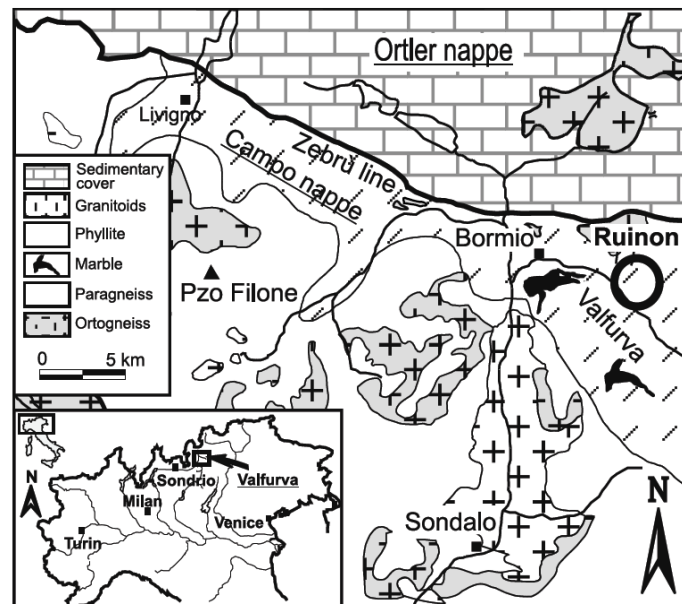


Figure 4.11-1. Test site location and geological setting (Crosta and Agliardi, 2003).

The bedrock is cut by four main sets of alpine and recent fractures strongly controlling the geometry of slope instabilities in rock. Late Pleistocene and Holocene deposits, mainly consisting of glacial, talus, and landslide deposits cover most of the slope. The entire slope up to 3000 m a.s.l. (Figure 4.11-2) has been affected by a large deep-seated slope deformation (DSGSD), recognized and analyzed by Agliardi et al. (2001). The phenomenon is controlled by pre-existing structural features and characterized by scarps, counterscarps, and trenches, cutting the bedrock as well as till and rock glacier deposits of the Holocene age and strongly influencing the Ruinon rockslide geometry. Rockslide accumulations of the Holocene age have also been detected close to the rockslide area.

The rockslide occurs in the lower sector of the DSGSD (Figure 4.11-2), and has been known for decades. Since 1960, the slope has been involved in repeated instability as a result of exceptionally heavy rainfall periods (1960, 1983, 1987, 1997). Observed associated slope instabilities have consisted of debris flows (sometimes causing road traffic interruption), rockfalls, and the progressive development of scarps and fractures with differential movements along the middle slope sector. Since 1997, the movement started accelerating and showing high, seasonally changing displacement rates (Crosta and Agliardi, 2003).

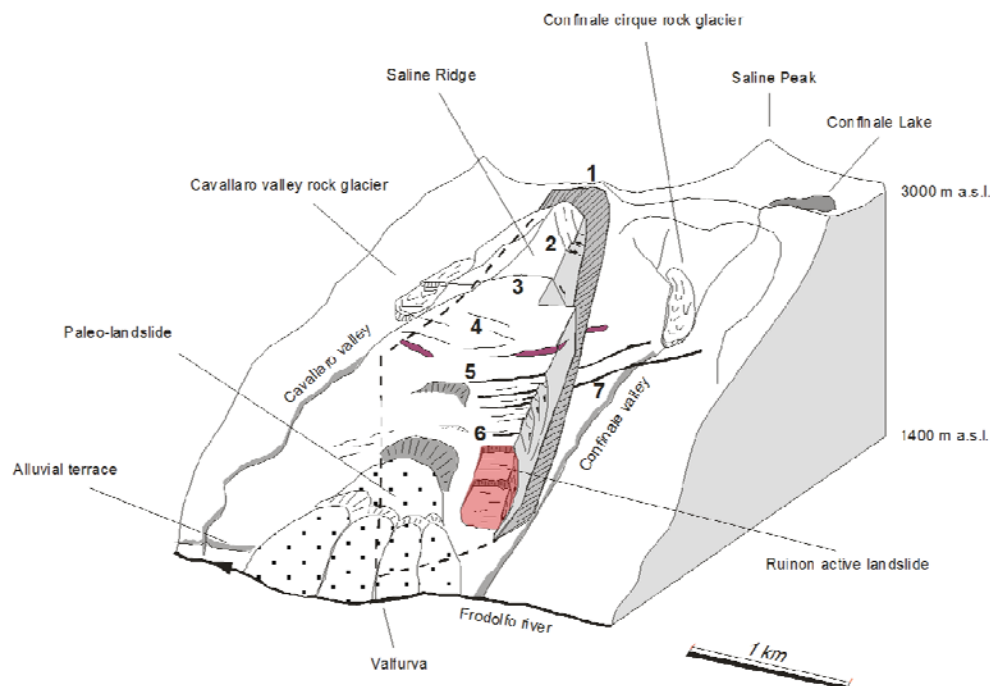


Figure 4.11-2. The Ruinon rockslide in the context of the Saline Ridge DSGSD (Agliardi et al., 2001).

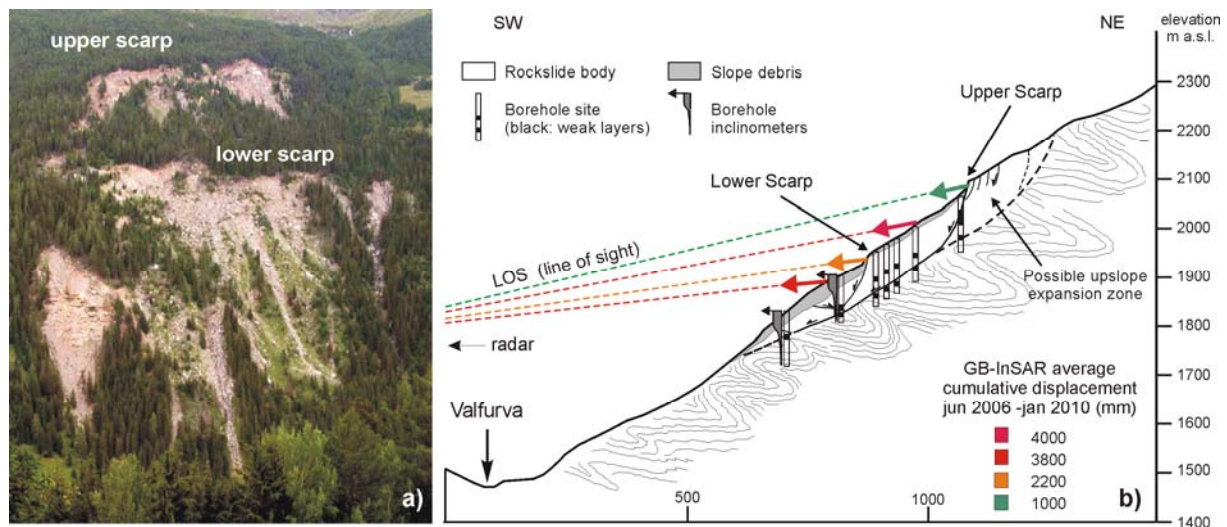


Figure 4.11-3. a) Front view and b) geological cross section (Agliardi et al., 2011) of the Ruinon rockslide, showing the main morphological features, rockslide shear surfaces, site investigations, and general distribution of measured displacements.

The rockslide is characterised by two separate main scarps, namely the Upper Scarp (2100 m a.s.l.), up to 30 m high and chiefly exposing disturbed rock masses, and the Lower Scarp (1950 m a.s.l.), which involves disrupted rock and a cover of both glacial and scree debris up to 30 m in thickness (Figure 4.11-3). Scarps and trenches located upslope from the Upper Scarp suggest possible expansion up to 2200 m a.s.l.

The rockslide has been investigated since 1988 by Regione Lombardia and, later, by ARPA Lombardia (Environmental Protection Agency of Regione Lombardia). Geotechnical site investigations were carried out in different stages between 1988-2004 and include: six full-core boreholes drilled up to 130 m in depth and equipped with inclinometer casings; three boreholes equipped with piezometers and pore pressure sensors; and two boreholes instrumented with multibase borehole extensometers. Field investigations included geological and geomorphological surveys, rock mass characterisation, combined with analysis of LiDAR topography, multitemporal interpretation of aerial photos and orthophotos, and geomechanical borehole core logging.

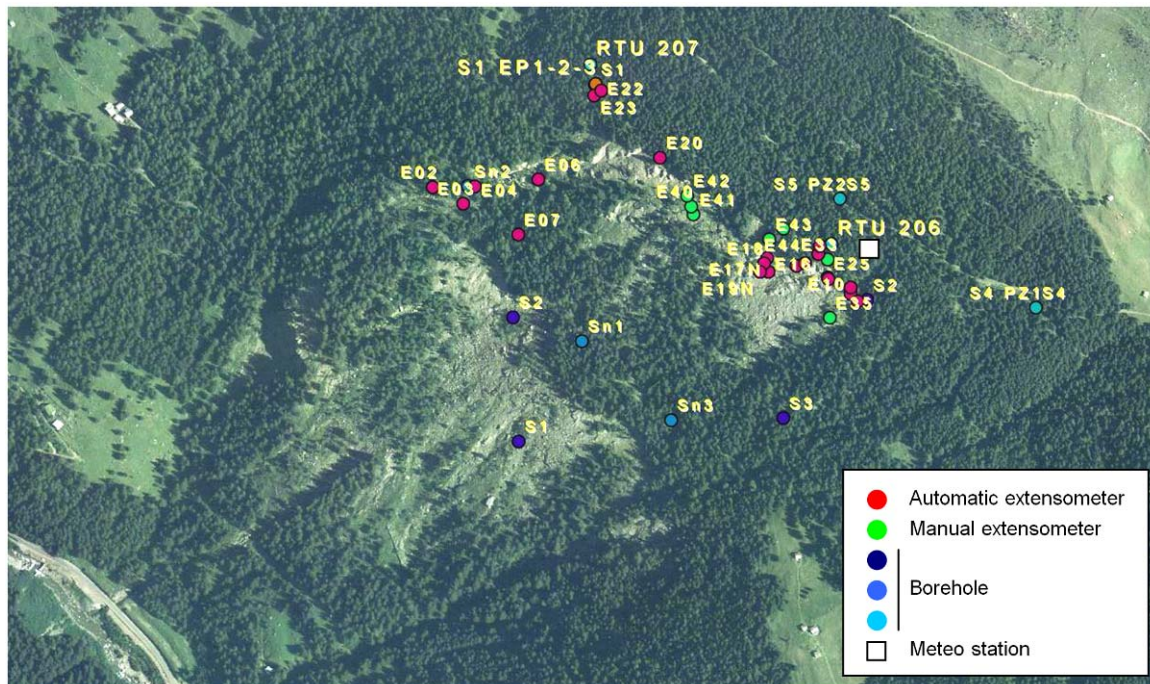


Figure 4.11-4. Simplified layout of the ground-based monitoring network, including a meteo station, data loggers, manual extensometer baselines, and automatic extensometers. The locations of boreholes drilled in the period 1988-2004 are also shown. Data and orthophoto (2006) courtesy of ARPA Lombardia.

The above-mentioned investigations allowed to constrain the complex geometry, kinematics, and hydrology of the rockslide (Figure 4.11-3b). The rockslide consists of a compound sliding of about 13 Mm³ of phyllite along surfaces 30 to 70 m deep, both in debris and rock (Agliardi et al., 2001; Crosta and Agliardi, 2003; Casagli et al., 2010). Moreover, although the presently active rockslide extends between 1700 and 2120 m a.s.l., the distribution of scarps and trenches suggests a possible upslope expansion up to 2200 m a.s.l. (Figure 4.11-3), eventually involving a volume exceeding 20 Mm³. The Upper Scarp is located between 2100 and 2120 m a.s.l., and trends WNW–ESE, extending for more than 600 m. The scarp exposes a subvertical 30 m high rock outcrop, affected by rockfall, toppling, and large tension and hybrid cracks. The Lower Scarp developed between 1890 and 1930 m a.s.l. and cuts slope debris as well as disrupted rock masses. The scarp has been active since 1981 and has been subjected to rockfalls and slump failures often evolving into debris flows. During the 90s, these instabilities were often associated with water discharge from springs occurring between 1690 and 1850 m a.s.l., and aligned in a WNW–ESE trend. The Lower Scarp underwent a significant evolution since the beginning of 2001, and experienced increased displacements and retreat since 2008. A long southeast steeply dipping fracture, appearing in 1996–1997, bounds the rockslide along its northwest flank.

The inferred slide toe (1700 m a.s.l.) is suspended above the valley floor (1450 m a.s.l.), suggesting possible evolution into a rock avalanche in the event of catastrophic failure of the entire rockslide volume (worst case scenario). Other event scenarios include localized rockfall activity from the Upper Scarp, debris flow and debris slide activity from the Lower Scarp, as well as partial catastrophic collapse of individual rockslide sectors.

The major exposed element at risk is the SP29 road (former State Road 300) linking the Upper Valtellina and the Upper Camonica valleys through the Gavia Pass. Possible rockslide dam formation in case of catastrophic failure could be a concern for the Bormio municipality located a few kilometres downstream at the Valfurva valley outlet. Finally, prolonged road interruption during the winter season would also indirectly damage the Santa Caterina ski resort, located upstream in the valley.

4.11.2 DESIGN OF THE MONITORING NETWORK

Rockslide displacement measurements have been carried out since 1997 through a ground-based monitoring network, and in recent years by remote sensing techniques (i.e. satellite, PS-InSAR, and ground-based GB-InSAR, radar interferometry).

The monitoring network was implemented in different stages since 1997 from the Regione Lombardia Geological Survey. It included up to 50 distometer baselines (linked in chains crossing major scarps and fractures), 25 Invar wire extensometers, 17 GPS benchmarks, six borehole inclinometers, and two borehole multibase extensometers. Measurements were initially carried out manually every 7-15 days depending on the state of activity of the landslide, but measurement devices have progressively been connected to an automatic data logging and radio transmission system connected to the monitoring centre in Sondrio (presently operated by ARPA Lombardia, i.e. the public agency in charge). Some automatic wire extensometers have been combined with existing distometer baselines in order to increase measurement redundancy.

In 2000, 16 optical targets were added to the network to survey the evolution of debris-covered areas surrounding the Lower Scarp, where no measurement device could be installed. Unfortunately, most optical targets were lost in early 2001 because of the large displacements associated with the significant lower scarp retreat.

The presently operating ground-based network includes surface displacement measurement devices such as 18 automatic wire extensometer, 15 distometer baselines, 12 combined distometer-wire extensometer baselines, and GPS benchmarks, chiefly spread along the Upper Scarp and the right-hand flank of the rockslide (Figure 4.11-4). This network provides the longer and more continuous displacement time series (11-year time period), which allowed a sound characterisation of long-term rockslide behaviour and provided datasets for validating the subsequent analysis of remotely sensed displacement data.

A LiSALab GB InSAR sensor (by Ellegi s.r.l. for ARPA Lombardia) was installed in June 2006 (Casagli et al., 2010). The system is located on the opposite valley side (Figure 4.11-5), at a distance from the rockslide area ranging between 800 m (rockslide toe) and 1700 m (Upper Scarp). The system was initially installed as a test experiment, and later incorporated in the real-time monitoring network operated by ARPA Lombardia for civil protection purposes. In order to fit operational needs, the entire system (i.e. sensor, related hardware and software tools), has been specifically designed and implemented through the years to ensure the requested level of reliability, availability and robustness.

In the present configuration (Agliardi et al., 2011), the LiSALab system synthesizes an aperture of 3 m, covering a visible area of approximately 1 Km². The permanent monitoring settings of the system allow acquiring radar images and displacement maps with a range resolution of 1.5 m, an azimuth resolution between 2.6 and 5.2 m, providing approximately

five displacement maps per hour. The system has been equipped with rugged high-speed data transmission connections, a redundant power supply system, a near real-time connection with a weather station, and high-resolution webcams. The system now provides the most comprehensive and integrated information about the rockslide behavior and evolution, in order to undertake the risk mitigation actions requested by the civil protection plan. In this perspective, LiSALab GB InSAR is able to provide to remote users near- and real-time results in terms of geo-referenced displacement maps and time series at pre-defined points of interest (POI).

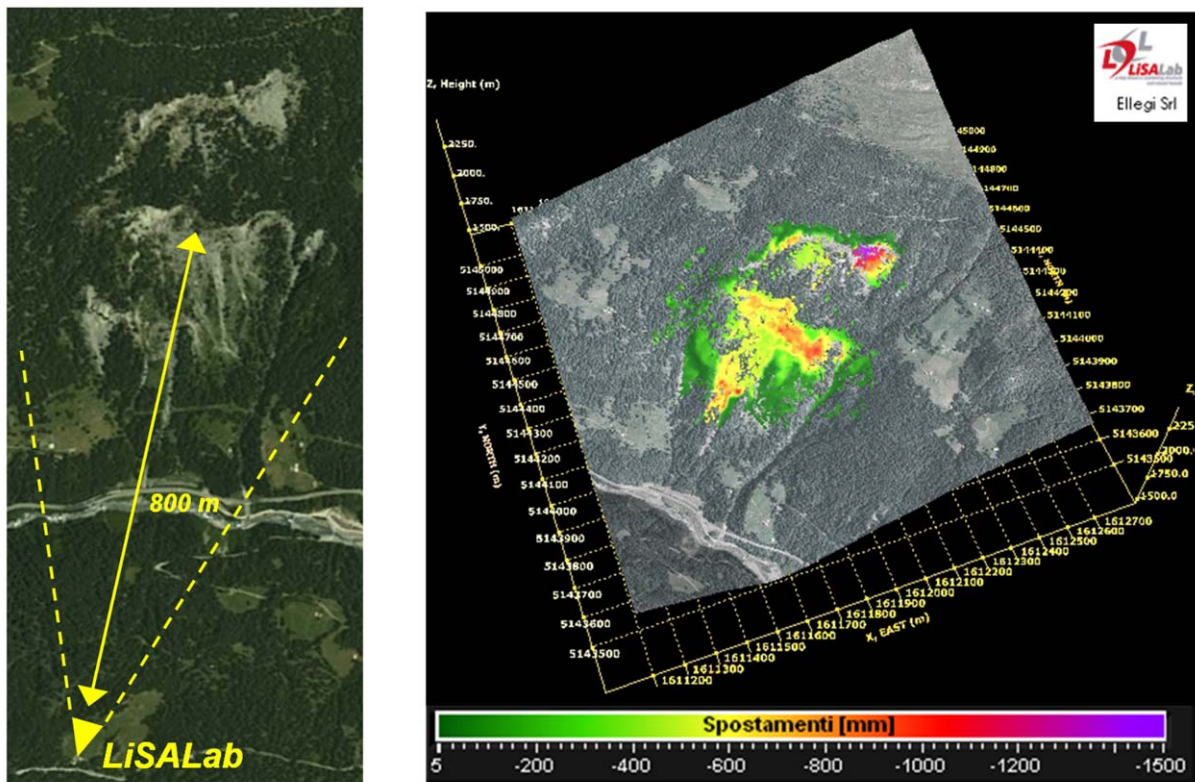


Figure 4.11-5. Layout of the GB InSAR monitoring system installed on the Ruinon rockslide in 2006 (LiSALab Technology provided by Ellegi s.r.l. for ARPA Lombardia).

4.11.3 ANALYSIS OF MONITORING DATA

4.11.3.1 Rockslide displacements

Data description

Monitoring data provided by the ground-based instrumentation allowed the identification of rockslide sectors characterised by different styles of activity and different responses to external triggers. Crosta and Agliardi (2003) identified three different patterns of displacement trends, namely: “brittle”, with stick-slip movement of limited rock mass volumes; “chaotic”, observed in areas of debris/disrupted rock and lacking a well-defined trend; and “seasonal creep” (Figure 4.11-6), with non-linear acceleration phases during wet seasons and resting periods during winter and early spring. Seasonal reactivations, associated with rainfall and snowmelt, have been superimposed over a general progressive trend from 1997 to 2002, whereas the rockslide experienced a stage of long-term stabilisation between 2003 and 2007. From 2008, the rockslide started accelerating again, suggesting that “seasonal” behaviour occurs at different timescales due to complex deformation and failure mechanisms (Figure 4.11-7).

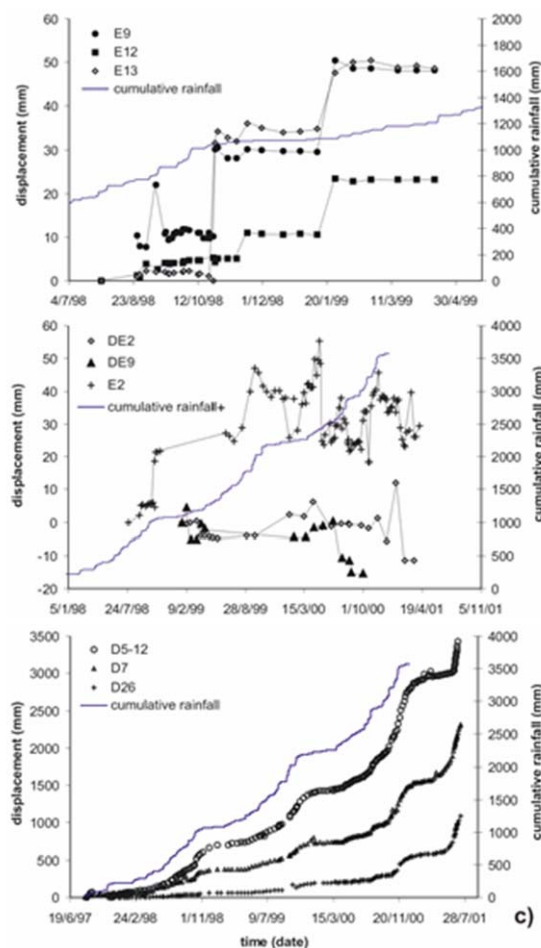


Figure 4.11-6. Displacement trend patterns outlined by Crosta and Agliardi (2003) based on surface displacement measurements provided by the ground-based geotechnical monitoring network in the period 1997-2001.

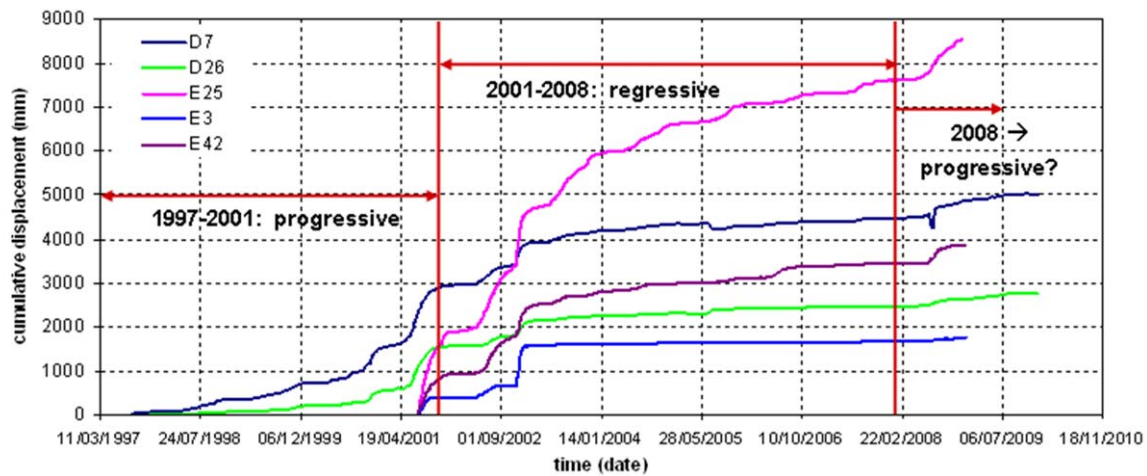


Figure 4.11-7. Long-term evolution of the Ruinon, from ground-based displacement measurements (modified after Agliardi et al., 2011).

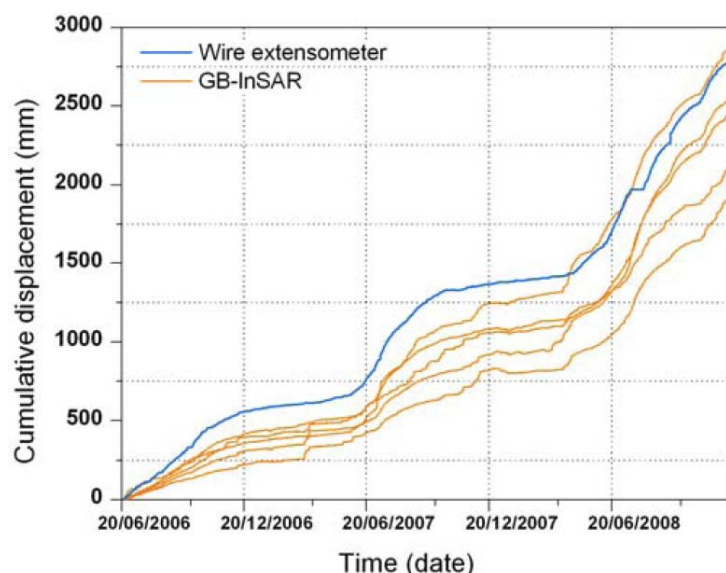


Figure 4.11-8. Comparison among displacements recorded by a wire extensometer and by GB InSAR (Line Of Sight displacements) at some slope locations nearby (Agliardi et al., 2011).

Data from ground-based instrumentation also allowed for validation/correction of the spatially-distributed displacement data provided by the GB InSAR system since June 22nd, 2006. Since displacements are measured along the radar Line of Sight (LOS), the recorded component of the local displacement vector varies at each slope location, requiring ground-truthing. The comparison between GB InSAR and wire extensometer data (Figure 4.11-8) revealed a good match among the recorded displacements, with extensometer data providing upper bounds (i.e. estimates of total displacement).

Data analysis: rockslide sub-areas

The spatially-distributed character of GB InSAR measurements provided the opportunity to refine the existing geological model of the rockslide in order to better understand its kinematics for early warning purposes. From this perspective, we analyzed the remote sensing displacement data up to February 10th, 2010 (Figure 4.11-8) and identified homogenous sub-areas characterized by similar behavior (Figure 4.11-11).

GB InSAR displacement maps have been automatically extracted as 5483 geo-referenced GridAscii files (one every six hours; grid size: 1500x1500 pixels; average cell size: 1 m) for further processing in ArcGISTM. As a first step, displacements have been cumulated over 30-day periods to obtain multi-temporal Cumulative Displacement (CD) maps. Incremental Displacement (ID) maps were also derived from CD.

Preliminary analysis of monthly CD maps allowed identifying the magnitude and spatial pattern of rockslide displacement fields, whereas ID maps provided insight into the temporal pattern of displacements (i.e. seasonality, major displacement events; examples in Figure 4.11-9).

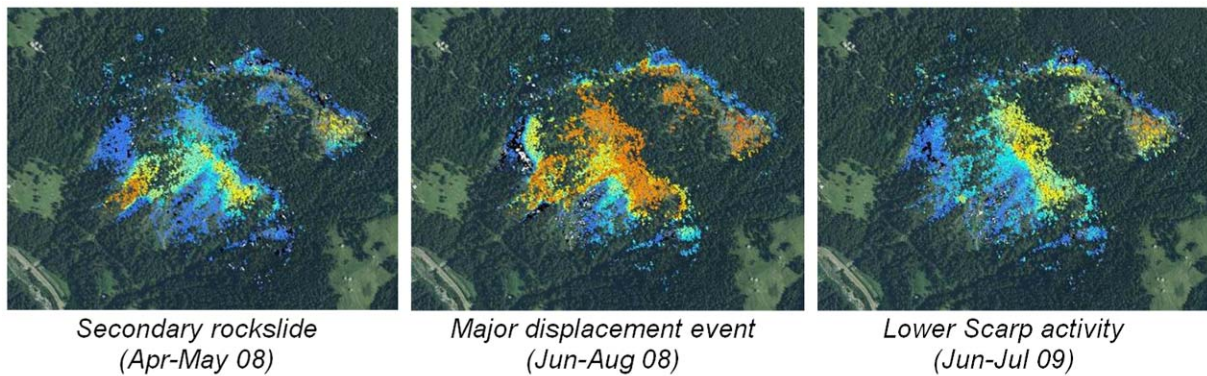


Figure 4.11-9. Different rockslide behaviors and displacement events outlined by ID maps.

The analysis of CD and ID maps (either raw or smoothed by neighbourhood statistical techniques) allowed the initial definition of sub-areas with a homogeneous displacement pattern and rate. This was refined through multi-temporal geomorphological mapping based on photo interpretation and field observations, aimed at identifying debris-covered areas, rock outcrops, major structures, and kinematic evidence.



Figure 4.11-10. Steps toward the identification of rockslide sub-areas: a) reclassification of CD maps; b) smoothing of CD maps by neighbourhood statistical techniques; c) comparison to geological and geomorphological field evidence (e.g. slope material, style of activity).

This allowed the identification of 13 sub-areas (Figure 4.11-5) with homogeneous landslide behaviour and style of activity, depending on the involved material (bedrock, fine or coarse debris cover) or on local structural controls (e.g. distance to major fractures and lineaments). These sub-areas have been further grouped into seven larger domains (A to G, Figure 4.11-11), which provide consistent information about the evolution of different rockslide sectors from a practical early warning perspective. In particular:

- domain “A” includes a fast-moving area involving disrupted rock masses at the eastern tip of the Upper Scarp, inferred to reflect the evolution of a quite large portion of the rockslide;
- domain “B” includes the Upper Scarp crown, characterised by small displacements and providing a passive feedback of rockslide global movement;
- domains “C” and “D” (Lower Scarp) include the rockslide displaced head, with a thin debris cover mantling the bedrock, reflecting large-scale rockslide movement, as well as domain “D”;
- domain “E” includes the thick rockslide debris and reworked glacial deposits downslope of the Lower Scarp, undergoing large displacements and responding to rainfall events through debris flows and debris slide activity;
- domain “F”: area involved in a large individual debris slide;
- domains “G”, including relatively stable areas, possibly providing passive feedbacks for catastrophic failure.

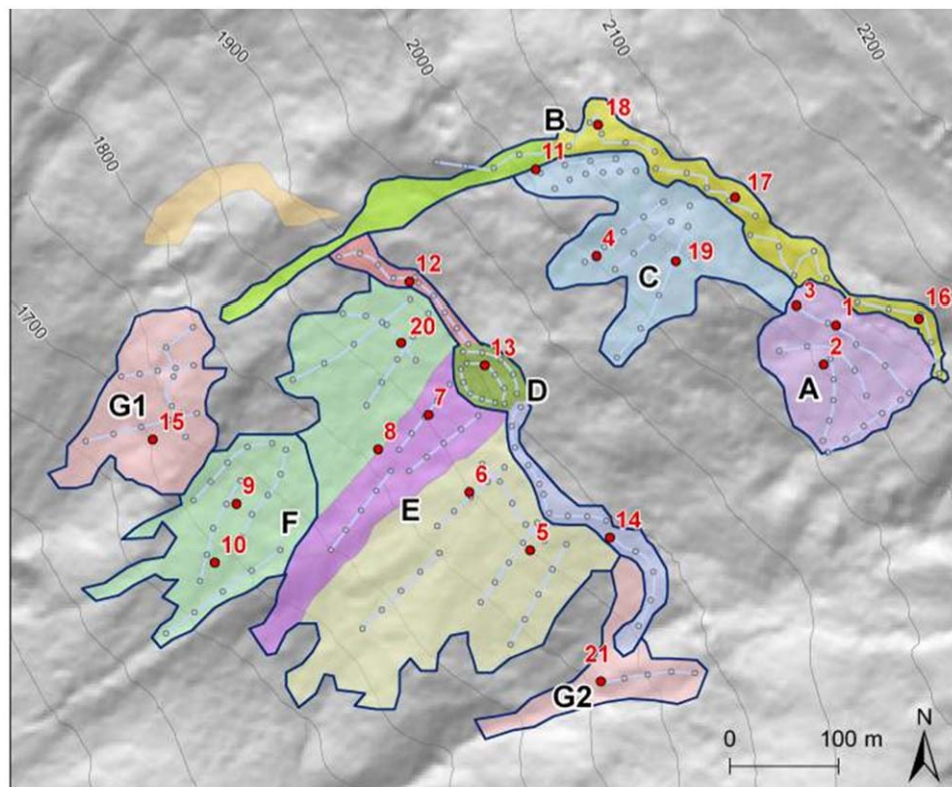


Figure 4.11-11. Thirteen rockslide homogeneous sub-areas, indicated by colours and identified with respect to: style of activity, displacement trend, and inferred instability mechanisms. Letters A to F indicate rockslide “early warning domains” (Agliardi et al. 2011).

Data analysis: extraction of displacement time series

We set up a virtual monitoring network made of 205 slope locations considered to be representative of specific kinematic features of the related sub-domains (Figure 4.11-11). For each location, we extracted displacement time series from the stack of 5483 Cumulative Displacement Maps (one every six hours). 132 continuous time histories (i.e. covering all five monitoring years) were validated against ground-truth and processed in order to remove the effects of “phase wrapping”. Corrected time series allowed a final refinement of rockslide sub-area zoning depending on: cumulative displacement and rate of displacement, sensitivity to and acceleration in consequence of specific triggering events (Figure 4.11-11).

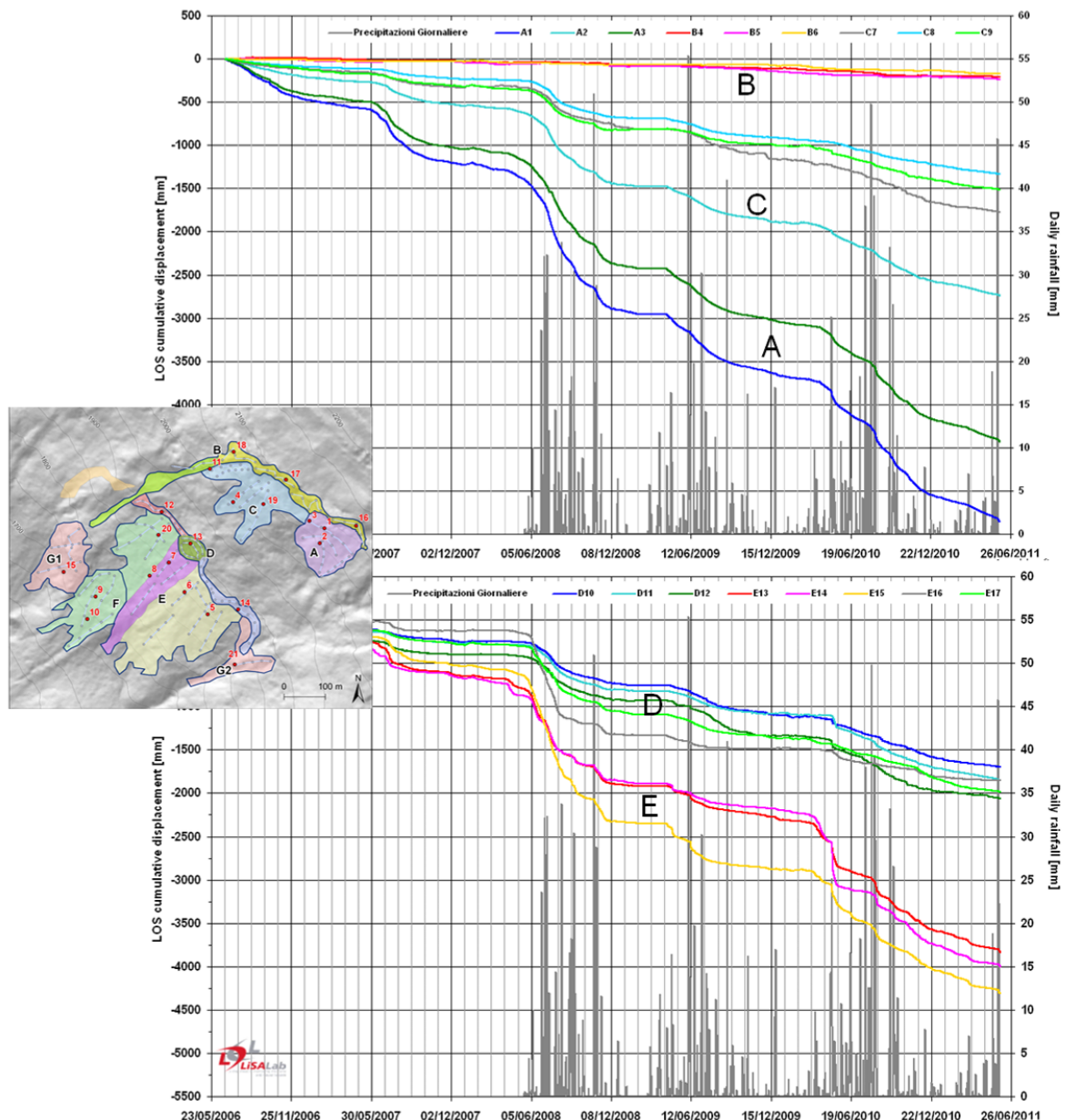


Figure 4.11-12. Displacement time series extracted by the GB InSAR dataset at specific points with well-characterised significance with respect to the evolution of the rockslide. These provide a description of the long-term evolution of different rockslide sectors (data Ellegi – LiSALab s.r.l. for ARPA Lombardia).

Early warning for rockslide collapse: alert velocity thresholds

Modelling the failure of large, complex rockslides at the Ruinon site would require detailed knowledge of rockslide geometry and structure, the constitutive behaviour of the involved materials, as well as the boundary conditions and related variations in space and time. This approach is usually unfeasible for early warning purposes because of the large underlying uncertainties and the required modelling effort, generally incompatible with real-time monitoring and decision-making.

Several empirical/phenomenological approaches based on the “slope creep” theory (Saito and Uezawa, 1961; Fukuzono, 1985; Voight, 1988) allow for the above-mentioned difficulties to be overcome when attempting to forecast rockslide failure through the analysis of time series monitoring data. For large landslides with complex kinematics and responses to external triggers, Crosta and Agliardi (2003) proposed a methodology to obtain physically-based alert velocity thresholds. The method is based on the Fukuzono-Voight equation (Voight, 1988), which establishes the following non-linear relationship between acceleration and displacement rate:

$$\ddot{\Omega} = A\dot{\Omega}^\alpha \tag{1}$$

where Ω is rockslide cumulative displacement, and A and α are empirical coefficients (constant in the case of time-invariant loading conditions and external actions).

Integration of Eq. 1 for $\alpha > 1$ and $\alpha \neq 2$ (Crosta and Agliardi, 2003) yields:

$$\Omega = \frac{1}{A(\alpha-2)} \left\{ \left[A(\alpha-1)t_f + \dot{\Omega}_f^{1-\alpha} \right]^{\frac{2-\alpha}{1-\alpha}} - \left[A(\alpha-1)(t_f-t) + \dot{\Omega}_f^{1-\alpha} \right]^{\frac{2-\alpha}{1-\alpha}} \right\} \tag{2}$$

where $t_f > t$ is the time of failure associated with the assumed displacement rate at failure (i.e. singularity or corresponding to a pre-defined high value of displacement rate), α is a dimensionless curve shape parameter, and A is a positive constant controlling the shape of the curve (Voight, 1988; Crosta and Agliardi, 2003)

Since seasonal behaviour usually hampers a reliable estimation of the time to complex rockslide failure, the authors used the equation, integrated to a power law of displacements vs. time, to fit time series of measured cumulative displacements (Figure 4.11-13). Non-linear fitting procedures allowed the derivation of model parameters (A , α , and t_f) typical of the current state of the physical system evolving towards failure. Synthetic velocity-time curves are then derived from these parameters (Figure 4.11-13), providing a quantitative basis to establish alert velocity threshold values. These correspond to different time intervals before expected failure conditions and are useful for early warning.

For the Ruinon rockslide, long-term time series of cumulated displacements does not show a continuous accelerating behavior, due to seasonality and long-term changes in rockslide evolution (from progressive to regressive, and *vice versa*). For this reason, the most critical periods of time series in the time window covered by GB InSAR (i.e. critical acceleration

stages showing an evolution close to catastrophic failure conditions) have been modeled by non-linear curve fitting of cumulative displacements.

The analysis has been carried out at 22 representative locations spread over the seven above-mentioned domains (Figure 4.11-11 and Figure 4.11-14). The periods considered were April-July 2008 and the summer of 2011.

Three early warning threshold levels (corresponding to different emergency plan actions) have been established according to Crosta and Agliardi (2003), namely: a) 30 days: attention; b) 15 days: pre-alarm; c) seven days: emergency.

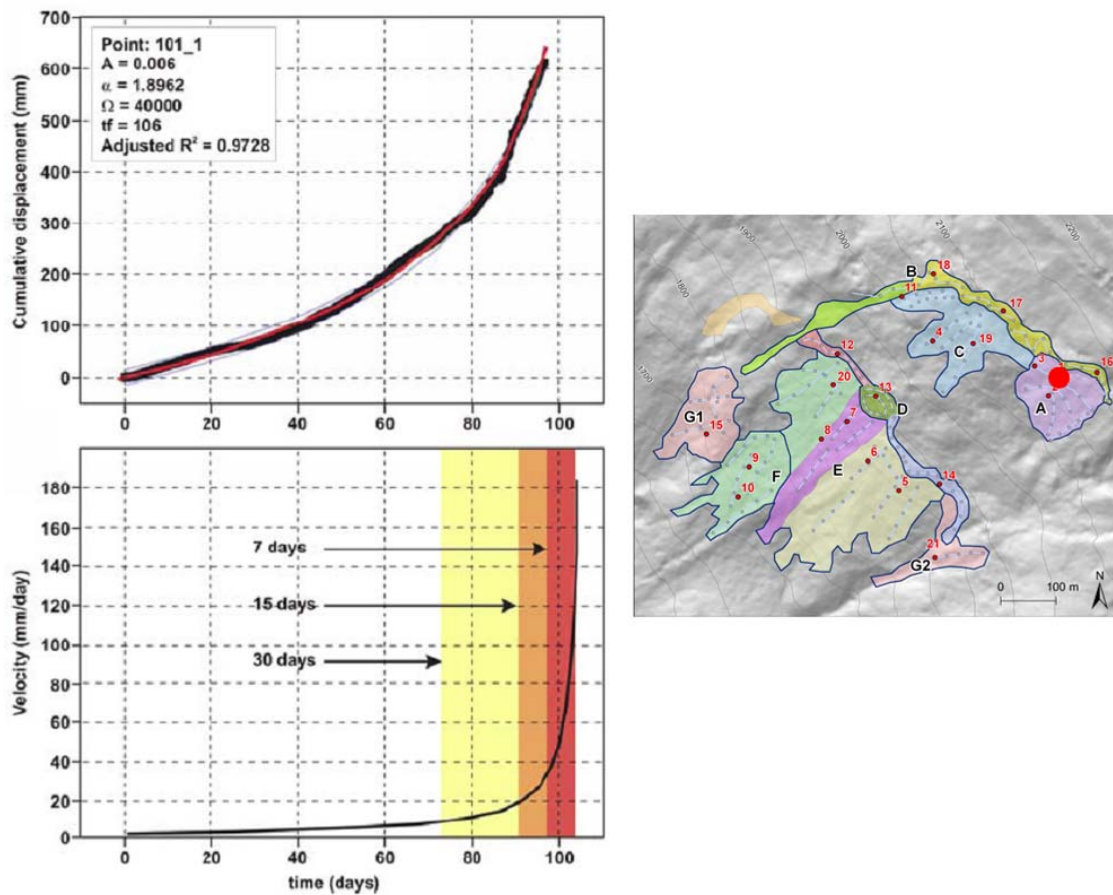


Figure 4.11-13. Alert velocity threshold definition by non-linear fit of cumulative displacement series (Ruion rockslide, year 2008; Agliardi et al., 2011).

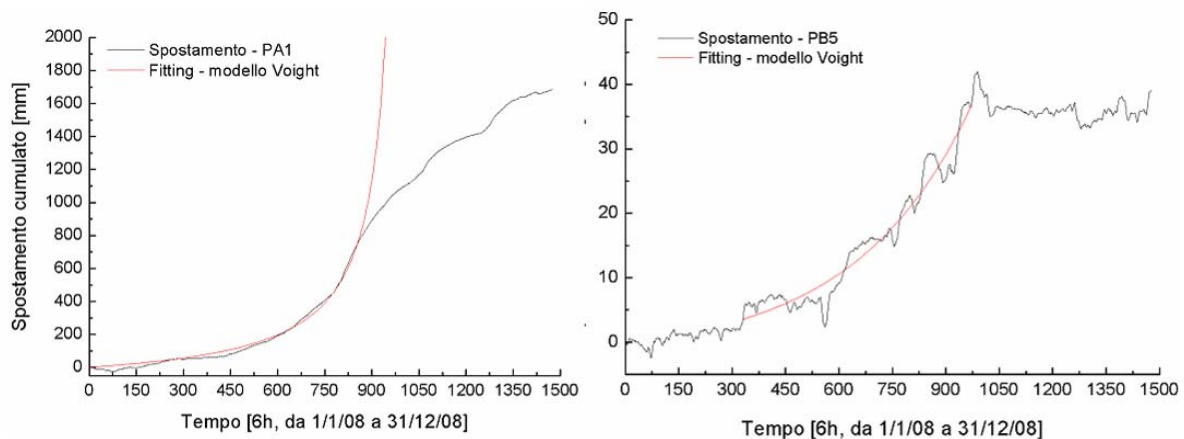


Figure 4.11-14. Examples of non-linear curve fitting of cumulative displacement series for the 2008 acceleration stage (sub-areas A and B; Agliardi et al., 2011).

4.11.3.2 Rainfall

Data description

The area is characterized by a typical continental-alpine rainfall regime (rainy summer and autumn) with an annual average, maximum, and minimum rainfall of 750, 1300, and 300 mm, respectively, calculated on the basis of the 1891–1990 rainfall record (Ceriani and Carelli, 1999).

Although long-term rainfall records have been provided by the Bormio and Santa Caterina rain gauges, these are located kilometres away from the Ruinon rockslide area. The rainfall levels have been measured directly on the rockslide area since January 2006, using an automatic rain gauge (combined with a meteo-station) which provide rainfall measurements every 30 minutes (Figure 4.11-15).

The mean annual precipitation evaluated within the monitoring period is 815 mm, with peaks exceeding 50 mm per day. Most of the rainfall concentrates in the late spring and summer, according to the local climatology.

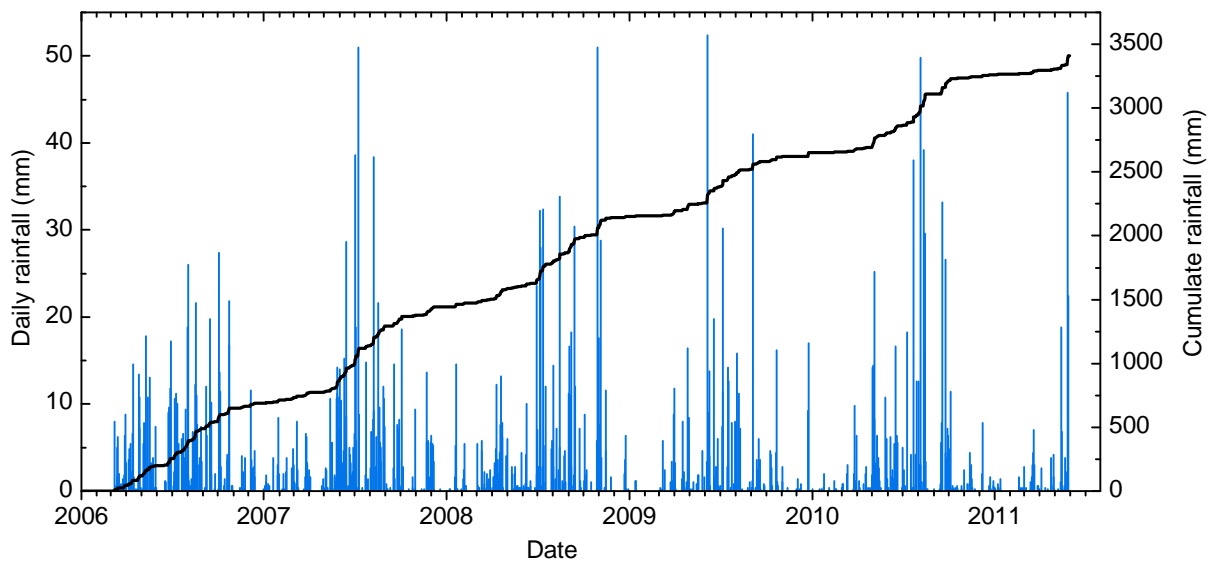


Figure 4.11-15. The figure portrays the complete rainfall dataset from January 2006 until May 30, 2011, in both daily and cumulative forms.

Rockslide reactivation: towards rainfall threshold

The qualitative comparison between displacement trends and rainfall time series (Figure 4.11-12) suggests a complex interplay between rainfall inputs and the Ruinon rockslide response. Time series of antecedent rainfall, cumulated over 1, 7, 15, 30, 45, 60, and 90 days was derived from available rain gauge datasets, and used to explore their controls on the overall rockslide response (Figure 4.11-16). The best correlation was found for 60-day cumulative rainfall, which results in increased displacement rates over values of 150-200 mm (Figure 4.11-17). Nevertheless, the results obtained for the whole rockslide lack statistical significance and are not related to the evolution of specific rockslide sub-areas. Thus they cannot be used as predictive tools, except for a preliminary evaluation of lower bounds of rockslide responses (e.g. associated to a quantile of observed displacements) to pre-defined rainfall input.

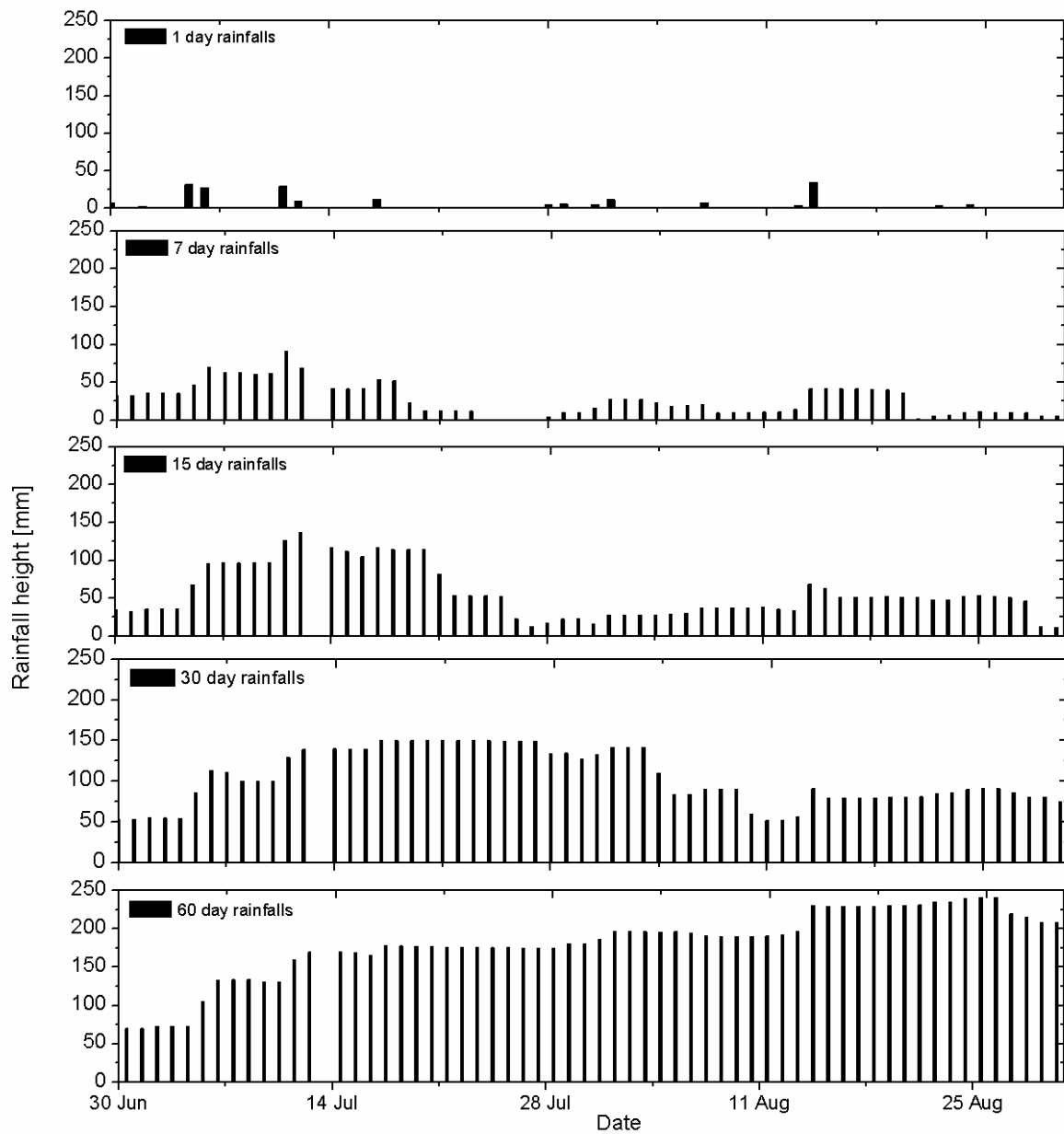


Figure 4.11-16. Antecedent rainfall cumulated over different time periods and referred to July-August 2008, characterized by significant critical acceleration of all rockslide sectors.

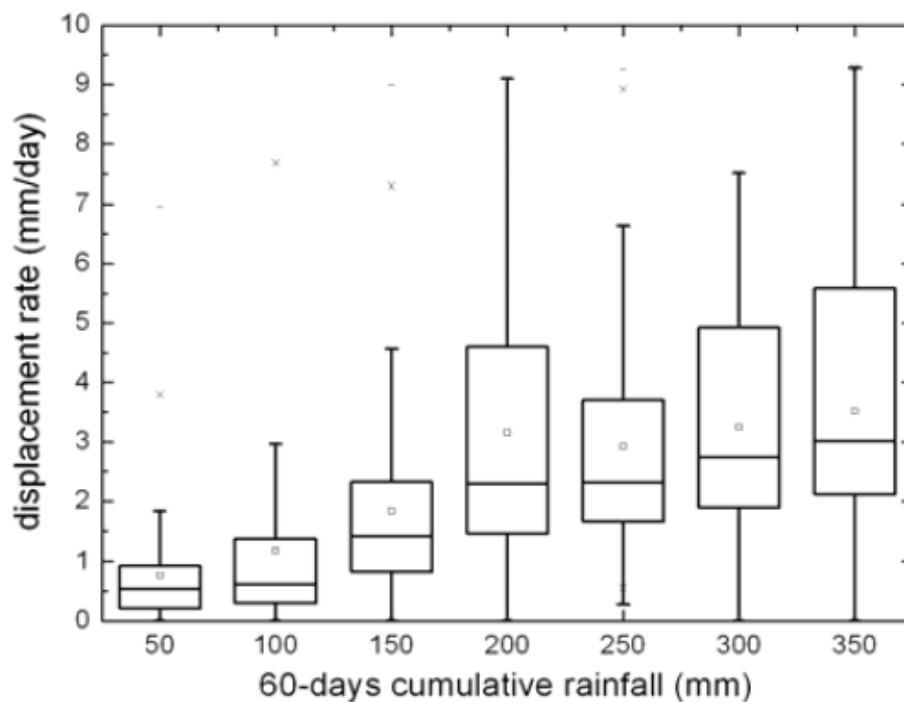


Figure 4.11-17. Relationship between displacement rates and antecedent 60-day rainfall, based on the entire available displacement and rainfall datasets (Agliardi et al., 2011).

The expected rockslide response to rainfall, outlined in this way, must be evaluated with respect to specific rainfall inputs (i.e. events, rainy periods) and for specific rockslide sectors (Figure 4.11-11). For this reason, we considered “rainfall events” to be rainfall time series subsets characterised by:

- 24-hour antecedent rain < 5 mm
- five-day antecedent rainfall < 10 mm

Rainfall time series extracted according to such criterion has been compared to rockslide displacement rates averaged over five days. The analysis allowed the identification of different types of rainfall displacement rate behaviors for different rockslide sub-areas (Figure 4.11-18). Areas with extensive and thick debris accumulations (e.g. A and E in Figure 4.11-11) show a clear and sudden response to individual rainfall inputs, with displacement rate peaks followed by exhaustion (Figure 4.11-18). On the opposite, rock outcrop areas (e.g. B in Figure 4.11-11) follow quite closely the rainfall patterns at the seasonal timescale but show no clear response or complex pulses with respect to individual rainfall periods. Along the Upper Scarp, most of the annual displacements occur until early spring, suggesting that the role of snowmelt may overcome that of rainfall inputs. In the debris-covered area below the Lower Scarp (“E” in Figure 4.11-11), most annual displacements usually follow well-defined, short periods of intense rainfall. In this area, the maximum response in terms of displacements and displacement rates should be expected.

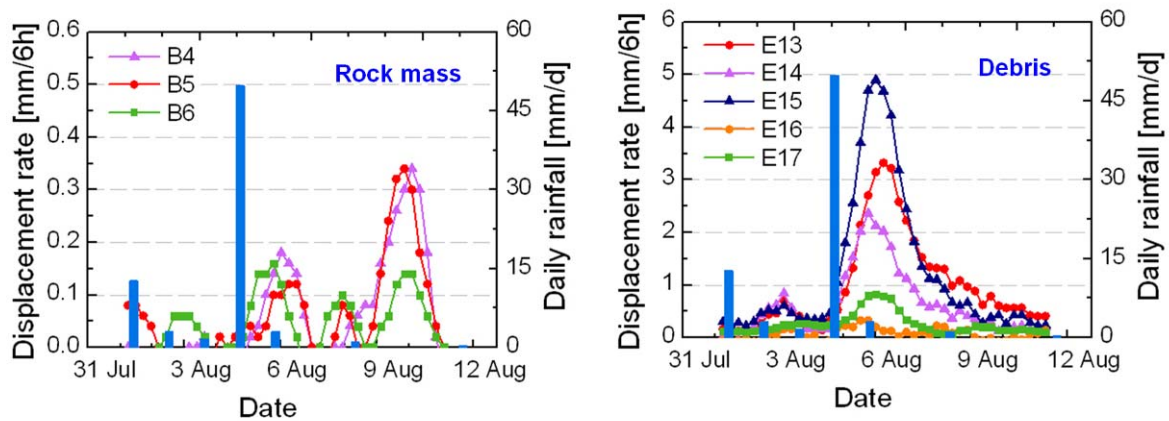


Figure 4.11-18. Different types of rainfall displacement rate responses outlined for different rockslide sectors, outlining the possible role of rainfall for the definition of early warning.

4.11.4 END-USER INVOLVEMENT AND ALARM CHAIN

The alert velocity threshold values resulting from the analysis summarized in Section 1.1.3.1 are being tested for operative use by the ARPA Lombardia Early Warning Centre, which is the regional authority in charge.

The early warning system currently exploits 21 “virtual sensors”, spread at key locations in the different rockslide domains and for which alert velocity threshold values have been evaluated. For each virtual sensor, displacement and displacement rate time series (six-hour to 15-minute displacement rates) are derived by GB InSAR streaming data, and a specific alert level is considered to be reached when threshold values are exceeded by at least two virtual sensors in a given rockslide domain.

Ongoing early warning system testing and threshold tuning is being carried out by means of the back analysis of time series related to the past, in order to obtain a statistical evaluation of false alarms and improve the reliability of predictions.

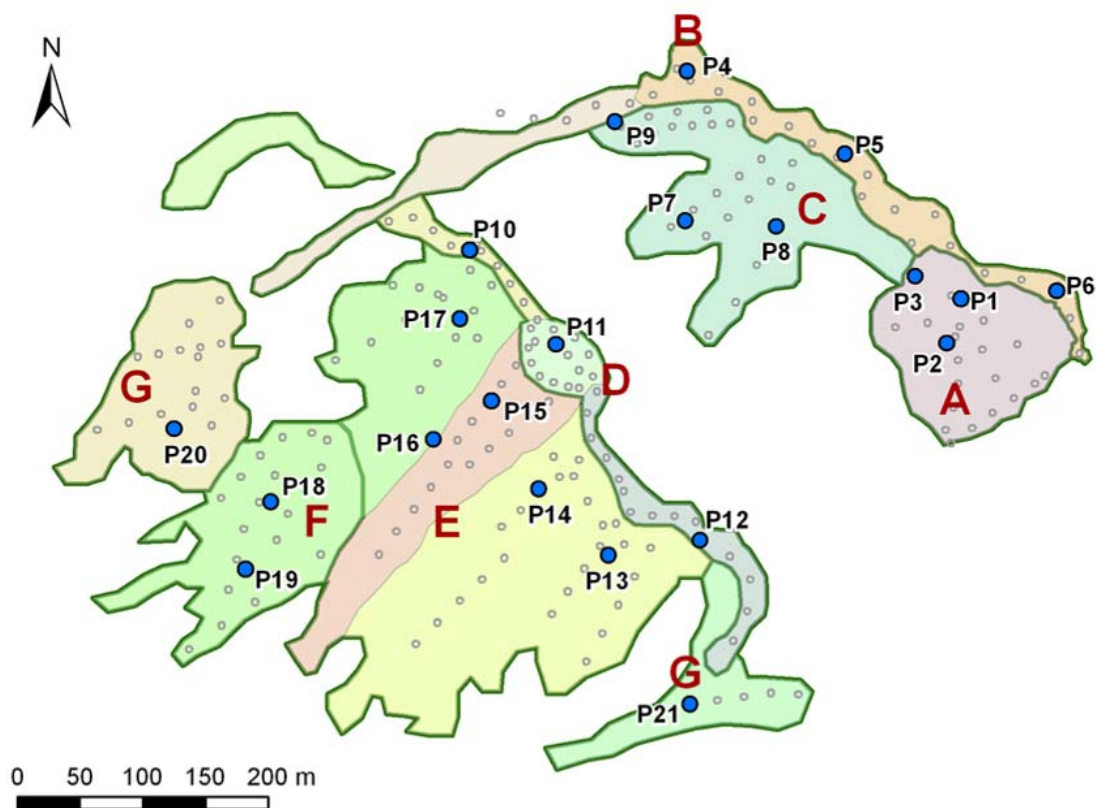


Figure 4.11-19. Monitoring locations currently considered setting up the early warning system (under testing).

4.11.5 SUMMARIZED EVALUATION OF PARAMETERS

Establishing physically-based threshold values of suitable descriptors for early warning of large rockslides is still difficult, due to their complex geometry, kinematics and hydrology, and due to the complex interactions among triggering agents and rockslide mechanisms. For these landslides, it is very difficult to identify individual displacement “events” and to correlate them with possible triggers (e.g. rainfall and snowmelt). Furthermore, rockslides often give different feedback to similar triggering events depending on the season or year. In addition, remote monitoring techniques such as GB InSAR have usually been used to describe and follow slope instability, but not for quantitative predictions of slope deformation and failure.

Different approaches have been attempted here to exploit GB InSAR data for early warning, in order to provide threshold values in terms of either displacement rate or rainfall to be used as civil protection management tools. We have proposed a novel approach to the quantitative analysis of GB InSAR data for early warning purposes. This allows the limitations of traditional ground-based instrumentation to be overcome by setting up a posteriori monitoring networks, based on radar displacement fields and constrained by refined geological models. GB InSAR provides a large amount of data even in debris-covered areas, when ground-based instrumentation fails. These data, validated by selected ground-based measurements, allows for the establishment of specific warning thresholds for homogeneous rockslide sub-areas.

Although the method had been developed with ground-based data (e.g. distometer baselines, wire extensometers), GB InSAR data proved to be the most flexible technique to apply this forecasting approach. In fact, GB InSAR a) provides spatially-distributed data from which the most suitable time series can be selected; b) provides real-time measurements to keep the analysis updated; c) provides high-frequency measurements resulting in nearly instantaneous velocity estimates for practical applications.

References

- Agliardi F., Crosta G., Zanchi A. (2001). Structural constraints on deep-seated slope deformation kinematics. *Engineering Geology*, 59 (1-2): 83-102.
- Agliardi, F., Crosta, G.B., Sosio, R., Rivolta, C., Mannucci, G. (2011). In situ and remote long term real-time monitoring of a large alpine rock slide. *Proceedings of the Second World Landslide Forum*, 3-7 October 2011, Rome, 6 pp.
- Crosta G B, Agliardi F (2003). Failure forecast for large rock slides by surface displacement measurements. *Canadian Geotechnical Journal*. 40(1): 176-191.
- Casagli N, Catani F, Del Ventisette C, Luzi G. (2010). Monitoring, prediction, and early warning using ground-based radar interferometry. *Landslides*. 7: 291–301
- Amitrano D., Helmstetter A. (2006). Brittle creep, damage, and time to failure in rocks. *Journal of Geophysical Research*. 111: B11201.
- Broadbent, C.D, Zavodni, Z.M. (1982). Influence of rock structure on stability. *Stability in Surface Mining*, 3, Soc. of Mining Engineers.
- Crosta, G.B., Agliardi, F. (2003). Failure forecast for large rock slides by surface displacement measurements. *Canadian Geotechnical Journal*. 40, 1: 176-191.
- Fukuzono, T. (1985). A new method for predicting the failure time of a slope. In: *Proc. 4th Inter. Conference and Field Workshop on Landslides*, Tokyo, Tokyo University Press: 145–150.
- Saito, M., Uezawa, H. (1961). Failure of soil due to creep. In: *Proceedings of the 5th International Conference on Soil Mechanics and Foundation Engineering*. 1: 315–318.
- Voight, B. (1988). A method for prediction of volcanic eruption. *Nature*. 332: 125–130.

4.12 SONNBLICK & MÖLLTALER GLACIER (AUSTRIA)

David Ottowitz, Birgit Jochum, Robert Supper, Alexander Römer
Geological Survey of Austria

ABSTRACT

The main focus at these two monitoring sites was put on the collection of a continuous geoelectric dataset in a high alpine region to study permafrost conditions and the freezing/melting processes of the subsurface. Due to various problems at the Sonnblick site we moved the monitoring system to the Mölltaler glacier, where the system worked without any significant interruption during the whole planned monitoring period. The monitoring results show distinct resistivity changes in time (freezing/melting processes) and the absence of permafrost. The lack of appropriate additional measurements constricted a detailed interpretation of the data.

Presented parameters: permafrost monitoring, soil temperature, resistivity.

4.12.1 GENERAL DESCRIPTION OF THE TEST SITE

The Sonnblick, which has an elevation of 3,105 m a.s.l., contains a very famous meteorological observatory on its summit. Changes of climate parameters due to global warming generate increased permafrost “warming” in Alpine regions, thus involving severe environmental and engineering problems. Underlying processes are still not completely understood. The geoelectrical method could be the method of choice to monitor these processes, due to the fact that we have high resistivity contrasts between frozen and melted soil. In this case permafrost “warming” induces several rockfalls in the summit region of the Sonnblick. Due to this instability, complex construction measures had to be performed in the time period from 2002 to 2006 to save the observatory (Figure 4.12-1).

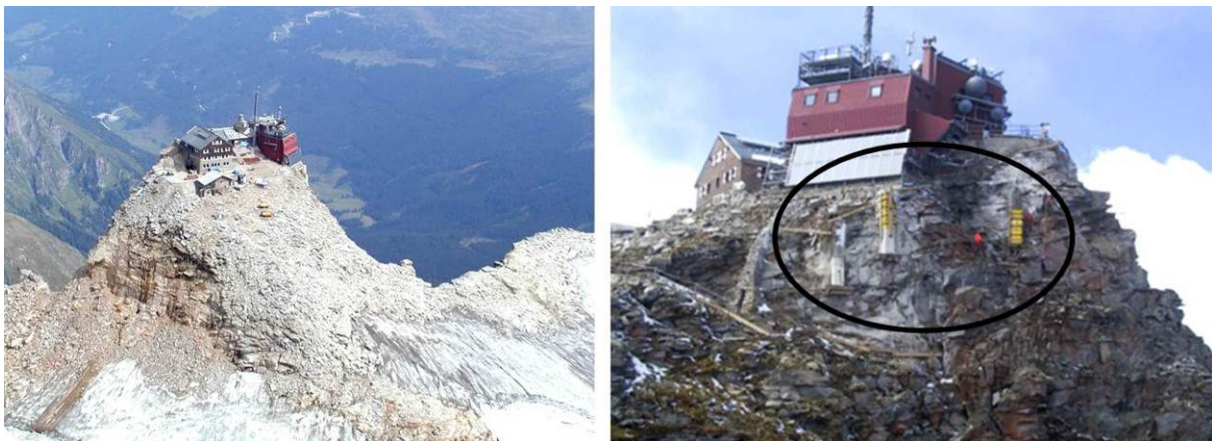


Figure 4.12-1. Sonnblick summit with observatory and Zittelhaus (left), constructions to stabilize the summit area (right) (Photos by M. Staudinger).

The main focus at this test site was put on the technological developments of the geoelectric system (GEOMON^{4d} (Supper et al. 2003, 2009, and 2010)), which were necessary due to the very high resistivity of frozen soil respectively rock and of course to the high alpine conditions (e.g. low temperature).

After a first test period on the Sonnblick, we realized that the data quality of the measurements was unsatisfactory, due to a large amount of different steel installations in the summit area. Because moving the system to another place on the mountain was not promising, we decided to search for a completely new site that was easily accessible.

Finally we decided to install our system in the skiing area of the Mölltaler Glacier close to the mountain station of the “Eissee” cable car (Figure 4.12-2).

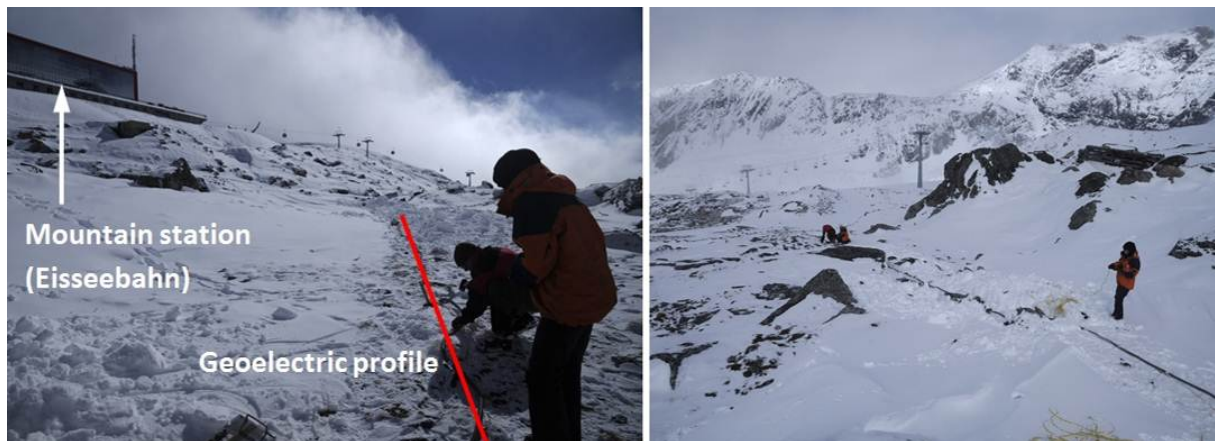


Figure 4.12-2. Position of the monitoring site Mölltaler Glacier.

The area of the monitoring system is placed about 5 km to the southwest of the Sonnblick and has an elevation of about 2,800 m a.s.l. (Figure 4.12-3). This short distance allows us to use different measurements (e.g. air temperature, precipitation, soil temperature) from the Sonnblick at least for a quantitative correlation with our geoelectric data.

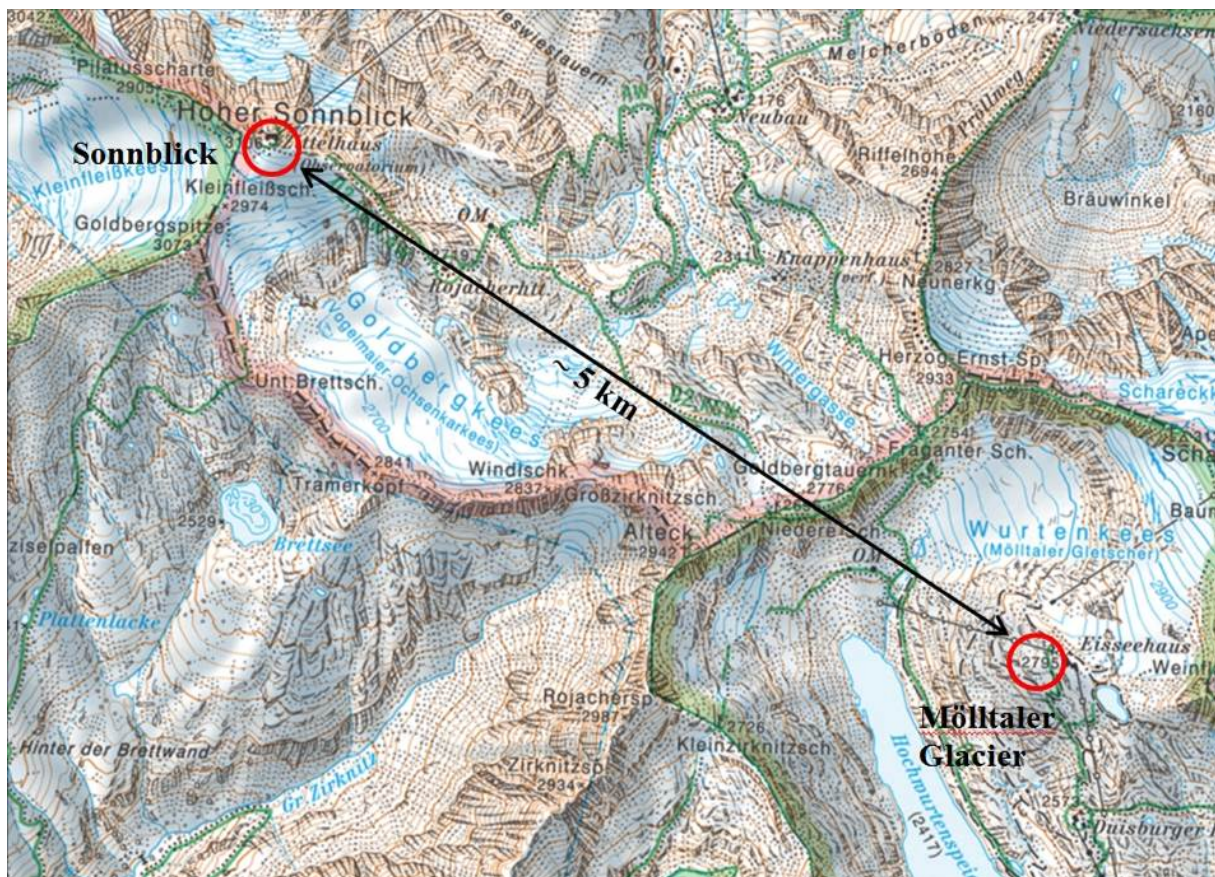


Figure 4.12-3. Location of the two monitoring sites (map ©Amap Fly 5.0, BEV, 2009).

Geological and geomorphic settings

Both test sites are placed within the subpenninic nappe system of the Tauern Window, which is a very complex geological unit (Figure 4.12-4). The particular part of the nappe system is called “Sonnblickkern” which consists mostly of “Zentralgneis”. The term “Zentralgneis” characterises felsic to intermediate metamorphic plutonites. From the petrographic point of view they are of aplitic, granitic, granodioritic, tonalitic and syenitic composition. Metabasites, which are also present at the monitoring sites, are metamorphic descendants of ophiolite sequences of early Palaeozoic age. The majority of the metabasites are fine- to intermediate-grained prasinites and amphibolites. The latter are partly also coarse-grained.

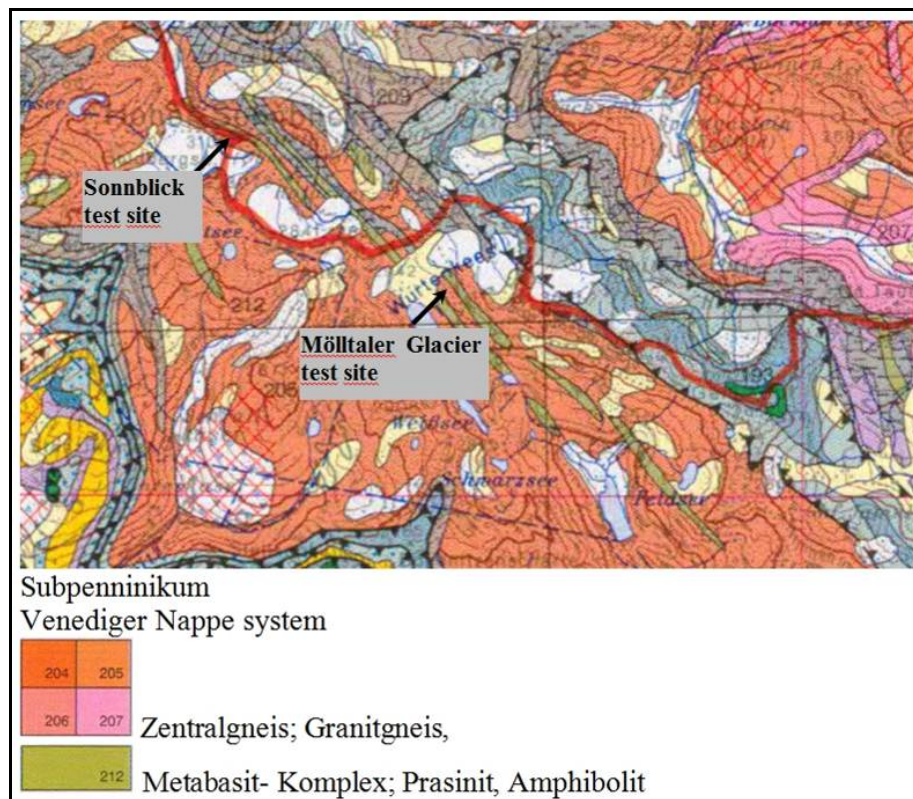


Figure 4.12-4. Excerpt of the Geological Map of Salzburg and the Legend, 1:200000, GSA, Vienna 2005, with the indication of site positions.

Characterization of the site

The summit area of the Sonnblick is very vulnerable to rockfalls which are induced by permafrost melting. The meteorological observatory and the Zittelhaus, which are placed on the top of the summit (see Figure 4.12-5), are indirectly affected by the rockfalls because they indicate a decreasing stability of the area.

At the site of Mölltaler Glacier there is no indication of mass movement or rockfall. The main focus here was on the collection of geoelectric data for a whole seasonal period to get information about permafrost conditions and freezing/melting processes at the monitoring site.

4.12.2 DESIGN OF THE MONITORING NETWORK

At the Sonnblick site several measurements have been performed by the Central Institute for Meteorology and Geodynamics (ZAMG) over a long time. This includes GPR, seismics, borehole measurements (e.g. soil temperature) and of course meteorological measurements.

For the geoelectric monitoring we used an adapted version of our GEOMON^{4D} (Supper et al. 2003, 2009, and 2010) system. The adaption concerns the voltage supply of the system, to enable measurements at areas with very high resistivity of the subsurface. The electricity was provided by the observatory.

Figure 4.12-5 shows the position of the geoelectric profile and the distribution of additional measurements.

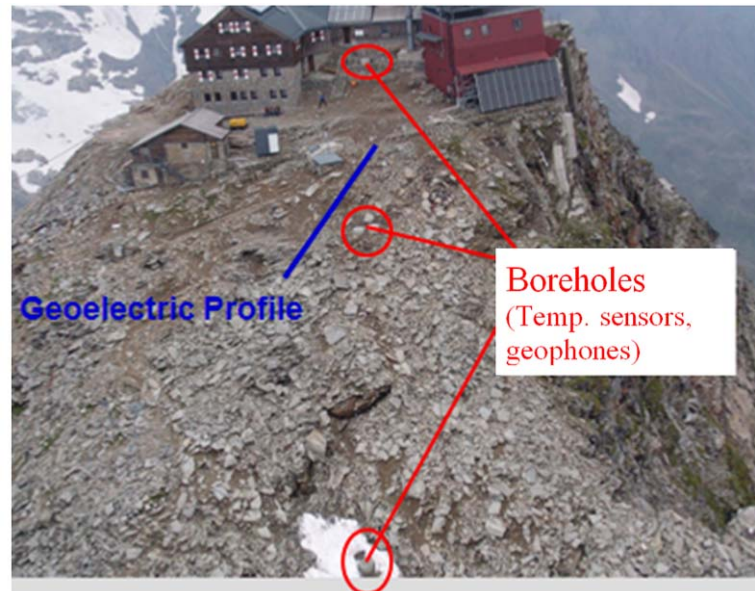


Figure 4.12-5. Position of the geoelectric profile and additional measurements (Photo by M. Staudinger).

Due to the exposed position of the system there were many problems with lightning strikes especially during summertime. In addition to that the data quality at this site was very bad, because of several steel installations in the summit area. This forced us to find a new monitoring site; continuous collection of high-quality data at the Sonnblick was impossible.

The new monitoring site at the Mölltaler glacier includes no additional measurements, but the distance to the Sonnblick is only about 5 km, so at least a quantitative implication of these measurements is possible. To ensure the data quality some geoelectric pre-investigations were performed at the planned monitoring site (Figure 4.12-6).

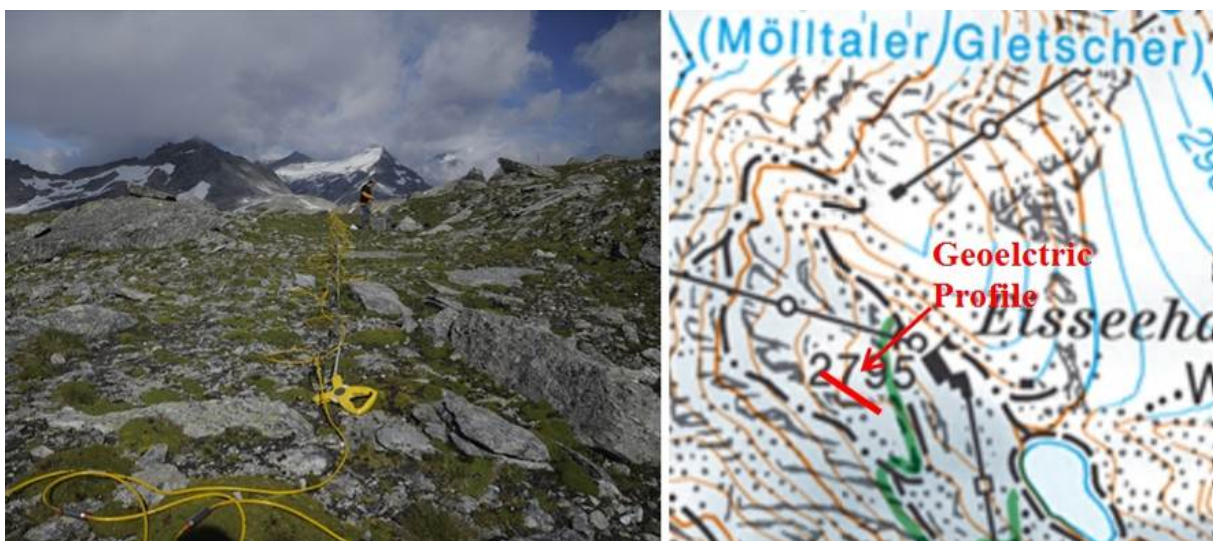


Figure 4.12-6. Geoelectric pre-investigations (left) and the detailed position of the monitoring profile (right) (map ©Amap Fly 5.0, BEV, 2009).

Because there was no possibility of a connection to the power grid we used a fuel cell system as a power supply which is described in detail in D4.8 (Chapter on Monitoring systems). The geoelectric monitoring system was installed in September 29th, 2010 and removed on August 22nd, 2011. The electrode spacing of the NW-SE oriented profile was 1 m and the measurement was performed once a day. The data was sent the following day by e-mail to the office in Vienna. At this measuring interval the very low fuel consumption of the fuel cell would enable continuous operation without maintenance for approximately nine months. Nevertheless, it was necessary to make some repairs already in June due to some damage by overvoltage and broken connections to some electrodes.

4.12.3 ANALYSIS OF MONITORING DATA

4.12.3.1 Resistivity

Freezing and melting processes of the subsurface have a very strong influence on the resistivity. As such, monitoring of this parameter seems to be a promising method for permafrost detection and for studying seasonal changes of the shallow part of the subsurface.

The monitoring profile on the Mölltaler Glacier had a length of 80 m with 1 m electrode spacing. This layout leads to a depth of penetration of about 15 m, which is much higher than the maximum depth where seasonal changes can be detected. Data processing respective to the inversion of the geoelectric data was performed with the AGI EarthImager 2D software. Figure 4.12-7 shows the inverted results of the whole monitoring period. It starts with the first resistivity model from October 9th, 2010 and it ends with June 24th, 2011. Although our monitoring period was until August 22nd, 2011 we omit results from the last two months, because of insignificant changes of the data. The interval between two resistivity models in Figure 4.12-7 is 15 days.

The interpretation of the monitoring results shows two important features. First of all the resistivity change in the shallow part of the depth section (about 3 m) shows the freezing and melting process very clearly. A continuous increase of the resistivity in this part can be seen from the inversion result 1 to 12, which corresponds to the date of March 24th. Later, the melting process, especially in the very shallow part of the depth section, leads to a decrease in the resistivity in result 13 and 14. The expansion of the high-resistivity area to larger depths in this time period correlates with the known time delay of minimum soil temperatures. The progress of the melting process shows very large resistivity changes between results 15 and 16. The comparison of the shallow part of the depth section of result 17 and 1 illustrates that we more or less reached the starting point.

At deeper parts of depth sections, hardly any changes took place. Consequently we conclude that although the profile was located at 2770 m, permafrost might not be present at depth due to the relatively low (15000 Ohmm) resistivities measured at depth.

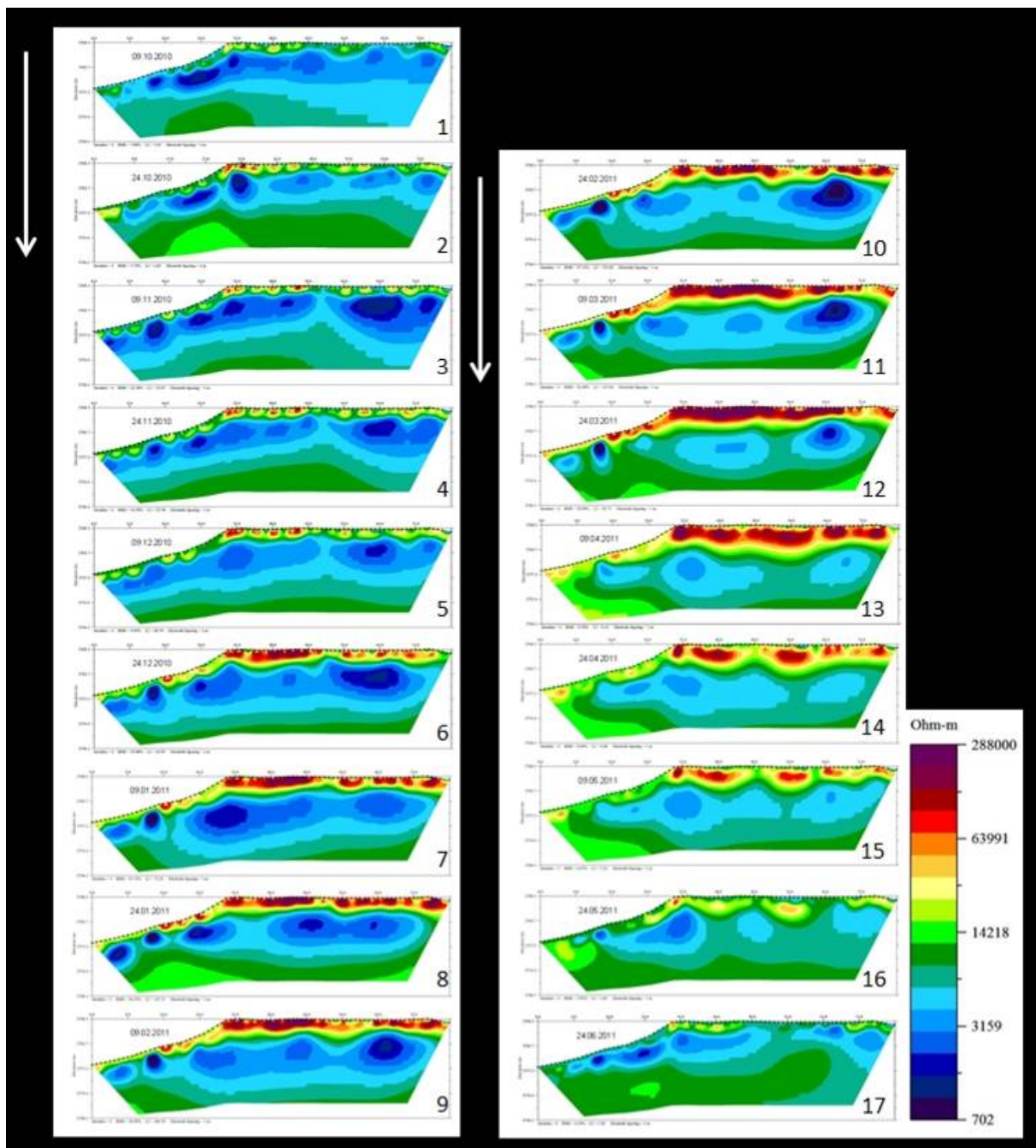


Figure 4.12-7. Inversion results of the whole monitoring period.

4.12.3.2 Soil temperature

Soil temperature was measured on the Sonnblick as mentioned in the chapter dealing with Design of the Monitoring Network see above (Figure 4.12-5). The measurements were performed by the Central Institute of Meteorology and Geodynamics and were kindly provided for an improved interpretation of our monitoring data. Figure 4.12-8 shows a selection of soil temperature data for all three available boreholes. It is clearly seen that positive temperatures of the soil are only present to a depth of 1 m and only during very short periods in the summertime. The rest of the year we have frozen conditions at all depths. A very interesting point is the difference of the temperature behaviour between these three locations (note varied scaling). This reflects the strong influence of different parameters (e.g.

slope angle, lithology) on soil temperature. It illustrates the importance of soil temperature measurements at the location of the geoelectric profile for exact, quantitative interpretations.

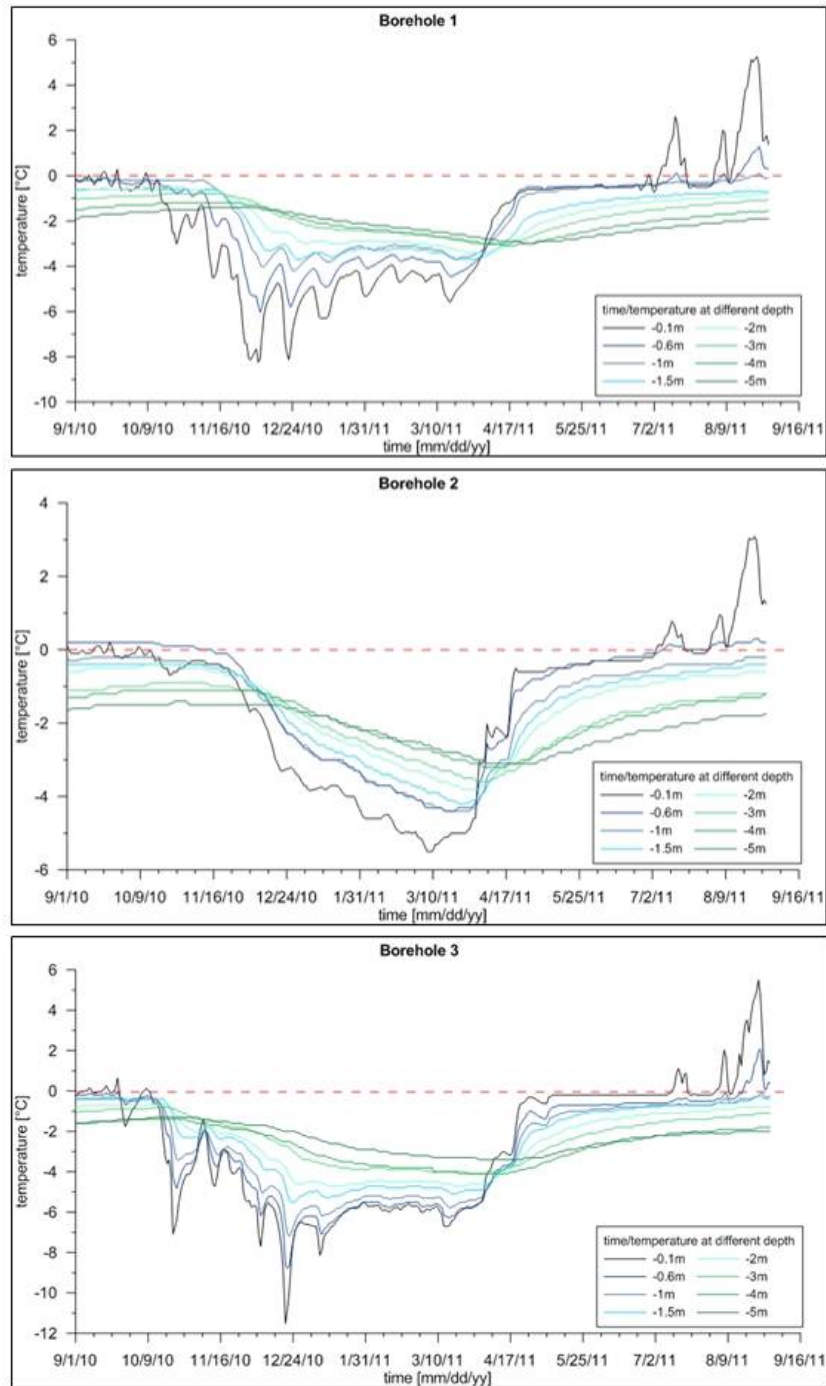


Figure 4.12-8. Changes of soil temperature in time at different depths at three different locations (temperature data provided by the Central Institute of Meteorology and Geodynamics, Vienna).

4.12.4 SUMMARIZED EVALUATION OF PARAMETERS

The correlation between soil temperature at different depths and resistivity should provide a better understanding of the principles responsible for resistivity changes at low temperatures. Unfortunately we did not have any information about soil temperature at the monitoring site. Our data source for this parameter is at a 5 km distance and at about 300 m higher altitude (at the Sonnblick). The fact that soil temperature is highly influenced by several conditions (e.g. slope angle, lithology) makes a qualitative correlation of our datasets impossible. The only thing that can be compared in a quantitative way is a long-term correlation.

Figure 4.12-9 shows the time series of apparent resistivity data for two measuring points, which corresponds to different depths, in comparison to the available data of soil temperature. The illustrated data series start with October 8th, 2010 and end with July 5th, 2011. Independent from depth, there is a clear correlation between low soil temperatures and high apparent resistivity. Due to different depths there is a clear time shift detectable between the areas of lowest soil temperatures as well as the areas of highest apparent resistivity. The strong variations of the apparent resistivity during winter (frozen conditions) are still a field of research.

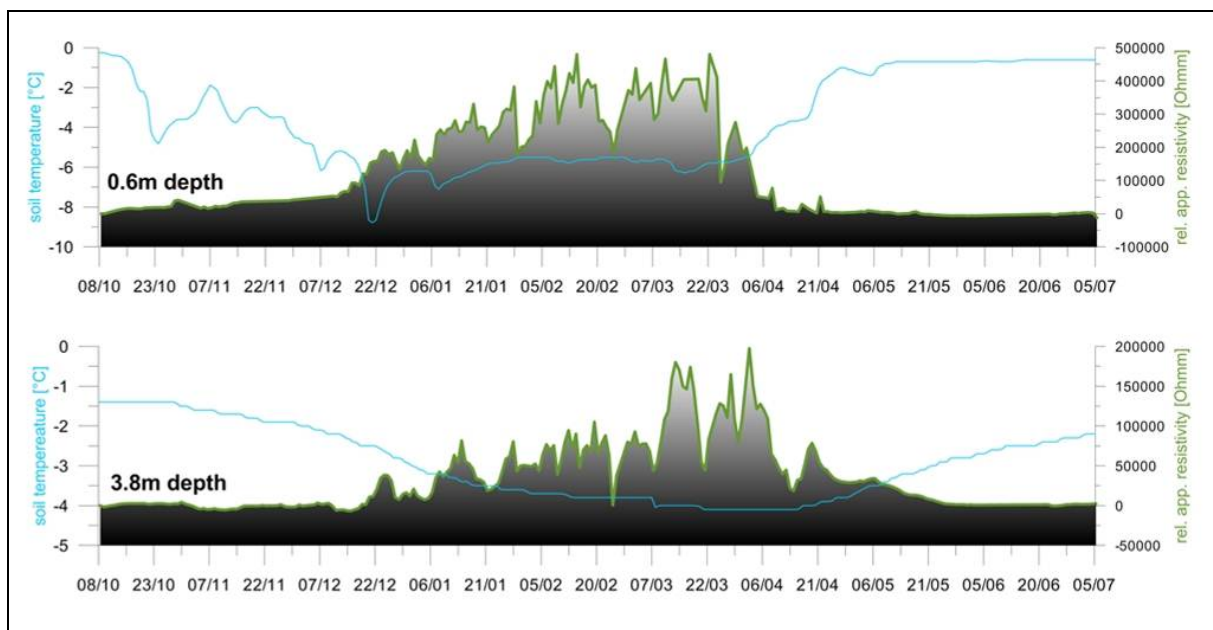


Figure 4.12-9. Correlation between apparent resistivity and soil temperature at different depths (temperature data provided by the Central Institute of Meteorology and Geodynamics, Vienna).

The monitoring system operated more or less without any significant interruption during the whole monitoring period. It is very reliable even in high alpine regions at temperatures below -20°C. Although we collected a high-quality geoelectric dataset, a detailed and verified interpretation was impossible due to the lack of additional measurements at the site. For future monitoring activities in permafrost regions we must consider the requirement for additional measurements. They should include at least one measuring point of soil temperature at two different depths at the monitoring profile. Nevertheless the main focus of this monitoring site,

to collect a geoelectric dataset in a high alpine (permafrost) region, with remarkable high resistivity of the subsurface for a full seasonal period, was successfully accomplished.

References:

- Supper, R., Römer, A., 2003. New Achievements in Developing a High Speed Geoelectrical Monitoring System for Landslide Monitoring. Proceedings of the Environmental and Engineering Geophysical Society, 9th Meeting Prag, Prag.
- Supper, R., Römer, A., Jochum, B., 2009. Geoelectrical measurements for natural hazard monitoring. SEGJ 9th International Symposium, Extended Abstracts, Sapporo.
- Supper, R., Baroň, I., Jochum, B., Ita, A., Winkler, E., Motschka, K., Moser, G., 2010. From structural investigation towards multi-parameter early warning systems: geophysical contributions to hazard mitigation at the landslide of Gschliefgraben (Gmunden, Upper Austria), Terra Abstracts, European Geosciences Union 2010.

4.13 SUPER-SAUZE (FRANCE)

Jean-Philippe Malet, Julien Travelletti and Patrice Ulrich
Centre National de la Recherche Scientifique, France

Julien Gance
Centre National de la Recherche Scientifique, France
Bureau de Recherches Géologiques et Minières, France

André Stumpf
Centre National de la Recherche Scientifique, France
International Institute for Geo-information Sciences and Earth Observation, Netherlands

Robert Supper, David Ottowitz, Birgit Jochum, Ivo Baroň
Geological Survey of Austria

ABSTRACT

The Super-Sauze landslide has developed in the black marl facies of the Barcelonnette Basin, in the southeast French Alps. The landslide, that has been active for decades, is in an intermediate stage of evolution and its volume is estimated at $0.7-10^6 \text{ m}^3$. The hazard caused by the mudslides is mainly related to the possibility of triggering of highly mobile debris/mudflow as was observed in 1999, 2000, 2006 and 2008. The landslide has been actively monitored since 1995 as it is considered a field laboratory for the understanding of flow-like landslides developed in clay-shales by the national OMIV Observatory (French Observatory on Landslides; <http://eost.u-strasbg.fr/omiv>). The landslide is investigated by the School and Observatory of Earth Sciences (CNRS & University of Strasbourg) and several monitoring techniques (continuous, campaigns) are used to characterize its dynamics and mechanisms in relation to climatic and hydrologic conditions. The Super-Sauze landslide has been the subject of many research studies and several PhD or post-doc projects. The monitoring system has been updated within the SafeLand project, also in combination with French (Project ANR-SISCA, Project ANR-TriggerLand) and Austrian research initiatives (FWF-contract TRP 175-N21), and the results of this instrumentation are presented.

Presented parameters: displacement, self-potential, resistivity, evolution of surface fissures in time.

4.13.1 GENERAL DESCRIPTION OF THE TEST SITE

The Super-Sauze mudslide is located on the north-facing slope of the Barcelonnette Basin (Southern French Alps). The landslide has developed in a torrential basin located in the upper part of Sauze torrent, on the left side of the Ubaye valley (

Figure 4.13-1).

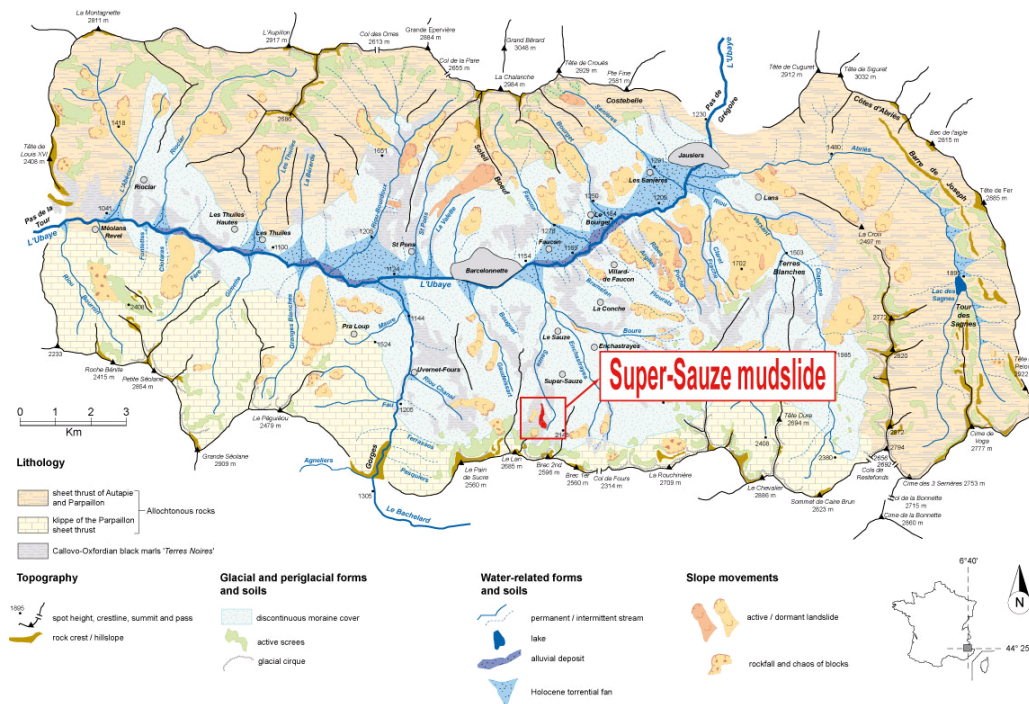


Figure 4.13-1. Location of the Barcelonnette Basin and the Super-Sauze landslide in the South French Alps.

Geological and geomorphic settings

The Southeastern part of the French Alps consists of sedimentary rocks composed of alternating marl and limestone sequences of Jurassic age. At Super-Sauze, the marls consist of stratified rocks, with fine bedding inherited from their original deposition by turbidity currents. The relatively low carbonate content (essentially calcite) varies from 20 to 35 % of the total volume. The detrital phase comprises mainly silt (predominantly quartz and feldspars) with a small proportion of clay materials (mainly illites and chlorites).

The landslide has developed in the upper part of the Sauze torrent characterized by a gully-type morphology (

Figure 4.13-2). The area features a conjugate normal fault system (N153°) affecting the autochthonous marls and the overlying limestone sheet thrusts, and a reversed fold (N215°) inclined at 35°. This results in opposite dip directions of the marls in this area. Quaternary deposits (moraine and rock glacier) are also partly overlying the marls in some parts of the catchment.

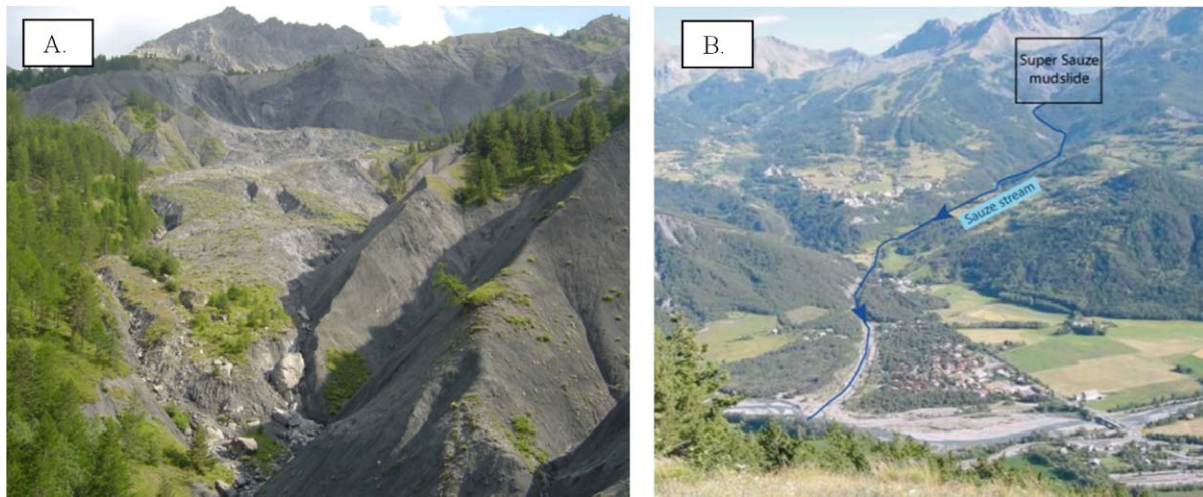


Figure 4.13-2. The Super-Sauze landslide from the bottom (2006) (A), and the risk catchment of the Sauze torrent (B).

Characterization of the site

The landslide is representative of the large gravitational phenomena developed in the clay-shales of southeast France (also such as, for instance, the La Valette landslide, the Poche landslide, the Villard-les-Dourbes landslide and the Boulc-Mondorès landslide).

In terms of geomorphology, the landslide is characterized by an ablation zone, a transit zone and a terminal zone that takes the form of a lobe (

Figure 4.13-2). The landslide is bordered by two lateral streams. In 2011, the landslide extended over a horizontal distance of 870 m and occurred between elevations of 2105 m at the crown and 1760 m at the toe with an average 25° slope gradient. The total volume is estimated at 750,000 m³ (Malet and Maquaire, 2003).

The dynamics are controlled by bedrock geometry, rock mass fabric, and hydrology. Morphological features induced by the sliding and flowing mode of the mudslide are easily recognizable. The contact between the landslide and the stable hillslopes comprises a shearing zone of a few meters' width characterized by tension cracks and shear surfaces marked by scratches in the direction of the movement (

Figure 4.13-3). Locally, compression levees are also clearly distinguishable (

Figure 4.13-3). A detailed morphological description of the mudslide can be found in Weber and Herrmann (2000).

On average, the surface displacement rates lie in the range of 0.002 to 0.03 m.day⁻¹ for the period of 1996-2011. But landslide crises with velocities up to 0.4 m.day⁻¹ may be observed each year in the spring season. Displacements along the landslide correspond mainly to the line of greatest slope.

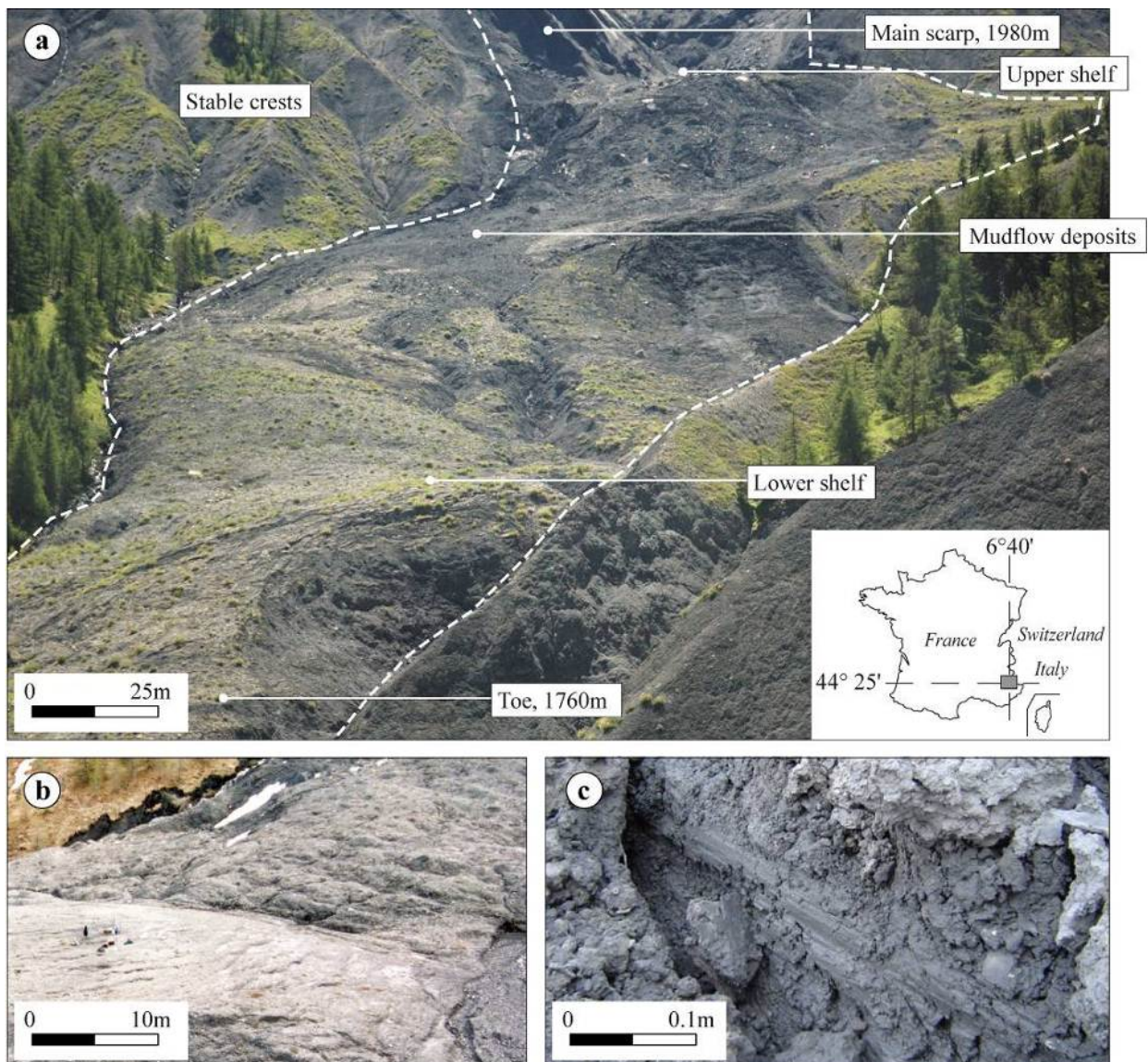


Figure 4.13-3. Geomorphologic features. a) Photograph of the landslide on 28th July 2008; b) Compression levees in the lower part; c) Striations indicating movement along shear surfaces along a stable crest in the central part.

Description of the history of the mass movement

In the beginning of the 1970s, plane and wedge failures occurred respectively on the eastern and western sides of the upstream part of the torrent, resulting in an accumulation of large marly rock panels and the formation of a main scarp (Figure 4.13-4). The panels have been progressively weathered and a matrix supported soil fabric has developed, integrating marly fragments of different sizes, and progressively filling up the gullies.

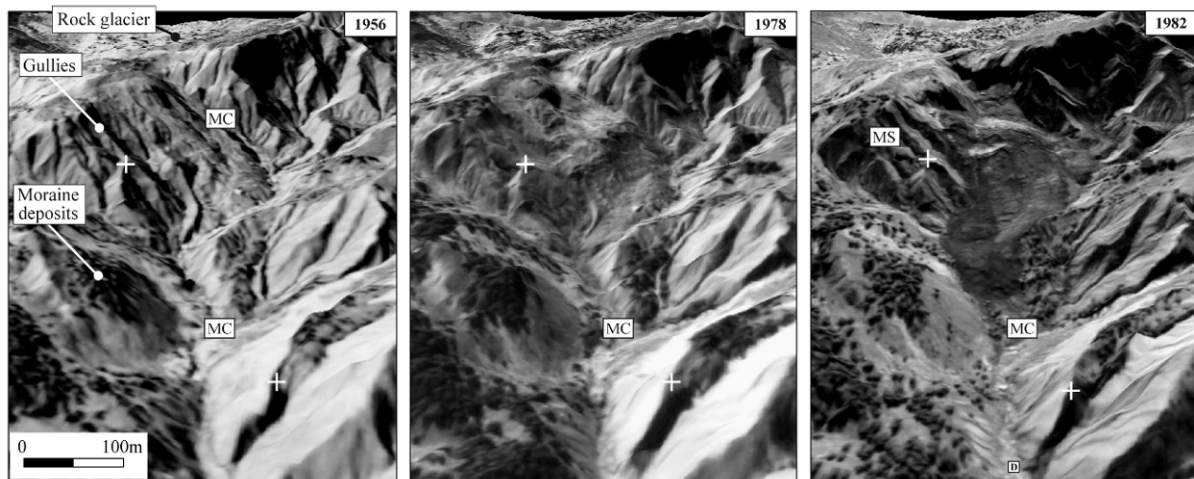


Figure 4.13-4. Morphological setting and evolution of the Super-Sauze mudslide, from 1956 (before failure) to 1982. The temporary storage of material at the toe of the main scarp and its weathering is clearly recognizable, before the downstream progression of the material in the main channel. (MC: main channel; MS: main scarp).

Beginning in the late 1970s, a rising level of soil accumulation in the gullies is observed (Figure 4.13-4). Since 1982, the material has progressed downstream by more than 200 m, with some changes in the rate of displacement according to the presence of obstacles. The bedrock geometry corresponds in the upper part to a succession of more or less parallel crests and gullies and, in the medium and lower parts, to a narrow incised channel. Consequently, the thickness of the mudslide is highly variable and varies between 0 and approximately 20 m.

4.13.2 DESIGN OF THE MONITORING NETWORK

Multi-sensor observations started in 1991 at Super-Sauze through campaigns, and a permanent monitoring system started to be built in 1995 (Malet, 2003) for the meteorological, hydrological and kinematic parameters. The permanent monitoring has been completed with a detailed geophysical and geotechnical investigation (dynamic penetration tests, percussion drillings, pressuremeter tests, inclinometer survey) combined with stereo-photogrammetric analyses in order to determine the structure of the accumulated mass. The strategy to define the internal structure of the landslide has consisted in cross-correlating this multisource information along five cross sections and then building a 3D geological model with a geological modeller (Travelletti & Malet, 2012).

Figure 4.13-5 indicates the current status of the permanent multi-sensor monitoring available on site (map, Figure 4.13-5A; cross-section, Figure 4.13-5B) and the location of the different geophysical and geotechnical profiles (Figure 4.13-5C).

A water balance station to monitor pressure heads, combined with several soil moisture sensors (of different technologies, e.g. TDR, FDR) installed in depth was installed in 1997. Twenty open standpipe piezometers with manual recordings and four piezometers with automatic recordings are installed on site on five cross-sections to define the geometry of the water reservoir and monitor the water levels. Cross-correlation of all information in a distributed database has allowed the construction of a hydrological and mechanical concept of the landslide (Malet et al., 2005). The displacements of the landslide have been observed since 1991 by combining a topometrical and GPS survey of a network of 40 benchmarks,

extensometer observations at one location (since 1999), aerial-photograph analysis, and, since 2007 by terrestrial laser scan acquisitions (Travelletti et al., 2012). Five cameras are also installed to monitor the displacements at a daily temporal resolution; the instrumentation consists in low-cost D70 Nikon reflex digital cameras installed on concrete pillars or on stable rods (Figure 4.13-7B). The acquisition system is controlled by a datalogger and the power is provided by a 40 W solar panel. A series of images is acquired daily at 11:00, 12:00, 13:00 and 14:00 GMT.

Since July 2011, three permanent GPS stations (Trimble NetRS) have also been installed on-site to provide continuous observation of movements to increase the temporal resolution of information and to implement an early warning system.

Since May 2011, permanent SP and resistivity monitoring is performed with the GEOMON^{4D} device from the Geological Survey of Austria, as part of an Austrian-funded project (FWF-Contract TRP 175-N21; Gance et al., 2012). The geoelectrical monitoring profile comprises 93 electrodes, laid out with irregular spacing to adapt the resolution to the expected processes. The general electrode spacing was 2 m, whereas in two areas it was decreased to 1 m and 0.5 m respectively. The relative position to other sensors is shown in

Figure 4.13-6. Twice a day a full resistivity section was measured, and SP measurements were performed hourly. For power supply, a solar-fuel cell combination is used, which performed well without interruption. Unfortunately due to a bios reset of the computer, no data is available between July 26th and October 27th. Additionally, problems were encountered from using a standard French GPRS net with which data transfer was not possible. Therefore, after a period of unsuccessful trials, the system was connected to the WLAN net connecting the other monitoring sensors.

The management of data acquisition and the maintenance of the systems are carried out by the French Observatory on Landslides (OMIV; <http://eost.u-strasbg.fr/omiv>).

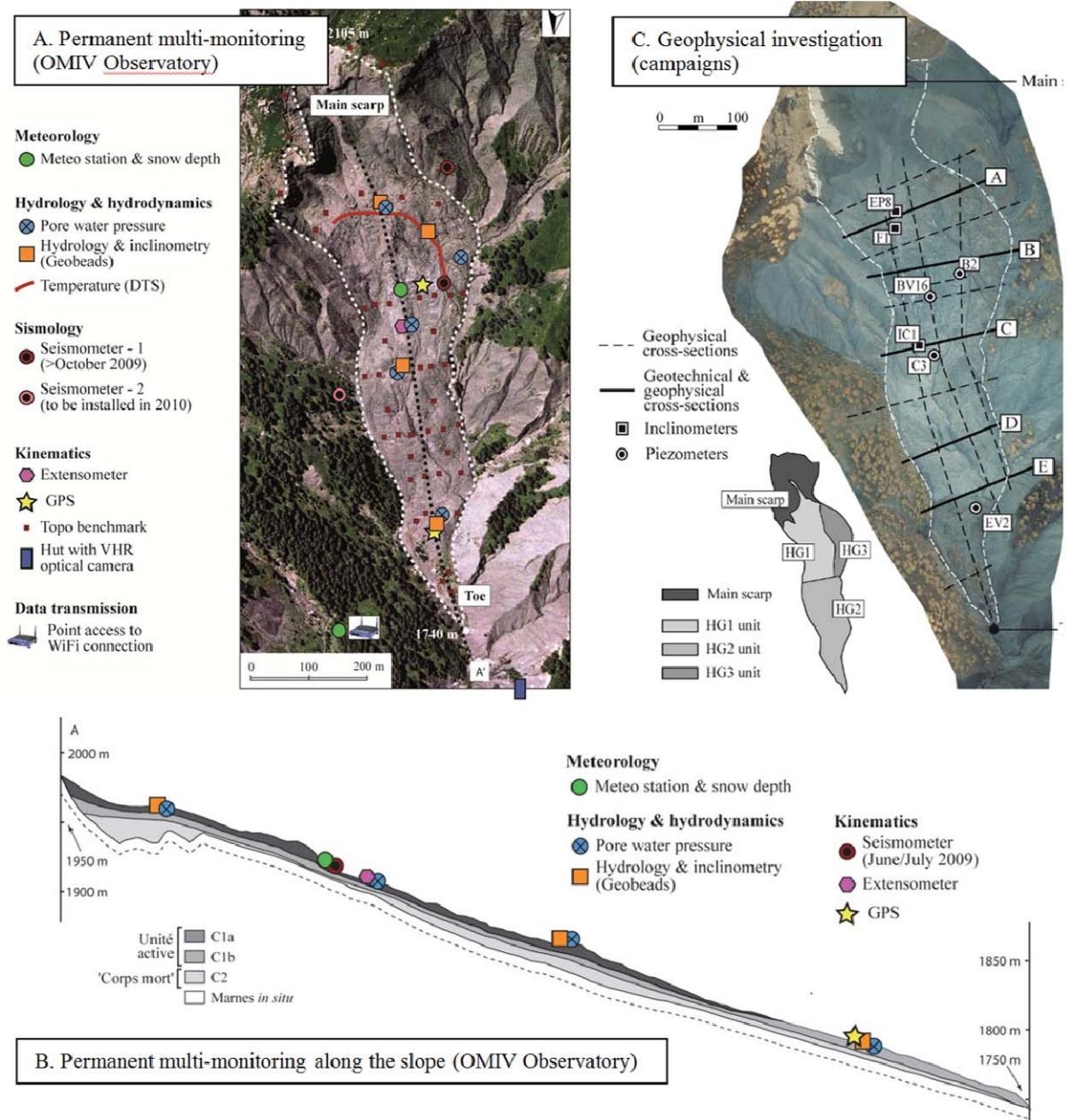


Figure 4.13-5. Location of the geotechnical, geophysical and hydrological investigations on the mudslide, and hydro-geomorphological units (HG) identified from the observations.



Figure 4.13-6. Layout of the geoelectrical monitoring profile: red=current electrodes, blue=potential electrodes, yellow=other sensors (north orientation is towards the top; Source: Google Earth).

4.13.3 ANALYSIS OF MONITORING DATA

4.13.3.1 Displacement from terrestrial image correlation, laser point clouds and GPS

Cross-correlation techniques applied both to very-high resolution optical images and to airborne and terrestrial LiDAR point clouds have been used to obtain an image of the landslide's displacement pattern since 2009. Using matching techniques, two-dimensional displacement fields can be derived by tracking objects in two images acquired at different times. The technique is based on the automatic identification of identical texture patterns within an image by maximizing a correlation function. A sub-pixel hierarchical correlation technique is used. The original images are first converted to gray-scale images, on which a 3x3-pixel Sobel convolution matrix is applied to highlight the ground surface texture. The gradient values are then correlated. Four successive degradations of the image resolution are applied following a pyramidal approach for changing the physical size of the correlation window and of the explored area by down-sampling the gradient values of the full resolution image (Figure 4.13-7A).

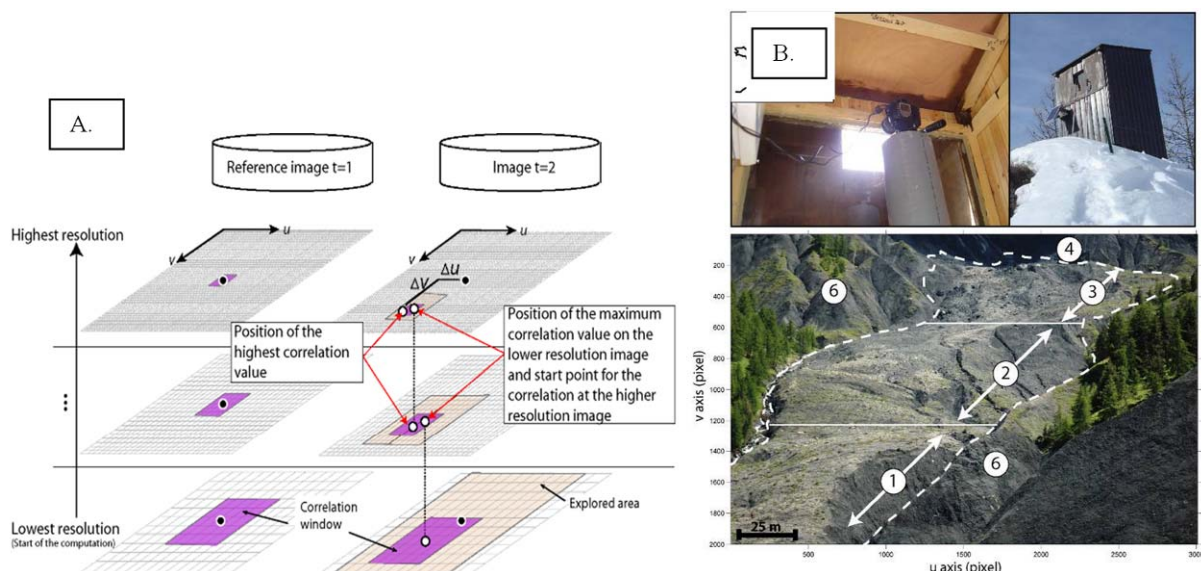


Figure 4.13-7. Principle of the normalized hierarchical image correlation technique (A), and its application to a series of images acquired in front of the Super-Sauze landslide from a stable crest (B).

The correlation results consist in matrices of displacement Δu and Δv along the u - and v -axes in the image plane with their associated correlation index (Figure 4.13-7A). In case of orthorectified airborne images, the pixel size is constant. Only the effective pixel size at the ground must be calculated to estimate metric displacements. In the case of terrestrial images, the image's pixel size is not constant due to the oblique acquisition; the displacements field correlated in the image plane cannot be directly interpreted in terms of metric displacements, and an orthorectification procedure is compulsory for a quantitative analysis.

A set of images acquired at the Super-Sauze landslide (Figure 4.13-7B) over the period of May-July 2009 is used to illustrate the potential of the technique for the characterization of the kinematics during an acceleration period (Travelletti et al., 2012). Figure 4.13-8A shows an example of displacement rates (in pixel.day^{-1}) of the ground surface in the image plane derived from image pairs from May 20–28 2009, June 1–4 2009 and June 9–13 June 2009.

The reference is the image from May 20th, 2009. The contrast in displacement rates between the landslide area and the stable area gives confidence on the calculated velocity field. One can notice that the pattern of displacement rate is heterogeneous spatially and temporally. The upper part of the landslide displays the highest velocity ranging from 1 to 7 pixels.day⁻¹ while the lower part displays velocity of less than 4 pixels.day⁻¹. From May 20th to June 13th, cumulated displacements of up to 110 pixels are observed in the upper part. The maximum displacement rate is observed around the 1st of June. Then, the landslide decelerates to a displacement rate of about 1 pixel.day⁻¹. Figure 4.13 8B shows the same displacement rates (in m.day⁻¹) of the ground surface in the local coordinate system after projection using photogrammetric techniques. This procedure allows a quantitative comparison to other sensor measurements.

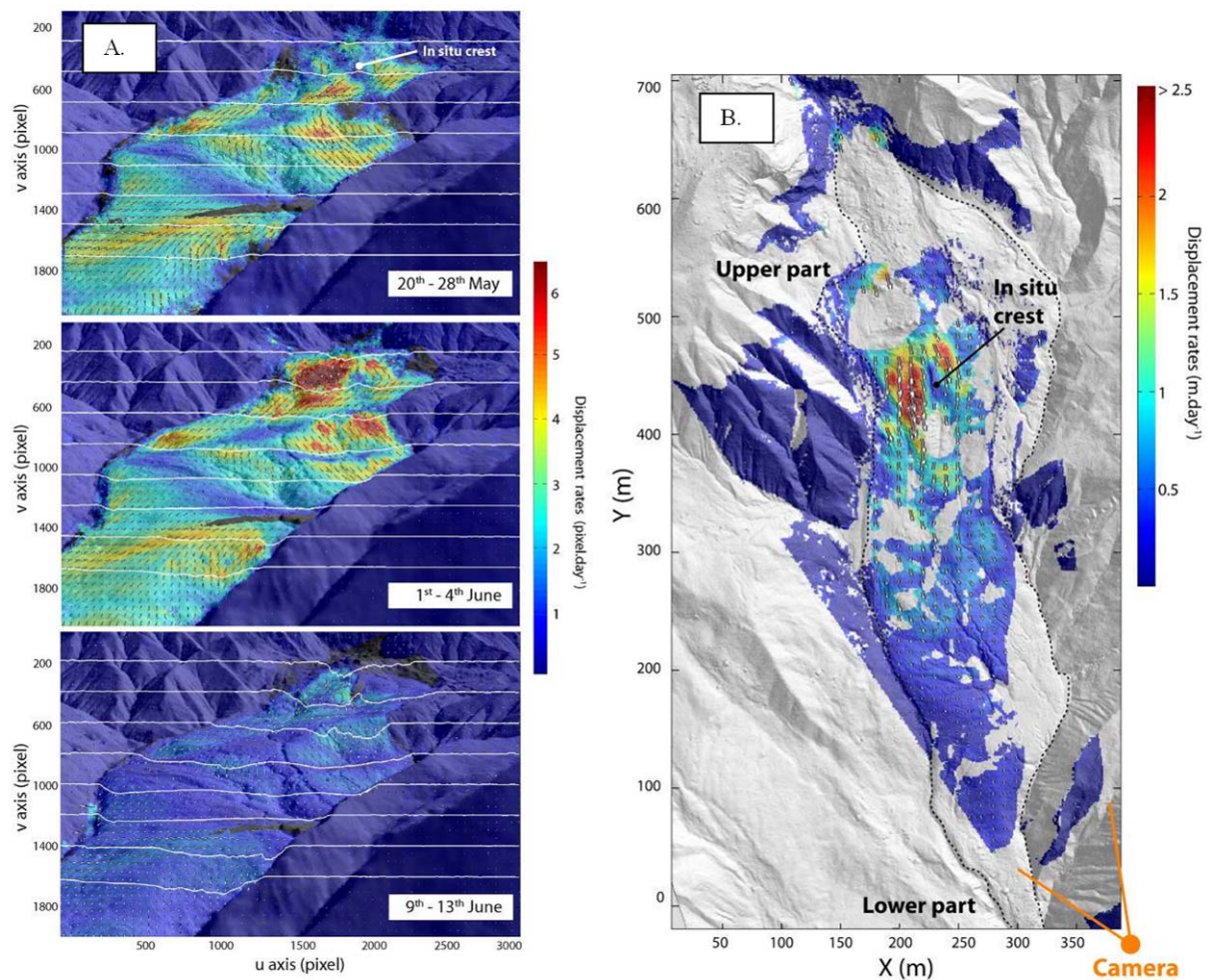


Figure 4.13-8. Displacement rates observed at Super-Sauze in 2009 from terrestrial photographs. Amplitude (color) and direction (arrows) in the image plane and cumulated displacements along eight profiles crossing the landslide over the period 20 May-25 June 2008 (in order to highlight the displacement direction, the arrow length is normalized for each image; A). Displacement rates map for the period 1-4 June 2008 in the local geographic coordinate system (B).

Image correlation techniques have been applied on repeated TLS (Terrestrial Laser Scans) acquisitions acquired at the site at five reference periods in the year (May, June, July, September, October) in order to characterize the 3D displacement field. The hypothesis is that for objects scanned from a unique view point, simple 2D correlation functions can be applied

on multi-temporal point clouds and yield the same range of accuracy as complex and time-consuming 3D surface matching algorithms. The performance of the cross-correlation algorithm is tested on datasets acquired at the toe of the Super-Sauze landslide. A long-range terrestrial laser scanner Optech ILRIS-3D was used for the monitoring (Travelletti et al., submitted). Ten acquisitions were acquired between October 2007 and May 2010 for the same base station at an average distance of 100 m from the landslide toe (Figure 4.13-9). At this distance, the laser diameter on the ground surface is estimated at between 3 to 5 cm. Only the last return pulse is registered to maximize the number of points reflected on the ground surface. The average point density at the ground surface varies from 153.0 pts.m⁻² to 234.9 pts.m⁻² with a standard deviation up to 351.7 pts.m⁻² and a maximal density of 1148.3 pts.m⁻². The distance between the point clouds to the position of the laser scanner is then determined and linearly interpolated in a regular grid.

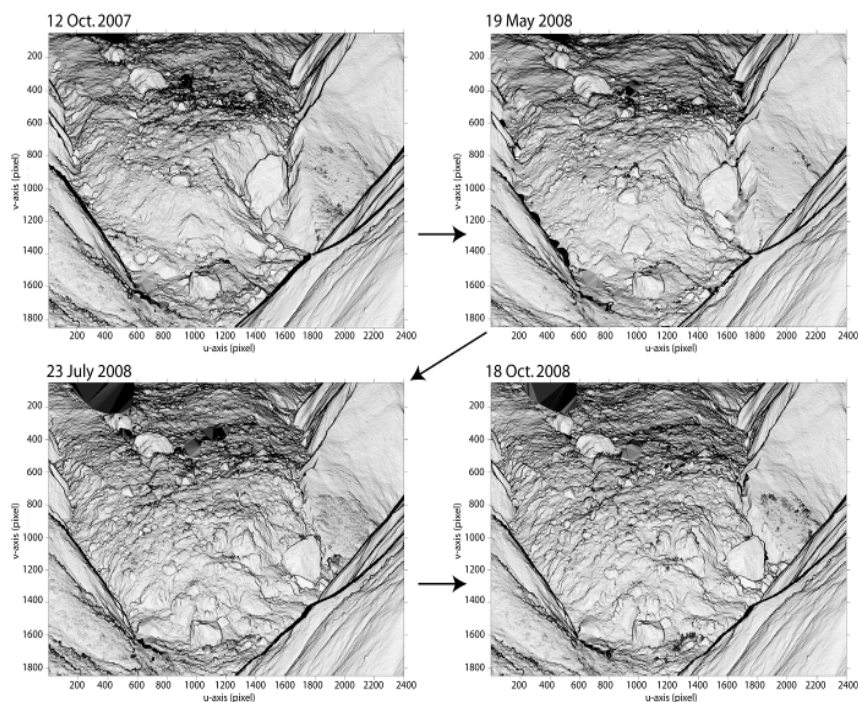


Figure 4.13-9. Images derived from the gradient calculation on the TLS point clouds for the period October 2007-October 2008 at Super-Sauze. The morphology of the landslide toe is very well represented and the progression of the landslide toe is highlighted (A); Comparison and validation of the displacements obtained by correlation with dGPS observations on a series of blocks (B).

Because the correlation function gives better results where the input data contains regions rapidly varying pixel information, the norm of the 2D gradient in u and v directions of the distance between the point clouds and the TLS station is calculated, to emphasize the morphology of the landslide. The generated images are then converted to grey-scale values (16 bits) and are used as inputs for the image correlation algorithm (Figure 4.13-9). The computed displacements are well reproduced for all periods of acquisition. Two acquisition periods (July-October 2008, July-October 2009) are presented to illustrate the performance of the approach and the behaviour of the landslide (Figure 4.13-10). For the period July-October 2008, displacements between 0.5 and 1.5 m are observed, corresponding to an average displacement rate of 0.6 to 1.7 cm.day⁻¹. The displacement field displays significant spatial heterogeneities. The largest displacements are detected in the front of the toe where the slope gradient increases. The detachment of a toe compartment is also highlighted in the front.

During the period July-October 2009, the landslide displays very different kinematics both in terms of magnitude and spatial distribution. Displacements are shorter and range from 0.1 m at the front to 0.6 m in the upper part, corresponding to an average displacement rate of 0.1 to 0.8 cm.day⁻¹. The computed displacements are validated by comparing the displacement values to dGPS observations of a series of blocks easily recognizable in the TLS point clouds. This comparison allows the evaluation of the accuracy of the approach by taking into account the noise in the data with the co-registering errors between two acquisitions. The displacements perfectly correlate ($r^2=0.99$), and a mean error and a standard deviation of 0.04 m and 0.03 m are determined (Figure 4.13-11). These results show that the error due to the co-registering is about 3 cm.

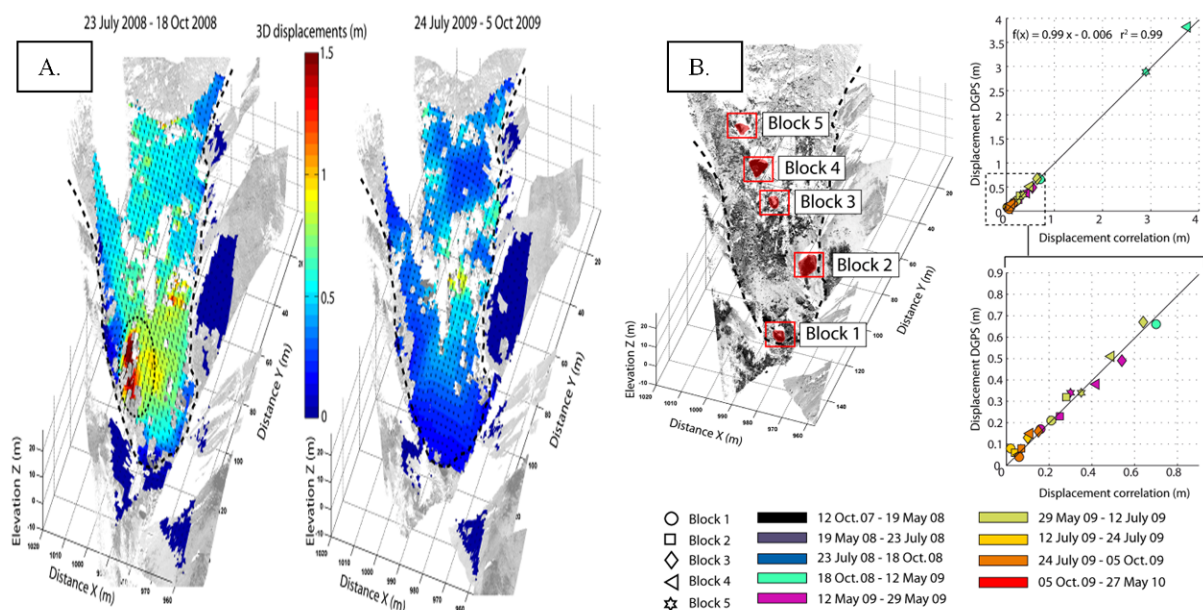


Figure 4.13-10. Displacement rates observed at Super-Sauze for the period 2007-2010 from repeated TLS acquisitions. 3D displacements field obtained by TLS measurements related to the acquisition periods of July-October of the years 2008 and 2009. The dashed circle indicates the detachment of compartment at the front of the toe (A); Comparison and validation of the displacements obtained by correlation with dGPS observations on a series of blocks (B).

The results of the monitoring through GPS (initiated with permanent GNSS receivers) in July 2011 also indicate a very variable kinematic regime, spatially from the top to the toe of the landslide where the displacement rates decrease, and temporarily in correlation with changing triggering conditions (rain event, snowmelt). The GPS data processing is detailed in Malet et al. (2011).

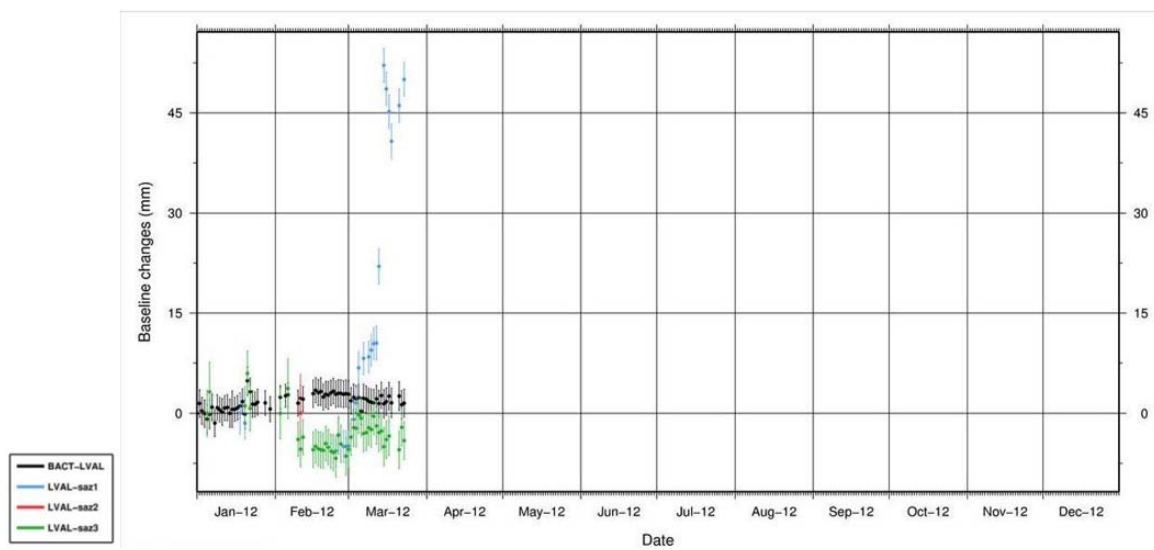


Figure 4.13-11. Displacement rates observed at Super-Sauze in early 2012 from permanent GPS observations. The displacement rates are expressed in terms of changes in baseline lengths to a stable reference GPS outside of the landslide (called BACT). Changes of a factor 10 are observed in the magnitude of displacement for the GPS SAZ2 & SAZ3 (at the bottom of the landslide) in comparison to the GPS SAZ1 (at the top of the landslide).

The very high-resolution cameras located in the upper and most active part of the landslide, near the GEOMON^{4D} monitoring system, are used to infer the displacements of local targets (e.g. styrene balls on top of the electrodes, GPS antenna for cross-validation). Stereo-photogrammetric techniques are used to co-register precisely the catalogues of images (using a Harris point-type procedure), automatically locate the targeted objects (using segmentation techniques) and finally, to track the displacement of the object in space and time (Figure 4.13-12). Comparisons of the displacement vectors obtained from the stereo-photogrammetric procedure to the reference displacement vectors observed by GPS indicates an accuracy of 5 cm at a target distance of 100 m.

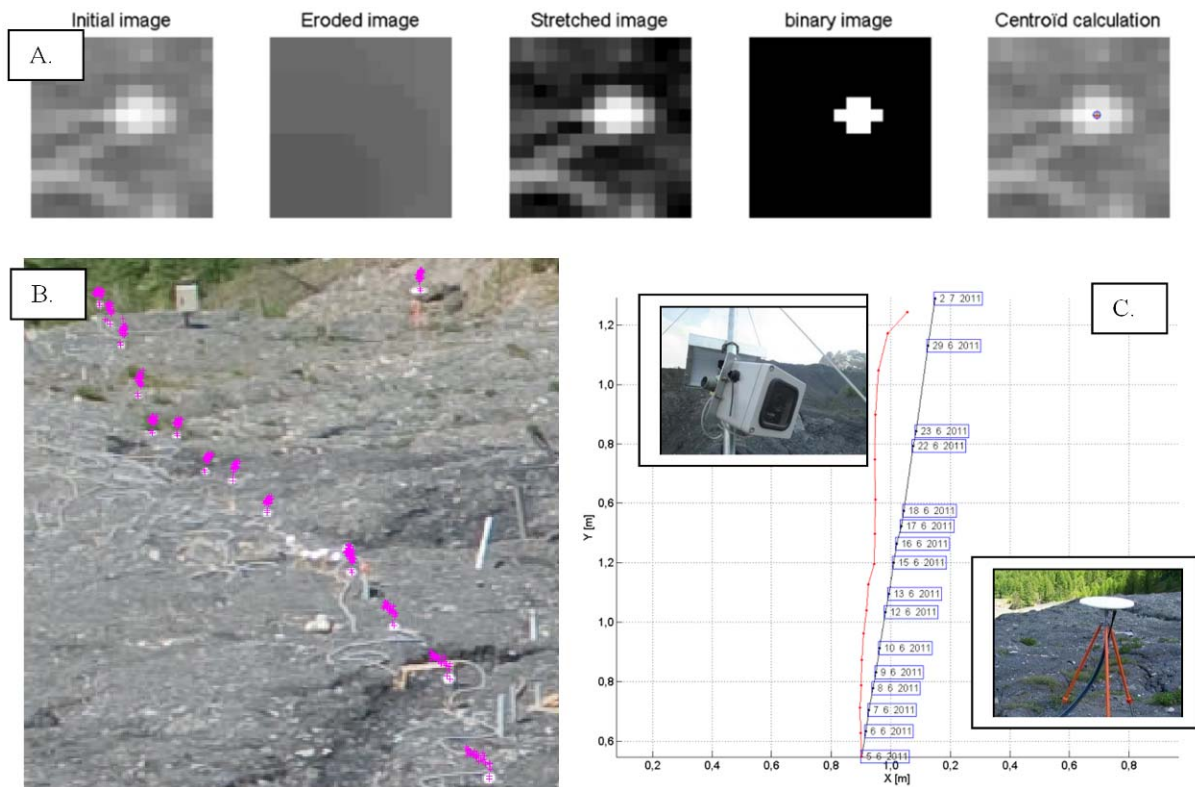


Figure 4.13-12. Time-lapse monitoring of target points (e.g. electrodes & GPS antenna) from terrestrial photographs. Automatic detection of the targets points using segmentation and mathematical morphology algorithms in grey-level images (A), Monitoring of the central position of the centroid of the target points (B), Evaluation of the quality of the stereophotogrammetric procedure by comparison with the coordinates of the GPS antenna (C).

4.13.3.2 Self-potential (SP) monitoring

The SP results especially during the first survey period (Figure 4.13-15) showed quite a large amount of noise with a diurnal period (Figure 4.13-18), which might be due to the crosstalk with some other sensors. However, the exact source is still undetermined.

It is interesting to note that during the whole month of June no SP anomalies were detected in correlation with rainfalls, whereas in July all major precipitation events were associated with distinct SP anomalies (Figure 4.13-13, Figure 4.13-14). The shapes of the SP anomalies are similar to the ones registered at the Gschlieffgraben site (sudden onset, continuous decrease). The delay time between the onset of precipitation and the SP signal is about four hours. One possible explanation for the absence of SP anomalies in June could be that during that period no subsurface water flow took place. However, resistivity values (Figure 4.13-19) show a direct response to rainfall (abrupt but small resistivity drop during rainfall, difference below 2 Ohmm) and a general smooth decay towards July.

During the second period beginning on October 27th, the situation looks different. Over summertime resistivity has generally increased arriving at the value shortly after the installation in May. Rainfall is again correlated with strong SP anomalies (Figure 4.13-17, Figure 4.13-16), but even after precipitation (duration November 2nd-6th) had stopped significant SP anomalies can be detected again and again (November 7th-12th) until the last large anomaly decays smoothly on November 12th. In the following period, the SP measurements show very smooth behaviour, and no anomalies can be detected until November 21st when a clear SP signal can again be observed. Anomalies usually show amplitudes between 0.2 and 0.4 V, similar to that recorded at other test sites.

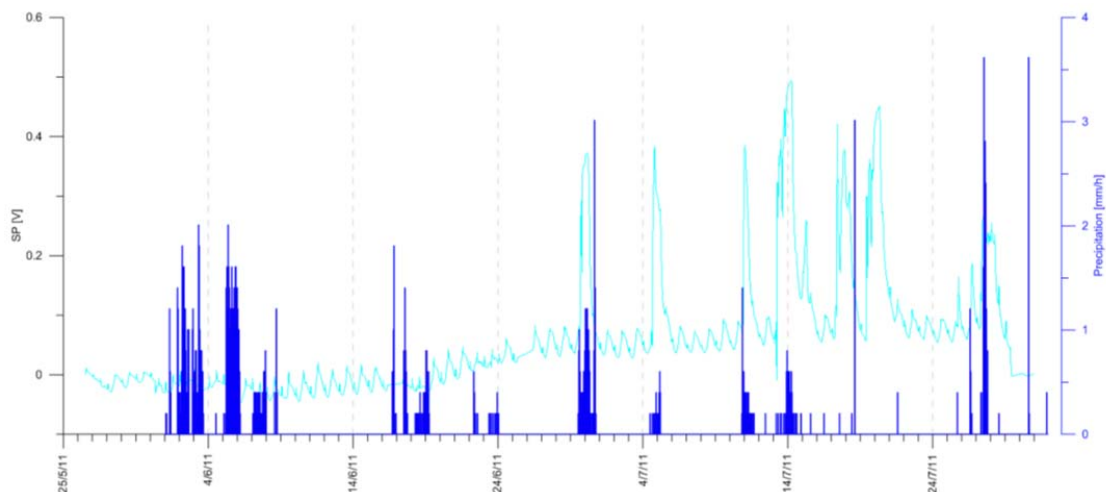


Figure 4.13-13. Result of SP monitoring within the first survey period, configuration with high noise signal.

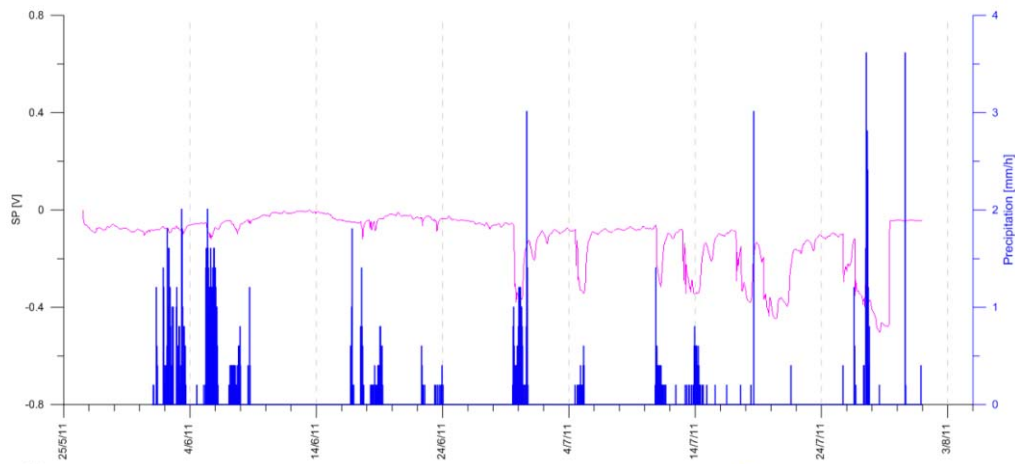


Figure 4.13-14. Result of SP monitoring within the first survey period

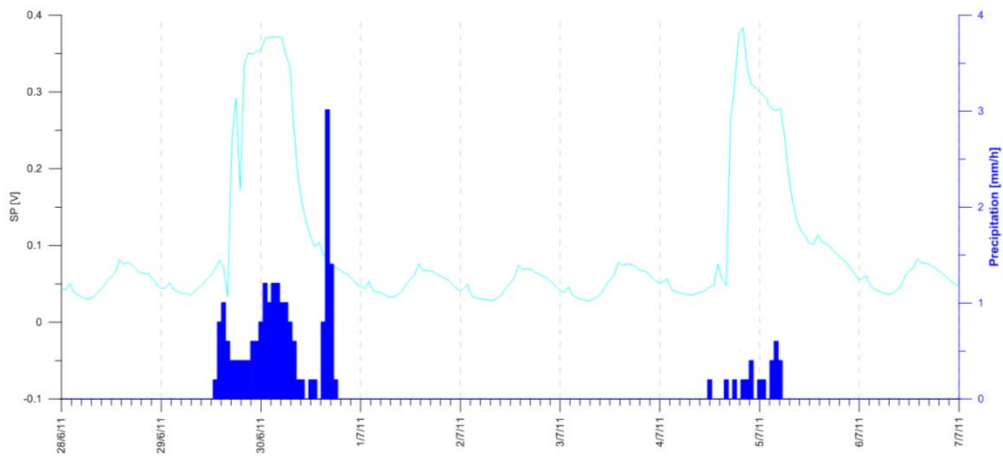


Figure 4.13-15. Result of SP monitoring within the first survey period: detail of two rain events.

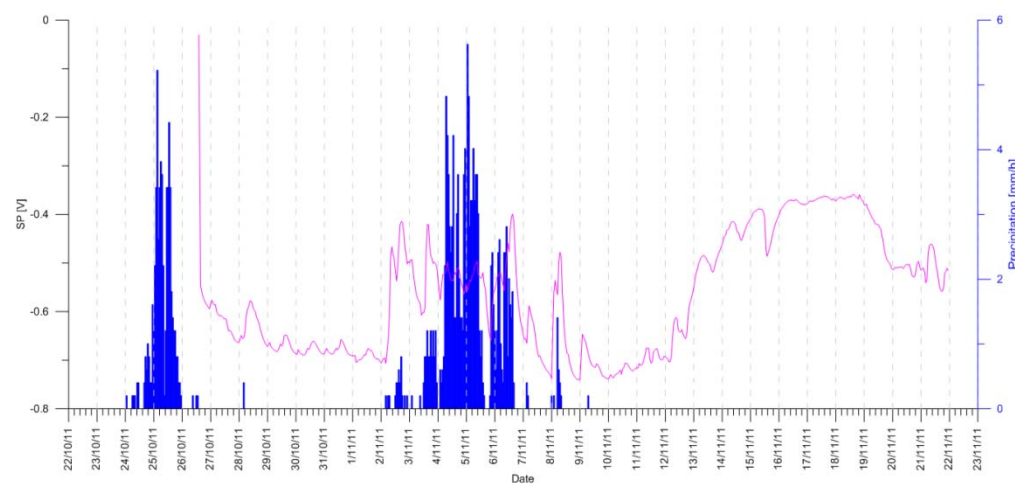


Figure 4.13-16. Result of SP monitoring within the second survey period.

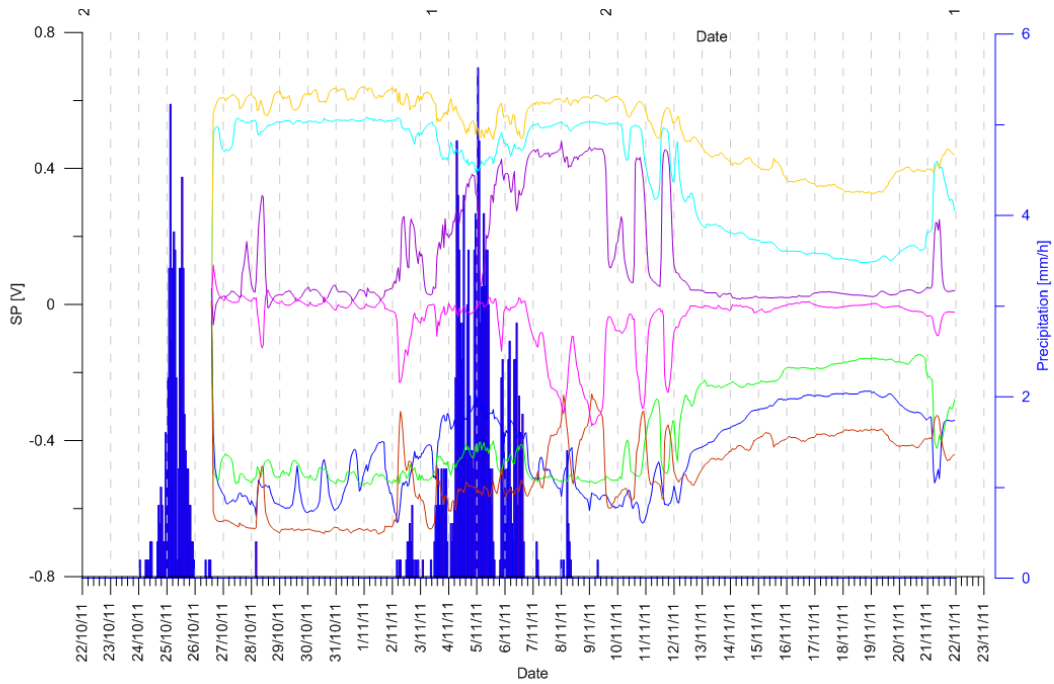


Figure 4.13-17. Result of SP monitoring within the second survey period.

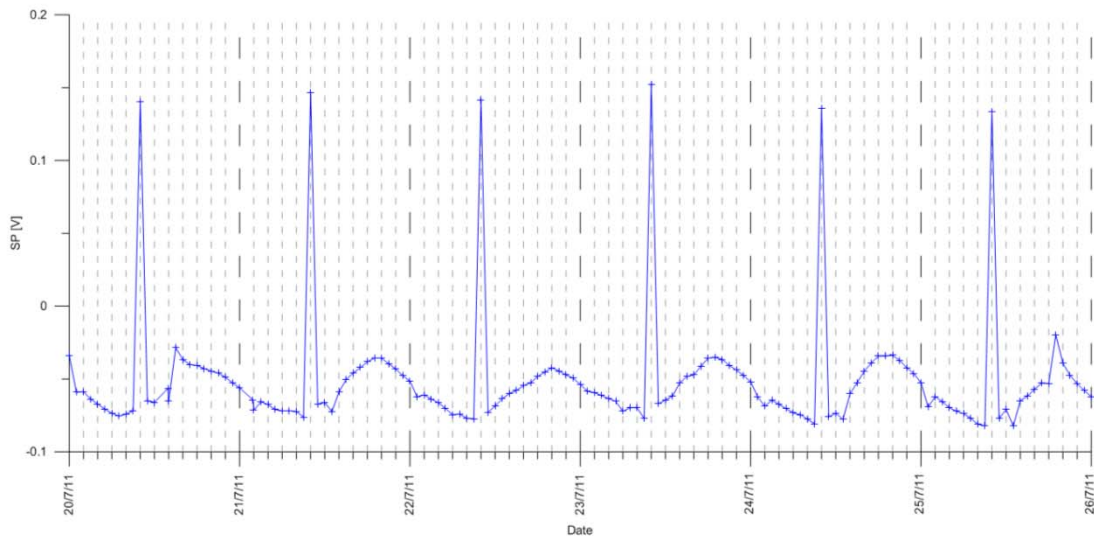


Figure 4.13-18. Detail graph of noise signal detected in some SP measurements with diurnal period.

4.13.3.3 Electrical resistivity monitoring

On the contrary, the results of resistivity monitoring show very constant values (with a small drop of less than 0.5 Ohmm during the rain period), until a continuous decay is initiated on November 12th. The minimum value is reached on November 18th; afterwards, resistivity rises again to the original level. This phase of decay exactly correlates with the period of smooth SP behavior. Figure 4.13-21 shows the results of the inversion of the resistivity data between November 2nd and November 22nd. In the beginning, absolutely no changes are visible. The first but very small detectable changes (almost 10 Ohmm, starting from an absolute value of approximately 40 Ohm.m) took place within a “dike-like” structure in the lower part of the section at depth on November 13th. On November 15th, also the resistivity of the surface layer started to decrease. On the 16th, resistivity started to drop significantly in both areas mentioned before, almost below 10 Ohm.m. Afterwards resistivity increases again until the 21st when the original values were nearly reached again. The interpretation of this data is quite difficult without the availability of additional data. One possible explanation is that during the phase of large SP anomalies, increased fluid flow took place which then triggered a movement around November 13th, initiating a compression of the subsurface layers. Consequently the pore space is reduced and water is pressed out, resulting in a decrease of resistivity in layers with a higher clay content (pore water, which has a higher resistivity than pure clay, is pressed out) and an increase of resistivity in rather sandy layers due to a reduction of porosity (original resistivity above 50 Ohm.m). This theory could fully explain the observed results, however it remains highly speculative without a correlation with other data (displacement, water conductivity).

A simple inflow of water from deeper areas could only explain the situation if it exhibits a very low electrical conductivity (high mineralization) below 10 Ohm.m.

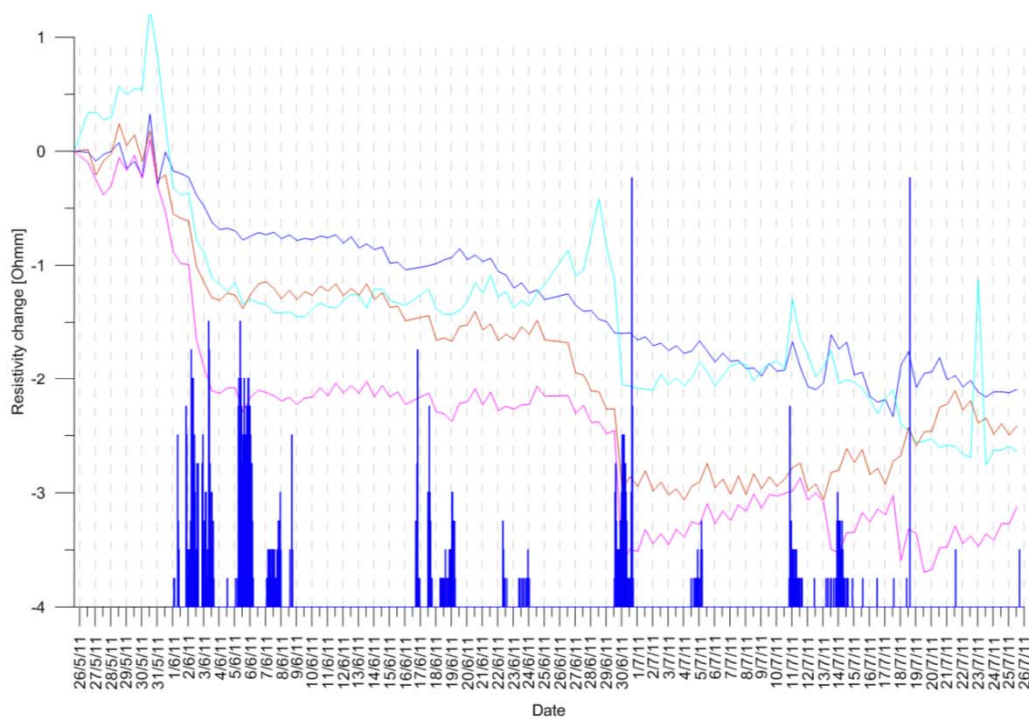


Figure 4.13-19. Results of resistivity monitoring within the first survey period.

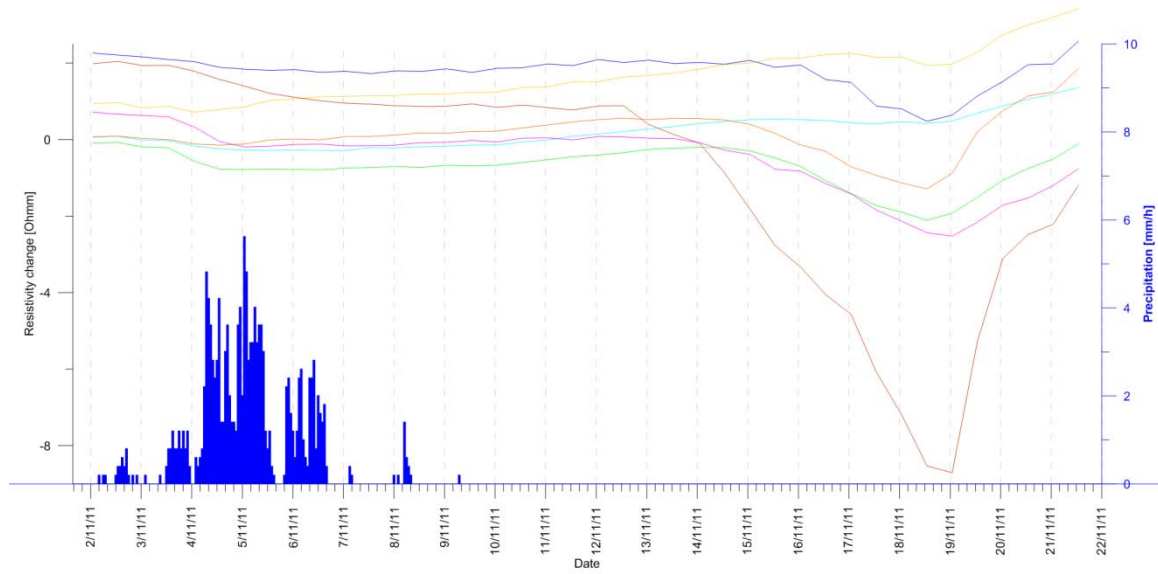


Figure 4.13-20. Results of resistivity monitoring within the first survey period.

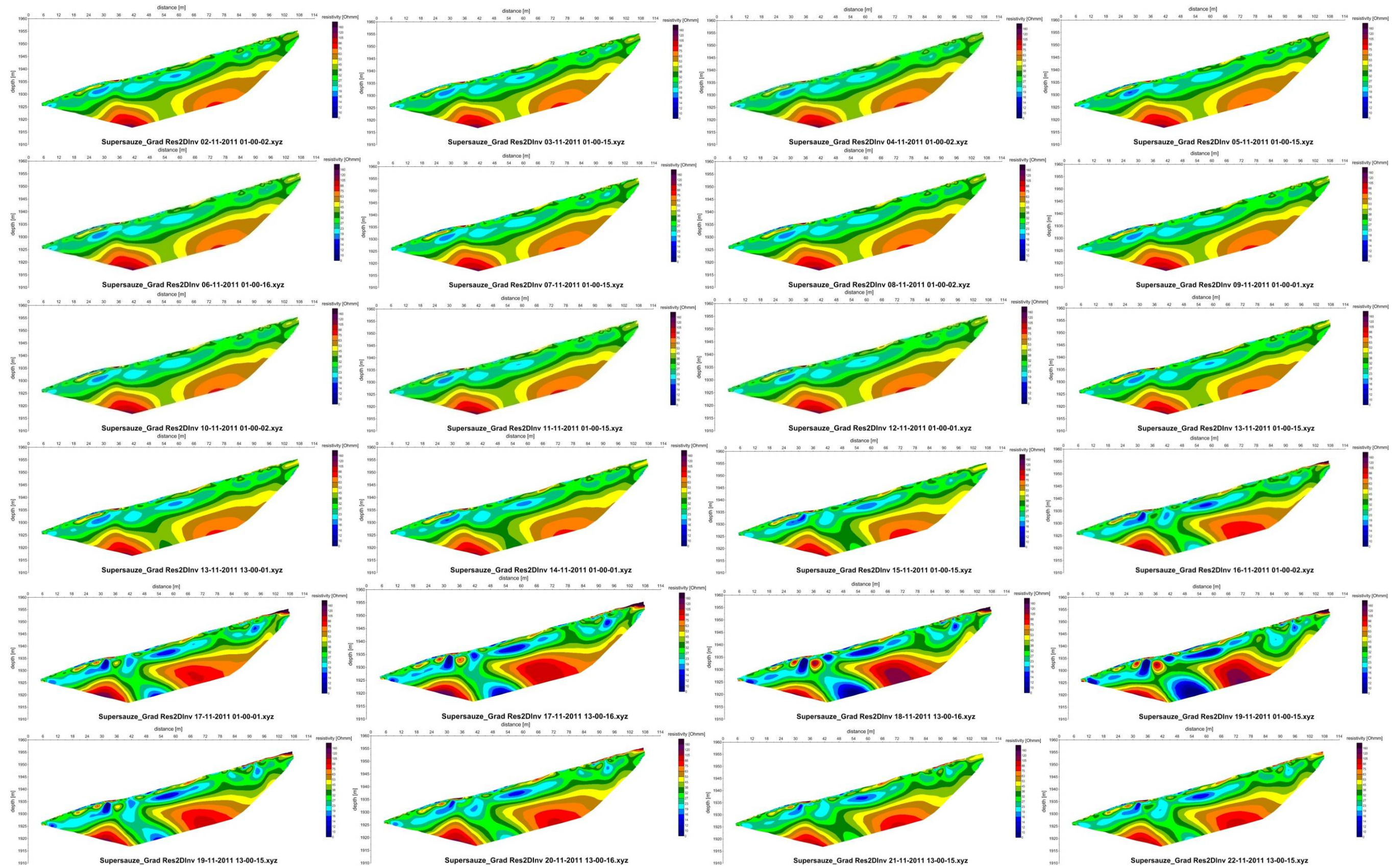


Figure 4.13-21. Inversion results of resistivity measurements for the period November 2nd to 22nd, 2011.

4.13.3.4 Evolution of surface fissures in time

Observations of features and structural patterns of earth surface landforms such as fissures can reveal information on the origin and mechanisms controlling a landslide. Therefore, considering the increasingly widespread availability of sub-decimetre resolution images from UAVs and other airborne platforms, we have targeted the development of a largely automatized image analysis technique to detect, map and characterize landslide surface fissures from VHR aerial images. The developed method is based on a combination of Gaussian directional filters, mathematical morphology and object-oriented image analysis (OOA) and was tested on a set of multi-temporal VHR images for the period of 2007-2009. It is hypothesized that the tracking of fissure patterns can be used as a proxy for possible rheologies of the material (Grandjean et al., 2011), and even as possible forerunners.

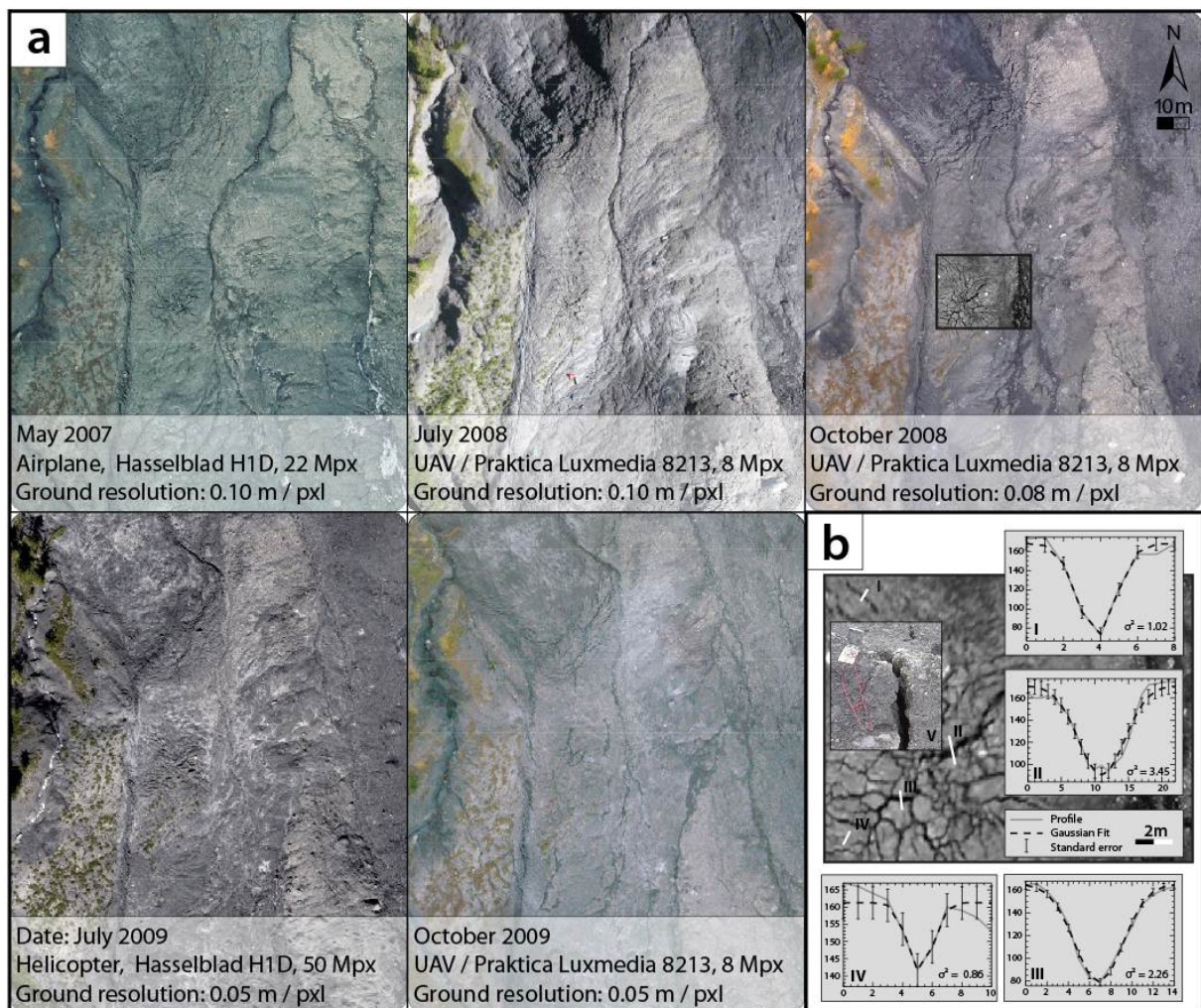


Figure 4.13-22. Examples of the processed data. (a) Subsets of orthophotographs acquired at five different dates with details of the acquisition systems and image ground resolutions. (b) Subset of the UAV image from October 2008 showing typical fissure patterns and (b-I-IV) grey-value profiles (green channel) approximated with Gaussian curves. (b-V).

The landslide clearly displays the signs of deformation in the form of ridges, bulges, lobes and fissures, but also markers of surface erosion such as rills and small gullies. Fissure widths of 0.01-0.40 m, lengths of more than 1.00 m and depths of up to 1.50 m can be observed in the field. In VHR airborne optical images, the fissures can be recognized as dark curvilinear structures (

Figure 4.13-22) as soon as their width approaches one pixel in size. Previous studies (Malet, 2003; Niethammer et al., 2011; Walter et al., 2011) already discussed relationships between the observed fissure patterns and strain resulting from a spatially heterogeneous displacement field and interactions between moving mass and the stable bedrock (Krzeminska et al., 2011). However, a full reconstruction of the complex bedrock geometry that may allow for a more detailed characterisation of the underlying deformation mechanisms has been completed only recently (Travelletti and Malet, 2011).

The image processing techniques comprise several stages: the first two stages of the developed workflow combine families of Gaussian-matched filters and morphological filters, and are followed by an object-oriented analysis to reduce the amount of false positive detection using contextual information and auxiliary topographic information. The detection results can be represented in raster maps or optionally, by center skeleton lines. Details on the procedure are given in Stumpf et al. (2011) and Stumpf et al. (submitted).

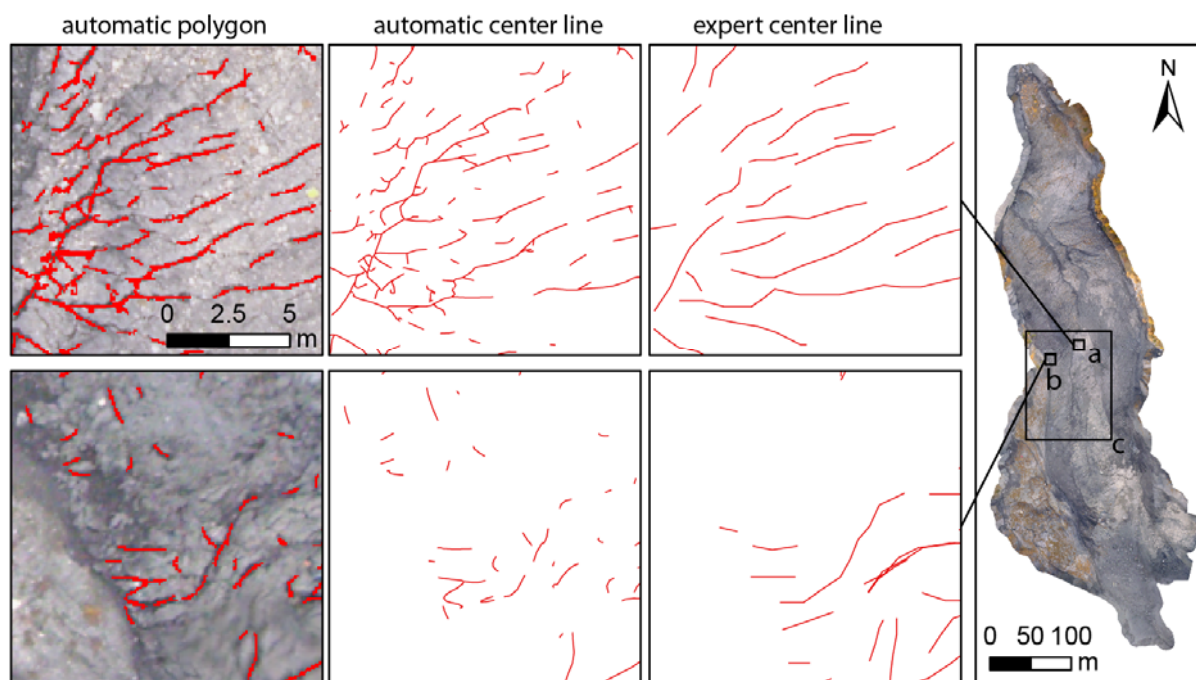


Figure 4.13-23. Example of comparison of the obtained fissure maps with the expert mapping for October 2010 (fissures in red). (a) Area with relatively high agreement of the mapped fissure patterns. (b) Area with relatively high rate of false negatives and false positives. The scale of the representations corresponds approximately to the scale used for the expert mapping (1:250). Central part of the landslide where the comparisons to expert mapping has been carried out (c).

Examples of results are presented in

Figure 4.13-23. The primary output of the developed processing routine is a map of the detected fissures represented by polygons.

Figure 4.13-23 displays an example of a comparison between an expert map and the result of the automatic detection. A first visual assessment of the obtained maps suggested better agreement of the fissure patterns in areas with high contrast and low texture (Figure 4.13-23a), whereas false positives and false negatives concentrated in sections with low contrast and increased surface texture (Figure 4.13-23b).

For a quantitative assessment of the mapping accuracy the obtained results were compared with the expert mappings at the central part of the landslide (Figure 4.13-23c) on all five dates. While several accuracy measures for geographic line datasets have been already proposed there is still no consensus about one generally applicable technique, and the metrics should be selected according to the problem at hand. Here we focused on three crucial aspects of the map accuracy that may have direct implications for their further use, namely the size of the affected (e.g. fissured) area, the length and density of the fissures, and their orientation.

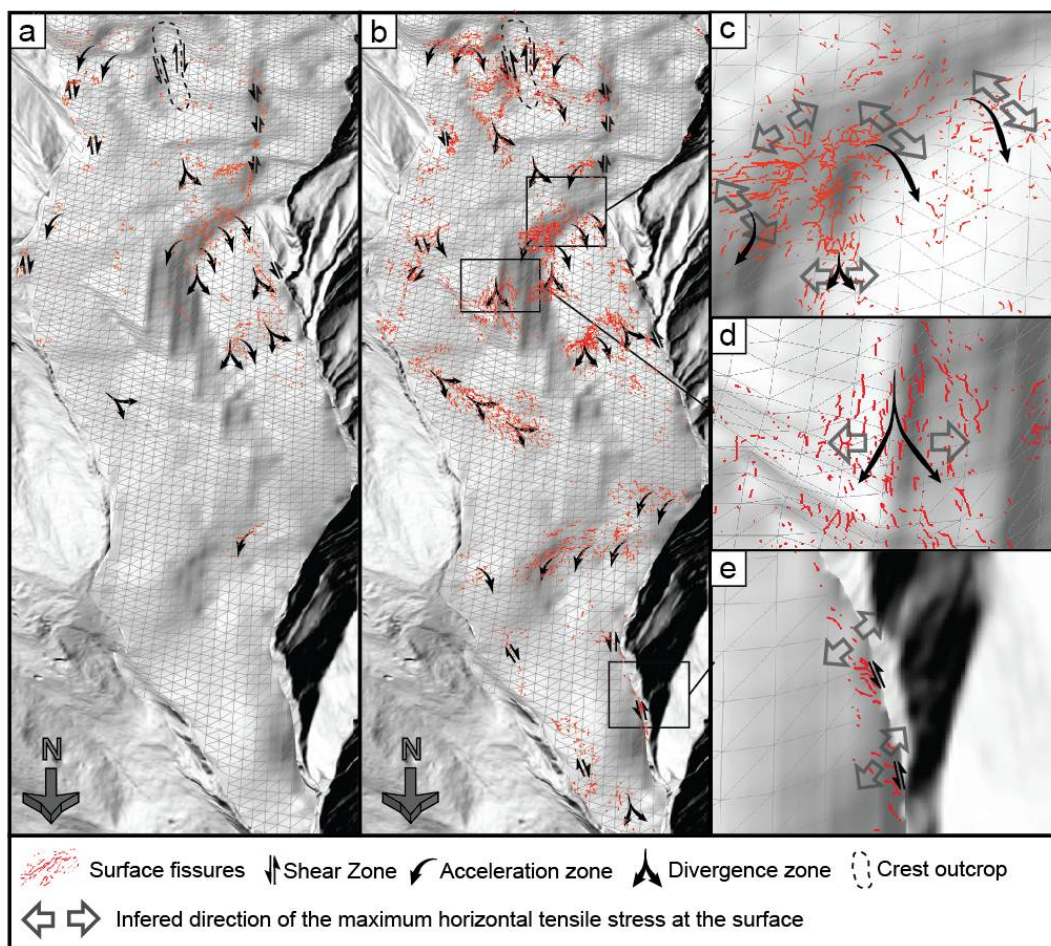


Figure 4.13-24. Pseudo 3D view showing the landslide dynamics inferred from the fissure patterns detected in the aerial images of (a) May 2007 and (b) October 2008. (c, d, e) Close up views for October 2008 showing

inferred landslide dynamics and stress vectors. The results are overlaid on a hillshade model of the topography of the stable bedrock proposed by Travelletti and Malet (2011).

Under conditions of homogenous illumination, a comparison of the results with expert mapping demonstrated detection rates of up to 65 % and orientation errors below 10°. In contrast, the technique is relatively sensitive to shading effects at full sunlight and prone to errors especially at a low sun incidence angle.

A joint interpretation of obtained fissure maps and of a 3D geometrical model of the stable bedrock demonstrated their complementary use for a better understanding of the geomorphological and geomechanical processes, such that the detected fissure pattern may be used for first approximation for mechanical processes in the recent deformation history of a slope. Comparing the detection results of May 2007 (

Figure 4.13-24a) and October 2008 (

Figure 4.13-24b), a significant increase in the abundance of fissures could be noted for the entire landslide. This can be attributed to a phase of strongly increased displacement rates (up to 3.5 m.day⁻¹) in early June 2008 (Travelletti, 2011). Although in October 2008, the displacement rates already consolidated again at average rates of between 0.01 and 0.03 m.day⁻¹, most of the fissures induced in June were preserved and evolved at the surface until October. Besides the general increase in the amount of fissures, it is intriguing to observe that at several local plots, similar fissure patterns can be observed at approximately the same positions through time, despite maximal displacements of up to 55 m between May 2007 and October 2009 (Niethammer et al., 2011). This indicates a recurrent continuous *in-situ* fissure formation where the fissures provide a close representation of the local strain field, similarly observed in the evolution of glacier crevasses.

Previous studies (Malet, 2003; Niethammer et al., 2011; Walter et al., 2011) already observed close relationships between the occurrence of fissures and the geometry of the stable bedrock at the Super-Sauze landslide. They also noted a general contrast between higher water content and rather ductile behaviour in the lower subsurface (< 1m) and typically lower water content of the topsoil, yielding more brittle behaviour at the surface. The surface fissures can therefore be understood as the response to stresses induced in the topsoil through coupling with ductile strain in the deeper subsurface. This model can be adopted as a basis to qualitatively estimate the patterns of flow and stresses from a joint interpretation (

Figure 4.13-23) of the detected fissure patterns and a geometrical model of the stable bedrock (Travelletti and Malet, 2011).

Considering the bedrock geometry and a formation of the open fissures normal to the direction of the least compressive stress, three different flow field patterns leading to the fissure formation at the Super-Sauze landslide can be suggested. First, lateral shear at external and internal landslide boundaries, aligned with the general flow field, leads to the formation of diagonal shear fissure arrays (

Figure 4.13-24e). Second, longitudinal acceleration and deceleration at topographic steps induces tensile stresses at the surface, resulting in transversal fissure arrays (

Figure 4.13-24c). Third, divergence of the flow field over topographic ridges and at the outlets of confining topographic channels induces lateral extension and tensile stresses, resulting in longitudinal fissure arrays (

Figure 4.13-24d). At several locations, those processes overlap and lead to the formation of mixed structures such as the radial fissure patterns displayed in

Figure 4.13-24c, resulting from lateral shear and longitudinal strain, and from local divergent stress field, respectively.

4.13.4 SUMMARIZED EVALUATION OF PARAMETERS

The ongoing monitoring programme at Super-Sauze is very challenging, in terms of field maintenance on site because of the large displacements, and because a quantitative and joint analysis of all the monitored parameters (kinematics, geophysics, hydrology) in terms of changes is beginning as part of OMIV Observatory. All processing techniques are being transferred online and time series of monitored parameters will be progressively broadcasted online on the OMIV website in 2012 and 2013.

References:

- Gance, J., Sailhac, P., Malet, J.-P., Grandjean, G., Supper, R., Jochum, B., Ottowitz, D. 2012. Monitoring water flows with time-lapse Electrical Resistivity Tomography at the Super-Sauze landslide. *Geophysical Research Abstracts Vol. 14, EGU2012-4292-2*.
- Grandjean, G., Bitri, A., Krzeminska, D.M., 2011. Characterisation of a landslide fissure pattern by integrating seismic azimuth tomography and geotechnical testing. *Hydrological Processes*, <http://dx.doi.org/doi:10.1002/hyp.7993>.
- Krzeminska, D.M., Bogaard, T.A., Van Asch, Th.W.J., Van Beek, L.P.H., 2011. A conceptual model of the hydrological influence of fissures on landslide activity. *Hydrology and Earth System Sciences*, 8(6), 11039-11073.
- Lampert, T.A., O'Keefe, S.E.M., 2011. A detailed investigation into low-level feature detection in spectrogram images. *Pattern Recognition*, 44(9), 2076-2092.
- Malet, J.-P., 2003. Les 'glissements de type écoulement' dans les marnes noires des Alpes du Sud. Morphologie, fonctionnement et modélisation hydro-mécanique. PhD Thesis, Université Louis Pasteur, Strasbourg (in French).
- Malet, J.-P., Auzet, A.-V., Maquaire, O., Ambroise, B., Descroix, L., Esteves, M., Vandervaere, J.-P., Truchet, E., 2003. Soil surface characteristics influence on infiltration in black marls: application to the Super-Sauze earth flow (southern Alps, France). *Earth Surface Processes and Landforms*, 28(5), 547-564.
- Malet, J.-P., Ulrich, P., Déprez, A., Masson, F., Lissak, C., Maquaire, O., 2011. Continuous monitoring and near-real time processing of GPS observations for landslide analysis: a methodological framework. In: Margottini, C., Canuti, P., Sassa, K. (Eds): *Proceedings of the Second World Landslide Forum*, 3-7 October 2011, Rome, Italy, Springer (to be published in 2012).
- Malet, J.-P., Maquaire, O. 2003. Hydrological behaviour of earthflows developed in clay-shales: investigation, concept and modelling. In Picarelli, L. (Ed). *The Occurrence and Mechanisms of Flows in Natural Slopes and Earthfills*, Sorrento, Italy, Patron Editore, Bologna: 175-193.
- Malet, J.-P., Van Asch, T.W.J., van Beek, L.P.H., Maquaire, O., 2005. Forecasting the behaviour of complex landslides with a spatially distributed hydrological model. *Natural Hazards and Earth System Sciences*, 5(1), 71-85.
- Maquaire, O., Flageollet, J.-C., Malet, J.-P., Schmutz, M., Weber, D., Klotz, S., Albouy, Y., Descloîtres, M., Dietrich, M., Guérin, R., et Schott, J.-J. 2001. Une approche multidisciplinaire pour la connaissance d'un glissement-coulée dans les marnes noires du Callovien-Oxfordien (Super-Sauze, Alpes-de-Haute-Provence, France). *Revue Française de Géotechnique*, 95/96: 15-31.
- Niethammer, U., James, M.R., Rothmund, S., Travelletti, J., Joswig, M., 2011. UAV-based remote sensing of the Super-Sauze landslide: Evaluation and results. *Engineering Geology*, <http://dx.doi.org/10.1016/j.enggeo.2011.03.012>.

- Stumpf, A., Niethammer, U., Rothmund, S., Mathieu, A., Malet, J.-P., Kerle, N., Joswig, M., 2011. Advanced image analysis for automated mapping of landslide surface fissures, In: Margottini, C., Sassa, K., Canuti, P. (Eds): Proceedings 2nd World Landslide Forum, Rome.
- Travelletti, J., 2011. Imagerie multi-paramètres et multi-résolutions pour l'observation et la caractérisation des mécanismes de glissements-coulées. PhD Thesis, Université de Caen Basse-Normandie, Caen.
- Travelletti, J., Delacourt, C., Allemand, P., Malet J.-P., Schmittbuhl, J., Toussaint, R., Bastard, M. 2012. Correlation of multi-temporal ground-based images for landslide monitoring: application, potential and limitations. *International Journal of Photogrammetry and Remote-Sensing*, 25p. doi: 10.1016/j.isprsjprs.2012.03.007
- Travelletti, J., Malet J.-P., Delacourt, C., (submitted, in review). Multi-date correlation of Terrestrial Laser Scanning data for the characterization of landslide kinematics. *Geomorphology*, 15p. (in review).
- Travelletti, J., Malet, J.-P., 2012. Characterization of the 3D geometry of flow-like landslides: A methodology based on the integration of heterogeneous multi-source data. *Engineering Geology*, <http://dx.doi.org/10.1016/j.enggeo.2011.05.003>.
- Walter, M., Arnhardt, C., Joswig, M., In Press. Seismic monitoring of rockfalls, slide quakes, and fissure development at the Super-Sauze mudslide, French Alps. *Engineering Geology*, <http://dx.doi.org/10.1016/j.enggeo.2011.11.002>.
- Walter, M., Niethammer, U., Rothmund, S., Joswig, M., 2009. Joint analysis of the Super-Sauze (French Alps) mudslide by nanoseismic monitoring and UAV-based remote sensing. *First Break*, 27(8), 53-60.
- Weber, D., Herrmann, A. 2000. Reconstitution de l'évolution géomorphologique de versants instables par photogrammétrie numérique : l'exemple du glissement de terrain de Super-Sauze (Alpes-de-Haute-Provence, France). *Bulletin de la Société Géologique de France*, 171: 637-648.

4.14 VALLCEBRE (SPAIN)

José Moya and Josep Gili

Universitat Politècnica de Catalunya

ABSTRACT

The Vallcebre landslide has been intensively monitored since 1996 and data on rainfall, groundwater level and ground displacement are measured on a regular basis. Data recorded at boreholes showed a practically immediate response of groundwater level to rainfall episodes and of landslide displacement to changes in groundwater. This allowed the simulation of landslide displacements and velocities from piezometric data. The good fit of the simulated values to the measured data indicated that groundwater level can be reliably used to predict the displacements of the landslide.

Presented parameters: displacement, velocity, groundwater level, precipitation.

4.14.1 GENERAL DESCRIPTION OF THE TEST SITE

The Vallcebre landslide is a large, active slope failure located in the upper Llobregat river basin, in the Eastern Pyrenees, 125 km north of Barcelona, Spain (Figure 4.14-1). The slope of the landslide is gentle (about 10° on average). The slide is 1200 m long and 600 m wide, and the entire landslide involves an area of 0.8 km². The landslide is of translational type and is formed by three main slide units (Figure 4.14-1). Each unit is formed by a gentle slope surface bounded in its head by a scarp of a few tens of meters high (Corominas et al, 2000; 2005). The mobilised material consists of a set of shale, gypsum, siltstone and claystone layers gliding over a thick limestone bed, all of which are of Upper Cretaceous-Lower Palaeocene age. The geological structure is defined by a syncline whose axis is nearly dipping towards the down-slope direction. In fact, the landslide originated at the “soft” mudrock core of the syncline.

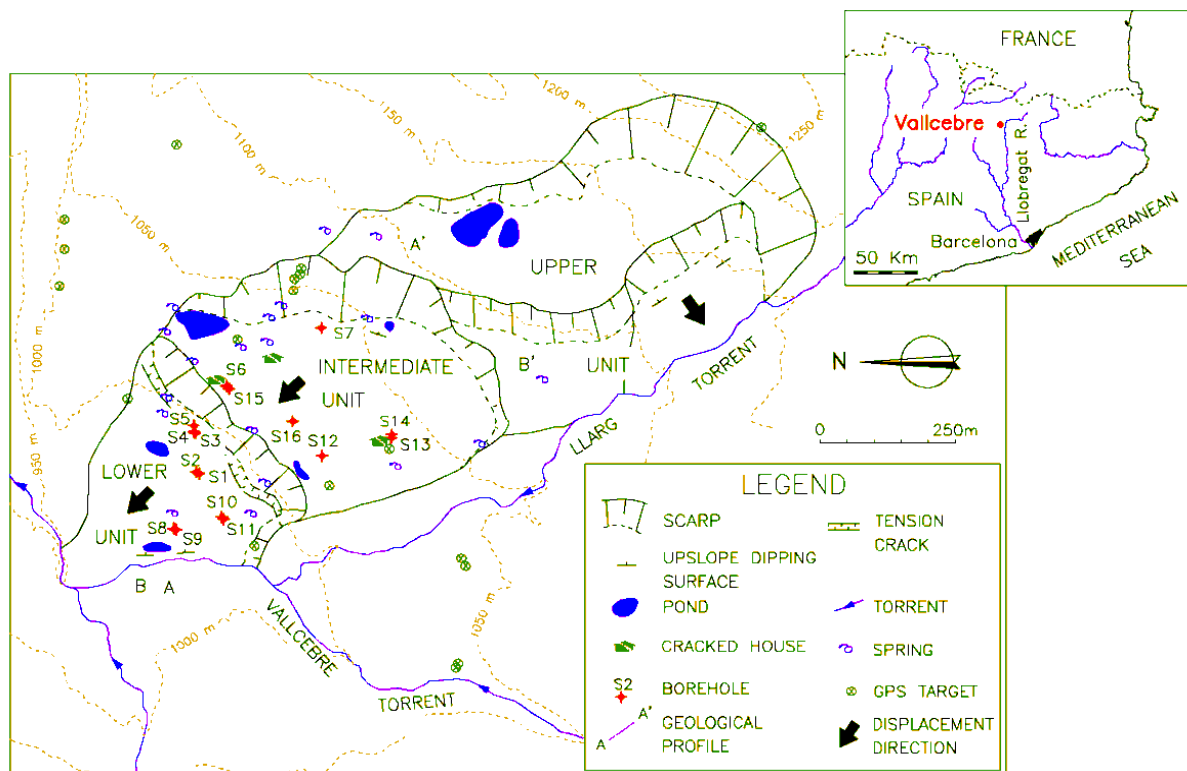


Figure 4.14–1. Geomorphological sketch of the Vallcebre landslide (Corominas et al. 2005).

Most of the evidence of surficial deformation is located in the boundaries of the slide units, such as distinct shear surfaces and tension cracks. A crack zone is located at the base of the head scarp of each landslide unit, where cracks re-open periodically. Within the landslide units, in contrast, the ground surface is only disturbed by minor scarps and by some cracking of farmhouse walls. These farmhouses and a few roads that pass through the landslide are the elements at risk that are present in the slope. Although there are some farmhouses located in the middle unit of the landslide, no houses are found in the lower landslide unit, which is the most active one.

The Vallcebre landslide is very slow and involves moderate risk. The landslide is very sensitive to changes in the water table. The main interest of the study of the Vallcebre landslide is not in the associated risk, but on its relatively simple geometry and geology and on its slow velocity. This allows easier testing of monitoring sensors and techniques and adjustment of mechanical and hydrological models to the slope behaviour. In that sense the Vallcebre landslide can be considered as a real-scale laboratory test.

4.14.2 DESIGN OF THE MONITORING NETWORK

The Vallcebre landslide was first monitored in 1987 using conventional surveying and photogrammetry. This early stage of monitoring confirmed the active character of the landslide. From July 1996 to April 1998, sixteen boreholes were drilled in the lower and

intermediate units of the landslide in order to log the geology and to set up an in-situ monitoring network (Figure 4.14–1). Eight boreholes were equipped with conventional inclinometers while the other six were equipped with wire extensometers and open pipe piezometers (see Corominas et al. 2000, 2005, and Gili et al. 2012a, for a description of the performance of wire extensometers). Since 1996, systematic loggings of rainfall, groundwater level changes, and landslide displacements in wire extensometers have been carried out every 20 minutes. Moreover, surface displacements have been measured using precise relative GPS on 30 control points since December 1995 (Gili et al. 2000). The aim was to obtain a more distributed view of the landslide displacement but also to calibrate the displacements gathered by wire extensometers during their early stage of operation (see also Corominas et al. 2000 and Gili et al. 2012a). GPS campaigns were frequently carried out from 1995 to 1998 (once every two months, on average), and since then they are currently executed once a year.

Three of the wire extensometers and all of the piezometers are still operational after 15 years of recording. The maintenance of these sensors involved periodical field campaigns every two to three months to check the power supply and the correct performance of the extensometers. Over the last two years, two main improvements were made to the in-situ monitoring network: the power supply range was enlarged by the installation of solar panels, and data transfer from dataloggers was shifted to a remote one using GSM modems, which, moreover, allows the implementation of a warning system.

Since 2006, differential interferometric radar techniques (DInSAR) have been used in the Vallcebre landslide, with the collaboration of the Institute of Geomatics (Crosetto et al. 2009 and Gili et al. 2012b). The aim was not only to improve the number and the distribution of the control points on the landslide, but to calibrate the radar techniques as well. A DInSAR monitoring of the landslide was carried out by analyzing 15 sets of SAR images from the Envisat satellite, which elapsed from December 2006 to December 2008. Seven corner reflectors were used in the analysis rather than natural reflectors because the landslide is densely vegetated and changes in the trees and in the grass cover are recorded seasonally. Since February 2010, SAR analysis has been based on the ground-based technique (GBSAR) from a number of mini-corner reflectors distributed throughout the lower unit of the landslide.

4.14.3 ANALYSIS OF MONITORING DATA

4.14.3.1 Landslide displacement

Since November 1996, horizontal displacements of up to 3.9 m have been observed. The continuous measurement in wire extensometers shows that the landslide has stopped moving only very occasionally since the monitoring started 15 years ago, although velocities reduced significantly during dry periods (Figure 4.14–2). On the other hand, the extensometer records indicated that several units of the landslide move at different rates. Extensometers S2 and S11 have shown the fastest displacements, with a maximum recorded rate of up to 14 mm/day. At these boreholes, the average annual displacement ranged from 200 to 660 mm, which corresponds to a mean daily velocity range of 0.6 to 1.8 mm/day. The other extensometers installed in this slide unit (S4, S5 and S9) exhibited lower rates, although in the same order of magnitude. At borehole S6, placed in the intermediate slide unit, the velocity is significantly

smaller indicating that the intermediate unit is less active than the lower one. Rapid movement of the lower landslide unit causes crack opening at the head scarp of this unit and removes support to the intermediate one.

4.14.3.2 Groundwater table

The groundwater level changes quickly along the landslide, reacting almost immediately to rainfall inputs, which suggests that water infiltration is controlled by fissures and pipes rather than by soil porosity/permeability. The extensometers recorded sudden changes in displacement rates that can be directly related to the fluctuations of the water table governed by rainfall. The relationship between groundwater level changes and landslide activity is particularly clear at borehole S2 (Figure 4.14–2). There is a strong level of synchronism between the two records. In addition, the rate of displacement is strongly correlated with water table data. The position of the groundwater level at an approximate depth of 6.22-6.24 m corresponds to a stable situation.

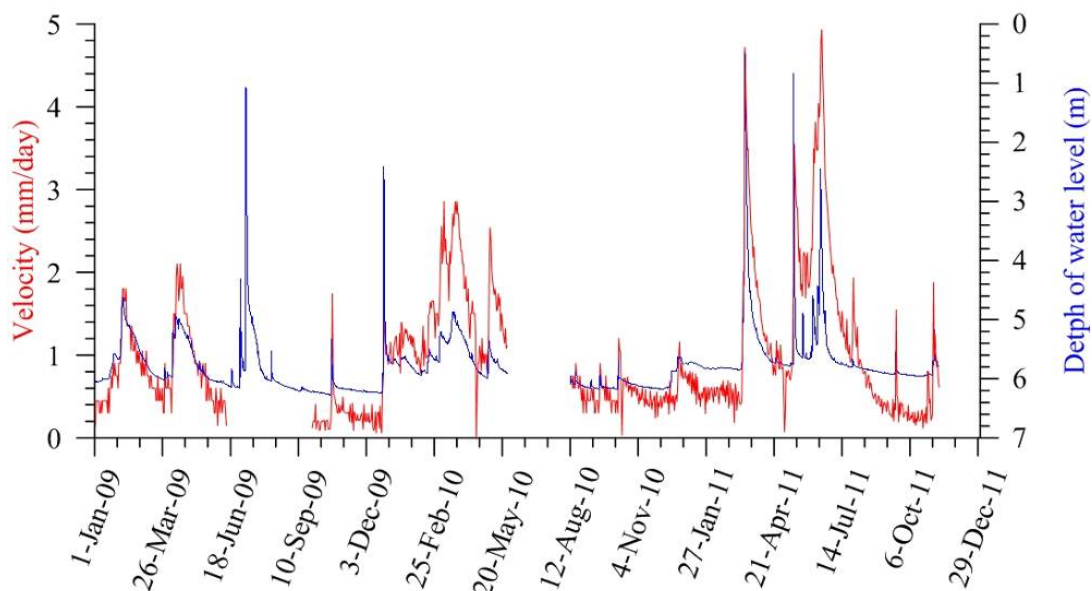


Figure 4.14–2. Water table (blue line) and landslide velocity (red line) of the Vallcebre landslide at borehole S2 over the last three years.

4.14.4 SUMMARIZED EVALUATION OF PARAMETERS

Several boreholes show a close relationship between landslide velocity and groundwater level (Figure 4.14–2, Corominas et al. 2005). This fact suggests that groundwater level can be used to predict landslide movements and, therefore, as an early warning parameter. A detailed analysis of the mentioned relationship revealed that a viscous strength force is operating in the landslide (Corominas et al. 2005). On the other hand, the landslide toe is tilted backwards and induces an additional resistance to the movement of the landslide. This effect has been recently incorporated in the simulation of landslide displacements from data recorded in the piezometers (Figure 4.14–3) (Ferrari et al. 2011).

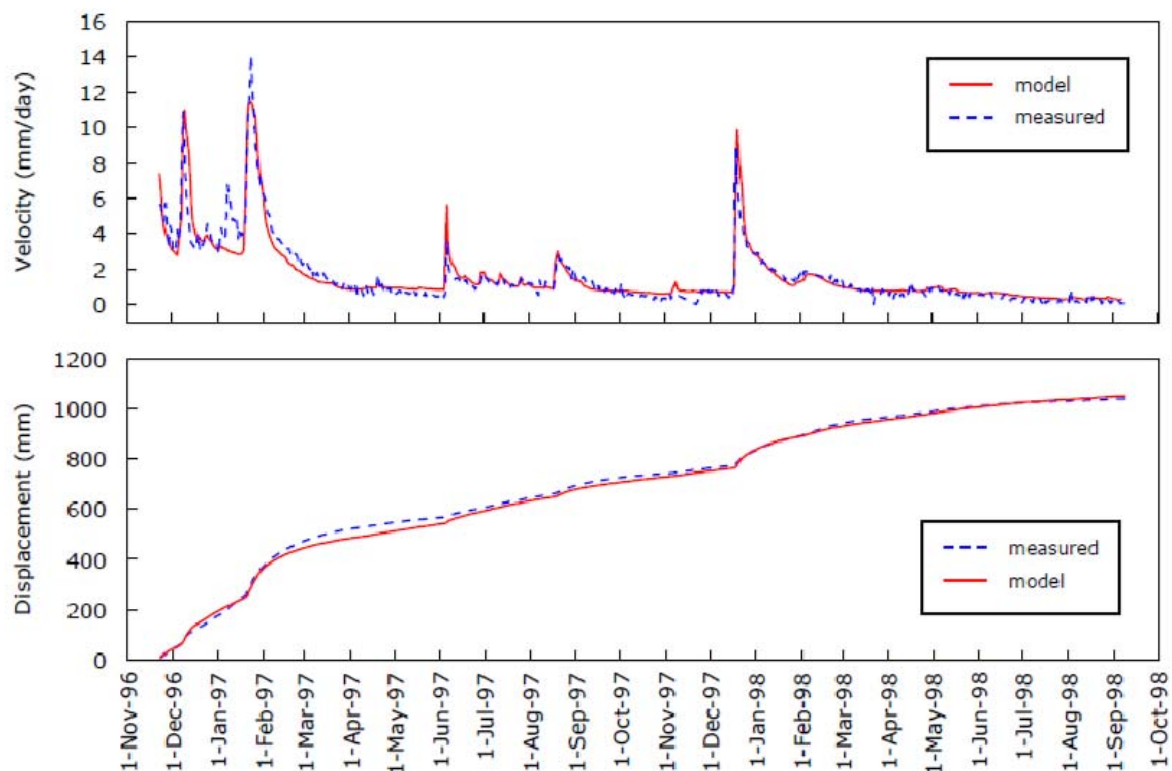


Figure 4.14–3. Measured and predicted displacements and velocities at borehole S2 from water level changes and considering a viscous strength component and the effect of the landslide foot evolution (Ferrari et al. 2011).

The agreement between computed and predicted displacements is generally good. Nevertheless, the quality of the simulation is conditioned by the assumption of a simplified geometry (infinite slope in Corominas et al. 2005; and two rigid sliding blocks in Ferrari et al. 2011). Obviously these analyses are more representative of local conditions. The following steps of the analysis will include the examination of the landslide behaviour at a global scale and 3D geometry (i.e., using coupled finite element models including flow and mechanical equations).

4.14.5 END-USER INVOLVEMENT AND ALARM CHAIN

As mentioned above, the Vallcebre landslide is very slow. The farmhouses located in the landslide are in the intermediate unit, which moves in a sliding manner with no appreciable differential movements. Therefore, the risk associated with the landslide can be regarded as moderate. End-users (the municipal government) have worked on the establishment of an alarm chain and, currently, in the management of future risk mitigation measures.

References:

- Corominas, J., Moya, J., Lloret, A., Gili, J.A., Angeli, M.G., Pasuto A., Silvano, S., 2000. Measurement of landslide displacements using a wire extensometer. *Engineering Geology*, 55: 149–166.
- Corominas, J., Moya, J., Ledesma, A., Lloret, A. Gili, J.A., 2005. Prediction of ground displacements and velocities from groundwater level changes at the Vallcebre landslide (Eastern Pyrenees, Spain). *Landslides*, 2: 83-96.
- Crosetto, M., Monserrat O., Pozzoli A., Gili J.A. (2009). Detección y medida de deformaciones del terreno utilizando interferometría diferencial SAR (in Spanish). *Proceed. VII Simposio Nacional sobre Taludes y Laderas Inestables*, Barcelona, oct. 2009. E. Alonso, J. Corominas, M. Hürlimann (Eds.). ISBN 978-84-96736-77-1, pp. 523-534.
- Ferrari, A., Ledesma, A., Gonzalez, D.A. and Corominas, J., 2011. Effects of the foot evolution on the behaviour of slow-moving landslides. *Engineering Geology*, 117: 217-228
- Gili, J.A., Corominas, J., Rius, J., 2000. Using Global Positioning System techniques in landslide monitoring. *Engineering Geology*, 55: 167-192.
- Gili, J.A., Corominas, J., Moya, J., 2012a. Wire extensometers. In: Tofani, V., Segoni, S., Catani, F., Nicola Casagli, N. (Eds.) *Evaluation report on innovative monitoring and remote sensing methods and future technology*. Deliverable 4.5 of the European Project SAFELAND. pp 12-16. Available at <http://www.safeland-fp7.eu>
- Gili, J.A., Corominas, J., Moya, J., 2012b. Borehole wire extensometers, Vallcebre (Spain). In: Tofani, V., Segoni, S., Catani, F., Nicola Casagli, N. (Eds.) *Evaluation report on innovative monitoring and remote sensing methods and future technology*. Deliverable 4.5 of the European Project SAFELAND. pp 96-100. Available at <http://www.safeland-fp7.eu>

4.15 VILLERVILLE (FRANCE)

Jean-Philippe Malet, Candide Lissak-Borges, and Olivier Maquaire
Centre National de la Recherche Scientifique (CNRS)

Thom Bogaard
Delft University of Technology

ABSTRACT

The ‘Cirque des Graves’ and the ‘Fosses du Macre’ landslides in Normandy (France) are slow-moving rotational and translational coastal landslides characterized by surface displacement of a few centimeters per year. The permanent landslide activity generates important economical and physical damages (building perturbations and destruction) in this area where the land pressure associated with coastal tourism is increasing. For these reasons, the landslides have been progressively monitored since 1984. Previous research has demonstrated the efficiency of traditional instrumentation and the use of Global Positioning System (GPS) techniques to detect very low amplitude movements. Surface displacements correlated with rainfall and groundwater level analysis allowed the identification of hydro-climatic thresholds initiating seasonal movements. Continuous monitoring at several points on the landslide allowed the following to be specified: 1) the slope kinematics, 2) the relationship between rainfall, groundwater level and velocity, 3) the temporal evolution of different landslide sectors/areas. To establish a near real-time warning system, the monitoring network is based on the combination of data collection on the triggering factors and on the slope response in kinematic terms. The monitoring system has been updated within the SafeLand project and French research initiatives (Project SISCA), and the results of this instrumentation are presented.

Presented parameters: displacement, ground deformation, pore-water pressure, precipitation, wind velocity.

4.15.1 GENERAL DESCRIPTION OF THE TEST SITE

The coastal slopes of the department of Calvados (Normandy) are frequently affected by landslides causing significant damage to construction and infrastructure.

This paper outlines the field monitoring investigation carried out at the ‘Cirque des Graves’ and the ‘Fosses du Macre’ landslides. The monitoring network has been installed since 1984 after the major event of January 1982 (Maquaire, 1990) and was completed in 2001 and 2008. The kinematics of these slow-moving landslides have been analyzed over several years, with daily observations of displacement and groundwater level in order to identify critical thresholds for the onset of major acceleration. Traditional methods such as total stations and distance-meters are commonly used to quantify the kinematics and its possible correlation with hydrological and climatic characteristics. Many landslides are monitored to define critical thresholds and to point out the relation between groundwater levels and slope velocity (Angeli et al., 1999, Angeli et al., 2000, Petley et al., 2005, Ayalew et al., 2005, Corsini et al., 2005). Most of these areas are instrumented with a network of benchmarks distributed along the slope at the surface, and with inclinometers and piezometers in depth. New monitoring techniques such as permanent GPS, ground-based laser scanning, and ground-based

photographs are used to either increase the accuracy of the displacement measurements or to obtain an image of the displacement field (Malet et al., 2002, Coe et al., 2003). On Normandy landslides, the monitoring network has been designed to record daily displacement rates, groundwater fluctuations and rainfall amounts.

The monitoring of unstable slopes influenced by hydrological factors necessitates high temporal resolution acquisitions to define the spatial and the temporal pattern of the hazard. Continuous monitoring allows a near real-time warning system to be set up to guarantee the population's safety.

Geological and geomorphic settings

The Normandy coastal slopes are important touristic areas with increasing land pressure. Consequently unstable slopes affect many private properties, tourist infrastructure and networks. The coastal main road (RD513), joining Honfleur to the east and Trouville to the west, is partially affected and in case of landslide events, may disconnect many villages. The study areas (the 'Cirque des Graves' and the 'Fosses du Macre' landslides) are located on the high cliffs of the Pays d'Auge plateau (up to 140 m) between Trouville and Honfleur (Figure 4.15–1). Both landslides cover approximately 8 ha surrounding the village of Villerville. Both can be defined as active, slow-moving, rotational landslides according to the Cruden and Varnes (1996) classification.

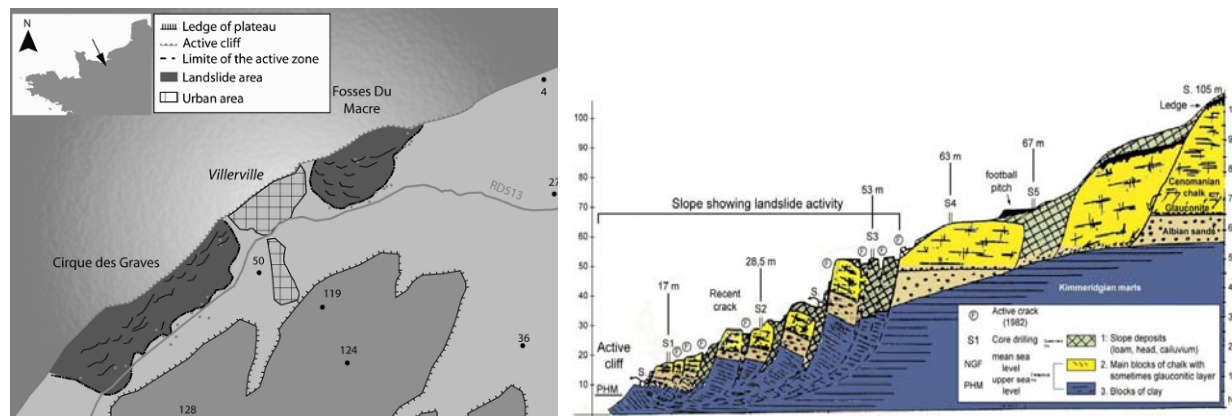


Figure 4.15–1. Location of the study area on the northeastern part of the Pays d'Auge coast, and Geological cross-section of the Cirque des Graves landslide. Altitude is in meters above sea level.

Characterization of the site

The heterogeneous geology consists of Cenomanian chalk and Albian sandstone on top of a thick layer of easily weathered Kimmeridgian marls (Flageollet and Helluin, 1987; Maquaire, 1990). The cliff coast is retreating by slow-moving, translational and rotational sliding Cenomanian chalk blocks.

Description of the history of the mass movement

The landslides have been officially considered as active since an important reactivation occurred in January 1982, however the slopes have not been stable for the last two centuries (Ballais et al., 1984). Since the first major reactivation, the slopes have been permanently affected by slow movement ($0.05\text{-}0.10\text{ m.yr}^{-1}$). Three other main accelerations occurred (February 1988, January 1995 and March 2001) in close relation to the hydro-climatic conditions. These multiple phenomena have generated many new scarps, several meters high, and tensile cracks that are still evolving. The principal part of the ‘Cirque des Graves’ landslide is affected by horizontal displacements between 0.005 to 0.1m.yr^{-1} . The toe of the landslide is affected by superficial failure and the development of muddy flows characterized by a high velocity (around 1m.yr^{-1}). The whole mass is affected by a combination of superficial and deep movements, including possible retrogression, enlargement or advancement of the limits of the landslide during major acceleration.

The morphology is typical of rotational landslides (Varnes, 1978). The Cenomanian chalk panels (Figure 4.15–3) are sliding on the Albian sand which overlays Kimmeridgian marls. The toe of the landslide is characterized by a chaotic morphology with shallow clayey flows overtopping sandy limestones. The morphology is also characterized by Quaternary slope deposits (Flageollet, 1992), and the oldest scarps are completely hidden by vegetation and/or modified by human intervention (Flageollet and Helluin, 1987).

4.15.2 DESIGN OF THE MONITORING NETWORK

The ‘Cirque des Graves’ landslide has been investigated since 1984 for a better understanding of the processes. To characterize the landslide, the actual monitoring network is comprised of 24 benchmarks implanted according to accessibility and vegetation constraints and to specific geomorphological features. The target is to identify the temporal and spatial heterogeneities of the surficial displacement pattern. Since 1984, the benchmark positions have been measured by non-continuous acquisitions with a total station. Since 2008, the displacements have been measured by non-permanent GPS campaigns (Trimble R5) to determine 3D positions. GPS techniques have been increasingly employed to monitor landslide movements (Gili et al., 2000, Malet et al., 2002; Squarzoni et al., 2005) and vertical subsidence of areas (Baldi et al., 2009). The results of previous research indicated that GPS is a viable alternative to other commonly used monitoring strategies. For the study cases, the protocol consists of repeated GPS observations of the benchmarks and horizontal tiltmeter surveys to characterize the angular surface displacement. The GPS observation time (e.g. real-time kinematic survey) for each benchmark is 17 minutes.

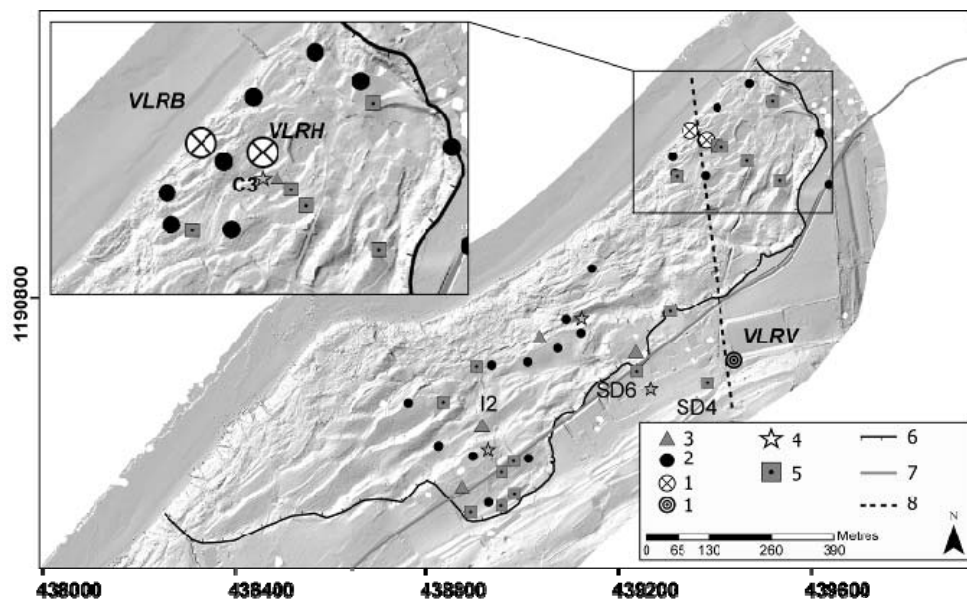


Figure 4.15–2. Monitoring network for the ‘Cirque des Graves’ landslide: 1) GPS receivers, 2) Topographic benchmarks, 3) Inclinerometers, 4) Pressure cells, 5) Piezometers, 6) Limits of the active zone, 7) Main road RD 513, 8) Interpretation profile of Figure 4.15–3.

Since July 2009, three permanent GPS stations (Trimble NetRS) have been installed to provide continuous observation of movements to increase the temporal resolution of information, and to implement an early warning system. The GPS antennas are installed on a stable 2.5 m in length concrete pillar for the reference point VLRV, and on ruggedized iron tripods sealed by concrete in the soil for the moving GPS within the landslide (VLRB, VLRH). These GPS systems are part of the French Observatory of landslides (OMIV, <http://eost.u-strasbg.fr/omiv>). The GPS reference station VLRV has been set up on the stable part of the slope, outside the landslide. Two GPS receivers (VLRH, VLRB) are located on the active part of the landslide, on two subsequent chalk panels. An automatic procedure was developed to download the daily observations (sessions of 24 hours of acquisition at a 30-second frequency) by internet. The baseline distance between VLRV and VLRH and VLRB is respectively 465 m and 480 m.

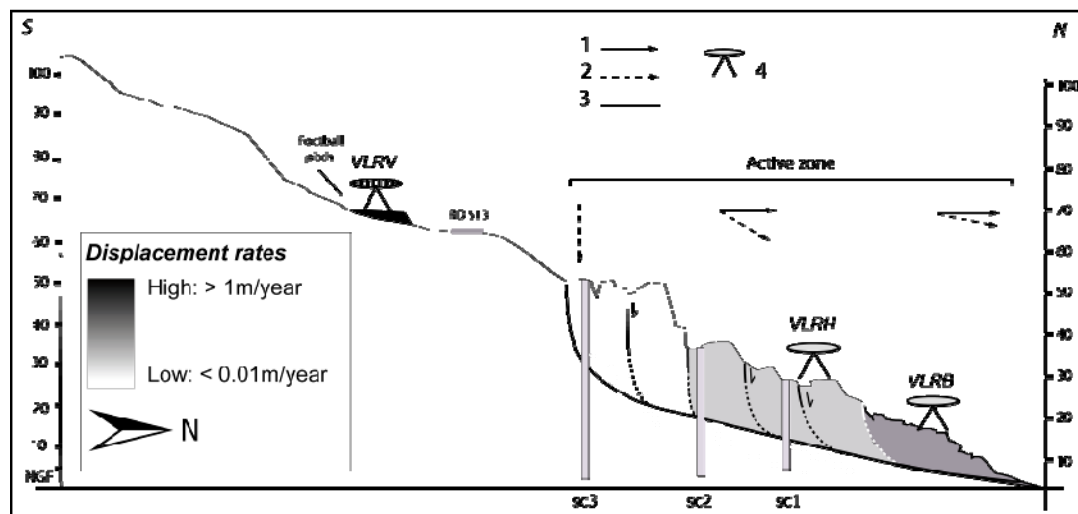


Figure 4.15-3. Geometry of the landslide at the cross-section located on Figure 4.15-2. The profile indicates the principal sliding surfaces and the displacement vectors at the surface: 1) Horizontal displacement, 2) Vertical displacement, 3) Sliding surface, 4) GPS receivers.

On the landslide body, five inclinometers were installed; four of them were installed at a depth of 20 m in 2006, and one of them at a depth of 9 m in 2009. Acquisitions of inclinometer data are carried out monthly. Permanent vertical tilt data are acquired by the recent installation of four multi-parametric probes (Geobeads designed by the AlertSolutions Company) (Peters et al., 2010). These vertical tiltmeters, installed along with pressure cells, are installed in borehole C3 (Figure 4.15-2) at several depths (Cell 1: -1.0 m, Cell 2: -2.0 m, Cell 3: -4.00 m, Cell 4: -5.80 m). The data, acquired at a six-minute temporal resolution, are transferred daily to the internet network to complete the alarm monitoring system.

The kinematic analysis is completed by a permanent survey of water level, pore-water pressure and rainfall at several positions (Figure 4.15-2). Seventeen piezometers (Figure 4.15-2) including three continuous groundwater sensors (SD4, I2, SD6), one multi-parameter datalogger (water and soil temperature, water conductivity, rain gauge; SD6), and one pore-water pressure sensor (Geobeads, C3) were installed. To complete the analysis, meteorologic observations of Météo-France (the French meteorologic survey agency) at Saint-Gatien (4 km from the landslide) and hydrogeologic observations of deep water levels at the BRGM well of Danestal (15 km from the landslide) are used. The rain data are available since 1949 and the groundwater data since 1974 for the Danestal piezometer. These regional data are used as a comparison with the observed local groundwater and meteorological data on the landslide.

The management of data acquisition and the maintenance of the system are carried out by the French Observatory on Landslides (OMIV).

4.15.3 ANALYSIS OF MONITORING DATA

4.15.3.1 Displacement

An analysis of GPS data allows for identifying the direction, amplitude and rate of movement. The GPS data acquired from the repeated campaigns are processed using Trimble Geomatic office. The horizontal and vertical accuracy are estimated at 0.007, 0.012, 0.013 m for X, Y and Z using the standard deviation. Over the period of November 2008-August 2010, this GPS survey allowed for determining horizontal velocity from 5 millimetres to 4 centimetres to the north (Figure 4.15–4).

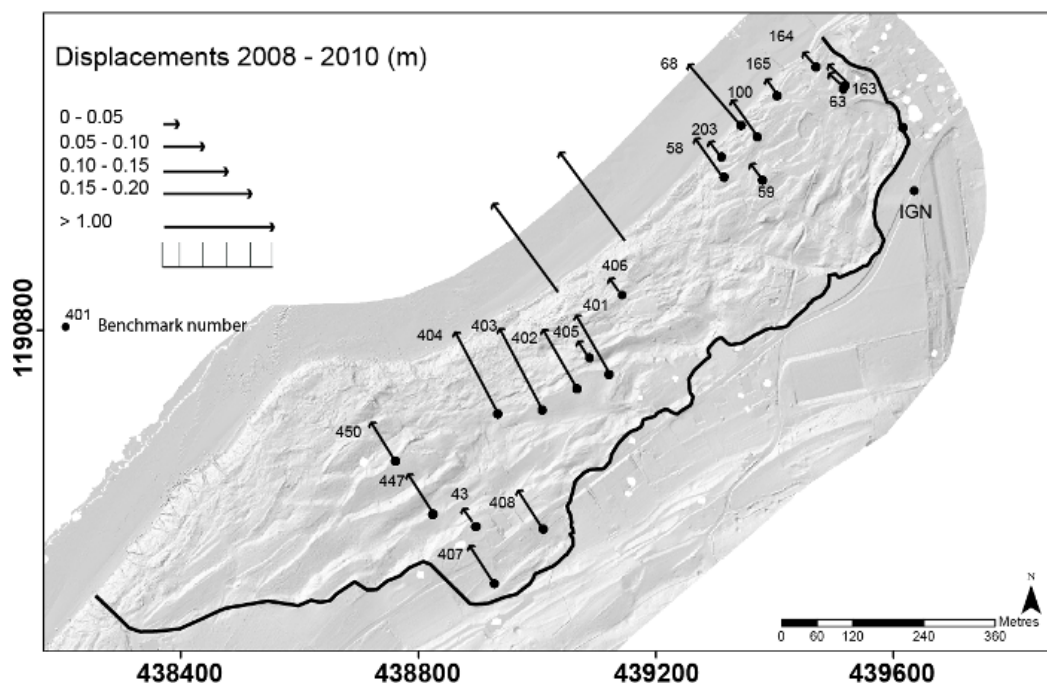


Figure 4.15–4. Cumulated displacements measured between 2008 and 2010.

Displacement vectors reveal differences in the rates and magnitude of displacement of four distinct areas (Figure 4.15–4): (1) the lowest part of the slope is the most active part with superficial displacement of outcropping marl; (2) the central part, upstream of area 1, is affected by displacements of more than 0.15 m of cumulated displacements; (3) the east border of the active area is principally characterized by very low horizontal displacements (benchmarks 163, 164 East part) between a few centimetres and millimetres per year; (4) and the west part of the landslide is affected by moderate movement rates of a few centimetres.

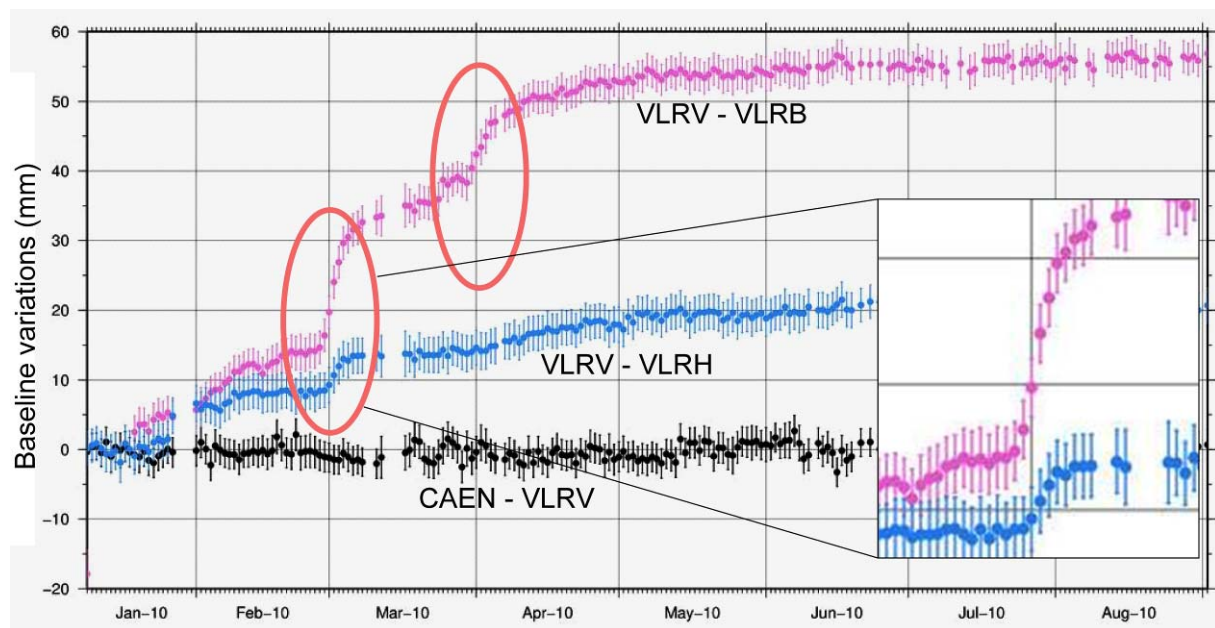


Figure 4.15–5. GPS baselines between VLRV (local reference station) – Caen (regional reference station, and VLRV-VLRH; VLRV-VLRB since January 2010. The baseline VLRV – CAEN allows to determine the accuracy on the GPS solutions, which is estimated at ca. 0.05 cm in all directions.

The continuous monitoring by GPS increases the accuracy on the determination of the displacement rates. The GPS data are processed daily using the Gamit/GlobK software, taking into account tropospheric and ionospheric models, and including additional GPS observations from a regional network of permanent stations to constrain the solution. An automated routine has been developed to process all the data by the OMIV-EOST team in Strasbourg as a duty of the French Observatory of Landslide (OMIV). The methodology to process the data and the accuracy is detailed in Déprez et al. (submitted).

The accuracy of the baseline length has been estimated at ± 0.005 m (Figure 4.15–5, Deprez, 2010). The first results show between January 2010 and July 2010, 0.06 m of cumulated displacements for VLRB station and 0.02 m for VLRH station. Two acceleration periods are observed at both stations, in January and February 2010, with a time lag of about five days between the stations (Figure 4.15–5). The permanent survey allows for asserting the existence of a lag time of acceleration between the compartments of the landslide.

4.15.3.2 Ground deformation

On several points of the landslide, deep movements were identified by inclinometer measurements with a slip surface between 15 and 17 m depth (Figure 4.15–3). In addition, ground deformation measurements with Geobeads probes have also been done since July 2010 (Figure 4.15–6).

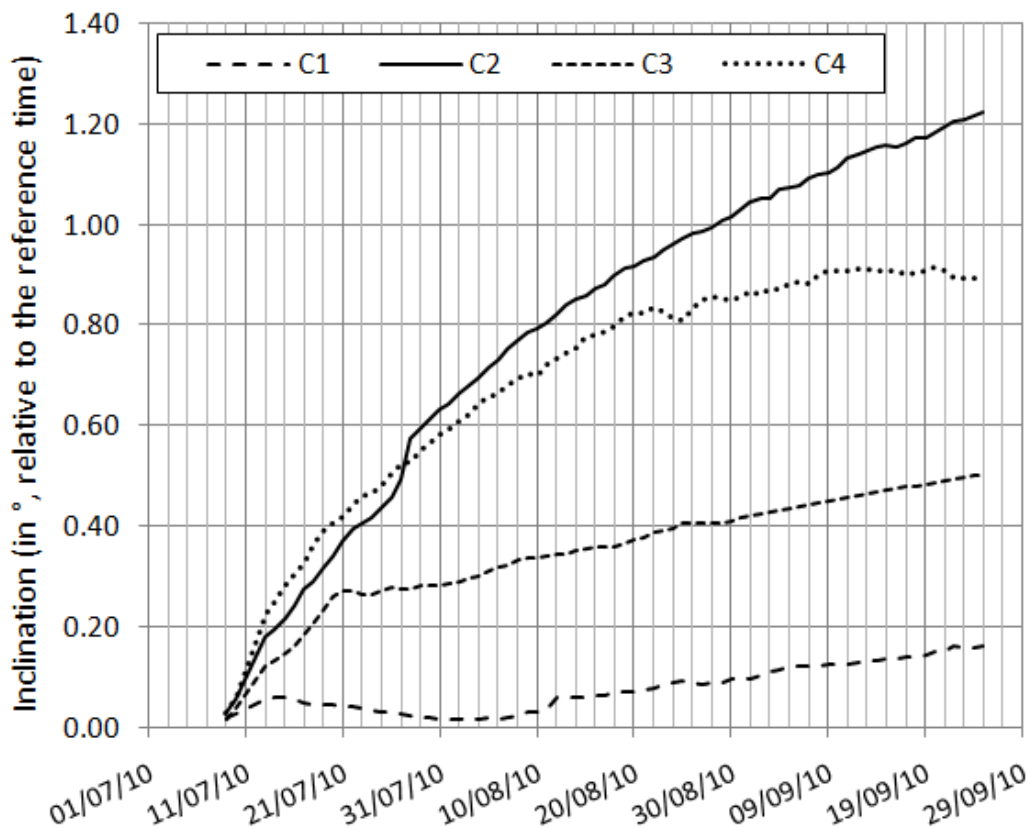


Figure 4.15–6. Cumulated tilt of Geobeads probes at several depth (C1: 1.00 m, C2: 2.00 m, C3: 4.00 m, C4: 5.80 m) in the slope.

The first three months of the probes’ registration (reduced activity period for the landslide) show continuous activity (Figure 4.15–6) of the landslide with a gradual inclination of the tiltmeters in C3 since their establishment. The position of the sensors is generated every six minutes. If any significant acceleration of the landslide occurs, a remarkable tilt of the probes will be recorded. Hitherto, no significant changes have been observed.

4.15.3.3 Pore-water pressure

The continuous recording in SD4, SD6, and I2 (Figure 4.15–2) highlights the effect of precipitation on groundwater fluctuation. For example, in November 2009 the groundwater in SD4 was still increasing (Figure 4.15–2 and 4.15–7) until four or five days after the end of rainfall. The groundwater discharge begins, but at the end of the month a new rainfall event triggers another increase in water level. The groundwater response is delayed about five days after the beginning of the episode (20/11/09) (Maquaire, 1990, Lissak et al., 2009).

Concerning pore pressure in C3, for the first three months of recording (July 2010–Sept 2010), no clear response to the infiltrating precipitation could be recorded because few rainfall episodes occurred within this period.

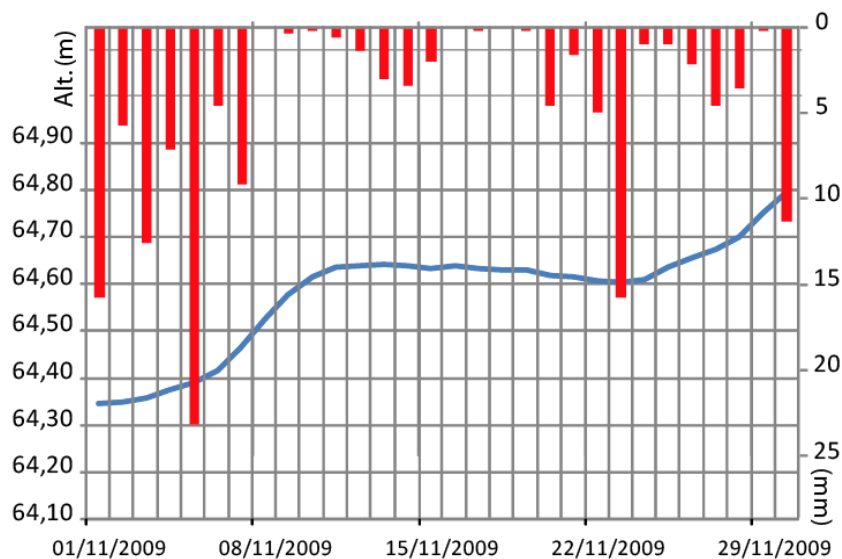


Figure 4.15–7. Example of the groundwater response (left axis) to precipitation (right axis) in SD4 piezometer (location in Figure 4.15–2).

The groundwater pattern within the landslide area does not change between the dry and wet season. The level is quite close to the surface but a clear difference exists throughout the landslide area in the annual amplitude of the groundwater level variations, ranging from several decimetres to 3 m. Seasonal trends of the water level on the landslide were analyzed for four piezometers having two years of continuous data. Using a harmonic analysis, the periodicity of the groundwater system can be determined. The analysis shows a clear seasonal trend: high groundwater levels in spring (April/May) and the lowest values around September. The signal is obviously superimposed to the seasonal trend corresponding to shorter time scale precipitation events. A cross correlation analysis of rainfall versus the groundwater level dynamics shows a 1-2 day time lag. The groundwater levels at the Pays d’Auge plateau are well represented by the Danestal piezometer; this piezometer is representative of the groundwater table observed in the limestone lithology that outcrops at the Villerville landslide (Lissak et al., 2009; Maquaire, 2000).

A further hydrological analysis was performed with a tentative hydrological modelling using monthly effective precipitation (P-PET) and groundwater level (h_t) data. The monthly groundwater level was modelled based on:

$$h_t = h_{t-1}e^{-\frac{dt}{k}} + f \cdot ([\max[(P - PET), 0]]) \cdot (1 - e^{-\frac{dt}{k}}) \quad [1]$$

for which h is the groundwater level, k the depletion constant, P-PET the effective rainfall and f denotes the rainfall multiplication factor in which also the effective porosity is included.

Three different conceptual models were used. The first is a standard linear reservoir. The second consists of two linear reservoirs with a rainfall threshold (a dual porosity system that becomes active when a rainfall threshold is passed). The third is a linear reservoir with a dual outlet, basically mimicking a groundwater system that accelerates when a groundwater threshold is passed (higher groundwater level taps a faster responding part of the subsurface). A standard optimization technique was used based on the RMSE and explained variance (R^2) between the observed and modelled groundwater level to obtain the best fit conceptual model. The simple linear reservoir was unable to mimic the more flashy behaviour at higher groundwater levels. The second conceptual model envisages a system where a precipitation threshold must be surpassed to activate faster responses within the subsurface; this improved the model results. Using two outlets, a regional groundwater system is mimicked that consists of a lower reservoir that behaves relatively modestly and a top reservoir that simulates the faster responses. The best fit (lowest RMSE) and best correlation between measured and modelled groundwater levels showed the groundwater threshold for Danestal at around 107 m.

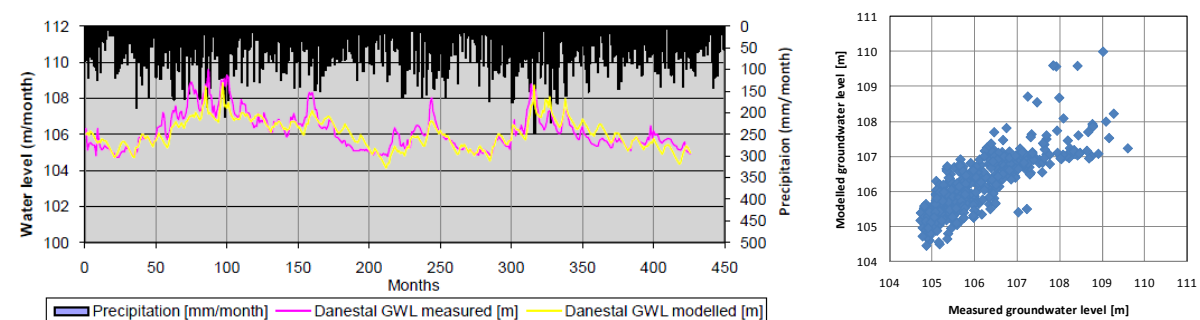


Figure 4.15–8. Model results for the dual outlet model using a threshold of 107 m. A) Time series starting 1974; B) Scatter plot.

4.15.3.4 Rainfall and wind velocity

To define rainfall–landslide thresholds (Keefer et al., 1987), GPS observations are linked to groundwater variations at the SD4 and SD6 piezometers and with the rain gauge implanted near SD6 (Figure 4.15–9) to estimate the chalk panel response to rainfall and groundwater variations. Analysis of the permanent GPS in correlation with the rainfall and the groundwater level data indicates that a low acceleration of a few millimetres is associated with at least five days of precipitations (Figure 4.15–9). On Figure 4.15–5, we can observe two acceleration periods for the VLRB station.

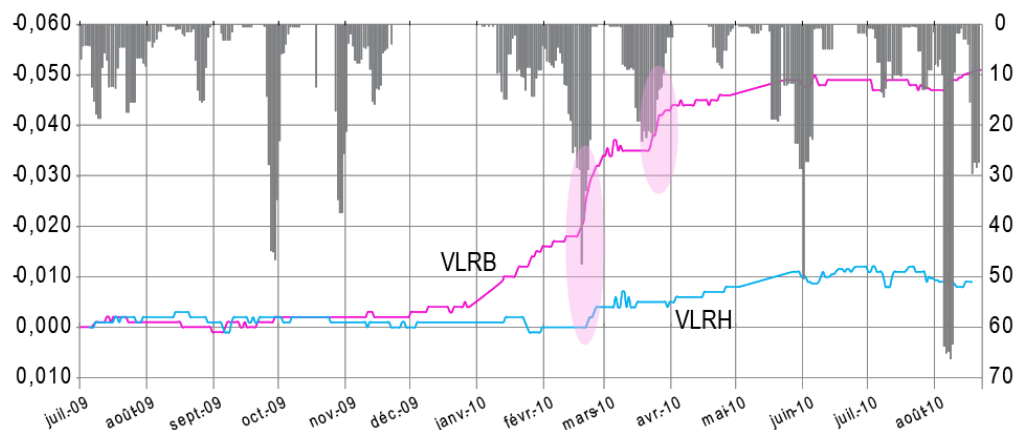


Figure 4.15–9. Cumulated horizontal displacements of VLRB and VLRH stations (left axis) and pluviometry (right axis) between July 2009 and August 2010. Left Y-axis: displacement (in m), Right Y-axis: precipitation (in mm).

We can estimate an approximate water level threshold about 66.20 m alt. at SD4 with several days of cumulated rainfall. At the end of March, the third acceleration of about 1 cm of displacement was only observed for the VLRB station. The station is located on the landslide toe which is in direct contact with the sea during high tides. A few days before the VLRB acceleration, the tidal coefficients were high. During the same periods, south-north winds were recorded at a speed of 30-35 km/h (Figure 4.15–10).

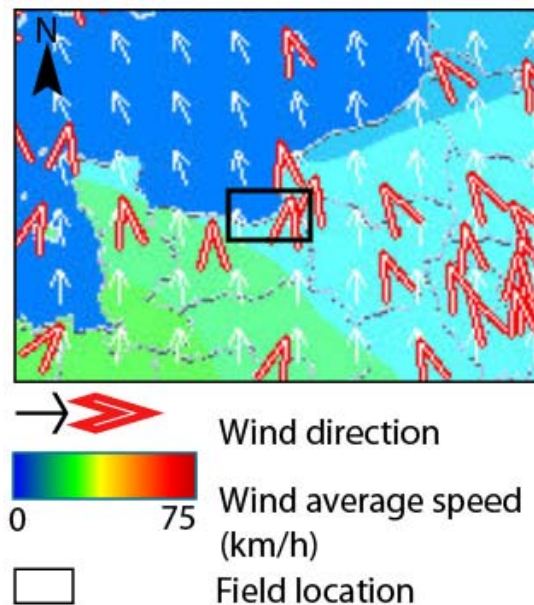


Figure 4.15–10. Extract from the wind map of March 25, 2010 (Meteociel.fr) a few days before VLRB acceleration to illustrate the wind conditions before and during the acceleration period.

The wind direction (Figure 4.15–10) did not allow the oversize wave phenomenon. Now we are only able to highlight the efficiency of the rainfall on the movement triggering. But, perhaps the sea action on the landslide toe could be proven during the next episode to explain the activity of the VLRB station when VLRH is stationary.

Guzzetti et al. (2007) define a threshold for a rainfall-induced landslide as “the rainfall, soil moisture or hydrological condition that, when reached or exceeded, is likely to trigger landslides”. Following Guzzetti et al. (2007) here, i) the empirical rainfall threshold was determined and ii) the antecedent condition threshold using the Danestal groundwater information. The local empirical threshold was established on the basis of cumulative rainfall, duration or their combination. The daily rainfall data of St. Gatien station was checked thoroughly to count the number of days having continuous rainfall. Continuous rainfall is here defined as a series of consecutive rainy days with a maximum of one dry day in between. Similarly, the cumulative effective rainfalls of those rainfall events of the landslide area were also analyzed.

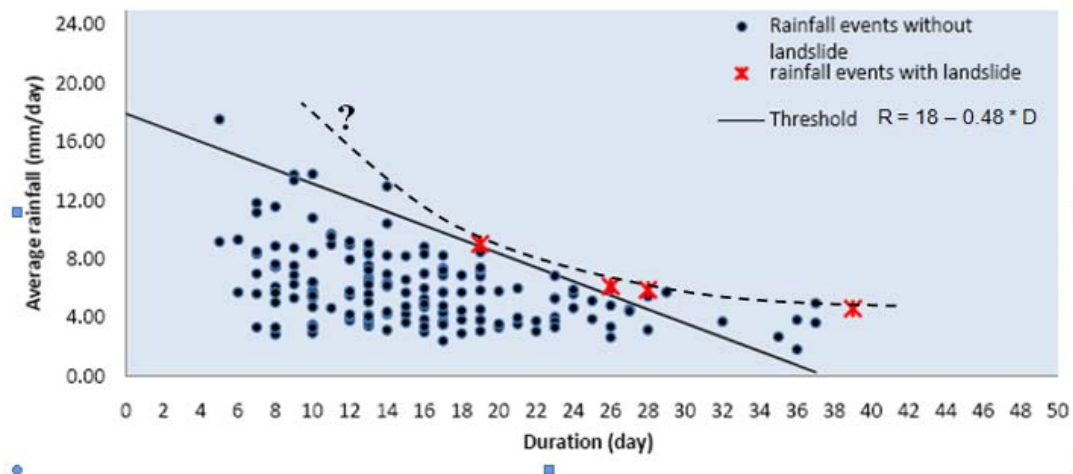


Figure 4.15–11. Empirical rainfall-duration threshold for Villerville landslide area. The empirical threshold equation is given by: $R = 18 - 0.48 * D$, with R is the average daily rainfall intensity in [mm/day] and D the duration in [days]. Dashed line indicates possible curved envelope threshold.

As only four landslide re-activations are known, the rainfall events without landslide activity are also plotted. Two thresholds are plotted: a linear threshold and a sketched curved envelope. This gives an indicative rainfall-duration threshold for one landslide area. The limited re-activation events make it impossible to argue in favour of the linear threshold or the curved envelope, which are indicated in Figure 11. More data, especially of landslide re-activations, are needed for that. Instead of using only rainfall information we also analyzed the relation between groundwater level as proxy for antecedent moisture condition, cumulative rainfall and landslide re-activation.

4.15.4 SUMMARIZED EVALUATION OF PARAMETERS

The first years of GPS permanent monitoring allowed the seasonal rates displacement of the very slow 'Cirque des Graves' landslide to be identified. A continuous monitoring is adequate to take into account the smallest movements before acceleration crisis. Because slow creeps occur until the point of catastrophic failure (Moss, 2000), it is important to differentiate the seasonal velocity of a landslide from a pre-crisis activity. The real-time monitoring is coupled with a warning system with an automatic treatment of GPS positions, water pressure, ground deformation and water level. Geodetic data are transferred daily and are able to be used.

The first years of monitoring put forward the temporal and spatial heterogeneity of the landslide. The landslide is comprised of nested panels responding to the same hydrological stress but moving with a different lag time of several days. The hydrological response of the landslide body is evident, but the behaviour of the toe of the landslide should be affected by other local hydrological processes.

References:

- Angeli, M.C., Pasuto A., Silvano S. 1999. Towards the definition of slope instability behaviour in the Alverà mudslide (Cortina d'Ampezzo, Italy). *Geomorphology* 30:201-211.
- Angeli, M.C., Pasuto A., Silvano S. 2000. A critical review of landslide monitoring experiences. *Engineering Geology* 55:133-147.
- Ayalew, L., Hiromitsu Y., Hideaki M., Takami K. 2005. Landslides in Sado Island of Japan: Part I. Case studies, monitoring techniques and environmental considerations. *Engineering Geology* 81: 419-431.
- Baldi, P., Casula, G., Cenni, N., Loddo, F., Pesci, A. 2009. GPS-based monitoring of land subsidence in the Po Plain (Northern Italy). *Earth and Planetary Science Letters* In Press, Corrected Proof.
- Ballais, J.-L., Maquaire, O., Ballais, H. 1984. Esquisse d'une histoire des mouvements de terrain dans le Calvados depuis 2 siècles. In: *Actes du Colloque "Mouvements de terrain"*, Documents du BRGM, N° 83, Ed. BRGM, Orléans, pp. 476-483.
- Coe, J. A. et al. 2003. Seasonal movement of the Slumgullion landslide determined from Global Positioning System surveys and field instrumentation, July 1998-March 2002. *Engineering Geology* 68: 67-101.
- Corsini, A., Pasuto, A., Soldati M., Zannoni A. 2005. Field monitoring of the Corvara landslide (Dolomites, Italy) and its relevance for hazard assessment. *Geomorphology* 66:149-165.
- Cruden, D. M., Varnes, D. J. 1996. Landslide types and processes. *Landslides, Investigation and Mitigation* 36-75.
- Déprez, A. 2010, Caractérisation de la cinématique de glissement de terrain ppar mesure GPS en continu et modélisation mécanique. Application aux sites de La Valette et de Villerville. Rapport de Mémoire de Master 2, Ecole et Observatoire des Sciences de la Terre, Strasbourg, 30p. et annexes.
- Déprez, A., Malet, J.-P., Masson, F. Ulrich, P. 2010 (submitted). Continuous monitoring and near-real time processing of GPS observations for landslide analysis: a methodological framework. *Engineering Geology*, 16p. (submitted).
- Flageollet, J.-C. 1992. Quaternary slope formations between Trouville and Honfleur. In: Flageollet, J.-C. (Ed.), *Proceedings of the European Intensive Course on the Prevention of Coastal Erosion and Submersion Risks*, CERG, Council of Europe, Major Hazards Agreement, Strasbourg, pp. 101-108.

- Flageollet, J.-C., Helluin, E. 1987. Morphological investigations of the sliding areas along the coast of Pays d'Auge, near Villerville, Normandy, France. In: *Proceedings of the 1st International Conference on Geomorphology*, Vol. 1, pp. 477-486.
- Gili, J. A., Corominas, J., Rius, J. 2000. Using Global Positioning System techniques in landslide monitoring. *Engineering Geology* 55:167-192.
- Guzzetti, F., Peruccacci, S., Rossi, M., Stark, C.P. 2007. Rainfall thresholds for the initiation of landslides in central and southern Europe. *Meteorology and Atmospheric Physics* 98: 239-267
- Keefer, D. K. et al. 1987. Real-time landslide warning during heavy rainfall. *Science* 238:921.
- Lissak, C., Maquaire, O., Malet, J.-P., Déprez, A., Masson, F., Ulrich, P., Peters, E.T. (2010). Multi-technique permanent monitoring of a slow-moving coastal landslide in Normandy. *Proceedings of the International Conference: Mountain Risks: Bringing Science to Society*, Nov 2010 Florence 2010. pp. 267-274.
- Lissak, C., Maquaire, O., Malet, J.-P. 2009. Role of hydrological process in landslide occurrence: Villerville-Cricqueboeuf landslides (Normandy coast, France). In: Malet, J.-P., Remaître, A., Boogard, T.A. (Eds) *Proceedings of the International Conference on Landslide Processes: from geomorphologic mapping to dynamic modelling*, Strasbourg, CERG Editions, pp. 175-180.
- Malet, J. -P., Maquaire, O., Calais, E. 2002. The use of Global Positioning System techniques for the continuous monitoring of landslides: application to the Super-Sauze earthflow (Alpes-de-Haute-Provence, France). *Geomorphology* 43:33-54.
- Maquaire, O. 1990. *Les mouvements de terrain de la côte du Calvados. Recherches et prévention*. Documents du BRGM., N° 197, Ed. BRGM, Orléans, 430 p.
- Mora, P. et al. 2003. Global Positioning Systems and digital photogrammetry for the monitoring of mass movements: application to the Ca' di Malta landslide (northern Apennines, Italy). *Engineering Geology* 68:103-121.
- Moss, J. L. 2000. Using the Global Positioning System to monitor dynamic ground deformation networks on potentially active landslides. *International Journal of Applied Earth Observation and Geoinformation* 2:24-32.
- Peters, E.T., Malet, J.-P., Bogaard, T.A. 2010. Multi-sensor monitoring network for real-time landslide forecasts in early warning systems. *Proceeding conference on Mountain Risks: bringing science to society*. Nov 2010, Florence 2010. Pp. 335-340.
- Petley, D.N., Mantovani, F., Bulmer, M.H., Zannoni, A. 2005. The use of surface monitoring data for the interpretation of landslide movement patterns. *Geomorphology* 66:133-147.
- Squarzoni, C., Delacourt, C., Allemand, P. 2005. Differential single-frequency GPS monitoring of the La Valette landslide (French Alps). *Engineering Geology* 79:215-229.
- Varnes, D. J. 1978. Slope movement types and processes. *Special report* 176:11-33.

5 DISCUSSION

The presented “*Report on evaluation of Mass Movement Indicators*” summarized the state of the art of monitoring parameters related to mass movements with an eye to mid- and short-term landslide forecasting and early warning, and presented the original results of the SafeLand working package 4.3, which we believe “moved the line” of science forward. The main aim was to cover the subject of slope instabilities as complexly as possible to provide necessary information on which parameters could be monitored. Thus, among the others, this study brings information complementary to the report D 4.8 of the SafeLand project entitled “*Guidelines for landslide monitoring and early warning systems in Europe – Design and required technology*”.

The monitoring parameters of landslides are reviewed in Chapter 2. The list of parameters includes basic definitions and formulas, units, typical values and possible applications for landslide monitoring. Each of these contributions is accompanied by a list of essential literature, making it easy for the reader to become oriented in the basic facts and the source data. The parameters are evaluated in Chapter 3 on the basis of a questionnaire study. Their relative abundance within the test sites and their early warning potential were assessed. And last but not least, Chapter 4 illustrated the review of the parameters through a manifold variety of examples from 15 test sites. These test sites represent the most prominent active slope failures throughout Europe monitored by the institutions united in the SafeLand project.

The most important parameters of landslide monitoring and EW were *displacement, velocity* and *acceleration*. Lovisolo reviewed these parameters in Chapter 2.1.1. Displacement can be monitored continuously by various techniques, both in superficial and in-depth conditions. Displacement measured along the vertical profile can be visualized both in differential and in cumulative ways; the cumulative way permits an estimation of the amount of displacements occurring throughout the profile, whereas the differential mode enables the identification of individual sliding surfaces and the most deformed areas. On the other hand, the detection of velocity and acceleration of displacements during monitoring is crucial to optimizing warning and intervention times. Several methods of landslide forecasting are also based on the mass movement velocity. Blikra and Kristensen (Chapter 4.1) compared the reliability of displacement data obtained from different sensors at the Åknes test site. The permanent GPS (GNSS) network has shown to be very robust and reliable, also contributing to near real-time data. The lasers directly measured displacement and thus mass movement, and are important parts of the early warning system due to their frequent measurements across the main back scarp. They noted that setting SMS messages on the laser measurements was a bit difficult, however, as the number of outliers was quite large and they received too many messages from the sensors. On the other hand, the extensometers in comparison with other sensors did not capture the entire movement of the rockslide; they only captured local displacement within the landslide body, and sometimes there were also movements backwards due to back-rotation of individual blocks. The extensometers would most likely supply frequent and reliable information of the movement, unless new crevasses were responsible for most of the movement. The extensometers are only able to expand up to a maximum level and beyond that they would fail, so they are not suited for monitoring the landslide in the latest stages of acceleration. However, the reliability of the sensors makes them very well suited for

automatic messages/alarms. In the case of robotic total stations, they experienced that the measurements were relative depending on the weather conditions and data was usually missing during bad conditions (rain, fog, snow). There were also major problems with ice and snow in the prisms. The other instrument – the crackmeters– only measured displacement across small extensional features and therefore did not capture the total displacement of the landslide. However, the crackmeters have the potential to record spreading activity in smaller cracks, which may be important for the landslide dynamics. Although they record very small amounts of the total movement, they are suited for automatic SMS messages and alarms. Unfortunately they would be difficult to use in the late stages of an event. A similar array of different sensors was presented by Blikra and Kristensen (Chapters 4.8 and 4.9) from other Norwegian test sites: Jettan and Mannen. These authors, however, considered the DMS to be the most effective tool for displacement monitoring as it provides quasi-continuous information of sliding planes in depth. Moreover, the system measures displacement or tilt for every meter, in addition to water pressure and temperature. This argument was proved also by Lovisolo et al. (Chapters 4.6 and 4.10) and Lovisolo in Supper et al. (Chapters 4.3 and 4.4). To complete the review of displacement monitoring instruments applied in the D 4.6 test sites, the GB InSAR and terrestrial laser scanner (TLS) must be mentioned. The high efficiency of the GB InSAR was approved by Agliardi (Chapter 4.11) at the Ruinon rockslide. A displacement time series extracted from GB-InSAR provides a large amount of data even in debris-covered areas. TLS together with optical image correlation techniques and dGPS was presented by Malet et al. (Chapter 4.13) as an effective technique for obtaining spatio-temporal displacement maps (and deformational maps) of entire instabilities. This could avoid misinterpreting or omitting only punctual displacement results from single on-site sensors.

Malet & Traveletti (Chapter 2.1.2) presented that *pre-failure strains* can be potentially useful precursors of main movements. Continuous strain measurements could contribute to understanding the failure mechanism and to the calibration/validation of coupled hydro-mechanical deformation models. Strain could be directly observed by means of “Object oriented analysis” on very high-resolution orthophotographs, by “Optical Fibers” which have the general advantage of being insensitive to electrical disturbances such as lightning, etc. or embedded extensometers installed in a Rosette array (separation in orientation of 120°).

Mass loss/increment balance is a new monitoring parameter proposed by Michoud et al. (Chapter 2.1.3) for landslide EW. This kind of parameter is regularly used for snow avalanches. Yet, three major issues must be overcome to implement it in landslide monitoring: (i) an automatic routine allowing continuous monitoring with a TLS device; (ii) the automation of the estimation of mass balances comparing two point clouds must be available; (iii) threshold values must be estimated with complex models that require a lot of input and a good conceptual model of the landslide to be as reliable as possible for alarms. However, further research is necessary.

Stumpf (Chapter 2.1.4) presented *macro-cracks and surface fissures* as another useful monitoring parameter. The presence and characteristics of surface fissures can be relevant inputs for early warning systems for three reasons: (i) the observation of newly occurring surface fissures is a basic qualitative warning sign which in most cases will raise the alert level and trigger further investigation. Thus, the main challenge is the timely detection of such

fissures that may often become visible only days or even hours before a catastrophic event; (ii) for the monitoring of known fissures, crackmeters (crack-gauges) are valuable instruments for measuring already minimal deformation at the most critical slope sections; (iii) an indirect use of information on the spatial distribution of surface fissures could be a more reliable parameterization of precipitation-based early warning systems, since the presence of fissures will influence the infiltration rate into the landslide body and along potential shear planes. As illustrated by Malet et al. (Chapter 4.13) in an example from the Super-Sauze test site, observations of features and structural patterns of earth surface landforms such as fissures can reveal information on the origin and mechanisms controlling a landslide. A joint interpretation of obtained fissure maps and of a 3D geometrical model of the stable bedrock demonstrated their complementary use for a better understanding of the geomorphological and geomechanical processes. Thereby, the detected fissure pattern may be used for first approximation for mechanical processes in the recent deformation history of a slope.

Micro seismicity/Acoustic emissions are described by Roth & Malet (Chapter 2.1.5) as an important landslide monitoring parameter for EW systems, complementary to directly observable parameters. It can be used to continuously observe the varying dynamic processes during landslide movement, in the pre-failure, failure and post-failure stage according to the case studies. They point out that it is necessary to monitor a site over long-term periods in order to assess the natural variations, to optimize the monitoring parameters and to be able to identify significant changes in seismic activity. They showed some short examples from the Åknes rockslide and the Super-Sauze mudslide. One can observe seismic signals generated by rockfalls (multiple onsets caused by the impact of tumbling rocks) and rockslide micro-events. Despite the lack of brittle material deformation that would generate impulsive fracture release within weak sediments of the Super-Sauze mudslide, it was possible to detect “landquake” events, giving information on the internal dynamics of the mudslide. Blikra & Kristenssen (Chapter 4.1.) presented results of the microseismic monitoring in the Åknes rockslide, conducted by a network comprised of eight 3-component geophones with real-time data transfer and processing. They proved that the microseismic events on the slope were associated with rockfalls, small scale rockslides and the general movement of the entire instability, and acceleration of the slope increased the microseismic activity. The cumulative amplitudes of the events are believed to be associated with an increase in the number and/or magnitude of seismic events. The data very nicely showed the increase of event magnitude during the spring. The implemented seismic system has shown to be robust and of high reliability, giving supplementary important information during increased displacements.

Another precursor of the main movements is *rockfall frequency*, as presented by Agliardi (Chapter 2.1.6), due to rock mass damage and progressive failure. Available information suggests that monitoring rockfall frequency may provide very useful information on the evolution of rock slope failure, but its reliable application as an early warning parameter requires additional research.

Hydrologic properties are those parameters that **directly describe the hydrological conditions** of the subsurface with respect to landslide triggering and reactivation. They are listed in the section 2.2.

Groundwater level and **pore-water pressure** are described by Lam & Heyerdahl (Chapter 2.2.4). These parameters are essential for any landslide monitoring and EW system at a slope scale, because their values, trends and fluctuations could be used as direct input to a slope stability model to assess the temporal frequency of instability. They should be applied in particular to slopes showing signs of distress and prolonged deformation, and exhibiting signs of potentially large-scale failure that is difficult and costly to stabilize. The groundwater level and/or pore-water pressure were monitored at 80% of presented test sites in order to couple them with displacement and other parameters. For more details, see the section below regarding the coupling of parameters.

Soil suction is presented by Cascini et al. (Chapter 2.2.2) as another new promising monitoring parameter of landslides, in which the increased water content causes the decrease of soil suction and, as a consequence, a decrease in shear strength. This reduction of suction values during infiltration may be a significant mechanism for shallow landslides on over-steepened hillslopes or where soils or regolith are underlain by permeable substrates. In both environments, shallow slope failure may occur prior to the formation of positive pore pressures. Whether shallow landslides commonly occur under partially saturated conditions is still controversial, in part because of the lack of instrumental data on the hydrologic conditions within a naturally occurring shallow landslide. Thus, it remains a subject of further research.

The information on the interaction between soil suction and soil humidity, and the role of the **soil humidity** as a potential monitoring parameter of landslides was further developed by Damiano and Picarelli (Chapter 2.2.3). Based on the literature they argued that monitoring of soil volumetric water content seems to be more useful than soil suction monitoring for early warning purposes, since water content grew smoothly during the entire infiltration processes while soil suction showed abrupt steep fronts attaining its final value long before slope failure. In the near future, devices such as TDR probes, which enable complete vertical profiles of the volumetric water content within landslides to be obtained, would represent fundamental tools for the timely alerting of landslide triggering as they capture a significant indicator of impending slope failure which is an important prediction of landslide triggering.

Lam & Heyerdahl (in Chapter 2.2.4) summarized the information on **water balance: inflow and outflow, surface flow**. Water balance is not a landslide indicator itself. However, its role in the early warning of landslides pertains to knowledge of the interaction between various elements of the whole hydrological cycle. The land-based portion of the hydrological cycle, such as *inflow of water* into catchment and landslide-prone areas and *outflow* from the system (e.g. surface flow - runoff and subsurface flow), is of the most interest in terms of the stability of hillsides. Although the entire *water balance* is not constituted as a direct landslide indicator, it may be an indicator of possible debris-flow initiation within a watershed. Such events are strongly connected to water discharge and erosion in channels; hence the hydrologic balance and assessment of resulting discharge may give guidance to early warning for such events. Many empirical models implicitly take this into account, using a long-term component for rainfall coupled with a short-term intense rainfall component as a basis for early warning. Real data on in/outflow were presented by Supper et al. (Chapter 4.7) from an example taken from the Gschlifgraben test site. The results showed the response of the

measured parameter to major rainfall, and the times of increased flow after these events. A comparison of results showed that in springtime, both the upper and lower sensors could detect almost the same flow whereas in the autumn an almost constant shift between both datasets could be recognized. This observation suggested some kind of leakage along the string.

Surface and subsurface water quality is presented by Malet et al. (Chapter 2.2.5) as a new joint hydro(geo)chemical parameter which could be monitored as a possible forerunner of failure or acceleration of active landslides. ‘Water quality’ is a term used to describe the chemical, physical, and biological characteristics of water, usually with respect to its suitability for a particular purpose. In the case of slope hydrology research, the use of water quality is related to the possibility of unravelling the hydrological processes controlling landslide triggering or kinematics. This section (i) *analyzed the impact hydro(geo)chemical processes have on physical properties of the soil material and rock slopes*, i.e. the relation to deformation rate and the relation between pore fluid composition and residual shear strength of soil material; and, (ii) *described the information on subsurface structure and composition*, i.e. on subsurface architecture and the hydrological information on the origin of water, flow paths and travel times (using isotope analyses) for early warning of failures associated with hard-rock and soft-sediment slopes. Hydrochemical information used in both hard and soft rocks enables clusters of water types to be displayed, which is useful for identifying the contribution of different aquifers to the landslide area. Kinetic-based modelling is shown to be very useful in the interpretation of hydro(geo)chemical information.

Ground geophysical properties means those geophysical parameters whose changes indirectly (using model calculations or data inversion) characterise changes in other parameters, in most cases in hydrological properties. These parameters can/could be used to predict the activation of a mass movement and they are listed in section 2.3.

Geoelectrical parameters, such as subsurface electrical resistivity, induced polarization (IP), and self-potential (SP) are presented by Supper et al. (Chapter 2.3.1). Since most of the European landslides are triggered by precipitation and high water content in the subsurface, and the electrical resistivity is mainly determined by the water content of the subsurface, the authors consider temporal changes of **electrical resistivity** to be a promising parameter for the monitoring of landslides. Other geoelectric parameters like **induced polarization** and **self-potential** could definitely have great potential for monitoring, but so far have hardly ever been investigated in detail; the authors describe these parameters and their possible use in landslide monitoring and EW in detail. The geoelectrical parameters were extensively illustrated by Supper et al. (Chapters 4.2, 4.3, 4.4, 4.7 and 4.12) and by Supper in Malet et al. (4.13). A variety of landslide, rainfall and freeze/thaw events, viewed from the perspective of spatiotemporal change of resistivity and self-potential of the subsurface, were presented using examples from the test sites of Ancona, Ampflwang, Bagnaschino, Gschliefgraben, Möltaller Glacier and Super-Sauze. They suggested a very high reliability of those parameters for landslide monitoring and EW. However, the authors stated that further research and technical development is still needed.

Seismic velocity as a possible monitoring parameter of landslides was described by Čarman & Kumelj (Chapter 2.3.2). Since seismic wave velocity reflects the elastic properties

of the medium, which are in turn dependant on water content and porosity among other factors, seismic velocity change may be indicative of change in water content. However, they stated, that geoelectric methods are probably more effective in this respect.

Based on a recent literature search, Baroň (Chapter 2.3.3) listed a new potentially promising monitoring parameter of landslides: *passive (pulse) electromagnetic emissions (PEE)*. When the substrate undergoes a change of strain and displacement within different material blocks, passive electromagnetic radiation occurs. This phenomenon could occur at different scales, from forming of micro-fissures up to dislocations separating major landslide blocks. However, it seems that the PEE measurements are often influenced by electromagnetic noise, especially in densely inhabited areas. This probably makes the acoustic emission a more useful parameter for landslide monitoring than PEE.

Supper (Chapter 2.3.4) described *proton magnetic resonance (PMR)* as another new promising geophysical parameter for landslide monitoring, which directly depends on the quantity of water in the subsurface and which has so far not been used for monitoring purposes. Due to advanced data acquisition technologies, water content (amplitude of signal) as well as hydraulic transmissivity (relaxation time) can be estimated for the model of a horizontally (multi-) layered subsurface. The major disadvantage of MRS is its sensitivity to noise, which is the major problem in inhabited regions of Europe. Another disadvantage is high cost of the equipment and the fact that several technical improvements are necessary to use this method for monitoring purposes.

The external processes that have an effect on the mass movement body and which are able to activate or accelerate it – the **external triggers** – were reviewed as well since they could be monitored in order to predict or just detect the reactivation or critical acceleration of mass movement. *Meteorological conditions* as a general monitoring parameter were reviewed by Mercogliano (Chapter 2.4.1). She presented especially general thresholds for cumulative rainfall and triggering of shallow, intermediate and deep-seated landslides. As presented in Chapter 4, the meteorological monitoring parameters were distinctly the most abundant within the studied test sites. They were monitored at 93 % of the test sites and were mostly used for correlation to other parameters.

Regional seismicity and earthquakes as possible monitoring parameters of landslides were summarized and evaluated by Čarman & Kumelj (Chapter 2.4.2). The earthquake events may affect landslides in a *(i) direct way* (mobilizations of landslides due to shear stress and dynamic loading, and/or landslide mass partial or complete liquefaction in slowly moving landslides or fast-moving debris flows), or an *(ii) indirect way* (changes in the landslide mass that may lead to increased water percolation and eventual activation of the landslide). The latter effect was also documented by Vecchiotti et al. (Chapter 4.3) in the Ancona test site. However, the tectonic earthquakes and their influence on landslides used to be monitored together with the microseismic parameters within the respective slope failures.

Morelli et al. (Chapter 2.4.3) presented a comprehensive review on how *volcanic activity* acts as a regional trigger of landslides. Volcanoes are highly dynamic structures that change their morphology mainly in response to both intrusive and extrusive phenomena. The magma emplacement may, for example, influence the stability of the flanks through the periodic filling and tapping of the magma reservoirs which leads to bulging and contracting cycles.

The emplacement of a magmatic body in the shape of intrusive dome (cryptodome) or minor intrusion along preferential rift zones (dykes) in which elevated pore fluid pressures are mechanically and thermally generated produce a cyclical increase of slope dip that can turn into destabilization and collapse in quite different amounts of time. In fact, a few months may elapse before a significant intrusive event triggers the formation of a landslide (the time varies according to the growth rate), while thousands of years are usually necessary to trigger collapses caused by progressive dyke-induced rifting. Destabilization also results from extrusive activity which may give rise to syn-eruptive (primary) or post eruptive (secondary) mass movements, or mass movements unrelated to eruptions. The review is well supported by essential literature and field examples. Unfortunately, no such test site was monitored and presented within the SafeLand project.

Tides are another factor that was included in the report as a possible landslide monitoring parameter by Zöchbauer (Chapter 2.4.4) but that was unfortunately not illustrated in any test site. The forces, generated from the sun and the moon, are possible factors leading to shear sliding processes, like earthquakes or glacier movements. In particular, the atmospheric tides can be responsible for movements of landslides that are nearly at failure; solid-earth tides are too small to change the stability in this shear sliding process. However, this parameter seems to be far from being a routine method of landslide monitoring and EW.

Single parameters provide information on slope failure behaviour, state and possible triggering, yet the **coupling of different types of parameters** from various sensors gives a much more complex and complete picture of the whole instability, and thus is really essential for effective early warning.

Blikra & Kristensen (Chapter 4.1) have shown the efficiency of coupling between different monitored parameters on an example from the Åknes test site. The parameters included meteorological data (precipitation/snowmelt), different surface displacement data (GPS, total station, laser, extensometers), seismic events (microseismic network), subsurface displacements (DMS column) and water level (piezometers). They noted that the change in alarm levels were always based on data from a combination of sensor types, and included an overall evaluation of the stability. They hierarchized the indicators, grouping them under “primary” or “supplementary” by their importance.

Primary indicators:

- **Surface displacements** (velocity and acceleration): GPS, total station, extensometers, lasers, crackmeters
- **Subsurface displacements**: DMS columns (inclinometers)

Supplementary indicators:

- **Water level**: piezometers in DMS column
- **Precipitation and snowmelt**: meteorological station
- **Seismic events**: seismograph and a microseismic network

They concluded that velocity thresholds for defining the alarm levels were different from instrument to instrument, and also differed according to the time period over which the data had been evaluated. Extensometer data over a period as short as one hour could serve as the

basis for a warning, whereas data from the total station and GPS were assessed over a longer period due to larger fluctuations and noise. Therefore they considered information coupled from different sensors to be the most reliable and important for evaluating alarm levels.

Agliardi et al (Chapter 4.11) approved the importance of monitoring the whole instability by means of not only the punctual information. They successfully applied GB-InSAR, which provided a large amount of data even from debris-covered areas of the Ruinon rockslide where ground-based instrumentation failed. Such spatially-distributed, improved information, validated by selected ground-based measurements, allowed for the establishment of new velocity and displacement thresholds for early warning purposes.

An approach of impending failure prediction presented by Lovisolo et al. (Chapters 4.6 and 4.10) and Lovisolo in Supper et al. (Chapters 4.3 and 4.4) is based on the coupling of very precise in-depth displacement velocity and groundwater level (GWL) fluctuations recorded by a multi-sensor “Differential Monitoring of Stability” system (DMS). Based on the real field data, they documented several cases of a distinct rise of GWL several hours prior to landslides’ re-activation, thus proving the high reliability of coupling GWL with high-accuracy displacement monitoring for short landslide forecasting and early warning. In agreement, Moya and Gili (Chapter 4.14) observed that data on the groundwater level recorded in boreholes practically immediately responded to rainfall episodes and subsequent landslide displacement. This allowed the simulation of landslide displacements and velocities from piezometric data. The good fit of the simulated values to the measured data indicated that groundwater level can reliably be used to predict the displacements of the landslide.

Also Malet et al. (Chapter 4.15) coupled several monitoring parameters at the Villerville test site in order to specify: 1) the slope kinematics, 2) the relationship between rainfall, groundwater level and velocity, 3) the temporal evolution of the different landslide sectors/areas. To establish a near real-time warning system, the monitoring network should be based on a combination of data collection on the triggering factors and on the slope response in kinematic terms.

The importance of coupling geoelectric parameters, such as self-potential and resistivity, with other parameters was exemplified by Supper et al. (Chapters 4.2, 4.3, 4.4, 4.7 and 4.12) and by Supper in Malet et al. (4.13). To understand the role of those geoelectric parameters for landslide monitoring and EW, one must correlate them with precise in-depth mass movement displacement and with the subsurface physical conditions (such as the temperature of the substrate and water content or groundwater level, respectively). The coupling with other external factors such as precipitation or snow melting, which act indirectly, would be important as well especially for setting up the thresholds.

Crosta et al. (Chapter 4.5) presented another approach: coupling the real monitoring data with the modelled ones. The motion on the Bindo-Cortenova slope during the 2005-2009 period has been modelled numerically by means of a 1D pseudo-dynamic visco-plastic method, based on Perzyna's theory. The viscous nucleus in the 1D block model has been assumed to be linear or non-linear and the parameters were calibrated and compared to laboratory determined properties. Geo-mechanical, geo-morphologic and piezometric data have been used as input data. Ground-based displacements have been used to calibrate and validate the model on a long temporal series (2004-2010), and this demonstrated the high reliability of coupling numerical models with real monitoring data for EW.

By our knowledge, the analyzed data from these test sites brought forward the most complex and comprehensive study on landslide monitoring parameters yet. Yet, two main problems were encountered within this work package 4.3.

The project duration was only three years. To obtain meaningful results, data from several triggering events must be observed. Of course, such events cannot be predicted in the long term. Therefore, test sites had to be selected on their history and for having sufficient data for interpretation; in many cases, sites were chosen that had a long series of monitoring data already available. Unfortunately, on some sites no triggering events took place over the duration of the project (e.g. test site Gschlifgraben).

Secondly, financial support for test site equipment was limited. Therefore only some sites could be newly set up (e.g., Ampflwang, Gschlifgraben), and additional innovative equipment was added to already-equipped sites (e.g., Ancona, Bagnaschino, Super-Sauze). In several cases, additional financial support from other projects was given to support the field activities. The focus on evaluation, application and development of innovative technologies was mainly placed on DMS, GB InSAR and geoelectrical monitoring. Significant advances could be reached for mass movement monitoring with these technologies. The detailed results were already described above. To summarize, the following main conclusions could be derived:

- Almost all of the observed events were triggered by precipitation. Consequently, rainfall thresholds seem to be one of the most important early warning parameters. However, in many cases thresholds were found to be variable and in some cases were found to depend on the pre-conditioning of the subsurface (e.g. pre-wetting due to snowmelt). In some cases this pre-conditioning could be monitored (e.g. by geoelectrics), however more research on these relations must still be performed in future to derive unique warning levels.
- To allow detailed interpretation of the results and to establish correlations, a high data sampling interval is a necessity. The minimum value was found to be one hour, but if detailed correlations require investigation, we suggest an interval of ten minutes.
- Displacement, especially measured with the DMS system, proved to be the most reliable parameter for early warning purposes. The technology is mature and reliable. GB InSAR proved to be the technology of choice, especially for monitoring large mass movements with high rates of displacement. However, several developments must still occur to use this method as an early warning system. In any case, we see a high future potential for this method due to the fact that the whole landslide body can be monitored at the same time.
- For the first time, geoelectrical monitoring was applied at several sites simultaneously. It proved to be reliable as a measuring technology, however the potential of this method was not found to be as an early warning system, but rather as a method for investigating the processes leading to the triggering of a landslide or evaluating the scale of an event (e.g. test site Bagnaschino) once it occurred. Since only two real triggering events (at Bagnaschino and Ampflwang) could be monitored with this method so far, longer observation periods are necessary to derive the final concluding results.

- Actual early warning thresholds could only be derived at some sites. Consequently, future studies must be focused on this topic, and the SafeLand project results will provide a sound basis for this future research. Many more triggering events must be analyzed, which will require several long-term monitoring projects on several mass movements in different geological backgrounds. Therefore, we hope that the international initiatives that began at various sites within the SafeLand project will be continued. Only then will real progress be possible in future.

The editors of this report appreciate each author's efforts towards such a comprehensive and complex project, and believe that the report will substantially contribute to more effective landslide monitoring and early warning in order to save human lives and property.

6 CONCLUSIONS

The *Report on evaluation of Mass Movement Indicators* summarized the state of the art of monitoring parameters related to mass movements, and presented the original results from the test sites of the SafeLand project - working package 4.3, moving the horizon of the science a bit further. Based on the results achieved and presented, we can state that:

- Despite the financial and time constraints, the report seems to be one of the most complex and comprehensive studies on landslide monitoring parameters yet;
- Almost all of the observed events were triggered by precipitation;
- The most important parameters of the landslide monitoring and EW were evaluated *displacement, velocity* and *acceleration*; velocity thresholds for defining the alarm levels, however, differ from instrument to instrument, and differ according to the time period over which the data are evaluated (stage of evolution of the landslides);
- Other essential parameters for landslide EW are *precipitation, ground-water level fluctuations, pore-water pressure* and *micro seismicity / acoustic emissions*;
- New promising parameters for landslide monitoring and EW were presented, such as: *pre-failure strains, mass loss/increment balance, macro-cracks and surface fissures, rockfall frequency, soil suction, surface and subsurface water quality, electrical resistivity, induced polarization* and *self-potential, passive (pulse) electromagnetic emissions*, and external triggers, like *tides, regional seismicity and earthquakes, and volcanic activity*; they should be, however, subject of further research. Other parameters to be described in the report were evaluated of less importance;
- Single parameters give various information on slope failure behaviour, state and possible triggering; however **coupling of different types of parameters** from various sensors gives much more complex and complete picture of the whole instability and thus is really essential for effective early warning;
- To allow detailed interpretation of the results and to establish correlations, a high sampling interval of the data is necessary. The minimum value was found to be one hour, however if detailed correlations need to be investigated, we suggest an interval of ten minutes depending on the assumed velocity of the mass movement;
- The results from the SafeLand project provide a sound basis for future research of early warning parameters and thresholds. However, many more triggering events need to be analyzed, which requires several long term monitoring projects on several mass movements in different geological settings. Therefore we hope that the international initiatives started within SafeLand at several site will be continued. Only then real progress will be possible in future.